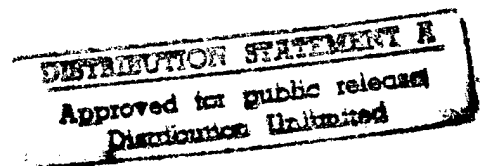# Materials Degradation and Fatigue
In Aerospace Structures

AFOSR University Research Initiative on Aging Aircraft
Schools of Engineering and Science, Purdue University

Final Report

for

Air Force Office of Scientific Research

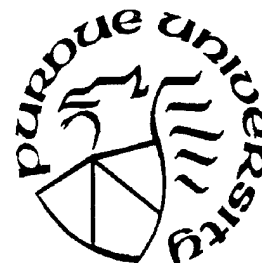Grant Number F49620-93-1-0377

prepared by

A. F. Grandt, Jr.

August 1997

19971006 006

School of Aeronautics and Astronautics
1282 Grissom Hall
Purdue University
W. Lafayette, IN 47907-1282
Telephone: (765) 494-5117
Fax: (765) 494-0307

REPORT DOCUMENTATION PAGE

Public reporting burden for this collection of information is estimated to average 1 hour per response, including the time for reviewing instructions, searching existing data sources, gathering and maintaining the data needed, and completing and reviewing the collection of information. Send comments regarding this burden estimate or any other aspect of this collection of information, including suggestions for reducing this burden, to Washington Headquarters Services, Directorate for Information Operations and Reports, 1215 Jefferson Davis Highway, Suite 1204, Arlington, VA 22202-4302, and to the Office of Management and Budget, Paperwork Reduction Project (0704-0188), Washington, DC 20503.

1. AGENCY USE ONLY *(Leave blank)*	2. REPORT DATE	3. REPORT TYPE AND DATES COVERED
	August 1997	Final Technical Report 1 Jul 93 to 30 Jun 97

4. TITLE AND SUBTITLE
Materials Degradation and Fatique in Aerospace Structures

5. FUNDING NUMBERS
F49620-93-1-0377

6. AUTHOR(S)
A. F. Grandt, Jr.

7. PERFORMING ORGANIZATION NAME(S) AND ADDRESS(ES)
School of Aerospace of Aeronuatics and Astronuatics
Purdue University
128 Grisson Hall
W. Lafayette, IN 47907-1282

8. PERFORMING ORGANIZATION REPORT NUMBER

9. SPONSORING/MONITORING AGENCY NAME(S) AND ADDRESS(ES)
AFOSR/NA
110 Duncan Ave, Suite B115
Bolling AFB, DC 20332-8050

10. SPONSORING/MONITORING AGENCY REPORT NUMBER
F49620-93-1-0377

11. SUPPLEMENTARY NOTES

12a. DISTRIBUTION AVAILABILITY STATEMENT
Approved for Public Release, Distribution Unlimited.

12b. DISTRIBUTION CODE

13. ABSTRACT *(Maximum 200 words)*

This report summarizes research conducted by the Purdue University Schools of Engineering and Science during a four-year AFOSR University Research Initiative focused on basic issues dealing with aging aircraft. The coordinated goals of the program fall into four main categories: damage development, prediction of crack growth and interaction, failure prevention techniques, and advanced analysis methods. The damage development goals addressed the failure mechanisms of corrosion, fatigue crack formation, and fretting. The general objective of the crack growth and interaction tasks was to develop techniques to predict the growth of service induced cracks and to determine the impact of widespread cracking on damage tolerance. The theme of the failure prevention projects was to develop procedures to extend the operational life of "older" aircraft by delaying service induced damage, repairing cracked structure, and employing fleet tracking methods to prioritize maintenance actions within a fleet of aircraft. Finally, research was directed at developing "advanced" analysis methods used in other research tasks. These projects dealt with adding statistical components to various materials evaluations and structural analyses, and developing ductile fracture criteria relative to aircraft materials and structures.

14. SUBJECT TERMS

15. NUMBER OF PAGES

16. PRICE CODE

17. SECURITY CLASSIFICATION OF REPORT	18. SECURITY CLASSIFICATION OF THIS PAGE	19. SECURITY CLASSIFICATION OF ABSTRACT	20. LIMITATION OF ABSTRACT
Unclassified	Unclassifie	Unclassified	UL

DTIC QUALITY INSPECTED 3

Materials Degradation and Fatigue
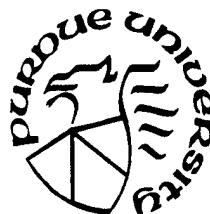# In Aerospace Structures

AFOSR University Research Initiative on Aging Aircraft
Schools of Engineering and Science, Purdue University

Final Report

for

Air Force Office of Scientific Research

Grant Number F49620-93-1-0377

prepared by

A. F. Grandt, Jr.

August 1997

School of Aeronautics and Astronautics
1282 Grissom Hall
Purdue University
W. Lafayette, IN 47907-1282
Telephone: (765) 494-5117
Fax: 765 494-0307

Table of Contents

FOREWORD

This is the final report of research conducted on Air Force Office of Scientific Research Grant No. F49620-93-1-0377, "Materials Degradation and Fatigue of Aerospace Structures." This four-year grant began on July 1, 1993, and was concluded on June 30, 1997. It was part of the AFOSR University Research Initiative (URI) in Aging Aircraft. Prof. A. F. Grandt, Jr. from the Purdue School of Aeronautics and Astronautics was the Principal Investigator, and Dr. Walter F. Jones was the AFOSR program manager. Other Purdue University investigators include: Profs. T. N. Farris, B. M. Hillberry, E. P. Kvam, G. P. McCabe, and C. T. Sun. These faculty were assisted by a team of undergraduate and graduate students from the Purdue Schools of Engineering and Science.

1.   EXECUTIVE SUMMARY

The Purdue University Schools of Engineering and Science have formed an interdisciplinary team of materials scientists, structural engineers, and statisticians to address basic research issues associated with aging aircraft. The effort was supported by an AFOSR University Research Initiative for the period July 1, 1993 to June 30, 1997. This research grant has resulted in over 75 journal or conference papers and reports, along with 18 M. S. or Ph.D. theses. The coordinated goals of the research program fall into four main categories: damage development, prediction of crack growth and interaction, failure prevention techniques, and advanced analysis methods.

The thrust of the damage development goals was to determine a fundamental understanding of how service induced damage develops in older aircraft. The failure mechanisms of corrosion, fatigue crack formation, and fretting were addressed with a series of interrelated projects coordinated by graduate research assistants. These projects dealt with understanding how cracks form at inclusions or corrosion damage, quantifying the influence of corrosion on the remaining fatigue life of a structure, and with fretting fatigue as a mechanism for crack development.

The general objective of the crack growth and interaction task was to develop techniques to predict the growth of service induced cracks and to determine the impact of widespread cracking on damage tolerance. These projects involved testing specimens from retired aircraft components to determine if the fatigue crack growth resistance of "aged" material has degraded with service usage, and determining the influence of multiple site damage (MSD) on damage tolerance and fatigue life.

The general theme of the failure prevention projects was to develop procedures to extend the operational life of "older" aircraft by delaying service induced damage, repairing cracked structure, and employing fleet tracking methods to prioritize maintenance actions within a fleet of aircraft. Projects in this task dealt with developing adhesively bonded composite patches to repair cracks in metal structure, examining the ability of corrosion prevention compounds to improve the stress corrosion cracking resistance of aluminum alloys, and determining methods to monitor aircraft usage with respect to their potential for developing corrosion or fatigue damage during service.

Finally, research was directed at developing "advanced" analysis methods used in other research tasks. These projects dealt with adding statistical components to various materials evaluations and structural analyses, and developing ductile fracture criteria relative to aircraft materials and structures.

2.0 INTRODUCTION

2.1 Background

The growing ages of the nation's commercial and military aircraft fleets, combined with their large replacement costs, pose significant challenges to those responsible for providing reliable and safe air operations in an era of fiscal constraint. The situation is complicated by an uncertain economic future that requires attention to maintaining many present aircraft beyond their original design or economic lifetimes.

While there are many economic and public policy matters involved with the aging aircraft topic, fatigue and material degradation due to corrosion are two of the more important technical issues limiting the design, maintenance, and operation of long life aircraft. Although these issues have been successfully approached in the past through detailed damage tolerance design and durability methods, the special requirements of the aging aircraft problem highlight the need for additional research, and for new approaches for treating the detrimental effects of fatigue and corrosion.

The objective of the Purdue Aging Aircraft Program is to solve fundamental problems, which presently limit the safe operation of aircraft beyond their original design or current economic lifetimes. The general objectives are summarized as follows.

- Characterization of initial and service induced damage and mechanisms that lead to crack formation through corrosion, fatigue, and fretting at joints.

- Determination of how cracks, once formed, grow through corrosion and fatigue, with emphasis on the development of crack interaction and fracture criteria for multiple-site-damage.

- Development and assessment of failure prevention tools such as bonded composite patches, corrosion prevention compounds, and simple structural monitoring techniques to identify individual aircraft for further inspection and/or maintenance actions.

- Development of advanced methods for stochastic risk analysis and for crack growth analysis in ductile materials.

2.2 Research Personnel

The research program was conducted by an interdisciplinary team of six faculty aided by graduate and undergraduate students from the Purdue University Schools of Aeronautics and Astronautics, Materials Engineering, Mechanical Engineering, and Department of Statistics. The faculty and students involved in this effort during the 1996-97 fiscal year are summarized below. Participants in other years were identified in prior annual reports.

2.2.1 Faculty

Alten F. (Skip) Grandt, Jr. (Principal Investigator) Professor, School of Aeronautics and Astronautics, 1282 Grissom Hall, Purdue University, West Lafayette, IN 47907-1282, Tel: (765) 494-5141, Fax: (765) 494-0307, e-mail: grandt@ecn.purdue.edu. **Topics:** fatigue, fracture mechanics, multiple-site damage, residual strength, corrosion.

Thomas N. Farris, Professor, School of Aeronautics and Astronautics, 1282 Grissom Hall, Purdue University, West Lafayette, IN 47907-1282, Tel: (765) 494-5134, Fax: (765) 494-0307, e-mail: farrist@ecn.purdue.edu. **Topics:** tribiology, fretting fatigue, fracture mechanics, boundary elements.

Ben M. Hillberry, Professor, School of Mechanical Engineering, 1288 Mechanical Engineering Building, Purdue University, West Lafayette, IN 47907-1288, Tel: (765) 494-5721, Fax: (765) 494-0539, email: hillberr@ecn.purdue.edu. **Topics:** fatigue, fracture, crack formation, statistical and probabilistic modeling.

Eric P. Kvam, Associate Professor, School of Materials Engineering, 1289 MSEE Building, Purdue University, West Lafayette, IN 47907-1289, Tel: (765) 494-4097, Fax: (765) 494-1204, e-mail: kvam@ecn.purdue.edu. **Topics:** materials characterization, microscopy, corrosion.

George P. McCabe, Professor, Department of Statistics, 1399 Mathematics Building, Purdue University, West Lafayette, IN 47907-1399, Tel: (765) 494-6047, Fax: (765) 494-0558, e-mail: mccabe@vm.cc.purdue.edu. **Topics:** statistics, design of experiments, reliability.

C. T. Sun, Neil A. Armstrong Distinguished Professor, School of Aeronautics and Astronautics, 1282 Grissom Hall, Purdue University, West Lafayette, IN 47907-1282, Tel: (765) 494-5130, Fax: (765) 494-0307, e-mail: sun@ecn.purdue.edu. **Topics:** composite materials, fracture mechanics, smart materials and structures.

2.2.2 Students

The following graduate students were involved in the research during the 1996-97 final year. Students indicated by an asterisk (*) made substantial contributions to the URI objectives, but were not financially supported by the AFOSR grant. Several other students also received supplemental funding from fellowships and other department sources, effectively leveraging AFOSR support on the project.

School of Aeronautics and Astronautics

Matthew Gates, Pat Golden*, Ganapathy Harish, Markus Heinimann, John Klug, Scott Maley, Pamela McVeigh, Jason Scheuring, Darren Sexton*, Xu-Ming Su, Matthew Szolwinski, Hsing Wang

School of Materials Engineering

Lisa Schild

School of Mechanical Engineering

Beth DeBartolo, Karl Gruenberg, Ben Knight, Monty Moshier, John Zamber

Department of Statistics

Zugheng Jin, Cheng Yu Sun*

3.0 ACCOMPLISHMENTS

3.1 Introduction

This chapter summarizes the publications and other accomplishments resulting from the research on the AFOSR University Research Initiative on Aging Aircraft. Since detailed descriptions of project goals and approaches have been described in prior annual reports, this section focuses on summarizing publications and presentations prepared during the 1996-97 fiscal year.

3.2 List of Publications and Presentations

Year 4

The following papers and presentations resulted from the July 1, 1996 to June 30, 1997 period. Papers indicated by * are reprinted in Appendix A of this report.

*1. J. N. Scheuring and A. F. Grandt, Jr., "Mechanical Properties of Aircraft Materials Subjected to Long Periods of Service Usage," *Journal of Engineering Materials and Technology* (1997).

*2 J. H. Elsner, E. P. Kvam, and A. F. Grandt, Jr., "Modeling and Microstructure Analysis of Fatigue Initiation Life Extension by Reductions in Microporosity," *Metallurgical and Materials Transactions A, Volume 28A,* May 1997, pp. 1157-1167.

*3 I. A. Golinkin, D. D. Ruff, W. P. Kvam, G. P. McCabe, and A. F. Grandt, Jr., "Applications of Analysis of Variance (ANOVA) Statistical Methods to Braking Load Corrosion Test," *Journal of Testing and Evaluation* (1997).

*4 M. C. Cherry, S. Mall, M. B. Heinimann, and A. F. Grandt, Jr., "Residual Strength of Unstiffened Aluminum Panels with Multiple Site Damage," *Engineering Fracture Mechanics* (1997).

*5 M. B. Heinimann and A. F. Grandt, Jr., "Analysis of Stiffened Panels with Multiple Site Damage," Proc. of the 1996 USAF Structural Integrity Program Conference (December 3-5, 1996, San Antonio, Texas), WL-TR-97-4055, Volume II, June 1997, Materials Directorate, Wright Laboratory, Air Force Material Command, Wright-Patterson AFB, OH 45433-7734, pp. 655-682.

*6 M. D. Gates and A. F. Grandt, Jr., "Crack Gage Approach to Monitoring Fatigue Damage Potential in Aircraft," 1997 Society for Experimental Mechanics Spring Conference on Experimental and Applied Mechanics, June 2-4, 1997, Bellevue, Washington.

*7   A. F. Grandt, Jr., T. N. Farris and B. M. Hillberry, "Analysis of the Formation and Propagation of Widespread Fatigue Damage," Proc ICAF: *Fatigue in New and Aging Aircraft, Ed P. Poole and R. Cook, Scotland, June 1997, In-Press.*

*8   A. F. Grandt, Jr., D. Sexton, P. Golden, G. H. Bray, R. J. Bucci, and M. Kulak, "A Comparison of 2024-T3 and 2524-T3 Aluminum Alloys Under Widespread Damage Scenarios," *Fatigue in New and Aging Aircraft, Ed P. Poole and R. Cook, Scotland, June 1997, In-Press.*

*9   M. P. Heinimann and A. F. Grandt, Jr., "Fatigue Analysis of Stiffened Panels with Multiple Site Damage," The First Joint DoD/FAA/NASA Conference on Aging Aircraft, Ogden, Utah, 8-10 July 1997.

10   G. Harish, M. P. Szolwinski, and T. N. Farris, "Finite Element Modeling of Rivet Installation and Riveted Joints for the Prediction of Fretting Crack Nucleation," The First Joint DoD/FAA/NASA Conference on Aging Aircraft, Ogden, Utah, 8-10 July 1997.

*11   M. P. Szolwinski, G. Harish, T. N. Farris, and T. Sakagami, "An Experimental Study of Fretting Crack Nucleation in Airframe Alloys: A Life Prediction and Maintenance Perspective," The First Joint DoD/FAA/NASA Conference on Aging Aircraft, Ogden, Utah, 8-10 July 1997.

12.   M. P. Szolwinski, and T. N. Farris, "Mechanics of Fretting Fatigue Crack Formation," *Wear*, 198 pp. 93-107 (1996).

13   P. A. McVeigh and T. N. Farris, "Finite Element Analysis of Fretting Stresses," *ASME Journal of Tribology*, In-Press.

14   G. Harish, T. N. Farris, "3D Modeling of Skin/Rivet Contact," AIAA Journal, Submitted.

15   T. N. Farris, A. F. Grandt, Jr., G. Harish, P. A. McVeigh, M. P. Szolwinski, and H. S. Wang, "Fretting Fatigue Crack Nucleation and Propagation in Structural Joints," *Proc. Air Force 4th Aging Aircraft Conference*, Colorado Springs, July 1996, In-Press.

*16   M. P. Szolwinski, G. Harish, P. A. McVeigh, and T. N. Farris, "The Role of Fretting Crack Nucleation in the Onset of WFD: Analysis and Experiments," *Proc. FAA-NASA Symp. On Continued Airworthiness of Aircraft Structures*, Atlanta, August 1996, In-Press.

*17   G. .Harish and T. N. Farris, "Modeling of Skin/Rivet Contact: Application to Fretting Fatigue," *Proc. 38th AIAA/ASME/ASCE/ASC Structures, Structural Dynamics, and Materials Conf.*, Kissimmee, FL, April 1997, pp. 2761-2771.

18   B. M. Hillberry, S. M. Rohrbaugh. P. J. Laz, and E. A. DeBartolo, "Total Fatigue Life Prediction Model: A MSD Application," *Proc. USAF Fourth Aging Aircraft Conference*, Colorado Springs, July 1996. In-Press.

19   B. M. Hillberry, P. J. Laz, E. A. DeBartolo, and S. M. Rohrbaugh, "Total Fatigue Life Prediction Model: What We Have Learned," FAA/USAF Workshop on the Application of Probabilistic Methods to Gas Turbine Engines, Fairborn, Ohio, 3-9 October 1996.

20   B. M. Hillberry, "A Probabilistic Fatigue Analysis of Multiple Site Damage in Aircraft," presented at Ohio State University, 10 October 1996.

*21   P. J. Laz and B. M. Hillberry, "Fatigue Life Prediction for Crack Formation at Inclusions in 2024-T3 Aluminum," accepted for publication by the *International Journal of Fatigue*.

22   X. M. Su and C. T. Sun, "A Plane Strain Core Model for Crack Growth in Ductile Materials," Proceedings of the ASME Aerospace Division, AD-Vol. 5, 1996, pp. 217-226.

*23   C. T. Sun and X. Su, "Effect of Crack Interactions on Ductile Fracture," Proc. FAA/NASA Symposium on Continued Airworthiness of Aircraft Structures," Atlanta, August 1996, In-Press.

24   X. M. Su and C. T. Sun, "3-D Singular Stress in a Cracked Plate," Proc. 9th International Conf. On Fracture, April 1-5, 1997, Sydney, Australia.

*25   J. Klug, S. Maley, and C. T. Sun, "Characterization of Fracture and Fatigue Behavior of Bonded Composite Repairs," The First Joint DoD/FAA/NASA Conference on Aging Aircraft, Ogden, Utah, 8-10 July 1997.

26   J. C. Klug, S. Maley, and C. T. Sun, "Analysis of Cracked Aluminum Plates Repaired with Bonded Composite Patches," Proc. USAF 4th Aging Aircraft Conf., Colorado Springs, July 1996, In-Press.

*27   J. C. Klug and C. T. Sun, "Large Deflection Effects of Cracked Aluminum Plates Repaired with Bonded Composite Patches," submitted to *Journal of Composite Structures*.

Year 3

        The following papers and presentations resulted from the July 1, 1995 to June 30, 1996 period.

1   B. M. Hillberry, A. F. Grandt, Jr., T. N. Farris, and G. P. McCabe, "Widespread Fatigue Analysis of Aircraft Structures," Proc. Air Force 3rd Aging Aircraft Conference, Wright-Patterson AFB, Ohio, 26-28 September 1995.

2   A. F. Grandt, Jr., B. M. Hillberry, E. P. Kvam, G. P. McCabe, J. N. Scheuring, and I. Golinkin, "Evaluating the Effects of Corrosion on Structural Fatigue Life," Proc. Air Force 3rd Aging Aircraft Conference, Wright-Patterson AFB, Ohio, 26-28 September 1995.

3   C. T. Sun, J. C. Klug, and M. R. Lena, "Debonding and Thermal Residual Stress Effects on Bonded Composite Patch Repair," Proc. Air Force 3rd Aging Aircraft Conference. Wright-Patterson AFB, Ohio, 26-28 September 1995.

4   X. M. Su and C. T. Sun, "A Ductile Fracture Criterion Derived From Numerical Simulations," Proceedings of the 24th Midwestern Mechanics Conference, 1-4 October 1995, Ames, Iowa.

5   P. J. Laz and B. M. Hillberry, "A Probabilistic Approach to the Generation of EIFS Distributions Derived from Inclusion Characteristics," Structural Integrity in Aging Aircraft, Eds. C. I. Cheng and C. T. Sun, AD-Vol. 47, ASME 1995 International Mechanical Engineering Congress and Exposition, San Francisco, November 1995, pp. 81-85.

6   J. N. Scheuring and A. F. Grandt, Jr., "An Evaluation of Aging Aircraft Material Properties," Structural Integrity in Aging Aircraft, AD-Vol. 47, ASME, Eds. C. I. Chang and C. T. Sun, 1995 International Mechanical Engineering Congress & Exposition, San Francisco, CA, November 1995, pages 99-110.

7   M. P. Szolwinski and T. N. Farris, "Mechanics of Fretting Fatigue Crack Formation," Structural Integrity in Aging Aircraft, Eds. C. I. Cheng and C. T. Sun, AD-Vol. 47, ASME, 1995 International Mechanical Engineering Congress and Exposition, San Francisco, CA, November 1995, pp. 141-157. Also to appear in Wear.

8   B. M. Hillberry and P. J. Laz, "Probabilistic Model for Fatigue Life Prediction Due to Cracks Forming at Inclusions," Application of Probabilistic Design Methodologies to Gas Turbine Rotating Components," Federal Aviation Administration and Air Force Wright Laboratory Workshop, Atlantic City, N. J., November 1995.

9   M. R. Lena and C. T. Sun, "Use of Composite Patches as Reinforcements and Crack Arrestors in Aircraft Structures," in Structural Integrity in Aging Aircraft, AD-Vol. 47, ASME, C. I Chang and C. T. Sun, Eds., Proc. of 1995 International Mechanical Engineering Congress and Exposition, San Francisco, CA, 12-17 November 1995.

10   P. J. Laz, S. M. Rohrbaugh, and B. M. Hillberry, "A Probabilistic Model for Predicting Fatigue Life for Crack Nucleation at Inclusions Using FASTRAN," Proceedings of 1995 USAF Structural Integrity Program Conference, San

Antonio, Texas, November 1995.

11   H. L. Wang, K. Buhler and A. F. Grandt, Jr., "Evaluation of Multiple Site Damage in Lap Joint Specimens," Proc. of 1995 USAF Structural Integrity Program Conference, San Antonio, Texas, November 28-30, 1995.

12   M. P. Szolwinski, G. Harish, and T. N. Farris, "Experimental Observations of the Effect of Contact Parameters on Fretting Fatigue Crack Nucleation," Proc. of 1995 USAF Structural Integrity Program Conference, San Antonio, Texas, November 1995.

13   C. T. Sun, J. C. Klug, and C. Arendt, "Analysis of Cracked Aluminum Plates Repaired With Bonded Composite Plates," AIAA Journal, Vol. 34, No. 2, February 1996, pp. 369-374.

14   I. A. Golinkin, E. P. Kvam, D. D. Ruff, G. P. McCabe, and A. F. Grandt, Jr., "Application of the Breaking Load Test to Evaluating Effectiveness of Fluid Film Corrosion Preventative Compound of Stress Corrosion Resistance of Aluminum Alloy 2024-T351," Technical Report, prepared for Eureka Chemical Company, February 1996.

15   T. N. Farris, A. F. Grandt, Jr., G. Harish, and H. L. Wang, "Analysis of Widespread Fatigue Damage in Structural Joints," Proc. of 41st International SAMPE Symposium and Exhibition, Anaheim, California, March 24-28, 1996, pp. 65-79.

16   P. J. Laz and B. M. Hillberry, "The Role of Inclusions in Fatigue Crack Formation in Aluminum in 2024-T3," G. Lutjering and H. Nowack, Eds., Proceedings, Sixth International Fatigue Congress, Vol. 2, p. 1293-1299, Berlin, May 1996.

17   E. A. DeBartolo, P. J. Laz and B. M. Hillberry, "A Model for Probabilistic Crack Growth to Account for Crack Coalescence," G. Lutjering and H. Nowack, Eds., Proceedings, Sixth International Fatigue Congress, Vol. 2, p. 1311-1319, Berlin, May 1996.

18   J. C. Klug and C. T. Sun, "Large Deflection Effects of Cracked Aluminum Plates Repaired with Bonded Composite Patches," Proceedings of the First International Conference on Composite Science and Technology, 18-20 June 1996, Dunban, South Africa.

19   P. A. McVeigh and T. N. Farris, "Finite Element Analysis of Fretting Stresses," submitted to *ASME Journal of Tribology*.

20   J. N. Scheuring and A. F. Grandt, Jr., "Mechanical Properties of Aged Aircraft Material Subjected to Service Usage," submitted to the *Journal of Engineering*

Materials and Technology.

21   J. H. Elsner, E. P. Kvam, and A. F. Grandt, Jr., "Microstructure Analysis of Fatigue Initiation Life Extension by Reductions in Microporosity," submitted to *Metallurgical and Materials Transactions, A.*

22   I. A. Golinkin, D. D. Ruff, W. P. Kvam, G. P. McCabe, and A. F. Grandt, Jr., "Applications of Analysis of Variance (ANOVA) Statistical Methods to Breaking Load Corrosion Test," submitted to *Journal of Testing and Evaluation.*

23   J. H. Elsner, E. P. Kvam, and A. F. Grandt, Jr., "Fracture Mechanics Analysis of Small Crack Growth and Fatigue Initiation Life Extension by Reductions in Microporosity," submitted to *Fatigue and Fracture of Engineering Materials and Structures.*

24   X. M. Su and C. T. Sun, "On Singular Stress At the Crack Tip of a Thick Plate Under In-Plane Loading," to appear in the *International Journal of Fracture.*

25   J. H. Barker, and T. D. Wade, "Aircraft Corrosion Monitoring," *The Coast Guard Engineer's Digest*, Vol. 33, No. 263, Fall 1995, pp. 27-40.

Year 2

The following papers and presentations resulted from the second year's research (July 1, 1994 to June 30, 1995).

1. K. Buhler and A. F. Grandt, Jr., "Analysis of Multiple Site Damage With Implications for Nondestructive Evaluation," *Twenty-first Annual Review of Progress in Quantitative NDE, Snowmass Village, CO, July 31-August 5, 1994.*

2. A. F. Grandt, Jr., "Assessing the Influence of Corrosion and Multiple-Site Damage on Fatigue Life," *Corrosion, Tribology, Lubrication and Materials Fatigue Under Extreme Conditions,* AFOSR/URI Meeting, University of Illinois, Urbana, Illinois, August 17-18, 1994 (presentation only).

3. T. N. Farris, "Mechanics of Fretting Fatigue," *Corrosion, Tribology, Lubrication and Materials Fatigue Under Extreme Conditions,* AFOSR/URI Meeting, University of Illinois, Urbana, Illinois, August 17-18, 1994 (presentation only).

4. T. L. Weng and C. T. Sun, "A Global-Local Fracture Criterion for Ductile Materials," *1994 USAF Structural Integrity Program Conference,* San Antonio, TEXAS, December 6-8, 1994.

5. J. N. Scheuring and A. F. Grandt, Jr. "An Evaluation of Fatigue Properties of Aging Aircraft Materials," *1994 USAF Structural Integrity Program Conference,* San Antonio, TEXAS, December 6-8, 1994.

6. A. F. Grandt, Jr., "Evaluation of Aged Aircraft Materials," *Corrosion/Fatigue Program Planning Meeting,* Wright-Patterson AFB, Ohio, February 8, 1995 (presentation only).

7. B. M. Hillberry, "A Probabilistic Fatigue Model," *Corrosion/Fatigue Program Planning Meeting,* Wright-Patterson AFB, Ohio, February 8, 1995 (presentation only).

8. A. F. Grandt, Jr., "Purdue/AFOSR Aging Aircraft Research Program," NASA Airframe Structural Integrity Program Review, Langley Research Center, VA, March 20-21, 1995 (presentation only).

9. C. T. Sun, J. Klug, and C. Arendt, "Analysis of Cracked Aluminum Plates Repaired with Bonded Composite Patches," *Proceedings of the 36th AIAA/ASME/ASCE/AHS/ASC Structures, Structural Dynamics, and Materials Conference (SDM),* New Orleans, LA, April 10-14, 1995. (Also accepted for publication in AIAA Journal.)

10. P. J. Laz and B. M. Hillberry, "A Probabilistic Model for Predicting Fatigue Life Due to Crack Formation at Inclusions," *ICAF '95, International Committee on Aeronautical Fatigue, 18th Symposium,* Melbourne, Australia, May 3-5, 1995.

11. S. M. Rohrbaugh, B. M. Hillberry, and D. Ruff, "A Probabilistic Fatigue Analysis of Multiple Site Damage: Influence of the Number of Fastener Holes," *ICAF '95, International Committee on Aeronautical Fatigue, 18th Symposium,* Melbourne, Australia, May 3-5, 1995.

12. M. P. Szolwinski and T. N. Farris, "Three Dimensional Analysis of Fretting Fatigue Crack Initiation," 49th Annual STLE Meeting, Pittsburgh, PA, May 1995 (presentation only).

13. A. F. Grandt, Jr., "Analysis of Multiple Site Damage in Aging Aircraft," *Symposium on Aging Structures,* Joint Applied Mechanics and Materials Summer Conference, ASME, Los Angles, CA, June 28-30, 1995 (abstract only).

Year 1

The following papers and presentations resulted from the first year's research (July 1, 1993 to June 30, 1994).

1. J. H. Elsner, E. P. Kvam, and A. F. Grandt, Jr., "Fatigue Crack Initiation in 7050 Plate With Controlled Porosity," 1993 Materials Week, American Society for Metals Annual Conference, Pittsburgh, PA, October 17, 1993 (Presentation only).

2. A. F. Grandt, Jr., A. J. Hinkle, C. E. Zezula, and J. H. Elsner, "The Influence of Initial

Quality on the Durability of 7050-T7451 Aluminum Plate," 1993 USAF Structural Integrity Program Conference, San Antonio, TEXAS, November 30 - December 2, 1993 (published in conference proceedings).

3. A. F. Grandt, Jr., "Multiple Site Damage and Other Aging Issues," presentations to USAF Scientific Advisory Board, Materials Degradation Panel. — January 19, 1994, Washington, DC — February 24, 1994, Wright-Patterson AFB, Ohio

4. E. J. Moukawsher, A. F. Grandt, Jr., and M. A. Neussel, "Analysis of Panels with Multiple Site Damage," AIAA Paper No. 94-1459, AIAA SDM Conference, Hilton Head, SC, April 18-21, 1994.

5. M. P. Szolwinski and T. N. Farris, "Fretting Fatigue Crack Initiation: Aging Aircraft Concerns," AIAA Paper No. 4, AIAA-94-1591-CP, AIAA SDM Conference, Hilton Head, SC, April 18-21, 1994.

6. K. Buhler, A. F. Grandt, Jr., and E. J. Moukawsher, "Fatigue Analysis of Multiple Site Damage at a Row of Holes in a Wide Panel," FAA/NASA International Symposium on Advanced Structural Integrity Methods for Airframe Durability and Damage Tolerance, Hampton, VA, May 4-6, 1994 (published in conference proceedings.)

7. S. M. Rohrbaugh, B. M. Hillberry, A. F. Grandt, Jr., and G. McCabe, "A Probabilistic Fatigue Analysis of Multiple Site Damage, FAA/NASA International Symposium on Advanced Structural Integrity Methods for Airframe Durability and Damage Tolerance, Hampton, VA, May 4-6, 1994 (published in conference proceedings).

8. C. P. Arendt, and C. T. Sun, "Bending Effects of Unsymmetric Adhesively Bonded Composite Repairs on Cracked Aluminum Panels," FAA/NASA International Symposium on Advanced Structural Integrity Methods for Airframe Durability and Damage Tolerance, Hampton, VA, May 4-6, 1994 (published in conference proceedings).

9. A. F. Grandt, Jr., "Materials Degradation and Fatigue in Aerospace Structures," Second Air Force Aging Aircraft Conference, Oklahoma Air Logistics Center, Tinker, AFB, Oklahoma, May 17-19 (vu-graphs published in conference proceedings).

10. C. P. Arendt, "Bending Effects of Unsymmetrically Bonded Composite Repairs on Cracked Aluminum Panels," presentation to the USAF Engineers investigating composite repairs at Warner Robins AFB, May 23, 1994.

11. A. F. Grandt, Jr., M. T. Doerfler, R. J. Bucci, and M. Kulak, "A Fracture Mechanics Based Approach for Quantifying Corrosion Damage," 1994 Tri-Service Conference on Corrosion, Orlando, FL, June 20-24, 1994 (published in conference proceedings).

3.3 List of Graduate Theses

The following Purdue University graduate theses were prepared by students associated with this research project.

1. J. C. Klug, "Fracture and Fatigue of Bonded Composite Repairs," Ph.D. Thesis, School of Aeronautics and Astronautics, Purdue University, August 1997.

2. D. G. Sexton, "A Comparison of the Fatigue Damage Resistance and Residual Strength of 2024-T3 and 2524-T3 Panels Containing Multiple Site Damage," M. S. Thesis, School of Aeronautics and Astronautics, Purdue University, August 1997.

3. M. D. Gates, "A Crack Gage Approach to Monitoring Fatigue Damage Potential in Aircraft," M. S. Thesis, School of Aeronautics and Astronautics, Purdue University, May 1997.

4. M. B. Heinimann, "Analysis of Stiffened Panels with Multiple-Site Damage," Ph.D. Thesis, School of Aeronautics and Astronautics, Purdue University, May 1997.

5. X. Su, "Three Dimensional Effects in Elastic-Plastic Fracture," Ph.D. Thesis, School of Aeronautics and Astronautics, Purdue University, December 1996.

6. G. Harish, "Modeling of Plate/Fastener Contact: Application to Fretting Fatigue," M. S. Thesis, School of Aeronautics and Astronautics, Purdue University, August 1996.

7. S. M. Rohrbaugh, "Probabilistic Fatigue Damage Model for a 2024-T3 Aluminum Alloy," M. S. Thesis, School of Mechanical Engineering, Purdue University, August 1996.

8. P. J. Laz, "A Probabilistic Approach to Predicting Fatigue Life for Crack Formation at Inclusions," M. S. Thesis, School of Mechanical Engineering, Purdue University, May 1996.

9. E. A. DeBartolo, "The Effect of Particle Clusters on Fatigue Behavior of 2024-T3 Aluminum," M. S. Thesis, School of Mechanical Engineering, Purdue University, May 1996.

10. D. Ruff, "Weighted Cramer-Von Mises Estimation of a Distribution," Ph.D. Thesis, Department of Statistics, Purdue University, May 1996.

11. I. A. Golinkin, "Stress Corrosion Cracking of Aluminum Structural Alloys and Statistics of Failure," Ph.D. Thesis, School of Materials Engineering, Purdue University, December 1995.

12. P. A. McVeigh, "Finite Element Analysis of Fretting Fatigue Stresses, M. S. Thesis, School of Aeronautics & Astronautics, Purdue University, December 1995.

13. J. N. Scheuring, "An Evaluation of Aging Aircraft Material Properties," M. S. Thesis, School of Aeronautics and Astronautics, Purdue University, August 1995.

14. M. R. Lena, "Repair and Reinforcement of Cracked Aluminum Plates with Adhesively Bonded Composite Patches," M. S. Thesis, School of Aeronautics and Astronautics, Purdue University, May 1995.

15. M. P. Szolwinski, "Mechanics of Fretting Fatigue Crack Formation," M. S. Thesis, School of Aeronautics and Astronautics, Purdue University, August 1995.

16. K. Buhler, "A Study of Fatigue Crack Growth of Panels Containing Multiple Site Damage," M. S. Thesis, School of Aeronautics and Astronautics, Purdue University, December 1994.

17. J. H. Elsner, "Fatigue Crack Initiation of Aluminum Alloy 7050-T7451," M. S. Thesis, School of Materials Engineering, Purdue University, December 1994.

18. C. P. Arendt, "An Efficient Plate Finite Element Model for Analysis of Cracked Metallic Plates repaired with Composite Patches," M. S. Thesis, School of Aeronautics and Astronautics, Purdue University, August 1994.

3.4 Faculty/Student Recognition

The following awards were received by the Purdue research team during the past year (July 1, 1996 to June 30, 1997).

1. Professor C. T. Sun, named recipient of the 1997 AIAA Structures, Structural Dynamics and Materials Award. This award is presented for outstanding recent technical or scientific contribution in aerospace structures, structural dynamics, or materials, 31 January 1997.

2. Professor A. F. Grandt, Jr. named Fellow, American Institute of Aeronautics and Astronautics, May 1997.

3. Markus B. Heinimann, shared first place for best student presentation, ASTM E-08 committee meetings, May 1997.

3.5 Other Developments

Other laboratory developments, curriculum revisions, and technical interactions resulting from this project are described in previous annual reports.

APPENDIX A
REPRINTS OF TECHNICAL PAPERS

The following papers were prepared during the past year (July 1, 1996 to June 30, 1997) and are reproduced here in the following section.

A 1
- M. P. Szolwinski, G. Harish, P. A. McVeigh, and T. N. Farris, "The Role of Fretting Crack Nucleation in the Onset of Widespread Fatigue Damage: Analysis and Experiment," 1996 FAA-NASA Symposium on the Continued Airworthiness of Aircraft Structures, Atlanta, August 1996.

A 2
- H. Ganapathy and T. N. Faris, "Modeling of Skin/Rivet Contact: Application to Fretting Fatigue," Proc. of 38th AIAA/ASME/ASCE Structures, Structural Dynamics and Materials Conference, Vol. . 4, pages 2761-2771, April 1997.

A 3
- M. P. Szolwinski, G. Harish, T. N. Farris, and T. Sakagami, "An Experimental Study of Fretting Fatigue Crack Nucleation in Airframe Alloys: A Life Prediction and Maintenance Perspective," First Joint DoD/FAA/NASA Conference on Aging Aircraft, Ogden, Utah, July 1997.

A 4
- J. N. Scheuring and A. F. Grandt, Jr., "Mechanical Properties of Aircraft Materials Subjected to Long Periods of Service Usage," *Journal of Engineering Materials and Technology* (1997).

A 5
- J. H. Elsner, E. P. Kvam, and A. F. Grandt, Jr., "Modeling and Microstructure Analysis of Fatigue Initiation Life Extension by Reductions in Microporosity," *Metallurgical and Materials Transactions A, Volume 28A*, May 1997, pp. 1157-1167.

A 6
- M. C. Cherry, S. Mall, M. B. Heinimann, and A. F. Grandt, Jr., "Residual Strength of Unstiffened Aluminum Panels with Multiple Site Damage," *Engineering Fracture Mechanics* (1997).

A 7
- M. B. Heinimann and A. F. Grandt, Jr., "Analysis of Stiffened Panels with Multiple Site Damage," Proc. of the 1996 USAF Structural Integrity Program Conference (December 3-5, 1996, San Antonio, Texas), WL-TR-97-4055, Volume II, June 1997, Materials Directorate, Wright Laboratory, Air Force Material Command, Wright-Patterson AFB, OH 45433-7734, pp. 655-682.

A 8
- M. D. Gates and A. F. Grandt, Jr., "Crack Gage Approach to Monitoring Fatigue Damage Potential in Aircraft," 1997 Society for Experimental Mechanics Spring Conference on Experimental and Applied Mechanics, June 2-4, 1997, Bellevue, Washington.

A9
- A. F. Grandt, Jr., T. N. Farris and B. M. Hillberry, "Analysis of the Formation and Propagation of Widespread Fatigue Damage," Proc ICAF: *Fatigue in New and Aging Aircraft, Ed P. Poole and R. Cook, Scotland, June 1997, In-Press.*

A10
- A. F. Grandt, Jr., D. Sexton, P. Golden, G. H. Bray, R. J. Bucci, and M. Kulak, "A Comparison of 2024-T3 and 2524-T3 Aluminum Alloys Under Widespread Damage Scenarios," *Fatigue in New and Aging Aircraft, Ed P. Poole and R. Cook, Scotland, June 1997, In-Press.*

A11
- M. P. Heinimann and A. F. Grandt, Jr., "Fatigue Analysis of Stiffened Panels with Multiple Site Damage," The First Joint DoD/FAA/NASA Conference on Aging Aircraft, Ogden, Utah, 8-10 July 1997.

A12
- I. A. Golinkin, D. D. Ruff, E. P. Kvam, G. P. McCabe, and A. F. Grandt, Jr., "Application of Analysis of Variance (ANOVA) Statistical Methods to Breaking Load Corrosion Test," *Journal of Testing and Evaluation,* to appear November 1997.

A13
- P. J. Laz and B. M. Hillberry, "Fatigue Life Prediction for Crack Formation at Inclusions in 2024-T3 Aluminum," submitted to *International Journal of Fatigue.*

A14
- J. Klug, S. Maley, and C. T. Sun, "Characterization of Fracture and Fatigue Behavior of Bonded Composite Repair," The First Joint DoD/FAA/NASA Conference on Aging Aircraft, Ogden, Utah, 8-10 July 1997.

A15
- J. C. Klug and C. T. Sun, "Large Deflection Effects of Cracked Aluminum Plates Repaired with Bonded Composite Patches," submitted to *Journal of Composite Structures.*

A16
- C. T. Sun and X. M. Su, "Effect of Crack Interaction on Ductile Fracture," Proc. of FAA-NASA Symp. On Continued Airworthiness of Aircraft Structures, Atlanta, 1996.

A17
- X. M. Su and C. T. Sun, "On Singular Stress at the Crack Tip of a Thick Plate Under In-Plane Loading," *International Journal of Fracture*, Vol. 82, pp. 237-252, 1996.

THE ROLE OF FRETTING CRACK NUCLEATION IN THE ONSET OF WIDESPREAD FATIGUE DAMAGE: ANALYSIS AND EXPERIMENTS*

Matthew P. Szolwinski, G. Harish, Pamela A. McVeigh and Thomas N. Farris
School of Aeronautics & Astronautics
Purdue University
West Lafayette, IN

SUMMARY

The localized contact stresses, strains and surface microslip induced by fretting at fastener/hole or joint interfaces serve to accelerate the nucleation of widespread fatigue damage (WFD) when compared to the sole action of the global structural loads. Analytical, numerical and experimental approaches are integrated to predict the nucleation of cracks under the fretting contact stresses. Multiaxial fatigue theory, uniaxial strain-life material data and finite element analysis are combined to predict the nucleation of cracks by fretting contact in a reduced experimental model of an aircraft joint. Finite element analysis is combined with multiaxial fatigue theory to predict lives of actual aircraft joints.

INTRODUCTION

Fretting, the damage process that manifests itself when nominally-clamped surfaces are subjected to oscillatory loads or external vibrations, is not a recently-discovered malady. In fact, damage from fretting contact was reported as early as 1911 by researchers carrying out fatigue tests of steel who discovered "red rust...due to the varying stress between the test-specimen and its holder" (fretting corrosion) (ref. 1). Those interested in the design and maintenance of both fixed and rotary-wing aircraft after World War II gave concurrent acute attention to the role fretting plays in the degradation of the airframe structure and mechanical components (ref. 2). In spite of its importance, very little work analyzing the nucleation of cracks under the influence of fretting contact has been available. Instead, researchers have focused primarily on either reporting the effect of fretting on the reduction in total fatigue life or analyzing the effect of the fretting contact on surface cracks.
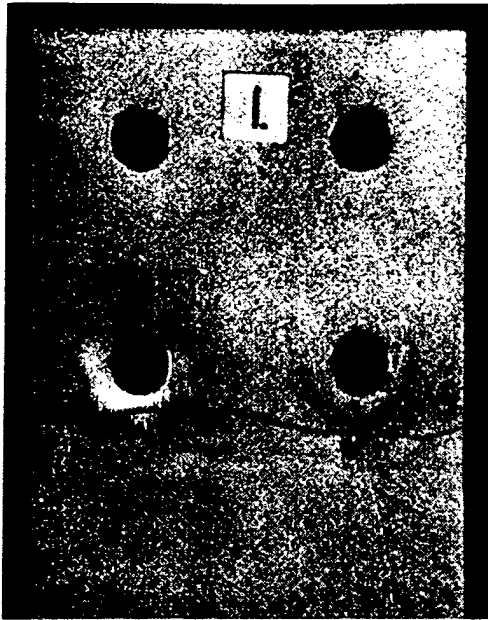
Figure 1: Fatigue failure of a lap splice attributed to fretting (ref. 3).

The current objective is to understand the ability of fretting to initiate and accelerate widespread fatigue damage (WFD) in airframe joints. Both periodic teardown inspections and laboratory simulations of common riveted aircraft lap splice joints have revealed evidence of fretting crack nucleation near the rivet/skin interface and at the faying surfaces of riveted joints, as shown in Figure 1. (refs. 3, 4). To ascertain accurately a more complete understanding of the effect of fretting and, possibly fretting corrosion, on the onset of widespread fatigue damage in aging airframes, the highly-localized microslip distribution and contact stresses related to the fretting action present in these structural members must be considered in detail.

This paper describes research efforts in two related areas: (1) understanding the mechanics of fretting fatigue crack nucleation, with particular emphasis on the development of predictive capability rooted in a blend of analytical and experimental methodologies and (2) accurate finite element modeling of a typical lap splice joint that incorporates the intimate localized contact between both the fastener and hole and faying surfaces of the sheets. Blending the results from these endeavors has led to the current phase of research: assessing the effects of rivet installation on fretting fatigue crack nucleation in aircraft joints. The following highlights achievements and ongoing work in each of these areas to elucidate the development of this current research objective.

PREDICTION OF FRETTING FATIGUE CRACK NUCLEATION

The synergistic competition among the wear, fatigue and corrosive phenomena associated with fretting contact is driven by the highly localized microslip distribution and contact stresses that vary non-proportionally with any bulk or global loading. Development of an understanding of the mechanics of fretting fatigue crack nucleation requires the careful characterization of the cyclic stresses, strains and displacements associated with fretting. This effort is made complicated by many effects, including the fact that the local coefficient of friction changes during the life of the fretting surfaces.

Analytical and Numerical Models for Cyclic Fretting Contact Stress Field

An analytical model of the surface tractions and stresses associated with the two-dimensional fretting problem was proposed independently by both Cattaneo (ref. 5) an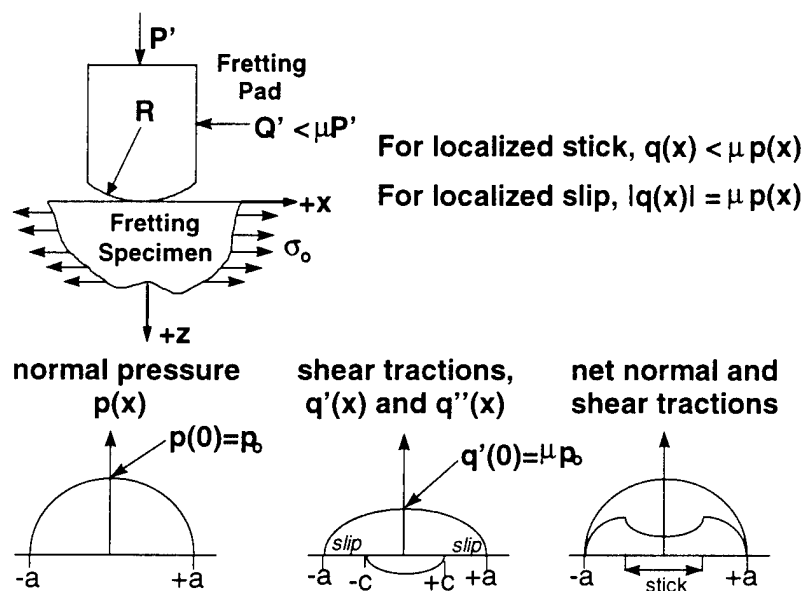d Mindlin (ref. 6) in 1938 and 1949, respectively. Assuming Hertzian contact of isotropic, elastic cylinders subjected to a monotonic tangential loading and a Coulomb law of sliding friction on a localized basis, a condition of "stick" or no relative motion between the contact surfaces in a central stick zone can be imposed, as illustrated in Figure 2. In the stick zone, the local shear traction $q(x)$, is less than the local frictional force, $\mu p(x)$ while in the regions of slip, $|q(x)| = \mu p(x)$.

For localized stick, $q(x) < \mu p(x)$

For localized slip, $|q(x)| = \mu p(x)$

Figure 2: A schematic of the surface tractions associated with fretting.

Closed-form solutions for the stresses, strains and surface displacements associated with given normal and tangential loads (P and Q) and coefficient of friction in the slip zones (μ) are available (ref. 7). The bulk tension shown in Figure 2 leads to a non-symmetric stick zone (ref. 8). Results from a wide range of loading parameters point toward the source of crack nucleation due to fretting: a sharp tensile peak in the tangential stress, σ_{xx} at the edge of the contact zone, $x = +a$ (see Figure 3). The analytical expression for the component of σ_{xx} due to the fretting alone reduces conveniently to (ref. 9):

$$(\sigma_{xx})_{\text{fretting}} = 2p_o \sqrt{\mu Q/P} \qquad (1)$$

where p_o is the maximum Hertzian pressure and μ is the coefficient of friction in the slip zones. The effect of the applied bulk stress component in the x-direction (σ_o) can be approximated by superposing it with $(\sigma_{xx})_{\text{fretting}}$, as shown in Figure 3. Thus for contact pressures in the ranges of 25 to 30 ksi, bulk stresses on the order of 12 to 14 ksi and nominal values of $Q/P = 0.3$ and $\mu = 0.6$, the fretting contact provides a stress concentration $[(\sigma_{xx})_{\text{total}}/(\sigma_o)]$ between approximately 2.5 and 2.8.
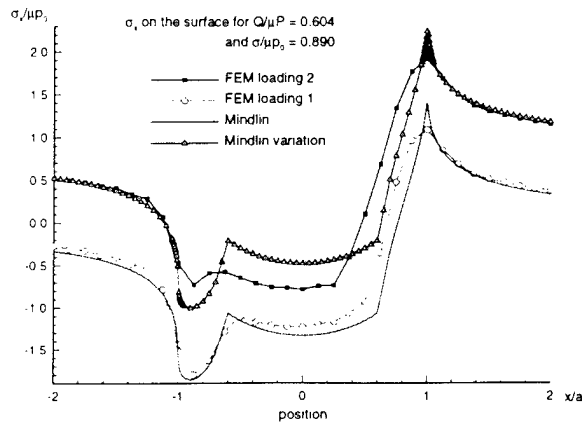
Figure 3: Tangential stress, σ_{xx}, along the contact surface. FEM loading 1 and the Mindlin cases involve no bulk stress while FEM loading 2 and the Mindlin variation cases incorporate the bulk stress σ_o. For the given set of conditions ($Q/\mu P$) and ($\sigma_o/\mu p_o$), no reversal of microslip at the contact surface occurs.
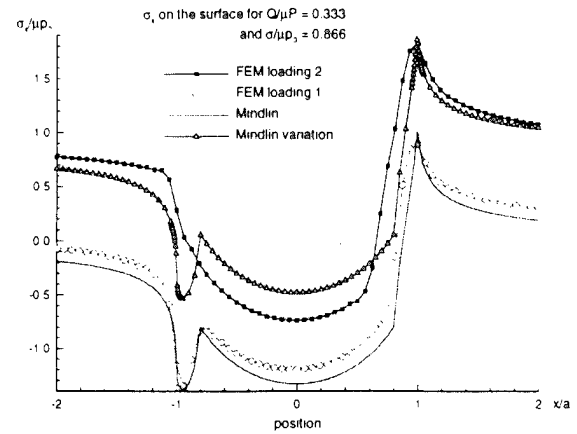
Figure 4: Tangential stress, σ_{xx}, along the contact surface, for a case of reversed slip. Again, FEM loading 1 and the Mindlin cases involve no bulk stress while FEM loading 2 and the Mindlin variation cases incorporate the bulk stress σ_o. Note that even while the Mindlin solutions do not account for the slip reversal, the predicted values of σ_{xx} at the trailing edge ($x/a = +1$) agree well with the FEM values.

Fretting and Multiaxial Fatigue Theory: Analysis and Experiments

As the ratio of the tangential load to normal load, Q/P, changes with an oscillatory tangential load, the cyclic stresses and strains are non-proportional in nature, leading to a state of multiaxial fatigue at all points. Any attempt to predict nucleation of fatigue cracks due to the influence of fretting must account for this fact. Based on the hypothesis that the peak in tensile stress at the trailing edge ($x/a = +1$) of contact drives the observed nucleation of fretting cracks perpendicular to the contact surface (ref. 10), Szolwinski and Farris (ref. 7) attempted to correlate published experimental observations of fretting fatigue crack failures with predictions made with multiaxial fatigue theory based on principal planes (ref. 11), uniaxial strain-life constants and the aforementioned fretting contact elastic stress analysis. The relationship between reversals to nucleation (defined as a crack of length 1 mm) and the product of strain amplitude and maximum stress during a complete loading cycle normal to the principal plane (the plane of the nucleated crack) is:

$$\Gamma = \sigma_{max}(\Delta\varepsilon/2) = [(\sigma_f')^2/E](2N_f)^{2b} + \varepsilon_f'(2N_f)^{b+c} \qquad (4)$$

This is the familiar uniaxial strain-life Smith-Watson-Topper equation with uniaxial fatigue constants that has been shown to hold for cases of multiaxial fatigue (ref. 11). The expression, coupled with the two-

dimensional stress analysis, identifies the location and orientation of the critical plane of crack nucleation as the trailing edge of contact perpendicular to the contact surface, respectively, agreeing with published observations (ref. 10).

The experimental setup presented in Figure 5 has been constructed at Purdue University to generate and monitor precisely the requisite loads necessary for fretting fatigue for verification of the postulated multiaxial fatigue predictive model. The fretting test fixture, designed around a 22-kip servo-hydraulic load frame, induces fretting between a cylindrical pad and flat specimen, a geometrical configuration identical to the one assumed in the analytical and FEM models. The fixture and associated data acquisition hardware and software (the details of which are presented elsewhere (ref. 12)) allow for complete control over the variables necessary to characterize the contact stress field: (1) Q/P, (2) σ_o, (3) p_o, and (4) $2a$, the width of the contact zone.
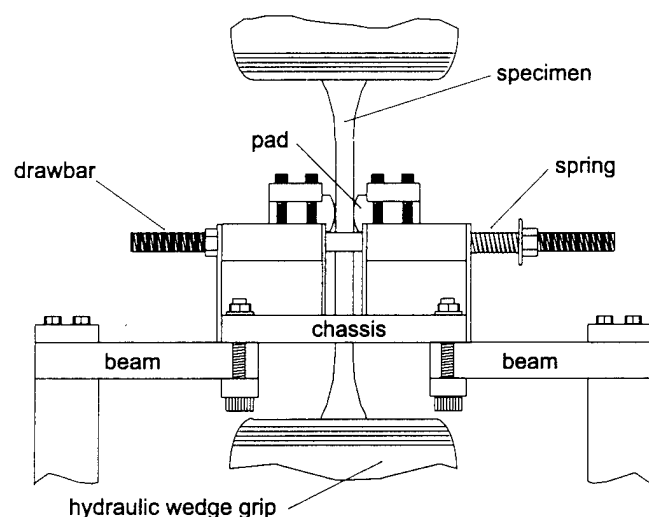
Figure 5: Experimental setup used in the fretting fatigue crack nucleation studies at Purdue University.

Aluminum 2024-T351 specimens and cylindrical pads have been used in the tests. Each specimen is run to fracture for a given maximum Hertzian contact pressure and amplitudes of bulk stress and Q/P. By measuirng these quantities and having determined the steady-state coefficient of friction in the slip zones to be $\mu = 0.6$ (ref. 12), a prediction can be made for the number of cycles required to nucleate a crack of 1 mm in the specimens. A propagation life for each test is estimated by assuming a thumbnail crack of depth 1 mm is grown through the specimen by the bulk stress using a Paris-law approach. It has been calculated that this propagation phase occurs in the latter 25-40% of total cycles to failure. Figure 6 displays fretting data both generated at Purdue and published data (ref. 10) for which the requisite loads and experimental parameters were known. To this end, the nucleation life for each experiment has been plotted as the number of cycles to failure minus the estimated propagation life.

For the sake of comparison, two theoretical curves are plotted along with the experimental data. The first, for 2024-T351, uses strain-life constants generated by Blatt (ref. 13). The material in the

published study was only identified as a 4% copper (by weight) aluminum alloy. As a result, a second curve using strain-life constants for 2024-T4 alloy is also plotted on the graph (ref. 14). While it appears from even a cursory review of the data that the multiaxial fatigue-based theory is able to predict accurately fretting fatigue crack nucleation, a statistically-designed set of tests is currently underway to provide further support to this claim.
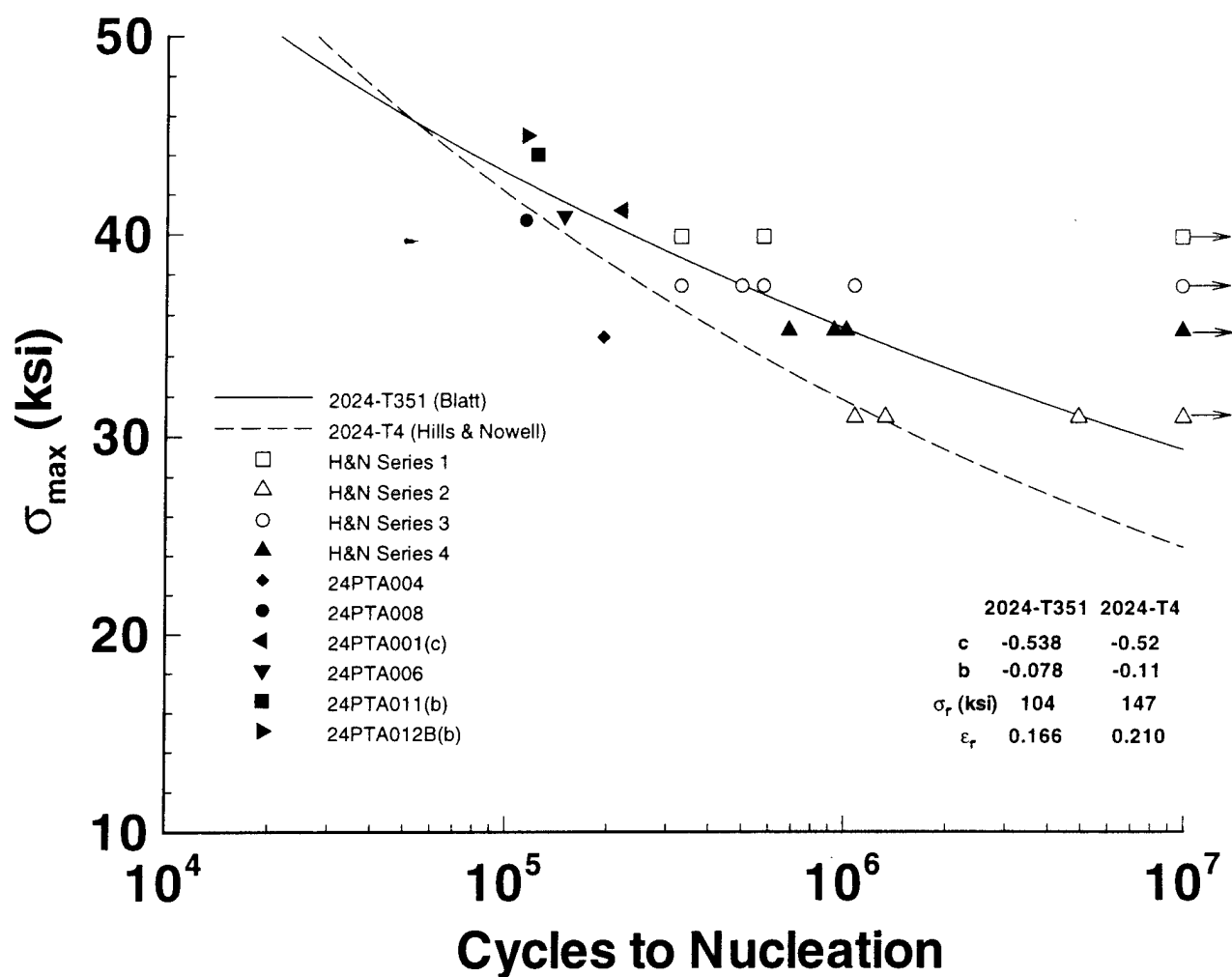

Figure 6: Comparison between nucleation lives as predicted by the multiaxial fatigue-based approach and experimental observations. For the series of tests conducted at Purdue, the steady-state coefficient of friction in the slip zones was determined to be $\mu = 0.60$.

MODELING OF JOINT CONFIGURATIONS WITH APPLICATIONS TO FRETTING FATIGUE

With the confidence in the capability to predict fretting crack nucleation from contact stresses and strains, the next logical step is to quantify the stresses and strains present in common joint configurations. Such an effort has been undertaken using finite element modeling with the expressed goal of verifying the presence of interfacial tractions and contact stresses indicative of fretting in lap splice joints.

Two separate finite element models of a skin panel with an infinite row of rivets are formulated using plane-strain quadrilateral elements and three-dimensional shell elements, respectively. Material properties of 2024-T3 aluminum were assumed for each component. The calculations are performed using ANSYS™, a finite element software package provided to Purdue University on an academic license by Swanson Analysis, Inc. Each model consists of a typical "cell" composed of one half-rivet and the portion of the skin around it. A complete lap joint may be thought of as being built up with these "cells." Symmetry conditions are imposed on both the top and bottom of the model to simulate the presence of the infinite row of rivets. The presence of multiple rivet rows is accounted for by the elastic supports (on one side for the 2-D model and on either side— one for each shell—for the shell model). By varying the stiffness of these elastic supports, the amount of load being transferred through the rivet can be controlled. To simulate global loading, a uniform tensile traction is applied on the remaining free edge or edges, with the rivet fixed at its center to prevent rigid body motion. Note that the applied global loading causes partial loss of contact between the rivet and plate as no shrink-effect due to rivet bucking is included in the present analysis.
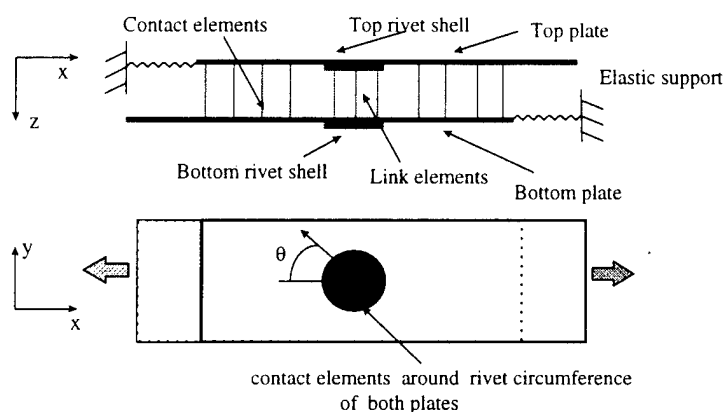

Figure 7: Schematic of shell model.

The three-dimensional model is represented schematically in Figure 7. This model incorporates contact elements along the rivet/skin interface as well as on the interface between the two plates, which are modeled as shells. For reasons of consistency, the rivets are also modeled as shells. Constraint conditions are imposed to force the two rivet shells to act as one body. The stiffnesses of the interface elements between the plates are calculated by assuming that the plates deform like rods under the action of an axial load provided by transverse pressure applied to the plates. With this approach, the effect of clamping the rivet head can be studied through application of axisymmetric pressure on an annular area around the rivet shells (ref. 15). The pressure is assumed to go fall to zero on both sides of this annulus in order to ensure a continuous profile. Note, though, there is no transverse shear stress capability in the current model.

With integration of this clamping pressure into the three-dimensional shell model, it is found that interfacial friction at the faying surfaces accounts for some of the load transfer through the joint; hence load transfer through the rivet is less than the overall load transfer through the rivet assembly. This division of load transfer is also observed upon unloading and subsequent reloading, as the stress distribution is nearly identical to the one present after the initial loading. This result may be explained by examining the manner in which the load is being transferred: With the initial loading, the plate/plate contact is initially stuck and the interfacial friction force transmits the load. Thus the rivet does not experience any loading until the plates attempt to move into contact with it. However, this contact will only commence when the plate/plate interface begins to slip nearly globally at the faying surfaces. Only after this point will the rivet begin to take up the bulk of the additional load. Similarly, when the load is released, the rivet will begin to unload only when the plates begin to move in the opposite direction. This
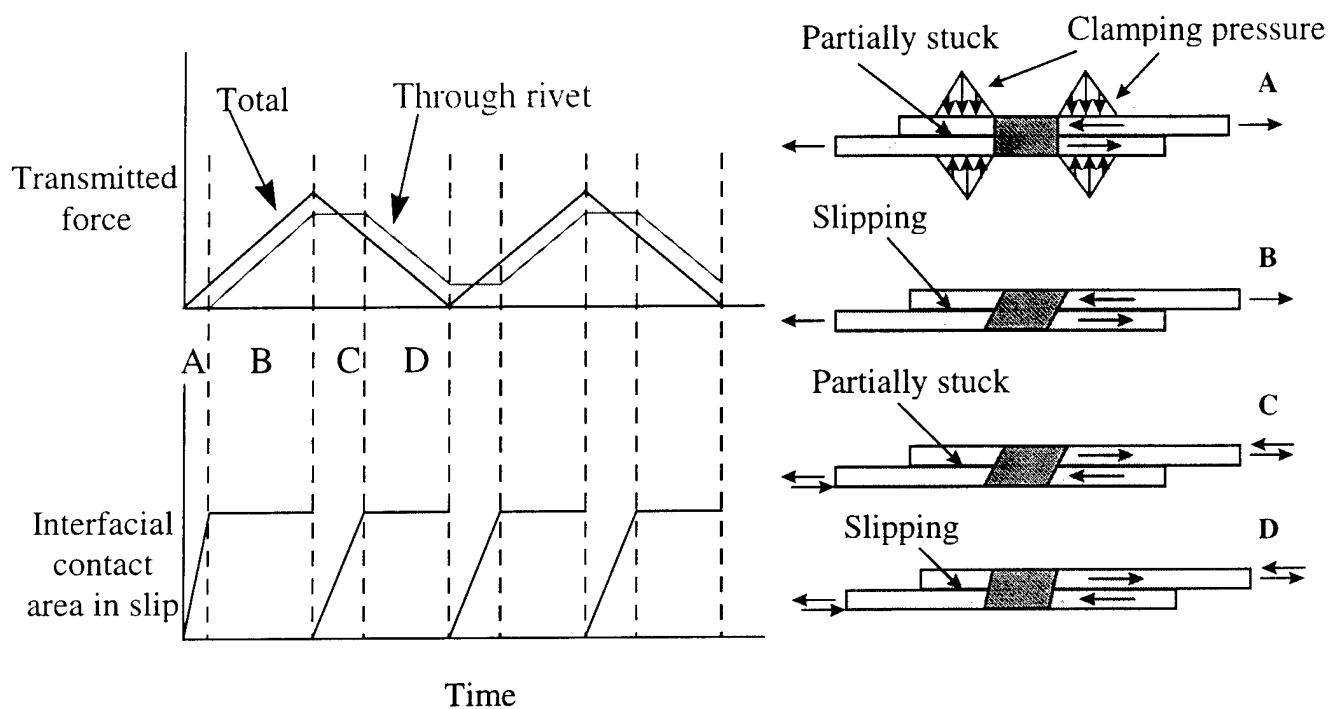
Figure 8: Schematic of load transfer mechanisms.

requires reversed slip (slip in the direction opposite to slip due to the initial loading) to occur in the plate/plate interface. Finally, when reloading occurs, the slip again has to reverse before the rivet takes up any more load. Thus, the fraction of the contact area in slip at any given time looks similar to the schematic given in Figure 8. Such a stick/slip action indicative of fretting leads to high localized contact stresses both at the faying surfaces and the rivet/skin interface.

Also, an increase in rivet head clamping results in a higher interfacial frictional force between the two plates causing a state of stress highly favorable to crack nucleation, especially as the interface is a hidden surface. This stress, combined with high slip amplitudes, can cause extensive wear and fatigue damage to the surfaces. For a given value of elastic support stiffness, the influence of interfacial friction is to increase load transfer ratio, but at a lower maximum tangential stress. The penalty lies in extending the zone of fretting damage.
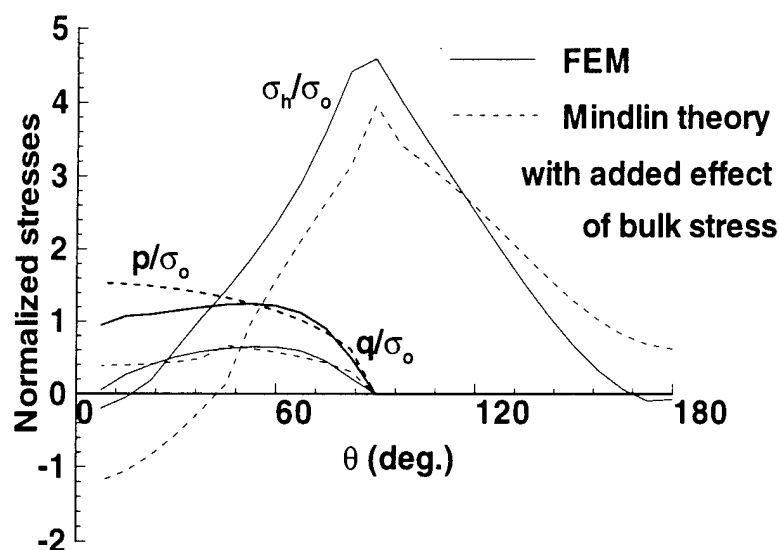
Figure 9: Normalized contact stresses at fastener hole at the mid-plane of the top plate. The applied clamping force is 75 lb. and 40% of applied load is transferred through the rivet assembly. The assumed coefficient of friction at the fastener/skin interface is $\mu = 0.5$.

The contact between the fastener and plate spans roughly half the interface, centered around $\theta = 0°$. This is in good agreement with the results published by Narayana and Dayananda (ref.16). The stress results are expressed in the form of stress distribution around the fastener hole for a given LTR and coefficient of friction. The normal pressure, p, the shear traction on the plate at the interface, q, and the tangential stress around the fastener hole, σ_h, are plotted as functions of the angular coordinate θ in Figure 9.

From these results, it can be concluded that the contact between the fastener and plate can be approximated by the analytical tractions derived for the Mindlin case. This conclusion is supported by the distinct "fretting-like" stick-slip behavior in the contact, the nominally-Hertzian pressure distribution and the shear traction that follows the pressure distribution in the slip region, where $q(\theta) = \mu p(\theta)$. In the stick region, q decreases slowly as θ approaches zero. The region of slip is dependent on the coefficient of friction, varying from 15° to 60° of arc as the coefficient of friction increases from 0.2 to 0.7. The tangential stress (or hoop stress, σ_h) shows a tensile peak at the edge of contact ($\theta = 0°$), similar to the results presented earlier in Figure 3. This stress then decays away from the edge of contact. In general, increases in the coefficient of friction result in a decrease in the maximum value of normal pressure and an increase in the maximum tangential stress. The tangential stress peak coupled with the stick-slip behavior must be included in any analysis of nucleation of cracks at and around fastener holes.

Results from this model also provide insight into load transfer ratio and rivet spacing. As the stiffness of the elastic support is varied, the load taken up by the rivet changes accordingly. In the model, the resistive stiffness is the series sum of two springs with stiffnesses equal to that of the support and the region of the panel aft of the rivet. Thus, in order to reduce the rivet load, rivet spacing must be decreased in conjunction with an increase in the number of rivets.

The origin of the tractions at the plate/fastener interface can be identified as the combination of stress concentrations due to the fastener hole and the plate/fastener contact. The stress concentration solution is determined by solving the same model without the fastener, but with all other boundary conditions intact and superposing contact stresses as determined by Mindlin theory, assuming a contact area and slip zone size as given by the full model. The tangential stress is calculated as the sum of the Mindlin solution stress and the stress due to the effect of the stress concentration provided by the hole.

Close to the trailing edge of contact, which is the primary point of interest, the values predicted by the analytical approach theory are quite reasonable when compared to the FEM results. The 3-D model results also compares well to the 2-D results (ref. 17) which is expected as the mid-plane results are basically devoid of bending stresses. It is also important to note that the stick/slip condition is evaluated on basis of nodal forces and not stresses. Hence only mid-plane values can be expected to conform strictly to Coulomb friction theory.

As shown, the use of finite element modeling of a typical joint configuration to predict and analyze probable zones of fretting is a useful approach. It may be the only way to understand the behavior of the rivet/skin contact subjected to complex loadings in the presence of cracks which may have been nucleated by fretting. This type of analysis is of particular significance for design of rivet size and spacing and the implications of rivet installation procedures in the context of widespread fatigue damage.

CONCLUSION

The combination of appropriate stresses and multiaxial fatigue theory allows the prediction of fretting crack nucleation in a two-dimensional experimental approximation of the rivet/skin interface. As the three-dimensional fastener/skin interfacial stress state calculated by finite element analysis is similar to that of the experiment, it is believed that the onset of widespread fatigue damage at the fastener/skin interface can be predicted. Further experimental and analytical work, particularly in the area of the stresses

induced during the rivet installation process, is required to predict fretting at the faying surfaces of lap joints.

REFERENCES

1. Eden, E. M; Rose, W. N.; and Cunningham, F. L.: The Endurance of Metals. *Proceedings of the Institution of Mechanical Engineers*, part 3, 1911, pp. 839-924.

2. Rahm, A. E.; and Wurster, H. J.: Fretting Corrosion in Aircraft and Aircraft Accessories. *Lubrication Engineering*, vol. 7, February 1951, pp. 22-40.

3. Harris, W. J.: *Metallic Fatigue*. Pergamon, 1961.

4. Müller, R. P. G.: An Experimental and Analytical Investigation on the Fatigue Behavior of Fuselage Riveted Lap Joints. Ph.D. thesis. Delft University of Technology, The Netherlands, 1995.

5. Cattaneo, C.: Sul Contatto di Due Corpi Elastici: Distribuzione Locale Degli Sforze. *Rendiconti dell' Accademia nazionale dei Lincei*, vol. 27, 1938, pp. 342-348, pp. 434-436, pp. 474-478.

6. Mindlin, R. D.: Compliance of Elastic Bodies in Contact. *Journal of Applied Mechanics*, vol. 16, 1949, pp. 259-268.

7. Szolwinski, M. P.; and Farris, T. N.: Mechanics of Fretting Fatigue Crack Formation. *Wear*, 1996, in press.

8. McVeigh, P. A.; and Farris, T. N.: Finite Element Analysis of Fretting Stresses. *Journal of Tribology*, 1996, in press

9. Hills, D. A.; Nowell, D.; and Sackfield, A.: Surface Fatigue Considerations in Fretting. *Interface Dynamics*, eds. Dowson, D.; Taylor, C. M.; Godet, M.; and Berthe, D., Elsevier, 1988, pp. 35-40.

10. Hills, D. A.; Nowell, D. and O'Connor, J. J.: On the Mechanics of Fretting Fatigue. *Wear*, 1988, vol. 125, pp. 129-156.

11. Socie, D.: Critical Plane Approaches for Multiaxial Fatigue Damage Assessment. *Advances in Multiaxial Fatigue*, ASTM STP 1191, 1993, pp. 7-36.

12. Szolwinski, M. P.; Harish, G.; and Farris, T. N.: Experimental Observation of the Effect of Contact Parameters on Fretting Fatigue Crack Nucleation. *Proceedings of the 1995 USAF Structural Integrity Program Conference*, San Antonio, 1995.

13. Blatt, P. A.: Evaluation of Fatigue Crack Initiation Behavior of an Experimental Ternary Aluminum-Lithium Alloy. M. S. thesis, Purdue University, West Lafayette, 1990.

14. Hertzberg, R. W.: *Deformation and Fracture Mechanics of Engineering Materials*. Wiley, 1976.

15. Reithmaier, L.: *Standard Aircraft Handbook.* 4th ed., Tab Books, 1986.

16. Narayana, K. B.; and Dayananda, T. S.: Cracks Emanating from Pin-Loaded Joints. *Engg. Fracture Mechanics*, vol. 47, 1994, pp. 29-38.

17. Farris, T. N.; Grandt, A. F., Jr.; Harish, G.; and Wang, H. L.: Analysis of Widespread Fatigue Damage in Structural Joints. *Proceedings of 41st International SAMPE Symposium and Exhibition*, Anaheim, 1996.

MODELING OF SKIN/RIVET CONTACT: APPLICATION TO FRETTING FATIGUE

Harish Ganapathy and T.N. Farris*
School of Aeronautics and Astronautics
Purdue University
1282, Grissom Hall
West Lafayette, IN 47907-1282

ABSTRACT

Fretting is a contact damage mechanism arising from microslip associated with small-scale oscillatory motion of nominally clamped structural members. Fretting has been observed near aircraft skin fastener holes. The present work, focusing on fretting as a crack nucleation mechanism in lapjoints, analyzes the contact at a typical skin/rivet interface using both plane and shell finite elements. Contact elements implementing the Coulomb friction law keep track of contact status between interacting surfaces. The shell model accounts for bending, contact between the skin panels and rivet clamping pressure. Elastic supports control the load transferred and simulate various rivet configurations. No interference is considered. There is loss of contact between the skin and rivet on loading. The distinct stick-slip zones, combined with high tensile stresses at the edge of contact, are indicative of fretting, resulting in crack nucleation at the edge of contact. The tensile stress decays rapidly away from the edge of contact. The slip displacement has values typically associated with fretting fatigue. The interface between the two skin panels is also a region of fretting damage. Crack nucleation lives are predicted using a multiaxial fatigue theory. The top row of rivets has the smallest predicted life. For low remote stresses, increase in friction coefficient increases life, while for high remote stresses, life decreases with increase in coefficient of friction. Increasing rivet head clamping pressure increases the life. Plasticity blunts effects of friction coefficient and clamping. An approximate solution, that does not require finite element analysis, estimates the crack nucleation life for any rivet configuration quickly.

INTRODUCTION

Fretting is a damage process resulting from a combination of wear, corrosion and fatigue driven by micro-motion and stresses at the contact zone. The first analysis of Hertzian contact with the additional complexity of a tangential force having magnitude less than that required to produce gross sliding was done by Mindlin and independently by Cattaneo.[1,2] These analyses reveal the division of contact into regions of stick and slip, which is relevant to fretting observations.

Fretting fatigue is observed in roller bearings, riveted lap-joints, dovetail notches of turbine blades and even artificial hip joints.[3,4] In the recent past, various researchers have studied the fretting of lapjoints in the laboratory.[5-7]

Fretting in engineering materials is a three-stage mechanism.[8] The first stage involves the removal of thin oxide layer on the material surface through wear. As the oxide degrades in the first few cycles, the underlying material of the contact surfaces forms microwelds through an adhesive process.[9] This causes the accumulation of wear debris between the contact surfaces. The coefficient of friction increases in the first few hundred cycles of fretting contact, coincidentally with wear debris accumulation.[10-12] As the cycles keep accumulating there is plastic deformation near the surface and additional wear promoting more oxide formation.[13] This near surface plastic deformation promotes the nucleation of cracks. Fretting fatigue results when one or more of these microcracks penetrate into the bulk of the material. Fretting can cause an order of magnitude change in expected fatigue life.

Fretting fatigue crack nucleation has generated renewed interest of late, especially with regard to aging aircraft. The United States Air Force (USAF) is looking to extend the lives of some of its aging fleets (e.g. KC 135 and C 141). Also, some of the
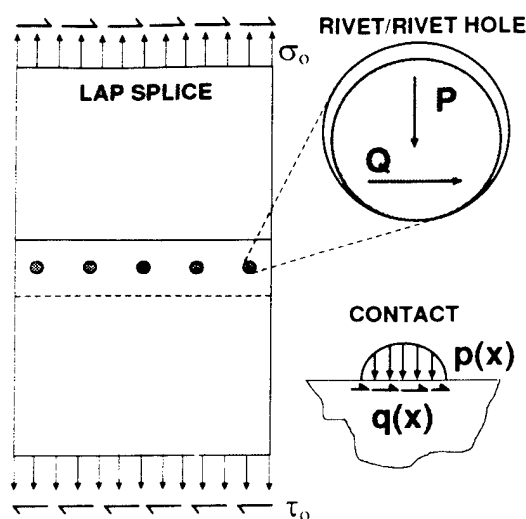
---

*Professor, Senior Member AIAA

Figure 1: Fretting and aircraft

planes are actually operating at loads higher than the design loads.[14] This has lead to a philosophy of aircraft, both new and old, being inspected periodically. Particular emphasis is being laid on Multiple Site Damage (MSD).[15] MSD is characterized by a multitude of cracks in a structural member, all of which, while not individually catastrophic, can cause premature failure by their combined effect. Teardown inspections of KC 135, C 5A and C-141 have revealed the existence of MSD cracks at fastener holes, one of the prime locations of fretting fatigue damage. Farris et al. have discussed how fretting is a possible mechanism for the formation of MSD.[16] This is illustrated through Figure 1 which shows the global loading on a lap splice and the local contact at the rivet/skin interface, involving both normal and shear loading. A careful study of the parameters involved in fretting, and the development of an appropriate theory with applicability to the actual practical structural members is thus necessitated. This paper develops a method for treating the fatigue of lap splices as fretting, leading to an approximate prediction of crack nucleation life. A parallel experimental study is also underway.[17]

FINITE ELEMENT MODEL

Any good theory must satisfy two criteria: it must agree with experimental results and must have a solid physical basis. While the former is achieved through experiments simulating field behavior, the latter involves modeling of the phenomenon under investigation to isolate the parameters governing it. The study of crack nucleation in lapjoints involves calculating the state of stress in the lapjoint and its influence on nucleating the crack. Since the complex phenomena of contact and plasticity govern this behavior, closed form solutions are not available. The Finite Element Method (FEM) provides numerical solutions to problems of this nature. The solution involves the following steps: identification of skin/rivet configurations to be studied; reduction to discrete model (with accompanying assumptions); solution of discrete model and interpretation of results within framework of assumptions.

A typical lapjoint is analyzed using 2-D plane strain quadrilaterals as well as 3-D shell elements. The 2-D model is discussed first because it shows the details of the rivet/skin contact. The 3-D model is required to include the effects of skin/skin load transfer and rivet head clamping pressure. The models discussed in this paper assume a three row lapjoint with infinite rivets in each row. They comprise one-half rivet and the region of skin panel around it. The rivet diameter is $0.2in$, while the rivet spacing is $1in$. With appropriate boundary conditions and spring elements, the models simulate the presence of multiple rows of rivets. The commercial code ANSYS, provided to Purdue on an academic license, is used for solution of the problem. The rivet and plate are assumed to be 2024-T351 Aluminum. The Young's modulus is $10.6Msi$, while Poisson's ratio is 0.33. By varying the stiffness of the spring elements, the amount of load being transferred to the rivet can be controlled, allowing the modeling of any rivet configuration. While the model is loaded by a remote tensile load, the periodic boundary conditions (on boundaries parallel to direction of principal traction) create a non-uniform traction in the orthogonal direction. The effect of subsequent rivets behind the rivet of interest is modeled by the spring elements and the traction that they exert. The loads are applied gradually to facilitate the solution of the nonlinear problem. The contact between the interacting surfaces is tracked by using contact elements, which transmit only compressive normal stresses. They also transmit shear traction, subject to a maximum of μ (coefficient of friction) times the normal stress. When this limit is exceeded, the contact element starts to slip, allowing relative motion between the two surfaces it connects. When the shear traction is less than this limit, the two surfaces are said to be stuck, with no relative motion.
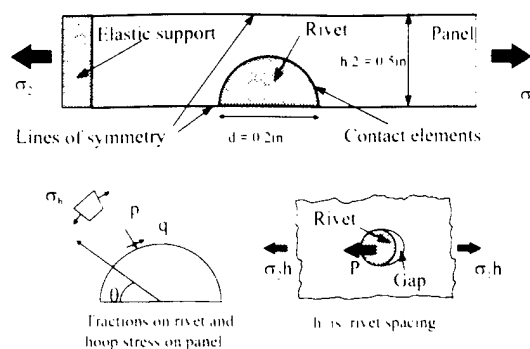
Figure 2: Schematic of 2-dimensional model

Figure 3: Schematic of shell model

2-Dimensional model

This section addresses the special features of the 2-D model (Figure 2). The 2-D model is built using 818 plane strain eight-noded quadrilaterals (PLANE82). The contact between the skin and rivet is modeled with 180 2-D point-to-surface contact elements. By adjusting the stiffness of the elastic support, the effect of the subsequent rows of rivets is controllable. Figure 2 also shows the directions of the tractions on the rivet and the nature of contact under tensile loading. The center of the rivet is fixed to provide a frame of reference to eliminate rigid body motion. The effect of local contact stresses is assumed to be negligible at a distance of five radii from the contact, so that the stresses may be assumed to be constant across the width at this distance. This is crucial to simulate various rivet locations and load transfer ratios (LTR). Since the problem is very close to a receding contact problem, the stresses can be scaled by the applied traction.[18] This eliminates the need to solve the problem for various load magnitudes. The value of the effective stiffness of the panel region behind the rivet is the sum of the stiffness of the elastic support and the panel lying between the rivet and the support. The coefficient of friction is varied between 0.2 and 0.7. The applied load is kept at $10ksi$. The stiffness of the support is varied from zero (free edge) to a very large value (fixed edge — corresponding to an infinite number of rivets). The basis of this approach is that the contact of one rivet does not change the nature of contact of the rivets behind it — except by changing the effective load seen by the succeeding rivets.

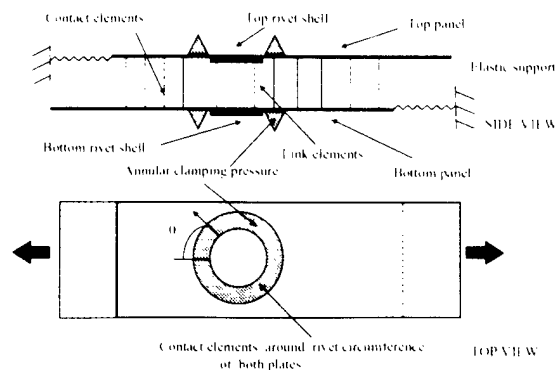The 2-D model does not incorporate the interfacial friction between the panels, which accounts for some of the load transfer. The rivet head clamp-ing pressure and bending of the panels are also not included. No plasticity model is implemented, so that stresses are assumed elastic. The shell model addresses these issues.

3-Dimensional shell model

The dimensions of a typical aircraft skin lap joint are characteristic of the realm of validity of Mindlin shell theory. The skin panels are approximated by shells along their neutral axis. The rivet is also modeled as two parallel shells, each aligned with one of the panels to assure consistency of the model. The two shells comprising the rivet are linked together by constraints. Each panel is $3in$ long and $0.5in$ wide. The overlap region is $2in$ by $0.5in$. The thickness of each panel is $0.07in$. Taking advantage of symmetry, only one-half of a rivet is modeled. Appropriate boundary conditions are used to simulate the existence of an infinite number of rivets in each row and also the effect of the succeeding rows of rivets. Both the panels have a symmetry condition parallel to the applied traction. There is an elastic support for each plate similar to the one used for the 2-dimensional model. Figure 3 shows a schematic of the shell model.

The rivet shells are fixed at their center to eliminate rigid body motion. The section of the panel near the rivets may be considered equivalent to a collection of unit structures, each consisting of a half-rivet and adjacent zone of the two plates. Clamping pressure is applied on the panel to simulate a clamped rivet head. An annulus with outer radius equal to 1.3 times the rivet radius is chosen for applying pressure.[19] The pressure is assumed to go to zero at both edges of the plate to ensure a smooth profile. For consistency, the sum of the forces acting over the two ends of the top plate and the bot-

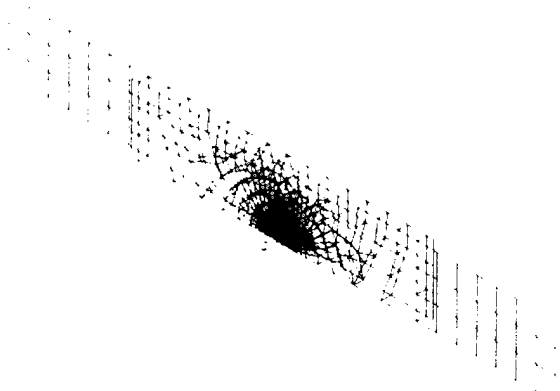Figure 5: Deformed mesh for 2-dimensional model

Figure 4: Finite element mesh for shell model

tom plate must be equal. The rivet by itself should not provide any reaction, implying that the support stiffnesses cannot be arbitrarily chosen, but must be found iteratively.

The skin panels and the rivet are modeled by 4-noded Mindlin shell elements (SHELL43 in ANSYS). The two rivet shells are connected by link elements and appropriate constraint conditions to ensure that their behavior is akin that of a single rivet. The model has 852 nodes with 768 shell elements and 267 contact elements. There are 24 elements around the circumference of the rivet. The mesh is shown in Figure 4.

The panel/rivet and panel/panel contact is tracked by 3-dimensional point-to-point contact elements. Even though this is a 3-dimensional problem, the nature of contact is expected to be roughly the same regardless of load. Hence, these elements are particularly appropriate as the contact area can be estimated apriori and does not change appreciably with load. The panel/rivet contact is modeled by 50 contact elements, half for each panel. There are 217 contact elements between the two panels. Here, since the shells are modeled along their centerlines, the distance between them can be changed due to compression of the plates. Hence, a soft contact algorithm with normal stiffness in compression emulating rod-like behavior in the through thickness direction is used.

Displacement compatibility is imposed at the mid-plane of the cylinder formed by the two rivet shells using the following equation:

$$(u_i + 0.5\theta_i t)_{bottom} = (u_i - 0.5\theta_i t)_{top} \qquad (1)$$
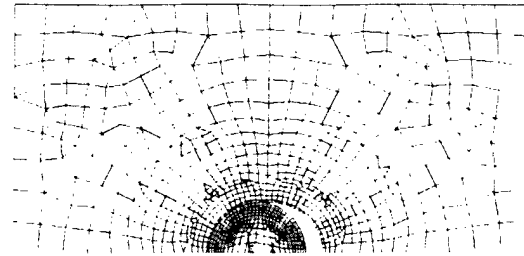
where t is the thickness of each of the shells forming the rivet and u_i is the translational displacement in the i direction, and θ_i is the angular displacement (in the i direction) of the normal section to the neutral axis (in undeformed state). Link elements with weighted stiffness (calculated from the areas of the adjoining elements containing the nodes forming the link element) emulate the through thickness stiffness.

RESULTS

Figures 5 and 6 show the displacement profile for the plane and shell model respectively. It is clearly seen that contact is centered around $\theta = 0^o$ with the half-contact angle being nearly 90°. This also shows that the dominant contact mechanism is the global motion of the plate into the rivet. The other mechanism is the tendency of the panel hole to deform locally into an ellipse under load. The observed contact region is in agreement with the results of Narayana and Dayananda.[20] The contact zones exhibit stick-slip behavior. The hoop stress has a maximum near the edge of contact, and decays away from the edge of contact. This behavior is characteristic of fretting. Experiments indicate that for 2024-T351 aluminum, μ is about 0.2 at the beginning of fretting and increases to a stable value of about 0.65 after a few hundred cycles.[17] In an actual skin/rivet assembly, the coefficient of friction would reach a stable value within a few hundred cycles.

2-Dimensional Model

Figure 7 shows the results, expressed in the form of stress distribution around the fastener hole, for a typical configuration. The normal pressure, p, the shear traction on the plate at the interface, q, and
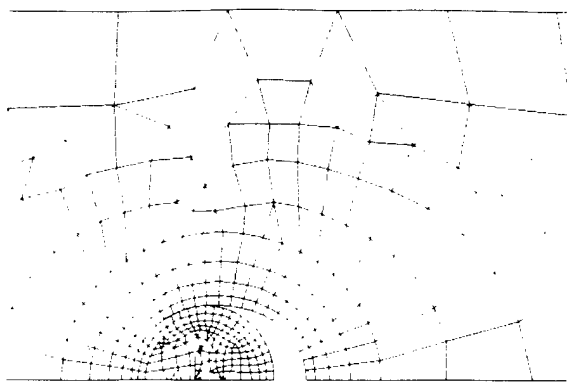
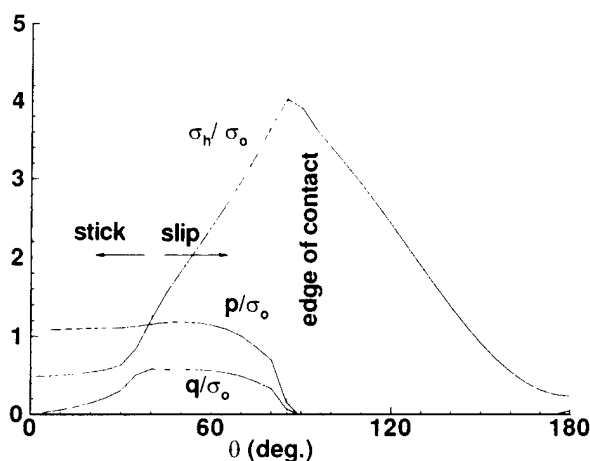Figure 6: Deformed mesh for shell model. Only part of one panel is shown to demonstrate the loss of contact

Figure 7: Contact stresses for plane model. LTR = 0.30, $\mu = 0.5$

the tangential stress around the fastener hole, σ_h, are plotted as functions of the angular coordinate θ, which has been defined in Figure 2. The stresses are made non-dimensional by dividing by the remote applied uniform tension, σ_o. The most important observation from these plots is that a distinct stick-slip behavior is present in the contact. This is also verified by checking the status of the contact elements. Wherever the contact elements report no contact, the normal pressure and shear traction are assumed to be zero.

The pressure distribution is nearly semi-elliptic in nature and resembles the Hertzian pressure distribution. However, at high LTR, the pressure reaches a maximum at a value of θ different from zero. This is due to the effect of local deformation of the panel

hole discussed earlier which causes the region around θ to move radially away causing a reduction in normal pressure. Also the small sharp dip at $\theta = 0''$ is due to the effect of the symmetry condition imposed on this node. The shear traction follows the pressure distribution in the slip region, where $q = \mu p$. In the stick region, q decreases slowly as θ goes to zero. Again, the non-zero value at $\theta = 0$ results purely as a consequence of numerical approximation of the FEM. The region of slip is dependent on the coefficient of friction. It varies from $60''$ to $15''$ of arc as the coefficient of friction varies from 0.2 to 0.7.

The tangential stress (or hoop stress, σ_h) shows a tensile peak at the edge of contact ($\theta = 0''$). The stress decays away from the edge of contact. However, the tangential stress seems to stabilize in the stick region. The tangential stress is derived from three sources - the stress concentration due to the rivet hole, the normal pressure and the shear traction. The tangential stress peak coupled with the stick-slip behavior is very conducive to the nucleation of fretting fatigue cracks at the edge of contact. For a given support stiffness and applied remote traction, as μ increases, the maximum normal pressure drops, the shear traction increases, and the region of stick becomes larger. The increased shear traction causes increases tangential tension at the edge of contact. However, other researchers have reported that in the presence of a crack, the tangential stress reduces with increase in μ.[20]

3-Dimensional Shell Model

While the shell model also illustrates important features like the loss of contact and tensile stress peak at the edge of contact, this section discusses additional features available only in the shell model. The shell model highlights the localized bending in the proximity of the rivet, caused by the two skin panels pulling the rivet in opposite directions. The plasticity is modeled as kinematic hardening with an initial yield stress $\sigma_y = 48ksi$ and a hardening modulus $E_t = 0.225Msi$.

Figure 8 shows the stress distribution at the mid-surface of one panel for a purely elastic case. Figure 9 shows the contact stresses when plasticity has set in. Once again, the tangential stress (or hoop stress, σ_h) shows a tensile peak at the edge of contact ($\theta = 0^o$). On unloading, there is a residual pressure distribution, which is also shown in Figure 8. This residual pressure is due to the locked-in slip zones as well as plasticity.

Even in the presence of plasticity, the tensile peak at the edge of contact is observed. This peak value now remains close to the material yield stress
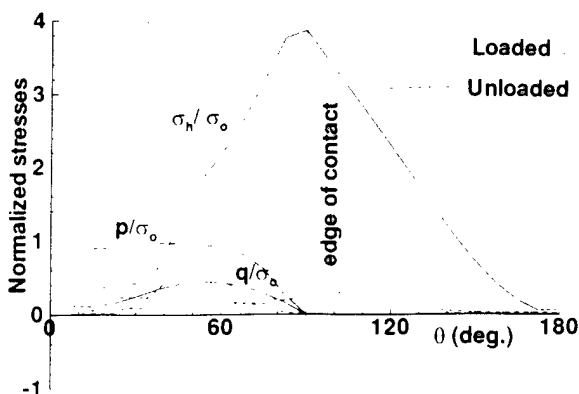
Figure 8: Contact stresses for shell model : LTR = 0.37, μ = 0.65 , peak clamping pressure is 8ksi, σ_o = 10ksi

Figure 9: Contact stresses for shell model in plastic regime. LTR=0.37;μ = 0.65. peak clamping pressure is 8ksi, σ_o = 16ksi.

(as the work hardening rate is very small for 2024-T351 Aluminum.). There is a redistribution of any additional remote load. Consequently, the pressure distribution no longer resembles a Hertzian distribution. Due to the action of the bulk of the panel which is elastic, the plastic region is constrained. On unloading, the tangential stress becomes negative near the edge of contact. Also the residual pressure is very low. However, the plasticity is confined to the first cycle only and subsequent cycles are elastic and cycle between the two states shown in Figure 9.

Figure 10 shows the decay of hoop stress radially away from contact in the $\theta = 0^o$ direction. The stress concentration and contact stresses both decay quite rapidly with distance from the hole. The gradient is quite steep even when plasticity sets in. Thus, this problem involves high stress gradients in addition to contact, frictional dissipation and plasticity.

Variation with friction and rivet head clamping

For a given load transfer ratio (of the rivet assembly), as the coefficient of friction increases, the interfacial friction takes up more load, resulting in less load transfer through the rivet itself. However, the local stresses at the rivet/skin interface tend to increase with coefficient of friction. For small values of remote stress, the first phenomenon dominates, resulting in lower stress values overall. For moderate values of remote stress, the relief due to interfacial friction diminishes and stress values at the panel/rivet interface increase with coefficient of friction. However, in the plastic regime, the coefficient of friction has a small effect on the stress (and strain)
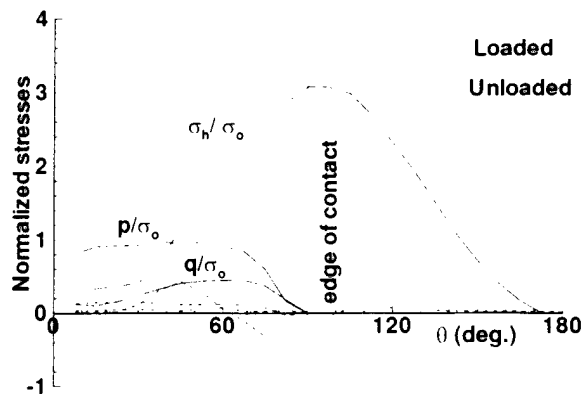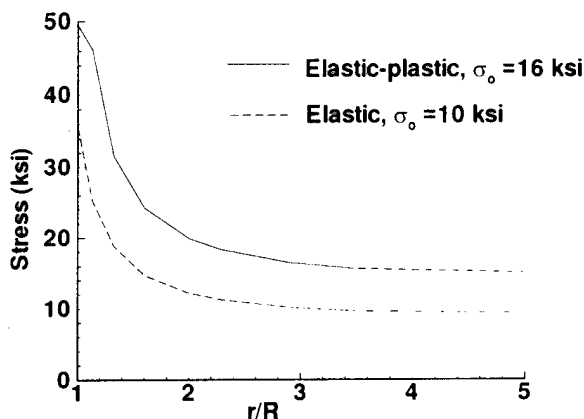

Figure 10: Variation of hoop stress away from contact in radial direction. μ = 0.2, LTR=0.375 R is radius of rivet.

states.

Higher clamping pressures result in higher interfacial load transfer and hence reduced stress levels at the panel/rivet interface. Again, the onset of plasticity negates any stress relief due to high clamping pressure. The clamping pressure diffuses through the thickness to encompass a larger area at the interface between the plates. Thus a larger area is available for interfacial load transfer, leading to some stress relief.

Both of the above mentioned effects may be explained by considering the behavior of the region around the edge of contact after yielding. As subsequent load is applied, this region takes up very little of it and the stress levels remain nearly the same. Hence, while the yielding may initiate at different
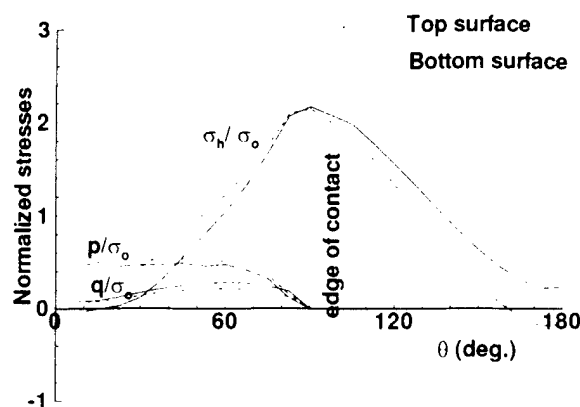
Figure 11: Effect of bending on stresses at contact interface for middle row rivet. LTR = 0.26, μ = 0.5, remote stress =14ksi, peak clamping pressure is 12ksi.

Figure 12: Partition of load between rivet and interfacial friction between panels.

levels of loading for various configurations, the final state after complete loading is close to that at yielding for all configurations.

Figure 11 shows the effect of bending on the stresses at the panel/rivet interface. It is observed that the ratio of q to p in the slip region is less than the value imparted to the contact elements via input. This is a consequence of the contact algorithm using force at discrete nodes to calculate slip in contrast to the stress-based approach that is more appropriate for a continuum elastic body. Also, as frictional force is not always in the X-Y plane, when slip is imminent, q, is not always be equal to μp. Thus, the value μ_{eff} refers to the effective coefficient of friction that is seen in the plane of the panel. The normal pressure increases from top to bottom while shear stress at the interface decreases in magnitude from top to bottom. The hoop stress increases from top to bottom in the contact zone, but has an opposite trend in the region of no contact. The bending stress is quite small near the edge of contact, which is the crucial location for fretting crack formation. An important observation is that the stick/slip condition is evaluated on basis of nodal forces and not stresses. Hence, strictly, only mid-plane values can be expected to conform to coulomb friction theory.

The panel/panel interface carries some load and hence load transfer through the rivet itself is reduced. The tensile load is now reduced to zero and increased once again to its maximum value. The stress distribution after reloading is almost identical to the one seen after the initial loading. This result
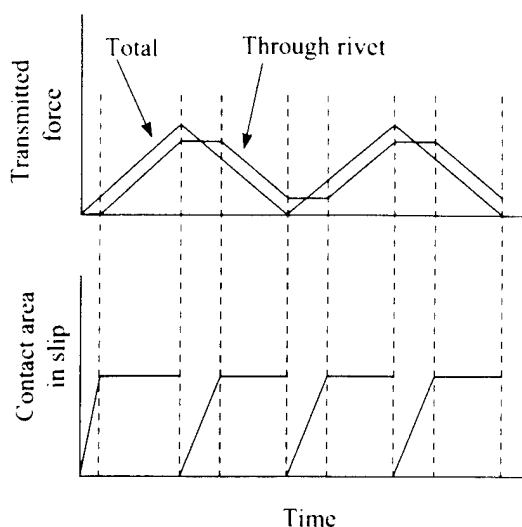
may be explained by examining the manner in which the load is being transferred. When the plate/plate contact is initially stuck, the initial loading is taken up by the interfacial frictional force. The rivet will not experience any load until the plate tries to move into it. So the plate/plate interface has to slip nearly everywhere, following which the rivet will take up the bulk of the additional load. Similarly, when the load is released, the rivet will experience a reduction in load only when the panels undergo reversed slip (i.e. slip in direction opposite the direction of original slip). Finally, when reloading occurs, the slip has to reverse again before the rivet takes up any more load. Thus, the fraction of the contact area in slip at any given time looks similar to the schematic given in Figure 12. Also, the load transferred by the rivet and panel/panel interface is shown. This behavior leads to high stresses during the time the interface is stuck. Also, the higher the clamping load, the more the interfacial frictional force between the two plates, causing a state of stress highly favorable to crack nucleation, especially as the interface is a hidden surface. This, when combined with high slip amplitudes, can cause extensive damage to the surfaces and nucleate cracks.

Relative displacements

One of the characteristic features of fretting is the stick-slip behavior of the contact. The relative displacements between the top plate shell and top rivet shell are shown in Figure 13. The gap displacement refers to relative normal displacement between
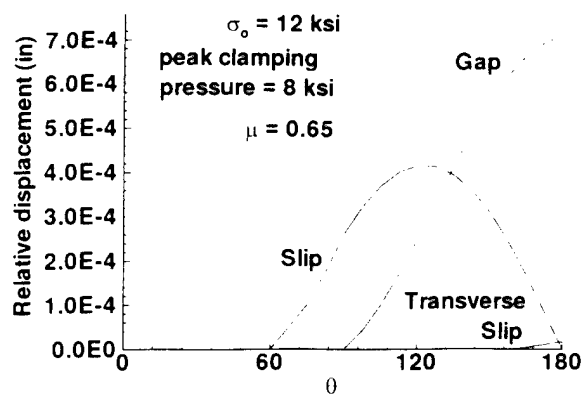
Figure 13: Slip displacements between panel and rivet. Top row. LTR = 0.375

the plate and rivet. Naturally, this gap is zero in the contact region where the rivet and the plate are in contact. The gap is positive elsewhere, indicating loss of contact. The slip displacement refers to relative motion along the hoop direction. The slip displacements are zero in the stick region and increase towards the trailing edge. The shell model also brings out the slip in the third direction. This is called transverse slip. If no clamping force is present, this transverse displacement is quite significant. It also changes the direction along which the frictional force acts. The transverse slip is however, nearly zero in for the case of the clamped rivet head. This can be attributed in part to the effect of the clamping force resisting motion of the plate in the transverse direction. The maximum slip displacement in the contact region occurs at the edge and is nearly 400μin. This is consistent with the values reported for a lap joint.[21] For comparison, the maximum slip amplitude for the skin/skin contact is about 60μin at the location given by $\theta = 135^o$ and $r = 1.6R$, where r is radial distance from the hole and R is the radius of the rivet. This slip may be related to the formation of cracks at the skin/skin interface away form the skin/rivet contact. The slip displacement beyond the contact area does not have any particular significance.

CRACK NUCLEATION

Szolwinski and Farris have used the multiaxial theory, proposed by Socie (derived from the Smith-Watson-Topper equation), to predict fretting crack nucleation.[22][24] Their predictions are in good agreement with the experiments of Nowell and Hills and preliminary data collected at Purdue.[25][26] The life,
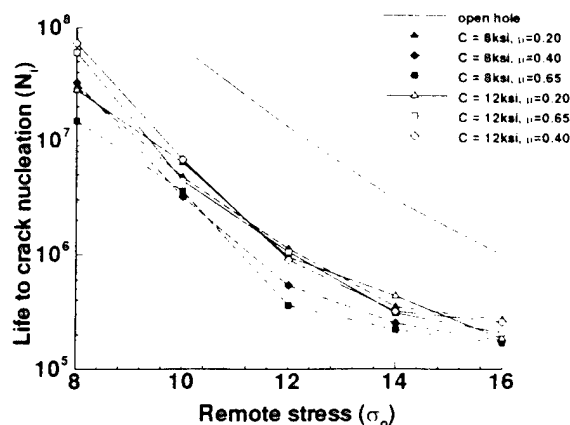

Figure 14: Predicted crack nucleation lives using multiaxial fatigue theory

N_i (in cycles), to nucleate a crack of length 0.03937in on the plane perpendicular to the applied load is given by

$$\Gamma = \sigma_{max} \frac{\Delta\epsilon}{2} = \sigma_f'(2N_i)^b + \epsilon_f(2N_i)^c \qquad (2)$$

The values of the fatigue constants σ_f', ϵ_f, b and c are 147ksi, 0.22, −0.12 and −0.52 respectively. The critical parameter is identified as Γ, the maximum value of the product of maximum normal stress and normal strain amplitude. For lapjoints without interference, this maximum occurs near the edge of skin/rivet contact.

Figure 14 shows the predicted lives to crack nucleation for various configurations. The stress levels and hence, the nucleation lives are much higher for the middle row which sees less remote load and reduced stress concentration. Also the open hole fatigue data is plotted for comparison. The data for the middle row falls above the open hole curve and is not plotted. Note that this theory is used only to translate the effect of various parameters into impact on nucleation life. A different theory would give similar quantitative results, with possible scale changes. In general, the lives are affected by the remote applied tension, the coefficient of friction and rivet head clamping pressure. As the remote load increases, the life to nucleation reduces. Owing to more load transfer and higher stress concentration, the top row is more susceptible to fretting crack nucleation as compared to the middle row. The effects of friction, clamping pressure, and plasticity are considered below.

Below a critical remote stress value, life increases with increase in friction coefficient upto a

certain value. Beyond this, the increase in interfacial friction is unable to compensate for the increase in local contact stresses at the skin/rivet contact. This critical value for the friction coefficient and remote stress depends on the clamping pressure. For example, when clamping with $8ksi$ maximum pressure, the optimum coefficient of friction for highest life is 0.4, while it is 0.6 when the maximum pressure is increased to $12ksi$. Beyond the critical stress, life decreases with increase in coefficient of friction. Higher clamping pressures decrease the load seen by the rivet itself, resulting in higher nucleation lives.

However, as mentioned earlier, in the plastic regime, beyond a certain value of load transferred into the rivet, the edge of contact experiences little change in stress and elastic strain amplitude. Hence, the effects of friction coefficient and clamping pressure on life, are diminished in the plastic regime.

ANALYTICAL MODEL

The origin of the stresses at the skin/rivet interface can be identified as the stress concentration due to the hole and the skin/rivet contact. The plate with a hole subjected to biaxial tension is a relatively simple problem. The Mindlin theory gives a good solution for the contact of two cylinders with a tangential force in addition to the normal force. McVeigh and Farris have shown that the Mindlin solution can be used to approximate more complicated situations.[27]

The decomposition of the model into a stress concentration problem and a Mindlin problem in the half-plane is shown in Figure 15. The normal force for the Mindlin problem is assumed to be twice the integral of the pressure force over the contact area (The 2 comes about because the FEM model contains only half of the contact area). An approximate solution is attempted by assuming that the pressure is distributed in accordance with Hertzian theory over a 90° arc of half-contact. The tangential force can then be calculated from

$$\frac{c}{a} = \sqrt{1 - \frac{Q}{\mu P}} \qquad (3)$$

The Mindlin theory can then be used to determine shear stress distribution.[28] The tangential stress is calculated as the sum of the Mindlin solution stress and the stress due to the stress concentration effect. Note that while the plate/fastener contact is symmetric with antisymmetric shear traction about $\theta = 0^o$, the Mindlin problem assumes symmetric shear traction. The value for Q required in the
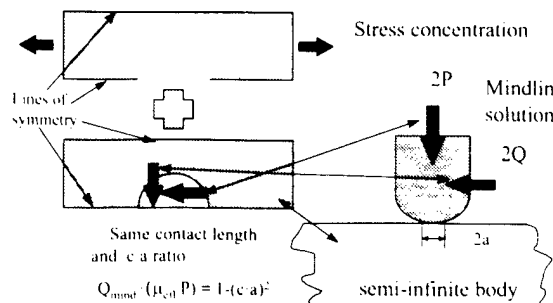

Figure 15: Decomposition of contact problem into stress concentration and Mindlin problem with symmetric shear traction

Mindlin problem is found by solving Equation 3 using the stick zone size, c, calculated from the finite element solution. The stress concentration is determined by solving the same model without the rivet, but with all other boundary conditions kept the same. This is similar to the problem of a plate with a hole subjected to biaxial tension, except that the relative values of the applied tension along the two axes is governed by the Poisson's ratio of the material. Also, the present analysis accounts for the effects of the symmetry boundary condition imposed on the plate. An approximate value for the maximum stress concentration factor for this problem is given by $3 - \nu$, where ν is the Poisson's ratio. For the case of the shell model, the load transferred through the rivet is obtained from FEM and the above procedure is followed. Though bending is not considered, the bending stresses in the region of interest are so small that this approximation is valid. An estimate of the interfacial frictional force would be μF, where μ is the coefficient of friction and F is the clamping force.

Figures 16 shows the comparison of the FEM solution with the Mindlin theory added on to the stress concentration. The tendency of the panel hole to deform locally into an elliptical shape under the action of the remote load causes the maximum pressure to move away from $\theta = 0^0$ location (where the Hertzian pressure is maximum).

The shear stress obtained from the Mindlin solution is for an antisymmetric shear traction problem, while the problem of interest is symmetric about $\theta = 0^0$. The solution of the symmetric shear problem does not yield itself to a closed form solution and
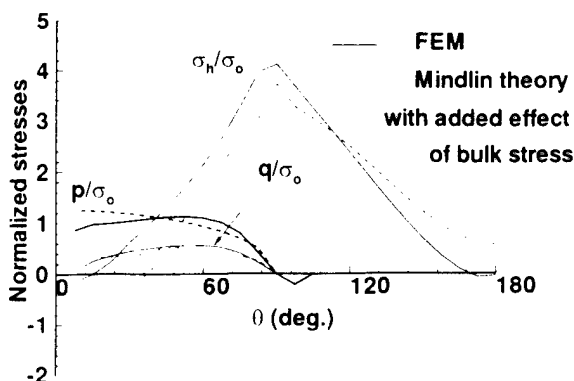
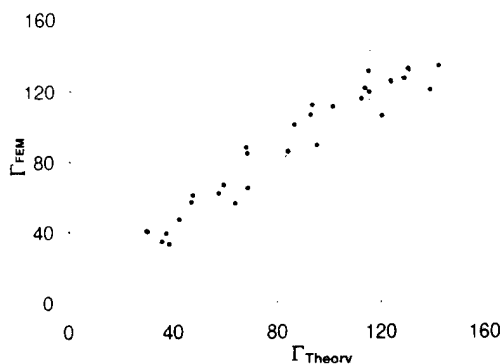Figure 16: Comparison between FEM result and analytical solution

Figure 17: Comparison of FEM result with theory. The solid line corresponds to exact correlation.

requires numerical solution. Hence, to preserve usefulness, the antisymmetric shear traction problem is chosen as the analytical approximation. This causes the shear stress and the tangential stress to deviate quite rapidly from the FEM values near the center of contact. However, close to the trailing edge, which is the primary point of interest, the values predicted by the approximate theory is quite reasonable when compared to the FEM result. Also, the finite element result for $Q/\mu P$ is in good agreement with the value predicted by Equation 3 for the observed slip zone size. Thus, the nature of the skin/rivet contact is characteristic of a fretting contact and is conducive to fretting crack nucleation.

Figure 17 shows the comparison of this analytical model with the FEM results for the top row of rivets with the following assumptions: The load transfer ratio is taken as 0.375. The interfacial friction in direction of load (assumed to be μF) is subtracted from the load transferred through the rivet.

The c/a value is assumed to be equal to μ itself. No bending is considered. The maximum hoop stress is limited to σ_y. The strain is calculated as if the stresses were elastic. The effect of the interfacial shear stress on Γ is neglected. Even with all the assumptions, the theoretical values for Γ values offer a reasonable estimate of the FEM results. These Γ values can be used in Equation 2 to predict crack nucleation life.

CONCLUSIONS

Fretting is one of the causes of crack nucleation in riveted lapjoints. For rivet joints with no interference, fretting damage can occur at the interface between the rivet and skin panel as well as between the two plates. The finite element method has been used to demonstrate the prevalence of conditions suitable for fretting induced crack nucleation. A multiaxial fatigue model is used to predict number of cycles to nucleate a crack. It shows that the critical location is at the skin/rivet contact. Higher clamping pressures increase the life by transferring more load through interfacial friction between the skin panels, thus reducing severity of stress near the rivet/skin interface. At low stresses, higher friction coefficient causes less load to go into the rivet itself, causing higher predicted lives. At moderate stress values, higher coefficient of friction reduces nucleation life. However, these effects are diminished in the presence of plasticity. The top row of rivets (which transfer the most load) are shown have the smallest predicted life. A simple analytical model has been developed to estimate crack nucleation life for an arbitrary lapjoint.

ACKNOWLEDGMENT

REFERENCES

[1] R. D. Mindlin. Compliance of elastic bodies in contact. *Journal of Applied Mechanics*, pages 259-268, Sep 1949.

[2] C. Cattaneo. Sul contatto di due corpi elastici: Distribuzione locale degli sforzi. *Rendiconti dell' academia nazionale die lincei*, 27, 1938.

[3] B. J. Kalb. Friction stresses between blade and disk dovetail possible case of numerous dovetail problems. In USAF *Structural Integrity Conference*, 1991.

[4] R. B. Waterhouse. Fretting fatigue in aqueous electrolytes. In *Fretting Fatigue*, chapter 7, pages 159–176. Applied Science, London, 1981.

[5] K. Iyer, G. T. Hahn, P. C. Bastias, and C. A. Rubin. Analysis of fretting conditions in pinned connections. *Wear*, 181:524–530, 1995.

[6] C. Petiot, L. Vincent, K. Dang Van, N. Maouche, J. Foulquier, and B. Journet. An analysis of fretting fatigue failure combined with numerical calculations to predict crack nucleation. *Wear*, 181:101–111, 1995.

[7] R. P. G. Müller. *An Experimental and Analytical Investigation on the Fatigue Behavior of Fuselage Riveted Lap Joints*. PhD thesis, Delft University of Technology, Delft, The Netherlands, 1995.

[8] P. L. Hurricks. Mechanism of fretting. *Wear*, 15:389–409, 1970.

[9] R. B. Waterhouse and D. E. Taylor. The initiation of fatigue cracks in a 0.7% carbon steel by fretting. *Wear*, 17:139–147, 1971.

[10] K. Nishioka and K. Hirakawa. Fundamental investigations of fretting fatigue, part 3. *Bulletin of JSME*, 12(51):397–407, 1969.

[11] K. Endo and H. Goto. Initiation and propagation of fretting fatigue cracks. *Wear*, 38:311–324, 1976.

[12] D. A. Hills, D. Nowell, and J. J. O'Connor. On the mechanics of fretting fatigue. *Wear*, 125:129–146, 1988.

[13] R. B. Waterhouse. *Fretting Corrosion*. Pergamon Press, Oxford, 1972.

[14] J. Lincoln. USAF aging aircraft program. *Aerospace Engineering*, 11-13, Oct. 1994.

[15] J. W. Lincoln. Life management approach for USAF aircraft. In *AGARD Conference Proceedings 506*, volume 17, Dec 1991.

[16] T. N. Farris, A. F. Grandt, G. Harish, and H. L. Wang. Analysis of widespread fatigue damage in structural joints. In *41st International SAMPE Symposium and Exhibition*, pages 65–79, Anaheim, 1996. SAMPE.

[17] M. P. Szolwinski, G. Harish, and T. N. Farris. Experimental observation of the effect of contact paramters on fretting crack nucleation. In *Proc. of the 1995 USAF Structural Integrity Program Conference*, pages 237–252, San Antonio, TX, 1995.

[18] J. Dundurs. Properties of elastic bodies in contact. In A. D. de Pater and J. J. Kalker, editors, *Proc. Symp. Intl. Union of Theoretical and Applied Mechanics*, pages 54–66. Delft University Press, 1974.

[19] L. Reithmaier, editor. *Standard Aircraft Handbook*. Tab Books, Blue Ridge Summit, PA, 4 edition, 1986.

[20] K. B. Narayana and T. S. Dayananda. Cracks emanating from pin-loaded joints. *Engg. Fracture Mechanics*, 47:29–38, 1994.

[21] W. J. Harris. *Metallic Fatigue*. Pergamon press, New York, 1961.

[22] M. P. Szolwinski and T. N. Farris. Mechanics of fretting fatigue crack nucleation. *Wear*, 198:93–107, 1996.

[23] D. Socie. Critical plane approaches for multiaxial fatigue damage assessment. In *Advances in Multiaxial Fatigue ASTM STP 1191*, pages 7–36. ASTM, Philadelphia, 1993.

[24] K. N. Smith, P. Watson, and T. H. Topper. A stress-strain function for the fatigue of metals. *Journal of Materials*, 5(4):767–778, 1970.

[25] D. Nowell and D. A. Hills. Crack initiation criteria in fretting fatigue. *Wear*, 136:329–343, 1990.

[26] M. P. Szolwinski, G. Harish, P. A. McVeigh, and T. N. Farris. The role of fretting crack nucleation in the onset of widespread fatigue damage : Analysis and experiments. In *FAA-NASA Symposium on the Continued Airworthiness of Aircraft Structures*, Atlanta, Georgia, 1996.

[27] P. A. McVeigh and T. N. Farris. Finite element analysis of fretting stresses. *Journal of Tribology*, 119:in press, 1997.

[28] R. D. Mindlin and H. Deresiewicz. Elastic spheres in contact under oblique forces. *Journal of Applied Mechanics*, pages 327–344, Sep 1953.

An Experimental Study of Fretting Fatigue Crack Nucleation in Airframe Alloys: A Life Prediction and Maintenance Perspective*

Mr. Matthew P. Szolwinski, Mr. G. Harish, and Prof. Thomas N. Farris
School of Aeronautics & Astronautics
Purdue University
West Lafayette, IN 47907-1282

Prof. Takahide Sakagami**
Department of Mechanical Engineering
Osaka University
Osaka 565 Japan

INTRODUCTION

Consideration of the localized details of the stick/slip interface behavior known as fretting is crucial to those interested in assessing the impact of this damage process on the lifetime of contacting structural components. This stick/slip phenomenon arises when the sliding force applied to one of the contacting bodies is less than the global frictional force required to cause gross relative motion of the surfaces. The near-surface contact stresses, strains and surface microslip drive the synergistic triad of wear, corrosion and fatigue damage phenomena that can degrade severely the surfaces of the contacting components. Fretting-induced damage is observed widely in contacting assemblies as diversified as bearings (Hutchings, 1992), the dovetail notch/turbine blade pair (Lindley & Nix, 1994) and mechanically-fastened joints, both structural (Hattori, 1994) and biological (Forsyth, 1981).

Interest in the role of fretting in fatigue crack formation has been recently re-catalyzed by the organizations and individuals concerned with maintaining the fleets of aging aircraft—both military and civilian. Catastrophic failures of critical structural members can occur due to the interaction and subsequent rapid linkage of small and many times undetectable cracks emanating

from at and around the fastener/sheet interfaces in aircraft joints. This damage state, dubbed widespread fatigue damage (WFD), was cited as the cause of the in-flight disintegration of a portion of an Aloha Airlines 737 fuselage section in 1988 (Hackett, 1988) and has been reported along with evidence of fretting wear and corrosion products in teardown analyses of in-service aircraft (Hoeppner et al., 1996).

Of course, any attempt to understand the mechanics of crack nucleation under the influence of fretting must address the nature of the cyclic contact stresses and strains and the intimately-related tribological characteristics of the contacting surfaces. Szolwinski and Farris (1996) present closed-form analytical expressions for the cyclic stresses and strains induced in both two- and three-dimensional fretting contact. Evaluation of these expressions over a wide range of loading parameters highlights the presence of a tensile peak in the tangential stress at the edge of contact. In light of experimental observations both presented in the literature (Nowell & Hills, 1990) and reported in fretting fatigue experiments conducted by the authors (Szolwinski, et al., 1995, Szolwinski et al. 1996) in which cracks were observed to nucleate at the trailing edge of contact, it is proposed that this tensile stress can be used to predict fretting crack nucleation.

The coefficient of friction at the interface of the contacting surfaces is an important factor in both the distribution and magnitude of the fretting surface and subsurface contact stresses, including this peak in the tangential stress at the trailing edge of contact. The effective global coefficient of friction, of course, is related to the nature of the contact surfaces. The combination of cyclic contact stresses and surface microslip wearing the surfaces and the accumulation of corrosion products in the contact region results in an increase in the coefficient of friction at the contact surfaces as fretting load cycles accumulate. Thus, quantifying accurately the evolution of friction coefficient under the influence of fretting contact is required in characterizing accurately the stress field responsible for nucleating fatigue cracks.

The focus of this document is to present experimental results capturing the evolution of friction under a range of fretting conditions. Of particular interest is the use of a multi-element infrared camera to measure contact temperature changes due to both frictional heating and thermoelastic effects. Results from these efforts are then utilized as an input to work targeted at

validating a fretting crack nucleation life prediction method with a recently-completed set of fretting fatigue experiments using 2024-T351 aluminum.

CHARACTERIZATION OF THE EVOLUTION OF FRICTION COEFFICIENT UNDER THE INFLUENCE OF FRETTING

Several researchers have observed the increase in friction coefficient under the influence of fretting wear. In most common types of fretting experimental setups (see Attia/Waterhouse, 1992 for several in-depth presentations of various types of fretting test methods and equipment), increases in friction coefficient at the contact surfaces are reflected in associated increases in the tangential or sliding forces measured in the experiment. Such observations were reported in early studies of fretting in steel (Endo, et al., 1974), with the tangential force increasing rapidly during the first few load cycles of the tests to a nearly-stabilized level for the duration of the test.

Vingsbo and Söderberg (1988) and Vincent (1994), in work designed to capture graphically varied regimes of fretting conditions due to evolution in friction coefficient, introduce the notion of a fretting map. This tool correlates loading conditions and fretting cycles with modes of stick/slip behavior for qualitative prediction of material response. Of particular interest in many fretting experimental setups and structural components is the so-called "mixed regime" of fretting contact, characterized by gross sliding early in the test or service life, with the eventual evolution of stick/slip conditions driven by the wear-induced growth in frictional coefficient.

In two separate series of tests conducted with fretting in aluminum alloys, Hoeppner, et al. (1996) and Hills, et al. (1988) report similar trends in tangential force measurements. Global friction coefficients are reported as the ratio of measured tangential force to applied normal force for a condition of gross sliding. Note that the investigators in the former set of experiments measured a condition of slip throughout the contact area, not stick/slip conditions. Under these conditions, stabilized ratios of tangential to normal forces ranged from 1.0 to over 2.0.

The experimental setup (illustrated schematically in Figure 1 and presented in greater detail elsewhere, Szolwinski, et al., 1995) used in the current investigation generates fretting conditions falling within the mixed regime, more similar to those present in the experiments of Hills, et al (1988). Carefully-controlled and monitored fretting contact is established between cylindrical fretting pads mounted in a loading chassis and opposing flat faces of a traditional "dog bone" specimen clamped between grips of an Instron 22 kip servo-hydraulic load frame with digital controller. As the lower grip/actuator pair applies a sinusoidal waveform, the chassis serves to induce an in-phase oscillatory tangential load on the fretting pads. A custom-designed supervisory and control data acquisition (SCADA) system is used to monitor the array of analog
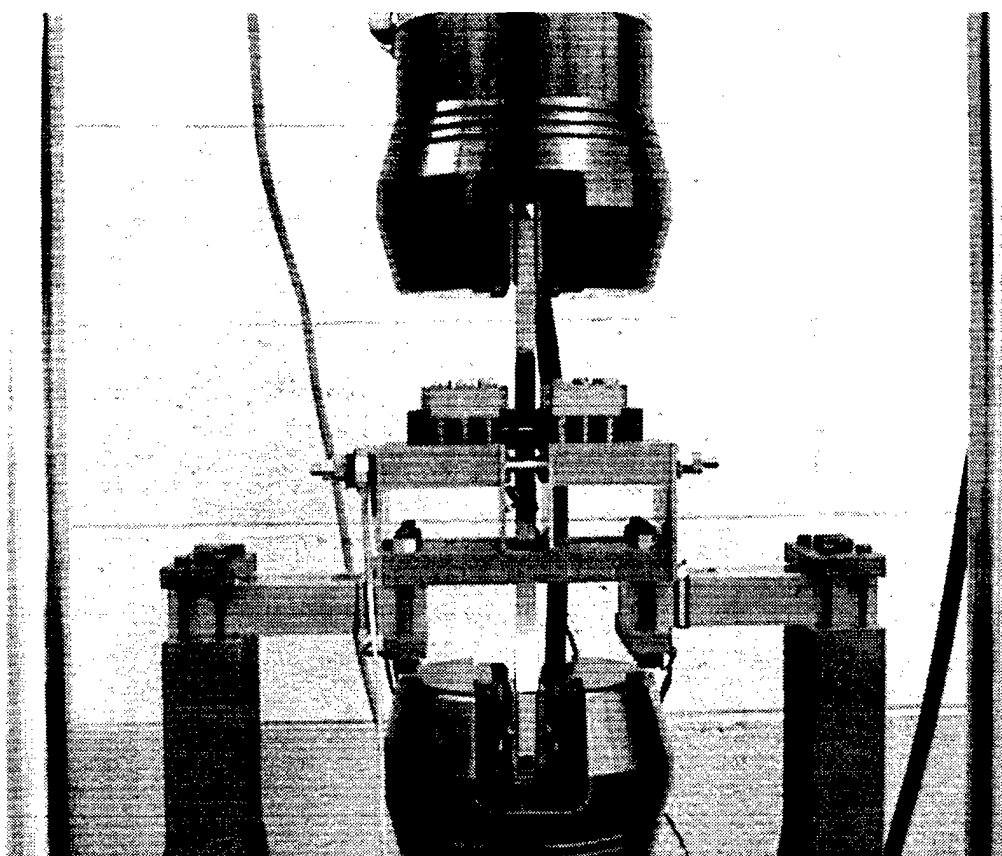
Figure 1: A photograph of the fretting fatigue test fixture.

and digital data signals providing load and displacement information required to characterize the contact stress field and test conditions. These include the normal and tangential loads applied to

the pads, bulk loading applied to the specimen, and actuator displacement. An integrated suite of virtual instruments with graphical user interfaces (GUI) powered by National Instruments LabVIEW running on a personal computer allows for on-line, real-time control, monitoring and post-processing of experimental conditions as measured by the array of analog and digital sensor output shown in Figure 2.
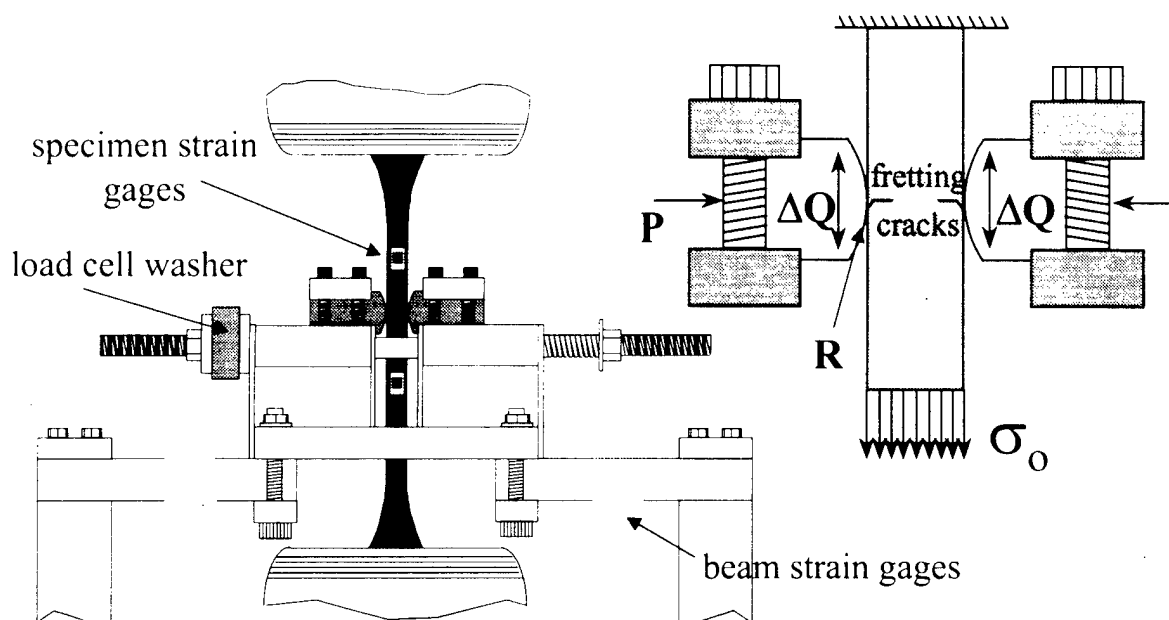
Figure 2: Schematic of forces involved in fretting experiments. P is normal load applied to pads of radius R, Q is tangential load on pads and σ_o is bulk stress amplitude.

Table 1 presents the loading parameters used in the investigation of friction coefficient evolution. Pad and specimen preparation involved treatment of the surface with sandcloth (300

Table 1: A summary of geometric and loading parameters involved in the evolution of friction experiments.

Parameter	Sequence 1
Normal load, P (lb)	1200
Steady-state tangential/normal load (Q/P)	0.39
Bulk stress amplitude, σ_o (ksi)	12
Pad radius, R (in)	5

grit followed by 600 grit) followed by a final polishing step with a cloth wheel and wax-based rouge. Average roughness (R_a) values of the pads were in the range 8 to 12 μin. It is noted that while no standard for fretting tests exists currently, the values of surface roughness for the pads and specimens fell near the range mandated by the ASTM standard for sliding wear tests (ASTM G 115-93).

After establishing contact between the pads and specimen faces, a constant-amplitude bulk load 10 Hz waveform corresponding to a bulk stress amplitude of 12 ksi was applied to the specimen. A monotonic increase in tangential force was observed for nearly the first 50 cycles of each test, as conditions of gross sliding dominated the contact. After saturation of the tangential force and application of a prescribed number of total cycles, the constant-amplitude waveform was halted and followed with application of a 2 Hz waveform that increased in amplitude at a rate of 100 pounds/cycle. Cessation of the test occurred upon detection of gross sliding corresponding to a rapid decrease in the applied tangential force waveform. It should be noted that the use of the increasing amplitude waveform, rather than the monotonic ramp loading employed by Hills, et al. (1988), was chosen to detect the onset of sliding during conditions of cyclic fretting loading rather than monotonic fretting loading.

Subsequent analysis of the applied loads at the onset of gross sliding during application of the dithered waveform allowed for determination of the effective coefficient of friction, μ_{eff}, at the contact interfaces as $\mu_{eff} = Q/P$. Using this approach the evolution of effective frictional coefficient versus cycle number is presented in Figure 3. The data during the initial 50 cycles is "continuous," as gross sliding occurs and the friction coefficient may be determined cycle to cycle. The average coefficient of friction rises from an initial value of 0.15 to a stabilized value around 0.50. A natural-log based fit for the friction rise under stick/slip conditions is provided in Figure 3 for the range $50 < N < 1000$.
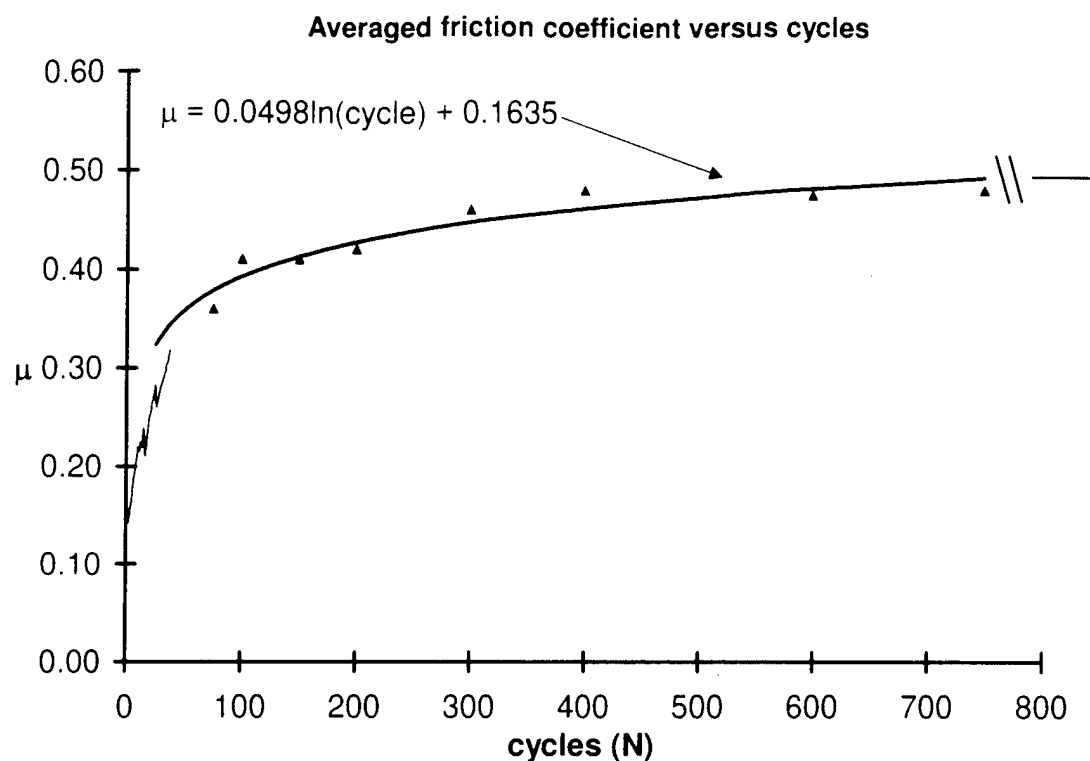
Figure 3: A plot of the average friction coefficient versus cycles obtained from the sequence 1 friction experiments.

The surface roughness in the slip zones shows a localized increase, as shown in a profilometer (form Talysurf) trace of a fretting pad surface after a fretting fatigue test (Figure 4). It is logical to expect that the coefficient of friction in the slip zones attains a higher value than that in the region of stick due in part to this increase in surface roughness. Hills & Nowell (1994) offer a method to estimate the slip zone coefficient from measurement of μ_{eff}. Following this approach, the steady-state value of effective friction coefficient of 0.50 is used to estimate a slip zone coefficient of friction value of $\mu_{slip} \sim 0.65$. This value is used in calculating the distribution of surface tractions and resulting contact stress field in the fretting fatigue crack nucleation model described later.
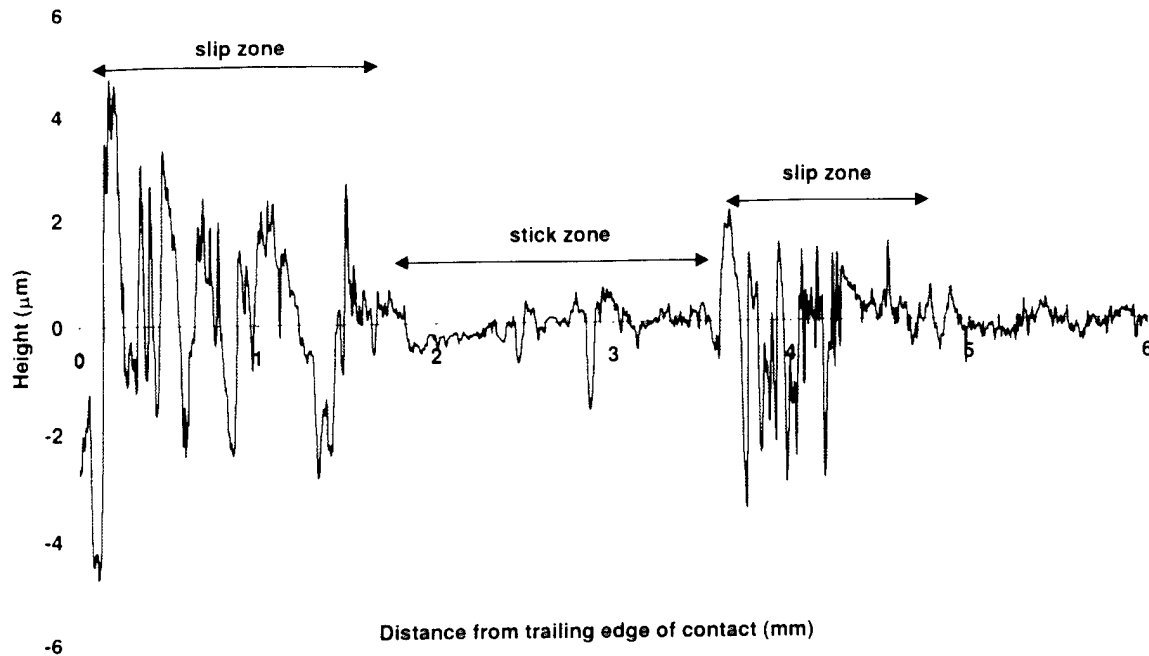
Figure 4: Profilometer trace of the surface of a fretting pad from a fretting fatigue test. Note the increase in surface roughness in the slip zones as demarcated on the graph.

Infrared Thermography

Additional verification of the mixed regime conditions evidenced by the previous results was performed with a powerful new tool for in-situ, non-invasive measurement of temperature fields. While others (Weick, et al, 1994) have performed temperature measurements of material under fretting conditions, the contact was between ceramic specimens and a sapphire indenter.

The setup, displayed in Figure 5, centers around a modular forward looking infrared (FLIR) sensor manufactured by Amber Technologies that relies on an InSb focal plane array to convert thermal radiation into intensity values with a sensitivity that corresponds to temperature changes of 0.025 K. To correlate the intensity values with temperatures, a flat black aluminum plate with attached thermocouple was moved through a heating and cooling cycle, while intensity images were captured with the camera. The resulting calibration curve correlating intensities
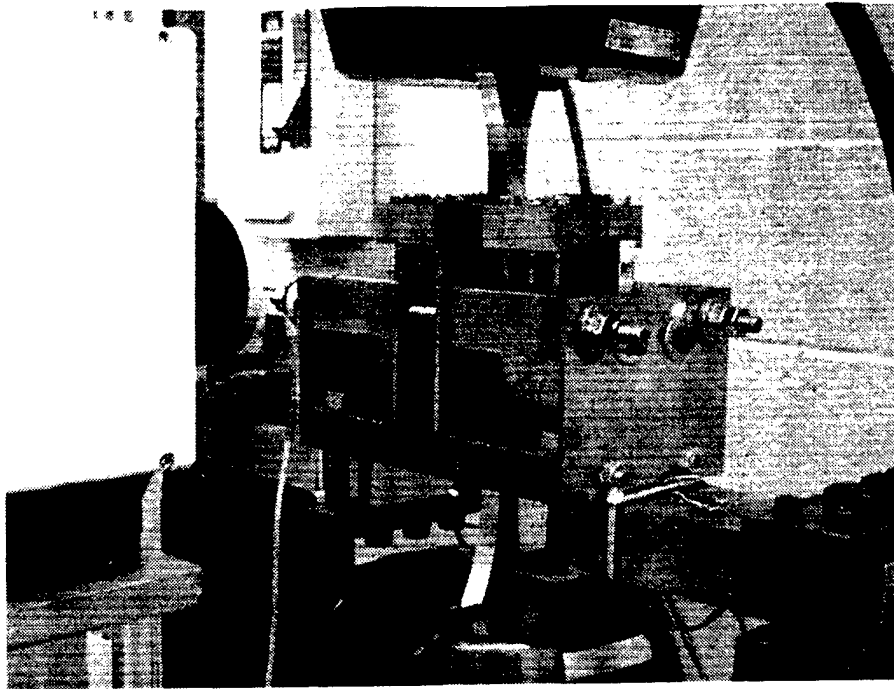
Figure 5: A photograph of the experimental setup used to measure contact temperatures arising from mixed-mode fretting contact.

with thermocouple measurements was used to generate the sequence of temperature maps presented in Figures 6 and 7. In the current experimental setup, temperature changes can be expected from two sources: (1) thermoelastic effects or temperature changes related to the change in principal strains in the material, and (2) frictional heating due to the shear traction at the contact surface.

In the fretting experiments, the camera was focused on an area of approximately 1 cm^2 around the pad/specimen interface at the onset of a fretting fatigue test conducted at 2 Hz in a climate-controlled laboratory. To increase the emissivity of the exposed surfaces, a thin coating of flat black spray paint was applied to the surfaces. Ten frames of intensity data were captured per cycle through the first 150 cycles of the test and subsequently post-processed into two-dimensional arrays of pixel intensity values. In each of the images, the horizontal line in the middle of the image is a marker band engraved on the center of the fretting pad to demarcate the middle of the contact zone. Increases in temperature correspond to higher intensities (brighter

pixels). The thermoelastic effect is particularly pronounced near the bottom of the specimen (left side of the images) due to the cyclic bulk loading. Tension in the specimen results in a global decrease in temperature and darkening of the specimen, while compression leads to a temperature increase and subsequent brightening. No such effect is observed in the pad as it is not subjected directly to bulk loading.

The frictional effect, however, is readily observed in images of the pad captured from the early stages of the fretting test (cycle 15, right area of Figure 6) in which conditions of gross sliding dominate the contact. The images reveal a patch of heating centered at the middle of the contact region with the greatest temperature rises appearing at the point of maximum magnitude of tangential loading on the pads. The loads correspond to the maximum bulk compression (Figure 6(a)) and tension (Figure 6(b)) in the specimen and maximum thermoelastic temperature effects in the specimen. It is important to note that even under these conditions, the maximum cyclic temperature rise is only on the order of 1°C, miniscule with respect to levels required to initiate any phase changes in metallic materials and certainly well below the 50-100°C range

(a)   (b)
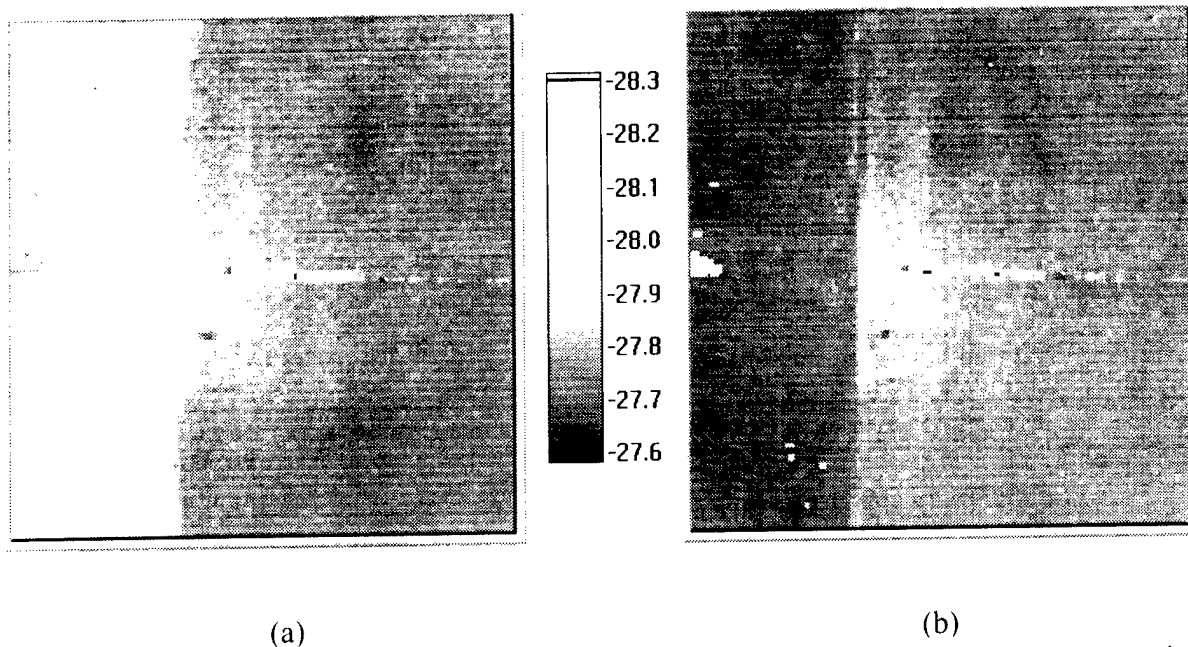
Figure 6: Temperature maps taken during cycle 15 at points of maximum bulk compression (a) and bulk tension (b) in the specimen. The frictional heating associated with gross sliding at the surface causes a temperature rise over the entire length of the contact surface. The image area is 10.7 mm by 10.7 mm at 128 x 128 resolution. Temperatures are expressed in °C.

calculated by Attia (1994) for fretting in steel. This patch of localized heating distributed over the length of the entire contact surface can be attributed to frictional heating generated by the gross sliding behavior of the pad/specimen interface and its frequency is twice that of the applied loading.

(a)   (b)
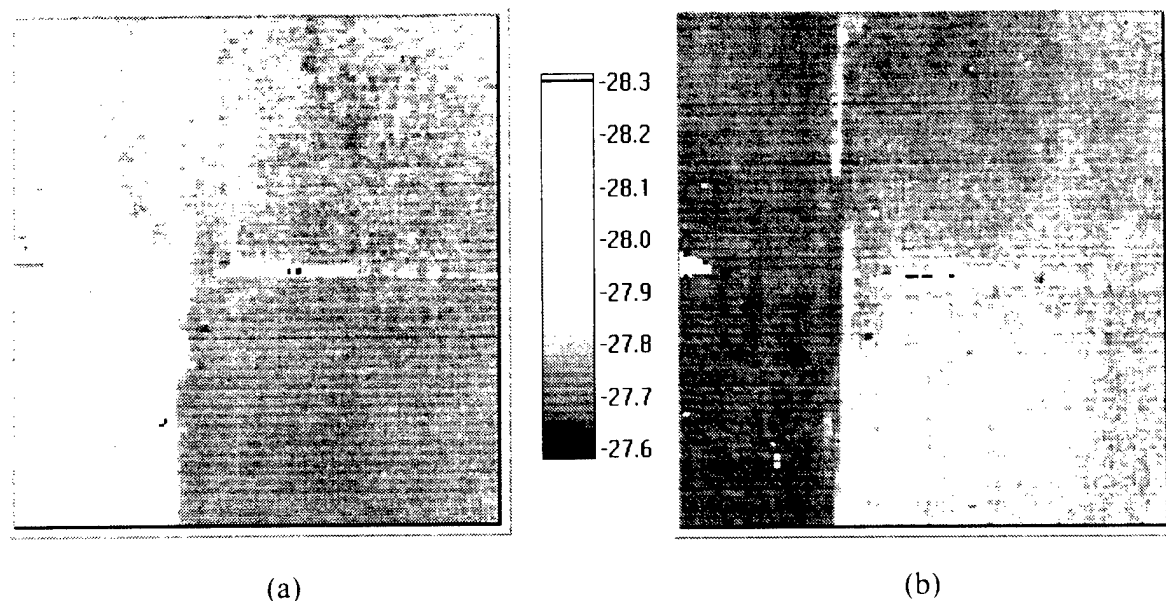
Figure 7: Temperature maps taken during cycle 150 at points of maximum bulk compression (a) and bulk tension (b) in the specimen. Gone is the distribution of heating across the entire contact area due to gross sliding. The image area is 10.7 mm by 10.7 mm. Temperatures are expressed in °C.

Images after cycle 45, though, show markedly different characteristics in the surface and subsurface temperature field, as can be discovered by comparing Figures 6 and 7. Also recall from the friction data presented earlier, evidence of global sliding disappeared around 50 cycles in each of the experiments, with the onset of stick/slip conditions. With the aid of the high-speed temperature measurements, direct visual evidence of the change in both the interfacial conditions and resulting contact stress can be captured both in-situ and in real time. The onset of the stick/slip conditions ushers in the disappearance of the intense (bright) temperature rise distributed across the entire contact surface and occurring at a frequency twice that of the bulk and tangential loading just described.

Instead, the temperature fields in the pads and specimens are dominated not by the frictional heating occurring near the positive and negative maxima in tangential loading, but rather by the thermoelastic effects due to the contact stress field.

For compressive loading in the specimen in Figure 7(a), the effective tangential load on the pad is directed upward. The contact stress field is characterized by a region of high gradients in tensile stress tangential to the surface at the trailing (lower) edge of contact and compressive tangential stresses at the leading (upper) edge of contact. The increase in tension translates into localized decreases in temperature and a darkening of trailing edge area of the pad, while the compression at the leading edge results in increases in the temperature field. At the point of maximum tension in the specimen, the direction of the tangential loading and the nature of the contact stress field are reversed, with similar effects observed in the temperature map, Figure 7(b). These thermoelastic effects mask any effects of frictional heating in the slip zones. Further details of these stress distributions are described in Szolwinski & Farris (1996) and McVeigh & Farris, (1997).

The temperature effects are exaggerated in the specimen due to the intensifying superposition of the thermoelastic temperature changes attributable to both the bulk loading and contact stresses. At the point of maximum bulk compression in the specimen (Figure 7(a)), the trailing edge of contact in the specimen experiences compressive tangential stresses due to both the bulk loading and contact, resulting in the observed temperature increases. At the point of maximum bulk tension (Figure 7(b)), a decline in measured temperature due to the bulk and contact compressive stresses is noted, as expected.

APPLICATION OF RESULTS TO PREDICTION OF CRACK NUCLEATION

In applying the results of these qualitative and quantitative data on the frictional behavior at the surface, it is critical to note that this region of intensive tensile stress at the trailing edge of contact corresponds exactly to the observed site of crack nucleation in the fretting fatigue tests conducted with this experimental setup. And as stated earlier, the coefficient of friction in the

slip zones determined from the initial series of tests is responsible for both the magnitude and distribution of the contact stresses driving the crack nucleation at and near the surface.

Statistically-designed experiments performed to correlate the value of tensile peak in stress at the trailing edge of contact and subsequent crack nucleation has been completed
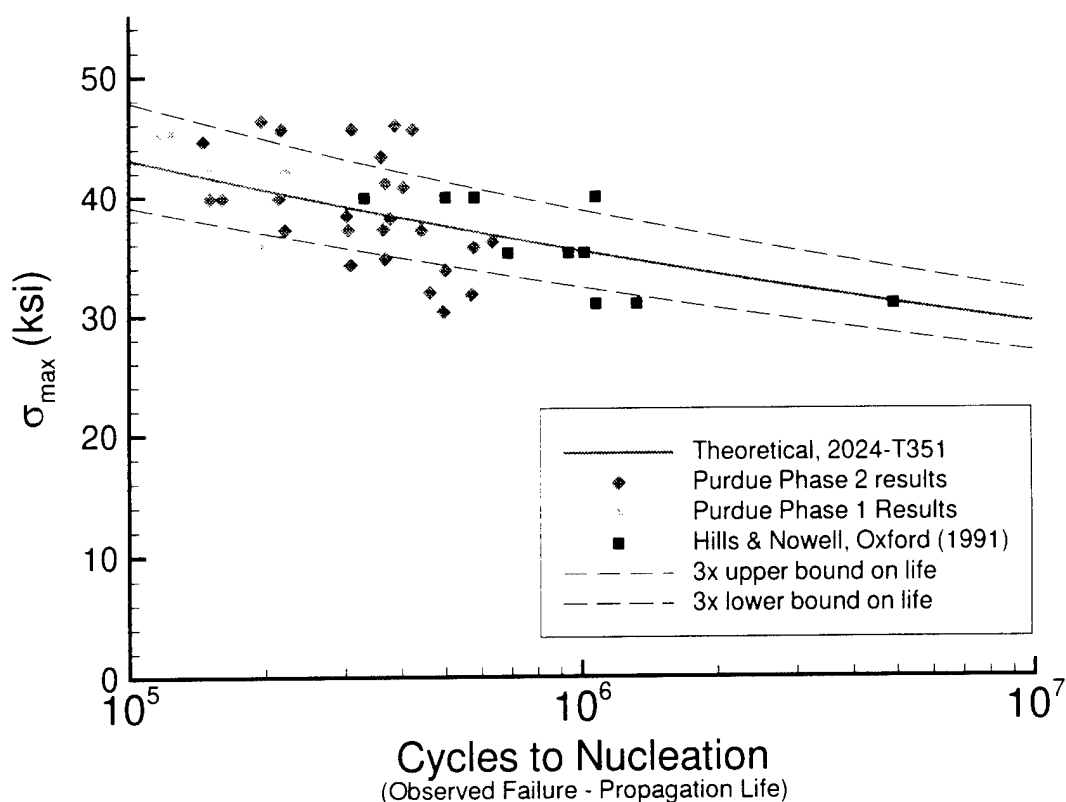
Figure 8: A comparison of theoretical fretting crack nucleation life predictions and estimated nucleation lives from experiments conducted by the authors ($\mu = 0.65$) and in the literature. Efforts are underway to apply a similar model to titanium engine alloys.

recently, with the results presented in Figure 8. Note that σ_{max} is controlled by several experimental parameters including P, σ_o and R. A comprehensive statistical analysis of the data is underway currently, to establish confidence limits in the predictive capability of the multiaxial fatigue model used to generate the life predictions.

CONCLUSIONS

Controlled fretting fatigue tests are used to track the evolution of friction coefficient and corresponding changes from gross sliding to stick/slip conditions. These results are corroborated by full-field infrared thermography that also illustrates the effect of changing friction coefficient on the stress field. The steady-state friction coefficient is used to calculate stresses that are combined with a multiaxial fatigue model to predict fretting crack nucleation lives. The predicted lives correlate well with measurements of failure lives less estimates of propagation lives. Ongoing work involves finite element analysis that includes the thermoelastic effect for combination with infrared thermography to substantiate the relative locations of stick and slip. In addition, work on a modified experimental setup is in progress for a series of fretting fatigue tests on a titanium alloy common in aircraft engine blades, Ti 6 Al V4.

REFERENCES

Hutchings, I. M., *Tribology*, CRC Press, Boca Raton, 1992.

Lindley, T. C. and Nix, K. J., "An Appraisal of the Factors Which Influence the Initiation of Cracking by Fretting Fatigue in Power Plant", in *Fretting Fatigue*, ESIS 18 (Edited by R. B. Waterhouse and T. C. Lindley), Mechanical Engineering Publications, Sheffield, England, 1994, 239-256.

Forsyth, P. J. E., "Occurrence of Fretting Fatigue Failures in Practice," in *Fretting Fatigue* (Edited by R. B. Waterhouse), Applied Science Publishers, London, 1981.

Hattori, T., "Fretting Fatigue Problems in Structural Design", in *Fretting Fatigue*, ESIS 18 (Edited by R. B. Waterhouse and T. C. Lindley), Mechanical Engineering Publications, Sheffield, England, 1994, 437-451.

Hackett, G., "Whoosh! She Was Gone," *Newsweek*, 9 May 1988, 16-17.

Hoeppner, D. W., Elliot III, C. B., and Moesser, M. W., "The Role of Fretting Fatigue on Aircraft Rivet Hole Cracking," DOT/FAA/AR-96/10, Federal Aviation Administration Technical Report, October 1996.

Szolwinski, M. P. and Farris, T. N., "Mechanics of Fretting Fatigue Crack Nucleation," *Wear*, 198 (1996), 93-107.

Nowell, D. and Hills, D. A., "Crack Initiation Criteria in Fretting Fatigue," *Wear*, 136 (1990), 329-343.

Szolwinski, M. P., Harish, G. and Farris, T. N., "Experimental Observations of the Effect of Contact Parameters on Fretting Fatigue Crack Nucleation," in *Proceedings of the 1995 USAF Structural Integrity Program Conference*, San Antonio, 1995, 237-265.

Szolwinski, M. P., Harish, G., McVeigh, P. A. and Farris, T. N., "The Role of Fretting Crack Nucleation in the Onset of Widespread Fatigue Damage: Analysis and Experiments," in *Proceedings of the 1996 FAA-NASA Symposium on the Continued Airworthiness of Aircraft Structures*, Atlanta, Georgia, 1996, in press.

Standardization of Fretting Fatigue Test Methods and Equipment, ASTM STP 1159 (Edited by M. H. Attia and R. B. Waterhouse), ASTM, Philadelphia, 1992.

Endo, K., Goto, H. and Fukunaga, T., "Behaviors of Frictional Force in Fretting Fatigue," *Bulletin of the JSME*, 17 (1974), 647-654.

Vingsbo, O. and Söderberg, S., "On Fretting Maps," *Wear*, 126 (1988), 131-147.

Vincent, L., "Materials and Fretting," in *Fretting Fatigue*, ESIS 18 (Edited by R. B. Waterhouse and T. C. Lindley), Mechanical Engineering Publications, Sheffield, England, 1994, 323-338.

Hills, D. A., Nowell, D. and O'Connor, J. J., "On the Mechanics of Fretting Fatigue," *Wear*, 125 (1988), 129-146.

Hills, D. A. and Nowell, D., *Mechanics of Fretting Fatigue*, Kluwer, Dordrecht, 1994.

Weick, B. L., Furey, M. J. and Vick, B., "Surface Temperatures Generated with Ceramic Materials in Oscillating/Fretting Contact," *Journal of Tribology*, 116 (1994), 260-267.

Attia, M. H., "Friction-Induced Thermo-Elastic Effects in the Contact Zone Due to Fretting Action", in *Fretting Fatigue*, ESIS 18 (Edited by R. B. Waterhouse and T. C. Lindley), Mechanical Engineering Publications, Sheffield, England, 1994, 307-319.

McVeigh, P. A. and Farris, T. N., "Finite Element Analysis of Fretting Stresses," *Journal of Tribology*, 1996, in press.

This set of proofs shows author's marks
or queries. Author or Editor will please
indicate all corrections on the set.

Page Proofs

Mechanical Properties of Aircraft Materials Subjected to Long Periods of Service Usage

J. N. Scheuring
School of Aeronautics and Astronautics,
Purdue University,
West Lafayette, IN 47907-1282

A. F. Grandt, Jr.
Professor, School of Aeronautics
and Astronautics.
Purdue University,
West Lafayette, IN 47907-1282

This paper evaluates changes in the behavior of aircraft materials which result from aging and/or corrosion that occurs during long periods of service usage. The primary objective was to determine whether damage tolerant analyses for older aircraft should employ updated properties that more accurately represent the current state of the material, or if the virgin material properties continue to properly characterize the aged/corroded alloy. Specifically, tensile stress-strain curves, cyclic stress life (SN) tests, and fatigue crack growth tests were used to characterize the "aged aircraft" material. These properties were compared with handbook properties for virgin material of the same pedigree. The aluminum alloys tested were obtained from fuselage and wing panels of retired KC-135 aircraft. Computer controlled tests were conducted using specimens machined from the retired aircraft components. Different configurations were used to observe the effects of aging and/or corrosion on material behavior. In the crack growth specimens, various levels of corrosion were observed. thus the crack growth rates could be categorized as a function of the level of corrosion present. The SN and da/dN-ΔK curves for the "aged" only materials were compared with the fatigue properties of virgin material of the same alloy. Similar comparisons were performed for the tensile stress-strain properties.

Introduction

Aircraft fleets are being required to fly beyond their original intended life expectancies. Continued operation requires updated analyses to determine how much longer these aircraft can be safely flown. A number of these analyses require basic mechanical properties, such as crack growth rate, Young's modulus, etc., as an input. One question that arises during these analyses is whether the original material properties employed for design calculations continue to adequately describe the current state of the material. If, for example, the material properties have changed due to chronological aging, corrosion, surface roughness, or other factors, analyses regarding the future integrity of the structure could be in error. Ideally, one would get the actual mechanical properties from the component being studied; however, this is not always feasible or even possible in some cases. Thus the primary question of this study is "Has service usage significantly changed the mechanical properties of aircraft materials?"

While much work has been performed in obtaining mechanical properties for aircraft aluminum alloys, they are based on material that is in a virgin state. Several studies performed in the past that dealt with materials with prior service usage of aircraft alloys are Gruff and Hutcheson (1969) and Everett (1975). Gruff and Hutcheson primarily looked at the effects corrosion and service usage on the stress-life properties of joined and unjoined panels of various 2xxx and 7xxx aluminum alloys in sheet form from an RA-5C aircraft and concluded that the lives of the materials with prior service usage were shorter than those of virgin material from published literature of the time. Everett was concerned with the effects of service usage of 7075-T6 plate and 7178-T6 extrusion from a C-130B transport center wing box with 6385 flight hours. In Everett's work, he was looked at the following mechanical properties and compared them to current literature of the time period: fatigue crack

growth rates, fracture toughness, tensile properties, and notched and unnotched fatigue strengths. He indicated that there were no significant differences in the mechanical properties between the service and new materials.

The purpose of this project is to characterize basic mechanical properties of materials that have seen prior service usage. In this study, material from large transport aircraft, aluminum alloys in sheet form, are analyzed after many hours of service usage to determine the effects, or lack thereof, that the usage has had on the mechanical properties. Not included in this study are the effects of joints, strengtheners, rivets, etc. Within the scope of this project, the main factors of interest are the effects of natural aging, service loading, and corrosion. The monotonic tensile stress-strain, cyclic axial stress-life, and fatigue crack propagation properties were measured in large transport aircraft alloys that had seen long periods of service usage. Since the original mechanical properties of these specific sheets of material are not known, comparisons are made here with handbook values for the alloys in question. The goal was to determine if these "average" mechanical properties are still representative of structural components which have seen extended service. In the event that there were significant degradation in material behavior, engineers would be required to perform extensive testing programs to quantify the current mechanical state of materials in older aircraft.

Material

The materials considered here are the 2024-T3, 7075-T6, and 7178-T6 aluminum alloys, typical of older, large transport aircraft materials. Six panels were obtained from three different aircraft: a retired C/KC-135; a retired Boeing 707-320C which had seen 20 years of service consisting of 19,967 flight cycles and 46,685 flight hours; and an active C/KC-135. The results completed to date for the 2024-T3, 7075-T6, and 7178-T6 aluminum alloys are presented in this paper. Although these materials were taken primarily from the wing and fuselage panels of the aircraft, access panels and doubler structures were also tested. A brief summary of the panels is given in Table 1.

Table 1 Brief summary of the materials in this study tested to data

Panel	Material	Thickness	Aircraft	Corrosion
Fuselage Lap Joint	7075-T6	2.057 mm (0.081 in)	Retired KC-135 #62-0291	Light
Up. Wing Skin Joint	7178-T6	5.08 mm (0.20 in)	Retired 707-320C	Light
Access	2024-T3	1.524 mm (0.06 in)	Active KC-135 xxxx-2618	Moderate
Fuselage	2024-T3	1.143 mm (0.045 in)	Active KC-135 xxxx-2618	Moderate
Doubler	2024-T3	1.27 mm (0.05 in)	Active KC-135 xxxx-2618	Moderate

The materials were tested in one of three surface conditions. The first condition, Type I, was the chronologically aged and in situ condition in which the material was taken from a joint or area that was visibly corroded, and the material was not altered from the as received condition. In this study, the term "aged" will be used to denote material that has had prior service usage; not to be confused with the metallurgical "aging" process. The second surface finish, Type II, was the condition in which material was taken from areas in which no corrosion was visible and, again, the surface was left in the as received condition. The third condition, Type III, employed specimens that had all defects and corrosion removed by a polishing procedure.

A chemical analysis was used to determine potential, but unexpected, changes in the material composition during prior service usage in addition to verifying that the alloy was the correct alloy. A Wavelength Dispersive Spectroscopy (WDS) elemental characterization was employed to determine elemental weight percent (WT percent) of the aged alloys. The WT percent was then compared with published handbook values such as the *ASM Handbook* (1990). The elemental breakdown of the alloy is given as a function of position across the thickness of the material, Scheuring (1995). Measurements were taken within 30 microns of the alloy-corrosion or alloy-paint interface while the alloy only measurements were taken from the center of the thickness of the specimen. In comparing the 2024-T3, taken from the access panel described in Table 1, the only large WT percent difference occurs in silicon, WT percent$_{AGED}$ = 0.08 percent in comparison to WT percent$_{HDBK}$ = 0.5 percent. The 7075-T6 fuselage WT percent's were all within acceptable ranges for this material, with the most noticeable aberration being the main alloying element, zinc, with a WT percent near the maximum range value. The main alloying elements in the 7178-T6 upper wing skin, copper and zinc, were slightly lower than the lower bounds of the nominal range of the handbook values, see Scheuring (1995) for complete details on the chemical composition analysis.

Specimens were taken primarily from the joints, as this is where the most severe surface corrosion was observed. However, specimen size limitations were caused by rivet holes commonly found in aircraft structures. The monotonic tensile specimens were ASTM E-8 (1993) Standard Subsize Axial Dogbone specimens. To perform stress-life (SN) tests, constant radius specimens, ASTM E-466 (1993), were employed for the unnotched axial stress-life (SN) tests. The SN specimens were flat, rectangular cross-section specimens that were narrowed from 12.7 mm (0.50 in.) to 6.35 mm (0.25 in.) with a radius of curvature of 50.8 mm (2.0 in.). For the fatigue crack growth tests, ASTM E-647 (1993) standard compact tension specimens

with a width of approximately W = 28.19 mm (1.11 in.) were used. The thin thickness of the aircraft components examined limited the size of the CT specimens. All crack growth specimens met the specimen width/thickness requirements, except for specimen 1612N1-CT6 which slightly exceeded (by 0.08 percent) the maximum ASTM width/thickness for CT specimens. Table 2 summarizes the tests completed to date as well as the pertinent geometric dimensions of the test specimens.

As with any material with corrosion, thickness measurements become important. In this study, several thickness measurements were utilized. In Fig. 1, the various thickness measurements utilized are represented. The first is the overall outer edge to outer edge measurement made with a digital micrometer (± 0.0005 in.), which includes the corrosion products, paint, and load bearing alloy. The second type of thickness measurement is similar to the first, but rather than using a digital micrometer, a 40× optical microscope and digital traverse (± 0.00005 in.) were employed. The final type of thickness measurement is also an optical measurement, but does not include the corrosion products and the paint, i.e., only measures the thickness of the load bearing alloy. It was determined that the most reliable thickness measurement was the optical measuring only the load bearing alloy. For the CT crack growth specimens, the thickness measurements were averaged over the surface where actual fatigue crack growth occurred, see Fig. 1, which did not including the precracking or the fracture regions. The inherent variability of thickness of the corroded material was investigated utilizing an immersion ultrasound, but no new information was obtained.

In the cyclic stress-life and fatigue crack growth tests, the temperature was 22.2°C + 1.1°C (72°F $\pm$ 2°F) while the relative humidity was maintained above 85 percent. These environmental conditions were chosen to coordinate with other concurrent USAF Aging Aircraft Studies, Nieser (1994). To achieve the environmental testing parameters, environmental chambers were employed. The relative humidity was checked in the chamber with the use of a hygrometer in the chamber itself while humid air from a bubbler (Scheuring, 1995) was pumped in to maintain the high relative humidity.

Results and Discussion

Tensile tests were utilized as one type of test to observe the behavior of the alloys. Standard ASTM E-8 tensile tests were

Table 2 Test matrix of aluminum alloys tested to date for monotonic stress-strain, unnotched SN, and crack growth tests

Material	Crack Growth	SN Unnotched	Monotonic
2024-T3	22 Compact Tension	43 Constant Radius	5 Axial Dogbone
Width	29.19 mm (1.11 in)	6.35 mm (0.25 in)	6.35 mm (0.25 in)
Thickness	2.032 mm (0.08 in)	1.14-2.07 mm (0.045-0.079 in)	1.778 mm (0.07 in)
Gage Length	N/A	N/A	38.1 mm (1.5 in)
7075-T6	13 Compact Tension	15 Constant Radius	9 Axial Dogbone
Width	29.19 mm (1.11 in)	6.35 mm (0.25 in)	6.35 mm (0.25 in)
Thickness	1.905 mm (0.075 in)	1.905 mm (0.075 in)	1.905 mm (0.075 in)
Gage Length	N/A	N/A	38.1 mm (1.5 in)
7178-T6	4 Compact Tension	None	5 Axial Dogbone
Width	76.2 mm (3.00 in)	none	4.877 mm (0.192 in)
Thickness	4.877 mm (0.192 in)	none	5.080 mm (0.20 in)
Gage Length	N/A	none	38.1 mm (1.5 in)

/ 940d$$jy04   04-03-97 23:55:23   asmel   ASME: J Materials

performed to determine the yield strength and the ultimate strength while the Young's modulus was determined using ASTM E-111(1993). The yield strength presented is based on the 0.02 percent Offset Yield criterion. A summary of the pertinent results is shown in Table 3 along with the expected handbook values, which are either statistical B or typical values as indicated in the table. The actual stress-strain curves can be found in Scheuring (1995) for each individual specimen. Tests were conducted on all three types of surface conditions. Type I, II, and III. All three configurations had the edges polished to remove machining effects from the specimens. No appreciable difference was found for any of the three alloys in the yield or ultimate strength, although the Young's modulus for all three materials was, on average, approximately 5 percent lower than *ASM Metal Handbook* (1990) and MIL-HDBK-5G (1994) handbook values for materials of the same pedigree.

Constant amplitude axial cyclic stress life tests were performed on the 2024-T3 and 7075-T6 alloys to observe the various effects of corrosion and aging. The flat specimens had rectangular cross-sections with a nominal gage width of 6.35 mm (0.25 in.). Specimens were again tested in one of three surface configurations; Type I, II, and III. The Type III specimens were polished to a mirror finish on all edges and faces while the other two surface configurations had only their edges polished. The machining of the edges of all the specimens was employed to try to force the specimens to fail on the surface of the specimen (which was of interest due to the corrosion on the surface) rather than the edges.

The SN results for the 2024-T3 alloy are shown in Fig. 2 along with the MIL-HDBK-5E (1987) data. Figure 3 illustrates results for tests on the fuselage panel in the three surface configurations and also test results for virgin 2024-T3 specimens. These virgin material specimens served to validate the test setup since they failed, on average, near the expected MIL-HDBK-5E (1987) handbook value of 100,000 cycles. All tests were performed at a stress ratio of $R = 0.02$ in air with relative humidity $>$ 85 percent at a temperature of 22.2°C (72°F). The applied stresses were based on the optical thickness of the specimen at the gage section, hence the stress levels were based on the load bearing material only, see Fig. 1 for clarification.

Table 3 Summary of Tensile Properties for aged aircraft materials in this study and comparison to current handbook values

2024-T3	Exp	Reference (B values)
Young's Modulus	68.5 GPa (9.94 Msi)	72 4 GPa (10 50 Msi)
Yield Strength	333 MPa (48.4 ksi)	276 MPa (47 0 ksi)
Ultimate Strength	440 MPa (63.8 ksi)	421 MPa (63.0 ksi)
Ref	MIL-HDBK-5G, 1994	
7075-T6	Exp	Reference (B values)
Young's Modulus	67.0 GPa (9.72 Msi)	71 0 GPa (10.3 Msi)
Yield Strength	507 MPa (73.5 ksi)	462 MPa (69.0 ksi)
Ultimate Strength	563 MPa (81.7 ksi)	524 MPa (77.0 ksi)
Ref	MIL-HDBK-5G, 1994	
7178-T6	Exp	Reference (Typical)
Young's Modulus	70 1 GPa (10.16 Msi)	71 7 GPa (10.40 Msi)
Yield Strength	542 MPa (78.6 ksi)	538 MPa (78.0 ksi)
Ultimate Strength	590 MPa (85.6 ksi)	607 MPa (88.0 ksi)
Ref	Metals Handbook, Vol. 2, 1990	

It is observed that Type III specimens failed on average, at or past the expected handbook limit while specimens with a non-smooth surface, Type I and Type II, failed at approximately one quarter of the expected lifetime. These tests indicate that, for unnotched specimens, the overriding factor is surface finish (as is influenced by the presence of corrosion and other surface defects) rather than the age of the material. As can be seen in Fig. 3, the fuselage panel specimens exceeded the expected failure value when the surface was polished, but specimens from the same panel, nonpolished surface finish, failed at noticeably lower number of cycles. In Type I specimens, the scatter was much lower than the Type III and virgin material. This is due to the nature of the SN test itself. Since the Type III specimens already had stress concentrators in the form of pits, corrosion, surface flaws, etc., it is assumed that cracks formed more rapidly than in Type I specimens.

The results for tests on different 2024-T3 panels at an applied stress level of 345 MPa (50 ksi) are shown in Fig. 4. The modern virgin material is again shown for reference. All three panels had aged and corroded specimens that failed at approximately one-quarter of the expected handbook despite different levels of corrosion present on the different panels.

A similar stress-life study was performed for 7075-T6 alloy. The results for the three configurations are shown in Fig. 5 in addition to MIL-HDBK-5E (1987) values. The specimens were tested at a maximum stress $\sigma_{max} = 345$ MPa (50.0 ksi) and load ratio $R = 0.00$. Figure 5 indicates, for this stress level and load ratio, that the surface finish is again more prominent than the age of the material. This is shown by the fact that the Type III specimens failed at an average of 83,000 cycles, the Type II specimens at 28,000 cycles, and the Type I specimens at 21,000 cycles while failure was expected at 100,000 cycles by MIL-HDBK-5E.

Also observed in this study are the fatigue crack growth rates of the 2024-T3, 7075-T6, and 7178-T6 alloys. The crack length was monitored by computer controlled compliance measurements. Compact tension specimens were one of two sizes, either
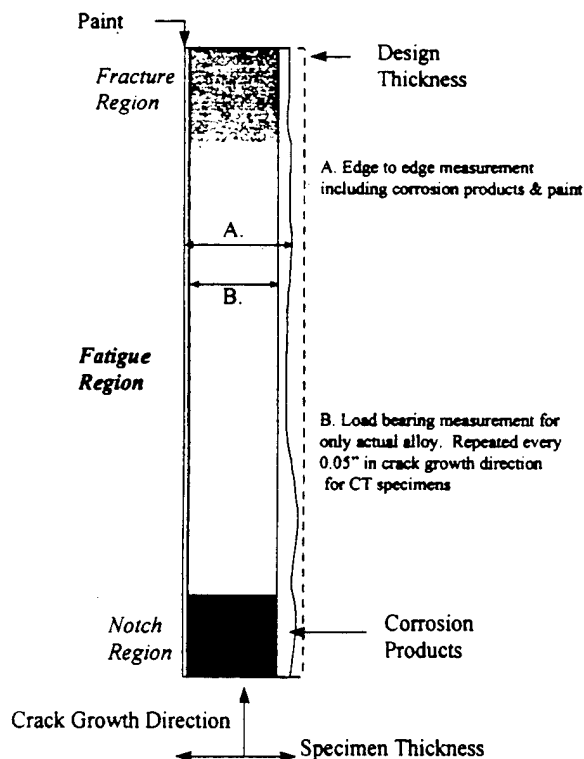

Fig. 1 Schematic of different thickness' of aged and corroded material

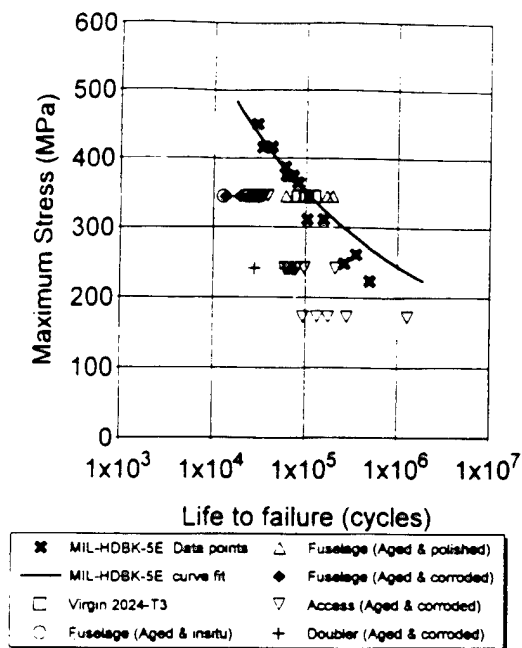/ 940d$$jy04   04-03-97 23:55:23   asmel   ASME: J Materials

Fig. 2 Results of 2024-T3 SN tests in comparison with current handbook values. Three different panels in different configurations of 2024-T3 are compared to the handbook values.
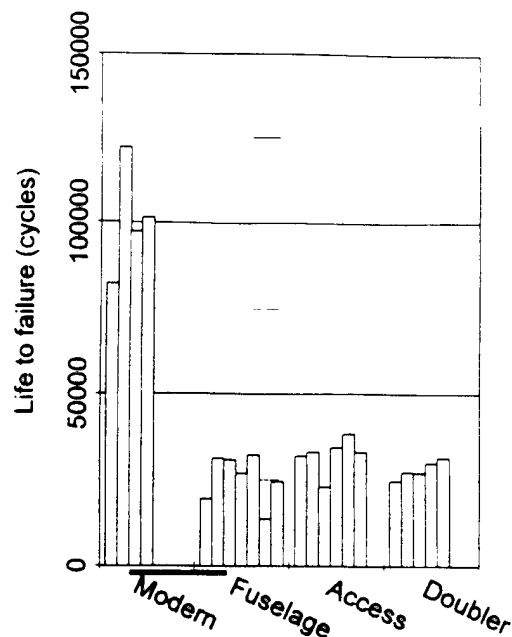

Fig. 4 Unnotched SN tests for 2024-T3. Comparison of different types of 2024-T3 panels at 345 MPa (50 ksi) and R = 0.02.

a width W = 28.194 mm (1.11 in.) for thinner panels with riveted joints, or W = 76.2 mm (3.0 in.) for thicker panels with enough material for larger Compact Tension specimens. All specimens were tested at load ratio R = 0.10 at a frequency of 10 Hz at an temperature T = 72°F ± 2°F (22.2°C + 1.1°C) and a relative humidity RH > 85 percent.

Fig. 3 2024-T3 surface roughness comparison for a single fuselage panel tested at 345 MPa (50.0 ksi) and a load ratio R = 0.02

A comparison of the fatigue crack growth results for the 7178-T6 alloy is presented in Fig. 6. The data were generated from four CT specimens, machined from a retired Boeing 707-320C upper wing skin, with a nominal thickness of 5.08 mm (0.20 in.) that showed little visible signs of corrosion or degradation. The data scatter from specimen to specimen was relatively small, as depicted by the narrow scatter band. Also shown in Fig. 6 are crack growth rates for Damage Tolerant Design Handbook (1994) data at similarly low R ratios, R = 0.02 and R = 0.05. The data generated in this study lie within the scatter of the handbook data, seeming to imply that little, if any, change had occurred in the fatigue crack growth behavior for this aged aircraft material.

Fatigue crack growth rates for "lightly" corroded 7075-T6 specimens, Type I, tested at R = 0.1 are presented in Fig. 7, along with Damage Tolerant Design Handbook data for virgin material at similar load ratios. The corrosion level at which the 7075-T6 was similar to ASTM G-34 (1987) EA levels. Hence, the specimen to specimen scatter in this alloy is larger than that of the 7178-T6 material, which showed no visible corrosion. When comparing these data to the Damage Tolerant Design Handbook, the lightly corroded material shows no appreciable degradation and lies within reasonable limits of the handbook data scatter. In addition, but not depicted, two Type I specimens were tested in dry lab air, RH = 20 ± 10 percent (the others were tested at RH ≥ 85 percent) to observe the effects of high humidity on testing, but no observable differences were found in the crack growth rates.

Figure 8 compares the data in Fig. 7 with results of three tests with specimens taken from the same panel, but polished on all surfaces to remove all visible corrosion, Type III specimens. As seen in Fig. 8, there is little difference in the fatigue crack growth rates between the two surface configurations. Thus, the "lightly" corroded 7075-T6 specimens had similar crack growth rates to polished specimens when the appropriate load bearing thickness measurement was utilized.

Figure 9 illustrates results of tests of Type I material conducted at a higher load ratio, R = 0.5, on the 7075-T6 material. Also shown in Fig. 9 are the Damage Tolerant Design Handbook data sets for various environmental conditions and specimen thickness at the same load ratio. The fatigue crack growth
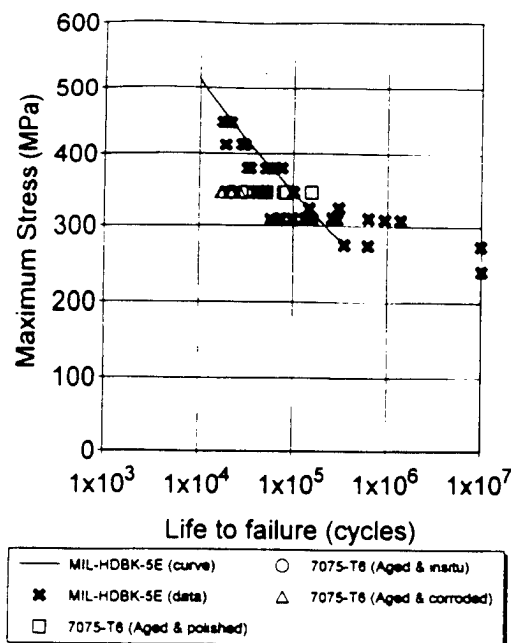
Fig. 5 SN results for 7075-T6 for one level of stress for the various configurations in comparison to the current MIL-HDBK-5E values tested at 345 MPa (50.0 ksi) and R = 0.00
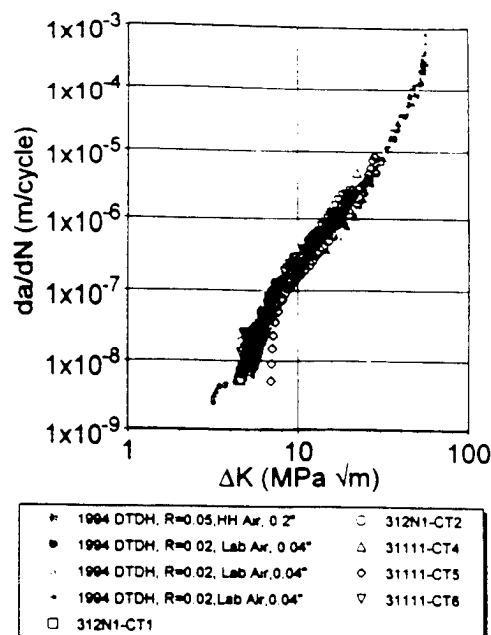

Fig. 7 7075-T6 crack growth curve comparison between this study and Damage Tolerant Design Handbook data for CT specimens that are lightly corroded

rates for the Type I specimens in this study lie within the scatter of the handbook data sets, seeming to imply that the effects of prior service usage on the fatigue crack growth rate diminish as the load ratio increases.

Figure 10 presents the results for ten 2024-T3 alloy specimens obtained from Type I panels. Data at this load ratio, R = 0.10, are compared to several handbook data sets including the *Damage Tolerant Design Handbook and Virkler* (1978), a large experimental data set of which only the upper and lower bounds are illustrated. The fatigue crack growth rates in all ΔK regimes seems to be slightly faster than the handbook values, with the

doubler panel crack growth rates faster than the access panel crack growth rates. The scatterband for the doubler structure is slightly larger than that of access panel. Both panels exhibited what appeared to be moderate to heavy surface corrosion, similar to that of ASTM G-34 (1987) EB to EC levels.

Tests were also conducted on two 2024-T3 panels in which the corrosion was polished off the surface, leaving a Type III specimen. Results for these tests are compared in Fig. 11 with the Type I data. For the Type III data, the scatterband was similar to the Type I material for each panel. Type III crack growth rates are slightly faster than their Type I counterparts in most of the ΔK regimes. This is could likely be accounted
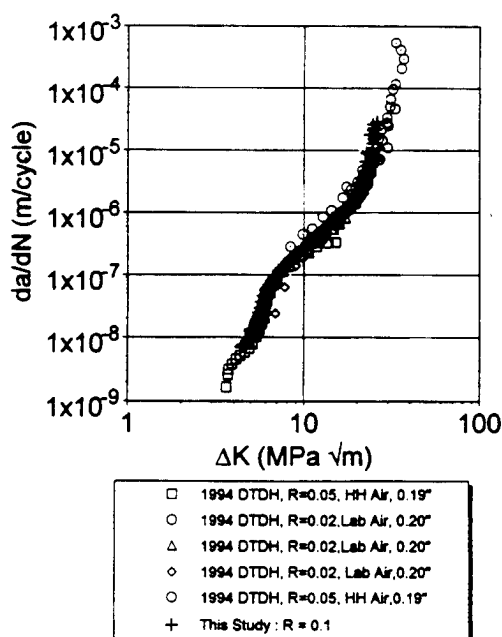

Fig. 6 7178-T6 crack growth comparison between this study and *Damage Tolerant Design Handbook* for CT specimens, no visible surface corrosion
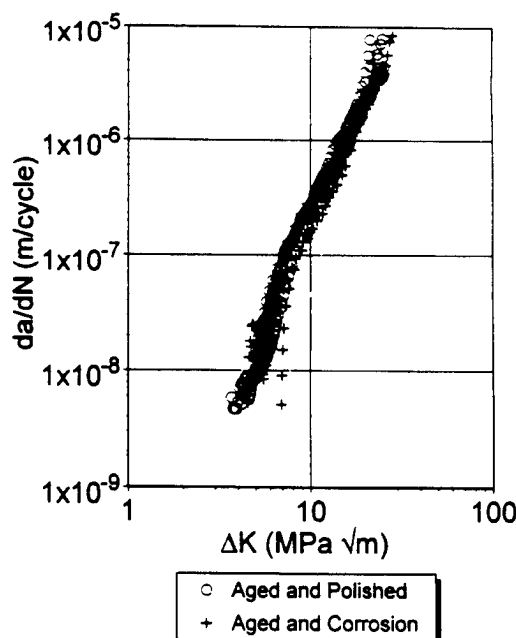

Fig. 8 7075-T6 aged and corroded specimens compared to aged and polished specimens from the same panel
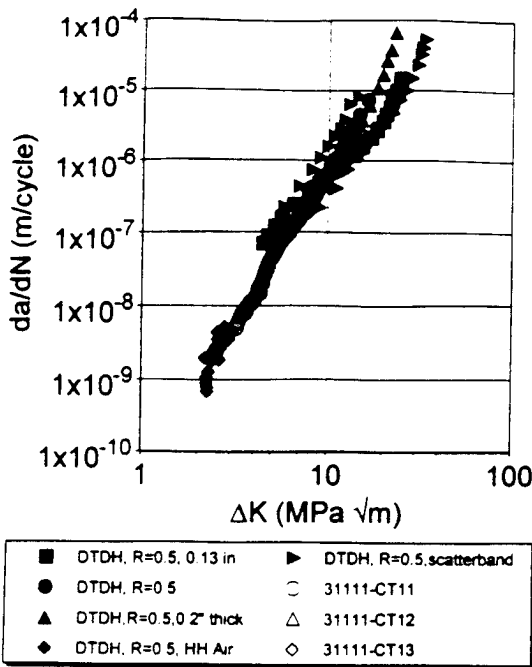
Fig. 9 Aged and corroded 7075-T6 material tested at $R = 0.5$ and compared to DTDH data

Fig. 11 Fatigue crack growth for 2024-T3 which compares aged and corroded material to aged only materials from the same panels of 2024-T3

for in the optical thickness measurements in which an average value was utilized for both types of surface conditions. The average thickness value would be more accurate for the Type III specimens, but could be less accurate for the Type I specimens as the thickness varied more through the width of the specimens that had corrosion products and paint/primer present. The Type I specimens also exhibited a slightly faster fatigue crack growth rates than the *Damage Tolerant Design Handbook* data.

Figure 12 illustrates results of tests conducted on 2024-T3 alloys that were Type I, from the access and doubler panels at a load ratio $R = 0.50$. Both the doubler and access panel crack growth rates lie within the *Damage Tolerant Design Handbook* data presented in Fig. 12. This result is consistent with the 7075-T6 material; as the load ratio R increases, the effects of corrosion and aging on the fatigue crack growth rate diminish.

The crack growth results presented in this paper are based primarily on two measurements, the crack length and the specimen thickness. The crack length measurement was compliance
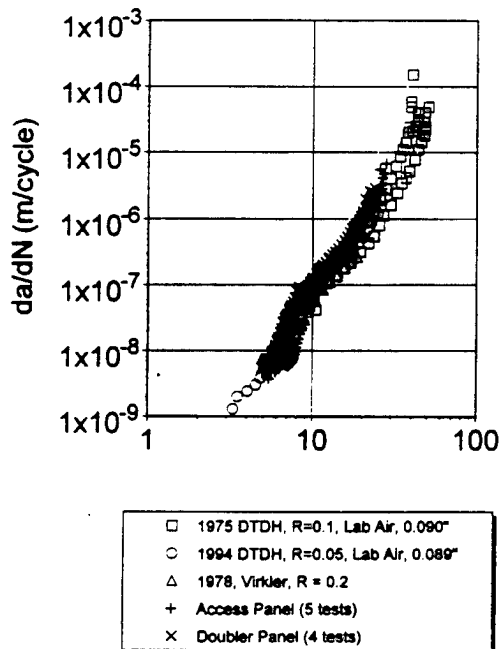

Fig. 10 Crack growth comparison for aged and corroded 2024-T3 from an access panel and a doubler panel to the *Damage Tolerant Design Handbook*
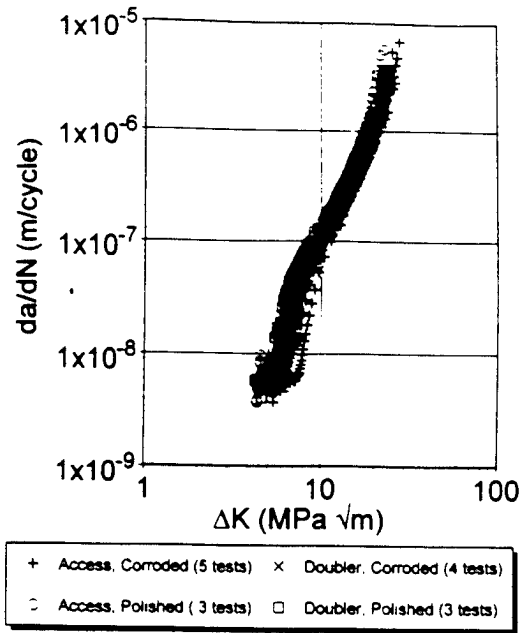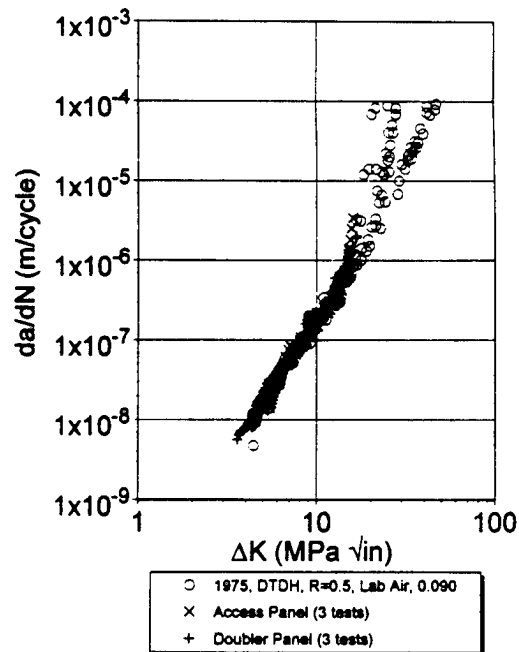

Fig. 12 Comparison of aged and corroded 2024-T3 tested at a load ratio of $R = 0.50$ for the access panel and the doubler structure

based, and optically checked during each test. The thickness measurements were somewhat less robust in nature. The fatigue crack growth results presented in this paper are based on an optically averaged measurement of the thickness of the load bearing material in the crack growth region of the specimen, performed after the test, see Fig. 1 for clarification.

Exclusion of the corrosion products from the thickness, apparently does not explain the faster crack growth rates observed in the 2024-T3 material. Crack growth rates for materials that were moderately corroded, comparable to ASTM G-34 EB or EC level (subjective to authors opinion), are all slightly faster than the handbook data of the same pedigree. To account for the increased fatigue crack growth rates, all of the unaccountables, such as influence of corrosion on the material or hydrogen embrittlement, can all be lumped into the specimen thickness comparison as an exercise to get an idea of the general trend of the crack growth rate increase. An example from the 2024-T3 aged and corroded material from the access panel tested at $R = 0.10$ is described below. The data were fit with the following hyperbolic sine curve:

$$\log \frac{da}{dN} = C_1 \sinh \left[C_2 (\log \Delta K + C_3) \right] + C_4 \qquad (1)$$

where C_i = experimental parameters where data fit are then shifted to match the handbook data by changing the thickness of the aged and corroded specimens to match the handbook data. This is accomplished by a simple transformation of ΔK by the following formula:

$$\Delta K_{new} = \Delta K_{Hndbook} = \Delta K_{old} \frac{t_{old}}{t_{new}} \qquad (2)$$

The results indicate that the corrosion and aging processes would be similar to a 5–15 percent thickness loss for the corroded material to match to handbook data 2024-T3 specimens. Note that this apparent thickness loss is in addition to actual specimen thickness changes which, as described above, have already been accounted for.

Summary and Conclusions

Stress-strain, cyclic stress-life, and fatigue crack growth tests were conducted on materials taken from aircraft with prior service usage. Several conclusions can be drawn from these tests.

• The alloys examined in this study appear to have retained the same elemental weight percentage composition after years of service usage, as expected. The elemental analysis shows that each alloy still contains approximately the same WT percent of each element with respect to the current acceptable ranges for today's alloys.

• Tensile stress-strain tests were performed on all three materials, 2024-T3, 7075-T6, and 7178-T6. The yield and ultimate strengths of the "used" materials agree with handbook data for virgin material while the Young's modulus was 2 to 5.5 percent below handbook data.

• The cyclic axial stress-life tests indicate that an aluminum alloy in the insitu condition will have a failure life that is shorter than a smooth, polished alloy of the same pedigree, as seen in the corroded 2024-T3 and 7075-T6.

• The minimally corroded materials tested at $R = 0.10$ have similar crack growth behavior to that reported for virgin materials. This observation is based on tests conducted on lightly corroded 7075-T6 and uncorroded 7178-T6. Material that is aged only, but polished, shows a slight increase in fatigue crack growth rate comparable to that of the aged and corroded materials. Tests were conducted on lightly corroded 7075-T6 and two moderately corroded 2024-T3 panels.

• At a stress ratio of $R = 0.10$, fatigue crack growth rates for moderately corroded 2024-T3 appear to be slightly faster

than handbook values in all fatigue crack growth regimes. Additionally, the crack growth rate scatterband increased as the corrosion level increased. When the load bearing thickness was used to compute the cyclic stress intensity factor, the variability from specimen to specimen was smaller, but the crack growth rates were still faster than the published data for virgin material.

• Fatigue crack growth tests were also conducted on the 7075-T6 and 2024-T3 aged and corroded materials at a load ratio $R = 0.5$. The aged and corroded test results indicate that the effects of prior service usage diminish with increasing load ratio as the tests showed no large aberration from the handbook values for both lightly corroded 7075-T6 and moderately corroded 2024-T3.

• In utilizing aged and corroded materials, or performing analyses on material that has seen prior service usage, one important aspect of the analysis is to utilize a thickness measurement that will encompass the load bearing alloy only.

References

Damage Tolerant Design Handbook, 1994, *A Compilation of Fracture and Crack Growth Data for High-Strength Alloys,* Chapter 8, Vol. 4, University of Dayton Research Institute, Sponsored by Materials Laboratory Air Force Wright Aeronautical Laboratories.

Everett, R. A., 1975, "Effect of Service Usage on Tensile, Fatigue, and Fracture Properties of 7075-T6 and 7178-T6 aluminum Alloys," NASA Technical Memorandum X-3165, Feb.

Gruff, J. J., and J. G. Hutcheson, 1969, "Effects of Corrosive Environments on Fatigue Life of Aluminum Alloys Under Maneuver Spectrum Loading," *Proceedings of Air Force Conference on Fatigue and Fracture of Aircraft Structures and Materials,* Miami Beach, FL, Dec. 15-18.

Personal correspondence with Mr. Donald E. Nieser, USAF Oklahoma Air Logistics Center, Tinker Air Force Base, Oklahoma, 1994-1995.

Metals Handbook, Tenth Edition, Volume 2, Properties and Selection: Nonferrous Alloys and Special Purpose Materials, ASM International, 1990.

Military Standardization Handbook, MIL-HDBK-5G, Military Materials and Elements for Aerospace Vehicle Structures, DOD, 1994.

Scheuring, J. N., 1995, "An Evaluation of Aging Aircraft Materials," M.S. thesis, School of Aeronautics and Astronautics, Purdue University, Aug.

"Standard for Constant Amplitude Testing of Metallic Materials," American Society of Testing and Materials, E466-87, *1993 Annual Book of ASTM Standards,* Section 3, Vol. 1, 1993.

"Standard Test Method for Exfoliation Corrosion Susceptibility in 2XXX and 7XXX Aluminum Alloys," American Society of Testing and Materials, G 34-86, *1987 Annual Book of ASTM Standards,* Section 3, Vol. 2, 1987.

"Standard Test Method for Measurement of Fatigue Crack Growth Rates," American Society of Testing and Materials, E647-93, *1993 Annual Book of ASTM Standards,* Section 3, Vol. 1, 1993.

"Standard Test Method for Tension Testing of Metallic Materials," American Society of Testing and Materials, E8-93, *1993 Annual Book of ASTM Standards,* Section 3, Vol. 1, 1993.

"Standard Test Method for Young's Modulus, Tangent Modulus, and Chord Modulus," ASTM E-111, *American Society of Testing and Materials,* Vol. 3.01, pp. 291-296, 1993.

Virkler, D. A., 1978, "The Statistical Nature of Crack Propagation," M.S. thesis, School of Mechanical Engineering, Purdue University, May.

/ 940d$$jy04   04-03-97 23:55:23   asmel   ASME: J Materials

Modeling and Microstructure Analysis of Fatigue Initiation Life Extension by Reductions in Microporosity

J.H. ELSNER, E.P. KVAM, and A.F. GRANDT, Jr.

Fatigue initiation lifetimes were demonstrated to be related to the size and density of microporosity in the midplate region for three differently processed variations of aluminum alloy 7050-T7451. Metallographic and fractographic examination of double edge notched fatigue specimens was performed to characterize microstructural inhomogeneities. A greater size and density of micropores were found for those materials that had failed at shorter fatigue lifetimes. The specific crack-initiating feature was identified for each of the known cracks. Linear elastic fracture mechanics modeling of crack initiation from each of the micropore-induced cracks showed that this could be adequately accounted for by a stress intensity factor analysis proposed by Trantina and Barishpolsky.

I. INTRODUCTION

THIS article focuses on microstructural inhomogeneities that cause fatigue crack initiation in 7050-T7451 plate aluminum alloy. Alloy 7050 is commonly used for thick plate aerospace components that require high strength and good resistance to stress corrosion cracking. The main objective of the present work is to provide a quantitative description of micropore population in this alloy, and to evaluate the effect of micropore population on fatigue crack initiation by modeling crack growth emanating from a micropore. These modeling refinements can lead to better crack growth predictions.

The sizes of microstructural inhomogeneities have been shown to be critical in determining the fatigue lifetime of smooth axial fatigue specimens.[1] The total fatigue lifetime can be broken down into two distinct parts, the crack initiation and propagation lifetimes. Fatigue crack initiation has been shown to be a critical factor in determining the fatigue life of both double edge notched and smooth axial fatigue specimens of alloy 7050-T7451.[2] The fatigue life of these specimens in uniform testing conditions has been shown to vary mainly by differences in the initiation lifetimes. For example, Grandt et al.[2] showed that the life to initiate a surface crack (i.e., to reach 127 μm) under 124 MPa stress for three material variants was 20,000 cycles, 50,000 cycles, and 150,000 cycles, but the propagation life of each was 60,000 cycles. The fatigue lifetime was more than doubled just by an increase in the initiation lifetime.

Understanding what causes initiation and postponing the initiation event can lengthen fatigue lifetimes. Crack initiation from inhomogeneities often does not occur until after a crack incubation period, which may constitute the majority of the fatigue lifetime. The length of the initiation lifetime is thus directly related to the total fatigue lifetime. Characterization of the crack-inducing inhomogeneities can

lead to a better understanding of the initiation process and initial crack growth behavior.

Phenomenologically, mode I fatigue crack initiation can be defined when a tensile load creates two surfaces with an opening displacement. Practically, though, fatigue crack initiation is often defined by when a crack reaches a certain detectable length.[2,3,4] Fatigue cracks in ductile metals initiate from various features or by various mechanisms. Some microstructural protocrack features from which a fatigue crack may emanate include surface defects,[5,6,7] constituent particle inclusions,[3,4,8] and microporosity.[9,10,11]

Growth of long fatigue cracks is often modeled by the Paris equation:[12]

$$\frac{da}{dN} = C(\Delta K)^m \qquad [1]$$

where da/dN is the change in crack length per fatigue cycle, ΔK is the cyclic change in the stress intensity factor, and C and m are scaling constants. However, for a given material and crack driving force, small cracks behave differently than what is predicted by the Paris equation. Many researchers[13] have reported that small fatigue cracks grow at a faster rate than large cracks near the large crack threshold, ΔK_{th}.

Several factors can increase the apparent crack driving force. Some of the small crack phenomena include diminished closure effects,[14] large scale plasticity,[15] and microstructural dissimilitude.[16] Microstructural inhomogeneities, such as an inclusion or a micropore, will also commonly increase the crack driving force by acting as stress concentrators; this phenomenon will be analyzed further in this article.

Trantina and Barishpolsky investigated the effects of an inhomogeneity on the crack driving force in an infinite solid.[17] Their model assumed a micropore or particle with radius R and a crack of length b emanating from it, as shown in Figure 1. The stress intensity factor for the inhomogeneity was found to be

$$K_{TB} = Y_{TB}\sigma\sqrt{\pi b} \qquad [2]$$

where σ is the applied stress and b is the physical crack length. (Here, the TB subscript designates those terms specific to the Trantina–Barishpolsky model.) The geometric

J.H. ELSNER, formerly Graduate Student, School of Materials Engineering, Purdue University, 47907, is Research Engineer, AS&M, Wright-Patterson AFB, OH. E.P. KVAM, Associate Professor, School of Materials Engineering, and A.F. GRANDT, Jr., Professor, School of Aeronautics and Astronautics, are with Purdue University, West Lafayette, IN, 47907.
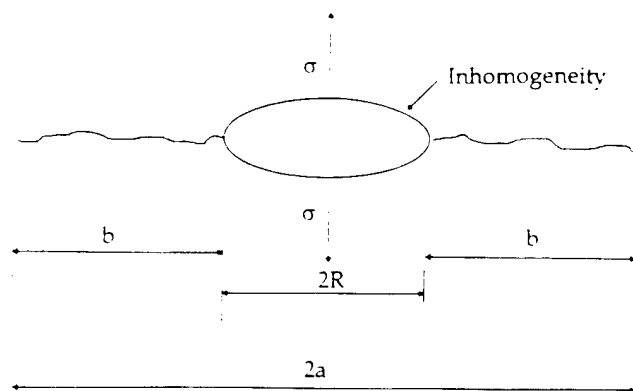Manuscript submitted March 29, 1996.

Fig. 1—Schematic representation of inhomogeneity with crack emanating from it, where $2R$ is the inhomogeneity diameter, $2b$ is the physical crack length only, $2a$ is the total crack length, and σ is the applied stress.

Fig. 3—Microstructure of 7050-T7451 etched with Keller's etchant showing subgrain boundaries.
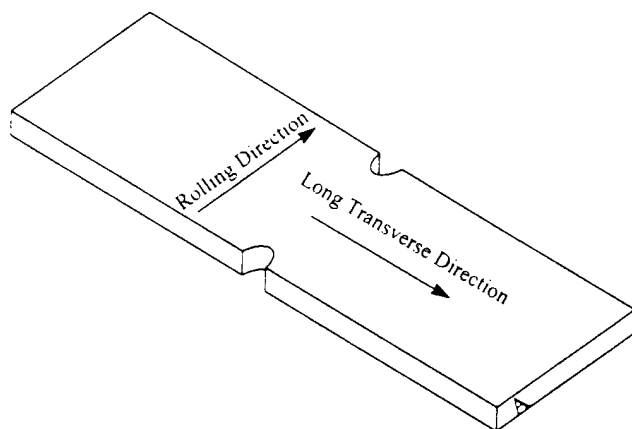

Fig. 2—Schematic representation of double edge notched specimen used for fatigue testing. Specimen orientation with respect to ingot is indicated.

term Y_{TB} was developed by curve fitting results from elastic-plastic finite element analyses, and is given by

$$Y_{TB} = \frac{2}{\pi} + T\left(1.12k_t - \frac{2}{\pi} - 1\right)\left(\frac{R}{b+R}\right)^{10} + \left(\frac{R}{b+R}\right)^{18} \quad [3]$$

where k_t is the stress concentration factor for a void, and T = 1 for a void, 2 for a bonded inclusion, and 0.3 for an unbonded inclusion. The Y_{TB} solution includes the Y solution for a circular "penny" crack in an infinite body, because once the crack is large enough that the microstructural inhomogeneity has no effect on the stress intensity (i.e., $b >> R$), $Y = 2/\pi$.

II. EXPERIMENTAL

Three different variations of alloy 7050 were used in this study. The first variant was 14.5-cm-thick plate material of 7050-T7451 from older standard processing conditions; this will be referred to as "old" material. The second variant was a 14.5-cm plate material, with improved processing parameters that reduced the size of microporosity in the alloy; this will be referred to as "new" material. The third material examined had been processed with the same im-
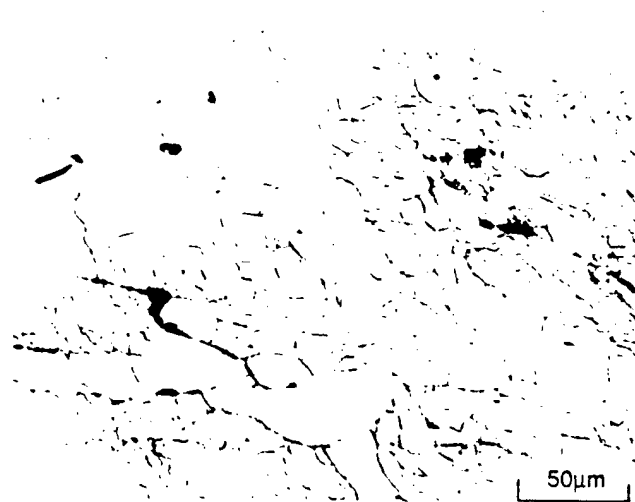
provements as the new material but was rolled to 7.5 cm instead of 14.5 cm in an effort to further reduce microporosity. This third material will be referred to as "7.5-cm" material. Microporosity was expected to be the primary cause of initiation in the thick plate formed from the old and new materials, so the 7.5-cm material was tested to compare initiation sites in the near absence of micropores.

Alloy 7050-T7451 was direct chilled ingot cast in a mold of cross-sectional size 40 by 130 cm and about 6-m long. Micropores formed, which tended to be most populous in the center of the ingot because it was the last to solidify. All of the fatigue specimens in this study were, therefore, fabricated from the high porosity midplane of the plate. The fatigue specimens fabricated from the midplane thus represented a worst case scenario for fatigue initiation, and would most accurately represent critical service conditions, because 7050 was designed primarily for thick plate applications. Processing steps for alloy 7050-T7451 included homogenizing, hot rolling to desired thickness, solutionizing, quenching, stretching, and age hardening.

A schematic of the double edge notched test specimen is shown in Figure 2. The rolling direction and long transverse direction of the ingot from which the specimens were processed are labeled on the specimen. The typical microstructure of the rolled alloy used here contained elongated grains, subgrains, and a certain amount of recrystallization. The material was electropolished in 20 pct perchloric acid 80 pct ethanol at 30 Vdc for 5 to 10 seconds and etched using Keller's reagent. The microstructure can be seen in Figure 3. In order to distinguish the grain boundaries from the subgrain boundaries, the material was electoetched in Graff–Sargent etch at 5 Vdc for about 5 to 10 seconds. The samples were then viewed with polarized light and an analyzer. Micrographs of the plane normal to the long transverse direction of the old, new, and 7.5-cm materials are shown in Figures 4(a) through (c), respectively. The mechanical rolling created a partially oriented grain structure, and a simple linear intercept method was used to determine the planar-linear orientation of the grains. The planar + linear = planar-linear orientations[18] of the old, new, and 7.5-cm material were 39 pct + 7 pct = 46 pct, 50 pct +
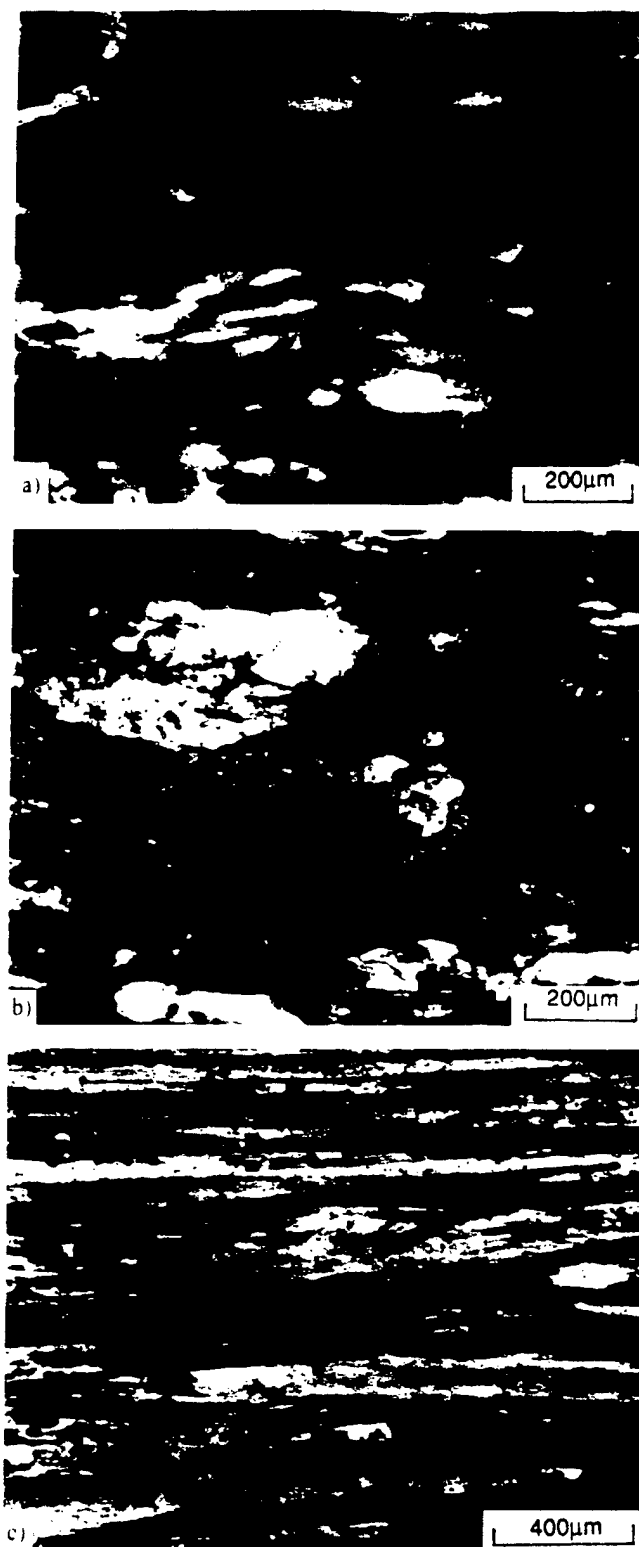
Fig. 4—Microstructure of 7050-T7451 etched in Graff–Sargent and viewed with polarized light and an analyzer showing contrasting grains for the (a) old material, (b) new material, and (c) 7.5-cm material. Views are perpendicular to the long transverse direction (plane A in Fig. 2).

10 pct = 60 pct. and 53 pct + 26 pct = 79 pct. respectively.

The principal strengthening precipitates in 7050-T7451 are η' and η.[19] These precipitates are on the order of 10

nm in size and are not expected to contribute to crack initiation. Constituent particles are products that form during solidification of the alloy and are known to result from iron or silicon impurities. Unlike the η' and η precipitates. these constituent particles can have a distinctly detrimental effect, deteriorating the fatigue resistance of the material by acting as fatigue crack initiation sites. The iron-bearing particles are typically of the composition Al_7Cu_2Fe, and the silicon particles are of the composition Mg_2Si. These particles will be referred to as Fe constituents and Si constituents, respectively.

The area fraction of Fe and Si constituent particles was relatively small. The total area fraction of Fe + Si constituents in the midplane of the new material was about 1 pct.[20] There was a greater number density of small Si constituent particles. but the Fe particles were much larger in size. which resulted in a higher area fraction.

Ideally. structural alloy materials should not contain microporosity; in sheet applications. the extreme mechanical deformation during rolling of the sheet effectively closes any microporosity. The thick plate examined here did contain microporosity. though. because there was not enough mechanical deformation to effectively close the porosity. A major use of alloy 7050 is in thick-plate applications. so this is relevant to the alloy's utility.

The microporosity was characterized here using a scanning electron microscope (SEM) and an image analysis system. The plane normal to the tensile direction was ground. then polished on 0.05-μm alumina. Three analysis planes. separated by at least 2 mm. were selected. Because micropore sizes could differ by several orders of magnitude. images were analyzed at magnifications of 100. 500. and 1500 times. Ten images at each magnification were analyzed on the three different planes for a total of 90 analysis fields (approximately 50 mm^2) for each material type.

A logarithmic histogram of the micropore population is given in Figure 5. Table I contains the micropore density. mean pore area. and area fraction. In this survey. the old material had six micropores of size range 1000 to 2100 μm^2 with an outlier at 8900 μm^2. The new material had ten micropores greater than 100 μm^2 with a maximum of 210 μm^2. and the 7.5-cm material had only three micropores greater than 100 μm^2 with a maximum of 170 μm^2. Figure 6 shows the distribution of micropores in the 100- to 1000-μm^2 range for the three materials.

The variation in the tensile mechanical properties of the materials was minimal between the old and new materials.[21] The only noticeable difference was that the percent elongation at failure in the short traverse direction was slightly lower in the old material. The tensile properties were regarded as a nonvariable in this study.

The fatigue test specimen geometry was a double edge notched flat sheet 25-cm long. 5-cm wide. and 0.46-cm thick. with semicircular 0.234-cm notches at the midline edges. The specimen design was selected because the local stress concentration of the notch would focus crack initiation in a relatively small volume of material. which could be closely monitored. The specimens (fabricated from the high-porosity midplate region) had their tensile axis oriented along the long transverse rolling direction. and the initial small cracks started widening along the short transverse direction. within the notch bores. Friction grips were
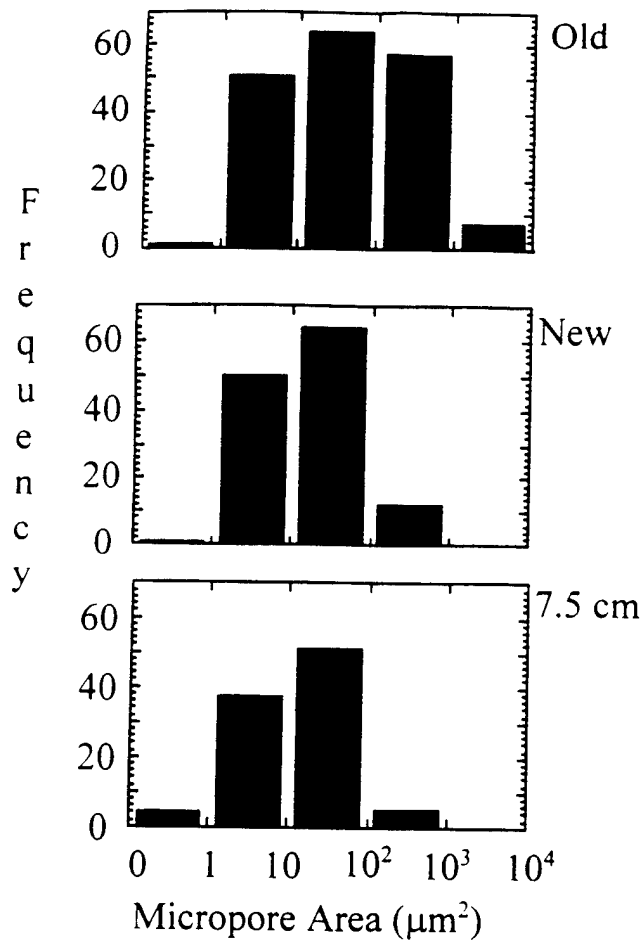
Fig. 5—Complete frequency distribution of micropore areas for old, new, and 7.5-cm material.

Table I. Micropore Density, Mean Area, and Area Fraction of the Old, New, and 7.5-cm Materials

Material Type	Density (mm^2)	Mean Area (μm^2)	Area Fraction (Pct)
Old	3.8	190	0.072
New	2.7	39	0.010
7.5 cm	2.1	31	0.0064

Fig. 6—Frequency distribution for micropore areas between 100 and 1000 μm^2.

used to hold the specimens in an MTS testing machine, and the specimens were tested at nominal notch stresses of 110, 124, and 138 MPa. Other testing conditions included a load ratio of 0.10, frequency of 10 Hz, temperature of 22 °C, and relative humidity ranging from 60 to 80 pct. The testing was stopped periodically to measure small fatigue crack growth within the notch bore using acetate tape replicas. Nine specimens of each material were fatigued until fracture. The actual fatigue testing of the specimens was conducted by Zezula[21] and is described in more detail in References 2 and 21.

III. FRACTOGRAPHY

Fractographic examination was performed to analyze the crack-initiating feature type and size in all of the fatigue-fractured specimens. Ultrasonic cleaning of the specimens in acetone before examination was used to remove acetate tape residue. All of the fracture surfaces were examined with an SEM at accelerating voltage of 25 kV and a working distance from 25 to 40 mm.

Many specimens had multiple initiation sites, and every initiation site on each fracture surface was examined. Numerical and graphical crack growth data (taken during testing, using replicas) were used to help identify all the initiation sites. Many specimens had crack growth in both

notches, or at multiple sites within a single notch. When multiple cracks grew in one notch, either the cracks would coalesce or the dominant crack would cause arrest of the other cracks.

The inhomogeneities that initiated cracks were characterized by type and size. The various types of identifiable inhomogeneities causing initiation included micropores, Fe constituent particles, Si constituent particles, and machining damage. If an inhomogeneity could not be classified in these categories, then it was said to be indeterminate. Figure 7 shows how the size of a micropore was characterized by its maximum width and length ($2R$ by c). The micropore area was determined by image analysis. Tables II through IV include inhomogeneity data for the old, new, and 7.5-cm materials, respectively.
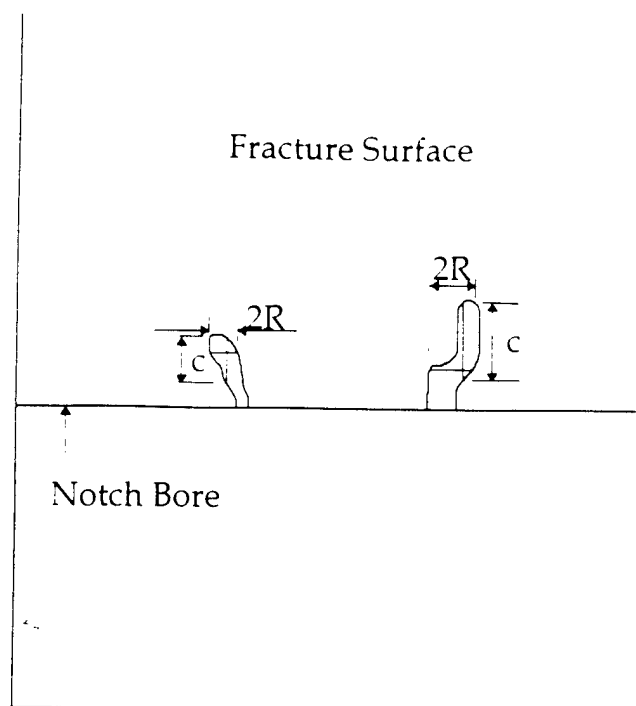
Fracture Surface

Notch Bore

Fig. 7—Schematic view of inhomogeneities showing definition of maximum width and depth dimensions.

Table II. Inhomogeneity Data for the Old Material

	Old Material		
Initiation Site	Inhomogeneity Type	Size 2R × c (μm)	Micropore Area (μm²)
1260	Fe constituent	15 × 15	—
1312	micropore	40 × 100	7900
1500	micropore	30 × 50	2000
1510	micropore	40 × 80	4300
1602	micropore	35 × 175	7800
1722	micropore	65 × 185	11,000
2011	micropore	35 × 55	1100
2112	micropore	30 × 70	600
2311	micropore	20 × 130	2400
2410	micropore	35 × 65	4700
2530	micropore	30 × 45	1180
3010	Fe constituent	20 × 10	—
3150	micropore	70 × 80**	3300
	micropore	40 × 50**	2000
3220	micropore	55 × 55	2500
3311	micropore	60 × 200	8700
3312	micropore	80 × 160	8900

**Micropores were separated by 90 μm and were the cause of initiation.

Table III. Inhomogeneity Data for the New Material

	New Material		
Initiation Site	Inhomogeneity Type	Size 2R × c (μm)	Micropore Area (μm²)
4110	micropore	25 × 43	1200
4310	micropore	20 × 20	400
5310	Fe constituent	5 × 40	
5411	micropore	25 × 40	1700
6213	micropore	13 × 40	400

Table IV. Inhomogeneity Data for the 7.5-cm Material

	7.5-cm Material	
Initiation Site	Inhomogeneity Type	Size 2R × c (μm)
72121	polish mark	10 × 4
7510	polish mark	15 × 3
81111	Fe constituent	15 × 60 (ss)
81122	Fe constituent	10 × 10
8310	Si constituent	7 × 10 (ss)
8510	Fe constituent	15 × 15 (ss)
9110	Fe constituent	10 × 20
9310	Fe constituent	15 × 15
9512	Fe constituent	10 × 15

Fig. 8—Micropore initiation site 2311 of old material.

Micropores were the dominant initiation sites in the 14.5-cm materials. The material was rolled, and so many micropores were elongated in the rolling direction. The outlines of the micropores on the fracture surfaces were usually smooth with an irregular elongated shape, and the surfaces of the micropores were usually smooth. It can be seen that the depth dimension in the rolling direction was generally larger than the width. Figures 8 and 9 show micropores from old and new materials, respectively.

The Fe or Si constituent particles tended to cause initiation in the absence of micropores. Mechanically rolling the material broke up the particles into stringers of smaller particles; the entire stringer, rather than any individual particle, usually appeared to have been the initiation site. Figures 10(a) and (b) show both halves of the only identified primary initiation site from a constituent particle in the new material. The Fe constituent particles were seen on both fracture surfaces, which suggested that the particles had fractured rather than debonded from the matrix. This has implications for the shape of the initiation site and stress concentration for small crack growth.
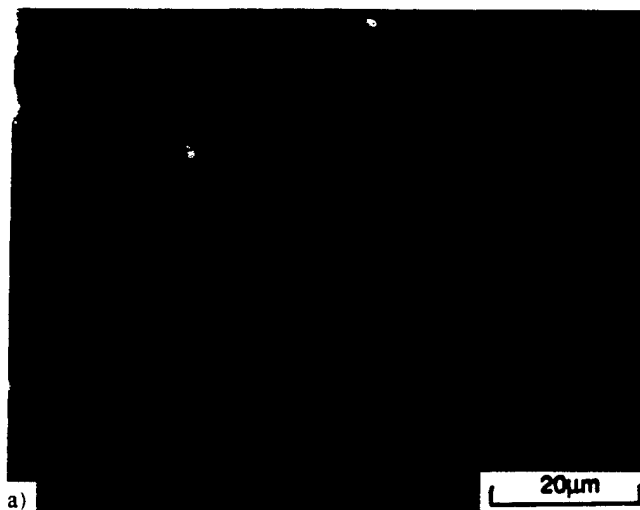
Figure 11 shows the only initiation site observed to result from a Si constituent particle. The cracked dark-contrast constituent particle in this figure was determined (by energy

Fig. 9—Micropore initiation site 5411 of new material.

Fig. 11—A dark contrast Si constituent particle of 7.5-cm material, initiation site 8310.
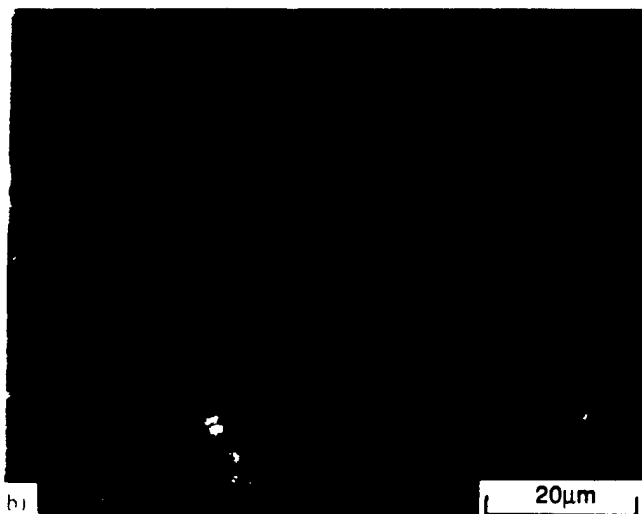

Fig. 10—(a) Stringers of bright Fe constituent particle of new material, initiation site 5310; and (b) the Fe constituents on the opposite fracture surface demonstrating that the particles fractured rather than debonded

dispersive X-ray spectroscopy) to be a Mg-Si type particle, probably Mg_2Si. The particle was observed to be fractured,

and was highly angular (faceted), which may have helped induce the fatigue crack initiation.

Initiation in most of the 7.5-cm material specimens was either caused by polishing marks or was indeterminate. Such initiation sites also occurred occasionally in the old and new materials. Figure 12(a) shows an indeterminate initiation site for a new material specimen. There is a protrusion, which was speculated to be grain boundary separation. Another indeterminate initiation site can be seen in Figure 12(b).

IV. INCUBATION LIFE CALCULATIONS

Substantial crack growth modeling was performed.[22] A summary of the procedures and results are outlined subsequently.

Crack growth data[23] were used to determine the observed incubation life. This life was defined by when the observable crack length $2a$ was greater than the inhomogeneity diameter $2R$ and the crack length had increased more than 10 pct during two consecutive 3000 cycle intervals. Linear elastic fracture mechanics was then used to determine numerically a calculated incubation life. These two lives will be referred to as observed incubation life and calculated incubation life, respectively.

Using the stress intensity factor solution for a notched specimen,[24] the Paris equation for crack growth in the notch bore had been determined to be[2]

$$\frac{da}{dn} = 1.46 * 10^{-7} (\Delta K)^{2.738} \frac{mm}{cycle} \qquad [4]$$

for ΔK in units of $MPa\sqrt{m}$.

The effective K solution for a crack growing from a particle or void in the bore of the notch was determined by multiplying geometric stress intensifier terms. Since the K solution for the notch (K_N) was already known, it could be multiplied by the geometric factor for the microstructural inhomogeneity (Y_F) to determine the K solution for the combination of the notch and inhomogeneity:
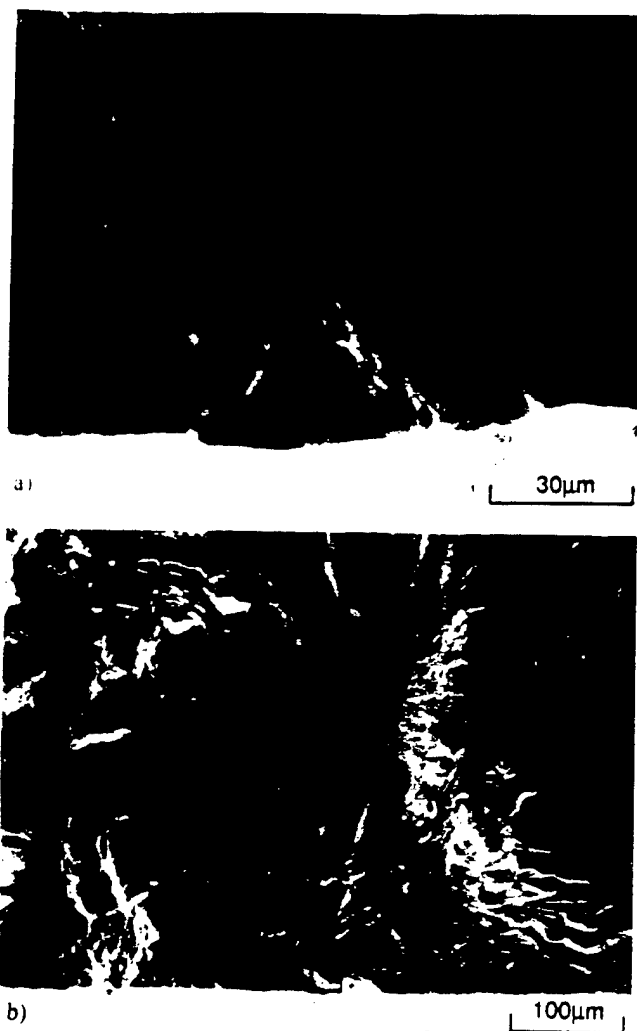
$$K = Y_F * K_N \qquad [5]$$

Fig. 12—Indeterminate initiation site of (a) new material. site 4610, showing a protrusion which is speculated to be grain boundary separation, and (b) 7.5-cm material, site 7010.

where Y_F is a variation of Y_{TB},[11] given by

$$Y_F = 1 + T(1.12k_t - 2)\left(\frac{R}{b+R}\right)^{10} + \left(\frac{R}{b+R}\right)^{1x} \quad [6]$$

The penny crack geometric term, $2/\pi$, was replaced by unity in the Trantina–Barishpolsky factor, because the crack shape was already included in the notch K factor. If $b >> R$, the solution in Eq. [6] reduced to the K_v solution, while if $b \approx 0$, then it reduced to $1.12*k_t*K_v$, which effectively multiplied the stress intensity factor by the stress concentration of the inhomogeneity. It should be noted also that the Trantina–Barishpolsky stress intensity factor defined the crack length as $2b$ (physical crack length only shown in Figure 1), whereas the model here defined the crack length as $2a$ (physical crack length plus inhomogeneity diameter).

Newman's K solution[24] is a function of the (unknown) crack depth, c. Since the crack depth could not be observed in situ, c was estimated using the empirical relationship[25]

$$\frac{c}{a} = 1.0 - 0.1\left(\frac{a}{t}\right) \quad [7]$$

where t is the half-thickness of the sample. This value of c

may not have been very accurate, particularly at small a values, because of the large inhomogeneity aspect ratio. Two c values were used in these analyses. The first analysis utilized the c value in Eq. [7]; however, the aspect ratio of the inhomogeneity was much larger than that predicted by Eq. [7]. To account for this discrepancy, another c value was calculated with consideration of the initial aspect ratio of the inhomogeneity.

Six different algorithms were compared. Three used the calculated initial aspect ratio, and three used the observed initial aspect ratio. In each set, one algorithm did not employ the Trantina–Barishpolsky geometric term, while the other two used a Trantina–Barishpolsky geometric factor, with a stress concentration factor k_t of 2 or 6. (The large k_t value of 6 was used to test the sensitivity of the modification.) The results of the six algorithms are listed in Table V.

These algorithms ran backward, from an observed crack length $2a > 127$ μm, until reverse cycle-by-cycle iteration had shrunk the parameter b to zero (leaving only the measured diameter of the corresponding initial inhomogeneity). The cycle count after that time was considered the calculated incubation life. This cycle count was compared to the observed incubation life.

If the Trantina–Barishpolsky geometric factor was not used, the calculated incubation life for either initial c/a aspect ratio was usually less than the observed incubation life. This implied that the non-Trantina–Barishpolsky calculated crack propagation was slower than the true crack propagation. If the Trantina–Barishpolsky correction factor was used, the calculated incubation life was similar to or greater than the observed incubation life.

The differences between the calculated and observed incubation lifetimes were small when the calculations were based on the measured initial micropore depth. The fit was tolerable, but not as good, when using only the calculated c value from Eq. [7].

The results of the algorithms with the Trantina–Barishpolsky modification much more accurately matched the data than the results of the algorithm without the modification, particularly when using the calculated c values. Some improvement was found for the larger k_t value, but this was small compared to the improvement over the nonmodified model.

Of the six algorithms considered, only the two incorporating both the Trantina–Barishpolsky modification and the observed aspect ratio could consistently produce accurate yet conservative propagation lifetimes. For design and failure prediction, these slightly conservative predictions would be strongly preferred. For design critical components subjected to fatigue, the modeling demonstrated here has shown that an inhomogeneity such as a micropore can accelerate crack incubation as well as initial crack growth rates, and these effects need to be accounted for in a similar manner shown here when predicting crack growth behavior.

V. DISCUSSION

The initial density and size of inhomogeneities in these materials were observed to be important to fatigue performance even when they caused minimal changes in tensile properties. Fatigue cracks initiated primarily at two differ-

Table V. The Observed and Predicted Incubation Lifetimes for Calculated (Equation [7]) and Observed Aspect Ratios

Initiation Site	Observed Incubation (Cycles)	Initial Aspect Ratio (c/a)*	Newman K (Cycles)	Newman K + TB K = 2 (Cycles)	Newman K + TB K = 6 (Cycles)	Cycle Count 2a > 127 μm
			LEFM Calculated Incubation Life			
Old						
1722	10.001	calculated	1	4845	6276	16,004
		6	5611	14,846	15,332	
2311	15,003	calculated	1	1	1	26,006
		13	7534	14,846	15,332	
3311	10,000	calculated	1	5634	6429	13,000
		7	6800	10,385	10,657	
3312	13,000	calculated	6496	14,241	14,964	18,000
		4	13,445	16,485	16,762	
New	4310	162,511	calculated	126,260	158,002	160,136	200,004
		2	145,244	166,018	167,179	
5411	29,990	calculated	7372	28,031	29,451	50,020
		3	26,990	36,945	37,530	
6213	55,000	calculated	20,337	40,577	41,942	80,000
		6	49,288	57,040	57,485	

*The calculated aspect ratio is always less than one and follows Eq. [7].
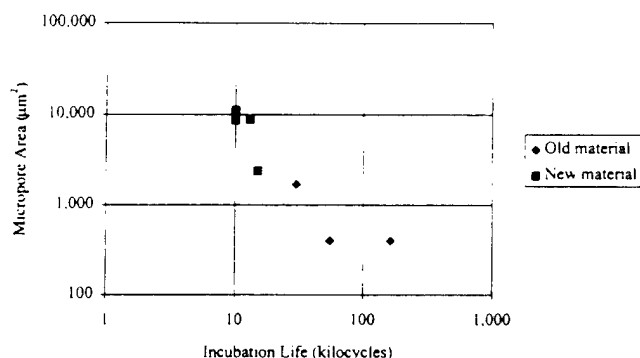
Fig. 13—Inverse trend of incubation life and micropore area for double edge notched specimens.

Fig. 14—Inverse relationship of micropore length and fatigue lifetime.[1]

ent types of microstructural inhomogeneities in alloy 7050-T7451, micropores and constituent particles. The size of micropores was greatest in the old material and decreased in both the new and 7.5-cm materials; the frequency was greatest in the thicker plate material and decreased in the 7.5-cm material. The dominant identifiable initiation sites for the old, new, and 7.5-cm materials were micropores, either micropores or constituent particles, and constituent particles, respectively. There thus appeared to be a quality-related transition from micropores to constituent particles.

The differences in the total fatigue lifetimes had been attributed mainly to the differences in initiation life,[2] with substantial improvement in time to initiation as microporosity diminished. Large micropores tended to initiate fatigue cracks first, while constituent particles tended to become initiation sites only when the size and density of the micropores became small enough. The additional rolling to reduce the 7.5-cm material from 14.5 cm mainly reduced the frequency of the porosity. Those constituent particles that initiated observable fatigue cracks appeared to have fractured rather than debonded.

The average area of a micropore causing initiation, determined from fractographic analysis, decreased from 4500 to 920 μm² between the old and new materials, respectively. The areas were both about an order of magnitude

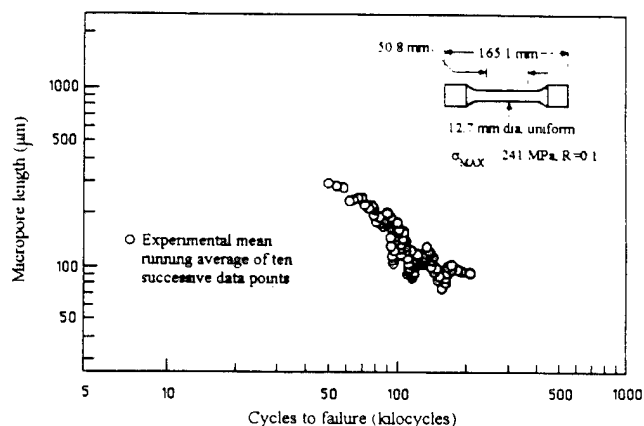larger than the mean micropore areas found from metallography, which were 190 and 39 μm², respectively. This was expected because larger micropores should form cracks more easily than smaller micropores and because cracks would tend to initiate from the largest micropores in the area of the stress concentrator. The incubation life and total fatigue life depend on the size of microporosity. Figure 13 shows a trend of an inverse relationship between micropore area and incubation life, and Figure 14 (from Reference 1) shows the same trend of micropore length and fatigue life. In addition to the larger micropores decreasing fatigue life because of the larger initial crack, larger micropores also seem to create a crack sooner that smaller pores.

The expected number of a crack-initiating micropores in the notch was related to the micropore distribution, density of micropores, and volume of material in the expected region of initiation. The micropore distributions were given in Figure 5. The cumulative distribution of micropore areas ..tted on probability paper can be seen in Figures 15(a) through (c). The smallest micropore observed from fractography causing initiation was 400 μm². Assuming a crack-initiating micropore must be 400 μm² or larger, the probability of any single micropore being this large was
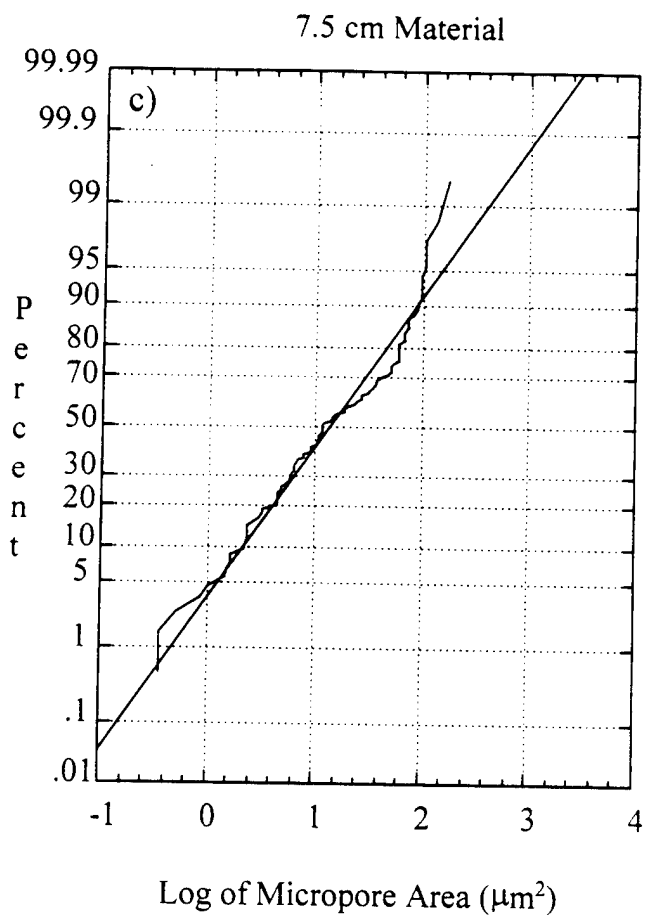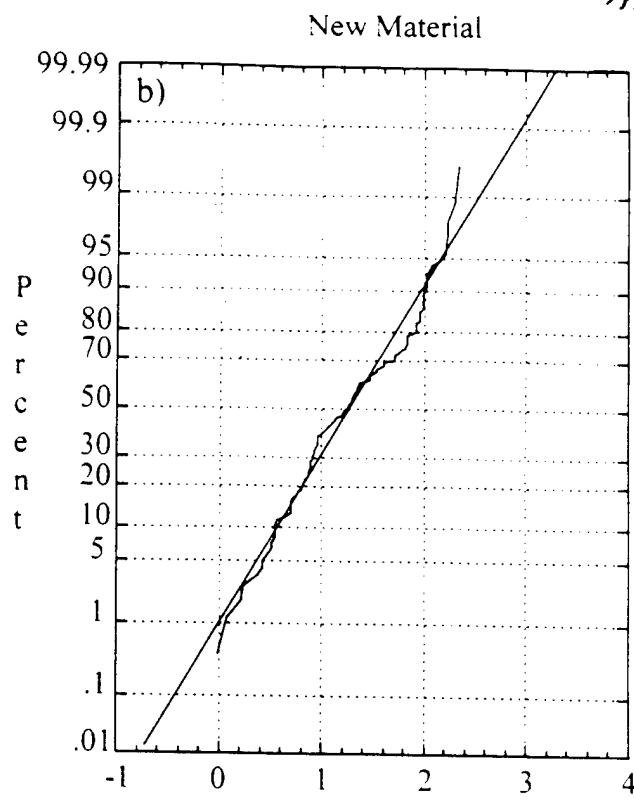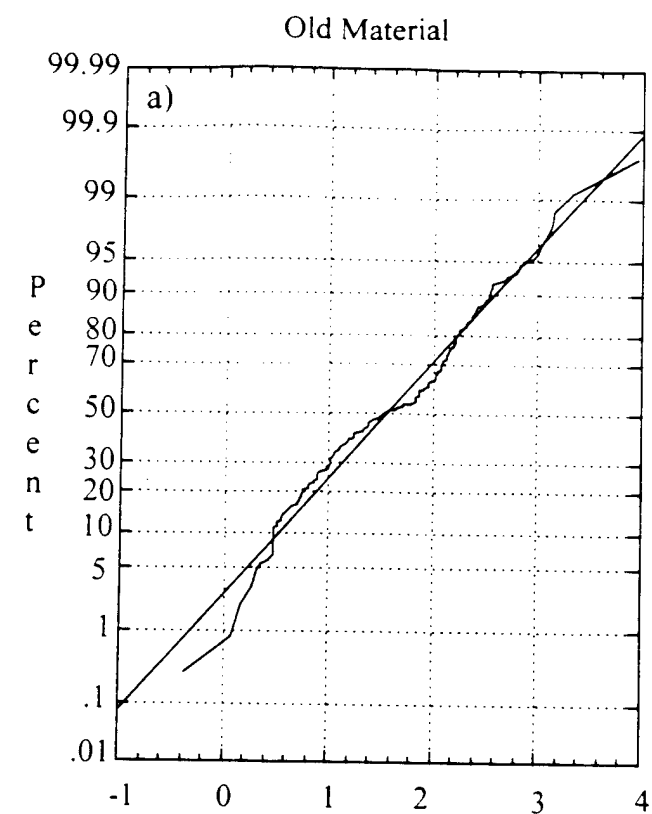
Fig. 15—Cumulative probability function plotted on probability paper for (a) old material, (b) new material, and (c) 7.5-cm material.

found to be 0.1, 0.01, and 0.01 for the old, new, and 7.5-cm materials, respectively.

The density of the micropores was determined by Saltykov's method.[2] The method estimates the volume density from the area density and assumes spherical pores. The density of the micropores were 240, 280, and 130 per mm³ for the old, new, and 7.5-cm materials, respectively.

The volume of material, where the micropores were expected to initiate cracks, was estimated by two methods. Cracks initiated at various angles from the radial centerline of the notch. In the extreme case, a crack initiated from a micropore 20 deg from the centerline. Using a finite element program, the constant stress contour was found corresponding to the stress at the surface at ±20 deg. This contour reached 150 μm below the notch surface at the centerline. This cross-sectional area was determined to be 0.18 mm², so the total volume within each notch that was at or above this stress was 0.18 mm² (4.6 mm) = 0.83 mm³.

An alternate method to find the volume of material containing possible crack-initiating micropores considered surface effects. Because almost all of the crack-initiating micropores intersected the surface, this volume was determined by multiplying the arc length (±20 deg times the radius) by the diameter of the smallest crack-initiating micropore (20 μm) by the notch width. The corresponding volume was (1.6 mm)(0.020 mm)(4.6 mm) = 0.15 mm³.

The expected number of crack-initiating micropores in the notch was calculated by multiplying the probability that a given micropore was at least 400 μm² times the micropore density times the volume. In doing so, the numbers of crack-initiating micropores for the old, new, and 7.5-cm materials were 20, 2.3, and 1.1, respectively, when calculations were based on the volume size of 0.83 mm³. For the volume size of 0.15 mm³, the values were 3.6, 0.42, and 0.20, respectively. The numbers for the smaller volume, which represented only pores that intersected the surface, were closer to what was observed. Fractography had shown that micropore initiation was the cause of failure in almost all of the old material (often with multiple sites per notch), about half of the new material, and none of the 7.5-cm material. This demonstrated that the boundary conditions of the free surface had an important role in crack formation in notched specimens.

One factor affecting the small crack growth rate was large scale plasticity, because the formation of a plastic zone around a micropore near the notch was expected at the stresses encountered in these experiments. The applied stresses were ~28 pct of the yield strength, and the stress concentrator of the notch (k_t = 3), along with a micropore in the vicinity of the notch, would produce a stress above the yield strength. The difference in the calculated and observed initiation times might be partly attributed to the plastic zone size around the cracks in early stages of growth. The plastic zone size could not be calculated using linear elastic fracture mechanics (LEFM) principles, because the expected large plastic zone to crack size ratio (from the high applied stresses) violated LEFM assumptions. The size of the plastic zone must be small compared to the size of the crack for LEFM principles to be valid. This was not the case for the initial crack emanating from an inhomogeneity at the stress levels encountered in this study. The plastic zone resulting from the presence of a micropore or

constituent particle would be larger than expected from the presence of a crack alone.

Small cracks have been known to grow at a faster rate than large cracks for a given crack driving force,[3] and this could be attributed to microstructural dissimilitude, such as when the plastic zone or crack encounters a grain boundary. Differences between "small" and embryonic (those less than 127 μm in size) cracks, on the other hand, could be attributed to inhomogeneities and an unusually large plastic zone around the micropore.

Even though LEFM predictions were not strictly valid, they gave close estimates of fatigue lifetimes. The LEFM principles are constantly being improved upon because (1) they have worked in the past and have an established good history and (2) there is not a convenient alternative that does a better job of prediction. The modifications, however, tend to make LEFM models more complicated. For example, determining the scaling constants in Eq. [1] is normally the first step for fatigue crack growth predictions. Then, small crack growth predictions have been added into the model, and the effects of microstructural inhomogeneities have been added on top of that. Although these models have been refined to produce good conservative estimates, they ignore some of the actual metallurgical phenomena of fatigue crack advancement.

VI. CONCLUSIONS

Fatigue initiation time differences were demonstrated to be related to the size and density of microporosity in the midplate region for three differently processed variations of aluminum alloy 7050-T7451 plate. Greater size and density of micropores in the highly stressed region of notched fatigue samples were found for those materials that had failed at shorter fatigue lifetimes. Only when microporosity had been suppressed did other microstructural features act as fatigue initiation sites.

Modeling of crack initiation showed that higher stress concentrations, due to the open pores, could be adequately accounted for by a stress intensity factor analysis proposed by Trantina and Barishpolsky.[17] This analysis was found to be overly conservative for cracked constituent particles, however.

ACKNOWLEDGMENTS

REFERENCES

1. P.E. Magnusen, A.J. Hinkle, W.T. Kaiser, R.J. Bucci, and R.L. Rolf: *J. Test. Eval.*, 1990, vol. 18 (6), pp. 439-45.
2. A.F. Grandt, Jr., A.J. Hinkle, C.E. Zezula, and J.H. Elsner: *Proc. 1993 USAF Structural Integrity Program Conf.*, T.D. Cooper, J.W. Lincoln, and J.L. Rudd, eds., Wright-Patterson AFB, OH, 1994, pp. 255-67.
3. S. Güngör and L. Edwards: *Mater. Sci. Eng.*, 1993, vol. A160 pp. 17-24.

4. P. Li, N.J. Marchand, and B. Ilschner: *Mater. Sci. Eng.*, 1989, vol. A119, pp. 41-50.

5. C. Wiesner, H.U. Kunzi, and B. Ilschner: *Mater. Sci. Eng.*, 1991, vol. A145, pp. 151-58.

6. M. Goto and H. Nisitani: *Fatigue Fract. Eng. Mater. and Struct.*, 1992, vol. 15 (4), pp. 353-63.

7. R. Taggart, M. Ramulu, and T. Jolly: *Mater. Sci. Eng.*, 1989, vol. A119, pp. 73-80.

8. D.W. Hammond and S.A. Meguid: *Eng. Fract. Mech.*, 1990, vol. 37 (2), pp. 373-87.

9. J.R. Brockenbrough, R.J. Bucci, A.J. Hinkle, P.E. Magnusen, and S.M. Miyasato: Annual Report for ONR Contract No. N00014-91-C-0128, Office of Naval Research, Arlington, VA, Dec. 29, 1993.

10. A.J. Hinkle, P.E. Magnusen, R.L. Rolf, and R.J. Bucci: in *Structural Safety and Reliability*, A.H.-S. Ang, M. Shinozuka, and G.I. Schuleller, eds., American Society of Civil Engineers, New York, NY, 1989, pp. 1467-74.

11. B. Skallerud, T. Iveland, and G. Härkegard: *Eng. Fract. Mech.*, 1993, vol. 44 (6), pp. 857-74.

12. P.C. Paris, M.P. Gomez, and W.P. Anderson: *The Trend in Engineering at the University of Washington*, 1961, vol. 13, pp. 9-14.

13. R.O. Ritchie and J. Lankford: *Small Fatigue Cracks*, TMS, Warrendale, PA, 1986.

14. W.L. Morris: *Metall. Trans. A*, 1980, vol. 11A, pp. 1117-23.

15. K.S. Chan: in *Small Fatigue Cracks*, R.O. Ritchie and J. Lankford, eds., TMS, Warrendale, PA, 1986, pp. 407-25.

16. K.S. Chan and J. Lankford: *Acta Metall.*, 1988, vol. 36 (1), pp. 193-206.

17. G.G. Trantina and M. Barishpolsky: *Eng. Fract. Mech.*, 1984, vol. 20 (1), pp. 1-10.

18. E.E. Underwood: *Quantitative Stereology*, Addison-Wesley, Reading, MA, 1970, pp. 66-71.

19. M.A. Przystupa, J. Zhang, and A.J. Luevano: Annual Report for ONR Grant No. N00014-91-J-1299, Office of Naval Research, Arlington, VA, Feb. 10, 1992.

20. S.M. Miyasato, P.E. Magnusen, and A.J. Hinkle: Report for ONR Grant No. N00014-91-C-0128, Office of Naval Research, Arlington, VA, Nov. 3, 1993.

21. C.E. Zezula: Master's Thesis, Purdue University, West Lafayette, IN, May 1994.

22. J.H. Elsner: Master's Thesis, Purdue University, West Lafayette, IN, Dec. 1994.

23. A.F. Grandt, Jr. and C.E. Zezula: Addendum to Final Report for The Aluminum Company of America, Project Number TC919597TC, Purdue University, West Lafayette, IN, Apr. 1994.

24. J.C. Newman, Jr.: in *Small-Crack Test Methods*, ASTM STP 1149, J. Larsen and J.E. Allison, eds., ASTM, Philadelphia, PA, 1992, pp. 6-33.

25. M.H. Swain: in *Small-Crack Test Methods*, ASTM STP 1149, J. Larsen and J.E. Allison, eds., ASTM, Philadelphia, PA, 1992, pp. 34-56.

26. E.E. Underwood: *Quantitative Stereology*, Addison-Wesley, Reading, MA, 1970, pp. 123-26.

Page Proofs

RESIDUAL STRENGTH OF UNSTIFFENED ALUMINUM PANELS WITH MULTIPLE SITE DAMAGE

M. C. CHERRY and S. MALL†

Department of Aeronautics and Astronautics, Air Force Institute of Technology, Wright-Patterson Air Force Base, OH 45433, U.S.A.

R. HEINIMANN and A. F. GRANDT, JR

School of Aeronautics and Astronautics, Purdue University, West Lafayette, IN 47907, U.S.A.

Abstract—This study investigated the residual strength of unstiffened aluminum panels with widths of 381 mm and 229 mm containing multiple site damage (MSD). The MSD usually occurs at rivet holes, or other stress concentration locations within an aircraft structure. This study simulated rivet holes with MSD, by using holes of constant diameter with small cracks, evenly spaced across the midspan of specimens. The panels were prepared by either fatiguing MSD damage at rivet holes or simulating fatigue damage by saw cuts at each hole. Each specimen was subjected to a monotonically increasing tensile load until failure occurred across the midspan of the gauge section. Five different failure criteria which do not model the stable crack extension were evaluated to predict the residual strength (failure load) for each specimen geometry. These criteria provided a wide range of residual strength predictions for wide and narrow panels with MSD. A failure criterion which involved the plastic zone (yielding) of the lead and MSD cracks gave the most accurate prediction of failure load for panels with MSD damage. The width of the specimens did not affect, in general, the trends in the prediction of failure loads from the five failure criteria. © 1997 Elsevier Science Ltd

1. INTRODUCTION

MULTIPLE SITE damage (MSD) is characterized by the simultaneous presence of several cracks at various sites, such as at different holes in a structural element. This may become significant and critical when cracks are of sufficient size and density whereby the structure will no longer meet the present damage tolerance requirements, i.e. it may reduce the residual strength and fatigue life of an aerospace structural component below those based on a single lead crack approach without considering the interaction with the surrounding cracks[1].

Both military and commercial aircraft are being increasingly used beyond their designed lifetime. MSD poses a significant challenge to those who must assure the structural integrity of aging aircraft. Most commercial aircraft are designed and maintained according to the damage tolerance philosophy based on the principles of fracture mechanics [2]. This damage tolerance philosophy is based on a single lead crack in a structure. Several small MSD cracks, however, can cause a structure to fail catastrophically when these cracks are smaller than a single critical crack which the maintenance crew is looking for.

The objective of this study was, therefore, to investigate the effects of MSD on the residual strength of unstiffened flat aluminum panels. This was accomplished by testing the 381 mm and 229 mm wide 2024-T3 (bare) aluminum specimens with MSD. This study is the extension of a previous study where 229 mm wide specimens with MSD were tested [3]. Further, the present study examined the applicability of simple analytical approaches to predict the residual strength of a panel with MSD. The measured and predicted residual strengths were compared for both sets of tests. Although several rigorous criteria to predict the residual strength, which may involve complex treatments [4, 5], are available, this paper examines five relatively simple approaches to determine the range of their applicability. For the purpose of this study, residual strength is defined as the maximum stress a component can sustain before complete failure occurs in the presence of damage. Further, the specimens with 381 mm width will be referred to

---

†Author to whom all correspondence should be addressed.

as wide specimens in this study. However, they are not wide enough when compared to other tests reported in the literature[6, 7].

2. EXPERIMENTS

Experiments were performed on wide (381 mm) and narrow (229 mm) panels. The material used in this study was 2024-T3 aluminum with a thickness of 2.29 mm for the narrow panels and 1.016 mm for the wide panels. The grain direction was perpendicular to the loading direction. The wide specimens, to measure the residual strength, were 101.6 cm ×60.9 cm with a 38.1 cm width across the gauge section as shown in Fig. 1. These will be referred to as Wide Residual Strength (WRS) specimens in this study. Holes of diameter 3.175 mm were drilled into the gauge section of these specimens conforming to two configurations. The first configuration, Type A (WRS A), had a center lead crack with no other additional holes or MSD. It was used to obtain the apparent stress intensity factor (K_{app}) for the material. The second configuration, Type B (WRS B), included a center lead crack and holes with MSD. It was used to measure the residual strength with MSD. These two configurations can be seen in Fig. 2. Each configuration had two variations of lead crack encompassing either five center holes or seven center holes. Both configurations had a hole separation of 1.905 cm measured from the hole centers.
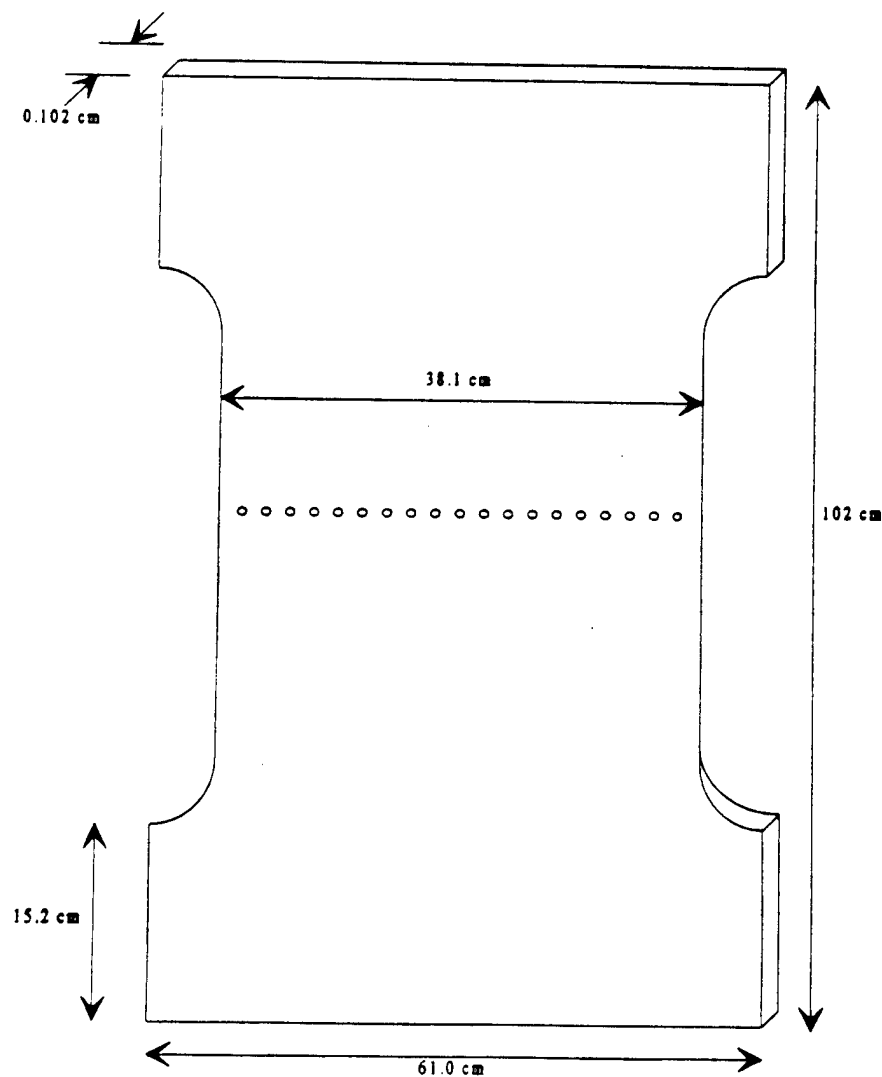

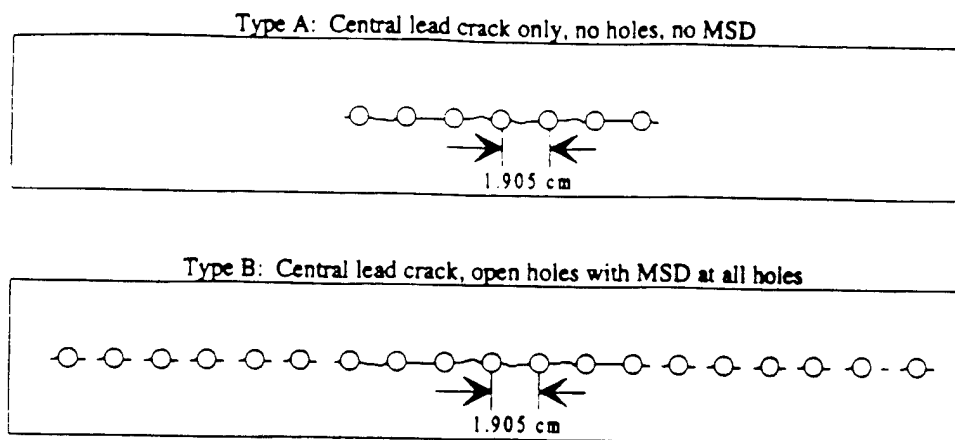Fig. 1. Wide residual strength (WRS) specimen.

Type A: Central lead crack only, no holes, no MSD

Type B: Central lead crack, open holes with MSD at all holes

Fig 2. Schematic of crack and hole configuration.

The MSD damage involved two cracks emanating from all holes. These MSD cracks were prepared by precracking under fatigue loading conditions or machining by a fine saw. WRS specimens with fatigued precracks were initially drilled with holes 2.12 mm in diameter. These holes were then notched on both sides by a jeweler's saw blade with a thickness of 0.30 mm. These specimens were then fatigued under a constant amplitude cyclic condition at a 75.8 MPa stress level to force fatigue cracks to grow from the notched holes. After the cracks grew by at least 0.762 mm, the holes were then drilled to the 3.175 mm diameter at which they were tested. This method gave real fatigue cracks emanating from the sides of holes.

WRS specimens with saw cuts were drilled with holes of 3.175 mm diameter, and then notched with a jeweler's saw. The central lead crack for all WRS specimens was cut by a Ingersoll-Rand HS 3000 Water Jet Cutting System with an Allen Bradley 8400 CNC controller. The final length of all cracks at different holes along with the central lead cracks of these specimens is given in Table 1. The WRS specimens with fatigued MSD cracks, WRS 5B and WRS 6B, are given in boldface. The crack lengths given for each hole are measured from the hole edge.

The narrow specimens, shown in Fig. 3, had the same geometry and material from the same lot as those tested by Moukawsher et al.[3]. The narrow panels tested in the present study were used to investigate the effects of using fine (0.30 mm thick) saw cuts to model fatigue cracks for residual strength measurement. These narrow panels will be referred to as Narrow Residual Strength (NRS) specimens. The NRS specimens were 68.6 cm × 33 cm with a 22.9 cm width across the test section and had a row of 4.06 mm diameter holes across the test sections. Two sets of NRS specimens were tested, one with a nominal central lead crack of 6.1 cm and the other with a nominal lead crack of 8.1 cm. MSD cracks were present at all the holes outside the lead crack. The lead and MSD crack lengths were machined to be identical to those in the specimens in ref.[3] used to measure the residual strength. In ref.[3], the lead and MSD cracks were fatigued while in the present study they were machined by using a fine saw (0.3 mm). For each specimen (with fatigued cracks) tested in ref. [3], two identical specimens (with saw cut cracks) were tested here. The lead and MSD crack lengths for the NRS specimens are given in Table 2. The anti-buckling guide was not used since no local out-of-plane buckling in the NRS and WRS tests was observed.

Four coupon specimens were tested in accordance with ASTM E8[8] in order to establish the tensile stress–strain relationship for the material used in this study. These specimens were machined with nominal dimensions of 203.2 mm × 50.8 mm with a gauge section width of 25.4 mm. The grain direction was again perpendicular to the loading direction. A uniaxial monotonic load was applied to the specimens until failure occurred in the gauge section. The tensile specimens were loaded under strain control mode at a loading rate of 5.08 mm per minute. The stress–strain data were acquired using an 25.4 mm extensometer. The 0.2% offset method was then used to determine the yield stress, σ_s and the ultimate stress, σ_u for the two

Table 1 Crack lengths (cm) for wide residual strength (WRS) specimens

Hole	WRS 1b	WRS 2b	WRS 3b	WRS 4b	WRS 5b	WRS 6b
1L	0.0833	0.0888	0.0272	0.0329	0.0193	0.1462
1R	0.0526	0.0803	0.0326	0.0249	0.0135	0.0464
2L	0.0560	0.0850	0.0269	0.0265	0.0114	0.2846
2R	0.0744	0.1074	0.0211	0.0344	0.0312	0.3137
3L	0.0803	0.1043	0.0217	0.0347	0.0060	0.3090
3R	0.0818	0.1052	0.0271	0.0359	0.0236	0.3000
4L	0.0884	0.0649	0.0291	0.0298	0.0033	0.1702
4R	0.0842	0.0752	0.0298	0.0342	0.0004	0.0061
5L	0.0636	0.0862	0.0293	0.0357	0.0144	0.2855
5R	0.0936	0.0719	0.0312	0.0265	0.0097	0.3059
6L	0.0828	0.0779	0.0189	0.0254	0.0720	0.1238
6R	0.0855	0.0610	0.0301	0.0465	0.0277	0.0775
7L	0.0884	•	0.0368	•	0.0572	•
7R	0.1124	•	0.0400	•	0.0396	•
8L	•	•	•	•	•	•
8R	•	•	•	•	•	•
9L	•	•	•	•	•	•
9R	•	•	•	•	•	•
10L	•	•	•	•	•	•
10R	•	•	•	•	•	•
11L	•	•	•	•	•	•
11R	•	•	•	•	•	•
12L	•	•	•	•	•	•
12R	•	•	•	•	•	•
13L	0.0771	•	0.0136	•	0.0119	•
13R	0.0699	•	0.0324	•	0.0213	•
14L	0.1182	0.1006	0.0481	0.0287	0.4408	0.1876
14R	0.0892	0.0902	0.0302	0.0331	0.4562	0.1858
15L	0.0986	0.0814	0.0164	0.0331	0.0702	0.0377
15R	0.0799	0.0767	0.0234	0.0316	0.2176	0.0418
16L	0.0677	0.0771	0.0301	0.0340	0.3656	0.0503
16R	0.0823	0.0683	0.0240	0.0231	0.3623	0.1146
17L	0.0927	0.0872	0.0255	0.0377	0.0244	0.0017
17R	0.0922	0.0834	0.0259	0.0466	0.2000	0.0058
18L	0.0753	0.0889	0.0177	0.0302	0.0145	0.0198
18R	0.0686	0.0850	0.0273	0.0453	0.0058	0.0231
19L	0.0620	0.0827	0.0348	0.0260	0.0809	0.0175
19R	0.0733	0.1053	0.0357	0.0533	0.1925	0.0603
Lead L	0.1391	0.1270	0.1270	0.4849	0.5042	0.1768
Lead R	0.1675	0.1575	0.4679	0.5884	0.1659	0.1471
Lead Crack	7.9266	11.7145	8.5728	12.5226	7.9498	11.7539

Note: L = left side of hole, R = right side of hole.
All crack lengths were measured from hole edge.
Bold face represent specimens with fatigued MSD cracks..

lots of 2024-T3 aluminum material used in this study. The σ_{ys} and σ_{ult} for the narrow specimens (NRS) in this study were 303 MPa and 434 MPa, respectively. The σ_{ys} and σ_{ult} for the wide specimens (WRS) in this study were 290 MPa and 400 MPa, respectively. The reported values for σ_{ys} and σ_{ult} in MIL-HDBK-5F are 290 MPa and 434 MPa, respectively[9].

2.1. Prediction of residual strength

The residual strength of a panel with a crack is defined as the maximum stress which it can withstand before failure occurs. When MSD is present, the residual strength can be greatly decreased below that which would otherwise be expected with a single lead crack. There have been several analytical techniques proposed to predict failure load of panel with a lead crack and MSD when subjected to a monotonically increasing load. Five of these techniques are briefly described below. As mentioned earlier, this study considered relatively simple analytic approaches which do not model the stable crack extension to determine their applicability by comparing the predicted failure loads with experimental data.

2.1.1. *Net ligament loss criterion*. The net ligament loss criterion, also referred to as net section yield, predicts failure based on the amount of material available to carry the load. Consequently, the failure load is a function of the material's yield strength, and the number of flaws
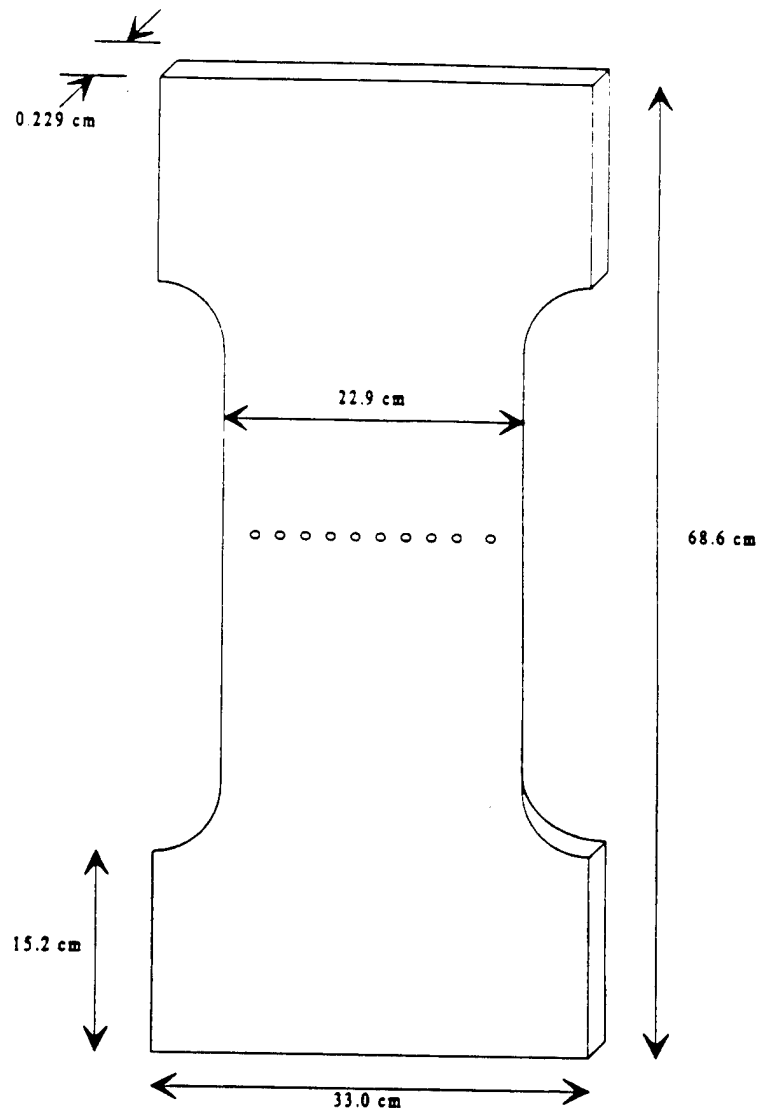
Fig. 3. Narrow residual strength (NRS) specimen.

included in the gauge section. These include the simulated rivet holes, the lead crack and the MSD crack lengths present in the specimen. The failure load, P_{net} is the load that causes the net section stress to equal or exceed the material's yield strength.

$$P_{net} = \sigma_{ys}(W - 2a_2 - nd - 2nl)t, \tag{1}$$

where:

P_{net} = failure load based on the net ligament loss criterion
σ_{ys} = material's yield strength
W = width of gauge section
a_2 = half crack length of the central lead crack
n = number of holes
d = average diameter of the holes
l = average half crack length of the MSD cracks
t = panel thickness at the row of holes.

2.1.2. *K-apparent criterion*. The K-apparent criterion is based on the linear elastic fracture mechanics. The primary assumption for this criterion is that there exists an effective fracture toughness for the thin sheet which allows more yielding than that under the plane strain condition. This is referred to here as K_{app} (K-apparent). Unlike the fracture toughness, K_{IC}, K_{app} is not strictly a material property, but can vary with different geometries and crack configuration.

Table 2. Crack lengths (cm) for narrow residual strength (NRS) specimens

Hole	NRS-01a	NRS-01b	NRS-01c	NRS-04a	NRS-04b	NRS-04c	NRS-04 d
1L	0.0508	0.0356	0.1397	0.4851	0.0356	0.2540	0.0356
1R	0.1397	0.0762	0.0864	0.5207	0.0254	0.2921	0.0127
2L	0.1778	0.0254	0.1499	0.4140	0.0356	0.1397	0.1346
2R	0.0483	0.0254	0.0508	0.3861	0.0254	0.1346	0.1372
3L	0.1626	0.0991	0.1524	0.3912	0.0381	0.0991	0.2210
3R	0.1880	0.1219	0.0533	0.0356	0.0635	0.1270	0.2718
4L	•	•	•	•	•	•	•
4R	•	•	•	•	•	•	•
5L	•	•	•	•	•	•	•
5R	•	•	•	•	•	•	•
6L	•	•	•	•	•	•	•
6R	•	•	•	•	•	•	•
7L	•	•	•	•	•	•	•
7R	•	•	•	•	•	•	•
8L	0.0914	0.0737	0.2083	•	•	•	•
8R	0.1448	0.0610	0.0508	•	•	•	•
9L	0.0508	0.0381	0.2692	0.1245	0.1448	0.3378	0.3378
9R	0.1168	0.0203	0.2540	0.0635	0.0914	0.2616	0.2718
10L	0.0660	0.0229	0.4293	0.1854	0.2565	0.1702	0.1981
10R	0.0838	0.0406	0.3200	0.1930	0.3277	0.1499	0.2083
11L	na	na	na	0.1321	0.4140	0.0152	0.0762
11R	na	na	na	0.1422	0.4191	0.0381	0.1041
Lead Crack	6.2992	6.1722	6.2586	8.1077	8.2194	8.1382	8.3566

Note: L = left side of hole. R = right side of hole.
All crack lengths were measured from hole edge.

To determine the values for K_{app} for the narrow and wide specimens in the present study, panels with the same width, 229 mm and 381 mm, having a lead crack and no MSD (Type A-configuration, Fig. 2) were used. The following equation was used to determine K_{app}:

$$K_{app} = \sigma \sqrt{\pi a \beta_w}.$$ (2)

where:

K_{app} = apparent stress intensity factor
σ = applied stress at fracture
W = specimen width
a = half of lead crack length
$\beta_w = \sec \pi a/W$ = finite width correction factor.

The K_{app} was calculated to be 78.9 MPa√m for the narrow specimen, and 83.2 MPa√m for the wide specimen in the present study.

To determine the predicted failure load for the specimens with MSD (Type B-configuration, Fig. 2) by this criterion, the stress intensity factor of the lead crack including crack interaction effects from MSD crack was used to determine the remotely applied load that would produce a stress intensity factor equal to or greater than the measured K_{app}.

2.1.3. *Ligament yield criterion[10]*. The ligament yield criterion predicts the residual strength of the panel with lead crack and MSD as the stress level which will cause the lead crack's plastic zone to touch the plastic zone of the MSD crack. The size of plastic zone is equal to Irwin's plastic zone radius[10].

$$R = \frac{1}{2\pi}\left(\frac{K}{\sigma_{ys}}\right)^2.$$ (3)

where:

R = plastic zone diameter in front of the crack
K = stress intensity factor at the crack tip
σ_{ys} = yield strength of the material.

As the remote stress level increases, the plastic zone sizes of different cracks will increase and will eventually touch. When the plastic zone of the lead crack meets the plastic zone from the nearest neighboring MSD crack, the ligament has effectively yielded. Once this occurs, the

Residual strength of unstiffened aluminum panels

7

Specimen
Center Line

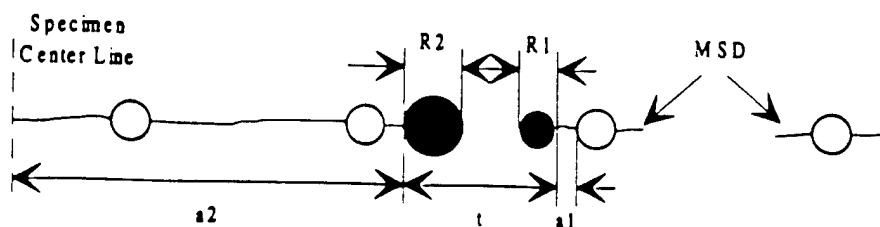R2   R1   MSD

a2   t   a1

Fig. 4. Schematic of plastic zones for ligament yield criterion.

lead crack effectively extends to the far end of the MSD crack. Figure 4 shows a schematic of this linkup criterion[10]. When the applied load reaches a level that causes the effective ligament to yield, the ligament will fail.

According to Swift[10], the predicted failure of a specimen with MSD is a function of the plastic zone size of the lead crack and the nearest neighboring MSD crack, the material's yield strength, and an interaction factor between the MSD crack and the lead crack. The interaction between the lead crack and its neighboring MSD crack can be determined from Rooke and Cartwright[11], or from Kamei and Yokobori[12]. For this study as in the previous study[3], the Kamei and Yokobori criterion was used. Figure 5 shows a schematic and the equations used by Kamei and Yokobori to determine the stress intensity factors for unequal length adjacent cracks.

The stress intensity factor for the lead and MSD cracks are found by the method of compounding. The stress intensity factor for the lead crack then becomes:

Remote Stress

2   1

2a   t   2b

Remote Stress
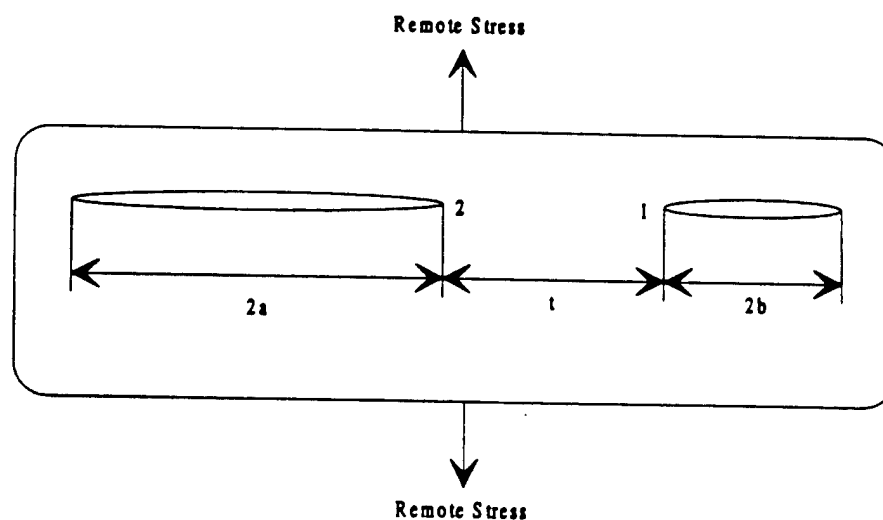
$$\beta_{i1} = \sqrt{1 + \frac{2a}{t}} \left[1 - \left(1 + \frac{t}{2b} \right) \frac{K(k) - E(k)}{K(k)} \right]$$

$$\beta_{i2} = \sqrt{1 + \frac{2b}{t}} \left[1 - \left(1 + \frac{t}{2a} \right) \frac{K(k) - E(k)}{K(k)} \right]$$

where: K(k) = Complete elliptic Integral of the first kind
E(k) = Complete elliptic integral of the second kind

$$k = 2 \sqrt{\frac{ab}{(2a + t)(2b + t)}}$$

Fig. 5. Schematic of Kamei–Yokobori crack interaction factor[12]

8   M C CHERRY et al.

$$K_2 = \left[\frac{P}{W'_{net}t} \right] \sqrt{\pi a_2} \beta_{12} \frac{W'_{net}}{W'_{lead}} . \tag{4}$$

where:

P = applied load
a_2 = lead crack half length
β_{12} = Kamei–Yokobori interaction factor for lead crack
W'_{net} = net section width of specimen
W'_{lead} = appropriate width for lead crack compounding.

The stress intensity factor for the MSD crack is based on the Bowie solution for a cracked hole [13] and includes the appropriate area for compounding as well as the interaction factor [eq. (5)].

$$K_1 = \left[\frac{P}{W_{net}t} \right] \sqrt{\pi a_1} \beta_h \beta_{11} \frac{W_{net}}{W_{MSD}} . \tag{5}$$

where:

a_1 = MSD crack length (from edge of hole)
β_{11} = Kamei–Yokobori interaction factor for MSD crack
$W_{MSD} = W_{net} + d + 2a_1$ = appropriate width for MSD crack compounding.

$$\beta_h = \left[\frac{F_1}{F_2 + \dfrac{a_b}{r}} + F_3 \right] = \text{Bowie factor,} \tag{6}$$

where:

a_b = MSD crack length measured from hole edge
r = radius of the hole
F_1, F_2, F_3 = hole configuration constants

for holes with cracks   for holes with only
emanating from both sides: one side cracked:
F_1 = 0.6865 F_1 = 0.8733
F_2 = 0.2772 F_2 = 0.3245
F_3 = 0.9439 F_3 = 0.6762.

The predicted failure load according to the Swift criterion then becomes:

$$P_{swift} = \sigma_{ys} t W_{net} \sqrt{ \frac{2b}{ \left[a_1 \beta_h^2 \beta_{11}^2 \left(\dfrac{W_{net}}{W_{MSD}} \right)^2 + a_2 \beta_{12}^2 \left(\dfrac{W_{net}}{W_{lead}} \right)^2 \right] } }, \tag{7}$$

where: .

P_{swift} = failure load based on the Swift criterion
b = crack tip separation.

2.1.4. *Average displacement criterion[14]*. The average displacement criterion proposed by Jeong and Brewer assumes that the stress across the ligament is uniform and equal to the material's ultimate strength. According to Jeong and Brewer, prior to specimen failure, the displacement of the crack faces is assumed to be zero in the direction parallel to the crack. The configuration with a single large lead crack surrounded by smaller MSD cracks was modeled as the superposition of two known cases. The two cases used were a single crack (from $x = 0$ to $x = c$) in an infinite medium subjected to remote tension, and the same single crack subjected to pressure loading on its crack faces. The locations of the crack tips used in this criterion and in the next criterion also by Jeong and Brewer can be seen in Fig. 6. Since the displacement of the crack faces along the ligament (from $x = a$ to $x = b$) after superposition should be zero, this criterion then becomes:
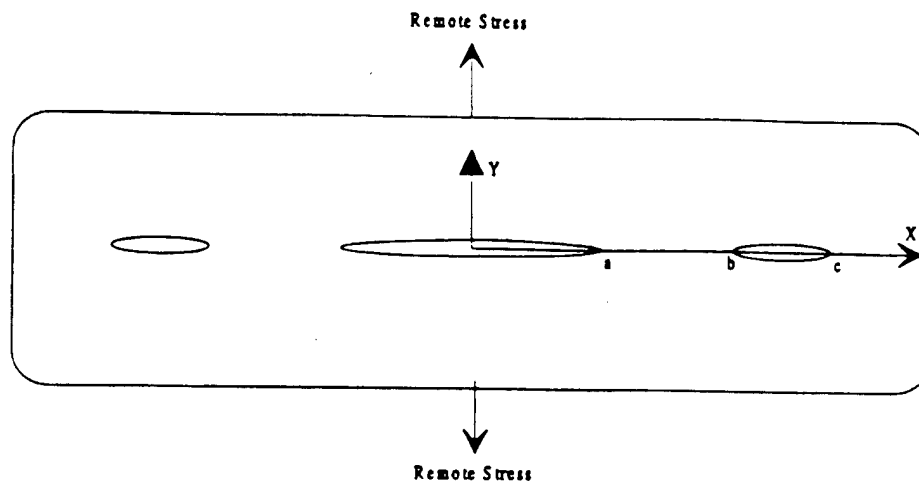
Fig. 6. Crack tip location definition for average stress and average displacement criterion.

$$\int_a^b \nu_1(x)\,dx + \int_a^b \nu_2(x)\,dx = 0, \tag{8}$$

where:

$\nu_1(x)$ = displacement of the crack face perpendicular to the crack (finite body uniform tension)
$\nu_2(x)$ = displacement of the crack face perpendicular to the crack (infinite body pressure loading).

$$\nu_1(x) = \frac{2\sigma_0}{E}\sqrt{c^2 - x^2} \tag{9}$$

$$\nu_2(x) = \frac{2\sigma_{ult}}{E\pi}\left\{ \begin{array}{l} (b-x)\cosh^{-1}\left(\dfrac{c^2 - bx}{c(b-x)}\right) - (a-x)\cosh^{-1}\left(\dfrac{c^2 - ax}{c(x-a)}\right) + \\[2mm] (b+x)\cosh^{-1}\left(\dfrac{c^2 + bx}{c(x+b)}\right) - (a+x)\cosh^{-1}\left(\dfrac{c^2 + ax}{c(x+a)}\right) + \\[2mm] 2\left(\sin^{-1}\left(\dfrac{b}{c}\right) - \sin^{-1}\left(\dfrac{a}{c}\right)\right)\sqrt{c^2 - x^2} \end{array} \right\}. \tag{10}$$

The predicted failure load, P_{avgd}, of the panel according to the average displacement criterion becomes:

$$P_{avgd} = \frac{2\sigma_{ult}W_{asd}t}{\pi}\frac{\int_a^b \nu_2(x)\,dx}{b\sqrt{c^2 - b^2} - a\sqrt{c^2 - a^2} + c^2\left[\sin^{-1}\left(\dfrac{b}{c}\right) - \sin^{-1}\left(\dfrac{a}{c}\right)\right]}, \tag{11}$$

where:

a,b,c = locations of the crack tips (see Fig. 6)
$W_{asd} = W_{net} + 2a_2 + 2(d + 2a_1)$ = appropriate width for average displacement and average stress criterion.

2.1.5. *Average stress criterion[14]*. Jeong and Brewer postulated that the stress in the ligament between the lead crack and its nearest neighboring MSD crack is uniform and equal to the material ultimate strength immediately prior to failure of the specimen. The average stress criterion models the various cracks individually. Linkup between the two adjacent cracks is assumed to occur when the average stress in the ligament between the crack tips is equal to the ultimate tensile strength of the material. The criterion can be expressed as:

M. C. CHERRY *et al*

Table 3. Measured residual strength of fatigue cracked and saw cut narrow panels (NRS) in kN

Specimen	Fatigue crack	Saw cut #1	% Difference	Saw cut #2	% Difference
NRS-01a	89.85	89.05	−0.89	88.43	−1.58
NRS-01b	103.42	102.08	−1.29	102.39	−0.99
NRS-01c	88.16	85.71	−2.77	85.49	−3.03
NRS-04a	57.42	70.37	22.54	68.63	19.52
NRS-04b	76.28	77.75	1.92	78.37	2.74
NRS-04c	72.32	73.93	2.21	74.64	3.20
NRS-04d	69.34	70.06	1.03	68.81	−0.77

$$P_{\text{avgst}} = \sigma_{\text{ult}} W_{\text{asd}} t \frac{b - a}{\int_a^b \frac{\left[(c^2 - a^2) \frac{E(k)}{K(k)} + a^2 \right] x - x^3}{\sqrt{(x^2 - a^2)(b^2 - x^2)(c^2 - x^2)}} \, dx} . \tag{12}$$

where:

P_{avgst} = specimen failure load based on the average stress criterion
$E(k)$ = complete elliptic integral of the first kind
$K(k)$ = complete elliptic integral of the second kind
k = geometry factor.

$$k = \sqrt{\frac{c^2 - b^2}{c^2 - a^2}}. \tag{12a}$$

3. DISCUSSION OF RESULTS

The use of saw cuts to model fatigue cracks when measuring residual strength, and the effectiveness of the above mentioned five failure criteria to predict residual strength of a panel with a lead crack and MSD are discussed in this section.

3.2. *Saw cut versus fatigue crack*

The residual strength tests performed by Moukawsher *et al.* [3] with the lead and MSD cracks created by fatigue were repeated here using saw cuts to create the lead and MSD cracks. The comparison of the residual strength from fatigue cracks and saw cuts is shown in Table 3. As described earlier, two identical specimens with saw cut cracks were tested for each configuration. Table 3 shows that the residual strength from the saw cut specimens, in general, is within 3% of its counterpart from the fatigue crack specimens. The residual strength from the two identical saw cut specimens were within 2% of each other. One of the fatigue crack specimen (NRS-04a) had a significantly lower residual strength than that from the saw cut specimen. It is suspected that there was some problem during the testing of fatigue crack specimen since the

Table 4. Failure load comparison with prediction from failure criteria for narrow (NRS) and wide (WRS) residual strength specimens in kN

Specimen	Measured failure load	Net ligament loss	K_{app}	Ligament yield	Average displacement	Average stress
NRS-01a	89.11	86.78	118.72	97.93	69.48	68.23
NRS-01b	102.63	90.74	121.56	109.36	75.66	74.68
NRS-01c	86.45	79.17	119.65	90.34	64.99	63.83
NRS-04a	69.50	62.32	100.66	81.01	60.09	59.20
NRS-04b	77.47	68.54	100.66	80.75	60.67	59.65
NRS-04c	73.63	68.05	96.88	70.72	53.29	52.13
NRS-04d	69.40	66.76	93.99	65.51	49.64	48.53
WRS 1b	67.08	66.19	88.13	66.58	43.16	42.54
WRS 2b	53.91	56.18	70.14	55.55	36.93	36.41
WRS 3b	61.61	67.51	84.51	62.35	39.58	39.10
WRS 4b	49.86	56.00	66.67	50.48	31.59	30.96
WRS 5b	62.32	65.02	88.24	61.36	43.91	43.46
WRS 6b	47.64	54.06	69.57	51.44	34.11	33.46

Residual strength of unstiffened aluminum panels   11

Table 5. Absolute error comparison of failure criteria for narrow (NRS) and wide (WRS) specimens in percent

Specimen	Net ligament loss	K_{app}	Ligament yield	Average displacement	Average stress
NRS-01a	2.61	33.23	9.90	22.03	23.43
NRS-01b	11.59	18.45	6.56	26.28	27.23
NRS-01c	8.42	38.40	4.50	24.83	26.17
NRS-04a	10.34	44.83	16.56	13.54	14.82
NRS-04b	11.52	29.93	4.23	21.68	23.00
NRS-04c	7.57	31.57	3.95	27.63	29.20
NRS-04 d	3.80	35.42	5.61	28.48	30.08
WRS 1b	1.33	31.39	0.75	35.66	36.59
WRS 2b	4.21	30.11	3.04	31.49	32.46
WRS 3b	9.58	37.16	1.20	35.76	36.53
WRS 4b	12.32	33.72	1.25	36.63	37.91
WRS 5b	4.33	41.59	1.54	29.54	30.27
WRS 6b	13.47	46.03	7.97	28.40	29.77
Average	7.78	34.76	5.16	27.84	29.03

results of two saw cut tests are within 2% of each other. Two of the wide panels (WRS 5b and WRS 6b) had fatigue cracks rather than saw cuts. The crack lengths did not match those of the saw cut specimens, so no direct comparison was made.

3.3. Prediction of failure loads

The predicted loads from all five criteria along with the experimental counterpart of the present study are given in Table 4. The absolute errors between the predicted and measured failure loads are given in Table 5. The experimental failure loads, in the present study are compared
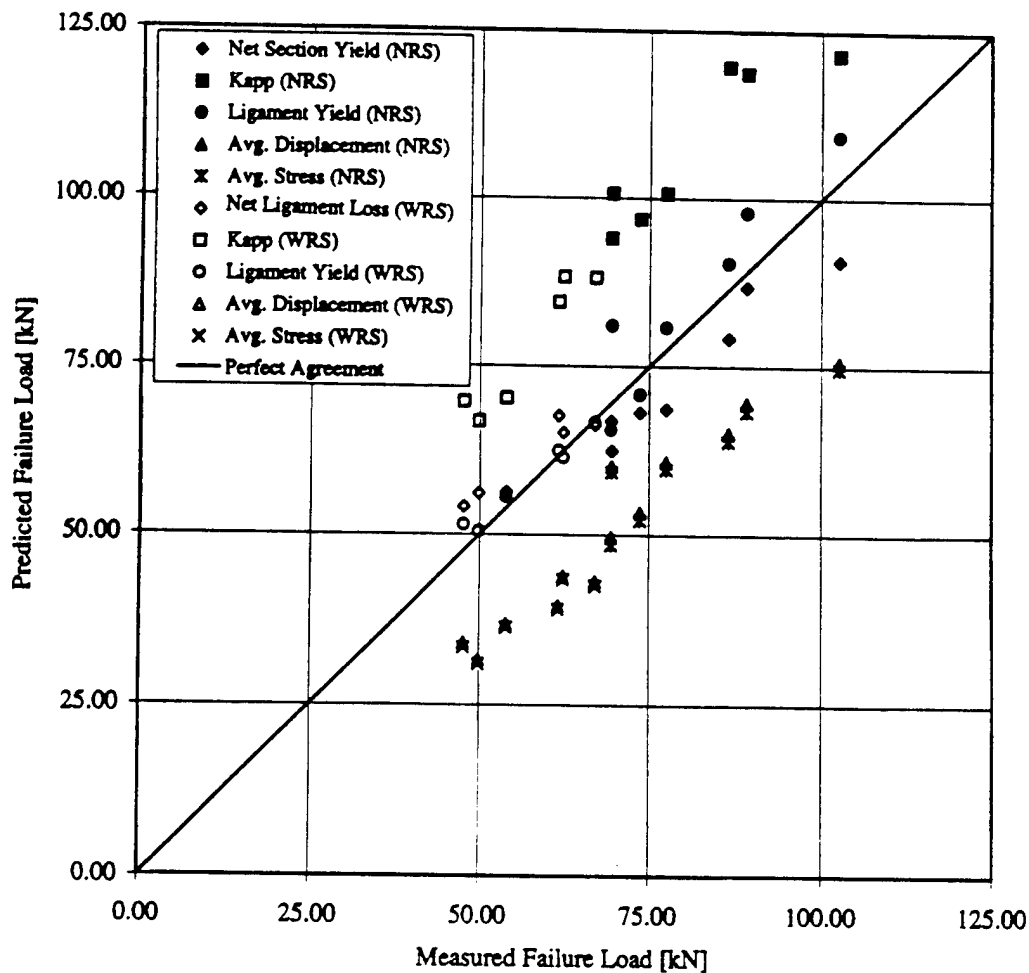

Fig. 7. Comparison of predicted and measured failure loads.

with the predicted failure loads for each specimen using the five failure criteria in Fig. 7. For the narrow specimens (NRS), the actual reported failure load is the average of the one fatigue crack specimen and the two saw cut specimens of the same geometry, except for NRS-04a, where the fatigue crack result was discarded, and the two saw cut specimens were averaged. The 45 degree line in Fig. 7 represents perfect agreement between predicted and actual failure loads. These results are discussed in detail next. A comparison of the relative errors, i.e. average error for all specimens from all five criteria for both narrow and wide specimens, is shown in Fig. 8.

3.3.6. *Net ligament loss criterion.* The net ligament loss criterion produces good results for both the narrow and wide specimens with an average error of 7.8%. This criterion overpredicts residual strength by an average of 7.1%, for wide specimens, while it underpredicts the residual strength by an average of 8.9% for the narrow panels.

3.3.7. *K-apparent criterion.* This criterion assumes linear elastic fracture mechanics approach and uses the stress intensity factor of the lead crack including the interaction from the MSD. The results of both the narrow and wide panels showed that this criterion consistently overestimates the residual strength of panels with MSD with an average error of 34.8%.

3.3.8. *Ligament yield criterion.* The ligament yield criterion, in this study, used Irwin's plastic zone radius as the plastic zone size, as suggested by Swift[10], and the material yield stress to determine the plastic zone sizes. This criterion gave the best results for both the wide and narrow panels (average difference was 5.2%). The ligament yield criterion was very accurate for the wide panels (average error was 2.6%) and reasonably accurate for the narrow panels (average difference was 7.3%)

3.3.9. *Average displacement criterion.* The average displacement criterion greatly underestimates the residual strength of panels with MSD with an average error of 27.8%.
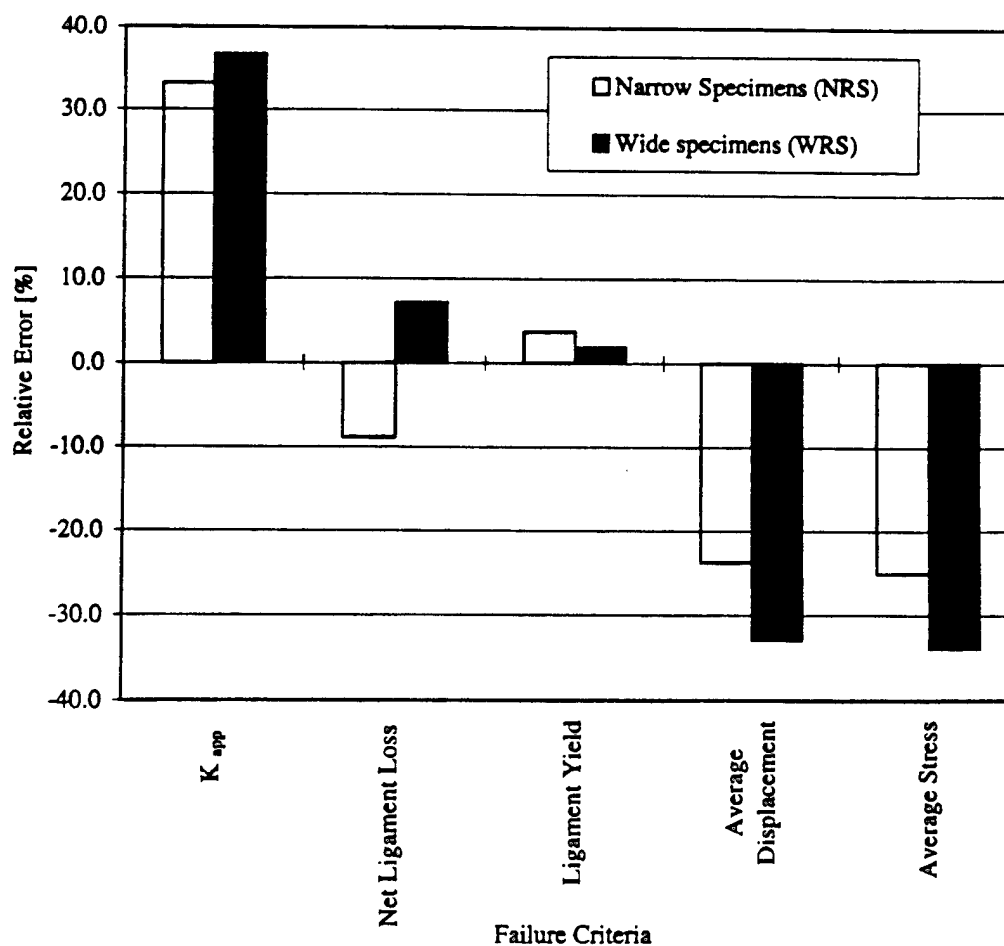

Fig. 8. Comparison of relative (average) error for all five failure criteria.

3.3.10. *Average stress criterion.* The average stress criterion, like the average displacement criterion underestimates the residual strength with an average error of $29°_0$.

The width of the specimens did not affect, in general, the trends in the prediction of failure loads from the five failure criteria. Only the net ligament loss criterion produced significant difference between the narrow and wide panels. The net ligament loss criterion was unconservative for wide specimens and conservative for narrow specimens. The ligament yield criterion gave excellent results for the wide specimens (average error 2.6%, and no error larger than 8%), but not quite as good for narrow panels (with an average error of 7.6% with a maximum error of 16.5%).

4. CONCLUSIONS

Unstiffened aluminum panels with multiple site damage were tested to determine their residual strengths. The test results were compared with the failure loads predicted by five simple failure criteria where stable crack extension is not modeled. The use of saw cuts to model fatigue cracks for the measurement of residual strength was examined.

Saw cuts can be used to model fatigue lead and short MSD cracks for residual strength testing where stable crack extension is not an issue. The residual strength of the saw cut specimens and the fatigue cracked specimens of the same geometry were within 3% of each other.

The five failure criteria produced a wide range of residual strength predictions for wide and narrow panels with multiple site damage. The *K*-apparent approach produced the most unconservative results. The ligament yield criterion produced the most accurate residual strength predictions in this study. The net ligament loss criterion also gave good results, but it was unconservative for the wider panels and conservative for the narrower ones. The average stress and average displacement criteria consistently produced excessively conservative predictions of residual strength. Only the net ligament loss criterion showed a difference in the prediction of residual strength between the narrow and wide panels.

5. REFERENCES

1. Mar, J. W., Preserving aging aircraft. *Aerospace America*, January 1996, pp. 38–43.
2. Mar, J. W., Structural integrity of aging airplanes: a perspective. In *Structural Integrity of Aging Airplanes*, ed. S. N. Alturi, S. G. Sampath and P. Tong. Springer-Verlag, Berlin, Heidelberg, 1991.
3. Moukawsher, E. J., Heinimann, M. B. and Grandt, A. F., Jr, Residual strength of panels with multiple site damage. *AIAA J.* (in press).
4. Newman, J. C., Dawicke, D. S., Sutton, M. A. and Bigelow, C. A., A fracture criterion for widespread cracking in thin-sheet aluminum alloys. *Presented to International Committee on Aeronautical Fatigue*, Stockholm, Sweden, June 1993.
5. Alturi, S. N. and Tong, P., Computational schemes for integrity analyses of fuselage panels in aging airplanes. In *Structural Integrity of Aging Airplanes*, ed. S. N. Alturi, S. G. Sampath and P. Tong. Springer-Verlag, Berlin, Heidelberg, 1991.
6. DeWitt, R., Fields, R. J., Low, III, S. R., Harne, D. E. and Foecke, T., Fracture testing of large-scale thin-sheet aluminum alloy. NIST Report prepared for FAA, May 1995.
7. Gruber, M. L., Wilkins, K. E. and Worden, R. E., Investigation of fuselage structure subject to widespread fatigue damage. *Presented at FAA–NASA Symposium, Continued Airworthiness of Aircraft Structures*, Atlanta, GA, U.S.A., August 1996.
8. Test methods of tension testing of metallic materials. ASTM E8-94C, American Society for Testing and Materials, July 1994.
9. Metallic materials and elements for aerospace vehicle structures. Mil-HDBK-5F. Department of Defense, Washington D.C., November 1990.
10. Swift, T., Widespread fatigue damage monitoring issues and concerns. *Presented at the 5th International Conference on Structural Airworthiness of New and Aging Aircraft*, Hamburg, Germany, June 1993.
11. Rooke, D. P. and Cartwright, D. J., *Compendium of Stress Intensity Factors*. Her Majesty's Stationery Office, London, 1976.
12. Kamei, A. and Yokobori, T., Two collinear asymmetrical elastic cracks. Report of the Research Institute for Strength and Fracture of Materials, Tohoku University, Vol. 10, Nos 1–4, pp. 41–42, 1974.
13. Grandt, A. F. Jr, Stress intensity factors for some thru-cracked fastener holes. *International Journal of Fracture*, 1975, 14(2), 283–294.
14. Jeong, D. Y. and Brewer, J. C., On the linkup of multiple cracks. *Engineering Fracture Mechanics*, 1995, 51(2), 233–238.

Presented at: 1996 USAF Aircraft Structural Integrity Program Conference
San Antonio, TX, December 3-5, 1996

Analysis of Stiffened Panels with Multiple Site Damage

*Mr. Markus B. Heinimann
Dr. Alten F. Grandt, Jr.
School of Aeronautics & Astronautics
1282 Grissom Hall
Purdue University
West Lafayette, IN 47907-1282

Abstract

This paper investigates the effect of multiple site damage (MSD) on stiffened panels. An analytical model based on displacement compatibility was used to analyze the link up and residual strength behavior of stiffened panels with lead and MSD cracks. Fifteen inch wide stiffened aluminum specimens with various lead and MSD crack lengths and two different stiffener configuration were tensile tested to determine crack link up and panel failure loads. A tip stress intensity reduction factor was verified experimentally through fatigue tests of stiffened panels, and used in two different link up and panel failure criteria to predict the lead crack link up and panel failure loads. The ligament yield criterion, modified for the stiffened panel, was shown to accurately predict the lead crack link up load. The apparent fracture toughness criterion consistently overpredicts link up loads for specimens with MSD. The stiffener failure criterion was shown to be able to predict panel failure to within less than 4 percent for specimens with a true lead crack. The net section failure criteria gives good results for specimens were the lead crack was arrested at a hole.

Introduction

Multiple site damage (MSD) is characterized by the simultaneous presence of several cracks at various sites, such as at different holes in a structural element. MSD may become significant and critical when cracks are of sufficient size and density whereby the structure will no longer meet the present damage tolerance requirements, i.e. it may reduce the lead crack residual strength and fatigue life of a structural component below those based on a single lead crack approach without considering the interaction with the surrounding cracks [1]

Since both military and commercial aircraft, are being increasingly used beyond their designed lifetime, MSD poses a significant challenge to those who must assure the structural integrity of aircraft. Most commercial aircraft are designed and maintained according to the "damage tolerance" philosophy based on the principles of fracture mechanics [2]. This damage tolerance philosophy is based on a single lead crack in a structure. Small MSD cracks, however, can cause a structure to catastrophically fail from smaller lead cracks than those which cause failure when MSD is not present.

Previous research at Purdue University and the Air Force Institute of Technology (AFIT) has examined the applicability of various simple failure criteria to predict crack link up in open hole panels with lead and MSD cracks [3, 4]. The current work aims to expand this model to include stiffeners, stringers and tear straps. Another project is examining the effects associated with lap joints.

An analytical model based on displacement compatibility between the sheet and the stiffener at the rivet locations [5, 6, 7] has been implemented here to quantify the effects of stiffeners on lead crack stress intensity factors. The model was verified by testing 15 inch wide panels with two different stiffener configurations and various lead and MSD crack geometries. The link up and ultimate failure loads were predicted using simple analytical failure criteria.

Open Hole MSD Background

Previous work at Purdue and AFIT [3, 4, 8] has resulted in the development of a model capable of predicting residual strength and fatigue crack growth in open hole panels with MSD. A number of different crack link up criteria proposed in the literature [9, 10] were evaluated and compared to the residual strength tests. The residual strength test specimens were made form Al2024-T3,

0.09 inches thick for the 9 inch wide panels, 0.04 inches thick for the 15 inch wide specimens. The specimens contained various lead and MSD crack configurations, which were fatigue cracks for the 9 inch wide specimens [3], and fine saw cuts in the 15 inch wide panels [4]. The ligament yield criterion proposed by Swift [9] was best able to predict the crack link up leading to sheet failure. Figure 1 shows a comparison of various simple analytical failure criteria and their ability to predict residual strength in 9 inch and 15 inch wide 2024-T3 aluminum panels which contained a row of cracked holes.

Since it is very difficult to precrack wide panels to obtain uniform MSD crack lengths, fine saw cuts or EDM notches often are used to as MSD and lead cracks [11]. In order to verify that the use of saw cuts to model lead and MSD cracks several of Moukawsher's residual strength test [3] were repeated using fine saw cuts (0.013 inches wide) rather than actual fatigue cracks to represent the MSD and lead crack.. For each of the 9 inch wide open hole specimens with fatigue lead and MSD cracks, two identical saw cut panels were tested. The residual strength of the saw cut panels was within 3% of the fatigue crack panel residual strength [4], leading to the conclusion that the use of fine saw cuts to model fatigue cracks in residual strength testing is acceptable. This conclusion is also supported in the literature. Broek reports, for example, that the use of jeweler's saw cuts instead of fatigue cracks in Aluminum alloy sheets does not effect the residual strength results [12]. Recent work by Dawicke, et al [13] indicates that using saw cuts instead of fatigue cracks has a significant effect on stable crack growth, but only a small effect on failure stress.

Stiffened Panel Model

The presence of stiffeners in a cracked panel has two basic effects that need to be modeled. First, the stiffeners reduce the crack tip stress intensity factor by increasing amounts as the crack approaches the stiffener. Second, the presence of the lead crack causes increased loading in the stiffener near the crack plane. The analysis outlined below can be used to determine the magnitude of both of these effects for a given specimen and crack configuration. The analysis of stiffened panels is accomplished using an analytical model. The model is based on displacement compatibility and has successfully been used in the past to analyze stiffened panels containing lead cracks [5, 6, 7]. The analysis employs the theory of elasticity to determine the displacements at the rivet locations, due to the applied remote stress and the unknown rivet forces, in a center cracked sheet and stiffeners. The rivet location displacements v_i in the sheet can be written as:

$$v_i = \sum_j A_{ij}(-Q_j) + B_i \sigma \qquad (1)$$

and the corresponding displacements v_i^{st} in the stiffener are given by:

$$v_i^{st} = \sum_j A_{ij}^{st} Q_j + B_i^{st} \sigma \qquad (2)$$

The matrix A_{ij} in Eq. 1 represents the displacements at the rivet location i in the sheet due to a unit force at rivet location j, B_i represents the displacement at the rivet location i in the sheet due to the applied remote stress σ. Similarly The matrix A_{ij}^{st} in Eq. 2 represents the displacements at the rivet location i in the stiffener due to a unit force at rivet location j, B_i^{st} represents the displacement at the rivet location i in the stiffener due to the applied remote stress σ. The displacements in the sheet and stiffener match at the rivet locations, therefore, equations 1 and 2 can be equated, and the resulting system can be solved for the unknown rivet forces, Q_i. Figure 2 shows schematically how the presence of the stiffener is modeled using the rivet forces Q_i. The stress intensity factor for the stiffened sheet can then be obtained using superposition of the stress intensity factor for a center crack subject to applied stress σ, and the stress intensity factor for a center crack subject to the point loads Q_i.

For convenience two non-dimensional parameters are introduced to describe the crack tip stress intensity reduction and the load transfer into the stiffener [7]. The tip stress reduction factor C is defined as the ratio of the stress intensity factor of the sheet with and without stiffeners (equation 3).

$$C = \frac{K_{stiffened}}{\sigma\sqrt{\pi a}} \qquad (3)$$

The stiffener load concentration factor L is defined as the ratio of the maximum stringer stress, which occurs in the crack plane, and the stress in the stringer at the end of the panel (equation 4).

$$L = \frac{\sigma_{max}}{\sigma_\infty}\bigg|_{stiffener} \qquad (4)$$

Because of symmetry only one quarter of the panel needs to be analyzed. The number of rivet locations that are considered determines the size of the system

of equations that needs to be solved. A computer code was written to determine the unknown rivet forces, tip stress reduction factor C, and load concentration factor L, given the material and geometric properties of the stiffened panel. The code was verified by comparison with the results obtained by Poe [6], using the same analytical method, and Vlieger [7], using finite elements. This comparison showed that using 20 rivet locations per quadrant results in a fully converged solution that matches both Poe [6] and Vlieger [7].

Modeling of MSD

The stiffened panel model outlined above does not include the presence of MSD cracks. Hence the presence of MSD in addition to the lead crack has to be modeled separately. A more complicated stiffened panel model proposed by Nishimura [14] allows for multiple cracks in the sheet.

The presence of multiple cracks in a sheet leads to crack interaction. The interaction between the lead and MSD cracks was modeled here using the Kamei-Yokobori interaction factor [15] as was done in the previous unstiffened panel work. [3, 4]. Figure 3 shows a schematic for the Kamei-Yokobori interaction factor as well as the equations used.

The area loss in a finite sheet due to MSD also has to be considered. It is modeled using appropriate areas in stress intensity factor compounding and load calculations for the failure criteria.

Panel Failure Criteria

Failure criteria in this stiffened panel research refers to criteria that determine the ultimate, and catastrophic failure of the stiffened panels. Two different panel failure criteria were examined in this project.

Stiffener Failure

The stiffener failure criteria predicts panel failure when the stress in the stiffener near the crack plane reaches the stiffener material's ultimate stress. This condition can be expressed by equation 5.

$$P_{stif} = \frac{\sigma_{ult\,st} \; \psi \; A_{st}}{L} \; \frac{A_{st} E_{st} + A_{net} E}{A_{st} E_{st}}$$

(5)

where: $\sigma_{ult\,st}$ = stiffener ultimate stress

L = stiffener load concentration (Eq. 4)

ψ = geometry factor

A_{st} = stiffener cross sectional area

E_{st} = stiffener elastic modulus

$A_{net} = (W - 2a - nd - 2n_{MSD}a_{MSD})\,t$ = net cross sectional area of sheet (i.e. excluding areas of holes, lead and MSD cracks)

a = lead crack half length

n = number of open holes with or without MSD

d = hole diameter

n_{MSD} = number of holes with MSD

a_{MSD} = MSD crack length

t = sheet thickness

E = sheet elastic modulus

The ratio term with the cross sectional areas and elastic moduli determines how much of the total load is carried by the stiffener, assuming stiffeners and sheet have the same strain away from the crack plane.

Net Section Failure

According to the net section failure criterion, panel failure occurs when the stress in the sheet and the stiffener both reach their respective ultimate stress. The expression for the net section failure criteria is shown in equation 6.

$$P_{section} = \sigma_{ult} A_{net} + \frac{\sigma_{ult\,st}\ \psi\ A_{st}}{L}\frac{A}{A_{lead}}$$

(6)

where: σ_{ult} = sheet ultimate stress

A = sheet gross cross sectional area

$A_{lead} = (W - nd - 2n_{MSD}a_{MSD})\,t$ = lead crack cross sectional area

W = Sheet width

n = number of open holes with or without MSD

d = hole diameter

n_{MSD} = number of holes with MSD

a_{MSD} = MSD crack length

t = sheet thickness

The ratio between the sheet cross sectional area and the lead crack area accounts for the load concentration in the stiffener due to the MSD area loss in the sheet.

Link Up Criteria

Because of the stiffener's arrest capabilities lead crack extension and link up with MSD cracks is possible without leading to panel failure. The two criteria discussed below are used to determine the loads which cause link up between lead and adjacent MSD cracks. Depending on lead crack length and panel configuration, multiple link-ups can occur before final panel failure.

K apparent

The apparent fracture toughness criterion predicts crack link up when the lead crack stress intensity factor exceeds the materials fracture toughness. The lead crack stress intensity factor is adjusted here using the Kamei-Yokobori factor to account for the presence of the MSD crack. Equation 7 gives the expression for the apparent fracture toughness criterion.

$$P_{K\,app} = \frac{K_c\,A_{net}}{\sqrt{\pi a \beta_{il}}\,C}\,\frac{A_{net}\,E + A_{st}\,E_{st}}{A_{net}\,E}$$

(7)

where: K_c = apparent fracture toughness of sheet
   a = lead half crack length
   β_{il} = Kamei-Yokobori interaction factor for lead crack
   C = Tip stress intensity reduction factor

Ligament Yield

The ligament yield criterion was proposed by Swift [9] and has been used successfully for unstiffened panels [3, 4, 10]. As shown in Fig. 4, crack link up is predicted to occur when the plastic zones ahead of the lead crack and the adjacent MSD crack "touch". Based on work by Cherry et. al. [4] the Irwin plastic zone radius combined with the material yield stress has been used to determine the plastic zone sizes in this project. Hence, the size of plastic zone is estimated to be equal to Irwin's plastic zone radius [9].

$$R = \frac{1}{2\pi} * \left(\frac{K}{\sigma_{ys}}\right)^2$$

(8)

where: R = plastic zone size in front of the crack

K = stress intensity factor at the crack tip

σ_{ys} = yield strength of the sheet material

As the remote stress level increases, the plastic zone sizes of different cracks will increase and will eventually linkup. When the plastic zones of the lead crack meet the plastic zone from the nearest neighboring MSD crack, the ligament has effectively yielded. Therefore, the lead crack effectively extends to the far end of the MSD crack. Figure 4 shows a schematic of this linkup criterion [9]. When the applied load reaches a level that causes the effective ligament between cracks to yield, the ligament will fail.

According to Swift, the predicted failure of a specimen with MSD is a function of the plastic zone size of the lead crack and its nearest neighboring MSD crack, the material's yield strength, and an interaction factor between the MSD crack, and the lead crack.

The stress intensity factor for the lead and MSD cracks are found by the method of compounding. The stress intensity factor for the lead crack then becomes (eq. 9)

$$K_2 = \left[\frac{P}{A_{net}}\right]\sqrt{\pi a}\ \beta_{il} C \frac{A_{net}}{A_{lead}} \tag{9}$$

where: P = applied load

The stress intensity factor for the MSD crack (eq. 10) is based on a fit to the Bowie solution for a cracked hole [16] and includes the appropriate area for compounding as well as the interaction factor for the adjacent crack tips.

$$K_1 = \left[\frac{P}{A_{net}}\right]\sqrt{\pi a_{MSD}}\ \beta_h \beta_{i\,MSD}\ \frac{A_{net}}{A_{MSD}} \tag{10}$$

where: a_{MSD} = MSD crack length (from edge of hole)

$\beta_{i\,MSD}$ = Kamei-Yokobori interaction factor for MSD crack

$A_{MSD} = A_{net} + (d + 2a_{MSD})t$ = appropriate area for MSD crack compounding

β_h = Bowie factor

$$\beta_h = \left[\frac{F_1}{F_2 + \frac{a_{MSD}}{r}} + F_3\right] \tag{11}$$

where: r = radius of the hole
    F1, F2, F3 = hole configuration constants
    for holes with cracks   or holes with only
    emanating from both sides: one side cracked:
    F1 - 0.6865   F1 - 0.8733
    F2 - 0.2772   F2 - 0.3245
    F3 - 0.9439   F3 - 0.6762

The predicted failure load according to the Swift criterion, then, becomes:

$$P_{swift} = \sigma_{ys} A_{net} \sqrt{\frac{2t}{\left(a_{MSD}\beta_h^2\beta_{iMSD}^2\left(\frac{A_{net}}{A_{MSD}}\right)^2 + a\beta_{i}^2C^2\left(\frac{A_{net}}{A_{lead}}\right)^2\right)}} \frac{A_{net}E + A_{st}E_{st}}{A_{net}E} \tag{12}$$

where: t = crack tip separation

For each crack configuration the link up and panel failure loads were calculated using the four criteria described above (Eqns. 5, 6, 7, 12). If the link up load was below the panel failure load, the lead crack was assumed to have linked up with the adjacent MSD crack and the process was repeated. Final panel failure was predicted when the panel failure load exceeded the link up load.

Specimen Geometry and Test Procedures

To verify the stiffened panel model and the failure criteria described above, a series of experiments using wide Aluminum panels was performed. The sheet material for all tests was Al 2024-T3 in the MRS condition, 0.063 inches thick, and all tests were performed with the specimens loaded in the L-T direction. The stiffener material was 0.09 inches thick Al 2024-T3. Stiffeners were riveted to both sides of the specimen to avoid out of plane deformation during testing. Standard aircraft riveting procedures were followed in bucking the MS20470AD-6 rivets using a pneumatic rivet gun [17]. Figure 5 shows the basic dimensions for

the stiffened panel specimens used in the verification program.. Although most of the residual strength tests employed 1.5 inch wide stiffeners, a few residual strength tests were performed using stiffeners that were only 0.75 inches wide. These two stiffener configurations will from here on be referred to as heavy and light stiffeners respectively. The analytical tip stress intensity reduction factors and load concentration factors for both stiffener cases are shown in Figure 6. Table 1 summarizes the lead and MSD crack lengths as well as the stiffener type for the residual strength tests. All residual strength specimens had the same MSD crack lengths at each open hole. Both the lead and the MSD cracks were made using a jeweler's saw with a blade thickness of 0.012 inches. The specimens were tested using a 100 kip servo-hydraulic test machine at the Fatigue and Fracture Test Facility of the Flight Dynamics Laboratory at Wright-Patterson Air Force Base. The loading was a performed at a constant load rate of 0.25 kips per second. Although buckling guides were employed for the unstiffened R-curve tests, they were not used for the stiffened panel residual strength tests. Link up and failure loads were recorded during the tests.

The same basic specimen without stiffeners and holes was used to perform three R-curve tests following ASTM E-561 [18]. The R-curve tests were performed in the same WPAFB facility as the residual strength tests. Stable crack extensions were monitored and measured using traveling microscopes. The resulting R-curve for the sheet material is shown in Figure 7.

Two stiffened panels with a lead crack, but without open holes were fatigue tested to experimentally verify the analytical tip stress intensity reduction factors using the backtracking method [19]. The fatigue tests were performed in the Fatigue and Fracture Lab of the School of Aeronautics and Astronautics at Purdue University. Each panel was tested at a different constant amplitude loading, and fatigue crack propagation of the lead crack was measured using traveling microscopes. The crack length versus cycle data was then converted to da/dN versus a using the procedure outlined in ASTM E-647 [20]. Using established baseline da/dN versus ΔK data for Al 2024-T3, an experimental stress intensity factor K_{exp} was then calculated for each crack length.

The results of these tests and comparison with analytical predictions are presented in the next section.

Results

The purpose of the experimental test program was to verify the analytical model for stiffened panels with lead and MSD cracks, and to determine which of the failure and link up criteria were most suitable.

Experimental Tip SIF Reduction Factors

The experimental stress intensity factor obtained from the two stiffened panel fatigue tests can be converted to experimental tip stress intensity reduction factors using equation 13.

$$C_{exp} = \frac{K_{exp}}{\sigma \sqrt{\pi a} \beta_w}$$ (13)

where: K_{exp} = experimental stress intensity factor

σ = applied remote stress

$\beta_w = \sqrt{\sec \frac{\pi a}{W}}$ = finite width correction factor

W = width of sheet

The comparison between the experimental and the analytical tip stress intensity reduction factor is shown in Figure 8. As figure 8 shows, the analytical and experimental results agree well with each other.

Reduction of Residual Strength due to MSD

The experimental residual strengths for the stiffened panel specimens are shown in Table 2. After link up all cracks arrested at the stiffener, except for MSD-13, where crack extension past the stiffener and panel failure were nearly simultaneous. Figure 9 shows the reduction in residual strength due to the presence of MSD. Note that the presence of MSD cracks that are only 0.05 inches long reduces stiffened panel residual strength by 24 percent for specimens with 4.5 and 6.0 inch lead cracks.. MSD cracks that are 0.1 inch long lead to a residual strength reduction of 32 percent, and more severe MSD cracks that are 0.15 inches long lead to a reduction in residual strength of 40 percent.

Link Up Criteria Comparison

The apparent fracture toughness and the ligament yield criterion outlined earlier were used to predict crack link up in the residual strength specimens. All specimens had one crack link up before failure, except for MSD-9, MSD-10 and MSD-13 which had two separate crack link ups. The actual and predicted first

link up loads are given in Table 3. The ligament yield criterion cannot be applied to the baseline tests (MSD-1 to MSD-4) because no MSD crack were present. For specimens with MSD, cracks the ligament yield criterion predicts the first link up well, with an average difference of 3.3 percent and no difference larger than 8 percent. The apparent fracture toughness criterion works well for the baseline cases (no MSD), but consistently overpredicts the link up load for specimens with MSD. The actual and predicted link up loads for the three specimens that had a second link up are given in Table 4. Note that for the second link up the apparent fracture toughness criterion gives much better results, while the ligament yield criterion does slightly worse than for the first link up. Neither criteria does very well for the second link up on MSD-13. This was the only specimen that had crack extension past the stiffener load line. The validity of the plastic zone expression across the stiffener load line is debatable and could have influenced the predictions. Comparison of the actual and predicted first and second link up loads are shown graphically in Figure 10.

Failure Criteria Comparison

Total panel failure was predicted whenever the predicted panel failure load was lower than the link up load. The net section failure and the stiffener failure criterion were used to predict panel failure loads. The actual and predicted panel failure loads are summarized in Table 5. The net section failure criteria is able to predict the failure load of the baseline specimens (MSD-1 to MSD-4) and the specimens with MSD and heavy stiffeners (MSD-4 to MSD-10) well with an average difference of less than 4.5 percent, but is very unconservative for the panels with the light stiffeners (MSD-11 to MSD-13). The stiffener failure criterion works well for specimens with MSD (MSD-5 to MSD-13) with an average difference of less than 3.5 percent, but underestimates the failure load of the baseline specimens. This is most likely due to the fact the after lead crack extension in the baseline specimen the lead crack end at a hole, which is a less severe situation than a lead crack of equal length, which is the case assumed by the stiffener failure criterion. Figure 11 summarizes the actual and predicted panel failure loads.

Work to Be Completed

This project brought to light some issues that need further attention. Currently the lead crack is being modeled as a center crack in a sheet. However, when the lead crack links up with the adjacent MSD crack, the crack lengths extending from the hole can be very small (0.05 inches in this work). It is not clear that the center crack model is an accurate representation of the stress intensity factor at the crack tip.

Specimen MSD-13 showed that when crack extension occurs past the stiffener line, neither of the current link-up criteria is able to accurately predict this link up. The ligament yield criterion that was shown to work well for all other cases, was not able to predict the second link up within less than 10 percent. The authors believe that the currently used plastic zone model is not a good approximation for plastic zone extending across stiffener load lines.

Consideration is also given to including stable crack extension before link up or failure in the various link up and failure criteria.

The analytical model was shown to work well for link up and residual strength predictions. Fatigue tests of stiffened panels with MSD and lead cracks will be conducted in the future to evaluate the model for fatigue crack growth calculations.

Summary

An analytical model based on displacement compatibility was used to analyze the link up and residual strength behavior of stiffened panels with lead and MSD cracks. The stiffened panel correction factors were used in two different link up and panel failure criteria to predict the lead crack link up and panel failure loads in 15 inch wide stiffened aluminum specimens. The ligament yield criterion, modified for the stiffened panel, has proven to be able to predict lead crack link up load within 4 percent. The apparent fracture toughness criterion consistently overpredicts link up loads for specimens with MSD. The stiffener failure criteria is been shown to be able to predict panel failure to within less than 4 percent for specimens with a true lead crack. The net section failure criteria gives good results for specimens were the lead crack was arrested at a hole.

Acknowledgments

References

1   Mar, J. W., "Preserving Aging Aircraft," Aerospace America, Jan. 1996, pp. 38-43.

2   Mar, J. W., "Structural Integrity of Aging Airplanes: A Perspective," Structural Integrity of Aging Airplanes, S. N. Alturi, S. G. Sampath, P. Tong, Editors, Springer-Verlag, Berlin, Heidelberg, 1991.

3   E.J. Moukawsher, M.B. Heinimann, A.F. Grandt, Jr., "Residual Strength of Panels with Multiple Site Damage," Journal of Aircraft, Vol. 33, No. 5, 1996.

4   M.C. Cherry, S. Mall, M.B. Heinimann, A.F. Grandt, Jr., "Residual Strength of Unstiffened Aluminum Panels with Multiple Site Damage," Submitted to Engineering Fracture Mechanics, August 1996.

5   Romualdi, J. P., Frasier, J. T., Irwin, G. P., "Crack-Extension-Force Near a Riveted Stiffener," NRL Report 4956, Naval Research Laboratory, Washington, D.C., 1957.

6   Poe, C.C., Jr., "Stress-Intensity Factor for a Cracked Sheet with Riveted and Uniformly Spaced Stringers", NASA TR R-358, 1971.

7   Vlieger, H., "The Residual Strength Characteristics of Stiffened Panels Containing Fatigue Cracks," Engineering Fracture Mechanics, Vol. 5, pp. 447-477, 1973.

8   Moukawsher, E. J., Neusel, M.A., and Grandt, A. F., Jr., "Analysis of Panels With Multiple Site Damage," AIAA Paper No. 94-1459, AIAA 35th SDM Conference, April 18-21, 1994, Hilton Head, SC.

9   Swift, T., "Widespread Fatigue Damage Monitoring Issues and Concerns," presented at the 5th International Conference on Structural Airworthiness of New and Aging Aircraft, Hamburg, Germany, June 16-18, 1993.

10   Jeong, D. Y., and Brewer, J. C., "On the Linkup of Multiple Cracks," Engineering Fracture Mechanics, Vol. 51, No. 2, 1995, pp. 233-238.

11   Broek, D., "The Effects of Multi-Site-Damage on the Arrest Capability of Aircraft Fuselage Structures," FractuREsearch TR 9302, 1993.

12   Broek, D., "The Residual Strength of Aluminum Alloy Sheet Containing Fatigue Cracks or Saw Cuts," NLR TR-M-2134, 1965.

13   Dawicke, D.S, Newman, J.C., Jr., Sutton, M.A., and Amstutz, B.E., "Stable Tearing Behavior of Thin-Sheet Material with Multiple Cracks," NASA Technical Memorandum 109131, July 1994.

14   Nishimura, T., "Stress Intensity Factors of Multiple Cracked Sheet With Riveted Stiffeners," *Journal of Engineering Materials and Technology,* Vol. 113, pp. 280-284, 1991.

15   Kamei, A., and Yokobori, T., "Two Collinear Asymmetrical Elastic Cracks," Report of the Research Institute for Strength and Fracture of Materials, Tohoku University, Vol. 10, Section 1-4, pp. 41-42, December 1974.

16   Grandt, A. F., Jr., "Stress Intensity Factors for Some Thru-Cracked Fastener Holes," International Journal of Fracture, Vol. 5, No. 2, April 1975, pp 283-294.

17   *Standard Aviation Maintenance Handbook,* EA-282-0, IAP, Inc.

18   "Standard Practice for R-Curve Determination," ASTM E561-94, Annual Book of ASTM Standards, Vol 03.01, American Society for Testing and Materials, 1996.

19   James, L. A. and Anderson, W. E., "A Simple Experimental Procedure for Stress Intensity Factor Calibration," Engineering Fracture Mechanics, Vol. 1, April 1969, pp. 565-568.

20   "Standard Test Methods Measurement of Fatigue Crack Growth Rates," ASTM E647-95a, Appendix X1.2, Annual Book of ASTM Standards, Vol 03.01, American Society for Testing and Materials, 1996.

Table 1: Summary of lead and MSD crack lengths and stiffener type for residual strength specimens

Specimen ID	Lead Crack Length (2a) [in]	MSD Crack Length [in]	Stiffener Type
MSD-1	5.982	-	heavy
MSD-2	5.975	-	heavy
MSD-3	4.525	-	heavy
MSD-4	4.520	-	heavy
MSD-5	5.992	0.051	heavy
MSD-6	6.003	0.149	heavy
MSD-7	5.982	0.103	heavy
MSD-8	5.976	0.058	heavy
MSD-9	4.471	0.054	heavy
MSD-10	4.48	0.098	heavy
MSD-11	6.025	0.053	light
MSD-12	6.026	0.048	light
MSD-13	5.975	0.097	light

Table 2: Summary of experimental residual strength of stiffened panels

Specimen ID	Lead Crack Length (2a) [in]	MSD Crack Length [in]	Actual Failure Load [kips]
MSD-1	5.982	-	47.25
MSD-2	5.975	-	49.97
MSD-3	4.525	-	51.36
MSD-4	4.520	-	52.02
MSD-5	5.992	0.051	38.16
MSD-6	6.003	0.149	30.90
MSD-7	5.982	0.103	34.11
MSD-8	5.976	0.058	37.81
MSD-9	4.471	0.054	37.09
MSD-10	4.48	0.098	34.04
MSD-11	6.025	0.053	23.53
MSD-12	6.026	0.048	24.35
MSD-13	5.975	0.097	20.29

Table 3: Actual and predicted first link up loads for stiffened specimens

Specimen ID	Actual First Link Up Load [kips]	App. Fracture Toughness Criterion [kips]	% Difference	Ligament Yield Criterion [kips]	% Difference
MSD-1	35.80	36.76	2.682		
MSD-2	35.60	36.76	3.258		
MSD-3	34.30	35.76	4.257		
MSD-4	34.90	35.76	2.464		
MSD-5	26.80	34.57	28.993	26.10	-2.612
MSD-6	13.60	25.85	90.074	13.85	1.838
MSD-7	20.50	30.19	47.268	19.61	-4.341
MSD-8	26.40	34.10	29.167	26.63	0.871
MSD-9	27.10	31.36	15.720	26.24	-3.173
MSD-10	21.20	27.75	30.896	20.31	-4.198
MSD-11	17.60	22.67	28.807	18.53	5.284
MSD-12	18.10	22.84	26.188	18.85	4.144
MSD-13	14.20	19.55	37.676	13.14	-7.465

Table 4: Actual and predicted loads for second link up for stiffened panel specimens.

Specimen ID	Actual First Link Up Load [kips]	App. Fracture Toughness Criterion [kips]	% Difference	Ligament Yield Criterion [kips]	% Difference
MSD-9	34.80	33.57	-3.534	37.77	8.53
MSD-10	29.50	28.71	-2.678	30.18	2.31
MSD-13	19.80	21.78	10.000	22.05	11.36

Table 5: Actual and predicted panel failure loads for stiffened panel specimens.

Specimen ID	Actual Panel Failure Load [kips]	Net Section Failure [kips]	% Difference	Stiffener Failure [kips]	% Difference
MSD-1	47.25	48.40	2.434	42.66	-9.714
MSD-2	49.97	48.42	-3.102	42.68	-14.589
MSD-3	51.36	54.24	5.607	49.40	-3.816
MSD-4	52.02	54.29	4.364	49.44	-4.960
MSD-5	38.16	40.68	6.604	37.10	-2.778
MSD-6	30.90	28.02	-9.320	30.79	-0.356
MSD-7	34.11	34.20	0.264	33.84	-0.792
]MSD-8	37.81	39.84	5.369	36.71	-2.909
MSD-9	37.09	39.92	7.630	36.77	-0.863
MSD-10	34.04	34.02	-0.059	33.84	-0.588
MSD-11	23.53	29.75	26.434	21.83	-7.225
MSD-12	24.35	30.79	26.448	22.30	-8.419
MSD-13	20.29	25.75	26.910	21.62	6.555

Figure 1: Comparison of actual and predicted failure loads by various analytical
failure criteria for residual strength tests with 9 inch (NRS) and 15 inch (PRS)
2024-T3 aluminum panels.
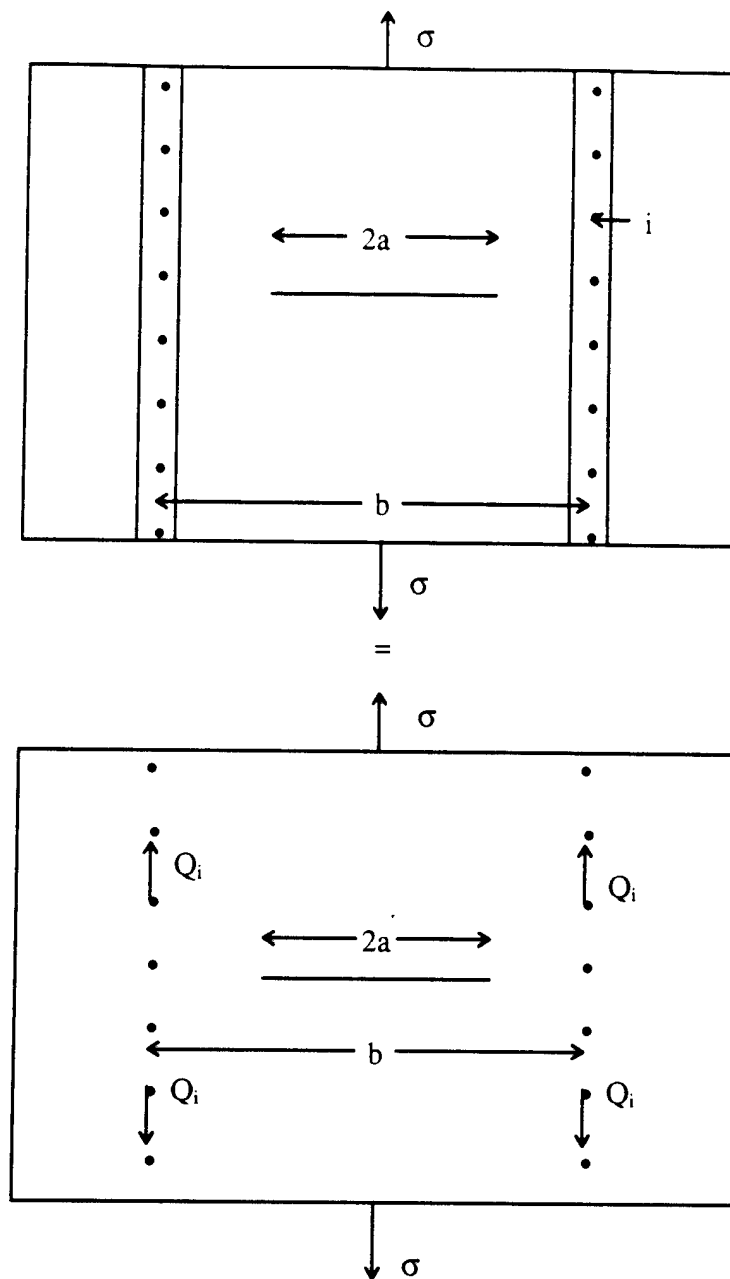
Figure 2: Schematic of stiffened panel model showing the modeling of the effects of the stiffeners using the rivet forces Q_i.

Remote Stress

Remote Stress
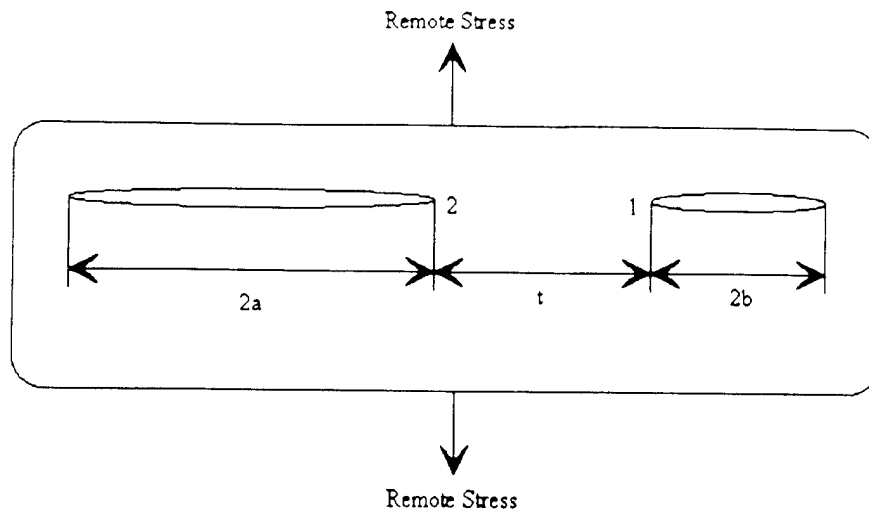
$$\beta_{l\,l} = \sqrt{1 + \frac{2b}{t}} \left[1 - \left(1 + \frac{t}{2a} \right) \frac{K(k) - E(k)}{K(k)} \right]$$

$$\beta_{l\,MSD} = \sqrt{1 + \frac{2a}{t}} \left[1 - \left(1 + \frac{t}{2b} \right) \frac{K(k) - E(k)}{K(k)} \right]$$

where: $K(k)$ = complete elliptic integral of the first kind
           $E(k)$ = complete elliptic integral of the second kind

$$k = 2\sqrt{\frac{ab}{(2a + t)(2b + t)}}$$

Figure 3: Definition of Kamei-Yokobori interaction factor for two planar crack of unequal length in an infinite plate [15].
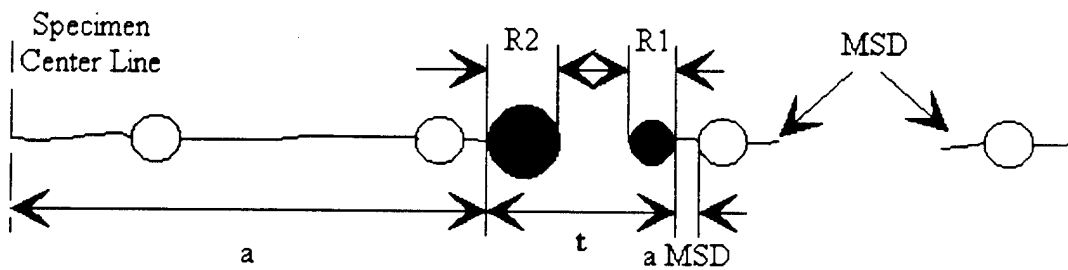
Figure 4: Schematic of the lead and MSD cracks and plastic zones for the ligament yield method [9].
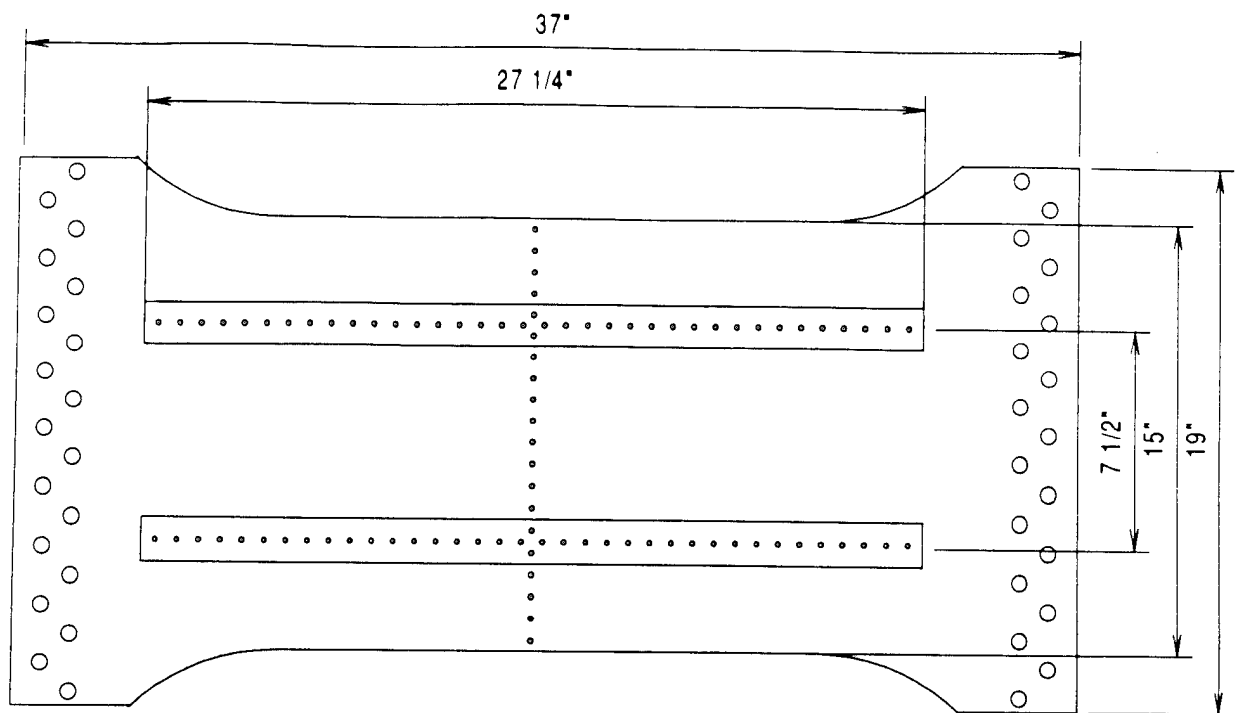
Figure 5: Schematic of stiffened panel specimen used for residual strength testing.

2.5

——— Heavy Stiffener, Tip SIF Reduction Factor (C)

—☐— Heavy Stiffener, Load Concentration Factor (L)

· · · · · Light Stiffener, Tip SIF Reduction Factor (C)

· · △ · · Light Stiffener, Load Concentration Factor (L)

2.0

Stiffened Panel Correction Factors (C & L)

1.5

L

1.0

2a

b

C

0.5

0.0

0.0   0.1   0.2   0.3   0.4   0.5   0.6

Non Dimensional Crack Length (a/b)
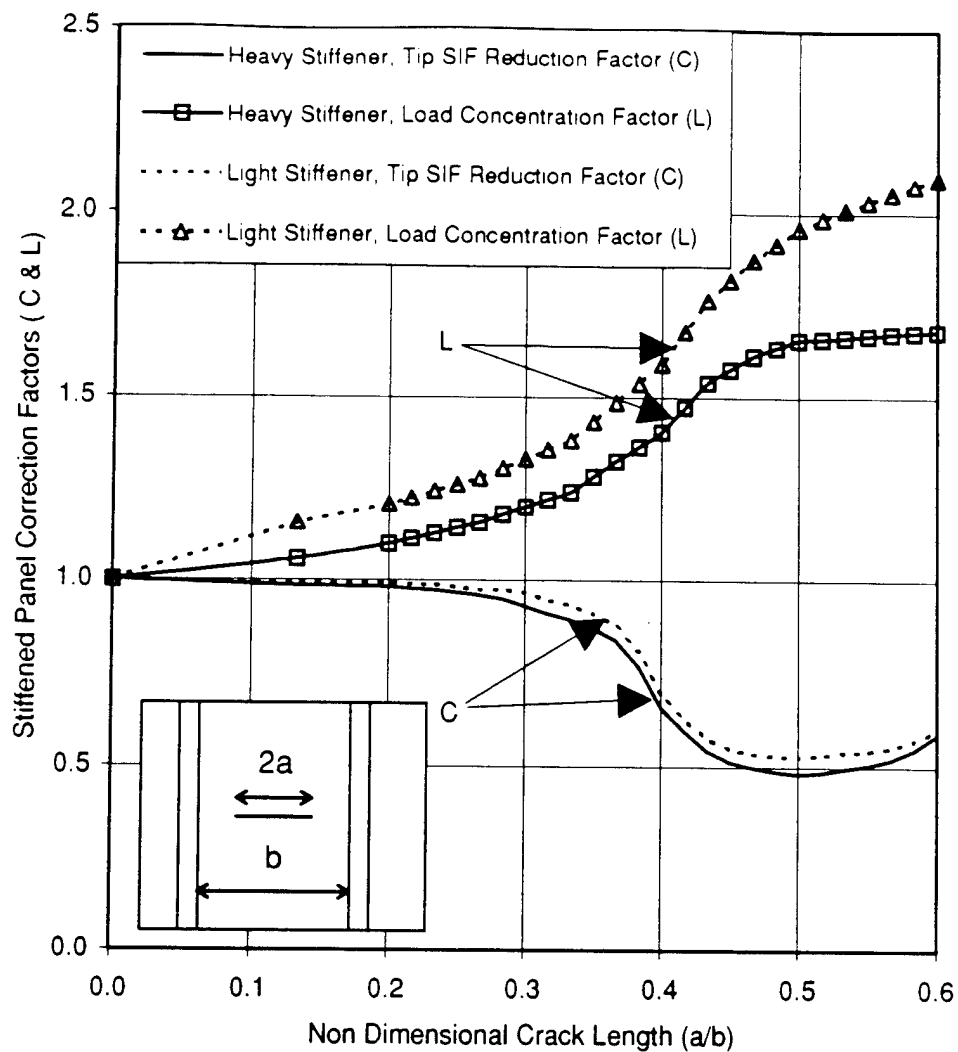
Figure 6: Analytical tip stress intensity reduction and load concentration factors for heavy and light stiffener residual strength specimens.
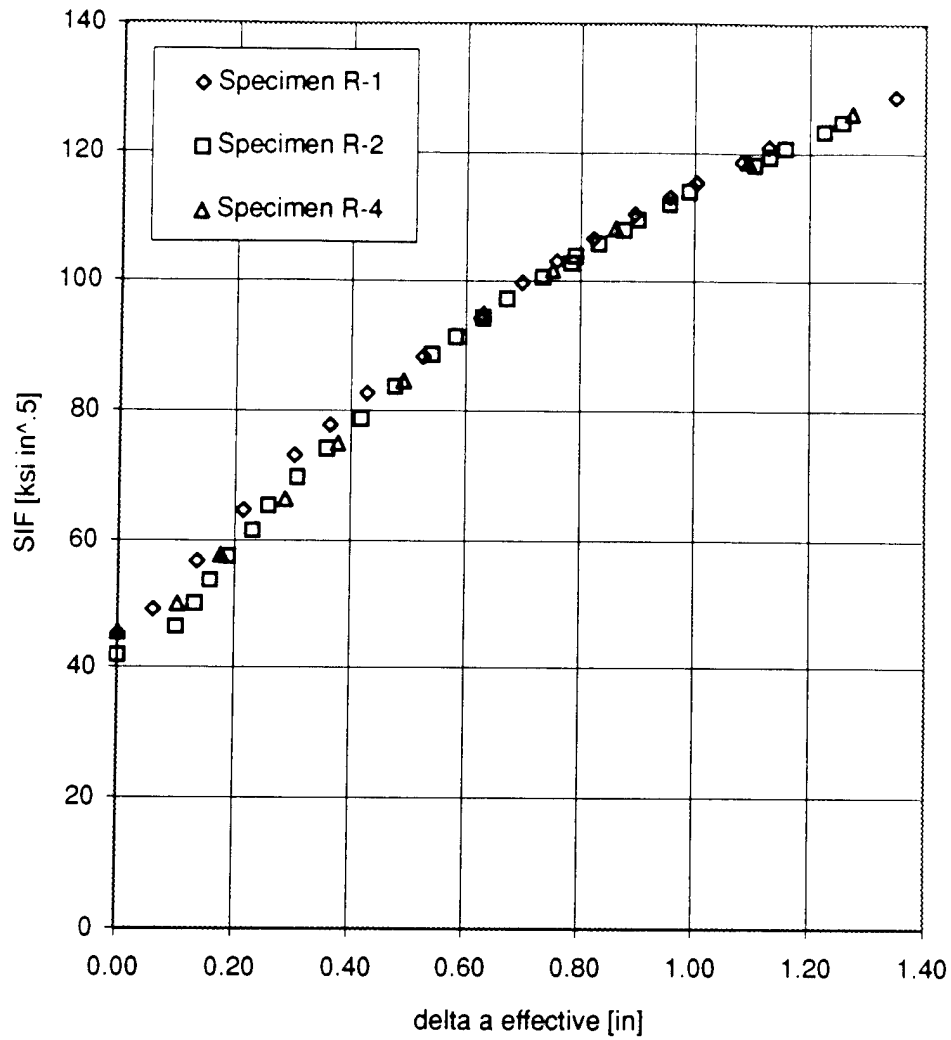
Figure 7: R-curve for Al 2024-T3 MRS in the L-T direction obtained from 15 inch wide specimens.
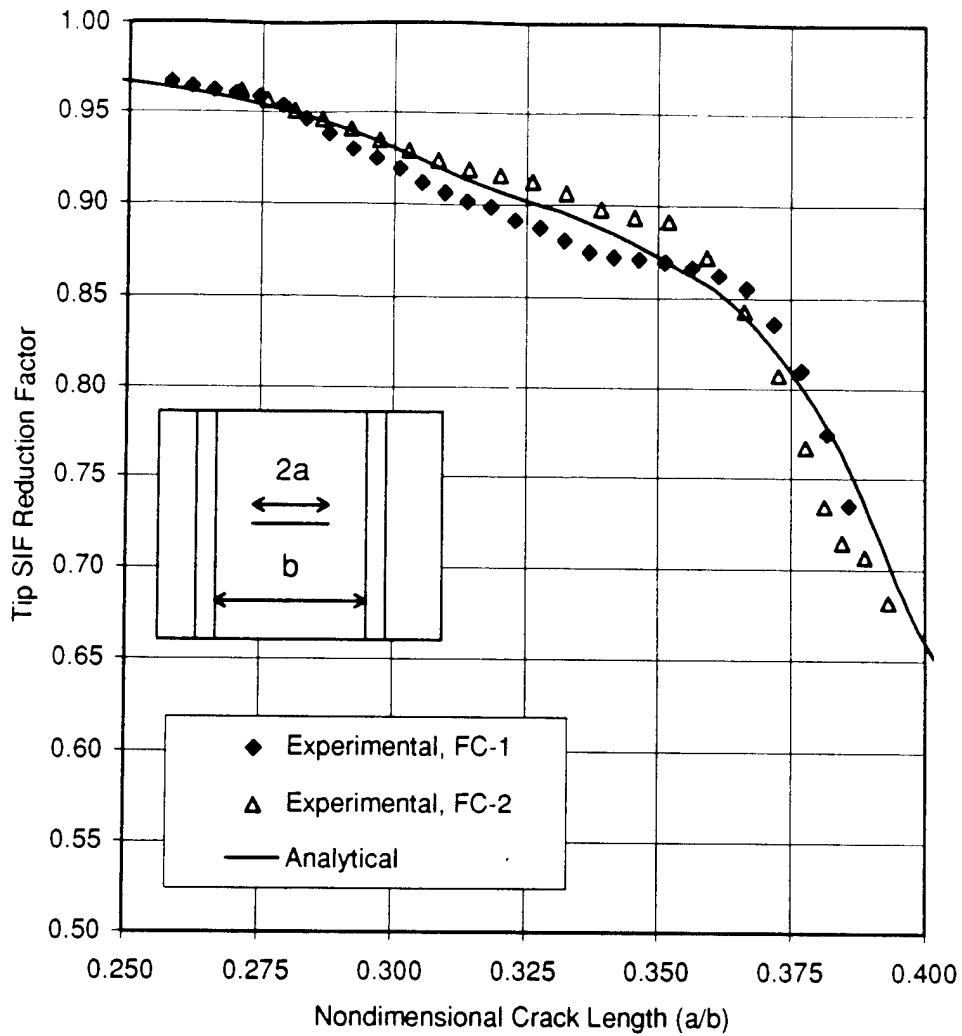
Figure 8: Comparison of analytical and experimental tip stress intensity reduction factors for 15 inch wide panel with heavy stiffeners.
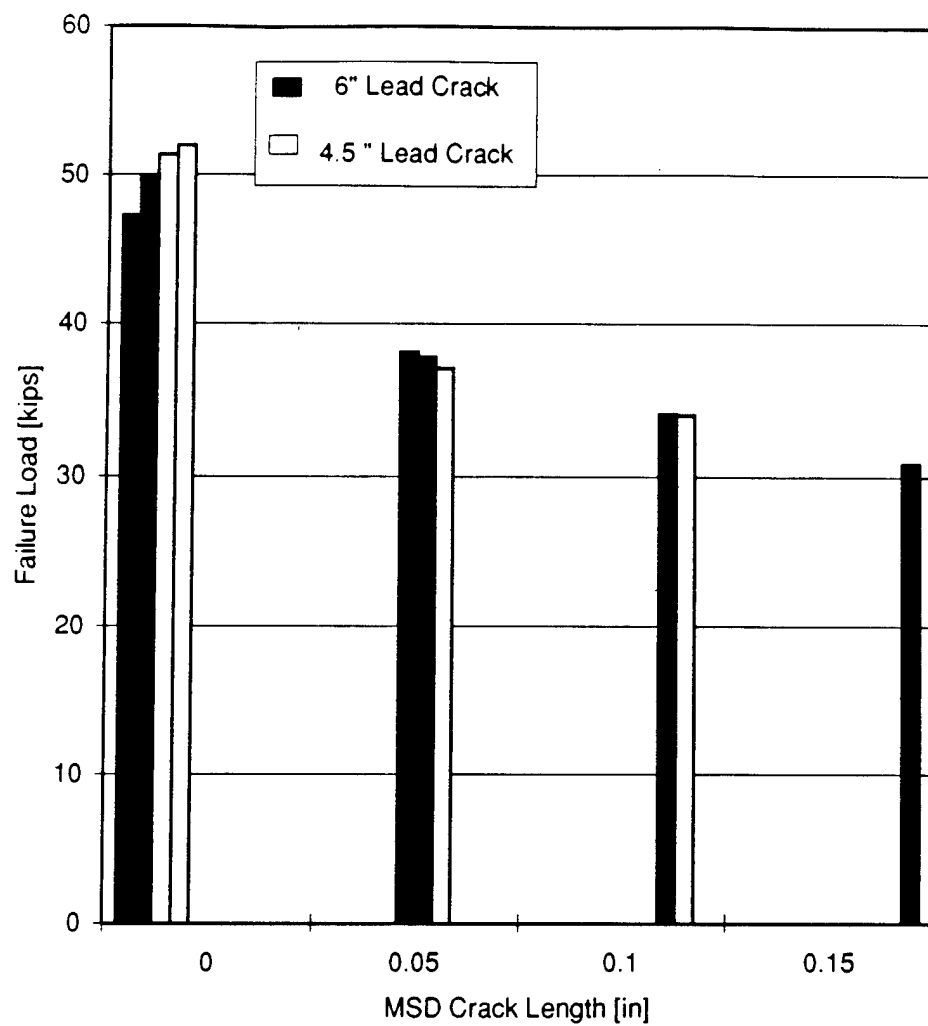
Figure 9: Reduction in residual strength of 15 inch 2024-T3 aluminum panels with heavy stiffeners due to MSD.
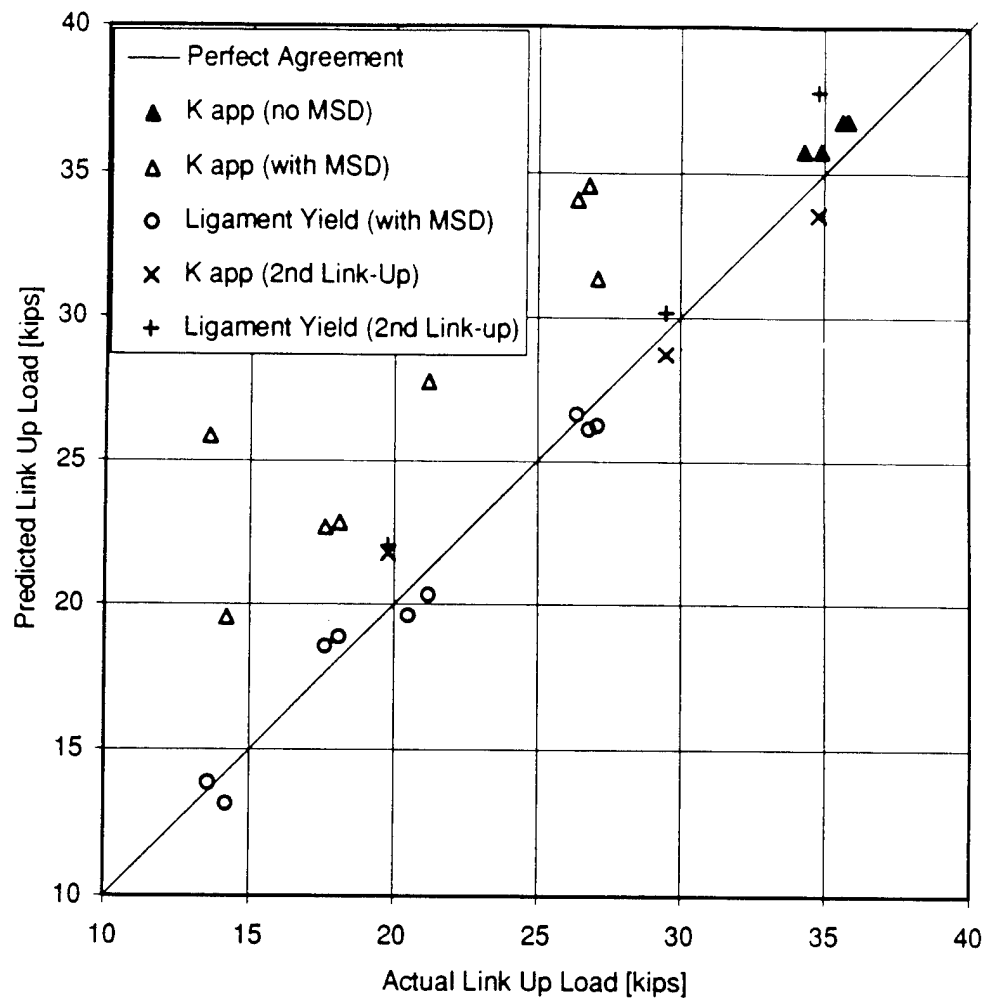
Figure 10: Comparison of actual and predicted link up loads by two different link up criteria for 15 inch wide, stiffened, 2024-T3 aluminum panels containing lead and in most cases MSD cracks.
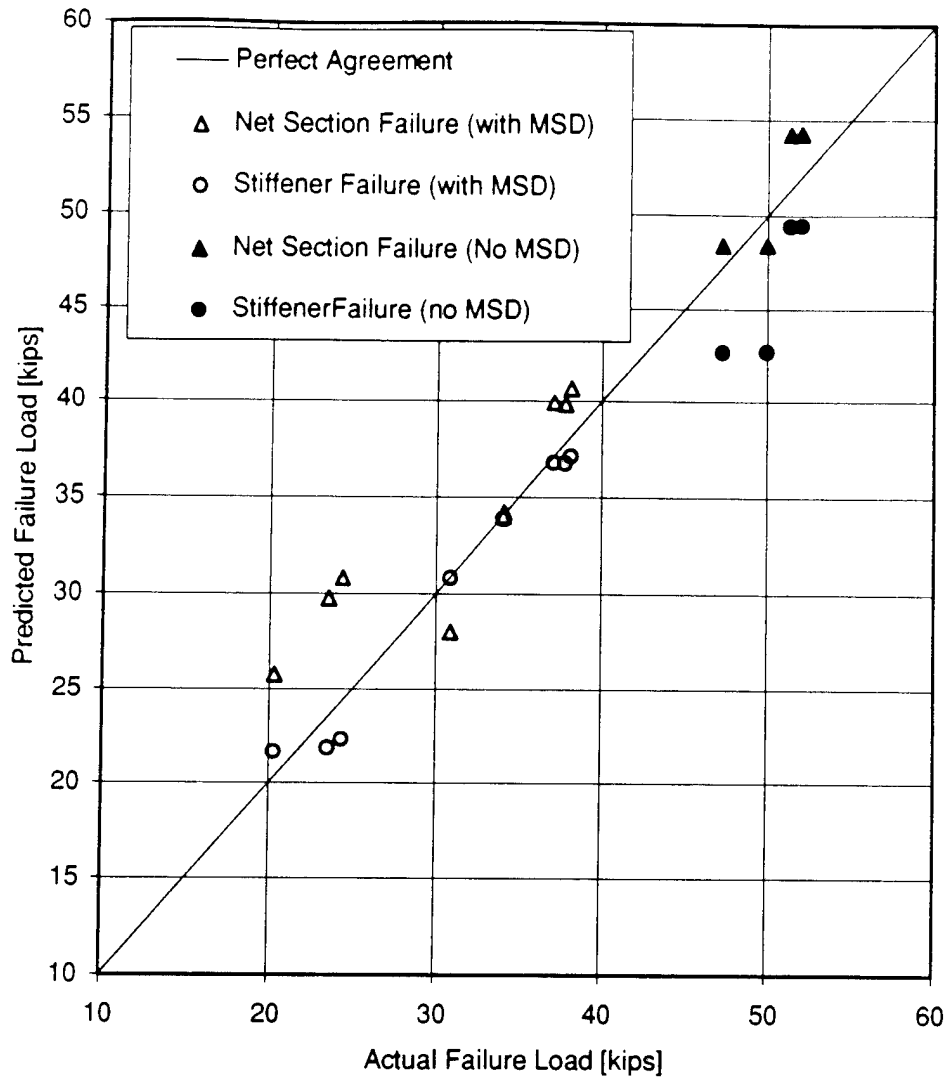
Figure 11: Comparison of actual and predicted panel failure loads by two different failure criteria for 15 inch wide, stiffened, 2024-T3 aluminum panels containing lead and in most cases MSD cracks.

Crack Gage Approach to Monitoring Fatigue Damage Potential in Aircraft

(1997 Society for Experimental Mechanics Spring Conf., Bellevue, WA, June 97)

M. D. Gates[1] and A. F. Grandt, Jr.[2]
School of Aeronautics and Astronautics, Purdue University
1282 Grissom Hall, West Lafayette, IN, 47907, USA

Introduction

Monitoring fatigue damage is a key component in ensuring the long and short-term safety of aircraft. Initial inspection and maintenance intervals are often determined using load assumptions made during design. Experience has shown, however, that aircraft are often subjected to loads which may differ significantly than those predicted during design. In addition, individual aircraft within a fleet often encounter large variations in load severity than those on the average.

Force management programs, such as that defined by the Air Force Structural Integrity Program (ASIP), ensure damage tolerance and durability of aircraft by refining inspection and maintenance intervals. One component of force management is the Individual Aircraft Tracking (IAT) program [1]. The objective of the IAT program is to use data acquisition and reduction tools to measure loads applied to individual aircraft and subsequently reduce these data to obtain updated information on structural integrity and predict potential flaw growth in key areas of the airframe for that particular aircraft [2].

Current tracking techniques, however, require instruments such as mechanical and electronic strain gages, acoustic emission monitors, counting accelerometers, flight load recorders, pilot logs and other devices to measure and record loads applied to the aircraft [3-5]. This load information must then be reduced using complicated computer algorithms into information pertaining to the extent of fatigue damage applied to the structure. For example, the B-1B IAT program [6] compiles stress histories from strain gage records and mission parameters such as gross weight, altitude, Mach number and aircraft geometry (wing angle and flap angle). These parameters are stored by a microprocessor-based solid state data collection and storage device, known as the Structural Data Collector (SDC). Internal loads within the primary airframe are then computed using a 77,000 element, 107,000 degree of freedom, half-airframe NASTRAN model. The accumulated structural damage is then estimated using a linear elastic fracture mechanics (LEFM) approach. Inevitably, however, the SDC does not provide records for all flights because the SDC may be inoperative, it may not installed in a particular aircraft, it may have a saturated memory or the collected data may be declared invalid [6].

The B-1B data collection and reduction scheme indicates that the current methods for IAT can be very complicated. These techniques require large capital, extensive effort and many assumptions in order to reduce the data into fatigue damage information. In addition, these methods may introduce errors which could lead to inspection intervals which are either too long or too short.

A much simpler and cheaper monitoring device may be the crack growth gage. The gage is simply a precracked coupon which is adhesively bonded to a load bearing structure, as shown schematically in Figure 1. Since the gage receives a predictable fraction of the loads applied to the structure, it responds with measurable crack growth. In this way, the gage acts as an analog computer by measuring loads applied to the structure, determining their effect on crack growth and responding with crack extension. The gage crack growth is then related to potential crack extension in the structure through the use of fracture mechanics "transfer functions." In this way, one has a simple method for monitoring potential fatigue damage.

Objectives

Experience has shown that crack gage coupons should be thin in order to reduce the load transferred to the gage and, thus, to reduce adhesive bond stresses. Thin gages can introduce potential problems, however, since variable amplitude loading may result in greater fatigue crack retardation in the thin gage than in a thicker structure. Past research examined a gage geometry to overcome this problem [7,8]. The geometry features deep-side grooves which are machined into the gage, as shown in Figure 2. The deep-side grooves create a stress state which simulates plane strain conditions, resulting in crack gages which experience variable amplitude fatigue crack growth which is similar to that encountered in the thicker structure.

Past research [7,8] has successfully demonstrated the crack growth gage concept, yet results could be improved. Specifically, past results indicated a less than ideal correlation between the structure crack length and the gage crack length. Figure 3 shows the "transfer functions," or structure versus gage crack lengths, for a series of tests performed in a previous research effort [8]. In order for the transfer function to be most useful, the gage crack length should grow at least as fast as the structure crack length, thereby "amplifying" the expected structural crack length. Hence, the transfer functions in the figure should have a lower slope in order to give more accurate information about the structural crack length.

As indicated in Figure 3, past research also suffered from variability in the experimental data. It is believed that the side-

---

groove machining method creates variances in residual stresses in the side grooves which lead to scatter in the crack gage behavior. While data from Virkler, Hillberry and Goel [9] indicate that scatter in fatigue life exists by as much as a factor of 1.45 to 1 in closely controlled constant amplitude experiments, past research showed variations in the structure and gage crack lengths beyond this "normal" scatter [8]. In addition, past research [7,8] showed that crack gages produced by different machine shops had different fatigue crack growth behavior, indicative of varying residual stresses.

The primary objective of this research is to develop a method of gage production and bonding which will yield consistent crack propagation. Specifically, the machining process will be targeted to improve the dimensional control of the side grooves in an attempt to reduce variances in the side-groove residual stresses. In addition, stress-relief heat treatment will be investigated as a means to reduce fatigue life scatter. Certain geometric and adhesion variables will also be modified in order to produce a more useful transfer function. It is hoped that by modifying an adhesion variable known as the "unbond length" (L_u in Figure 1), the fraction of load transferred from the parent structure to the gage will be increased, thereby increasing the gage crack growth rate and decreasing the slope of the transfer function.

Experimental Approach

The crack gages, as shown in Figure 2, were manufactured from a single sheet of 3.175 mm (0.125 in) thick 7075-T6 aluminum. The gages were machined to a size of 5.08 ± 0.025 cm (2.00 ± 0.01 in) by 15.24 ± 0.025 cm (6.00 ± 0.01 in), such that the rolling direction was oriented perpendicular to the direction of expected crack growth. The side grooves were machined using a 90° cutting tool. Using a feed rate of 4.45 cm/min (1.75 in/min) and a spindle speed of 225 rpm, three passes of the mill were made on each side of the gage to leave an average net thickness between the side grooves equal to 0.9500 mm (0.0374 in) with a standard deviation of 0.0584 mm (0.0023 in). This standard deviation was approximately 15% lower than the standard deviation achieved in the previous research [7]. A 7.6 mm (0.30 in) saw cut was then placed in one edge of the gage and the gage was pin loaded and precracked using ASTM standards [10] to a nominal length of 12.7 mm (0.50 in).

The carrier structures were machined from a single sheet of 0.635 cm (0.250 in) thick 7075-T651 aluminum such that the rolling direction was oriented perpendicular to the direction of expected crack growth. Each carrier was 66.04 ± 0.127 cm (26.00 ± 0.05 in) long by 7.62 ± 0.025 cm (3.00 ± 0.01 in) wide. The structure crack was simulated as a through the thickness single crack originating at a 0.635 cm (0.25 in) diameter hole. The hole was located 0.635 cm (0.25 in) from the centerline of the carrier so that the crack would be loaded more symmetrically during much of the test. The structure cracks were initiated and grown using ASTM standards to a nominal length of 0.1422 cm (0.056 in).

Unbonded precracked crack gages were tested under load control in order to determine the extent of variability in crack growth rates and crack gage lives. The gages were pin loaded in an MTS test machine at a constant amplitude of 2.22 kN (500 lb) with an

R-ratio of 0.05 and a frequency of 15 Hz. The crack growth rate was calculated using the seven point polynomial technique [10].

Other gages were heat treated in an attempt to relieve the residual stresses imposed in the side grooves during machining. These gages were heated to 343°C (650°F) followed by slow cooling over a period of about 2.5 hours to a safe handling temperature. A portion of these gages were then tested in the same procedure as above.

Heat treated gages were then adhesively bonded to the carrier structures using FM73 film epoxy adhesive. The aluminum surfaces were first carefully prepared using the phosphoric acid anodization (PAA) procedure [11-12]. The carrier/gage assemblies were placed in a vacuum bag with 634 mm Hg (25 in Hg) suction. The assemblies were pressure cured at 275.8 kPa (40 psi) by heating to 121°C (250°F) in 30 minutes, holding at that temperature and pressure for 90 minutes and cooling to 54°C (130°F) in 60 minutes. Figure 4 shows a completed carrier/gage assembly. Notice that the ends of the gages containing the pin loading holes were removed prior to bonding, leaving a nominal gage length of 10.62 cm (4.18 in).

The carrier/gage assemblies were then tested under load control at a constant amplitude stress of 110.3 MPa (16 ksi), with an R-ratio of 0.1 and a frequency of 3 Hz. The gage and structure crack lengths were measured visually every 1,000 cycles.

Experimental Results

The results of initial constant amplitude tests conducted on precracked unbonded side-grooved crack gages are shown in Figure 5. This figure indicates a scatter in the fatigue lives of 2.28 to 1. This scatter may be attributed to differences in the reduced thickness of the gages or differences in residual stress in the side grooves. The seven gages tested, however, were selected based on their similarity in reduced thickness. This indicates that variances in residual stresses in the side grooves greatly impact the fatigue crack growth behavior of the gages.

Given the high degree of variability in fatigue crack growth lives of the seven specimens shown in Figure 5, it was determined that a method of relieving the residual stresses was necessary. As described previously, heat treating was used to reduce the side-groove residual stresses. Three heat-treated gages were tested to failure in the same manner as the previous gages. Figure 6 presents the results of these tests. Dividing the longest fatigue life by the shortest fatigue life results in a scatter factor of only 1.24 to 1.

It was therefore concluded that the heat treatment method was effective at relieving the gage residual stresses. Heat-treated gages were subsequently bonded to carriers and tested under constant amplitude stress. Although problems were experienced with consistency in the adhesive bonding procedure, Figure 7 shows the experimental transfer functions for four tests in which the gages were bonded consistently. As the figure indicates, the four heat-treated gages behaved in a repeatable manner.

Theoretical Approach

A mathematical model has been previously developed [7] to relate the crack length in the coupon, a_g, with the crack length in the structural member, a_s. The theoretical model is developed by first assuming the edges of the coupon are attached to the structure (by adhesive bonding, for example) in such a way that when a remote stress, σ_S, is applied to the structure, an effective stress, σ_G, is transferred to the gage. This relationship can be represented by:

$$\sigma_G = f\sigma_s \qquad (1)$$

It has been shown that the load transfer function, f, depends on parameters such as gage geometry and material properties, but not on the stress level. The load transfer function can be found by stress analysis, based on either theoretical or experimental techniques [7, 8, 13, 14].

It can be assumed that the crack growth in the structure and the gage take the form:

$$\frac{da}{dN} = F(\Delta K) \qquad (2)$$

where $\frac{da}{dN}$ is the fatigue crack growth rate, ΔK is the cyclic stress intensity factor and F is an appropriate function relating the stress intensity factor, material properties and other load variables to the crack growth rate.

Noting that at any point in time the gage and structure have witnessed the same number of cycles, N, Equation (2) can be solved for cyclic life, N:

$$N = \int_{a_{iS}}^{a_{fS}} \frac{da}{F_S(\Delta K)} = \int_{a_{iG}}^{a_{fG}} \frac{da}{F_G(\Delta K)} \qquad (3)$$

where a is crack length, the subscripts i and f refer to initial and final, respectively, and the subscripts S and G refer to structure and gage, respectively.

By assuming a Paris equation [15] for the crack growth rate function $F(\Delta K)$, Equation (3) can be solved to give the desired transfer function relating the structure crack length to the gage crack length. The Paris equation is:

$$\frac{da}{dN} = C\Delta K^m = F(\Delta K) \qquad (4)$$

where C and m are material constants, and ΔK takes the form:

$$\Delta K = \Delta\sigma\sqrt{\pi a}\,\beta \qquad (5)$$

where $\Delta\sigma$ is the applied cyclic stress and β is the geometric shape function. Combining Equations (1) through (5) gives:

$$N = \int_{a_{iS}}^{a_{fS}} \frac{da}{C_S(\Delta\sigma_S\sqrt{\pi a}\beta_S)^{m_S}} = \int_{a_{iG}}^{a_{fG}} \frac{da}{C_G(f\Delta\sigma_S\sqrt{\pi a}\beta_G)^{m_G}} \qquad (6)$$

Note that a is the variable of integration and neither f nor β depend on the cyclic load $\Delta\sigma$.

By assuming the gage and structure have the same crack growth exponent, $m_S = m_G = m$ (note this is a reasonable assumption provided the gage and structure are made of similar materials), Equation (6) can be further reduced to:

$$\int_{a_{iS}}^{a_{fS}} \frac{da}{C_S(\sqrt{\pi a}\beta_S)^m} = \int_{a_{iG}}^{a_{fG}} \frac{da}{C_G(f\sqrt{\pi a}\beta_G)^m} \qquad (7)$$

While this equation can no longer provide information on cyclic life, N, it can now be numerically integrated to provide information on the structure crack length provided an initial structural crack length is assumed. Note that all stress level terms in Equation (7) effectively cancel, so that the relationship between the gage and structure crack lengths is independent of loading. Indeed, a distinct advantage of this model over current fatigue tracking methods is that it requires no knowledge of the load history.

Comparison of Experimental and Theoretical Results

The material properties (C_S, C_G, m) needed to solve Equation (7) for the present series of tests, along with the stress intensity factor solutions for the gage and structure cracks (β_S, β_G, f) are presented in Reference [16]. The gage stress intensity solution is dependent on the gage geometry, so for the four experimental cases tested, four prediction curves were generated. Figure 8 shows a comparison of the experimental and theoretical results. Notice that the experimental data follows the prediction curves very well, and that at longer gage crack lengths the prediction curve becomes slightly conservative. In addition, the original objective of increasing the gage crack growth rate has been achieved. The gage crack grew at a rate approximately twelve times greater than the structural crack, allowing for very accurate predictions of the structure crack length. Indeed, this rate could even be lowered, thus allowing for longer in-service life of the gage.

Conclusions

While the side groove has the potential to reduce the problems associated with fatigue retardation, its presence does complicate the implementation of the crack gage. Past research showed that side-grooved crack gages manufactured by different machine shops had different fatigue crack growth behavior. The current research also demonstrated that even with close control of the machining process, differences in fatigue lives were found in gages subjected to identical remote loads. It is believed that this variation in fatigue life was caused by differences in side-groove residual stresses created during manufacturing. Through the use of heat treatment, however, fatigue scatter was greatly reduced.

It should be noted that the initial objective of increasing the gage crack growth rate was achieved, though not by the technique initially proposed. Recall that increasing the gage crack growth rate was necessary to improve the prediction capabilities of the gage, and that increasing the gage unbond length (L_u in Figure 1) would achieve this objective. The heat treatment method, however, reduced the yield strength of the aluminum from 545 MPa (79 ksi) to 310 MPa (45 ksi). There was a similar reduction in ultimate strength, as well. This reduction increased the gage

crack growth rate greatly. Indeed, the bonded crack gages grew at a rate approximately twelve times greater than the structure crack. In past research, the crack gage grew at a rate slightly slower than the structure crack. Both this research as well as past research, however, used the same unbond length of 9.53 mm (0.375 in).

While the crack gage concept has been successfully demonstrated, in order for the technique to be most useful, a method for remotely monitoring the crack length in the gage is necessary. A device which could remotely monitor the gage crack length would eliminate the need for visual inspection and could also be linked to a data collection device for easy and rapid data reduction.

References

[1] "Aircraft Structural Integrity Program, Airplane Requirements," MIL-STD-1530A, Air Force Aeronautical Systems Division, 1975.

[2] Berens, A. P., et. al., "Handbook of Force Management Methods," Air Force Flight Dynamics Laboratory Technical Report AFWAL-TR-81-3079, 1981.

[3] Gould, P., "An Aircraft Structural Integrity Program - FAA Flight Inspection Beech 300 Fleet," Proceedings of the 1993 USAF Structural Integrity Program Conference, Wright Laboratory Technical Report WL-TR-94-4079, 34-66, 1994.

[4] Martin, B., Alford, R., "An Improved G-Tracking Method for Large Transport Aircraft," Proceedings of the 1993 USAF Structural Integrity Program Conference, Wright Laboratory Technical Report WL-TR-94-4079, 741-773, 1994.

[5] Van Way, C. B., Kudva, J. N., Marantidis, C., "Integration of Smart Structures Concepts for Improved Structural Integrity Monitoring of the T-38 Aircraft," Proceedings of the 1993 USAF Structural Integrity Program Conference, Wright Laboratory Technical Report WL-TR-94-4079, 835-846, 1994.

[6] Denyer, A. G., "B-1B Aircraft Structural Integrity Program," Proceedings of the 1995 USAF Structural Integrity Program Conference, Wright Laboratory Technical Report WL-TR-96-4093, Vol. I, 103-128, 1996.

[7] Dumanis-Modan, A., "Evaluation of the Crack Gage as an Advanced Individual Aircraft Tracking Concept," Ph.D. Thesis, School of Aeronautics and Astronautics, Purdue University, 1982.

[8] Grandt, A. F., Jr., Dumanis-Modan, A., "Evaluation of the Crack Growth Gage Concept as an Advanced Individual Aircraft Tracking Device," Air Force Flight Dynamics Laboratory Technical Report AFWAL-TR-83-3082, Vol. II, 1983.

[9] Virkler, D. A., Hillberry, B. M., Goel, P. K., "The Statistical Nature of Fatigue Crack Propagation," Air Force Flight Dynamics Laboratory Technical Report AFFDL-TR-78-43, 1978.

[10] "Standard Test Method for Measurement of Fatigue Crack Growth Rates," ASTM E647-95a, Annual Book of ASTM Standards, 1996.

[11] Clearfield, H. M., et. al., "Surface Preparation of Metals," Engineered Materials Handbook, Vol. 3, 259-264, 1990.

[12] Mahoney, L. C., "Surface Preparation for Adhesive Bonding," Handbook of Adhesives, Third Edition, 74-81, 1990.

[13] Ashbaugh, N. E., Grandt, A. F., Jr., "Single-Edge-Cracked Crack Growth Gage for Monitoring Possible Fatigue Crack Growth," Service Fatigue Loads Monitoring, Simulation and Analysis, ASTM STP 671, 94-117, 1979.

[14] Ori, J. A., Grandt, A. F., Jr., "Single-Edge-Cracked Crack Growth Gage," Fracture Mechanics, ASTM STP 677, 533-549, 1979.

[15] Paris, P. C., Erdogan, F., "A Critical Analysis of Crack Propagation Laws," Transactions of the ASME, Journal of Basic Engineering, 85-3, 528-534, 1963.

[16] Gates, M. D., "A Crack Gage Approach to Monitoring Fatigue Damage Potential in Aircraft," M.S. Thesis, School of Aeronautics and Astronautics Purdue University, 1997.
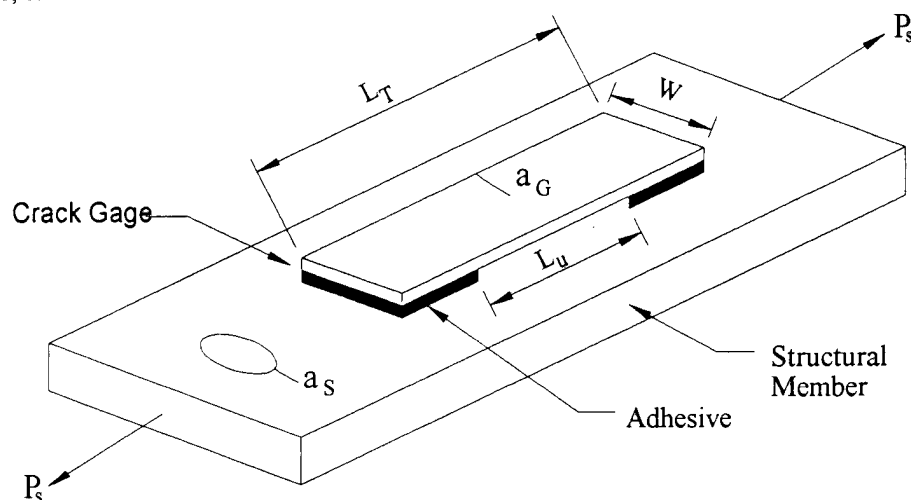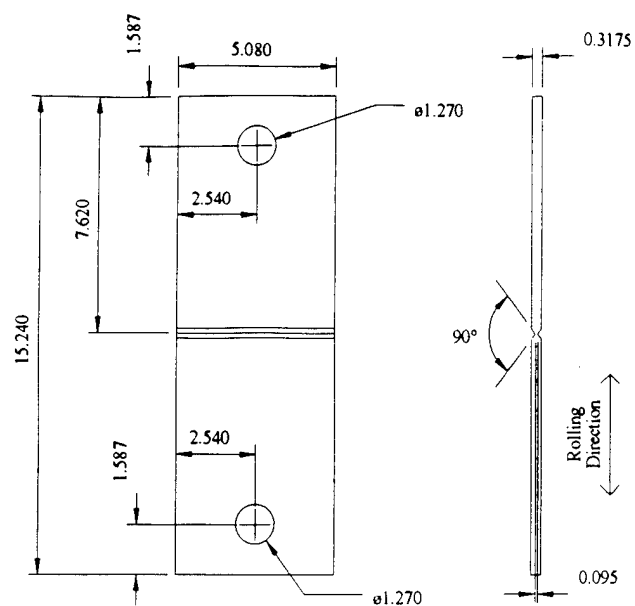
Figure 1: Schematic Drawing of Crack Gage Bonded to Structural Member

Note: All dimensions in cm

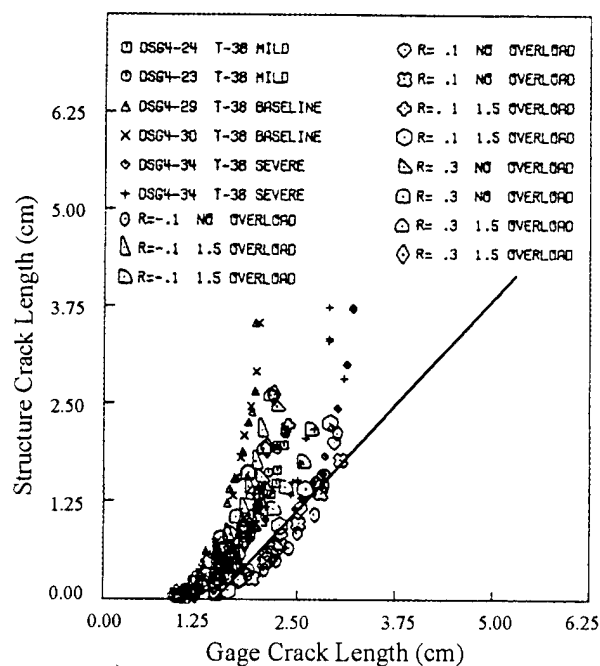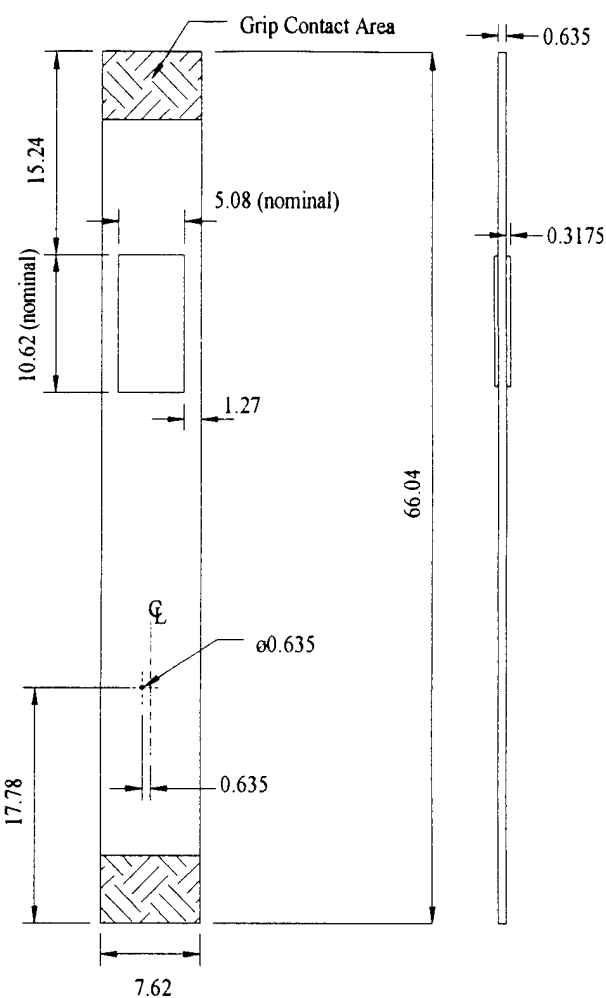Figure 2: Schematic of Side-grooved Crack Gage

Figure 3: Experimental Transfer Functions [after 8]

Notes: All dimensions in cm
Side grooves omitted for clarity

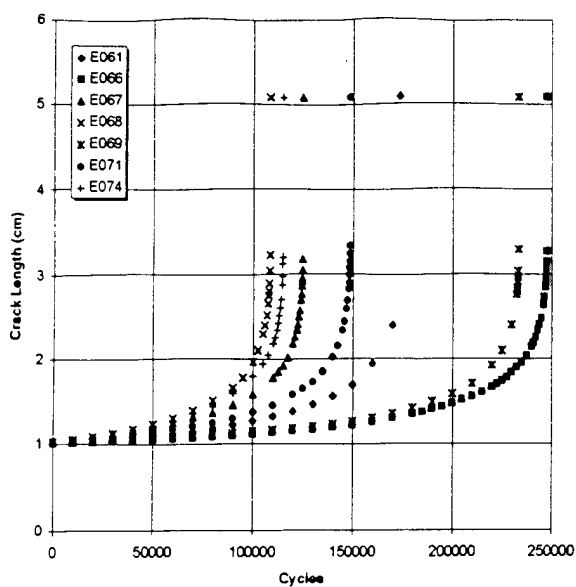Figure 4: Schematic of Carrier/Gage Assembly

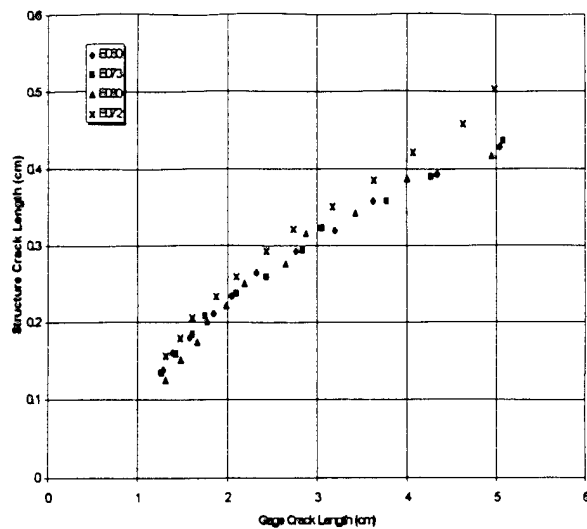Figure 5: Fatigue Lives for Non-heat-treated Crack Gages
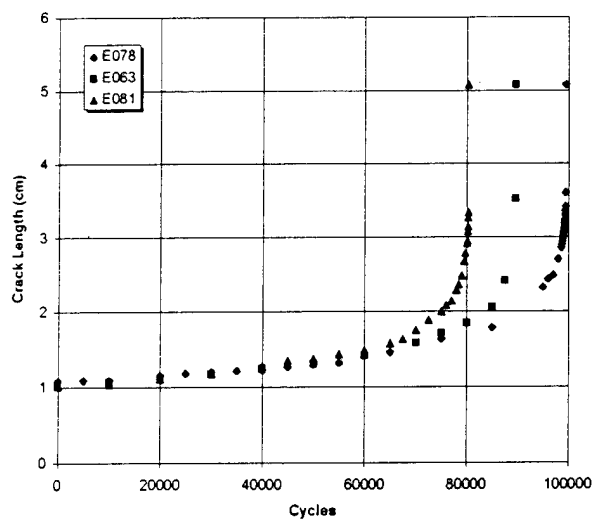

Figure 7: Experimental Transfer Functions

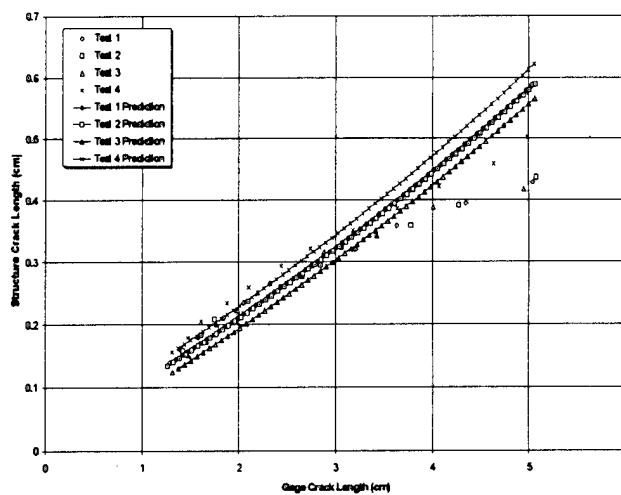Figure 6: Fatigue Lives for Heat-treated Crack Gages

Figure 8: Experimental and Predicted Transfer Functions

ANALYSIS OF THE FORMATION AND PROPAGATION OF WIDESPREAD
FATIGUE DAMAGE

A. F. Grandt, Jr.*, T. N. Farris*, and B. M. Hillberry†

This paper summarizes a basic research program dealing with predicting and observing the formation and propagation of widespread fatigue damage (WFD) in aerospace structures. A comprehensive effort is directed at determining how WFD develops from material inhomogeneitites, prior corrosion, or from fretting fatigue. Once cracks have formed at multiple locations, such as a row of rivets in a stiffened lap joint, procedures are developed to predict the subsequent growth, coalescence, and final failure load resulting from these multiple crack sources. Both deterministic and probabilistic approaches are considered and accentuated with comparison between predictions and controlled experiments.

INTRODUCTION

Purdue University has formed an interdisciplinary research team to address basic research issues associated with aging aircraft. The program is supported by the USAF Office of Scientific Research, and is focused on solving fundamental problems which limit the safe operation of aircraft beyond their original design or current lifetimes (1). The general program goals fall into the following four categories.

- Damage Development goals focused on determining how service induced damage develops in older aircraft through corrosion, fatigue crack formation, and fretting.

- Crack Growth And Interaction goals which deal with predicting the growth of service induced cracks and the impact of widespread fatigue damage (WFD) on residual strength and fatigue life.

*School of Aeronautics and Astronautics, and †School of Mechanical Engineering, Purdue University, W. Lafayette, Indiana 47907, USA.

Grandt, Farris, Hillberry

- <u>Failure Prevention</u> goals which focus on extending the operational life of "older" aircraft by delaying service induced damage, repairing cracked structure, and employing fleet tracking methods to prioritize maintenance actions within a fleet of aircraft.

- <u>Advanced Analysis Methods</u> developed to characterize crack growth in ductile materials, and to perform stochastic risk analyses to achieve the above general life analysis goals.

This paper focuses on efforts to predict the formation and propagation of widespread fatigue damage (WFD) which forms at material inhomogeneities, corrosion damage, or from fretting fatigue. Approaches are being developed to track the formation of this damage, its subsequent growth and coalescence into dominant cracks, and the consequences of WFD on residual strength.

CRACK GROWTH ANALYSIS

The WFD analysis scheme is based on a deterministic analysis for multiple-site damage (2). This fracture mechanics analysis predicts the growth, coalescence, and final fracture resulting from various combinations of small multiple site damage (MSD) cracks and large lead cracks which occur along a row of holes in a flat sheet. The multi-degree-of-freedom model allows individual cracks to grow independently, until interacting and linking up with adjacent cracks, or when growing into an uncracked hole (i.e., a "crack stopper"). The algorithm also employs a notch fatigue analysis to predict crack formation at holes which are initially uncracked, or to continue growing cracks which are momentarily stopped at the holes. Recent work (3-4) has developed stress intensity factor solutions for lead cracks which approach a stringer oriented perpendicular to the direction of crack growth, thus providing the capability to also analyze stiffened panels with WFD.

Numerical predictions for lead and MSD fatigue crack growth are compared with the results of several fatigue tests (2-3, 5) with both stiffened and unstiffened specimens in Figures. 1 and 2. Figure 1 shows a typical crack propagation diagram, which compares predicted and measured crack tip locations for an unstiffened panel fatigue test (5). This diagram indicates the type of detail that is obtained for multiply cracked specimens. Figure 2 summarizes predicted and measured fatigue lives for 4 stiffened (3) and 24 unstiffened (2,5) constant amplitude fatigue specimens that contain various combinations of lead and small multiple site damage cracks. Note that the WFD model does an excellent job of predicting the fatigue life of both stiffened and unstiffened panels with multiply cracked holes.

49- 2

Residual strength tests (3-4, 6) have also been conducted with both stiffened and unstiffened panels that contain MSD and lead cracks. The goal of these tests is to evaluate various residual strength criteria proposed for the multiple site damage problem. Although one objective of stiffeners is to provide a mechanism to arrest lead cracks before they can completely sever the panel, it is possible for the crack arrest capability to be defeated by small MSD that occurs on the opposite side of the stiffener. Figure 3 presents a summary of residual strength tests with stiffened 2024-T3 aluminum panels (4). These 1.6 mm (0.063 inch) thick panels were 38 cm (15 inch) wide and contained either 15.2 cm (6.0 inches) or .81 cm (4.5 inch) lead cracks, along with various MSD sizes. Symmetric stiffeners were riveted to the front and back sides of each specimen with a 19 cm (7.5 inch) spacing. Note that the residual strength of stiffened panels with relatively large lead cracks can be significantly reduced when small (1.27 mm to 3.81 mm = 0.05 to 0.15 inch) MSD cracks exist on the opposite side of the stiffener.

Figure 4 compares measured and predicted residual strength results for 22.9 cm (9 inch) and 38 cm (15 inch) wide unstiffened 2024-T3 aluminum panels that contain large lead cracks and small MSD cracks located at a row of open holes (3,6). Figure 5 compares the predicted and measured lead/MSD crack link-up loads for the stiffened panel specimen (4). Note that a relatively simple ligament yield model proposed by Swift (7) predicts the failure and lead/MSD crack link-up loads quite well for these residual strength tests (open and closed circles in Figures 4 and 5). The WFD crack growth program provides the option to select from these various residual strength criteria in order to determine final component life.

Other practical structural considerations are currently being added to the WFD analysis. A numerical model, for example, has been developed to determine the force transferred through fastener holes in various joint configurations (8). The model accounts for different plate thickness and material, as well as for the size and number of fastener rows. This load transfer information is used to compute the stress intensity factors (and, thus, fatigue crack growth rates) for MSD located at the fastener holes. One consequence of cracking at the holes is to change the load transfer among the various fastener rows. Figure 6 shows, for example, how cracking along the top row of fasteners in a three-row lap joint causes load shedding from that row to the uncracked fastener rows. While this particular result is for a "neat fit" fastener, recent research is extending the model to account for fastener interference (i.e., how tightly the fastener fills the hole) and rivet squeeze force. The degree of fastener interference depends on the rivet squeeze force along with other manufacturing parameters, and would be expected to vary widely in typical aircraft structure. As discussed later, probabilistic consideration of this effect can be accounted for in the WFD

Grandt, Farris, Hillberry

analysis, by letting fastener interference and/or rivet squeeze force be statistically varied input parameters.

CRACK FORMATION STUDIES

The goals of these tasks are to characterize the effects of microstructure, material anomalies, manufacturing damage, prior corrosion, fretting, and other potential sources that lead to widespread fatigue cracking. As described in the following subsections, two approaches to determine crack size distributions are being developed to serve as the initial damage state for crack growth analyses: 1) the Equivalent Initial Flaw Size (EIFS) method which incorporates an equivalent flaw size for the initial damage state distribution, and 2) a Total Life Prediction (TLP) model which characterizes the initiating crack size distribution by representing initial material fatigue quality in terms of inherent material inhomogeneities (e.g., constituent particles, porosity, etc.).

Equivalent Initial Flaw Size Characterization of Damage States

The Equivalent Initial Flaw Size approach for modeling the early stages of widespread fatigue assumes that a fictitious initial crack (or distribution of crack sizes) is inherent to the material and/or structural component of interest. The EIFS method treats the well known "scatter" in fatigue life by determining a "distribution" of initial crack sizes inherent to the manufactured component. The EIFS are chosen to represent initial material quality, along with manufacturing, and potential corrosion damage. By characterizing the initial material states in terms of initial flaw size distributions, crack growth mechanics can then determine the influence of applied stress and structural parameters on fatigue life. Probabilistic analyses may also be obtained by employing a deterministic crack growth framework with statistical inputs of various crack growth parameters (e.g., initial flaw size distributions, variations in material fatigue crack growth properties, fastener fit, variations in applied loads, etc.). The EIFS approach has previously been used to characterize initial manufacturing conditions (9, 10) material quality (11), and stress corrosion cracking (12).

Another EIFS approach is being developed to further evaluate the effects of corrosion on structural integrity. This approach characterizes initial corrosion damage in terms of two geometric parameters by assuming that corrosion can be approximated by a geometric structural change consisting of a general thickness reduction combined with a localized stress concentration due to pitting, etc. (13). The thickness loss leads to an increase in applied stress, while the localized damage is treated as an equivalent initial crack size distribution. These two parameters (thickness loss and EIFS distributions) may then be used as inputs to the general WFD analysis scheme, and statistical variations of thickness loss and

the EIFS could be used for Monte Carlo calculations which determine the influence of corrosion on remaining life. Estimates of the thickness loss and EIFS which represent the corroded material state would be obtained from measurements on naturally and artificially corroded materials.

The success of the EIFS approach for WFD applications depends on the ability to determine the appropriate initial flaw size distributions which represent damage states in older aircraft, and to predict the growth of these EIFS during subsequent service. Ongoing research to develop models to determine the sizes of fatigue cracking resulting from various sources is described below.

Total Life Prediction Model

A probabilistic Total Life Prediction (TLP) model has been developed to account for early crack formation at material defects, and short and long crack growth behavior (14-17). The model employs Monte Carlo simulations to predict fatigue lives for cracks which nucleate at voids or micropores. Size distributions of inclusion area, length, and width are obtained using a scanning electron microscope and image analysis software. The probabilistic model randomly selects inclusion sizes that are grown forward using a total fatigue life model that includes both small and large crack effects. The model predicts both the mean and variance, and, therefore, can readily predict minimum fatigue life.

The Total Life Prediction model shows very good agreement with Newman and Edwards' experimental data from the AGARD study (18). This comparison is shown below in Figure 7 as the cumulative distribution of the fatigue lives to initiate and grow a semi-circular crack to through thickness in a single edge notch specimen (17). Good agreement has been observed at two other stress levels. As described above, the prediction is based on the measured inclusion size distribution from an SEM image and a short and long crack growth model.

This TLP model has been incorporated into an MSD (2) analysis of a plate that contains a row of 10 open holes (17). The resulting probabilistic model predicted the total life of the panel to crack linkup of two adjacent holes where the cracks were assumed to initiate at an inclusion located at each side of every hole. The model consisted of 10,000 Monte Carlo simulations of 20 cracks growing for each simulation. This large number of trials allowed prediction of the expected fatigue life for 10^{-4} probability of panel failure. These results are shown in Figure 8.

The total life prediction model can also be used to determine an EIFS distribution for cracks forming at inclusions by back extrapolating a corner crack

geometry with long crack growth rate models and no threshold. As a result, the predicted EIFS distribution contains the corner crack shapes that are commonly employed for durability analyses. These derived EIFS distributions can then be utilized as the starting point for material induced WFD that can be analyzed by the crack growth model. An example (14) of an EIFS distribution obtained in this manner is shown in Figure 9.

The EIFS and TLP models are complimentary and can be readily implemented into probabilistic WFD predictions using MSD models. The EIFS approach is appropriate for characterizing induced damage, such as machining, fretting, and corrosion, whereas the TLP model relies on an appropriate defect stress intensity factor, early crack initiation, and a short crack growth model.

The TLP model for WFD is very promising and further research will focus on understanding the crack formation mechanisms at the microstructure level and determining the influence of service induced factors. The influence of residual stress on crack formation at inclusions and on short crack growth rate behavior is being studied and verified experimentally. Applications of the model to bolted holes and fretting conditions are also planned. Probabilistic models incorporating the TLP model into MSD applications will be verified with fatigue tests of corresponding MSD panels.

Fretting Fatigue Initiation of Widespread Fatigue Damage

Fretting fatigue is also being examined as a mechanism that leads to development of WFD at fastener/hole interfaces in lap joints or other airframe structural members where load transfer results in surface contact. Fretting is a contact damage mechanism arising from micro-slip associated with small-scale oscillatory motion of nominally clamped structural members. The combination of micro-slip at the contact surfaces, and the cyclic contact stresses associated with fretting, nucleates cracks at the contacting surfaces. Not surprisingly, fretting damage has been reported near aircraft skin fastener holes. The present work is designed to quantify the effect of fretting on fatigue crack nucleation in lap joint structures.

The first step toward the development of such a predictive methodology involved coupling the cyclic contact stress and strain fields with multiaxial fatigue theory for crack nucleation. Szolwinski and Farris (19) used this approach to predict fretting crack formation lives in an experiment aimed at producing fretting contact under controlled loads. A statistically-designed experimental test matrix is being used to validate this approach (20). To date, agreement between the predictions and observations is encouraging (Figure 10). These predictions are based on analytical approximations of the contact stress state based on measured

loads. The approximations have been justified using complete finite element modeling as illustrated in Figure 11 (21).

An effort to extend this approach to a lap joint configuration has been made using a three-dimensional finite element model of a rivet/lap joint assembly (22). Contact elements implementing the Coulomb friction law keep track of contact status between interacting surfaces. The shell elements incorporated in the model account for bending, contact between the skin panels, and rivet clamping pressure. Varying the stiffness of elastic supports allows for variation in the load transferred and simulation of various rivet configurations. When interference between the rivet and skin is not included in the model, there is loss of contact between the skin and rivet on loading. The corresponding distinct stick-slip zones, combined with high tensile stresses at the edge of contact, are indicative of fretting and portend crack nucleation at the edge of contact. Crack nucleation lives are predicted using the multiaxial fatigue theory described above. Exercising the model in conjunction with the multiaxial fatigue theory allows for quantification of factors such as friction coefficient, clamping pressure provided by the rivet head, and plasticity on crack nucleation lives.

The results from the finite element modeling also identify the interface between the two skin panels as a region of localized fretting damage. The load transferred through the rivet assembly is transferred through the skin/skin interface and between the skin/plate interface. The partition of load between the rivet and skin/skin interface is shown schematically in Figure 12. When the loading is applied for the first time, initially nearly all the load is taken up by the interfacial friction as the panels have to overcome this interfacial friction to move into the rivet and initiate contact at the panel/skin interface. Thus, the rivet begins to take up load only after the two panels slip with respect to each other. The rivet absorbs the subsequent loading. When unloading begins, once again the panels need to slip in the opposite direction in order to relieve the load on the rivet. This necessitates the reversal of the interfacial frictional load. During this phase of unloading the rivet itself does not experience significant change in load. When the unloading is complete, there is a frictional load between the two panels and a balancing load on the rivet. When reloading begins, once again the interfacial friction accounts for the initial part, and the rivet absorbs the subsequent loading. This mechanism now continues in a cyclic fashion. The presence of high slip amplitudes in conjunction with any high stresses can cause extensive damage to the faying surfaces and nucleate cracks. The amount of interfacial friction depends on the clamping pressure on the rivet. Efforts are underway to more fully model the clamping pressure and effect of the interference through finite element simulation of the riveting process.

PROBABILISTIC ANALYSIS

Although the basic fatigue crack growth program is deterministic in nature, probabilistic methods may be incorporated to assess the statistical influence of critical analysis parameters. Monte Carlo type calculations can determine the variation in life (or probability of fracture) resulting from the uncertainty in input parameters such as initial crack size, material properties, loading, or fastener fit. The initial damage state for the WFD calculations, for example, may employ equivalent initial flaw size (EIFS) distributions. These EIFS distributions could come from actual tear-down data, or may be based on tests and analyses which consider crack formation from various service induced sources.

As described previously, predictive models are being developed to estimate the WFD caused by fatigue cracking at material inhomogeneities, pre-corroded material state, and fretting. One could also incorporate the probability for other sources of cracking, such as engine bursts, bird strikes, or battle damage, along with the results of nondestructive inspection. In the latter case, the current crack size distributions could be periodically modified to represent those following inspection (i.e., incorporate probability of detection data in the calculations). Thus, by employing statistical descriptions of various input parameters, it is possible to determine the sensitivity of the probability of fracture from WFD to potentially critical issues.

An example of the probabilistic approach has been employed for an analysis of multiple site damage (23) in a wide plate with a single row of 30 open holes (see Figure 13). The statistical input variables considered in this example include equivalent initial flaw size distributions and stochastic descriptions of fatigue crack growth material properties. The holes were assumed to contain initial cracks randomly selected from an equivalent initial flaw size distribution reported for a fighter lower wing skin. The variability in fatigue crack growth rate was modeled by stochastic descriptions of crack growth parameters previously found for a modified Paris crack growth model. Different simulations were performed to determine the influence of both material variability and initial WFD on fatigue life (see Figure 14 for a typical result).

One of the results of those prior simulations was to show that the initial crack size distribution plays a more significant role on WFD life than the variability in fatigue crack growth material properties. Indeed, one of the main goals of such probabilistic studies is to determine the most critical parameters and/or those which induce the most variability. The results of these analyses will then help the design and maintenance engineers to focus attention on the most critical aspects of the WFD problem. Future plans include incorporating

Grandt, Farris, Hillberry

statistical variations in fastener fit and/or rivet clamp up force and their influence on load transfer through the structural joint. Variations in those input parameters will then be incorporated with EIFS distributions obtained from the crack formation models which estimate WFD caused by fatigue cracking at material inhomogeneities, pre-corroded material state, or by fretting. The EIFS input may also be based on the results of tear downs or nondestructive inspection capability. When completed, these series of calculations would demonstrate how to incorporate the effects of prior service and initial manufacturing or material condition on the analysis of WFD.

CONCLUDING REMARKS

The goal of this paper has been to summarize basic research on techniques to determine the formation of widespread fatigue damage and its subsequent influence on the residual strength. Research on crack formation models includes consideration of fretting and fatigue crack nucleation from material inhomogeneities and/or corrosion. Once individual cracks have formed at multiple locations, they are grown with fracture mechanics based algorithms that determine their initial growth and coalescence. Final fracture from dominant cracks, including interaction with smaller MSD flaws, is determined by various residual strength criteria. The basic WFD analysis model is being developed in the context of a structural joint, and includes the effects of load transfer through fasteners, fastener fit, as well as the influence of stiffeners on crack growth and arrest. A series of coupon and small component tests conducted to verify the predictive capabilities of the predictive techniques have given excellent results to date. Larger component tests are planned for the future. Monte Carlo simulations are also performed to obtain probabilistic treatment of the WFD problem. Such probabilistic calculations have been demonstrated with statistical inputs of initial crack size (i.e. EIFS distributions) and distributions of material crack growth properties. Future calculations are planned to include variations in fastener fit and riveting load as well as perhaps the consequences of inspection (via probability of detection curves).

ACKNOWLEDGMENTS

Grandt, Farris, Hillberry

N. Scheuring, H. L. Wang; (from the School of Mechanical Engineering) E. A. DeBartolo. P. J. Laz. S. M. Rohrbaugh.

REFERENCES

(1) Grandt, A. F., Jr. "Materials Degradation and Fatigue In Aerospace Structures." Third Annual Report for Air Force Office of Scientific Research Grant No. F49620-93-1-0377. School of Aeronautics and Astronautics, Purdue University, August 1996.

(2) Moukawsher, E. J., Grandt, Jr., A. F. and Neussl, M. A. "Fatigue Life of Panels With Multiple Site Damage." Journal of Aircraft, Vol. 33, No. 5, September – October 1996, pp. 1003 - 1013.

(3) Heinimann, M. B. "Analysis of Stiffened Panels with Multiple Site Damage," Ph. D. Thesis, School of Aeronautics and Astronautics, Purdue University, 1997.

(4) Heinimann, M. B. and Grandt, Jr., A. F. "Analysis of Stiffened Panels with Multiple Site Damage." 1996 USAF Structural Integrity Program Conference, San Antonio, Texas. December 3-5, 1996.

(5) Grandt, A. F., Jr., Sexton, D. G., Golden, P. J., Bray, G. H., Bucci, R. J. and Kulak, M. "A Comparison of 2024-T3 and 2524-T3 Aluminum Alloys Under Widespread Damage Scenarios," 19th ICAF Symposium, International Committee on Aeronautical Fatigue 1997, Edinburgh, 16-20 June 1997 (this proceedings).

(6) Moukawsher, E. J., Heinimann, M. B., and Grandt, Jr., A. F. "Residual Strength of Panels with Multiple Site Damage," Journal of Aircraft, Vol. 33, No. 5, September – October 1996, pp. 1014 - 1021.

(7) Swift, T. "Widespread Fatigue Damage Monitoring Issues and Concerns." 5th International Conference on Structural Airworthiness of New and Aging Aircraft, Hamburg, Germany, June 16-18. 1993.

(8) Wang, H. L., Buhler. K., and Grandt, Jr., A. F. "Evaluation of Multiple Site Damage in Lap Joint Specimens." Proc. of 1995 USAF Structural Integrity Program Conference, San Antonio, Texas. November 28-30, 1995.

(9) Rudd. J. L., Yang, J. N., Manning. S. D., and Yee, B. G. W. "Probabilistic Fracture Mechanics Analysis Methods for Structural Durability." Behavior of Short Cracks in Airframe Components. AGARD Conference Proceeding No 328, April 1983, p 10-1.

(10) Yang, J. N., Manning, S. D., Rudd, J. L. and Bader, R. M. "Investigation of Mechanistic-Based Equivalent Initial Flaw Size Approach. Proc. ICAF 95, International Committee on Aeronautical Fatigue, 18th Symposium, Melbourne, Australia, May 3-5, 1995.

(11) Magnusen, P. E., Hinkle, A. J., Kaiser, W., Bucci, R. J., Rolf, R. L. "Durability Assessment Based on Initial Material Quality," ASTM Journal of Testing and Evaluation, Nov. 1990, pp. 439-445.

(12) Lukasak, D. A., Bucci, R. J., Colvin, E. L. and Lifka, B. W. "Damage-Based Assessment of Stress Corrosion Performance among Aluminum Alloys," ASTM STP 1134, 1991.

(13) Doerfler, M. T., Grandt, Jr., A. F., Bucci, R. J. and Kulak, M. "A Fracture Mechanics Based Approach for Quantifying Corrosion Damage." Proceedings of 1994 Tri-Service Conference on Corrosion, Orlando, FL, June 20-24, 1994.

(14) Laz. P. J. and Hillberry, B. M. "A Probabilistic Approach to the Generation of EIFS Distributions Derived From Inclusion Characteristics," Structural Integrity in Aging Aircraft, AD-Vol. 47, ASME, 1995, pp. 81 - 85.

(15) DeBartolo, E. A., Laz, P. J. and Hillberry, B. M. "A Model for Probabilistic Crack Growth to Account for Crack Coalescence," Fatigue '96, Berlin, Germany, May, 1996.

(16) Laz, P. J. and Hillberry, B. M. "The Role of Inclusions in Fatigue Crack Formation in Aluminum 2024-T3," Fatigue '96, Berlin, May, 1996.

(17) Hillberry, B. M., Rohrbaugh, S. M., Laz, P. J. and DeBartolo, E. A. "Total Life Prediction Model: A MSD Application," Air Force Fourth Aging Aircraft Conference, Colorado Springs, Colorado, July 1996.

(18) Newman, J. C., Jr. and Edwards, P. R., "Short Crack Growth Behavior in an Aluminum Alloy - An AGARD Cooperative Test Program," AGARD R - 732, 1988

Grandt, Farris, Hillberry

(19) Szolwinski, M. P. and Farris, T. N. "Mechanics of Fretting Fatigue Crack Formation." Wear, Vol. 194, No. 3, pp. 355-367 (1996).

(20) Szolwinski, M.P., Harish, G., McVeigh, P.A. and Farris, T.N., "The Role of Fretting Crack Nucleation in the Onset of WFD: Analysis and Experiments." Proc. FAA-NASA Sym. On Continued Airworthiness of Aircraft Structure, Atlanta, GA, August 28-30, (in press), 1996.

(21) McVeigh, P.A. and Farris, T. N. "Finite Element Analysis of Fretting Stresses." ASME Journal of Tribiology, (in press), 1997.

(22) Harish, G. and Farris, T. N. "Modeling of Skin/Rivet Contact: Application to Fretting Fatigue." Proc. 38th SDM Conference, Kissimmee, FL, April 7-10, 1977, pp. 2761-2771.

(23) Rohrbaugh, S. M., Hillberry, B. M., Grandt, Jr., A. F. and McCabe, G. "A Probabilistic Fatigue Analysis of Multiple Site Damage," Proceedings of FAA/NASA International Symposium on Advanced Structural Integrity Methods for Airframe Durability and Damage Tolerance, Hampton, VA, May 4-6, 1994, NASA Conference Publication 3274, Part 2, C.F. Harris, Ed., pp. 635-652, September 1994.

Grandt, Farris, Hillberry
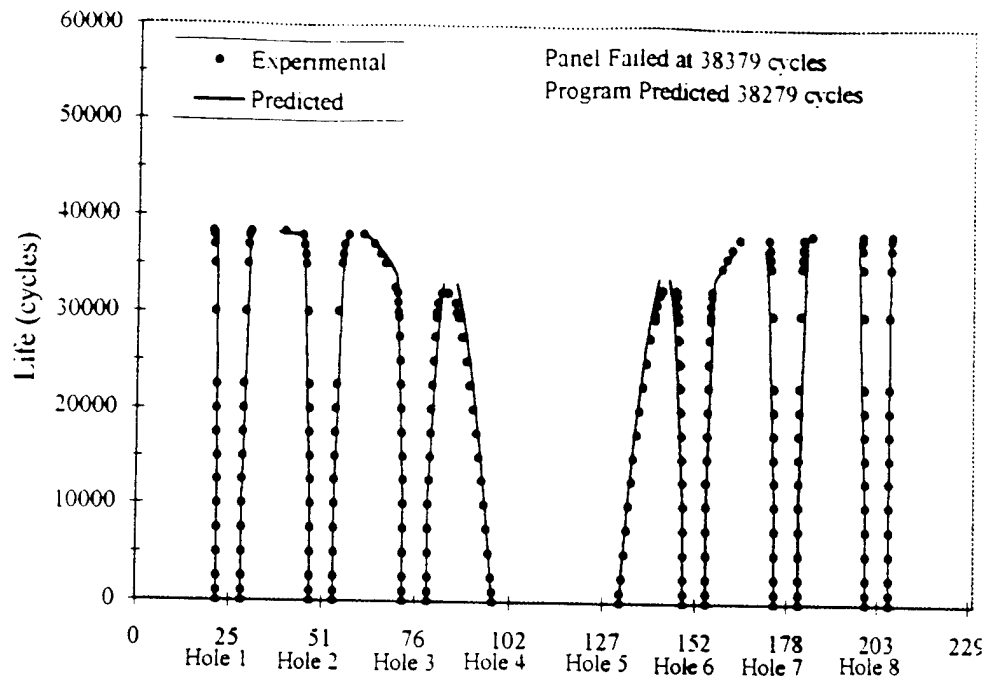
Figure 1   Comparison of measured and predicted fatigue crack growth in 2024-T3 specimen that contains a row of multiply cracked holes (5)
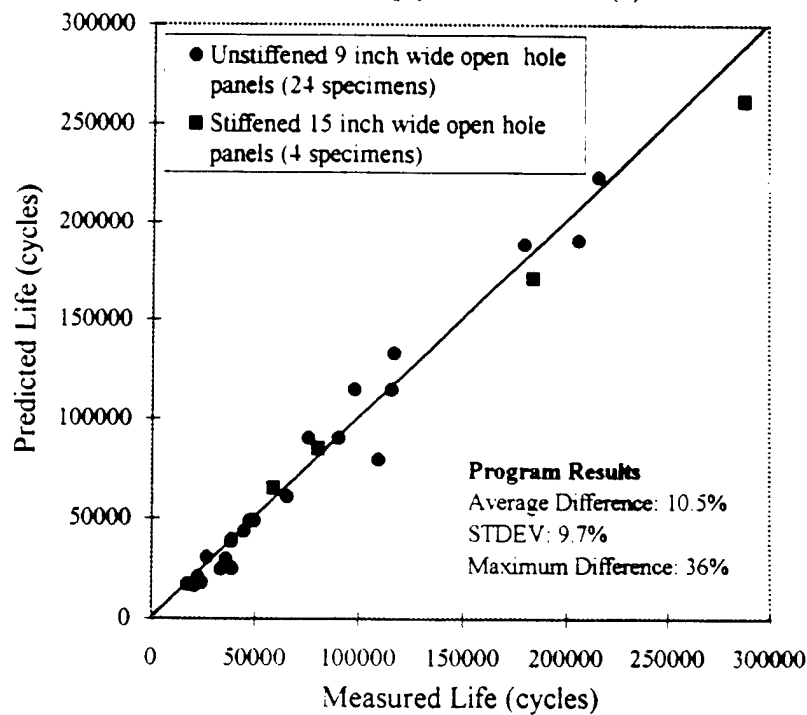
Figure 2   Comparison of measured and predicted fatigue lives for stiffened and unstiffened aluminum panels that contain multiply cracked holes (3)

A 12 - 13

Grandt, Farris, Hillberry
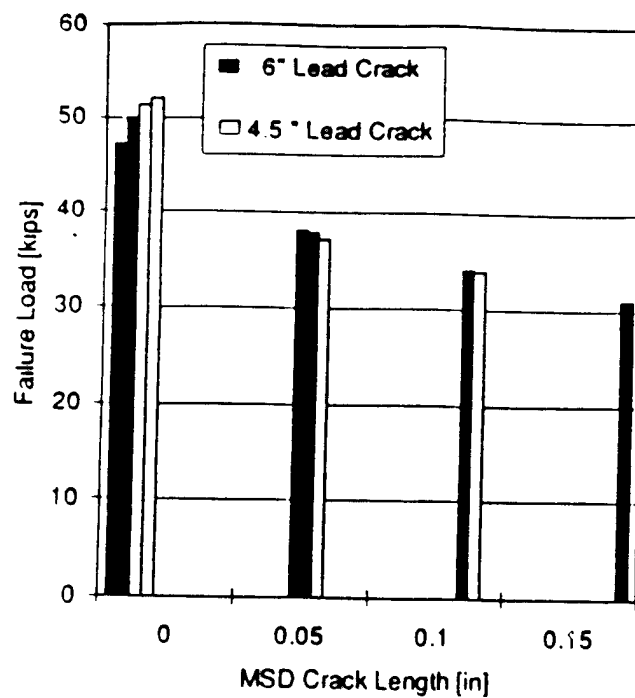
Figure 3 Residual strength of stiffened 2024-T3 panels which contain lead cracks and various MSD crack sizes located across stiffener from lead crack (3,4)
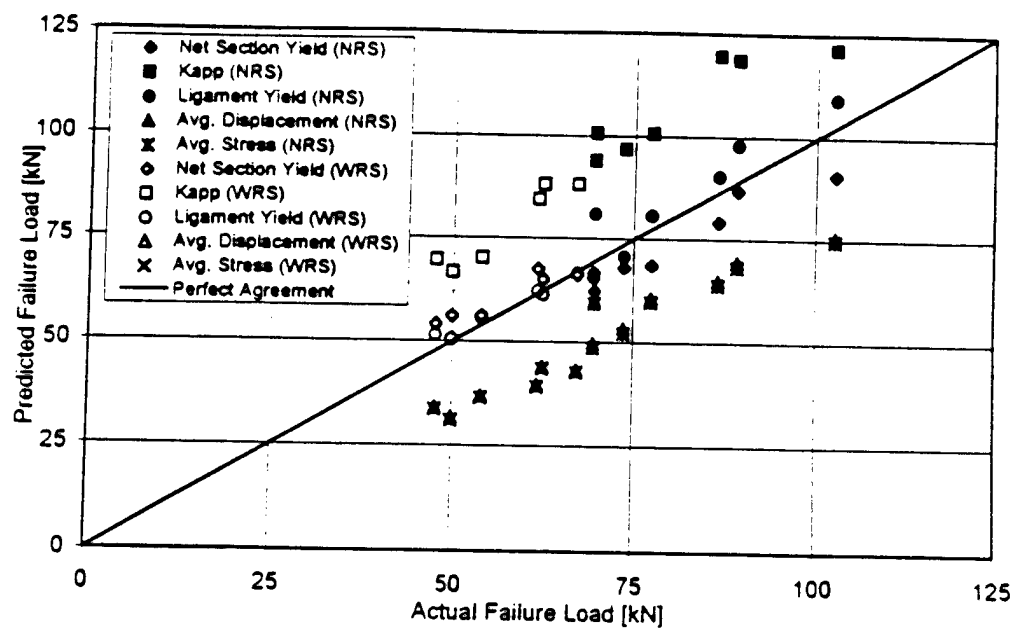
Figure 4 Measured panel loads for unstiffened MSD specimens compared with residual strengths predicted by various criteria (3).

Grandt, Farris, Hillberry

Figure 5   Comparison of measured and predicted link-up loads for stiffened 2024-T3 panels with lead and MSD cracks (3,4).
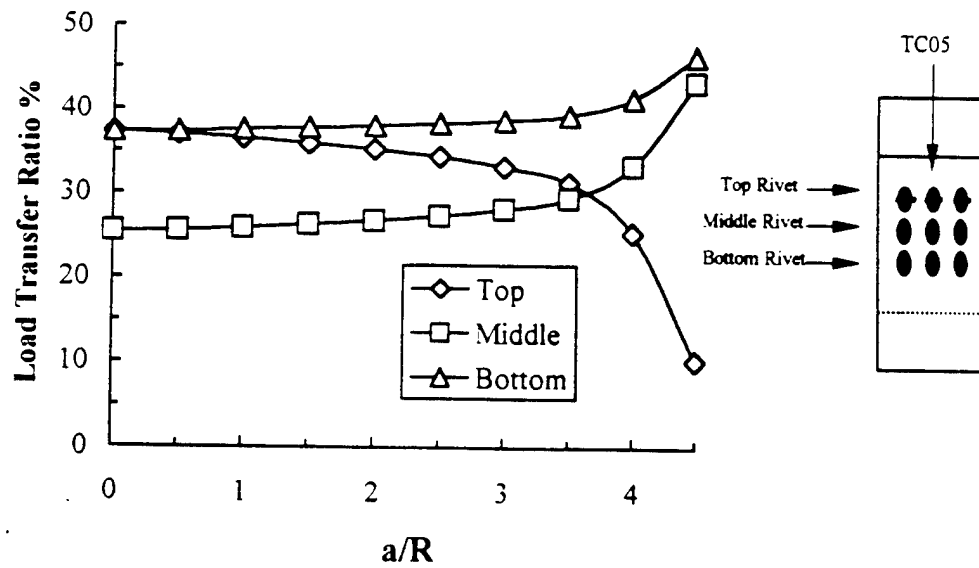
Figure 6   Change in fastener load transfer in a three-row lap joint caused by crack growth in top row of fasteners (8).

Grandt, Farris, Hillberry
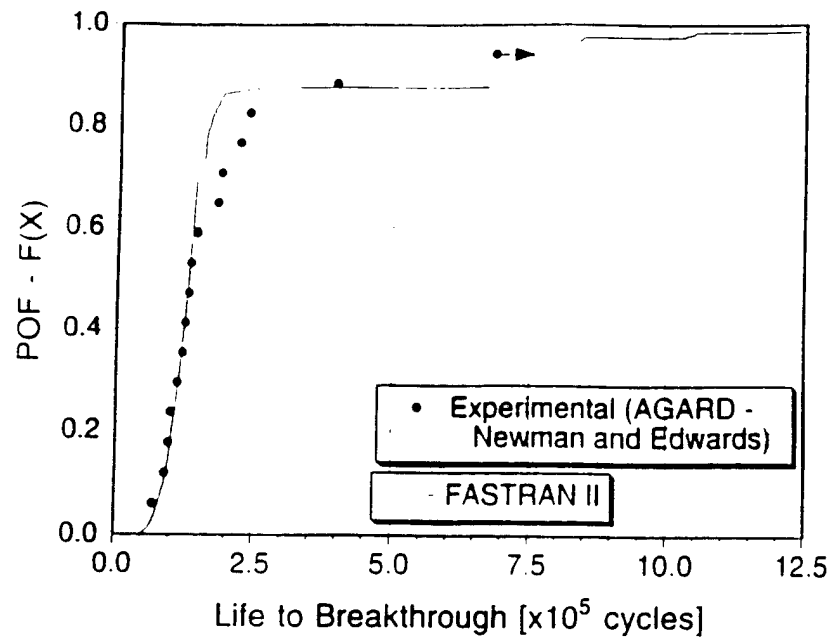
Figure 7 Cumulative distribution for probability of failure versus fatigue life predicted by the TLP model (maximum stress = 120 MPA, Reference 17).
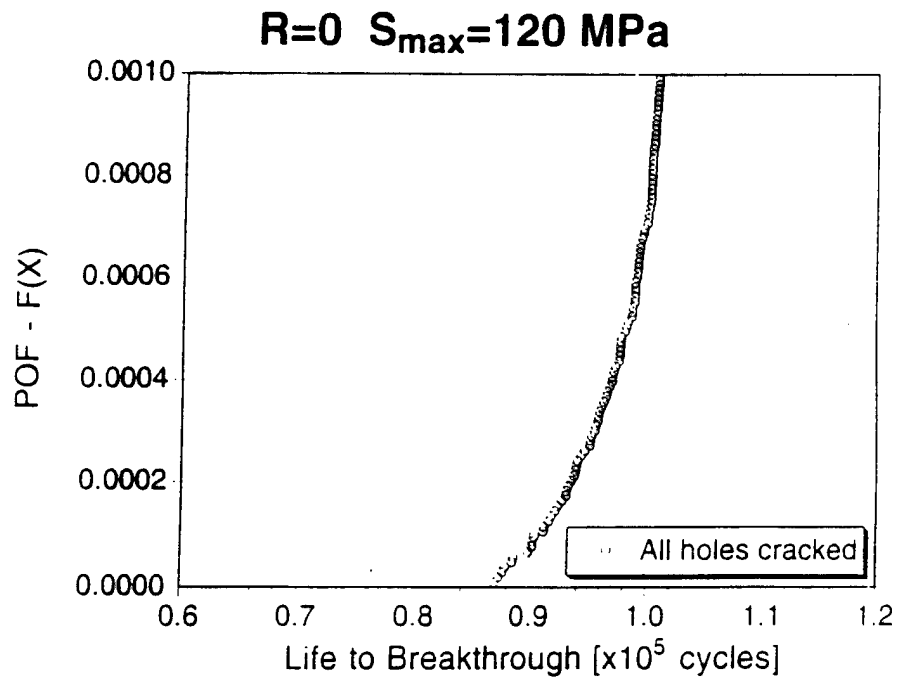
Figure 8 Probability of failure by ligament break for ten hole MSD panel simulation (17).

Grandt, Farris, Hillberry

Figure 9   Equivalent Initial Flaw Size distribution calculated from measured constituent particle distribution in 2024-T3 sheet (14).
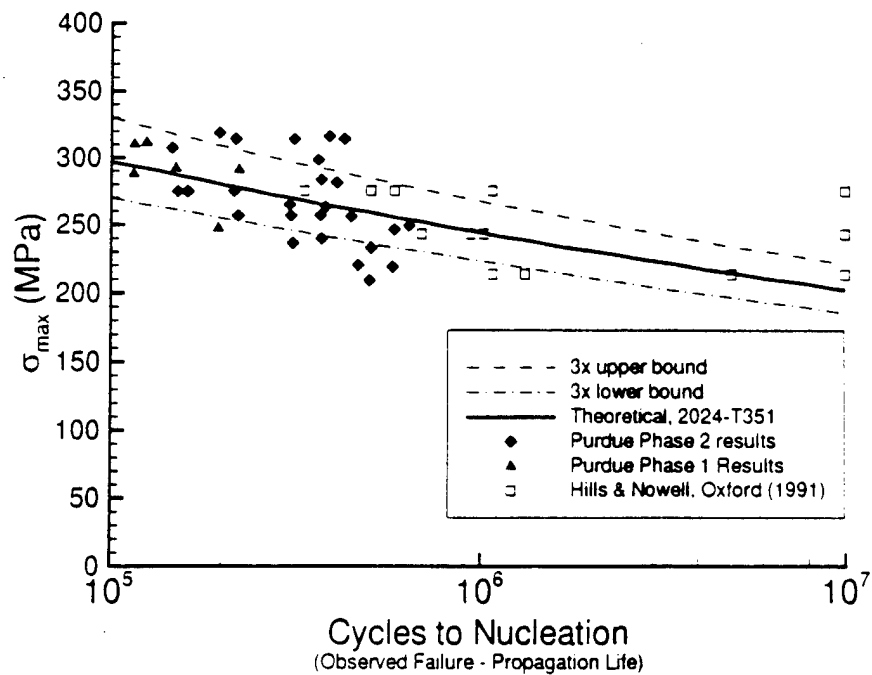
Figure 10   Comparison of experimental fatigue crack nucleation lives for fretting fatigue tests with predictions by multiaxial fatigue based approach (20).

Grandt, Farris, Hillberry
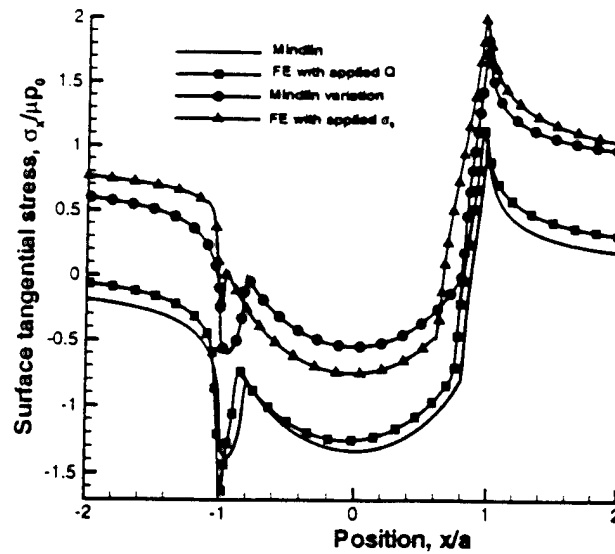
Figure 11   Comparison of approximate and finite element surface tangential stress that controls crack nucleation for given loads (21)
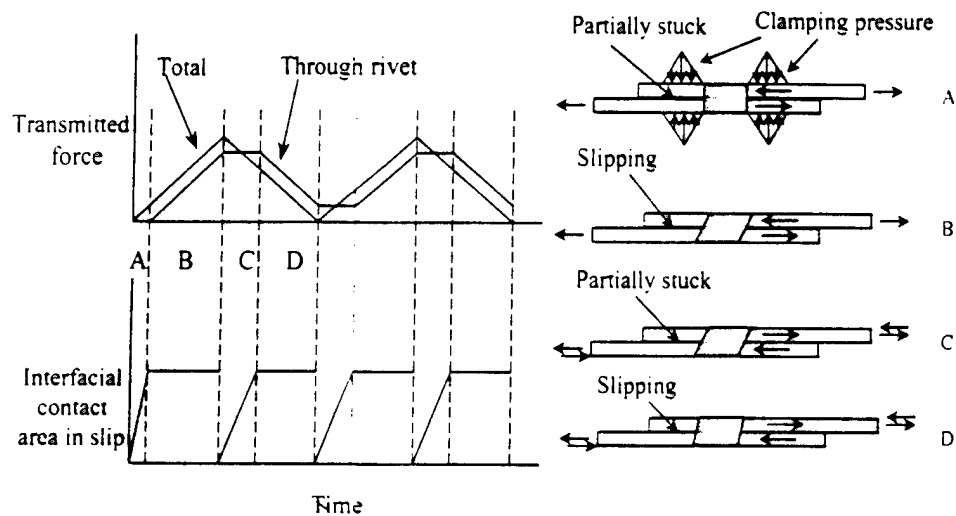
Figure 12   Schematic of load transfer mechanism in joint with clamp-up pressures (22).

A17 - 18

Figure 13   Open hole panel used for Monte Carlo simulations on effect of variable initial MSD and fatigue crack growth material properties on fatigue life (23).
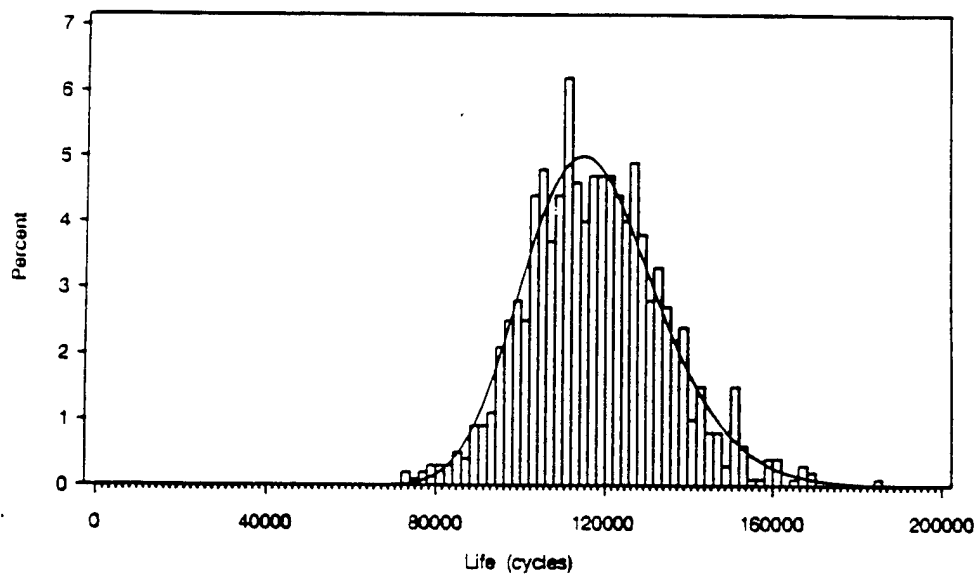
Figure 14   Fatigue life histogram showing influence of variability in initial crack size and fatigue crack growth material properties on life (23).

Grandt, Farris, Hillberry

FATIGUE IN NEW AND AGEING AIRCRAFT

A COMPARISON OF 2024-T3 AND 2524-T3 ALUMINUM ALLOYS UNDER MULTI-SITE DAMAGE SCENARIOS

A. F. Grandt, Jr.*; D. G. Sexton*, P. J. Golden*, G. H. Bray+, R. J. Bucci+, and M. Kulak+

This paper quantifies the improved resistance to the consequences of multi-site damage provided by new Alcoa aluminum alloy 2524-T3. This type of damage can develop in older aircraft in the form of fatigue and/or corrosion. Results from two types of tests are presented: (1) residual strength tests to assess the effect of multi-site damage on residual strength of a flat panel; and (2) fatigue tests to assess the effects of multi-site damage on fatigue life. With MSD present, 2524-T3 exhibited significant improvements in both residual strength and fatigue life relative to the incumbent alloy 2024-T3. The improvement in fatigue life was predicted from standard small coupon fatigue crack growth data using a multiple degree of freedom crack growth analysis. Potential advantages of the improved damage tolerance of 2524-T3 to aircraft manufacturer/operators are weight savings, lower operating costs, easier inspectability and increased safety.

INTRODUCTION

The service life of an airframe can potentially introduce multi-site damage (MSD) states such as widespread fatigue or widespread corrosion that may imperil the structural integrity of the aircraft. The inspection intervals set by standard residual strength and damage tolerant design are normally directed at the presence of a single crack, but may be inadequate in the presence of MSD. It is well known, for example, that small fatigue cracks located ahead of a larger lead crack can significantly reduce the residual strength and fatigue life normally associated with the lead crack (1-5). This realization and the desire for reliable, longer lasting aircraft with lower maintenance costs have given rise to requirements that non-pristine or aging structure be accounted for in design and maintenance strategies. This philosophical shift has created demand for affordable, replacement materials that can not only resist the occurrence of multi-site damage, but which offer improved structural damage tolerance when MSD is present.

* School of Aeronautics and Astronautics, Purdue University, 1282 Grissom Hall, W. Lafayette, IN 47907 USA
+ Alcoa Technical Center, 100 Technical Drive, Alcoa Center, PA 15069 USA

Presented at ICAF 97, International Committee On Aeronautical Fatigue, Edinburgh, 16-20 June 1997

An excellent example of one such material is new aluminum alloy 2524-T3 (formerly C188-T3) developed by Alcoa. Currently used in the Boeing 777 aircraft. 2524-T3 was designed for fuselage skin sheet as a replacement for 2024-T3, the industry standard since the DC-3. As shown in Table 1, 2524-T3 has superior fatigue crack growth resistance and fracture toughness Kc in comparison to 2024-T3 while maintaining equivalent tensile properties. Boeing utilized the improvements of 2524 in fracture toughness and fatigue crack growth resistance to obtain weight savings and reduced manufacturing costs in new structure over incumbent alloy 2024 design (6-8).

TABLE 1 – Typical Mechanical Properties for Clad 2524-T3 and 2024-T3 Aluminum Alloys (T-L Direction)

Alloy	Thickness (mm)	UTS (MPa)	TYS (MPa)	Elong (%)	Kc[a] MPa-m$^{1/2}$	da/dN@ ΔK=33[b] (mm/cycle)
2524-T3	0.81 - 1.59	420	303	19	174	2×10^{-3}
	1.60 - 3.26	441	310	21		
	3.27 - 6.32	441	303	22		
2024-T3	0.81 - 1.59	427	296	18	141	6.9×10^{-3}
	1.60 - 3.26	448	310	19		
	3.27 - 6.32	448	310	19		

a) M(T) specimen, T-L orientation, W = 40.6 cm (16 inch), $2a_0$ = 10.2 cm (4 inch) tested per ASTM B 646.
b) T-L orientation, tested per ASTM E 647 under constant ΔK conditions, R = 0.1, relative humidity > 90%.

A recent study by Bray et al. (9) focused on quantifying the improved resistance of bare 2524-T3 to the occurrence of MSD resulting from corrosion. With prior corrosion, approximately equivalent to one year exposure to a seacoast environment, the smooth fatigue strength of 2524 was approximately 10% higher and the lifetime to failure approximately 30 to 45% longer than that of 2024. A main factor contributing to the better performance of 2524 was a less damaging configuration of corrosion pits with respect to number, depth and/or shape, indicating 2524 is more resistant to the onset of MSD from corrosion.

The goal of the present study described in this paper is to quantify the beneficial effects of the improved damage tolerance provided by 2524-T3 once MSD is already present either in the form of corrosion or fatigue damage. The influence of MSD on lead crack residual strength and fatigue life to failure is

demonstrated with test results obtained for both 2524 and 2024 alloys.

TEST MATERIALS

The 2024-T3 and 2524-T3 materials used for the current study were purchased commercially in the form of 1.3 mm (0.05 inch) thick al-clad sheet. The strength and fracture toughness properties measured from specimens machined from these sheets are given in Table 2. The fracture toughness Kc was measured from 40.6 cm (16 inch) wide M(T) specimens tested per ASTM standard B 646 in the T-L orientation with an initial center crack length $2a_0$ =10.2 cm (4 inches). The R=0.05 fatigue crack growth properties for the two alloys in laboratory air are compared in Figure 1. These data were obtained from 10.2 cm (4 inch) wide M(T) specimens tested according to ASTM standard E 647. Again, note the significantly slower fatigue crack growth rates obtained for the 2524 alloy over much of the range of the cyclic stress intensity factor (ΔK) range.

TABLE 2 – Mechanical Properties of 2024-T3 and 2524-T3 Clad Alloys Used For This Study (T-L Direction)

Alloy	Thickness (mm)	UTS (MPa)	TYS (MPa)	Elong (%)	Kc[a] ($MPa\text{-}m^{1/2}$)
2524-T3	1.27	416	300	20.5	165
2024-T3	1.27	427	300	18.5	149

a) M(T) specimen, T-L orientation, W = 40.6cm (16 inch), $2a_0$ = 10.2cm (4 inch) tested per ASTM B 646.

MSD RESIDUAL STRENGTH TESTS

The goal of these tests was to determine how the residual strength of each alloy is influenced by small flaws (MSD) ahead of the lead crack. The lead crack is intended to model accidental damage or a large fatigue crack from a rogue flaw, while the small MSD is representative of wide spread fatigue or corrosion which could develop in an older aircraft. The residual strength tests conducted here employed 40.6 cm (16 inch) wide by 100 cm (40 inch) unstiffened panels with a 53 cm (21 inch) long test section. The specimens contained a central row of open holes oriented perpendicular to the applied tensile load. The open holes were 4 mm (5/32 inches) in diameter, and were located on 2.54 cm (1.0 inch) centers. An 11 cm (4.4 inch) nominal lead crack was formed by sawing the ligament between the five central holes, and then introducing 2.5 mm (0.10 inch) long electro discharge machine (EDM) notches at the end of this "slot." Small through-thickness MSD flaws were then introduced by EDM on each side of the remaining

holes in the plane of the lead crack. Several MSD flaw sizes were evaluated for each alloy, including a zero flaw size, 1.27 mm (0.05 inch), 2.5 mm (0.10 inch), and 3.8 mm (0.15 inch) MSD. All cracks were oriented in the T-L direction of the original aluminum sheets.

The panels were pulled to failure in remote tension in an electro-hydraulic test machine under displacement control. Extension of the lead crack (i.e., "slow" crack growth), and crack mouth opening displacement were obtained as a function of applied load. Link-ups between the lead crack and cracks emanating from the MSD flaws were also recorded visually with the aid of an optical microscope. The applied load versus lead crack length data are shown in Figures 2 and 3 for the two test materials. (Recall that all specimens contained an 11 cm (4.4 inch) long central lead crack.) A summary of residual strength as a function of MSD flaw size is given in Figure 4 for the two test materials. Note that although the presence of small MSD in the holes ahead of the lead crack does reduce specimen residual strength in both alloys, the 2524-T3 panels continue to have superior residual strength when MSD is present. The 2524-T3 panels demonstrated a 9-10.5% increase in residual strength in comparison to the 2024-T3 baseline for the various MSD flaw sizes investigated. Thus, when viewed as a replacement for 2024-T3, the 2524-T4 alloy gives a significant increase in the margin of safety for widespread fatigue damage scenarios that could develop in older aircraft.

MSD PANEL FATIGUE TESTS

The influence of MSD on fatigue life was also determined for the two test materials. The unstiffened panel fatigue specimens were 23 cm (9 inch) wide by 53 cm (21 inch) long with a 36 cm (14 inch) long test section. These panels also contained a single row of 4 mm (5/32 inch) diameter holes located on 25.4 mm (1 inch) centers oriented perpendicular to the applied tensile stress. A 3.4 cm (1.36 inch) lead crack was created by sawing the ligament between the two central holes and introducing a 2.5 mm (0.10 inch) long EDM slot at the end of the two holes. Various through-thickness MSD flaw sizes were then introduced at both sides of the remaining holes, with EDM slots oriented in the plane of the lead crack. Again, all cracks were oriented to grow in the T-L direction. These test specimens were then cycled to failure with an R = 0.05 peak gross stress of 59 MPa (8.56 ksi). Fatigue cracks quickly formed at the EDM slots and propagated to failure. The position of each crack tip (including the lead and MSD flaws) was recorded as a function of elapsed cycles with a traveling microscope. Five specimens of each material were tested in this manner: a single test with 2.5 mm (0.10 inch) MSD; and repeat tests for the 0 and 1.3 mm (0.05 inch) MSD conditions.

Figures 5 and 6 show typical crack propagation diagrams for the 2024-T3 and 2524-T3 specimens containing 1.3 mm (0.05 inch) MSD flaws at each hole. Figure 7 summarizes the fatigue lives for the 2524-T3 and 2024-T3 specimens as a function of MSD flaw size at the outboard holes (Recall that all the fatigue specimens also contained an initial 3.4 cm (1.36 inch) central lead crack). As anticipated, the fatigue life decreases with increasing MSD flaw size. The lives for the 2524-T3 specimens are 27 to 45% longer than the corresponding 2024-T3 specimens in all cases showing the superior performance of the 2524 material.

FATIGUE LIFE ANALYSIS

The fatigue life predictions shown in Figures 5-7 are based on a fracture mechanics procedure described in (4). That multi-degree-of-freedom crack growth analysis involves computing stress intensity factors (K) at each crack tip, and includes increases in K caused by interaction between adjacent cracks. The fatigue crack growth data given in Figure 1 are then used to determine the corresponding crack growth rates, and to incrementally advance individual crack tips. Link-up of adjacent cracks is based on the Swift ligament yield model outlined in Reference 2. Although not employed for the current experiments, the algorithm also includes a notch fatigue analysis to predict crack formation at holes which are initially uncracked, and to continue growing cracks which are momentarily stopped at holes. Recent work (10) has developed stress intensity factor solutions for lead cracks which approach a stringer oriented perpendicular to the direction of crack growth, thus providing the capability to also analyze stiffened panels with MSD. Reference 11 also discusses application of the predictive scheme to lap joint specimens with multiple cracks located at holes that contain load bearing fasteners.

The crack propagation diagrams given in Figures 5 and 6 specify the location of each crack tip as a function of elapsed cycles. The solid symbols represent the measured crack tip positions, while the solid lines are predictions based on the fracture mechanics model. Figure 8 compares the predicted and measured fatigue lives for the ten multiply cracked specimens examined here, and show excellent agreement between predicted and observed lives. Similar comparisons are given in Reference 4 for other unstiffened panel tests, in (10) for MSD experiments with stiffened panels, and in (11) for lap joint specimens. The current results, along with these other experiments indicate that the predictive model is quite capable of analyzing multiply cracked configurations that involve interactions between small MSD and larger lead cracks.

SUMMARY AND CONCLUSIONS

This paper has compared the resistance of 2524-T3 and 2024-T3 aluminum alloys

to multi-site damage scenarios that could develop in older aircraft. Both residual strength and fatigue lives were examined in flat panels containing a lead crack and multiple flaws at adjacent open holes representing fastener holes. Residual strength tests of panels that contained large lead cracks and MSD flaws ranging in size from zero to 3.8 mm (0.15 inch) indicated significantly improved damage tolerance for 2524-T3 relative to incumbent alloy 2024-T3. The residual strength of the 2524-T3 panels was 9 to 10.5% higher than that measured in the 2024-T3 panel having an equivalent flaw size. In the fatigue tests, 2524-T3 panels containing a small lead crack and MSD flaws ranging in size from zero to 2.5 mm (0.10 inch) exhibited a 27 to 45% increase in life compared to the equivalent 2024-T3 panel. A multiple degree of freedom computational crack growth analysis tool developed previously (4) was able to predict the observed differences in fatigue lifetime using fatigue crack growth curves for these materials obtained from small coupon tests.

Although both alloys have similar tensile properties, the results of this and previous work (6-9) indicate that significant advantages in damage tolerance are possible with 2524-T3 relative to the incumbent alloy 2024-T3 in fuselage skin sheet applications, both in new aircraft structure and in multi-site damage scenarios that might be found in aging aircraft. Potential advantages of 2524-T3 to aircraft manufacturer/operators are an increase in the allowable stress (weight savings), increase in inspection interval (lower operating costs), easier inspectability (larger crack sizes can be tolerated) and an increase in safety (reduced risk of failure).

ACKNOWLEDGMENTS

REFERENCES

1) Mar, J. W., "Structural Integrity of Aging Airplanes: A Perspective," Structural Integrity of Aging Airplanes, S. N. Atluri, S. G. Sampath, P. Tong, Eds, Springer-Verlag, 1991, pp. 241-273.

2) Swift, T., "Widespread Fatigue Damage Monitoring Issues and Concerns," 5th International Conference on Structural Airworthiness of New and Aging

Aircraft, Hamburg, Germany, June 16-18, 1993.

3) Moukawsher, E. J., Heinimann, M. B., and Grandt, A. F., Jr., "Residual Strength of Panels with Multiple Site Damage," Journal of Aircraft, Vol. 33, No. 5, 1996, pp. 1014-1021.

4) Moukawsher, E. J., Grandt, A. F., Jr., and Neussl, M. A., "Fatigue Life of Panels with Multiple Site Damage," Journal of Aircraft, Vol. 33, No. 5, 1996, pp. 1003-1013.

5) Heinimann, M. B. and Grandt, A. F., Jr., "Analysis of Stiffened Panels with Multiple Site Damage," Proc. of 1996 USAF Structural Integrity Program Conference, San Antonio, Texas, December 3-5, 1996.

6) Hyatt, M.V. and Axter, S.E., "Aluminum Alloy Development for Subsonic and Supersonic Aircraft," Science and Engineering of Light Metals (RASELM '91), Japan Institute of Light Metals, October 1991, pp. 273-280.

7) Staley, J.T., "Aluminum Alloys for Subsonic Aircraft," Aerospace Thermal Structures and Materials for a New Era, University of Virginia Thermal Structures Conference (2nd), Charlottesville, VA, October 19, 1994, pp. 343-358.

8) McGuire, J. and Varanasi, R., "Boeing Structural Design and Technology Improvements," Airliner, April-June 1996, pp. 12-19.

9) Bray, G.H., Bucci, R.J., Colvin, E.L. and Kulak, M., "Effect of Prior Corrosion on the S/N Fatigue Performance of Aluminum Sheet Alloys 2024-T3 and 2524-T3," Effects of the Environment on the Initiation of Crack Growth, ASTM STP 1298, W.A. Van der Sluys, R.S. Piascik, and R. Zawierucha, Eds., American Society for Testing and Materials, 1997.

10) Heinimann, M. B., "Analysis of Stiffened Panels with Multiple Site Damage," Ph.D. Thesis, School of Aeronautics and Astronautics, Purdue University, W. Lafayette, IN USA, 1997.

11) Wang, H. L., Buhler, K., and Grandt, A. F., Jr., "Evaluation of Multiple Site Damage in Lap Joint Specimens," Proc. of 1995 USAF Structural Integrity Program Conference, San Antonio, Texas, November 28-30, 1995.
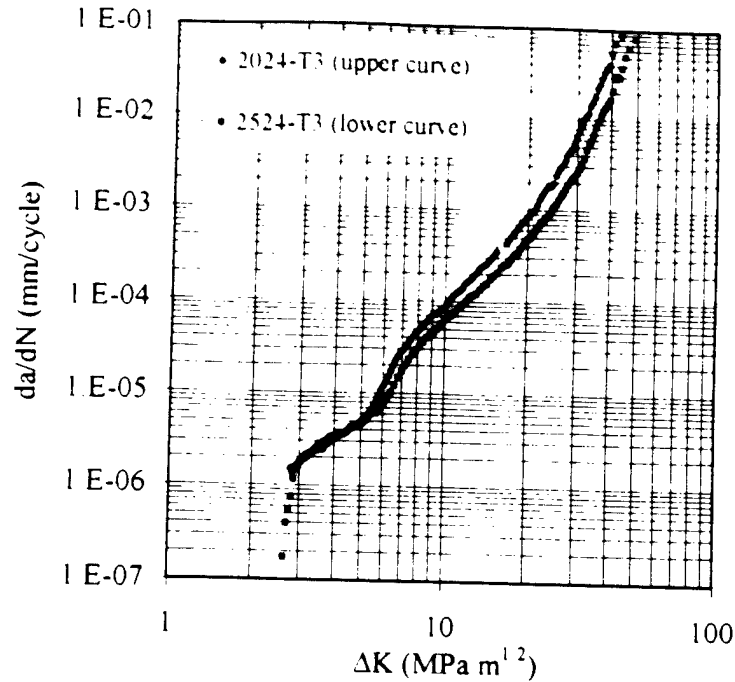
Figure 1 Fatigue crack growth rate data for 1.27 mm (0.05 inch) thick 2024-T3 and 2524-T3 test materials.

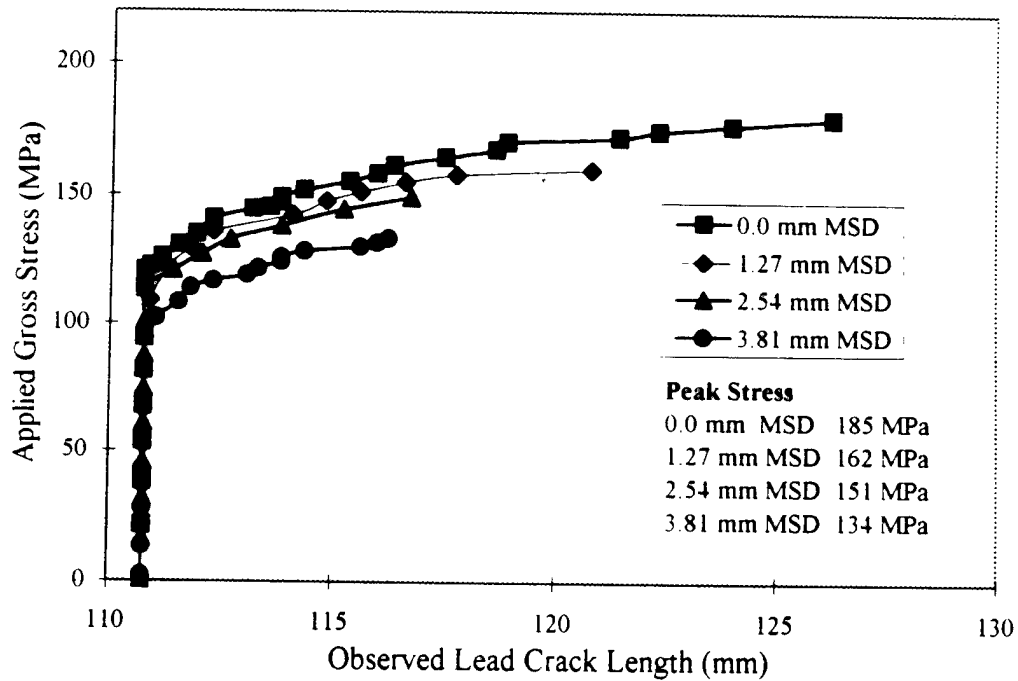Figure 2 Observed lead crack extension during residual strength tests of 2024-T3 specimens.
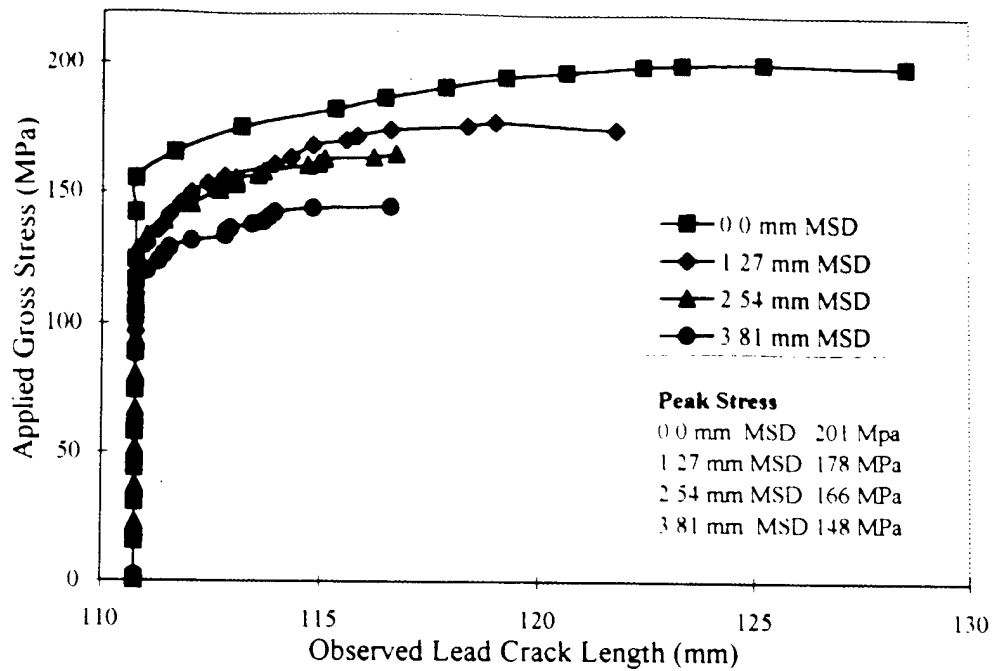
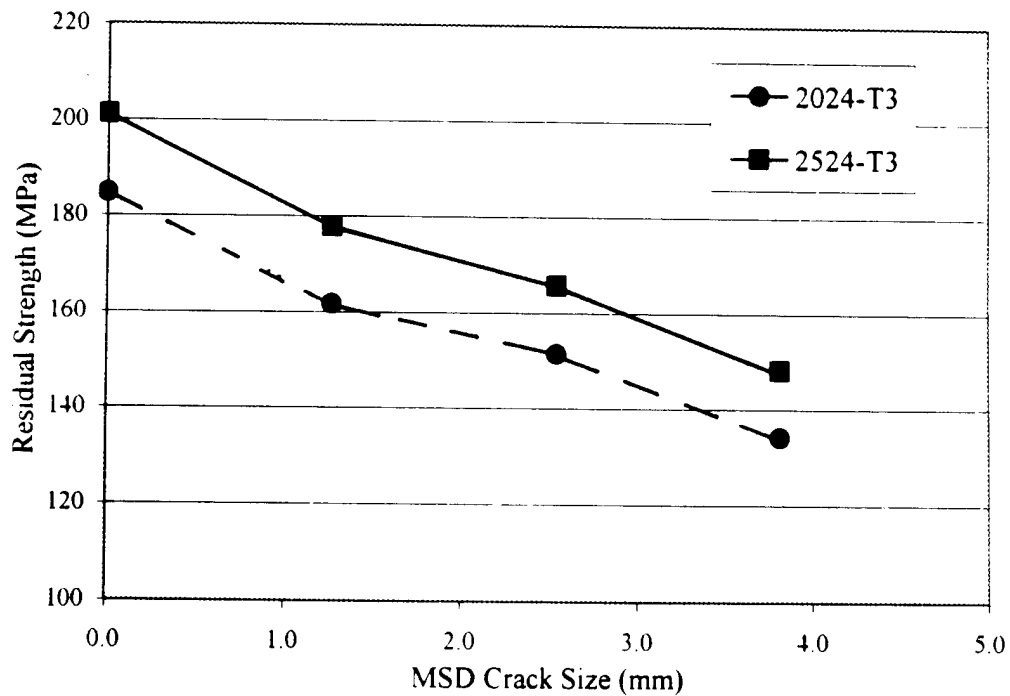Figure 3 Observed lead crack extension during residual strength tests of 2524-T3 specimens.

Figure 4 Comparison of residual strengths for 2024-T3 and 2524-T3 aluminum MSD panels.
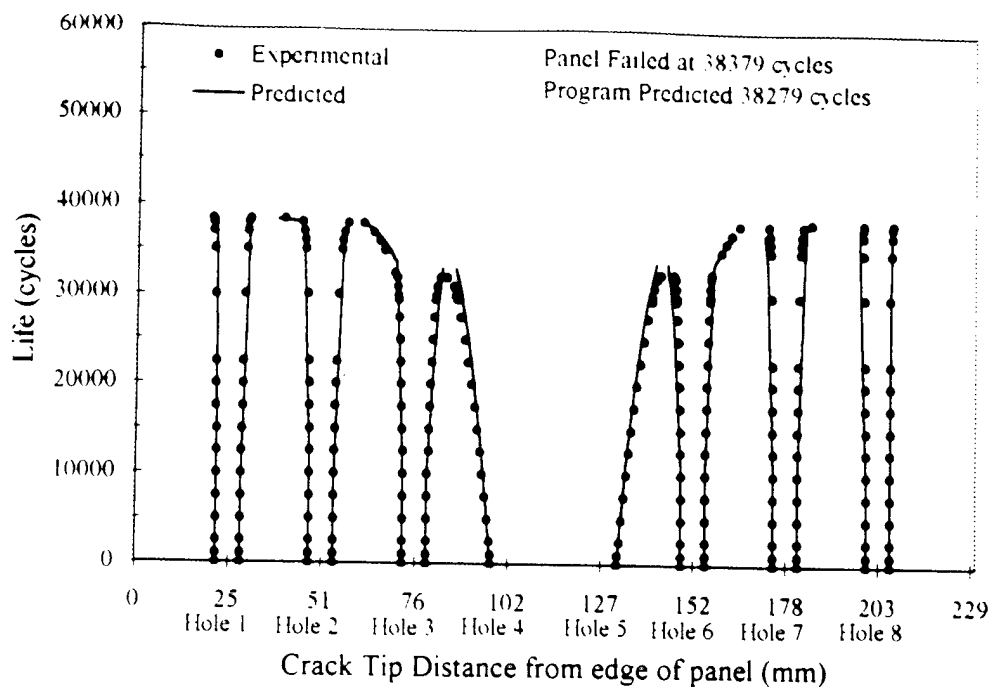
Figure 5 Fatigue crack propagation diagram for 2024-T3 specimen with 34 mm lead crack and 1.27 mm initial MSD.
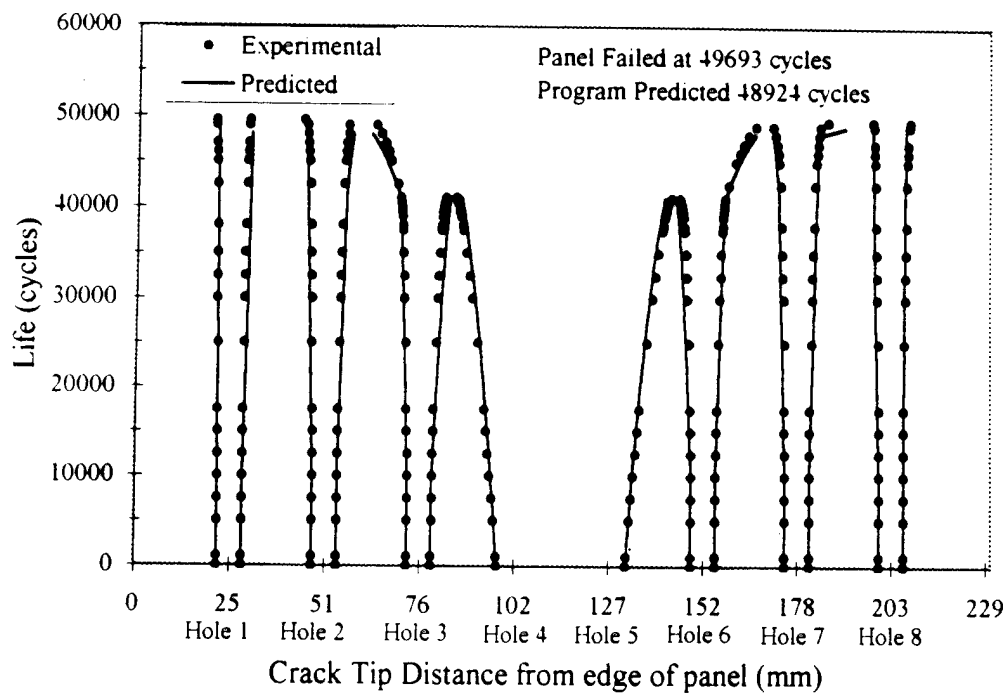
Figure 6 Fatigue crack propagation diagram for 2524-T3 specimen with 34 mm lead crack and 1.27 mm MSD.
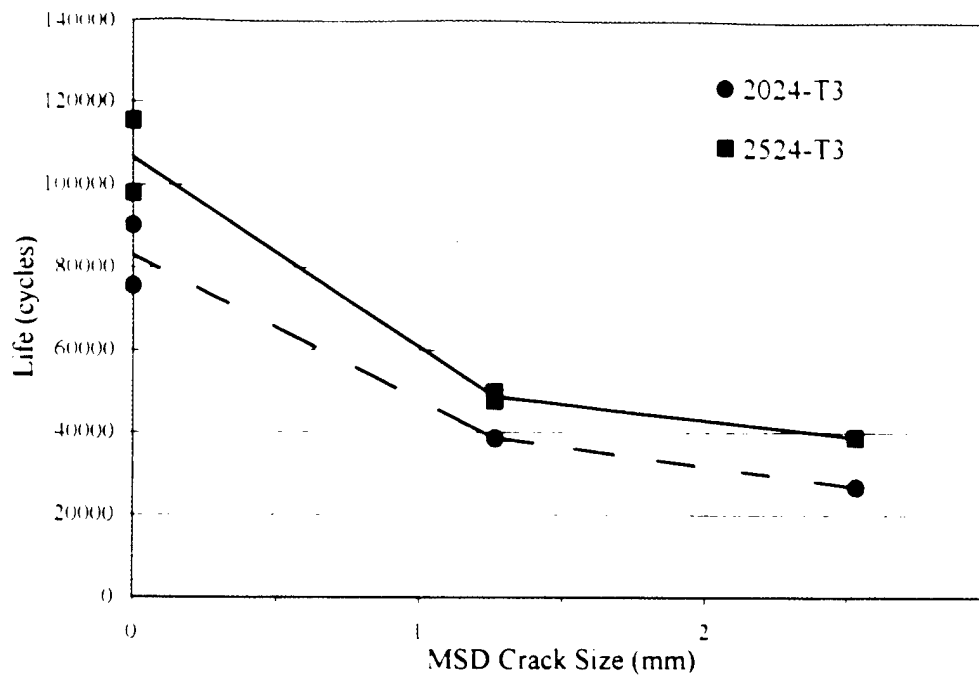
Figure 7 Comparison of fatigue lives for 2024-T3 and 2524-T3 aluminum specimens with 34 mm lead crack and various MSD crack sizes.
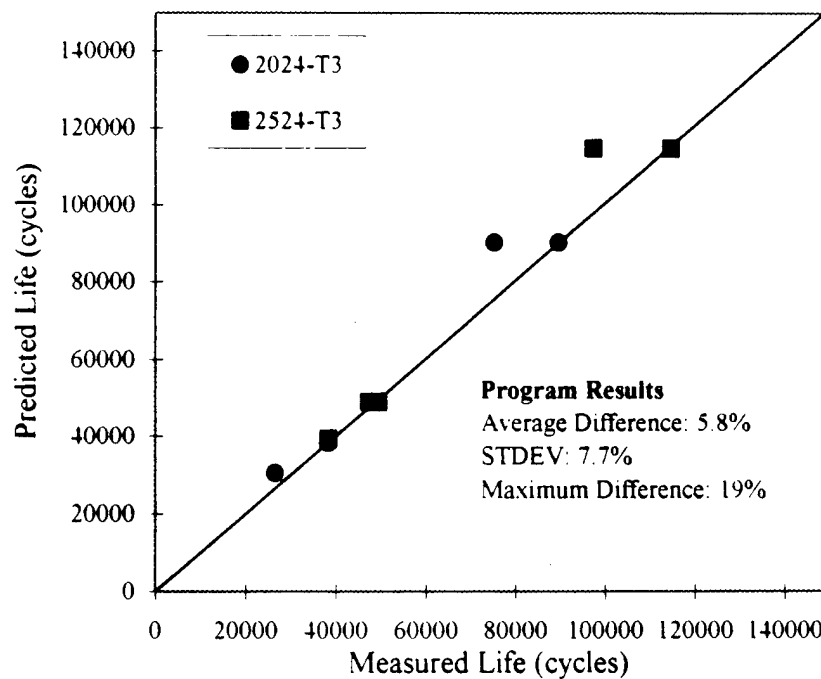
Figure 8 Comparison of measured and predicted fatigue lives for 2024-T3 and 2524-T3 specimens tested with lead and MSD cracks.

Fatigue Analysis of Stiffened Panels with Multiple Site Damage

*Dr. Markus B. Heinimann
Dr. Alten F. Grandt, Jr.
School of Aeronautics & Astronautics
1282 Grissom Hall
Purdue University
West Lafayette, IN 47907-1282

Abstract

This paper investigates the effect of multiple site damage (MSD) on stiffened panels. An analytical model based on displacement compatibility was used to analyze the link up and residual strength behavior of stiffened panels with lead and MSD cracks. Fifteen inch wide stiffened aluminum specimens with various lead and MSD crack lengths and two different stiffener configuration were tensile tested to determine crack link up and panel failure loads. A tip stress intensity reduction factor was verified experimentally through fatigue tests of stiffened panels, and used in two different link up and panel failure criteria to predict the lead crack link up and panel failure loads. The ligament yield criterion, modified for the stiffened panel, was shown to accurately predict the lead crack link up load. The apparent fracture toughness criterion consistently overpredicts link up loads for specimens with MSD. The stiffener failure criterion was shown to be able to predict panel failure to within less than 4 percent for specimens with a true lead crack. The net section failure criteria gives good results for specimens were the lead crack was arrested at a hole. The stiffened panel model was also implemented in MSD fatigue life prediction model. The stiffened panel fatigue model gave good predictions for four stiffened panel fatigue tests. A numerical study using the fatigue model was performed to study the effect of various MSD crack sizes, stiffener sizes and materials, as well as the presence of cracked stiffeners. The cracked stiffeners were modeled using an effective are approach. When lead cracks are present, knowledge the exact MSD crack length is not required. Rather, the use of a

reasonable average MSD crack lengths still results in good fatigue life predictions. When no lead cracks are present the parametric fatigue study indicates that the time to lead crack formation is the critical parameter. Once two MSD cracks have linked to form a lead crack, further link up occurs within a few cycles, until the lead crack reaches the stiffener. Increasing the stiffener size does not increase the lead crack formation life very much, but increasing the stiffness of the stiffener (i.e. going from aluminum to titanium) can increase lead crack formation life by a factor of 2 to 4. Cracks in the stiffeners have very little effect on the lead crack formation and propagation in the sheet.

Introduction

Multiple site damage (MSD) is characterized by the simultaneous presence of several cracks at various sites, such as at different holes in a structural element. MSD may become significant and critical when cracks are of sufficient size and density whereby the structure will no longer meet the present damage tolerance requirements, i.e. it may reduce the lead crack residual strength and fatigue life of a structural component below those based on a single lead crack approach without considering the interaction with the surrounding cracks [1]

Since both military and commercial aircraft, are being increasingly used beyond their designed lifetime, MSD poses a significant challenge to those who must assure the structural integrity of aircraft. Most commercial aircraft are designed and maintained according to the "damage tolerance" philosophy based on the principles of fracture mechanics [2]. This damage tolerance philosophy is based on a single lead crack in a structure. Small MSD cracks, however, can cause a structure to catastrophically fail from smaller lead cracks than those which cause failure when MSD is not present. The questions that need to be answered are: 1) what size of MSD will reduce the large damage residual strength below regulatory levels. 2) what is the crack growth life for initial flaws to reach the critical MSD size from question 1 [3].

Previous research at Purdue University and the Air Force Institute of Technology (AFIT) has examined the applicability of various simple failure criteria to predict crack link up in open hole panels with lead and MSD cracks [4, 5]. The current work aims to expand this model to include stiffeners, stringers and tear straps. Another project is examining the effects associated with lap joints.

An analytical model based on displacement compatibility between the sheet and the stiffener at the rivet locations [6, 7, 8] has been implemented here to quantify the effects of stiffeners on lead crack stress intensity factors. The model was verified by testing 15 inch wide panels with two different stiffener configurations and various lead and MSD crack geometries. The link up and ultimate failure loads were predicted using simple analytical failure criteria. The stiffened panel model was also implemented into a stiffened panel fatigue life prediction model. Four 15 inch wide stiffened panels with lead and MSD cracks were fatigue tested to validate the model. The stiffened panel fatigue model was also used in parametric studies to evaluate the

displacements in the sheet and stiffener match at the rivet locations, therefore, equations 1 and 2 can be equated, and the resulting system can be solved for the unknown rivet forces, Q_i. Figure 1 shows schematically how the presence of the stiffener is modeled using the rivet forces Q_i. The stress intensity factor for the stiffened sheet can then be obtained using superposition of the stress intensity factor for a center crack subject to applied stress σ, and the stress intensity factor for a center crack subject to the point loads Q_i.

For convenience two non-dimensional parameters are introduced to describe the crack tip stress intensity reduction and the load transfer into the stiffener [8]. The tip stress reduction factor C is defined as the ratio of the stress intensity factor of the sheet with and without stiffeners (equation 3).

$$C = \frac{K_{stiffened}}{\sigma\sqrt{\pi a}} \tag{3}$$

The stiffener load concentration factor L is defined as the ratio of the maximum stringer stress, which occurs in the crack plane, and the stress in the stringer at the end of the panel (equation 4).

$$L = \frac{\sigma_{max}}{\sigma_{\infty}}\bigg|_{stiffener} \tag{4}$$

Because of symmetry only one quarter of the panel needs to be analyzed. The number of rivet locations that are considered determines the size of the system of equations that needs to be solved. A computer code was written to determine the unknown rivet forces, tip stress reduction factor C, and load concentration factor L, given the material and geometric properties of the stiffened panel. The code was verified by comparison with the results obtained by Poe [7], using the same analytical method, and Vlieger [8], using finite elements. This comparison showed that using 20 rivet locations per quadrant results in a fully converged solution that matches both Poe [7] and Vlieger [8].

Modeling of MSD

The stiffened panel model outlined above does not include the presence of MSD cracks. Hence the presence of MSD in addition to the lead crack has to be modeled separately. A more complicated stiffened panel model proposed by Nishimura [13] allows for multiple cracks in the sheet.

The presence of multiple cracks in a sheet leads to crack interaction. The interaction between the lead and MSD cracks was modeled here using the Kamei-Yokobori interaction factor [14] as was done in the previous unstiffened panel work. [4, 5]. Figure 2 shows a schematic for the Kamei-Yokobori interaction factor as well as the equations used.

The area loss in a finite sheet due to MSD also has to be considered. It is modeled using appropriate areas in stress intensity factor compounding and load calculations for the failure criteria.

Panel Failure Criteria

Two different panel failure criteria were examined in this project to determine the ultimate, and catastrophic failure of the stiffened panels.

Stiffener Failure

The stiffener failure criteria predicts panel failure when the stress in the stiffener near the crack plane reaches the stiffener material's ultimate stress. This condition can be expressed by equation 5.

$$P_{suf} = \frac{\sigma_{ult\,st}\ \psi\ A_{st}}{L} \frac{A_{st}E_{st} + A_{net}E}{A_{st}E_{st}} \tag{5}$$

where:

$\sigma_{ult\,st}$ = stiffener ultimate stress

L = stiffener load concentration (Eq. 4)

ψ = geometry factor

A_{st} = stiffener cross sectional area

E_{st} = stiffener elastic modulus

$A_{net} = (W - 2a - nd - 2n_{MSD}a_{MSD})\,t$ = net cross sectional area of sheet (i.e. excluding areas of holes, lead and MSD cracks)

a = lead crack half length

n = number of open holes with or without MSD

d = hole diameter

n_{MSD} = number of holes with MSD

a_{MSD} = MSD crack length

t = sheet thickness

E = sheet elastic modulus

The ratio term with the cross sectional areas and elastic moduli determines how much of the total load is carried by the stiffener, assuming stiffeners and sheet have the same strain away from the crack plane.

Net Section Failure

According to the net section failure criterion, panel failure occurs when the stress in the sheet and the stiffener both reach their respective ultimate stress. The expression for the net section failure criteria is shown in equation 6.

$$P_{section} = \sigma_{ult} A_{net} + \frac{\sigma_{ult} \psi A_{st}}{L} \frac{A}{A_{lead}}$$

(6)

where:

σ_{ult} = sheet ultimate stress

A = sheet gross cross sectional area

$A_{lead} = (W - nd - 2n_{MSD} a_{MSD}) t$ = lead crack cross sectional area

W = Sheet width

n = number of open holes with or without MSD

d = hole diameter

n_{MSD} = number of holes with MSD

a_{MSD} = MSD crack length

t = sheet thickness

The ratio between the sheet cross sectional area and the lead crack area accounts for the load concentration in the stiffener due to the MSD area loss in the sheet.

Link Up Criteria

Because of the stiffener's arrest capabilities lead crack extension and link up with MSD cracks is possible without leading to panel failure. The two criteria discussed below are used to determine the loads which cause link up between lead and adjacent MSD cracks. Depending on lead crack length and panel configuration, multiple link-ups can occur before final panel failure.

K apparent

The apparent fracture toughness criterion predicts crack link up when the lead crack stress intensity factor exceeds the materials fracture toughness. The lead crack stress intensity factor is adjusted here using the Kamei-Yokobori factor to account for the presence of the MSD crack. Equation 7 gives the expression for the apparent fracture toughness criterion.

$$P_{K_{app}} = \frac{K_c A_{net}}{\sqrt{\pi a} \beta_{il} \beta_w C} \frac{A_{net} E + A_{st} E_{st}}{A_{net} E}$$

(7)

where:

K_c = apparent fracture toughness of sheet

a = lead half crack length

β_{il} = Kamei-Yokobori interaction factor for lead crack

$$\beta_{-} = \sqrt{\sec \frac{\pi a}{W}} = \text{finite width correction factor}$$

C = Tip stress intensity reduction factor

Ligament Yield

The ligament yield criterion was proposed by Swift [11] and has been used successfully for unstiffened panels [4, 5]. As shown in Fig. 3, crack link up is predicted to occur when the plastic zones ahead of the lead crack and the adjacent MSD crack "touch". Based on work by Cherry et. al. [5] the Irwin plastic zone radius combined with the material yield stress has been used to determine the plastic zone sizes in this project. Hence, the size of plastic zone is estimated to be equal to Irwin's plastic zone radius [11].

$$PZ = \frac{1}{2\pi} * \left(\frac{K}{\sigma_{ys}} \right)^2 \tag{8}$$

where:

PZ = plastic zone size in front of the crack
K = stress intensity factor at the crack tip
σ_{ys} = yield strength of the sheet material

As the remote stress level increases, the plastic zone sizes of different cracks will increase and will eventually linkup. When the plastic zones of the lead crack meet the plastic zone from the nearest neighboring MSD crack, the ligament has effectively yielded. Therefore, the lead crack effectively extends to the far end of the MSD crack. Figure 4 shows a schematic of this linkup criterion [11]. When the applied load reaches a level that causes the effective ligament between cracks to yield, the ligament will fail.

According to Swift, the predicted failure of a specimen with MSD is a function of the plastic zone size of the lead crack and its nearest neighboring MSD crack, the material's yield strength, and an interaction factor between the MSD crack, and the lead crack.

The stress intensity factor for the lead and MSD cracks are found by the method of compounding [15, 16]. The stress intensity factor for the lead crack then becomes (eq. 9)

$$K_{lead} = \left[\frac{P}{A_{net}} \right] \sqrt{\pi a_{lead}} \, C \, \beta_{ll} \, \beta_w \, \frac{A_{net}}{A_{lead}} \tag{9}$$

where:
P = applied load
C = tip stress intensity factor reduction factor

The stress intensity factor for the MSD crack is based on the Bowie solution for a cracked hole [17] and includes the appropriate area for compounding as well as the interaction factor (eq. 10).

$$K_{MSD} = \left[\frac{P}{A_{net}}\right]\sqrt{\pi a_{MSD}}\,\beta_h\beta_{MSD}\,\frac{A_{net}}{A_{MSD}} \qquad (10)$$

where:

a_{MSD} = MSD crack length (from edge of hole)

β_{MSD} = Kamei-Yokobori interaction factor for MSD crack

$A_{MSD} = A_{net} + (d + 2a_{MSD})t$ = appropriate area for MSD crack compounding

$$\beta_h = \left[\frac{F_1}{F_2 + \dfrac{a_{MSD}}{r}} + F_3\right] = \text{Bowie factor [17]} \quad (11)$$

where:

a_{MSD} = MSD crack length measured from hole edge

r = radius of the hole

F_1, F_2, F_3 = hole configuration constants

for holes with cracks emanating from both sides:	for holes with only one side cracked:
F1 = 0.6865	F1 = 0.8733
F2 = 0.2772	F2 = 0.3245
F3 = 0.9439	F3 = 0.6762

The predicted stiffened panel failure load according to the ligament yield criterion, then, becomes:

$$P_{swft} = \sigma_{ys}A_{net}\sqrt{\frac{2b}{\left(a_{MSD}\beta_h^2\beta_{MSD}^2\left(\dfrac{A_{net}}{A_{MSD}}\right)^2 + a_{lead}\beta_{l1}^2\beta_w^2 C^2\left(\dfrac{A_{net}}{A_{lead}}\right)^2\right)}\left[\frac{A_{net}E + A_{st}E_{st}}{A_{net}E}\right]} \qquad (12)$$

where: b = crack tip separation

For each crack configuration the link up and panel failure loads were calculated using the four criteria described above (Eqns. 5, 6, 7, 12). If the link up load was below the panel failure load, the lead crack was assumed to have linked up with the adjacent MSD crack and the process was repeated. Final panel failure was predicted when the panel failure load exceeded the link up load.

Stiffened Panel Fatigue Model

The purpose of the stiffened panel fatigue tests was to experimentally verify the fatigue life prediction code for stiffened panels that was developed as part of this study. The code is based

on the MSD fatigue life prediction code developed and verified for unstiffened open hole panels by Moukawsher and Neussl [9]. While the basic structure of the program has not been changed, several inconsistencies have been corrected and cleared up by Sexton [18]. Most notably the empirical 'correction' of the crack tip interaction factor employed by Moukawsher [9] has been eliminated here. (He scaled the crack tip spacing by a factor of 0.04 when using the Kamei-Yokobori interaction factor. The modified program was used to predict Moukawsher's fatigue tests [9] and resulted in predicted fatigue lives within 25 percent of the actual lives [18]. A brief description of the algorithm is given below.

The algorithm for the life prediction code is relatively simple in concept, and shown as a flow chart in Figure 4. The input consists of specimen geometry data, material data, including da/dN versus ΔK relationships, and tip stress intensity factor data in tabular form obtained from the stiffened panel model described earlier. Based on the initial configuration the stress intensity factor range (ΔK) for each crack tip is calculated, and the fatigue crack growth rate of each crack is determined using the da/dN versus ΔK relationship that was input. The number of cycles required to grow the fastest crack a specified amount (Δa) is calculated as follows (eqn 13).

$$\Delta N = \frac{\Delta a}{da / dN} \tag{13}$$

where: da/dN = crack growth rate for slowest crack.

The corresponding crack increment for all of the other cracks Δa_i, is then calculated using eqn. 14.

$$\Delta a_i = \Delta N \left(\frac{da}{dN} \right)_i \tag{14}$$

where: $\left(\dfrac{da}{dN} \right)_i$ = the crack growth rate at each separate crack tip.

This continues until one of the panel failure criteria is reached, or until that sheet had completely failed. The crack link-up criteria that are used are the apparent fracture toughness criterion, the ligament yield criteria, or the criterion that the cracks link up when the crack tip spacing goes to zero. Because the load ratio term goes to zero as the net section of the sheet decreases, it is possible to get run out predictions, where the load ratio is small enough that a lead crack that spans all the holes has a stress intensity factor below the threshold value. To avoid this numerical irregularity, a sheet net section failure criteria was added, so that the sheet is considered to have failed when the net section of the sheet is less than two percent of the gross cross-sectional area of the sheet.

Calculation of Stress Intensity Factors for Stiffened Panel Fatigue Model

As was discussed earlier the area compounding effect is noticeable in finite width test specimens, especially as the lead crack gets large. Area compounding is a way to account for the increased stress in finite width specimens due to the presence of multiple cracks and open holes. Without area compounding the predicted fatigue lives of the stiffened panel fatigue tests were factor of 8-11 too long, while with full area compounding, as shown in the ligament yield criteria

(eqns. 9, 10, 12) the predicted fatigue lives were a factor of 4-9 too short. The MSD stress intensity factor solution with a 'moderate' amount of compounding gave good agreement between the actual and predicted fatigue lives. The lead crack stress intensity factor is given by eqn. 15.

$$K_{ead} = \left[\frac{P}{A_{net}}\right]\sqrt{\pi a_{ead}}\, C\,\beta_t\, \frac{A_{net}}{A_{ead}}\left[\frac{A_{net}E}{A_{net}E + A_{st}E_{st}}\right]$$ (15)

The ratio term with the sheet net and stiffener areas and respective moduli is the familiar load ratio term. As a result of the finite width specimen, the load ratio decreases as the lead crack extends further across the specimen, and will approach zero when all the cracks have linked up (i.e. $A_{net}=0$). The stress intensity factor for the MSD crack is calculated using eqn 16.

$$K_{MSD} = \left[\frac{P}{A_{net}}\right]\sqrt{\pi a_{MSD}}\,\beta_h\,\beta_{MSD}\, C_{MSD}\, \frac{A_{net}}{A_{MSD:}}\left[\frac{A_{net}E}{A_{net}E + A_{st}E_{st}}\right]$$ (16)

Here all the parameters are as defined in the discussion of the link up criteria. The MSD stress intensity reduction factor C_{MSD} term was added here based on experimental observations. During the stiffened panel fatigue tests it was observed that MSD cracks near the stiffener grew at a slower rate than MSD cracks further from the stiffener. Therefore it was concluded that the tip stress intensity reduction effect of the stiffener that is observed, and modeled, for the lead crack, is also effecting the MSD cracks. The effect of the stiffeners on the lead crack in the form of the tip stress intensity reduction factor can be thought of as a stress distribution in the sheet. Hence an MSD crack near the stiffener would see the same stress, i.e. tip stress intensity reduction factor, as a lead crack with the same crack tip location as the MSD crack.

A common occurrence in fatigue crack growth test of panels with open holes (both stiffened and unstiffened) is the unsymmetric cracking of individual holes (i.e. the crack lengths on the left and right side of a hole are not identical). The curve fit to the Bowie solution given by eqn 11 assumes that either only a single crack exists, or that both cracks have the same length. The fatigue crack growth program developed by Neussl and Moukawsher [9] uses an approximation for unsymmetrically cracked holes. The approximation, as well as a comparison with some numerical stress intensity factors for unsymmetrically cracked holes is discussed an more detail in **Appendix A** of reference 19.

Cracked Stiffener Model

All of the previous discussion focused on the modeling of MSD in unstiffened and stiffened open hole panels, with the stiffeners uncracked. Luzar and Hug reported that during tear down and inspection of high time B707 aircraft lower wing skins, the majority of MSD cracks were found in the stiffeners [20]. This prompted the desire to include MSD cracking in the

stiffener in the modeling. Although the stiffened panel model used for this study does not include cracked stiffeners, models exist that are capable of dealing with cracked stiffeners [13, 21]. Implementing those models here was deemed beyond the scope of this project, and a simpler approach was employed for considering the effect of cracked stiffeners on the cracks in the sheet.

The approach to modeling stiffeners with MSD cracks is based on the idea of effective areas. The most likely, and also the most critical place, for a stiffener to have MSD cracks is at the rivet in the plane of the sheet cracks, because that is were the stiffener load concentration is highest. Cracks at that rivet location will change the displacement behavior of the stiffener between the rivets on either side of the cracked rivet. The displacement of the cracked stiffener section is modeled as the displacement of a finite width, center cracked sheet under remote tension which is given by ref.[22] as (see also Figure 5).

$$v_c(x,y) = \frac{\sigma}{E_{st}}\left\{ 2\sqrt{r_1 r_2} \sin\left(\frac{\phi_1 + \phi_2}{2}\right) - y - (1-\upsilon)\frac{y}{\sqrt{r_1 r_2}}\left[\frac{x \cos\left(\frac{\phi_1 + \phi_2}{2}\right) + y \sin\left(\frac{\phi_1 + \phi_2}{2}\right)}{-\sqrt{r_1 r_2}} \right] \right\}\beta_w \qquad (17)$$

where:

$v_c(x,y)$ = displacement in cracked sheet (stiffener) at location (x,y)

$r_1 = \sqrt{(x-a)^2 + y^2}$ see Figure 4.10 for definitions of parameters

$r_1 = \sqrt{(x-a)^2 + y^2}$

$\phi_1 = \tan^{-1}\left(\frac{y}{x-a}\right)$

$\phi_1 = \tan^{-1}\left(\frac{y}{x-a}\right)$

$\beta_w = \sqrt{\sec\frac{\pi a}{W}}$ = finite width correction factor

The displacement of the uncracked stiffener is modeled simply as the displacement of a strip of material under tension (eqn. 18).

$$v = \frac{\sigma}{E_{st}} y \qquad (18)$$

The effective area model assumes that under the same applied remote load, the cracked stiffener with cross sectional area A_{st}, has the same displacement as an uncracked stiffener with the effective cross sectional area A_{eff}. Only the most highly loaded rivet (the one on the crack plane) is assumed to be cracked, the location where the displacements need to match is the

adjoining rivet location. For convenience it assumed that the MSD cracks extend to the same size on either side of the cracked rivet. Matching displacements at the first rivet, and assuming symmetry about the y-axis means that the location (x,y) where the displacement for the cracked and uncracked stiffener (eqn. 17 and 18) is calculated is (0,p), were p is the rivet pitch. Making these substitutions and equating eqn 17 and 18, the effective area is given by eqn 19.

$$A_{ef} = A_{st} \frac{v(0,p)}{p}$$ (19)

where:

A_{eff} = effective cross-sectional area of cracked stiffener

A_{st} = stiffener cross-sectional area

$v(0,p)$ = eqn. 4.33 evaluated at x = 0, y = p

p = rivet pitch

Now modeling the cracked stiffener with an uncracked one with the effective area determined above, the stiffened panel and the fatigue crack growth models can be employed to predict sheet lead crack link up and sheet fatigue crack growth.

The cracked stiffener model described above makes many assumptions to be able to handle cracked stiffeners using the available analysis tools, and has not been verified through experiments. The effective area model for cracked stiffeners was however used in the parametric study reported later in this paper. Because of the limiting assumptions the cracked stiffener model was only applied to study link up stresses and fatigue crack growth in the sheet. Stiffener failure loads or stiffener crack growth require more elaborate models to predict.

Specimen Geometry and Test Procedures

To verify the stiffened panel failure criteria described above, a series of experiments using wide Aluminum panels was performed. The sheet material for all tests was Al 2024-T3 in the MRS condition, 0.063 inches thick, and all tests were performed with the specimens loaded in the L-T direction. The stiffener material was 0.09 inches thick Al 2024-T3 used in the T-L orientation. In addition to the residual strength and fatigue tests described below, a number of tests were performed to determine the material stress-strain curves and the fatigue crack growth properties. The details and results of those tests are given in ref. [19]. Table 1 summarizes the static material properties for the sheet and stiffener material, while Figure 6 gives the fatigue crack growth curve for the sheet material.

Stiffened Panel Residual Strength Specimens

The sheet was machined to the basic dimensions of the stiffened panel specimens, shown in Figure 7, using a CNC milling machine. Stiffeners were riveted to both sides of the specimen to avoid out of plane deformation during testing. Standard aircraft riveting procedures were

followed in bucking the MS20470AD-6 rivets using a pneumatic rivet gun [23]. Although most of the residual strength tests employed 1.5 inch wide stiffeners, a few residual strength tests were performed using stiffeners that were only 0.75 inches wide. These two stiffener configurations will from here on be referred to as heavy and light stiffeners respectively. The analytical tip stress intensity reduction factors and load concentration factors for both stiffener cases are shown in Figure 8. Table 2 summarizes the lead and MSD crack lengths as well as the stiffener type for the residual strength tests. All residual strength specimens had the same MSD crack lengths at each open hole. Both the lead and the MSD cracks were made using a jeweler's saw with a blade thickness of 0.012 inches. The specimens were tested using a 100 kip servo-hydraulic test machine at the Fatigue and Fracture Test Facility of the Flight Dynamics Laboratory at Wright-Patterson Air Force Base. The loading was a performed at a constant load rate of 0.25 kips per second. Although buckling guides were employed for the unstiffened R-curve tests, they were not used for the stiffened panel residual strength tests. Link up and failure loads were recorded during the tests.

Stiffened Panel Fatigue Test Specimens

The sheets and stiffeners for stiffened panel fatigue test specimens were machined the same way as for the stiffened panel residual strength tests described above. Instead of cutting the lead and MSD cracks with a jeweler's saw, only starter notches were cut at the open holes. All four fatigue test specimens were polished to facilitate optical detection of fatigue cracks and had 0.04 inch starter crack cut at all of the open holes. The panels were then precracked before the stiffeners were riveted on to get fatigue MSD cracks at all of the open holes. Precracking was performed with a maximum load of 5.5 kips and an R-ratio of 0.1 at a frequency of 5 Hz. The fatigue crack initiation and growth was monitored using 40x stereo microscope mounted on traveling bases with encoders. The goal of the precracking was to achieve 0.05 inch fatigue crack growth from each saw cut. Unfortunately fatigue crack initiation and growth in such wide panels is rarely very consistent. As a result all four fatigue specimens had unsymmetric fatigue precracking, with some hole having large cracks, and others just barely having initiated a fatigue crack. The final precrack lengths for the fatigue specimens are listed in Table 3. The ligaments between the central holes were than cut using the jeweler's saw to form lead cracks. Two of the specimens (FCM-1 and FCM-4) had short lead cracks of about 2.7 inches, while the remaining two panels (FCM-2 and FCM-3) had lead cracks of around 8.7 inches that extended under the stiffeners. The panels were then assembled by riveting the stiffeners onto the precracked sheets.

The assembled panels were than fatigue tested in a 20 kip servo hydraulic test frame using R-ratios of 0.1 at 5 Hz. Crack lengths were optically measured using 40x stereo microscopes mounted on traveling bases with encoders. The panels with the short lead cracks (FCM-1 and FCM-4) were fatigued with maximum loads of 6.5 kips and 7 kips respectively. Once the lead crack tip had grown under the stiffener the load was increased to overcome crack arrest and the panel was fatigue until the sheet failed completely. The panels with the long lead crack (FCM-2 and FCM-3) were fatigued using maximum loads of 10 kips and 9.5 kips respectively. The panels were cycled until the sheet failed completely. The lead crack lengths, applied loads and load change points of stiffened fatigue specimens are summarized in Table 4.

The results of the residual strength and fatigue tests and comparison with analytical predictions are presented in the next section.

Results

The purpose of the experimental test program was to verify the analytical model for stiffened panels with lead and MSD cracks, and to determine which of the failure and link up criteria were most suitable. The stiffened panel fatigue tests served to validate the stiffened panel fatigue crack growth model.

Reduction of Residual Strength due to MSD

The experimental residual strengths for the stiffened panel specimens are shown in Table 5. After link up all cracks arrested at the stiffener, except for MSD-13, where crack extension past the stiffener and panel failure were nearly simultaneous. Figure 9 shows the reduction in residual strength due to the presence of MSD. Note that the presence of MSD cracks that are only 0.05 inches long reduces stiffened panel residual strength by 24 percent for specimens with 4.5 and 6.0 inch lead cracks.. MSD cracks that are 0.1 inch long lead to a residual strength reduction of 32 percent, and more severe MSD cracks that are 0.15 inches long lead to a reduction in residual strength of 40 percent.

Link Up Criteria Comparison

The apparent fracture toughness and the ligament yield criterion outlined earlier were used to predict crack link up in the residual strength specimens. All specimens had one crack link up before failure, except for MSD-9, MSD-10 and MSD-13 which had two separate crack link ups. The actual and predicted first link up loads are given in Table 6. The ligament yield criterion cannot be applied to the baseline tests (MSD-1 to MSD-4) because no MSD crack were present. For specimens with MSD, cracks the ligament yield criterion predicts the first link up well, with an average difference of 3.3 percent and no difference larger than 8 percent. The apparent fracture toughness criterion works well for the baseline cases (no MSD), but consistently overpredicts the link up load for specimens with MSD. The actual and predicted link up loads for the three specimens that had a second link up are given in Table 7. Note that for the second link up the apparent fracture toughness criterion gives much better results, while the ligament yield criterion does slightly worse than for the first link up. Neither criteria does very well for the second link up on MSD-13. This was the only specimen that had crack extension past the stiffener load line. For the second link up the crack tip spacing approaches 0.5 inches. Broek et al reported that the ligament yield criterion tends to become unconservative [24] for crack tip spacings of greater than 0.5 inches. Comparison of the actual and predicted first and second link up loads are shown graphically in Figure 10.

Failure Criteria Comparison

Total panel failure was predicted whenever the predicted panel failure load was lower than the link up load. The net section failure and the stiffener failure criterion were used to predict panel failure loads. The actual and predicted panel failure loads are summarized in Table 5. The net section failure criteria is able to predict the failure load of the baseline specimens (MSD-1 to MSD-4) and the specimens with MSD and heavy stiffeners (MSD-4 to MSD-10) well with an average difference of less than 4.5 percent, but is very unconservative for the panels with the light stiffeners (MSD-11 to MSD-13). The stiffener failure criterion works well for specimens with MSD (MSD-5 to MSD-13) with an average difference of less than 3.5 percent, but underestimates the failure load of the baseline specimens. This is most likely due to the fact the after lead crack extension in the baseline specimen the lead crack end at a hole, which is a less severe situation than a lead crack of equal length, which is the case assumed by the stiffener failure criterion. Figure 11 summarizes the actual and predicted panel failure loads.

Stiffened Panel Fatigue Test Results

The stiffened panel fatigue tests are presented using crack propagation diagrams. The crack tip coordinate for each crack tip is plotted along the x-axis, with cycles in the y-axis. Predicted and actual crack tip positions are plotted on the same plot, using open symbols for the experimental data, and solid lines for the predictions. The location of the stiffener edges are shown by dotted lines. Note that for the stiffened panel fatigue tests failure is considered to have occurred when the sheet has completely failed. A single crack propagation diagram shows the growth and link up of all the cracks in a stiffened panel fatigue test specimen in one figure. The crack propagation diagrams for the stiffened panel fatigue specimens FCM-3 and FCM-4 are shown in Figure 12 and 13. A graphical comparison between experimental and predicted fatigue lives for the four stiffened panel fatigue tests is shown in Figure 14. The complete experimental stiffened panel fatigue crack growth data, including crack length versus cycle data is available in ref. [19]. Figure 14 shows that the stiffened panel fatigue model predicts the fatigue lives of the stiffened panel fatigue tests well. The average difference between actual and predicted fatigue lives is 8.1 percent, with no difference larger than 11 percent.

Parametric Stiffened Panel Fatigue Studies

The good agreement between the fatigue crack growth model and the fatigue tests validate the model for additional study. One of the areas of interest was the effect of MSD crack size on stiffened panel fatigue lives with lead and MSD cracks. In actual aircraft, it is impossible to know the size of every MSD crack. An average based on either inspection or damage tolerant design data is usually assumed. The effect of using average MSD crack lengths rather than actual crack lengths was examined by predicting the fatigue lives of the four stiffened panel specimens with various MSD crack lengths rather than the actual MSD crack lengths that are given in Table 3. The MSD cracks lengths used for the study were the average length for each test specimen, as well as the commonly used MSD crack sizes of 0.1 inches and 0.05 inches. The results are presented in graphical form in Figure 15 as the ratio of the predicted to the experimental lives for each specimen. Figure 15 shows that using the average, or 0.1 inches MSD crack size at each

hole has very little effect on predicted fatigue lives. Using the smaller (0.05 inches) MSD crack size makes the predictions unconservative, since the actual MSD crack size average for the specimens were between 0.084 and 0.143 inches. These results however indicate that it is not necessary to know all the MSD crack lengths for fatigue life predictions for panels with lead cracks. Using a reasonable average MSD crack size will still give good fatigue life predictions for stiffened panels with lead cracks. This conclusion should only be valid for the specimens tested for this project, but also for other stiffened panel cases where large lead and MSD cracks are present. The amount of MSD (number of holes with MSD and MSD length) for the specimens tested here was quite severe, cases with less sever MSD should show even more lead crack dominance.

One of the concerns with MSD is that it reduces the residual strength, the other major concern is that MSD cracks will link up to form large lead cracks in an aircraft structure. The fatigue model was used in a parametric study to determine the effects of parameters such as MSD crack length, stiffener size, stiffener materials, and MSD cracks in stiffeners on the lead crack formation lives of stiffened panels with only MSD. Area compounding is an issue in finite width specimens [19] such as the ones tested in this study. To reduce the effect of area compounding on the parametric study a 75 inch wide panel was considered. The center 15 inch section is identical to the stiffened panel specimen shown in Figure 7, with open holes, and MSD cracks. The 30 inch sections on either side of the center section have no open holes and no MSD or lead cracks. The stiffener spacing of the center section (7.5 inches) is continued across the whole panel. The parametric fatigue study looked at how MSD cracks would grow and link up to form lead cracks. The starting point for the fatigue study assumed MSD cracks at all of the open holes in the 15 inch center section. The loading for the fatigue crack growth predictions was 15 ksi gross section stress and an R-ratio of 0.1. The stiffened panel fatigue crack growth model was used to predict the growth and link up of the MSD cracks until a lead crack length (2a) of 9 inches was reached. The 9 inch lead crack length represents a lead crack that has grown past the stiffener load line, and has thus violated the crack arrest requirement.

Figure 16 shows the lead crack length versus cycle plot for a specimen with aluminum (2024-T3) stiffeners with a cross-sectional area of 0.27 in^2, and MSD cracks of 0.05 inches, 0.10 inches and 0.15 inches at all of the holes in the 15 inch center section. Figure 16 shows that for the vast majority of the fatigue life to reach a half lead crack length of 4.5 inches, no lead crack is present. When the two center holes link up to form a short lead crack, further link ups all the way to the stiffener occur within a few cycles. The MSD crack size has a very strong influence on the life to lead crack formation. The long (0.15 inches) MSD crack size forms a lead crack at 37 percent of the lead crack formation life for the 0.05 inch MSD cracks. Figure 16 also indicates that the shorter MSD crack cases have lead crack slowdown at the stiffener, e.g. the 0.05 inch MSD crack size takes almost 2,000 cycles to grow out from under the stiffener, while the same process only takes 100 cycles for the case with 0.15 inch long MSD.

Figure 17 shows the lead crack length versus cycle plot for specimens with different stiffener sizes and materials, and uniform 0.05 inch MSD cracks in the sheet. The stiffener materials considered: 1) 2024-T3 aluminum alloy, with the same material properties as the stiffened panel specimens tested in this study, and 2) Titanium 6Al-4V with a Young's modulus of

of 16.5 Mpsi. Figure 17 shows that the difference in lead crack formation life and life to 9 inch lead crack length for the three specimens with aluminum stiffeners are fairly close. The lead crack formation life for panels with aluminum stiffeners ranges from 6,900 cycles for the lightest aluminum stiffener to 8,700 for the heaviest aluminum stiffener. The titanium stiffener panels have significantly longer lead crack formation and 9 inch lead crack lives. A titanium stiffener with a cross section of 0.27 in² has a lead crack formation life that is twice as long as for the same size aluminum stiffener. For the titanium stiffener with a 0.54 in² cross section the lead crack formation life is 23,000 cycles, compared to 8,700 for the same size aluminum stiffener. The large difference between the titanium and aluminum stiffeners in fatigue lies in the difference in stiffness. The load ratio term (eqns 15, 16) is based on matched strains between the sheet and the stiffener away from the crack plane. Because titanium is much stiffer (Young's modulus of 16.5 Mpsi versus 10.5 Mpsi for 2024-T3) the titanium stiffeners take a much large fraction of the total load compared to the aluminum stiffeners. Thus the cracked sheet in the titanium stiffener cases experiences a lower stress than the sheet with aluminum stiffeners.

For the cracked stiffener parametric fatigue study, it is important to realize that the cracked stiffener model only models the effects of a cracked stiffener on the sheet. The fatigue crack growth of the MSD cracks in the stiffener are not modeled in this study. Figure 18 shows the lead crack length versus cycle plot for specimens with 0.27 in² aluminum stiffeners and 0.05 inch MSD cracks in the sheet, for four different stiffener MSD Crack lengths (0.0, 0.05, 0.15, 0.3 inches) as well was for a completely failed stiffener. Figure 18 shows that the lead crack formation and 9 inch lead crack lives are not significantly affected by the MSD crack length in the stiffener. The cracked stiffener model results in slightly shorter fatigue lives as the stiffener cracks get larger, but the difference is less than 200 cycles between lead crack formation for the uncracked stiffener and the stiffener with 0.3 inch cracks. During cyclic loading the cracks in the stiffener will certainly grow, just like the cracks in the sheet, but the cracked stiffener model used for this study cannot be used to predict the crack growth of the cracks in the stiffeners. However, if the cracks in the stiffener lead to complete stiffener failure, the lead crack formation life is significantly reduced, and the arrest capability is lost (see Fig. 18).

Conclusions

The authors believe that this project makes two major contributions to the aging aircraft structural integrity research community.

First, the use of a relatively simple stiffened panel model, combined with simple link up and failure criteria and linear elastic fracture mechanics results in a model that predicts the link up, failure and fatigue crack growth in stiffened panels. The accuracy obtained with this simple analytical model is comparable to that obtained with more complicated numerical models 20, 25, 26, 27]. Simple analytical models are ideally suited for structural design applications, trade studies or extensive statistical simulations.

The second contribution is the additional experimental residual strength and fatigue data for stiffened panels that was generated during this project [19]. These data will hopefully be useful to other researcher who want to verify their models and predictions.

The more detailed conclusions that can be drawn from the work presented in this paper are:

1. The presence of MSD cracks significantly decreases the residual strength of both unstiffened and stiffened panels. The reduction in residual strength varies between 23 and 40 percent depending on the lead and MSD crack geometries in the specimens examined.

2. A relatively simple analytical displacement compatibility model for the effects of stiffeners on a cracked panel can be used in the prediction of link up and failure loads in stiffened panel specimens with lead and MSD cracks. The same stiffener model also was successfully implemented in a stiffened panel fatigue crack growth model.

3. The lead crack link up loads in 15 inch wide stiffened panel specimens were predicted to within 3.5 percent by the ligament yield criterion with full area compounding, and to within 5.5 percent by the alternate ligament yield criterion with modified area compounding. The apparent fracture toughness criterion works well for the cases where no MSD is present, but overpredicts the link up loads for specimens with MSD by an average of 27 percent.

4. The stiffened panel model was used in a fatigue crack growth model for stiffened panel specimens with lead and MSD cracks. The stiffened panel fatigue crack growth model predicts the fatigue lives of four stiffened panel specimens with a difference of less than 11 percent for all specimens.

5. The residual strength and fatigue tests of the stiffened panel specimen indicate that area compounding effects are present in finite width test specimens. The effect of area compounding is especially severe in specimens with a large amount of damage, such as lead and MSD cracks, and open holes. Using wider specimens, and limiting the number of open holes and MSD cracks will reduce the area compounding effects.

6. A numerical study of the effect of MSD crack length on the fatigue life of stiffened panels with lead and MSD cracks showed that using reasonable MSD crack lengths in place of actual MSD crack lengths still results in good fatigue life predictions.

7. A simple model for the effects of MSD cracks in the stiffener on the crack link up and fatigue behavior in the sheet was developed. The cracked stiffener model was used in a parametric study of stiffened panel lead crack formation and growth lives. The cracked stiffener model cannot be used to predict stiffener failure loads, or stiffener fatigue crack growth.

8. The parametric fatigue study on 75 inch wide stiffened panels indicates that once two MSD cracks link up to form a lead crack further link ups occur within a few cycles until the lead crack reaches the stiffener line. The MSD crack size is the dominating factor in the lead

crack formation life, with MSD cracks of 0.15 inches having a lead crack formation life that is only 37 percent of the lead crack formation life of 0.05 inch MSD cracks. The parametric fatigue study also showed that the choice of stiffener material is more important than stiffener size. Stiffened panels with different size aluminum stiffeners had similar lead crack formation lives, while titanium stiffeners had lead crack formation lives that were factors of 2 to 4 longer. The cracked stiffener model was also used to study the effects of cracked stiffeners on the crack growth in the sheet. The cracks in the stiffener only have a very small effect on the lead crack formation and propagation in stiffened panels, until the stiffener fails. If the stiffener fails completely the lead crack formation life is significantly reduced and the crack arrest capability is lost.

Acknowledgments

References

1   Mar, J. W., "Preserving Aging Aircraft," Aerospace America, Jan. 1996, pp. 38-43.

2   Mar, J. W., "Structural Integrity of Aging Airplanes: A Perspective," Structural Integrity of Aging Airplanes, S. N. Alturi, S. G. Sampath, P. Tong, Editors, Springer-Verlag, Berlin, Heidelberg, 1991.

3   Swift, T., "Damage Tolerance in Pressurized Fuselages," 11th Plantema Memorial Lecture, Presented at 14th Symposium of the International Committee on Aeronautical Fatigue, Ottawa, Canada, June 1987.

4   Moukawsher, E.J., Heinimann, M.B., Grandt, A.F., Jr., "Residual Strength of Panels with Multiple Site Damage," Journal of Aircraft, Vol. 33, No. 5, 1996.

5   Cherry, M.C., Mall, S., Heinimann, M.B., Grandt, A.F., Jr., "Residual Strength of Unstiffened Aluminum Panels with Multiple Site Damage," Engineering Fracture Mechanics, (in press).

6   Romualdi, J.P., Frasier, J.T., Vin, G.P., "Crack-Extension-Force Near a Riveted Stiffener," NRL Report 4956, Naval Research Laboratory, Washington, D.C., 1957.

7   Poe, C.C., Jr., "Stress-Intensity Factor for a Cracked Sheet with Riveted and Uniformly Spaced Stringers", NASA TR R-358, 1971.

8   Vlieger, H., "The Residual Strength Characteristics of Stiffened Panels Containing Fatigue Cracks," *Engineering Fracture Mechanics*, Vol. 5, pp. 447-477, 1973.

9   Moukawsher, E.J. and Grandt, A.F., Jr., Neussl, M.A., "Fatigue Life of Panels with Multiple Site Damage," AIAA Journal of Aircraft, Vol. 33, No. 5, pp.1003-1013, 1996.

10   Heinimann, M.B., and Grandt, A.F., Jr. "Analysis of Stiffened Panels with Multiple Site Damage," presented at USAF Aircraft Structural Integrity Conference, San Antonio, TX, December 1996.

11   Swift, T., "Widespread Fatigue Damage Monitoring Issues and Concerns," presented at the 5th *International Conference on Structural Airworthiness of New and Aging Aircraft*, Hamburg, Germany, June 16-18, 1993.

12   Je   , D.Y., and Brewer, J.C., "On the Linkup of Multiple Cracks," Engineering Fracture M   anics, Vol. 51, No. 2, 1995, pp. 233-238.

13   Nishimura, T., "Stress Intensity Factors of Multiple Cracked Sheet With Riveted Stiffeners," *Journal of Engineering Materials and Technology*, Vol. 113, pp. 280-284, 1991.

14   Kamei, A., and Yokobori, T., "Two Collinear Asymmetrical Elastic Cracks," Report of the Research Institute for Strength and Fracture of Materials, Tohoku University, Vol. 10, Section 1-4, pp. 41-42, December 1974.

15   *ASM Handbook*, Vol. 19, Fatigue and Fracture, pp. 982-983, Materials Park, OH, December 1996.

16   Partl, O. and Schijve, J., "Multiple Site Damage in 2024-T3 Alloy Sheet," Delft University of Technology, LR-660, January, 1992.

17   Grandt, A.F., Jr., "Stress Intensity Factors for Some Thru-Cracked Fastener Holes," International Journal of Fracture, Vol. 5, No. 2, pp.283-294, April 1975.

18   Personal communication with D.G. Sexton, Graduate Student, School of Aeronautics & Astronautics, Purdue University, West Lafayette, IN, 1997.

19   Heinimann. M. B. "Analysis of Stiffened Panels with Multiple Site Damage". Ph D Thesis. School of Aeronautics & Astronautics. Purdue University. May 1997.

20   Luzar. J. and Hug. A.. "Lower Wing Disassembly and Inspection Results of Two High Time USAF B707 Aircraft." presented at USAF Aircraft Structural Integrity Program Conference. San Antonio. TX. December 3-5. 1996.

21   Atluri. S.N.. and Tong. P. "Computational Schemes for Integrity Analyses of Fuselage Panels in Aging Airplanes." *Structural Integrity of Aging Airplanes.* S. N. Alturi. S. G. Sampath. P. Tong. Editors. Springer-Verlag. Berlin. Heidelberg. 1991.

22   Westergaard. H.M.. "Bearing Pressures and Cracks." Journal of Applied Mechanics. Vol. 6. No. 2. June 1939.

23   *Standard Aviation Maintenance Handbook.* EA-282-0. IAP. Inc.

24   Broek. D.. Yeong. D.Y.. Thomson. D.. "Testing of Flat and Curved Panels with Multiple Cracks." presented at FAA-NASA Symposium on Advanced Structural Integrity Methods for Airframe Durability and Damage Tolerance. Hampton. VA. May 4-6. 1994.

25   Harris. C.E.. Starnes. J.H.. Jr.. Newman. J.C.. Jr.. "Developments of Advanced Structural Analysis Methodologies for Predicting Widespread Fatigue Damage in Aircraft Structures." NASA TM 110187. August 1995.

26   Newman. J.C.. Jr.. Dawicke. D.S. Sutton. M.A.. Bigelow, C.A.. "A Fracture Criterion for Widespread Cracking in Thin-Sheet Aluminum Alloys," Proceedings of the ICAF Conference. Vol. 1. pp. 443-467. 1993.

27   Newman. J.C.. Jr.. "FASTRAN II -A Fatigue Crack Growth Structural Analysis Program." NASA TM 104159. February 1992.

Table 1: Material properties for 2024-T3 0.09 inches thick (stiffener) and 2024-T3 MRS 0.063 thick (sheet) materials

Material	Young's Modulus [Mpsi]	Yield Stress [ksi]	Ultimate Stress [ksi]
2024-T3, 0.09" T-L Stiffener	10.2	44.0	63.0
2024-T3 MRS 0.063" L-T Sheet	10.5	51.5	67.0

Table 2: Summary of lead and MSD crack lengths and stiffener type for residual strength specimens

Specimen ID	Lead Crack Length (2a) [in]	MSD Crack Length [in]	Stiffener Type
MSD-1	5.982	-	heavy
MSD-2	5.975	-	heavy
MSD-3	4.525	-	heavy
MSD-4	4.520	-	heavy
MSD-5	5.992	0.051	heavy
MSD-6	6.003	0.149	heavy
MSD-7	5.982	0.103	heavy
MSD-8	5.976	0.058	heavy
MSD-9	4.471	0.054	heavy
MSD-10	4.48	0.098	heavy
MSD-11	6.025	0.053	light
MSD-12	6.026	0.048	light
MSD-13	5.975	0.097	light

Table 3: Fatigue precrack lengths measured from hole edge of stiffened panel fatigue test specimens.

Hole Nr.	Crack Tip	FCM-1	FCM-2	FCM-3	FCM-4
1	a_L	0.224	0.071	0.099	0.179
1	a_R	0.191	0.081	0.098	0.145
2	a_L	0.168	0.105	0.084	0.179
2	a_R	0.234	0.063	0.050	0.186
3	a_L	0.161	0.104	0.071	0.117
3	a_R	0.170	0.101	0.065	0.095
4	a_L	0.152	0.081	0.059	0.136
4	a_R	0.180	0.054	0.057	0.095
5	a_L	0.202	0.107	0.086	0.161
5	a_R	0.170	0.090	0.078	0.120
6	a_L	0.184	0.121	0.091	0.150
6	a_R	0.215	0.151	0.124	0.144
7	a_L	0.153	0.147	0.133	0.136
7	a_R	0.160	0.141	0.114	0.152
8	a_L	0.193	0.127	0.096	0.158
8	a_R	0.185	0.151	0.128	0.183
9	a_L	0.176	0.190	0.163	0.146
9	a_R	0.163	0.178	0.152	0.173
10	a_L	0.129	0.126	0.145	0.162
10	a_R	0.124	0.134	0.136	0.156
11	a_L	0.111	0.089	0.118	0.132
11	a_R	0.119	0.137	0.124	0.149
12	a_L	0.089	0.157	0.130	0.153
12	a_R	0.073	0.211	0.164	0.145
13	a_L	0.085	0.221	0.138	0.138
13	a_R	0.090	0.196	0.125	0.118
14	a_L	0.093	0.160	0.095	0.111
14	a_R	0.072	0.154	0.090	0.109
15	a_L	0.128	0.189	0.136	0.099
15	a_R	0.102	0.158	0.126	0.059
16	a_L	0.084	0.118	0.079	0.071
16	a_R	0.093	0.163	0.140	0.048
17	a_L	0.114	0.130	0.089	0.039
17	a_R	0.104	0.132	0.104	0.075
18	a_L	0.130	0.141	0.111	0.074
18	a_R	0.093	0.135	0.105	0.069
19	a_L	0.106	0.123	0.062	0.056
19	a_R	0.105	0.145	0.103	0.051
20	a_L	0.120	0.127	0.101	0.057
20	a_R	0.106	0.108	0.082	0.087

Table 4: Lead crack lengths, applied and load changes for stiffened panel fatigue test specimens.

	FCM-1	FCM-2	FCM-3	FCM-4
Lead Crack Length (2a)	2.690 in	8.712 in	8.668 in	2.768 in
Applied Load	6.5 kips	10.0 kips	9.5 kips	7.0 kips
Load Changed at	163,000 cycles	NA	NA	90,000 cycles
New Applied Load	11.0 kips	NA	NA	12.0 kips

Table 5: Summary of experimental residual strength of stiffened panels

Specimen ID	Lead Crack Length (2a) [in]	MSD Crack Length [in]	Actual Failure Load [kips]
MSD-1	5.982	-	47.25
MSD-2	5.975	-	49.97
MSD-3	4.525	-	51.36
MSD-4	4.520	-	52.02
MSD-5	5.992	0.051	38.16
MSD-6	6.003	0.149	30.90
MSD-7	5.982	0.103	34.11
MSD-8	5.976	0.058	37.81
MSD-9	4.471	0.054	37.09
MSD-10	4.48	0.098	34.04
MSD-11	6.025	0.053	23.53
MSD-12	6.026	0.048	24.35
MSD-13	5.975	0.097	20.29

Table 6: Actual and predicted first link up loads for stiffened specimens

Specimen ID	Measured First Link Up Load [kips]	App. Fracture Toughness Criterion [kips]	Ligament Yield Criterion [kips]
MSD-1	35.80	36.76	NA
MSD-2	35.60	36.76	NA
MSD-3	34.30	35.76	NA
MSD-4	34.90	35.76	NA
MSD-5	26.80	34.57	27.82
MSD-6	13.60	25.85	14.87
MSD-7	20.50	30.19	21.08
JMSD-8	26.40	34.10	26.81
MSD-9	27.10	31.36	27.92
MSD-10	21.20	27.75	21.23
MSD-11	17.60	22.67	18.65
MSD-12	18.10	22.84	19.27
MSD-13	14.20	19.55	13.82

Table 7: Actual and predicted loads for second link up for stiffened panel specimens.

Specimen ID	Measured Second Link Up Load [kips]	App. Fracture Toughness Criterion [kips]	Ligament Yield Criterion [kips]
MSD-9	34.80	33.57	37.52
MSD-10	29.50	28.71	30.92
MSD-13	19.80	21.78	22.45

Table 8: Actual and predicted panel failure loads for stiffened panel specimens.

Specimen ID	Actual Panel Failure Load [kips]	Net Section Failure [kips]	% Difference	Suffener Failure [kips]	% Difference
MSD-1	47.25	48.40	2.434	42.66	-9.714
MSD-2	49.97	48.42	-3.102	42.68	-14.589
MSD-3	51.36	54.24	5.607	49.40	-3.816
MSD-4	52.02	54.29	4.364	49.44	-4.960
MSD-5	38.16	40.68	6.604	37.10	-2.778
MSD-6	30.90	28.02	-9.320	30.79	-0.356
MSD-7	34.11	34.20	0.264	33.84	-0.792
]MSD-8	37.81	39.84	5.369	36.71	-2.909
MSD-9	37.09	39.92	7.630	36.77	-0.863
MSD-10	34.04	34.02	-0.059	33.84	-0.588
MSD-11	23.53	29.75	26.434	21.83	-7.225
MSD-12	24.35	30.79	26.448	22.30	-8.419
MSD-13	20.29	25.75	26.910	21.62	6.555

Figure 1: Schematic of stiffened panel model showing the modeling of the effects of the stiffeners using the rivet forces Q_i.

Remote Stress
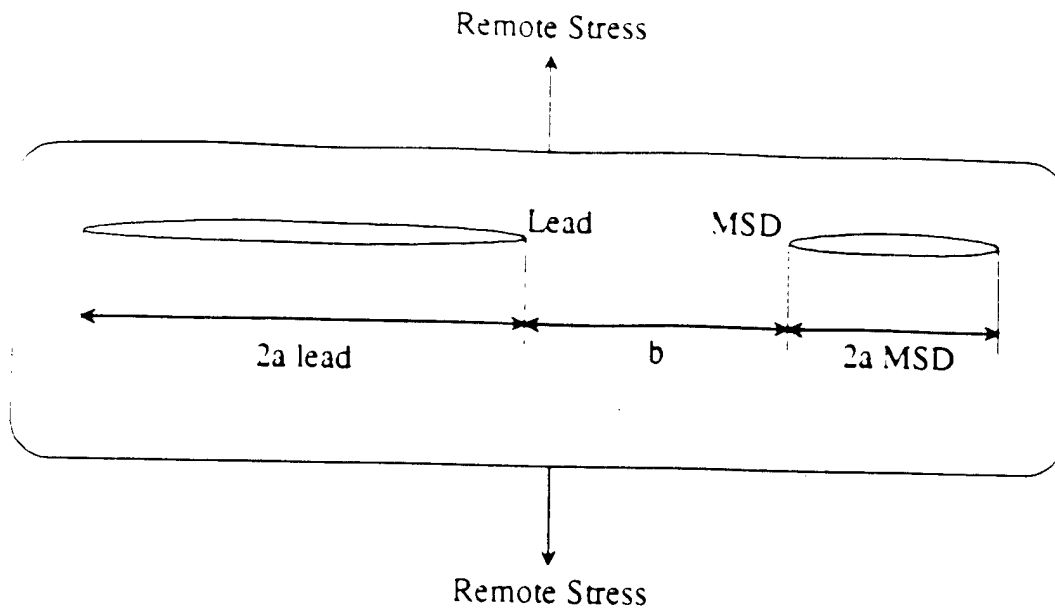
$$\beta_{l} = \sqrt{1 + \frac{2b}{t}\left[1 - \left(1 + \frac{t}{2a}\right)\frac{K(k) - E(k)}{K(k)}\right]}$$

$$\beta_{l\,MSD} = \sqrt{1 + \frac{2a}{t}\left[1 - \left(1 + \frac{t}{2b}\right)\frac{K(k) - E(k)}{K(k)}\right]}$$

where: $K(k)$ = complete elliptic integral of the first kind
            $E(k)$ = complete elliptic integral of the second kind

$$k = 2\sqrt{\frac{ab}{(2a + t)(2b + t)}}$$

Figure 2: Definition of Kamei-Yokobori interaction factor for two planar crack of unequal length in an infinite plate [15].

Figure 3: Schematic of the lead and MSD cracks and plastic zones for the ligament yield method [9].

```
┌─────────────────────┐          ┌──────────────────────────┐
│   Read Input Data   │          │ Print Final Results and Stop │
└─────────────────────┘          └──────────────────────────┘

┌─────────────────────┐     Yes
│ Check Failure Criteria │──────────────┐
└─────────────────────┘

           No

┌─────────────────────────┐   Yes
│ Intermediate Output Interval │──────────┐
└─────────────────────────┘              │
                                  ┌──────────────────────────┐
           No                     │ Print Intermediate Results │
┌─────────────────────────┐       └──────────────────────────┘
│ Compute SIF for Each Crack │
│          Tip             │
└─────────────────────────┘

┌─────────────────────┐
│  Update Crack Data  │
└─────────────────────┘

┌─────────────────────────┐
│ Compute da/dN for each Crack │
│          Tip             │
└─────────────────────────┘

┌─────────────────────────┐
│ Compute Cycle Increment for │
│    specified step size   │
└─────────────────────────┘

┌─────────────────────────┐
│ Grow Each Crack by Cycle │
│        Increment         │
└─────────────────────────┘

┌─────────────────────────┐
│  Check for Crack Link Ups │
└─────────────────────────┘
```
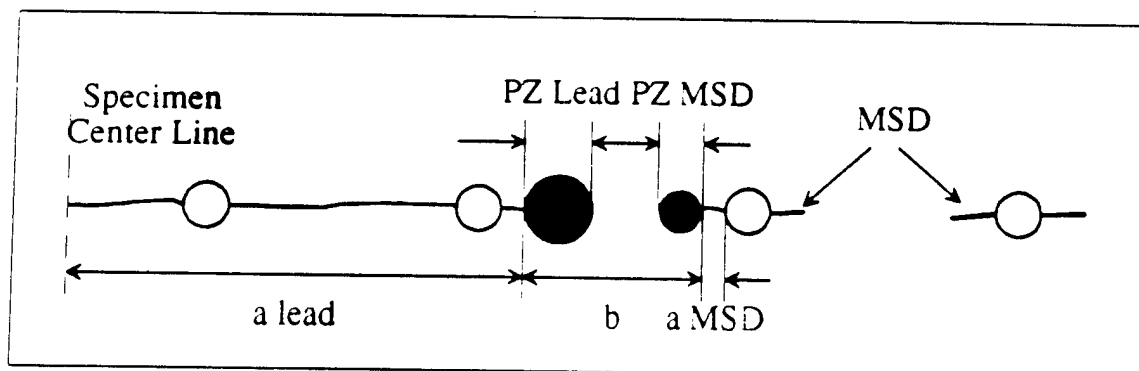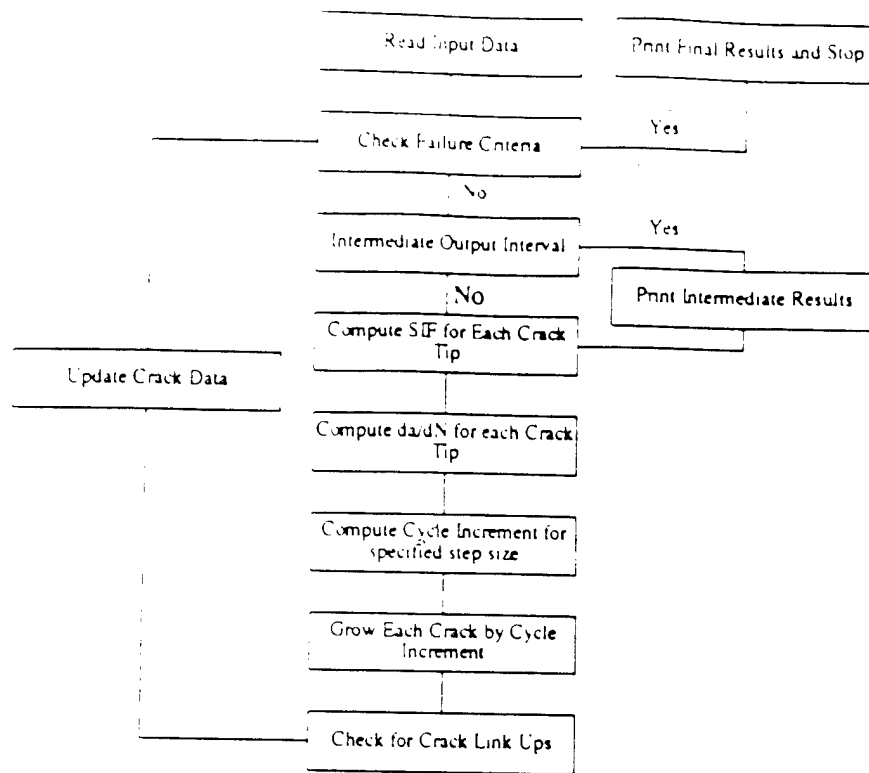
Figure4: Flow chart of stiffened panel fatigue life prediction algorithm

Lead Crack in
Sheet

Rivet Pitch, p

Cracked Stiffener
Modelled as:

Stiffener
MSD Cracks

Open Holes with
MSD in Sheet

Rivets
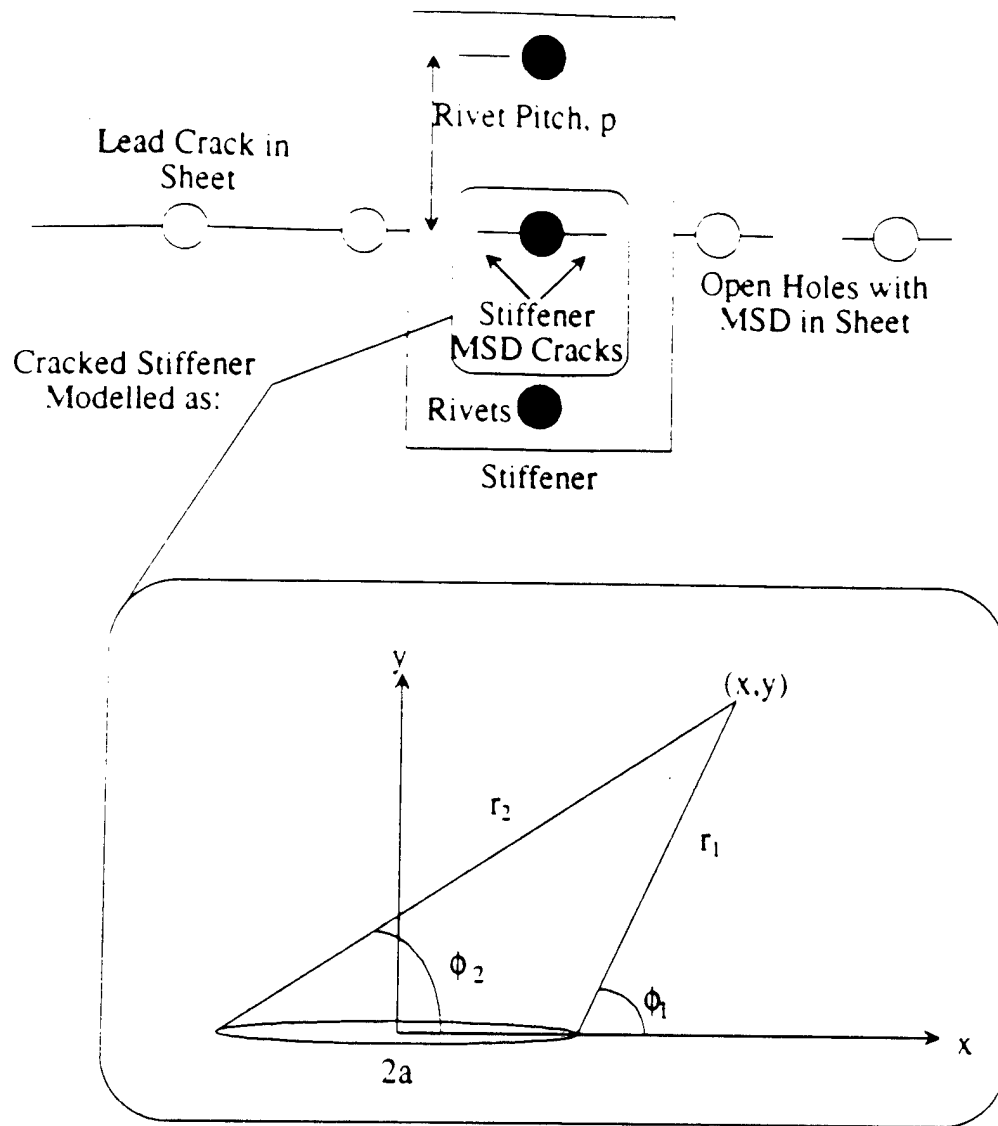
Stiffener

Figure 5: Definition of parameters for displacement calculation in cracked stiffener
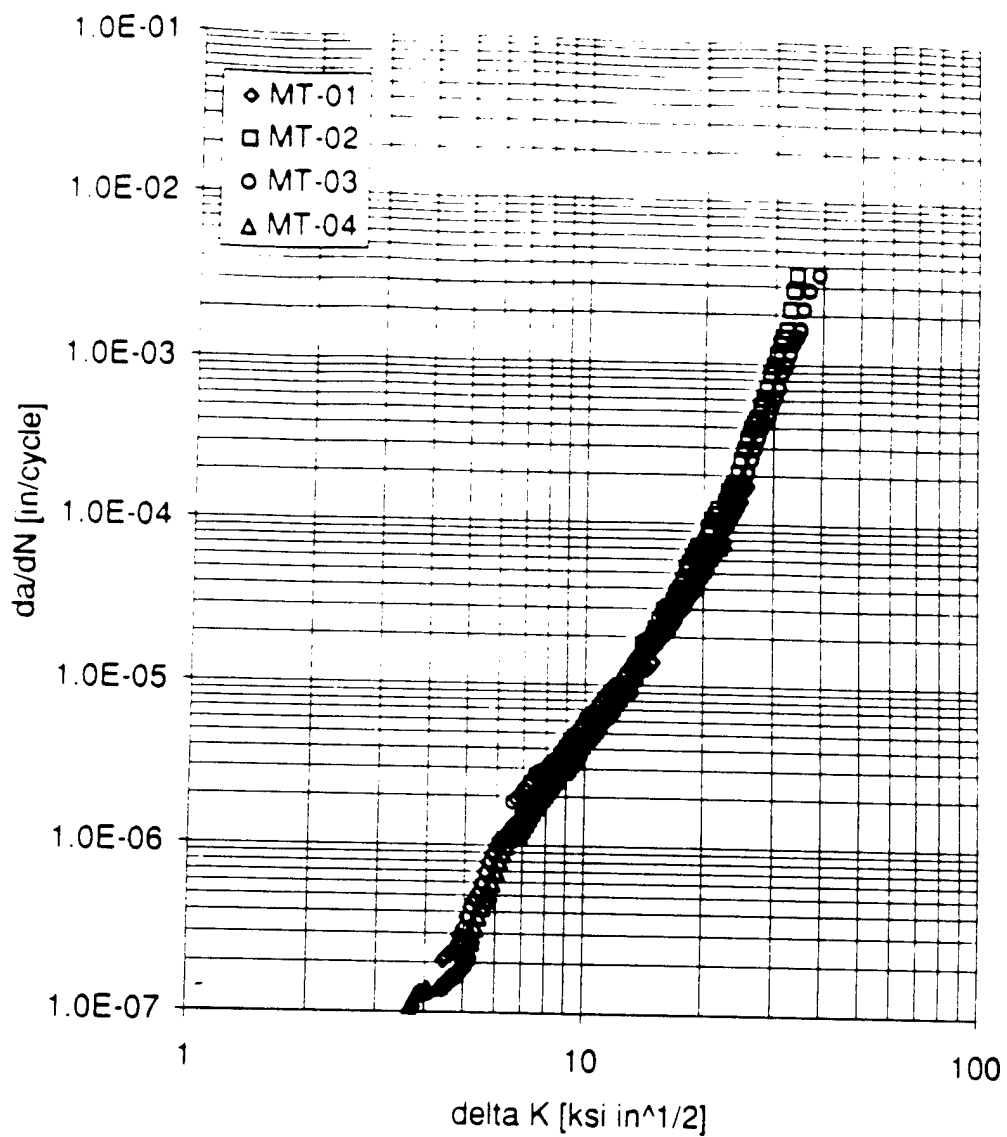
Figure 6: Fatigue crack growth curve for 2024-T3 MRS aluminum alloy, 0.063 inches thick, used for sheet material in stiffened panels.
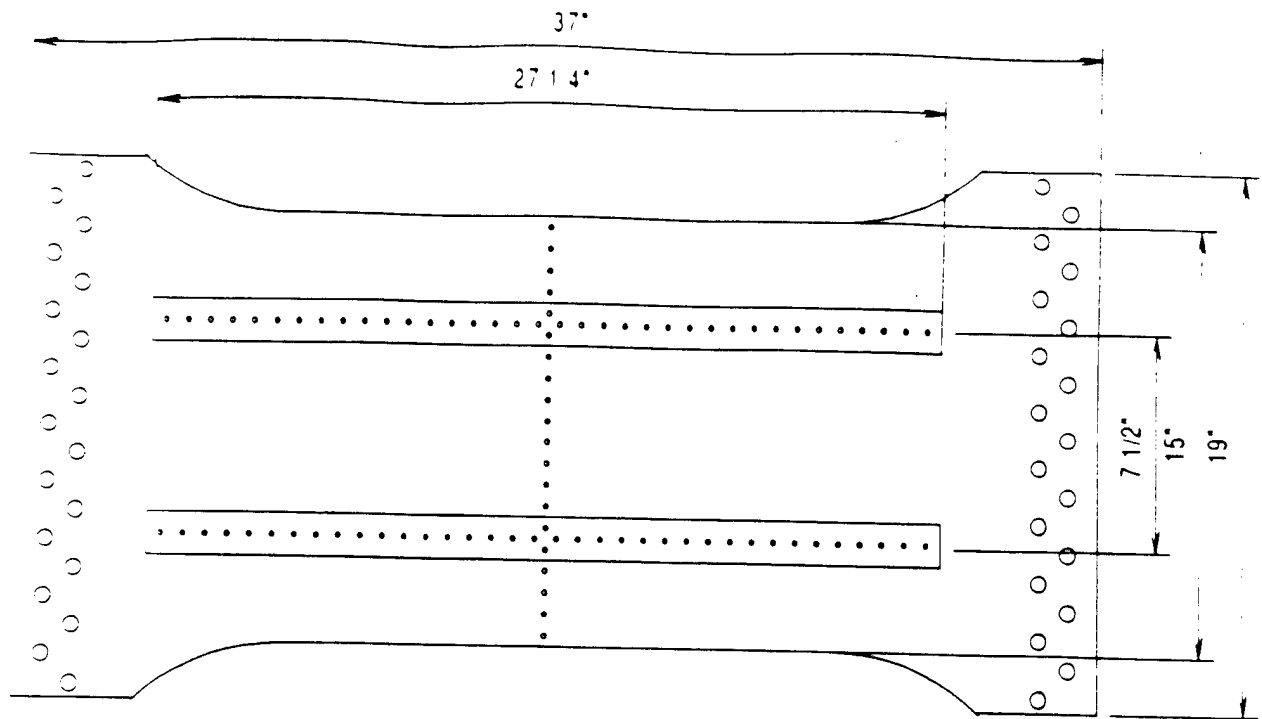
Figure 7: Schematic of stiffened panel specimen used for residual strength and fatigue testing.
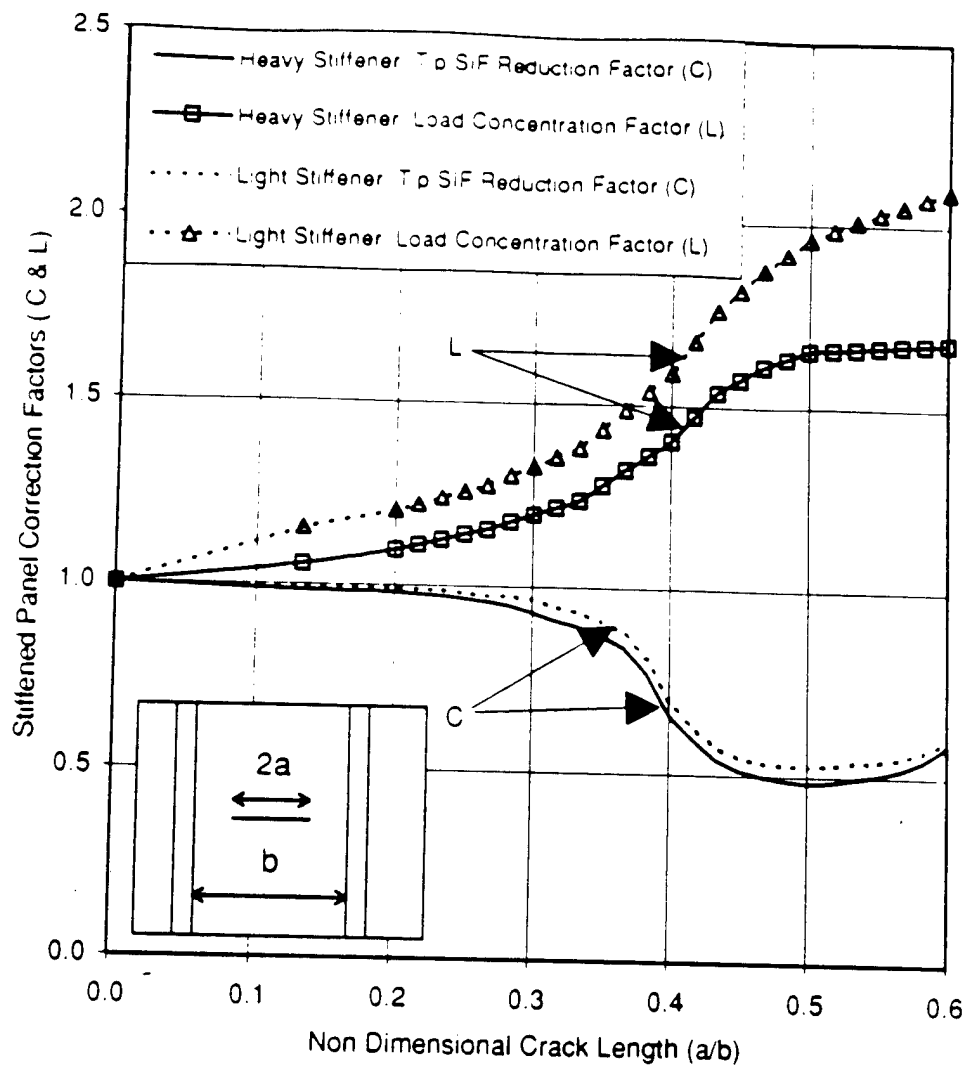
Figure 8: Analytical tip stress intensity reduction and load concentration factors for heavy and light stiffener residual strength specimens.
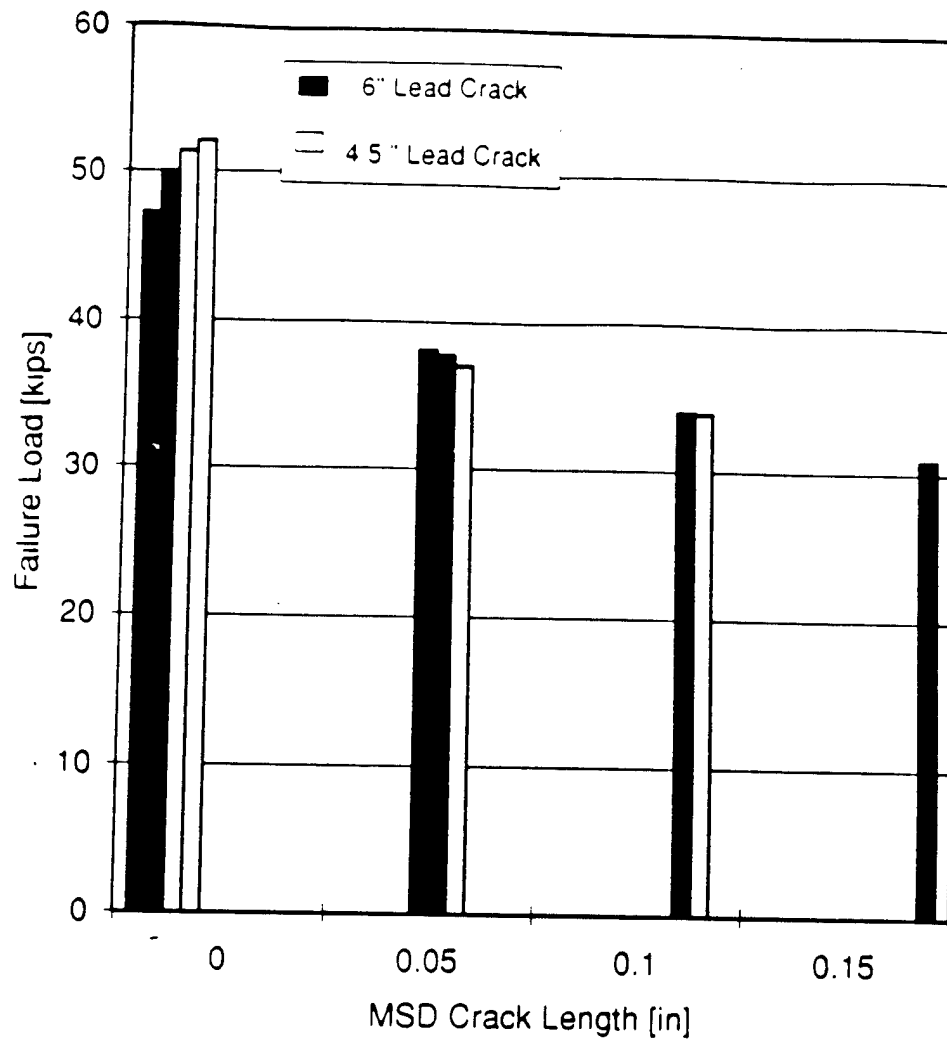
Figure 9: Reduction in residual strength of 15 inch 2024-T3 aluminum panels with heavy stiffeners due to MSD.
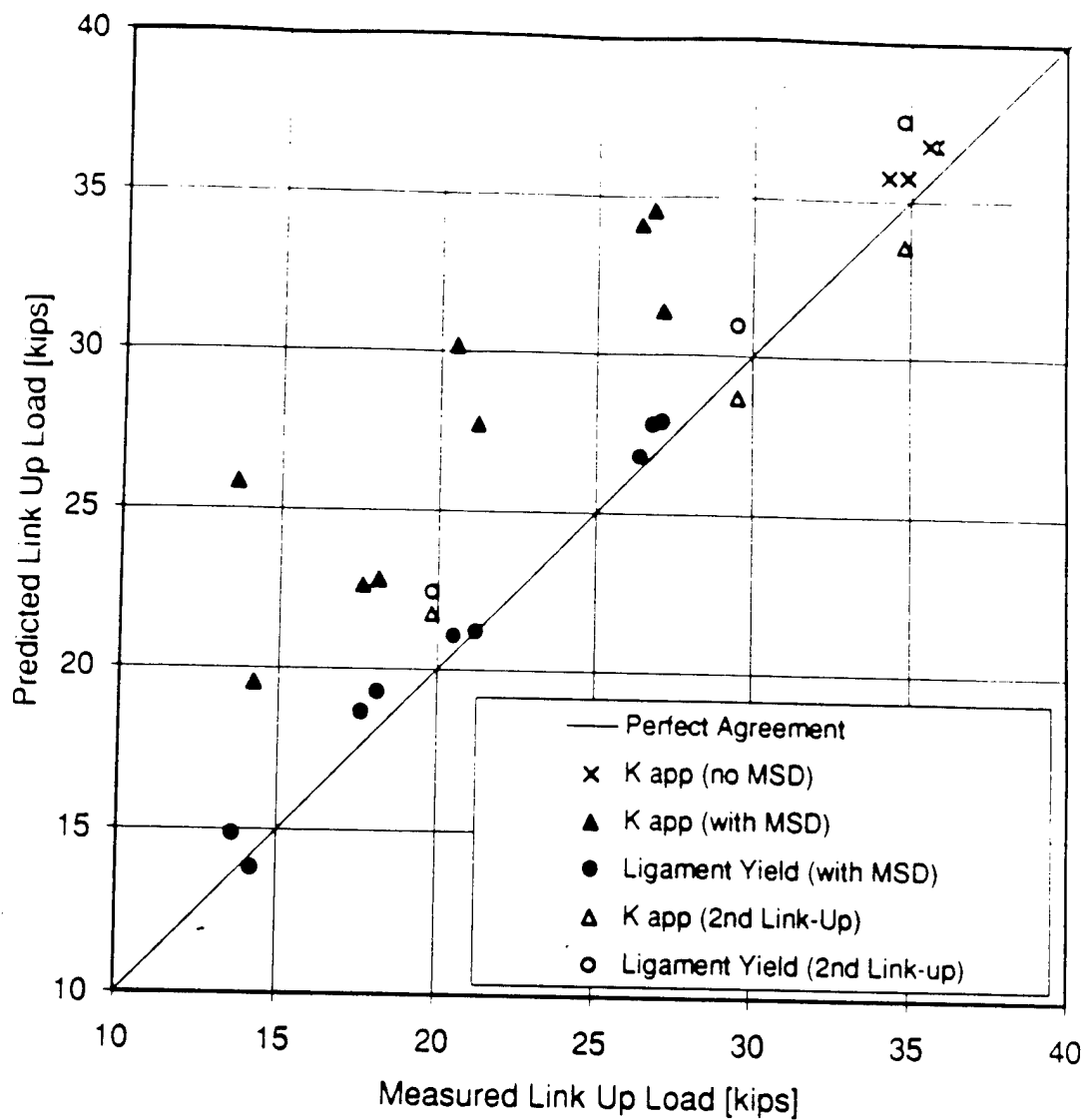
Figure 10: Comparison of measured and predicted link up loads by two different link up criteria for 15 inch wide, stiffened, 2024-T3 aluminum panels containing lead and in most cases MSD cracks.
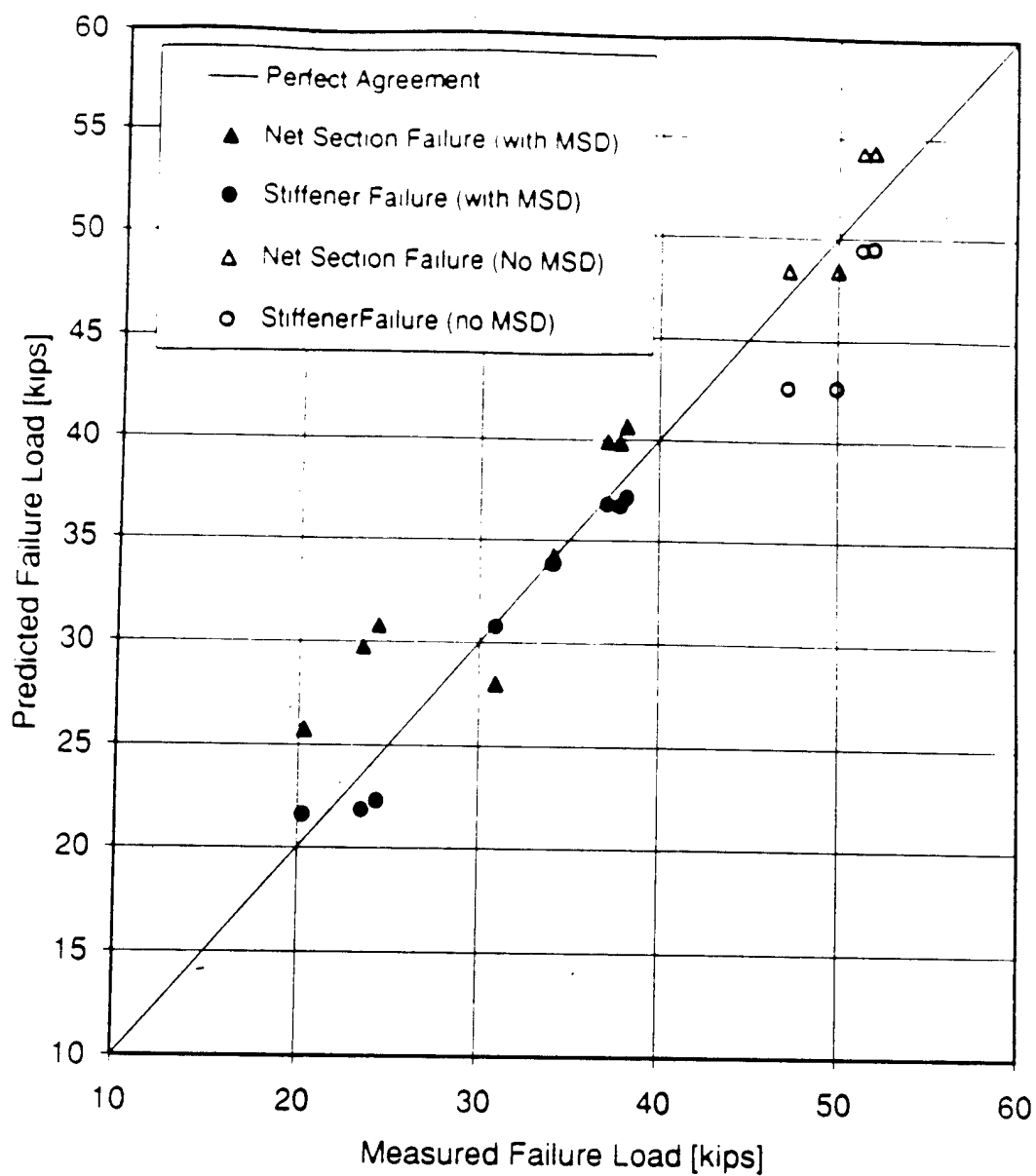
Figure 11: Comparison of measured and predicted panel failure loads by two different failure criteria for 15 inch wide, stiffened, 2024-T3 aluminum panels containing lead and in most cases MSD cracks.
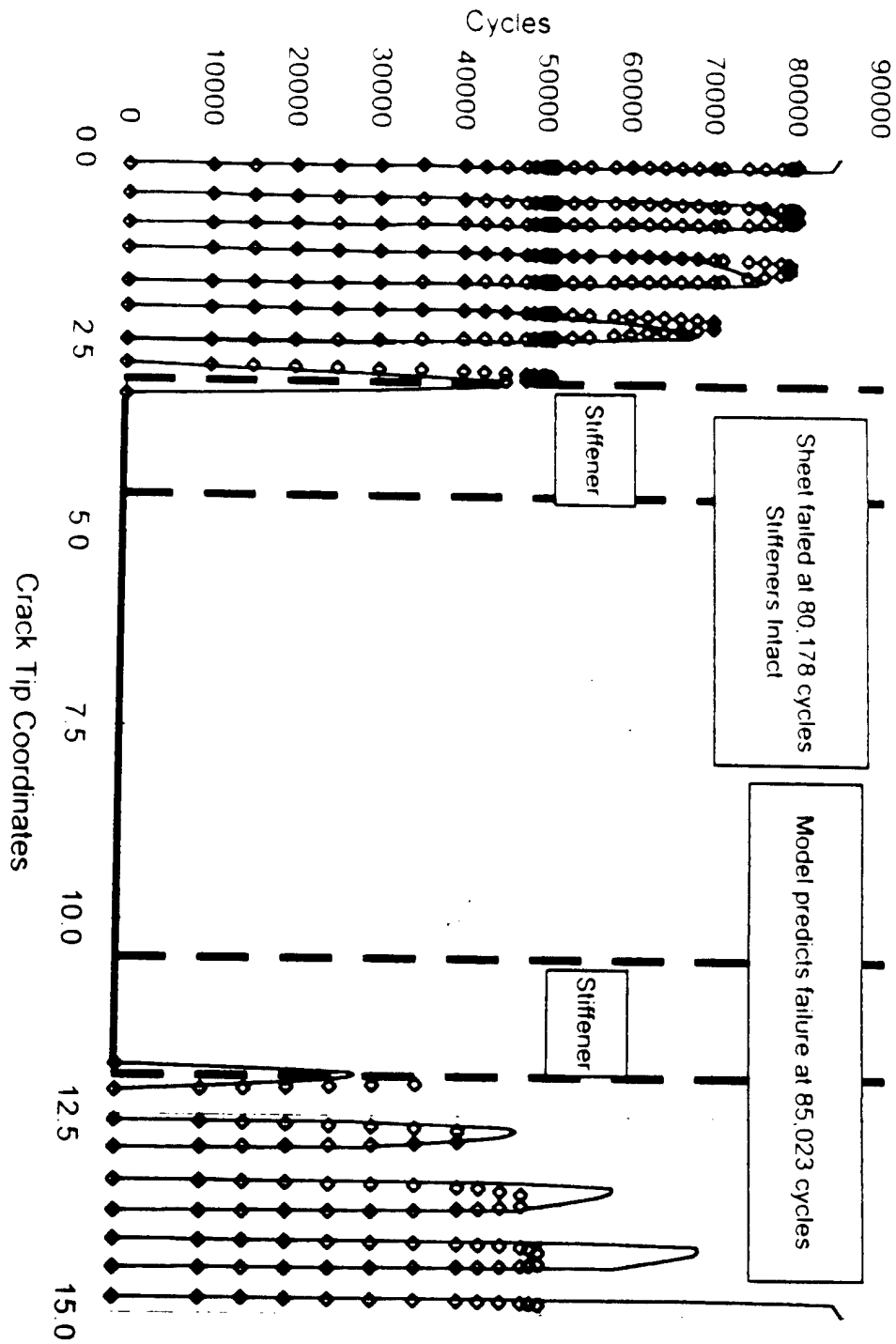
Figure 12: Crack propagation diagram for 15 inch wide stiffened panel specimen FCM-3 with lead and MSD cracks.
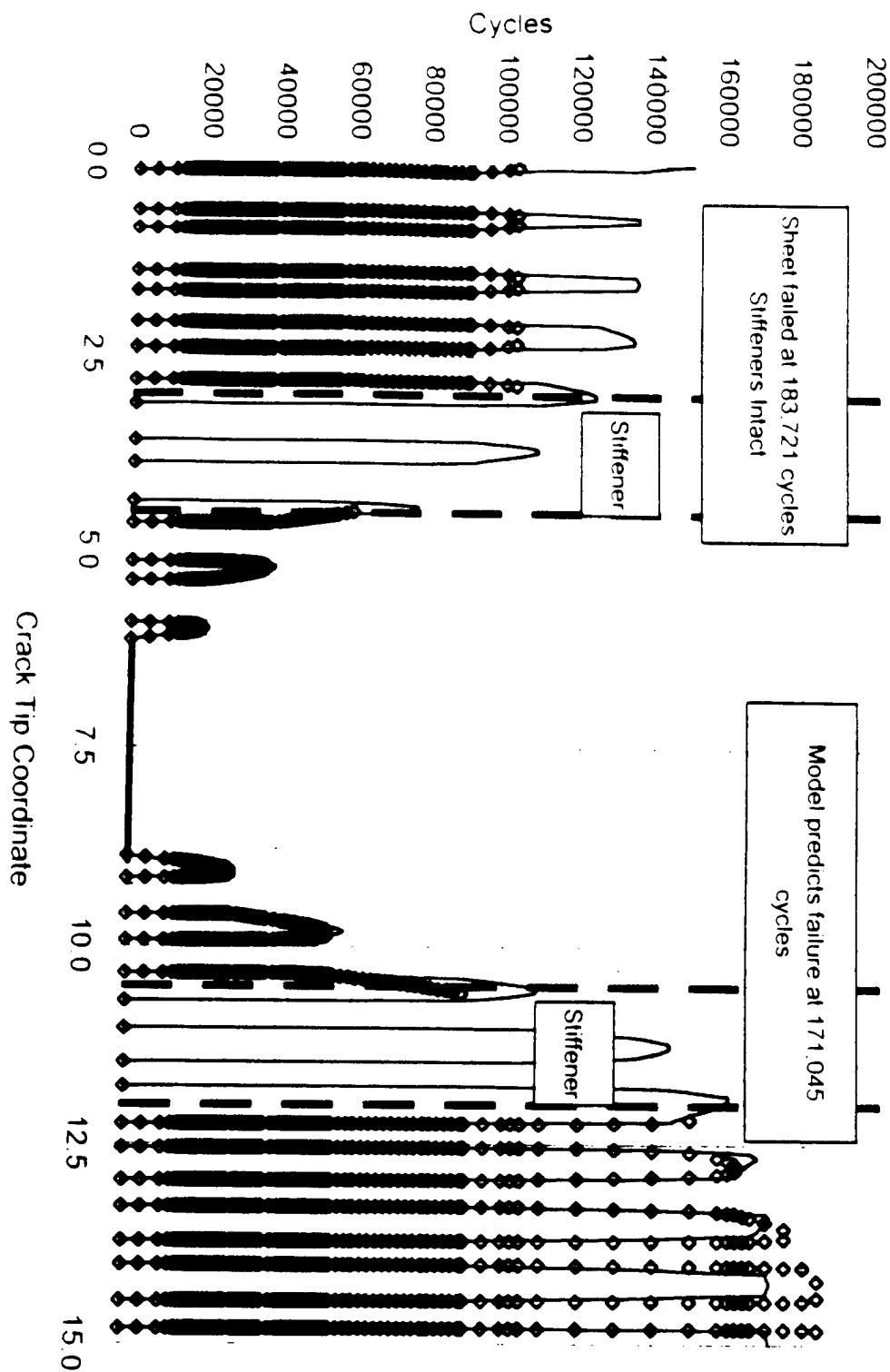
Figure 13: Crack propagation diagram for 15 inch wide stiffened panel specimen FCM-4 with lead and MSD cracks.
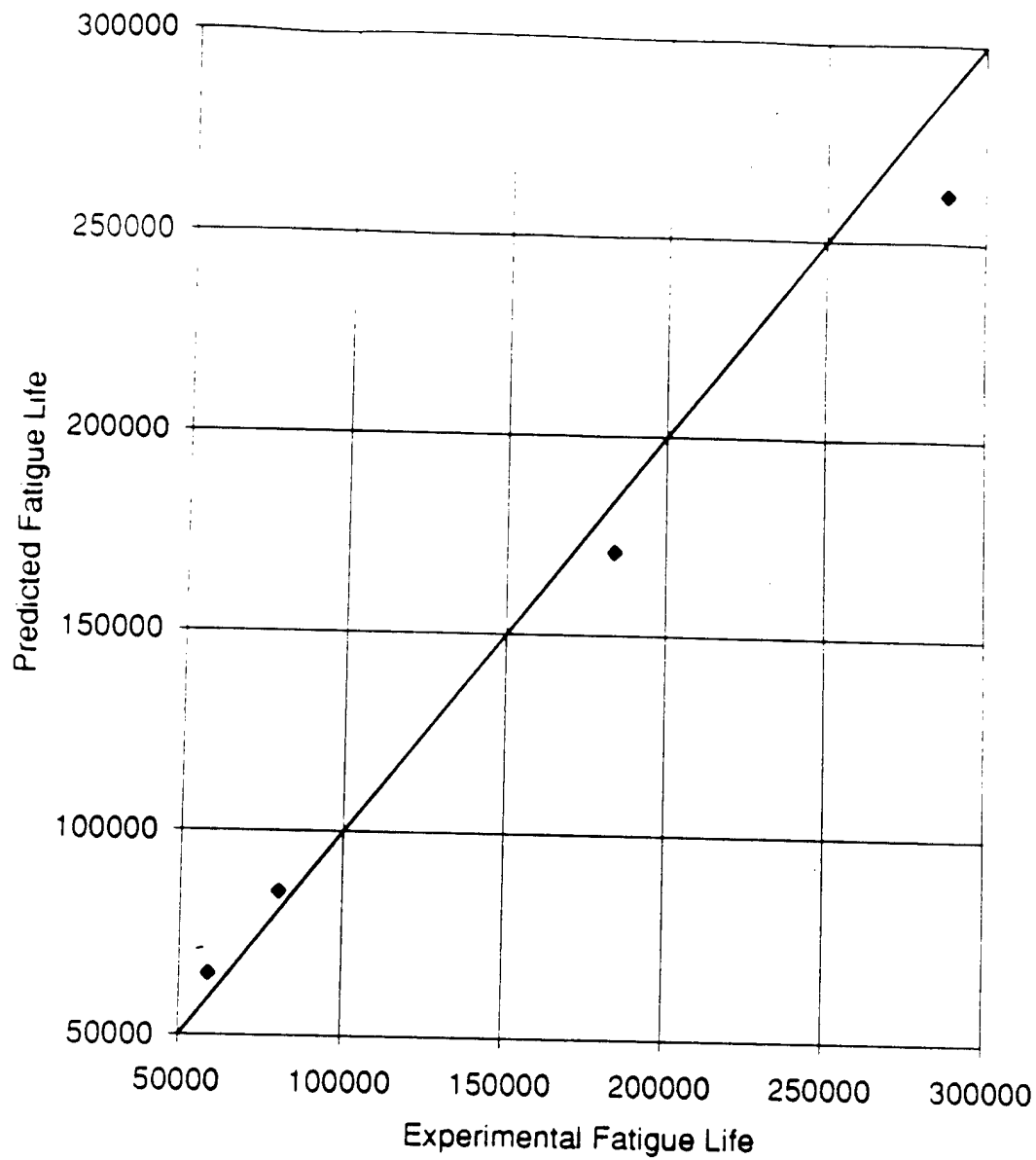
Figure 14: Comparison between actual and predicted fatigue lives for four 15 inch wide stiffened panel fatigue tests with lead and MSD cracks.
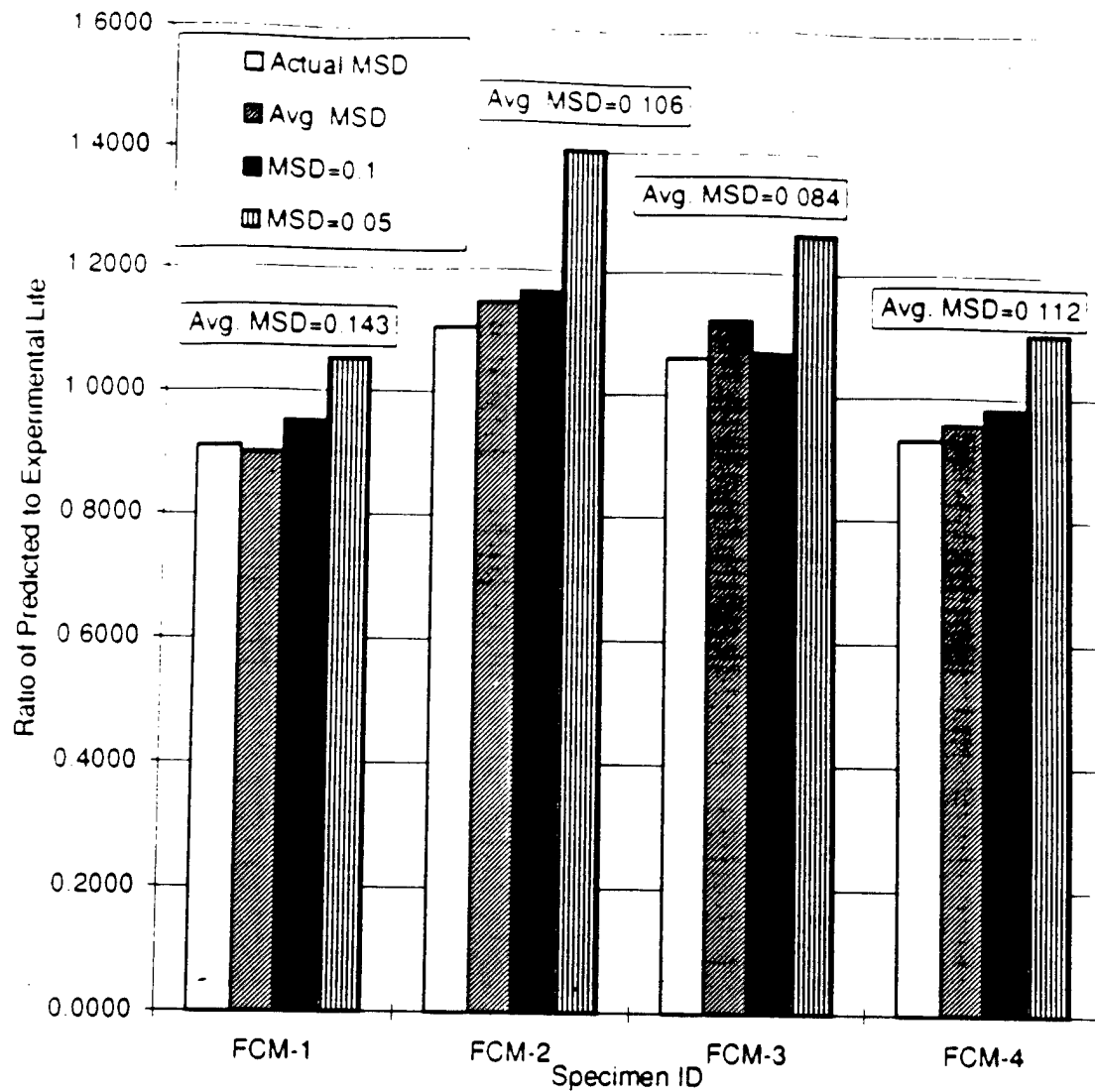
Figure 15: Effect of various MSD crack sizes on predicted fatigue life of stiffened panels with lead and MSD cracks.
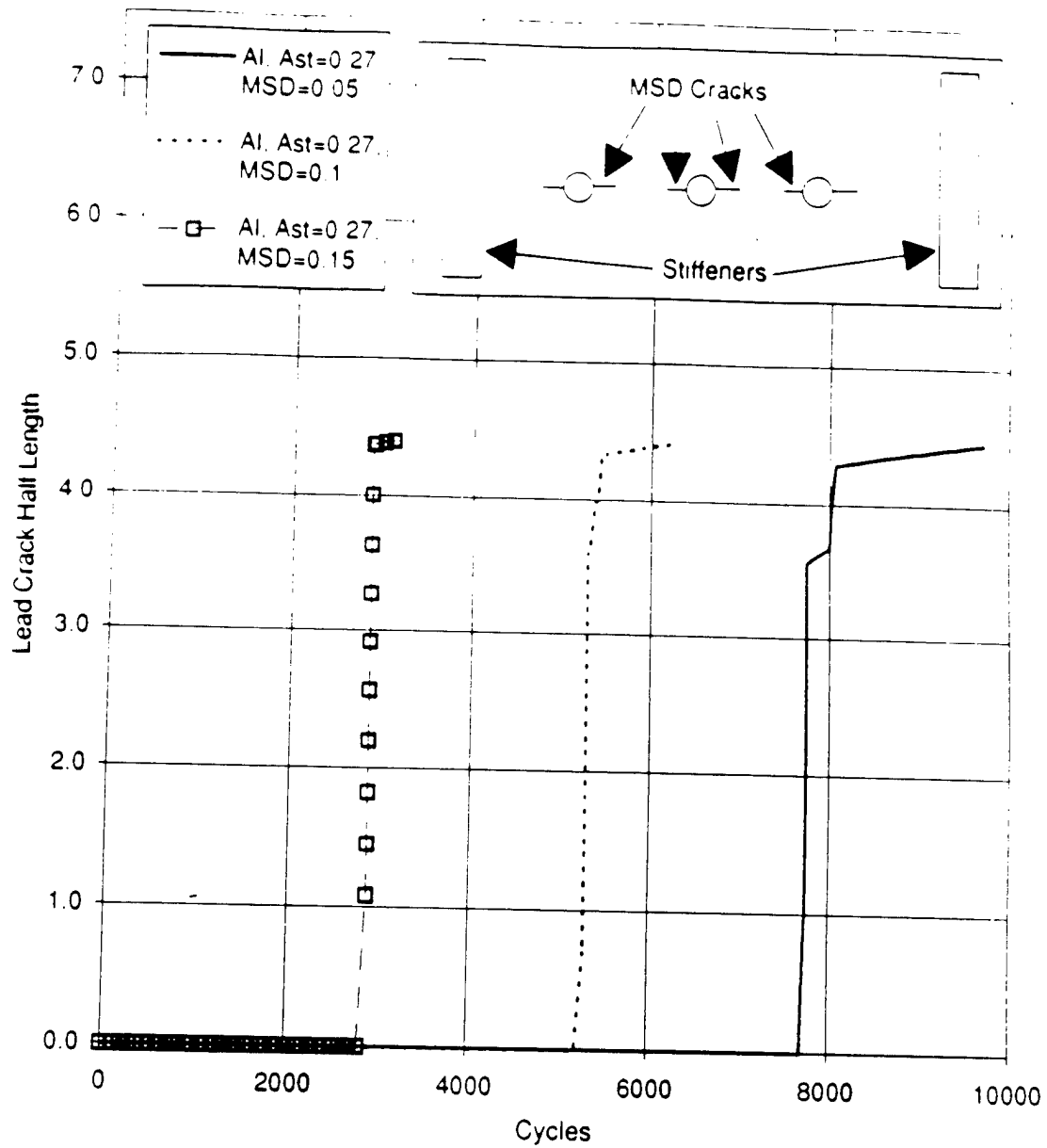
Figure 16: Lead crack versus cycle plot for stiffened panel with 0.27 in² stiffeners, and three different MSD crack sizes.
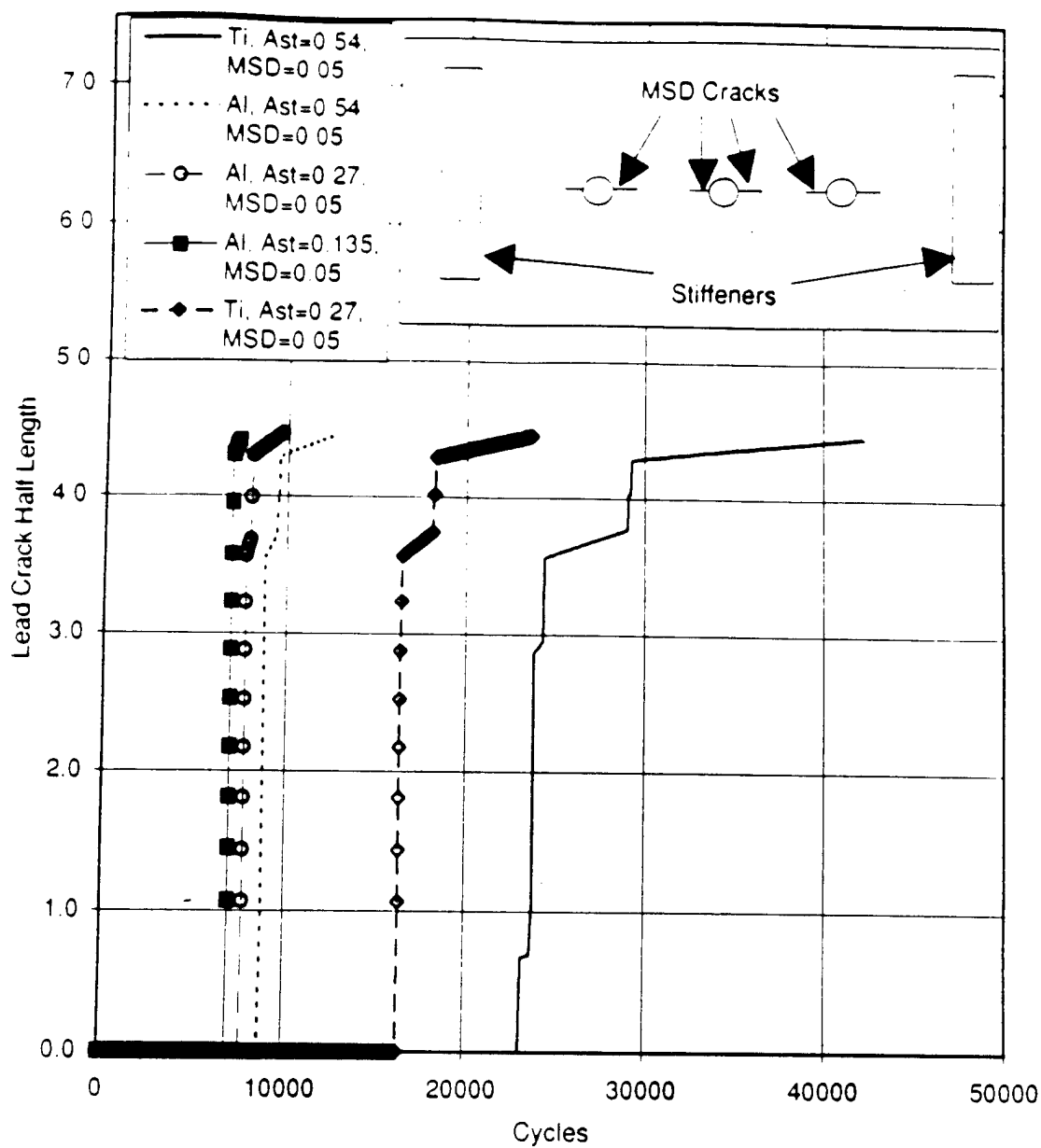
Figure 17: **Lead crack** versus cycle plot for stiffened panel with aluminum (Al) and titanium (Ti) stiffeners with cross sectional areas of 0.135 in², 0.27 in², and 0.54 in², and 0.05 inch MSD cracks in the sheet.
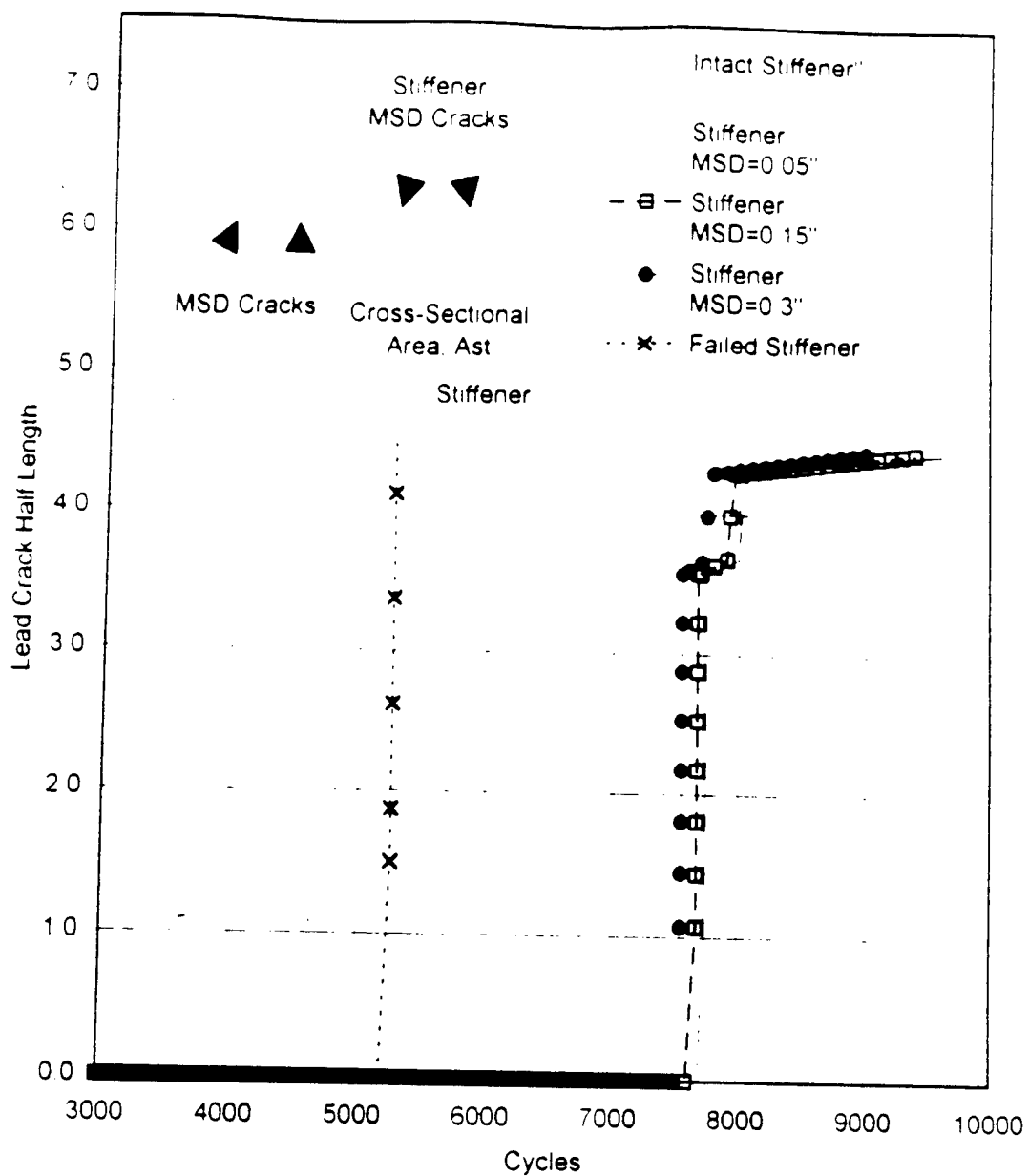
Figure 18: Lead crack versus cycle plot for stiffened panel with 0.27 in² aluminum stiffeners and 0.05 inch MSD cracks in the sheet, for 4 stiffener MSD crack lengths.

Application of Analysis of Variance (ANOVA) Statistical Methods to Breaking Load Corrosion Test

I.A. Golinkin,[1][*] D.D. Ruff ,[2] E.P. Kvam,[1] G.P. McCabe,[2] and A.F. Grandt, Jr.,[3]

[1]School of Materials Engineering, [2]Department of Statistics, and
[3]School of Aeronautics and Astronautics,
Purdue University, West Lafayette, IN 47907

[*]currently at:
        International Paper, Packaging Technology Center, Loveland, OH 45140

Abstract

The breaking load test was used for evaluating the effectiveness of a corrosion preventive compound to protect aluminum alloy 2024-T351 from stress corrosion cracking. This test determines the post-exposure fracture stress of smooth tensile coupons exposed to 3.5% NaCl alternate immersion while held at various stress levels. Three groups of specimens were examined: uncoated specimens, specimens coated before environmental exposure, and specimens coated after one day exposure. Statistical procedures based on analysis of variance methods were used to analyze the data. This statistical methodology shows much promise as a general approach to analysis of breaking load test data.

key words: breaking load test, analysis of variance, corrosion testing, stress corrosion cracking.

Introduction

Stress corrosion cracking (SCC), a premature failure due to synergistic action of sustained tensile stresses and corrosive environment, is commonly observed in structural alloys. Stress corrosion cracking resistance of materials is often evaluated by exposing smooth specimens to an aggressive environment at various stress levels [1,2]. Alternate immersion in 3.5% NaCl solution (ASTM G44-88) has been a common SCC test method, with results typically expressed as time-to-failure. Failure is defined in such tests as the actual fracture of specimens (or the visual evidence of the first crack of some predetermined size) as a function of applied stress. Pass/fail test results are used to estimate the threshold stress below which cracking does not occur [1,2]. The time-to-failure can be affected by size and geometry of the specimen, the method of loading (constant-stress or constant-strain), and fracture toughness of the material, rather than intrinsic materials properties, which is a significant limitation [1,2].

An improved approach to smooth specimen testing was developed at The ALCOA (Aluminum Company of America) Technical Center. This method, named the "breaking load" test, is based on the apparent decrease of the ultimate tensile strength, or the breaking strength, of the material after exposure to an aggressive environment [4-6]. It measures corrosion damage by comparing the post-exposure fracture stress (residual strength) of stressed specimens with the tensile strength of unstressed and unexposed specimens. Since post-exposure fracture stress reflects the extent of corrosion damage, residual strength data can be directly related to the so-called "effective flaw" size, which represents the maximum depth of corrosion attack in the specimen at the time of test [4-6]. Thus, the method enables evaluation of

materials in terms of their ability to initiate and propagate stress corrosion cracks, and eliminates problems associated with the effect of specimen size and geometry on experimental results. In contrast to traditional pass/fail testing, the breaking load method does not require the specimens to fail in the solution, and thus shortens markedly the duration of the test [4-6]. Extensive experimental work carried out by ALCOA indicated that the quantitative nature of the breaking load method opens new possibilities for investigation of stress corrosion cracking phenomena and other forms of environmental degradation, such as corrosion fatigue [4-6].

In these studies, the breaking load test was used to evaluate the effectiveness of a corrosion preventive compound on SCC of aluminum alloy 2024-T351. This evaluation incorporates statistical principles of experimental design and data analysis. A statistical procedure was outlined in the ASTM standard for the breaking load test [6]; the objective of this work is to further refine the ASTM procedure by incorporation of analysis of variance (ANOVA) statistical methods and to provide an accurate and efficient approach for data analysis using common statistical software packages.

Experimental Procedure

Alloy 2024-T351 used in these studies was supplied by ALCOA, Davenport Works, in the form of a 6.3 cm (2.5 inch) thick plate. The composition of the alloy is listed in Table 1. Short transverse round tension specimens of 3.175 mm (0.125 inch) diameter were prestressed and held in a constant-deflection type laboratory frame to stress levels of 0 MPa, 69 MPa (10 ksi) and 138 MPa (20 ksi), then exposed to 3.5% NaCl alternate immersion

testing (ASTM G 44-88) for 2 and 6 days. The choice of exposure time was based on statistical analysis of prior data, which indicated that for this alloy the most significant decrease in fracture stress occurred between two and six days. Three sets of specimens were used for this experiment: the control group (uncoated specimens) and the two groups of specimens that were coated with the corrosion preventive compound (Fluid Film®, aerosol type, Eureka Chemical Company) by spraying to a thickness of about 0.2 mm. These sets are referred to as "group 1" and "group 2". Specimens from "group 1" were coated before environmental exposure. The specimens from "group 2" were sprayed after being in the alternate immersion tank for one day to investigate the effectiveness of this compound to protect material that already had some degree of corrosion damage. All specimens were run at the same time. Specimens that did not fail after their exposure period in the corrosive solution were tensile tested to determine the post-exposure fracture stress. Corrosion exposure and mechanical testing were performed at the ALCOA Technical Center, Alcoa Center, PA.

Experimental Design and Statistical Methods

Five specimens were used for each combination of stress, time of exposure, and coating method. For each specimen, post exposure fracture stress was the variable analyzed. The five specimens for each condition were assigned at random from a collection of 90 specimens. This experimental design is called a completely randomized three-factor factorial design [8,9]. The three factors were stress, time of exposure, and coating method. The goal of the analysis was to explain how post-exposure fracture stress depends on

these three factors. The possible values for each factor are called levels. For this design there were 3 levels for stress (0 MPa, 69 MPa and 138 MPa), 2 levels for days of exposure (2 and 6 days), and 3 levels for coating method (none, coat before exposure and coat after one day exposure). Each combination of factors is called a cell. For this design there were 3x2x3 = 18 cells, each with five observations, giving a total of 18x5=90 observations. The usual method for analyzing this type of design is an analysis of variance (ANOVA) [8,9]. Here, we have a 3-way anova or a 3x2x3 anova.

The anova procedure is based on a statistical model that represents each observation as the sum of a cell mean and a random deviation from this mean. The cell means are modeled as the sum of a grand mean, main effects (one for each factor), two-way interactions (one for each pair of factors), and a three-way interaction [8,9]. The main effects express the differences among means for each factor, with levels averaged over all other factors. Two-way interactions express how the effect of a factor may depend on another factor. For example, if the post-exposure fracture stress is not different for days of exposure (2 versus 6) unless the stress is high, an interaction between stress and days of exposure would be an important part of the model. The three-way interaction expresses the effects of the three factors that are not modeled by the main effects and two-way interactions.

The anova procedure provides estimates of main effects, two-way interactions and the three-way interaction, along with an assessment of the size of these terms relative to the random deviations, based on the data collected and expressed as a test of statistical significance. The results of the tests of statistical significance are expressed as P-value; a P-value of .05 or less indicates that a proper interpretation of the data collected should include an explanation of these terms in the model. Interpretation of results where

there are statistically significant interactions can be simplified by careful examination of plots and by running additional analyses. For example, a statistically significant 3-way interaction found in this study was examined by running three 2-way anovas, one for each level of stress.

The validity of conclusions based on anova methodology depends on the extent to which the assumptions made for this analysis are satisfied. These assumptions include (a) independence of the observations and (b) random deviations from cell means that are normally distributed with a common standard deviation. The first assumption is reasonable because the specimens were randomly assigned to cells. The second assumption includes two parts: (i) normal distributions and (ii) standard deviations that do not vary across cells (the homogeneity assumption). Each of these can be examined with the data collected.

When standard deviations are not homogeneous, they often vary in a systematic way with the means. To explore this possibility, logarithms of the standard deviations are plotted versus logarithms of the means, as in Figure 5. If the relationship in this plot is approximately linear, then transforming the data by raising each observation to a particular power will produce data that are approximately homogeneous. Specifically, if $\log(s) = a + b \log(\bar{y})$, a simple linear regression of $\log(s)$ with $\log(\bar{y})$, then the suggested transformation is y^{1-b}. This type of transformation is called a power transformation or a Box-Cox transformation. The rationale is as follows. Suppose a random variable y has a mean μ and variance that is a function of μ, say $\sigma^2 = g(\mu)$. We want to find a function, say $f(y)$, such that its variance is approximately constant. Expanding $f(y)$ in a first order Taylor series about μ gives $f(y) - f(\mu) \approx (x - \mu) f'(\mu)$; squaring and taking expected values gives $\sigma^2 [f'(\mu)]^2$ as the approximate variance of $f(y)$. For the variance of $f(y)$ to be

approximately constant, we need $g(\mu) [f'(\mu)]^2$ to be constant, i.e., $f'(\mu) =$ $c/\sqrt{g(\mu)}$. This gives the integral equation $f(y) = \int (c/\sqrt{g(\mu)}) \, d\mu$. Now, if $\log(\sigma)$ = $a + b \log(\mu)$, then σ is proportional to μ^b, i.e., $g(\mu) = (e^a \mu^b)^2$. Substituting into the integral equation gives $f(y)$ proportional to $\int (1/\mu^b) \, d\mu = y^{1-b}$. Note that $b = 0$ corresponds to no transformation. Therefore, if the slope in the regression is not significantly different from zero, the data fail to provide evidence in favor of this type of transformation. Other methods to find transformations and to examine the homogeneity assumption can be found in texts on regression and analysis of variance methods, such as [8].

After the data have been transformed to meet the homogeneity assumption, the normality assumption is examined by constructing a normal quantile plot for the residuals (observations minus the cell means). This is a plot of the residuals *versus* computed values that would be expected if the residuals were normal. A straight line relationship is an indication that the normal assumption is reasonable.

Some specimens broke during exposure to the saline solution and, therefore, could not be tested. These are called censored observations. Analytical strategies include (a) using a strength of zero for the censored values (in this experiment it can be argued that because they broke as a consequence of the treatments, they have no post-exposure fracture stress); (b) imputing a value by selecting a uniform random number between zero and applied stress [5]; (c) using other advanced statistical methods that account for censored data; and (d) using time to failure data. A detailed description of this problem is beyond the scope of the current work. Fortunately, the conclusions were robust for the data collected in this experiment, in the sense

that they did not depend upon the particular choice of method for addressing the censoring problem. All the analyses were performed using Statistical Analysis Software (SAS).

Results and Discussion

Metallographic Observations

After environmental exposure, selected specimens were cleaned in nitric acid to remove loose corrosion debris, and examined in an optical microscope. Figure 1 compares specimens prestressed to 69 MPa (10 ksi) and subjected to alternate immersion testing for six days with and without coating. The surface of the specimen sprayed with corrosion preventive compound prior to exposure (Figure 1 a) does not reveal any significant evidence of corrosion damage. Also, the specimen that was coated after being in the corrosive environment for one day (Figure 1 b) had less surface damage than unprotected specimen (Figure 1 c). Longitudinal profiles of coated specimens are compared with control samples in Figures 2 and 3. Secondary cracks were not observed in specimens coated before environmental exposure, as shown in Figures 2 a and 3 a. These results indicate that application of the coating prior to exposure to an aggressive environment provided the most effective protection from SCC. Metallographic observations also showed that the severity of corrosion damage that developed in specimens coated after one day of alternate immersion was less than that of unprotected specimens. However, for some specimens from the 138 MPa (20 ksi) pre-exposure group, secondary cracks penetrated to a depth of

about 0.5 mm (Figure 3 b). Note that all of the uncoated control specimens exposed at this stress failed in the alternate immersion tank when the test duration was longer than two days. Therefore, even delayed application of the coating was still advantageous.

Statistical Analysis

Cell means and standard deviations for post-exposure fracture stress are given in Table 2. Specimens that failed in the alternate immersion tank are designated by asterisks, and the mean fracture stress of the surviving specimens is reported for those cells. To account for censored data in this experiment, two methods were employed. First, we simulated post-exposure fracture stress values for each specimen that failed in the solution by generating a uniform random number between zero and the applied stress. This methodology is based on the idea that, since the specimen failed at a particular exposure stress, the specimen's fracture stress was less than or equal to that stress value [5,6]. (Note that this measure does not take into account variables such as exposure time.) Means and standard deviations for cells with missing values were recalculated using the above method and are shown in bold face (see Table 2). Since none of the control group specimens stressed at 138 MPa (20 ksi) survived in the alternate immersion tank for 6 days (no uncensored data existed), this group was omitted from all the analyses. To assure that the final results were not dependent on the method of accounting for data censoring, all analyses were rerun with the post-exposure fracture stress values for failed specimens replaced by zero. None of the conclusions changed when this was done.

The logs of the standard deviations are plotted versus the logs of the means in Figure 5. There is a clear pattern, with the larger standard deviations being associated with the smaller means. Experimental work carried out at ALCOA Technical Center with 7000 series aluminum alloys [3-6], and prior testing done by Purdue University with 2000 series alloys, indicated that this pattern is typical for the breaking load test. To determine a transformation which would make the standard deviations approximately equal, we found the means and standard deviations of each cell and determined the regression $\log(s) = a + b \log(\bar{y})$. This yielded a slope of approximately -1.8, which suggested as a transformation $y^{2.8}$. This value is consistent with what was determined in a similar experiment using a different alloy (2024-T8). After the data were transformed, a three-way anova model was fit. The residuals were plotted, and appeared to be approximately normal.

In the three-way anova model, all interactions and main effects were significant (with p-values much lower than 0.05). To interpret these results, separate two-way anovas were run for each stress level. These means are displayed in Figure 5, expressed as percent of original strength by dividing them by the mean tensile strength of the unstressed, unexposed reference specimens (444 MPa). In each of these two-way analyses, the two-way interactions and main effects were found to be significant (most p-values much less than 0.05). Under the no stress condition, the two coating methods resulted in essentially no loss of strength. The uncoated specimens showed loss of strength, with a greater loss when exposed for 6 days. When stressed at 69 MPa (10 ksi), the specimens coated before exposure retained their strength. The specimens coated after exposure and the uncoated specimens lost about 20% of their strength at 2 days of exposure. At 6 days, the specimens coated

after exposure did not lose any additional strength, but the uncoated specimens lost an additional 20%. At 138 MPa (20 ksi), coating before exposure was effective in retaining full strength. When the coating was applied after exposure, there was a 30% loss at 2 days and an 80% loss at 6 days. The uncoated specimens lost 80% after 2 days; all specimens in this group failed in solution by 6 days. The low mean post-exposure fracture stress for the specimens that were coated after exposure was due to the relatively large flaws that developed in uncoated specimens during the one day exposure. Some of the secondary cracks penetrated to the depth of about 0.5 mm in 3.175 mm diameter specimens (see Figure 4). These results indicate that susceptible structural components might be coated with this corrosion preventive compound to provide effective protection from SCC. However, the long term effectiveness, periodicity of recoating, quantitative effectiveness, etc., have not been examined at all in this study. These, and several other aspects, would need substantial further testing before specific recommendations could be made with confidence.

Conclusions

1) This study has shown that the breaking load approach can serve as an effective accelerated test for evaluating corrosion preventive compounds. Analyses of variance (ANOVA) statistical methods were applied for such evaluations. This statistical procedure provided estimates of the effects of test parameters on residual strength for the three coating conditions, and can be used as an alternative method to analyze breaking load test results.

2) Prior experimental work done at ALCOA and the current data indicate that inequality of variance for various experimental conditions is common for the breaking load test and requires the use of transformations. The Box-Cox methodology outlined in the ASTM standard [6] is a convenient way to treat this problem.

3) Two methods were used in these analyses to represent residual strength of failed specimens (censored values): generating random numbers from zero to exposure stress, and substituting zero. Fortunately, for this case, conclusions of the analyses were robust, since the results were the same for both methods. Advanced statistical methods can be used to address this censored value problem.

4) This study showed that a corrosion preventive compound was effective in delaying the effects stress corrosion cracking in accelerated testing. The compound was most effective when applied prior to testing, but still showed significant effects when applied after some test-induced stress corrosion cracking had occurred. More thorough examination is required before specific recommendations can be made for field applications, but these experiments suggest the corrosion preventive compound may be useful in protecting stress corrosion susceptible regions.

Acknowledgments

A12- 13

work was supported by the Air Force Office of Scientific Research, Grant

References

[1]   R. H. Jones, *Stress-Corrosion Cracking,* ASM International, 1992.

[2]   B. F. Brown, *Stress-Corrosion Cracking in High Strength Steels and in Titanium and Aluminum Alloys,* Naval Research Laboratories, 1972.

[3]   D. O. Sprowls, et al, "A Study of Environmental Characterization of Conventional and Advanced Aluminum Alloys for Selection and Design, Phase II-The Breaking Load Test Method", ALCOA, NASA Contractor Report 172387.

[4]   D. A. Lukasak, R. J. Bucci, E. L. Colvin, and B. W. Lifka, "Damage-Based Assessment of Stress Corrosion Performance Among Aluminum Alloys", ASTM STP 1134, 1991, p. 101.

[5]   E. L. Colvin and M. R. Emptage, "The Breaking Load Method; Results and Statistical Modification From the ASTM Inter-Laboratory Test Program", *New Methods for Corrosion Testing of Aluminum Alloys,* ASTM STP 1134, V. S. Agarwala and G. M. Ugiansky, Eds., American Society for Testing and Materials, Philadelphia, 1992, p. 82.

[6]   ASTM Standard G-139, Standard Test Method For DeterminingStress Corrosion Cracking Resistance of Heat Treatable Aluminum Alloys With the Breaking Load Method.

[7]   G. E. P. Box and D. R. Cox, "An Analysis of Transformations", *Journal Royal Statistical Society,* Series B. 26, 1964, p. 211.

[8]   J. Neter, M. H. Kutner, C.J. Nachtsheim, and W. Wasserman, *Applied Linear Statistical Models,* Richard D. Irwin, Inc., 1996, 4th ed..

[9]   Miller and Freund, *Probability and Statistics for Engineers,* Prentice Hall, Engelwood Cliffs, New Jersey, 1994, p 630.

Table 1

Composition of aluminum alloy 2024-T351 plate material, wt%.

Cu	Mg	Mn	Fe	Zn	Ti	Cr	Si	Al
4.02	1.40	0.57	0.08	0.14	0.02	0.01	0.07	bal.

Table 2

Cell means and (standard deviations) of residual strength data for replicate specimens of AA 2024-T351 exposed to 3.5% NaCl alternate immersion. Failed specimens are indicated by an asterisk. Regular script in incomplete cells designate means and (standard deviations) of surviving specimens, whereas bold script uses random numbers.

Exposure stress (MPa)	Coating method					
	uncoated (control)		coated before exposure (group 1)		coated after one day exposure (group 2)	
	2 days	6 days	2 days	6 days	2 days	6 days
0	397.8 (2.1)	361.2 (5.5)	447.4 (3.4)	445.3 (2.1)	434.3 (1.4)	439.1 (5.5)
69	348.1 (16.5)	295.1 (23.4) **246.8 (111.0)** *	446.0 (2.1)	446.7 (4.1)	343.3 (16.5)	349.5 (28.9)
138	120.6 (121.3) **99.3 (115.8)** *	* * * * *	447.4 (4.1)	448.1 (4.1)	310.2 (85.5)	110.3 (102.7) **99.3 (55.8)** * * *

List of Figures

Figure 1 Photograph of short transverse specimens of alloy 2024-T351 exposed to 3.5% NaCl alternate immersion for 6 days at 69 MPa (10 ksi) stress: (a) control specimen, (b) specimen coated after one day exposure, (c) specimen coated before exposure

Figure 2 Longitudinal profiles of 3.175 mm diameter specimens of alloy 2024-T351 exposed to 3.5% NaCl alternate immersion for 6 days at 69 MPa (10 ksi) stress. (a) Specimen was coated prior to exposure, (b) control specimen.

Figure 3 Longitudinal profiles of 3.175 mm diameter specimens of alloy 2024-T351 exposed to 3.5% NaCl alternate immersion for 6 days at 139 MPa (20 ksi) stress. (a) Specimen was coated prior to exposure, (b) specimen was coated after one day exposure.

Figure 4 Log standard deviation plotted versus log cell means for the breaking load test results (Table 2) showing the observed trend of increase in standard deviation with decrease in mean post-exposure fracture stress. Only cells with complete data are included.
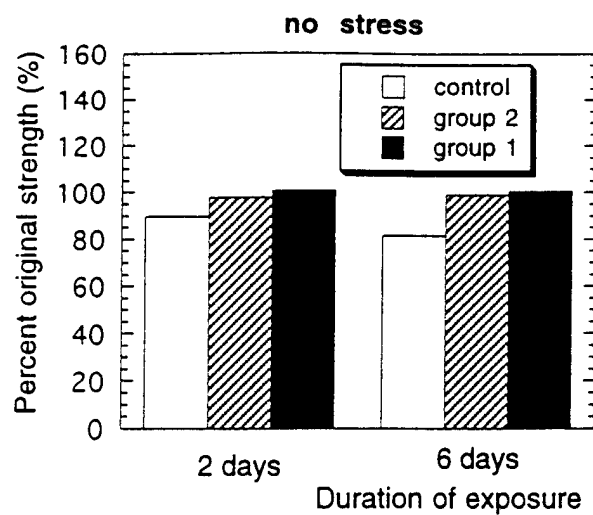
Figure 5 Comparisons of breaking load test results (means) for alloy 2024-T351 specimens coated with corrosion preventive compound.

1 cm

250 µm

250 µm

250 µm

250. µm
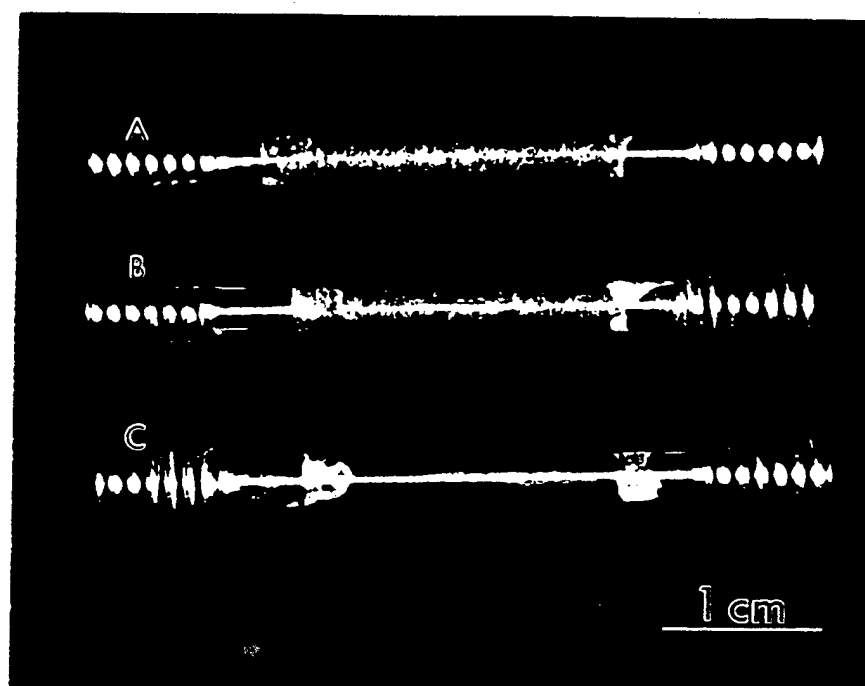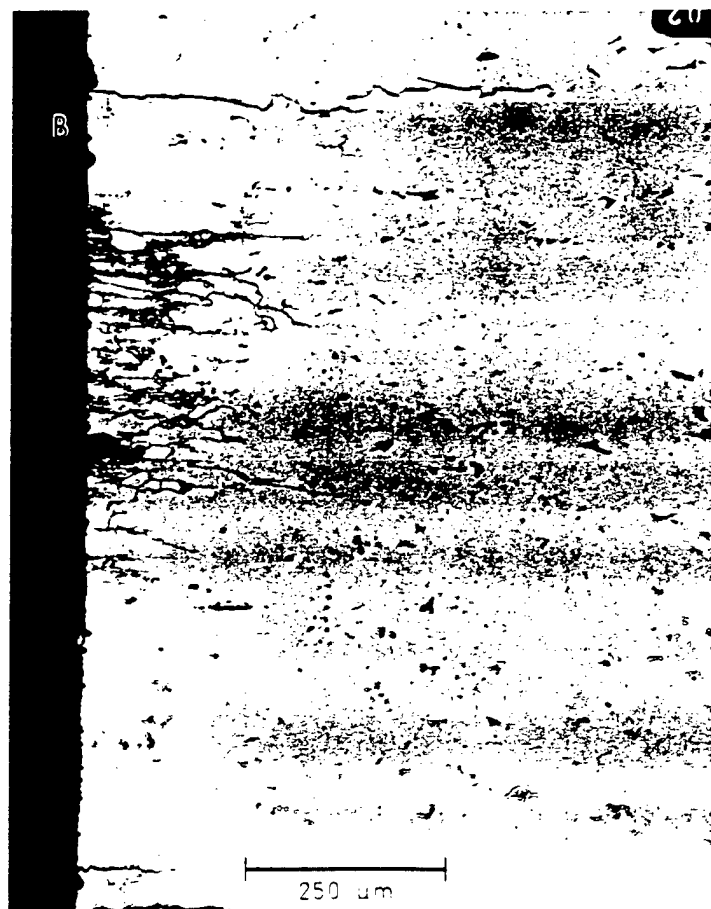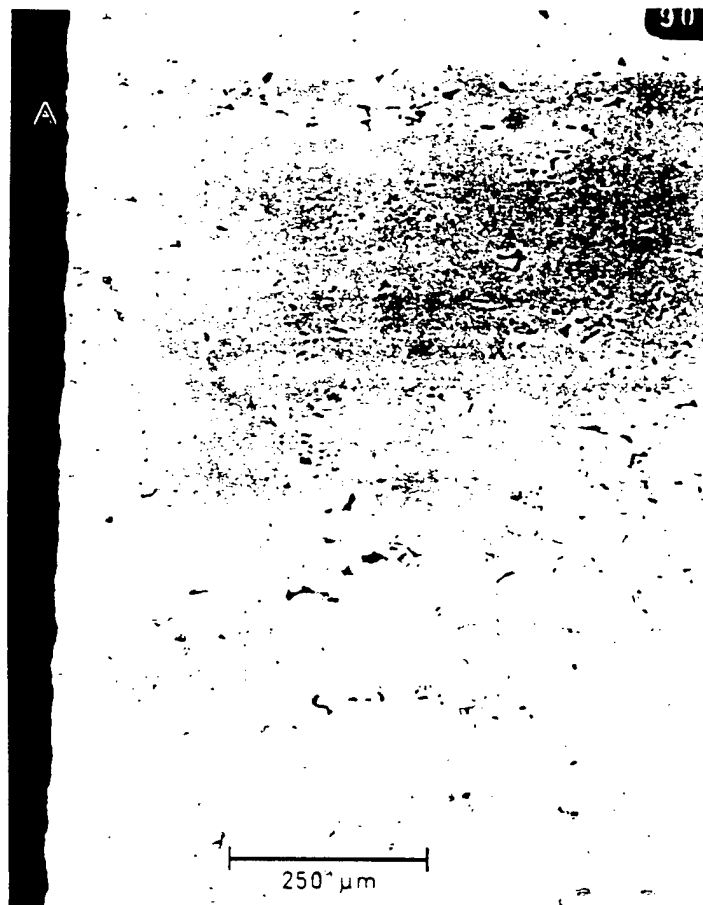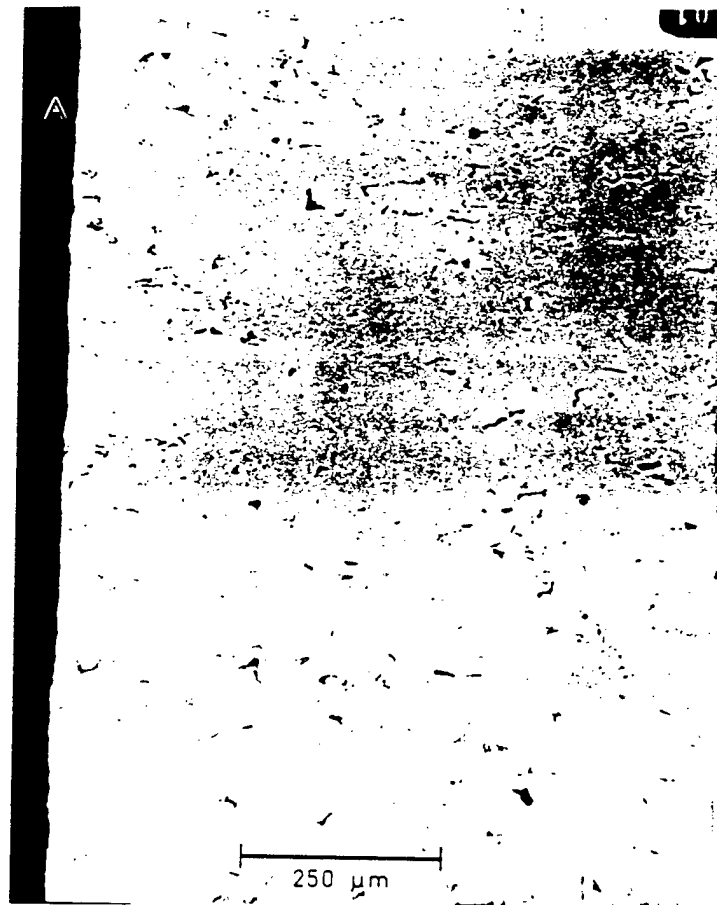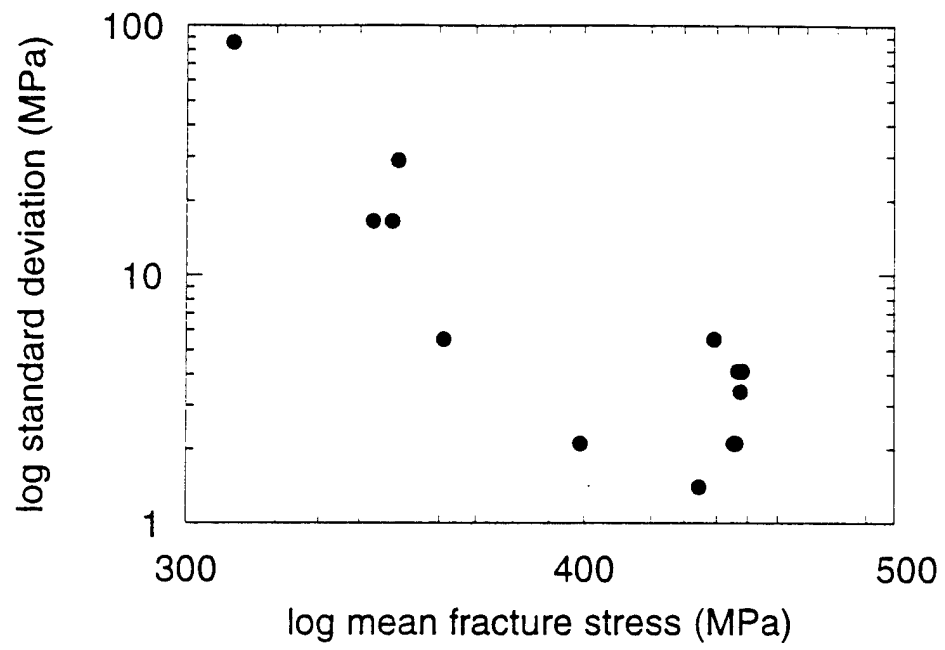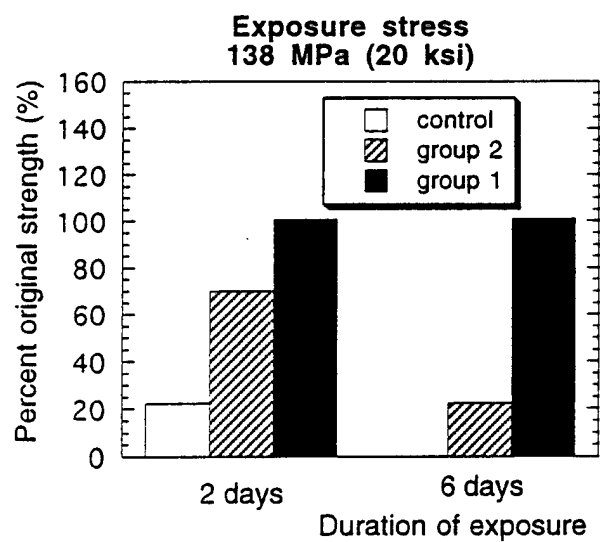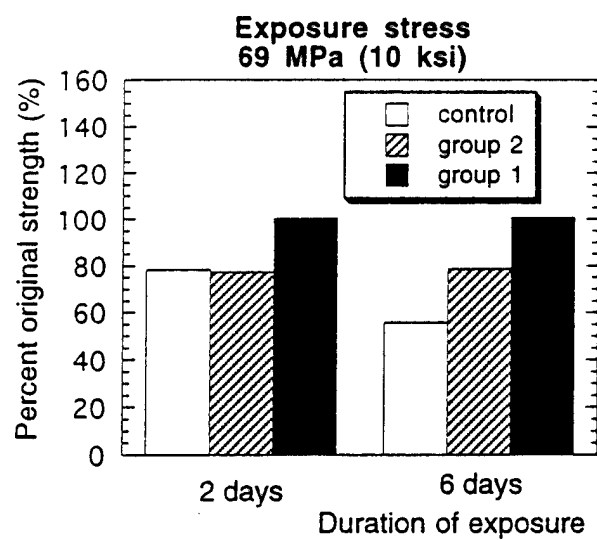
FATIGUE LIFE PREDICTION FROM INCLUSION INITIATED CRACKS

P.J. Laz[1] and B.M. Hillberry

School of Mechanical Engineering
Purdue University
West Lafayette, IN 47907

ABSTRACT

Fatigue cracks have often been observed to nucleate at inclusions or constituent particles in thin sheet 2024-T3 aluminum. Large amounts of scatter are commonly observed in the experimental fatigue lives and crack nucleation site data. This research attempts to address some of the stochastic issues associated with the fatigue process. An experimental program was conducted to investigate the influence of inclusions on fatigue crack formation. Inclusions were found to be the dominant crack nucleation site and the inclusion sizes that nucleated fatigue cracks were from the large particle tail of the overall inclusion size distribution. A probabilistic model has been developed to predict the observed variability in the experimental fatigue lives from the measured distribution of inclusion sizes. In order to model crack growth from a microstructurally sized defect (such as an inclusion), a total fatigue life prediction model accounting for the small crack effect must be utilized. The probabilistic model uses a Monte Carlo simulation and Newman's FASTRAN II model to predict fatigue life. The fatigue life distributions, that were generated with the probabilistic model, predicted the critical, lower experimental fatigue lives and the overall variability in fatigue lives under several loading conditions.

Key words: inclusions, life prediction, aluminum
Brief Title: Inclusion Initiated Fatigue

1. Graduate Research Assistant
2. Professor of Mechanical Engineering

Submitted to International Journal of Fatigue.

INTRODUCTION

The fatigue process and its mechanisms are largely influenced by the presence of material inhomogeneities. Fatigue cracks have been observed to form at inhomogeneities that are inherent to the material, like constituent particles and micropores, and at flaws acquired during service, like corrosion pits and machining scratches. This study focuses on a rolled thin sheet aluminum without microporosity and is primarily concerned with fatigue crack formation at inclusions.

Inclusions or secondary phase particles are common sites for fatigue crack nucleation in aluminum alloys [1-5]. The constituent particle's size and shape are important characteristics that influence crack nucleation. Also, differences in stiffness and thermal expansion between the inclusion and the surrounding matrix can introduce a localized stress concentration in and around a particle which increases the likelihood of fatigue crack formation [1]. Fatigue cracks often form at inclusions by one of three mechanisms: inclusion cracking, debonding of the interface between the inclusion and matrix, or cracking at lines of slip in the surrounding matrix [1-5].

Fatigue cracks were observed to initiate at slip lines around large (> 1 μm) inclusion clusters containing iron and silicon in 2024-T3 aluminum by Grosskreutz and Shaw [3]. Bowles and Schijve[4] observed that cyclic straining weakens and deteriorates the particle-matrix interface, increasing the susceptibility to debonding. Kung and Fine [5] observed that the shape of the various particles influenced the crack formation mechanism, resulting in cleavage of the elongated ß-phase (Al_7Cu_2Fe) particles and debonding of the spherical S-phase (Al_2CuMg) particles. Miyasato, Magnusen, and Hinkle [6] determined that Al_7Cu_2Fe and Mg_2Si were the most common constituent particles in a 7050-T7451 aluminum alloy. Although the Si containing particles were more numerous, they were smaller and played less of a role in fatigue crack formation than the larger Fe containing particles [6].

Newman *et al.* [7-9] found that fatigue cracks formed at inclusion and inclusion clusters in thin sheet 2024-T3 aluminum. The nucleation site was observed to quickly form a semi-elliptical surface crack approximately the size of the inclusion. The average observed defect (inclusion) size was 3 μm wide by 12 μm deep [8]. Kung and Fine [5] observed that most cracks initiated at constituent particle sizes greater than 6 μm. Murakami and Endo [10-12] used the square root of the cross-sectional area as a parameter to model the fatigue limit of internal and surface defects in steels. In addition, their experiments showed that fatigue strength is governed by one critical inclusion, not by the presence of many inclusions [11].

In summary, inclusions have been commonly observed as primary fatigue crack nucleation sites in aluminum alloys. The literature shows that the mechanisms of fatigue crack formation at constituent particles are dependent on the slip characteristics of the matrix, the relative properties of the inclusion and the matrix, the inclusion size and the strength of the particle matrix interface.

When a fatigue crack is small or roughly the size of a microstructural defect, its behavior is influenced primarily by microstructural features, including grains and inclusions [13]. The local properties of individual features often vary from the overall properties of the material and as a result, the crack growth behavior of small cracks differs from that of long cracks. The small crack effect is the phenomenon where small cracks grow at faster rates than long cracks and at stress intensity factors below the long crack threshold [7, 13-15]. These observations are significant because the growth of small cracks using long crack growth rate data results in non-conservative life predictions.

DETERMINISTIC CRACK GROWTH MODELING

The short and long crack growth behavior of fatigue cracks is distinguished by the relative size of the microstructure. When a fatigue crack spans two or more grains, the local effects are negligible and the crack can be considered a long crack that can be represented with linear elastic fracture mechanics (LEFM) [14]. When the fatigue crack is approximately the size of the microstructural features, the small crack effect must be considered. Newman [7] proposed that the small crack effect can be explained by plasticity effects and crack closure. Newman's closure model calculates the crack opening stress, S_o, when the crack becomes fully open. The crack-opening stress is used to determine the effective stress intensity factor range, ΔK_{eff}, according to the following equation [7]:

$$\Delta K_{eff} = \left(\frac{S_{max} - S_o}{S_{max} - S_{min}} \right) \Delta K \tag{1}$$

where S_{min}, S_{max} and S_o are the minimum, maximum and crack opening stresses, respectively. The crack closure model allows crack growth rate data at various R ratios (S_{min}/S_{max}) and stress levels to be collapsed to a single $\frac{da}{dN}$ versus ΔK_{eff} plot for a material.

When the crack is very small, it is assumed to be fully open, which implies that the opening stress is equal to the minimum stress ($S_o = S_{min}$) regardless of the stress ratio. In which case, the effective stress intensity factor range will equal the stress intensity factor range ($\Delta K_{eff} = \Delta K$) [7]. As the crack grows, it begins to undergo transient crack closure, which is accounted for by Newman's crack closure model. Newman's FASTRAN II computer program [16] is a life prediction model that utilizes the ΔK_{eff} crack growth rate data.

This type of total fatigue life model represents crack growth entirely as a propagation process by accounting for small crack growth. Crack propagation from a microstructural flaw represents a large portion (50-90%) of the total fatigue life of a specimen [8]. Fatigue cracks have been observed to form in the initial cycles of loading in plain carbon steels [14] and

aluminum alloys [7, 15, 17]. The total fatigue life of a specimen can be assumed to equal the number of cycles for crack propagation of a microstructural size flaw through the small and long crack growth regimes.

MATERIAL VARIABILITY

The microstructure of 2024-T3 aluminum contains constituent particles of various shapes and sizes. The material used in this study was 2.54 mm (0.1") thick. The aluminum was rolled into sheet during manufacturing, eliminating the presence of micropores. During the rolling process, the inclusions are often broken and cracked and a directionality with elongated grains is introduced in the material. The orientations of the microstructural planes for the single edge notch tension (SENT) specimen used in this study are shown in Figure 1.

The aluminum used in this study was produced in 1976 and was from the same lot tested by Virkler [18] in his study of long crack growth variability. The age of this material is significant because the particle size distribution and cleanliness of the microstructure are consistent with material presently on aging aircraft. The microstructure of the Short Transverse-Transverse (ST) plane obtained from the optical and scanning electron (SEM) microscopes is shown in Figures 2 and 3, respectively. The ST plane, perpendicular to the rolling and to the loading direction, was examined because fatigue cracks form at inclusions in this plane. Distributions of particle area, length, and width were collected for the ST plane using IMIX image analysis software [19] . A total of 3799 inclusions were analyzed in 16 locations on the ST plane. Each distribution of particle sizes was fit to a three parameter log-normal density function:

$$f(x) = \frac{1}{(x - \tau)\sigma\sqrt{2\pi}} \exp\left\{\frac{-(\ln(x - \tau) - \mu)^2}{2\sigma^2}\right\} \qquad (2)$$

where τ, σ and μ equal the threshold, shape and scale parameters, respectively. The distribution of particle areas is shown in Figure 4 and the coefficients for the log-normal distributions are contained in Table 1. The threshold parameter of the log-normal distribution was obtained by minimizing the Kolmogorov D statistic. The distribution of inclusion sizes collected for the ST plane for aluminum 2024-T3 is consistent with distributions reported in the literature by Miyasato, Magnusen and Hinkle [6] for aluminum 7050 and Bucci, Konish and Warren [20] for aluminum 2024.

EXPERIMENTAL TESTING

An experimental test program was conducted to obtain insight into the crack formation and growth processes and to investigate the characteristics of the crack nucleation sites. In this study, a single edge notch tensile (SENT) specimen similar to the AGARD specimen [7] was used. For the AGARD specimen, the nominal dimensions for specimen length, width, thickness, and notch radius are 305 mm, 50 mm, 2.3 mm, and 3.18 mm, respectively. In this study, the dimensions for specimen length, width, thickness, and notch radius are 203 mm, 45 mm, 2.54 mm, and 2.8125 mm, respectively. Both specimens have a stress concentration factor K_t of 3.17.

Crack nucleation and short crack growth are greatly influenced by surface preparation. Accordingly, machining and chemical polishing procedures, similar to those used in the AGARD studies [7], were used in an effort to reduce residual stresses and promote crack nucleation in the center of the notch. The notch was machined with a series of incrementally decreasing cuts and the specimen was then chemically polished for 5 minutes in a solution of 80% phosphoric acid, 5% acetic acid, 5% nitric acid and 10% de-ionized water, by volume [7].

The specimens were tested in a closed-loop servo-hydraulic test machine with an R ratio of 0.01 and an applied stress level range (ΔS) of 120 MPa. The life to breakthrough (through thickness crack) and life to failure were recorded for each specimen. Acetate replicas

were taken every 10,000 cycles according to the procedure for measuring crack growth from replicas developed by Swain [21]. The replicas were examined to determine the crack location and width of the inclusion that nucleated the crack. In addition, the fracture surfaces were analyzed to determine the length and width of these crack nucleating inclusions and their compositions using energy dispersive spectroscopy (EDS).

EXPERIMENTAL RESULTS

A total of seven experimental tests were conducted. One of the seven specimens was considered to have infinite life as no cracks formed within 500,000 cycles. The experimental fatigue lives, shown as a cumulative distribution function (CDF)[1] in Figure 5, are consistent with the results from the AGARD study. The fatigue lives were observed to have a large variability.

The crack nucleation sites were located by tracing cracks backward through the series of replicas. In every case, the cracks were traced back to an inclusion or a hole left where an inclusion had pulled out. The replicas were extremely helpful in determining the exact location of the crack nucleation sites, especially on the fracture surfaces where microstructural features were used as reference points. In several specimens, multiple fatigue cracks (1 to 5) were observed to nucleate along the bore of the notch and two cracks often coalesced to form a dominant crack. The amount of fatigue life in crack coalescence and growth of the dominant crack was small when compared to crack formation and growth of a small crack.

The sizes of the crack nucleating particles were measured from sputtered replicas (LS plane) and fracture surfaces (LS and ST planes). Figure 6 shows a typical crack nucleation site obtained from a replica of the LS plane and Figure 7 shows the same nucleation site on the actual fracture surface. The particle width (2a) and height were measured from the replicas. In

---

[1] The cumulative distribution function (CDF) is determined by ordering the experimental fatigue lives from lowest to highest, then plotting the data with the ordinate being the data points equally spaced between 0 and 1 and the abscissa being the fatigue lives.

the cases where the nucleation site was the dominant crack that led to failure, the inclusion width (2a) and length (c) in the ST plane were measured from the fracture surface. The crack nucleating particle was sometimes wider and more damaging than it appeared on the surface.

The sizes of the crack nucleating particles corresponded to the largest particles in the overall inclusion size distribution. This is best illustrated in the histograms shown in Figures 8 and 9 for the measured lengths and widths. The open bars show the measured histogram for the inclusion size distribution in the ST plane and the solid bars are the inclusion sizes corresponding to the dimensions of the observed nucleating flaw. These experimental measurements show that the distribution of particles that nucleated fatigue cracks were located in the tail of the overall distribution.

The composition of the crack nucleation sites was measured using EDS. The majority of particles that nucleated fatigue cracks contained iron, manganese, copper and aluminum. The iron containing particles were likely Al_7Cu_2Fe, which is consistent with the findings of Miyasato, Magnusen, and Hinkle [6], and Kung and Fine [5]. In several cases, the crack nucleating particles were observed to contain silicon, copper, and aluminum. These particles were possibly Mg_2Si particles, which are commonly found in aluminum alloys [6]. The magnesium was likely not detected because of limitations of EDS in detecting elements with low atomic numbers. The iron containing particles were generally larger and were the more commonly observed fatigue crack nucleation site.

In addition, the crack nucleation sites were observed to have formed in the notch within +/- 13.5 degrees from the normal. The angle of crack location is significant because there is a stress gradient that results from the presence of the notch. The region on the notch surface described by this angle corresponds to the notch surface area where the stress is within approximately 93% of the maximum according to Kirsch's elasticity solution for a hole in an infinite plate [22]. In addition, fatigue cracks were found to nucleate within the middle 50% of the specimen thickness. This result was expected as the chemical polishing rounded the notch corners which decreased the likelihood of a crack starting at the corner.

The experimental test program has shown that: 1) a large amount of variability is observed in fatigue life, 2) the fatigue cracks nucleated from inclusions and 3) the inclusion sizes that nucleated fatigue cracks varied in size, but were primarily from the upper tail of the distribution. The stochastic nature of fatigue and the experimental results encourages a probabilistic approach to modeling the fatigue process.

PROBABILISTIC MODELING

A probabilistic model has been developed by Laz and Hillberry [23, 24] (and since refined) that assumes the initial flaw sizes can be represented by the inclusion size distribution. The model uses a Monte Carlo simulation where, for each trial, a particle area is randomly selected from the previously determined log-normal distribution of particle areas. The resulting initiating flaw size is assumed to be a semi-circular crack with an area equal to that of the selected particle size, because fatigue cracks have been observed to quickly grow into a semi-circular shape (Pearson [17] and Newman and Edwards [7, 15]). The initial crack, which was assumed to be located at the center of the notch bore in the SENT specimen, was then grown forward using the deterministic life prediction model, FASTRAN II [16]. The number of cycles for the crack to form was assumed to be very small, and accordingly, fatigue life was modeled entirely as crack propagation. For this study, 1000 simulation trials in the Monte Carlo simulation were found to be sufficient.

FASTRAN II [16] is a life prediction program that uses a crack closure model to determine the opening stress level as the crack grows along the ΔK_{eff} crack growth curve. Newman's ΔK_{eff} crack growth curve for 2024-T3 aluminum [7] was used. Since ΔK_{eff} is corrected for the effects of plasticity and closure, this crack growth law is applicable for short and long cracks and is valid for constant and variable amplitude loading conditions. Also, the constraint factor transitions from flat to slant crack growth to account for the complex stress state in thin sheet materials.

The probabilistic model results in a predicted distribution of fatigue lives that can be compared to experimental values. Results can be presented for the experimental geometry from both this study and the AGARD study [7, 15] for a variety of stress levels.

The longest fatigue lives, which correspond to the smallest inclusion sizes, are governed by the ΔK threshold value. The threshold represents the ΔK value below which a crack will not propagate. Newman [7, 15] has reported a short crack ΔK_{th} of 1.05 MPa-m$^{1/2}$ for 2024-T3 aluminum. This value results in unrealistically long fatigue lives when incorporated into the FASTRAN II model. Accordingly for this study, to determine the threshold value (ΔK_{th}) to bound the upper portion of the cumulative distribution function, the experimental fatigue life data is utilized. The threshold value is determined by fitting the predicted data to the longest fatigue life that actually failed. A runout was not used as the fitting point, because it is assumed to have infinite life and does not correspond to an actual fatigue life. Experimental fatigue lives from three stress levels (R=0, S_{max} = 110, 120 and 145 MPa) [7] resulted in a ΔK_{th} of 1.36 MPa-m$^{1/2}$. The observation, that this threshold is applicable to all three of the stress levels analyzed, implies that ΔK is a valid threshold parameter.

PROBABILISTIC MODEL RESULTS

The probabilistic model was evaluated for the experimental specimen geometries and stress conditions from both this study (R=0.01 and ΔS = 120 MPa) and the AGARD study [7] (R=0.0 and ΔS = 110, 120 and 145 MPa). The resulting predicted fatigue life distributions can be compared to the experimental life data in an S-N curve (Figure 10). The probabilistic model conservatively predicts the most critical, shortest fatigue lives and the overall range of values. The shortest fatigue lifetimes correspond to the largest, most damaging inclusion sizes.

The predicted and experimental fatigue lives can be more clearly evaluated by comparing the cumulative distribution functions. The CDF comparison for the experimental results from this study are shown in Figure 11. The CDF results for the AGARD specimen

with an R ratio of 0 and maximum stress levels of 110, 120, and 145 MPa are shown in Figures 12, 13 and 14, respectively. At all three stress levels, the probabilistic model predicted the shortest fatigue lives and the variability in lifetimes. At the lower stress levels, the probabilistic model closely predicted the shorter fatigue lives, but underpredicted the longer lifetimes. The Kolmogorov D test showed that the differences between the predicted and experimental fatigue life distributions are not statistically significant.

In addition, a direct one-to-one comparison of fatigue life was made for the experimental specimens. In this case, the dominant fatigue crack nucleation site was used as the initial crack size input into the FASTRAN II life prediction model [16]. The resulting predicted and experimental fatigue life comparisons are shown in Figure 15. This prediction could not be carried out for specimen 5-049-3, because the crack size was too unsymmetric to be grown. For about half of the specimens, the FASTRAN II life predictions are close to the experimental values. In several cases, there are considerable differences between the predicted and experimental lives. This observation can likely be explained by the presence of other mechanisms in the fatigue behavior, mainly the combined effects of nucleation life and variability in the small crack growth regime. In the experimental tests at the 120 MPa stress level, 43% of the specimens nucleated cracks within the first 10,000 cycles. However, roughly 28% of the specimens had significant nucleation lives greater than 100,000 cycles. In addition, slow crack growth in the small crack regime was observed in several specimens. The slow growth rates are likely the result of a crack growing through a grain boundary or a grain of different orientation. The effects of nucleation life and small crack growth rate variability are significant and need to be investigated further.

CONCLUSIONS

The role of inclusions in fatigue crack formation has been investigated. An experimental test program was conducted on SENT specimens made from 2024-T3 aluminum.

Fatigue cracks were observed to form at inclusions and these crack nucleating inclusions were primarily from the tail of the inclusion size distribution. The distribution of inclusion sizes was used as the stochastic input into a probabilistic life prediction model to predict the variability in experimental fatigue lives. The probabilistic model, used in conjunction with the FASTRAN II crack closure model, accurately predicted the shortest experimental fatigue lives and the range of values. Further investigation into the effects of small crack growth rate variability and nucleation life is necessary.

ACKNOWLEDGMENT

REFERENCES

1. Suresh, S. Fatigue of Materials. Cambridge: Cambridge University Press. 1991.
2. Tanaka, K. and Mura, T. "A Theory of Fatigue Crack Initiation at Inclusions." Metallurgical Transactions A. 13A(January): 117-123. 1982.
3. Grosskreutz, J.C. and Shaw, C.G. "Critical Mechanisms in the Development of Fatigue Cracks in Aluminum 2024." 2nd International Conference on Fracture. Brighton. 1969.
4. Bowles, C.Q. and Schijve, J. "The Role of Inclusions in Fatigue Crack Initiation in an Aluminum Alloy." International Journal of Fracture. 9: 171-179. 1973.
5. Kung, C.Y. and Fine, M.E. "Fatigue Crack Initiation and Microcrack Growth in 2024-T4 and 2124-T4 Aluminum Alloys." Metallurgical Transactions A. 10A: 603-610. 1979.
6. Miyasato, S.M., Magnusen, P.E. and Hinkle, A.J. "Constituent Particle Distributions in 7050 Thick Plate." ONR Contract No: N00014-91-C-0128. ALCOA Technical Center. 1993.
7. Newman, J.C., Jr. and Edwards, P.R. "Short Crack Growth Behaviour in an Aluminum Alloy - An AGARD Cooperative Test Programme." AGARD R-732. 1988.
8. Newman, J.C., Jr., Phillips, E.P., Swain, M.H. and Everett, R.A., Jr. "Fatigue Mechanics: An Assessment of a Unified Approach to Life Prediction." Advances in Fatigue Lifetime Predictive Techniques, ASTM STP 1122. Mitchell, M.R. and Landgraf, R.W., ed. Philadelphia: American Society for Testing and Materials. 5-27. 1992.
9. Newman, J.C., Jr., Wu, X.R., Venneri, S.L. and Li, C.G. "Small Crack Effects in High-Strength Aluminum Alloys." NASA-RP-1309. 1994.
10. Murakami, Y. and Endo, M. "Effects of Defects, Inclusions, and Inhomogeneities on Fatigue Strength." Fatigue. 16(April): 163-182. 1994.
11. Murakami, Y. "Effects of Small Defects and Nonmetallic Inclusions on the Fatigue Strength of Metals." JSME International Journal, Series I. 32(2): 167-180. 1989.

12. Murakami, Y. and Endo, M. "Effects of Hardness and Crack Geometries on ΔK_{th} of Small Cracks Emanating from Small Defects." The Behaviour of Short Fatigue Cracks. Miller, K.J. and de los Rios, E.R., ed. London: Mechanical Engineering Publications. 275-293. 1986.
13. Hudak, S.J., Jr. "Small Crack Behavior and the Prediction of Fatigue Life." Transactions of the ASME. 103(January): 26-35. 1981.
14. Miller, K.J. "The Short Crack Problem." Fatigue of Engineering Materials and Structures. 5(3): 223-232. 1982.
15. Edwards, P.R. and Newman, J.C., Jr. "An AGARD Supplemental Test Programme on the Behaviour of Short Cracks Under Constant Amplitude and Aircraft Spectrum Loading." AGARD R-767. 1990.
16. Newman, J.C., Jr. "FASTRAN II - A Fatigue Crack Growth Structural Analysis Program." NASA-TM-104159. NASA Langley Research Center. 1992.
17. Pearson, S. "Initiation of Fatigue Cracks in Commercial Aluminum Alloys and the Subsequent Propagation of Very Short Cracks." Engineering Fracture Mechanics. 7: 235-247. 1975.
18. Virkler, D.A. "The Statistical Nature of Fatigue Crack Propagation." Journal of Engineering Materials and Technology, Transactions of the ASME. 101(2): 148-153. 1979.
19. IMIX Software. Princeton Gamma-Tech. 1993.
20. Bucci, R.J., Konish, H.J. and Warren, C.J. "Aluminum Technology Advances for Aircraft Safety and Global Competiveness." ASM International - Lafayette Chapter Meeting. 1995.
21. Swain, M.H. "Monitoring Small-Crack Growth by the Replication Method." Small-Crack Test Methods, ASTM STP 1149. Larsen, J.M. and Allison, J.E., ed. Philadelphia: American Society for Testing and Materials. 1992.
22. Timoshenko, S.P. and Goodier, J.N. Theory of Elasticity. New York: McGraw-Hill Pub. Co. 1934.
23. Laz, P. J., and Hillberry, B. M., "The Role of Inclusions in Fatigue Crack Formation in Aluminum 2024-T3," Fatigue 96, The Sixth International Fatigue Congress, Berlin, Germany, May 6-10, 1996.
24. Laz, P. J., and Hillberry, B. M., "A Probabilistic Model for Predicting Fatigue Life Due to Crack Formation at Inclusions," International Committee on Aeronautical Fatigue (ICAF), 18th Symposium, Melbourne, Australia, May 3-5, 1995.

Table 1. Log-normal density function coefficients for various particle characteristics in the ST plane.

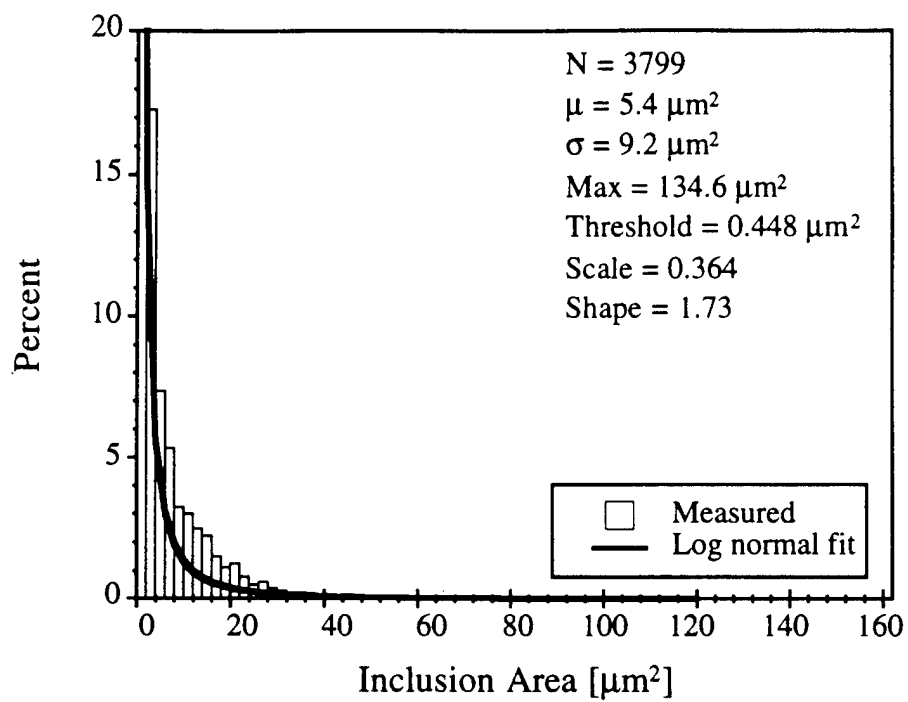| Characteristic	Threshold (τ)	Shape(σ)	Scale (μ)
Area [μm^2]	0.448	1.727	0.364
Width (2a) [μm]	0.259	0.795	0.331
Length (c) [μm]	0.522	0.900	0.433

Figure 1. Specimen planes in a single edge notch tension (SENT) specimen.

Figure 2. Sample microstructure of the ST plane of aluminum 2024-T3 under the scanning electron microscope at 400X.

Figure 3. Sample microstructure of the ST plane of aluminum 2024-T3 under the scanning electron microscope at 500X.

Figure 4. Distribution of inclusion areas obtained from the ST plane and the log-normal distribution.

Figure 5. Experimental cumulative distribution functions (CDF) for fatigue life to breakthrough.

Figure 6. SEM micrograph of a typical crack nucleation site taken from an acetate replica (60,000 cycles, 1000X).

Figure 7. SEM micrograph of a typical crack nucleation site taken from the fracture surface (2000X).

Figure 8. Comparison of the lengths of the crack nucleating particle sizes and the overall distributions.

Figure 9. Comparison of the widths of the crack nucleating particle sizes and the overall distributions.

Figure 10. S-N curve comparison of experimental and predicted fatigue lives.

Figure 11. Experimental and predicted cumulative distribution functions (CDF) for fatigue life to breakthrough. (This study's specimen, R=0.01, and $\Delta S = 120$ Mpa).

Figure 12. Experimental and predicted cumulative distribution functions (CDF) for fatigue life to breakthrough. (AGARD specimen, R=0, and $S_{max} = 110$ MPa).

Figure 13. Experimental and predicted cumulative distribution functions (CDF) for fatigue life to breakthrough. (AGARD specimen, R=0, and $S_{max} = 120$ Mpa).

Figure 14. Experimental and predicted cumulative distribution functions (CDF) for fatigue life to breakthrough. (AGARD specimen, R=0, and $S_{max} = 145$ MPa).

Figure 15. Comparison of experimental and predicted fatigue lives for individual specimens. (This study's specimen, R=0.01, and $\Delta S = 120$ Mpa).
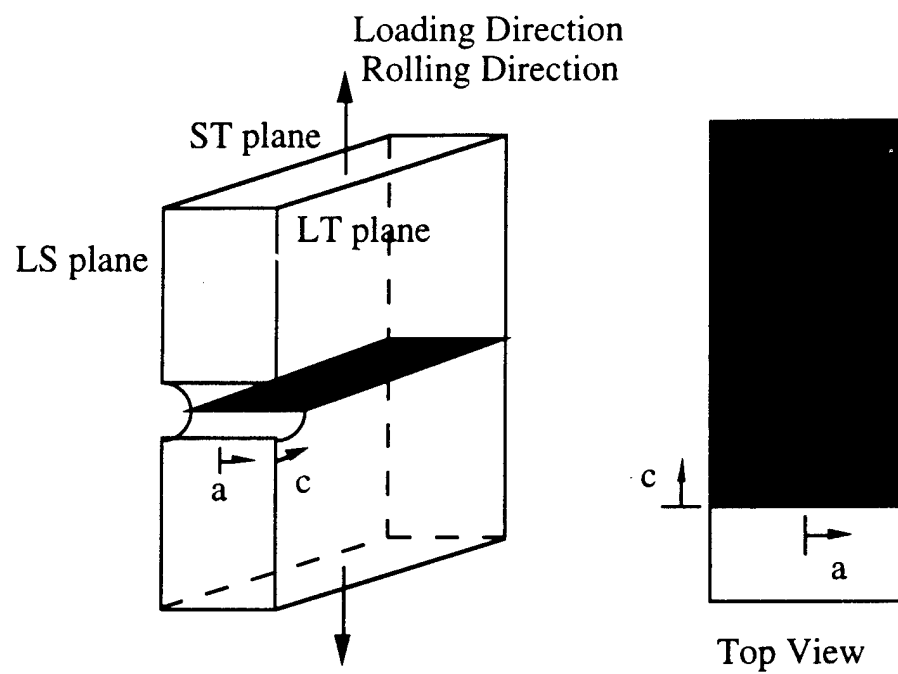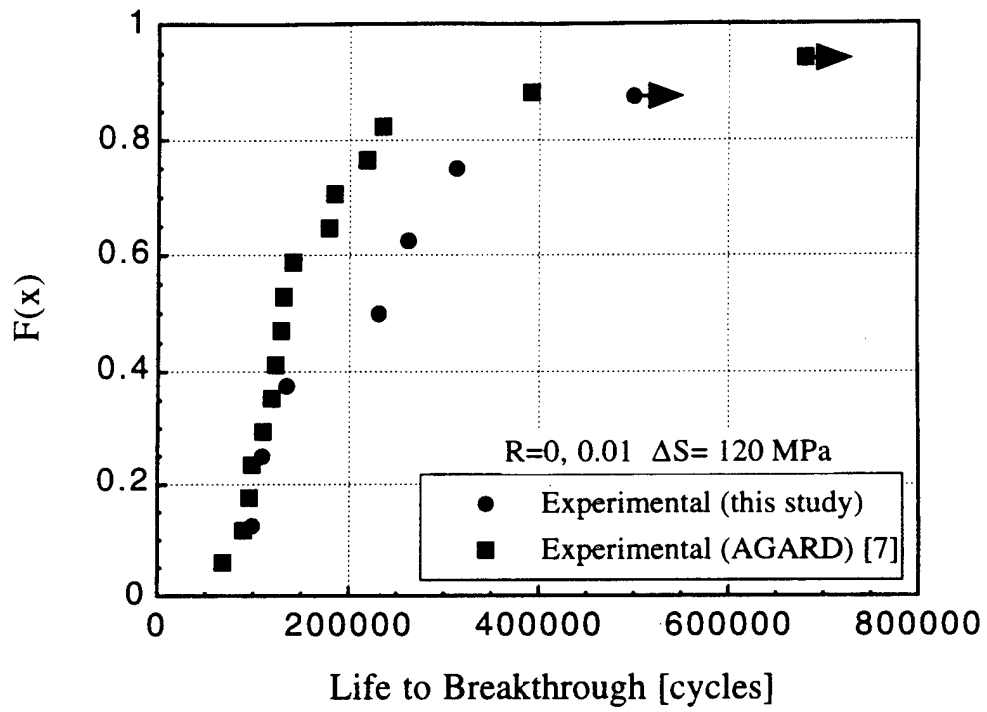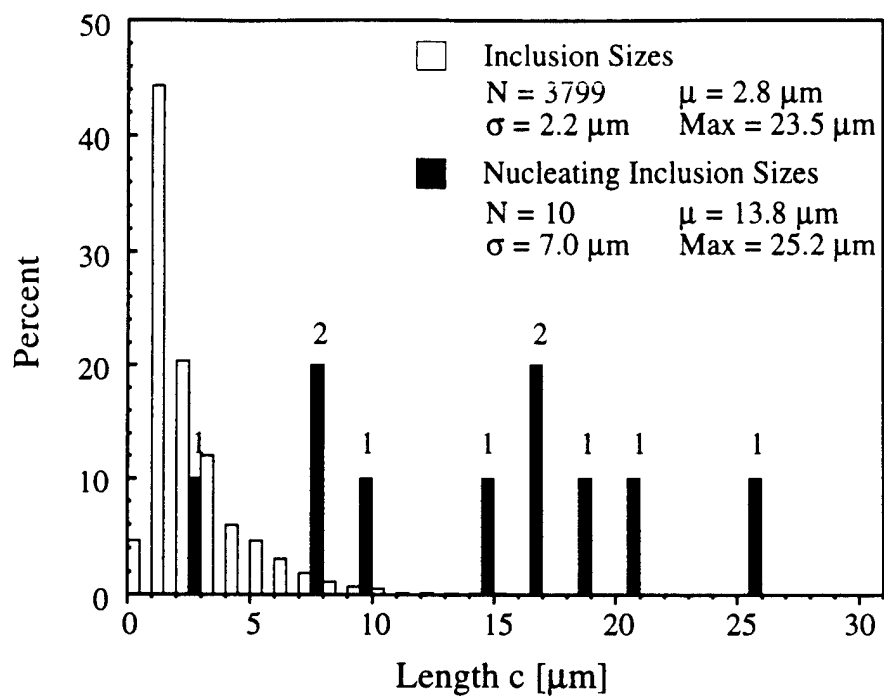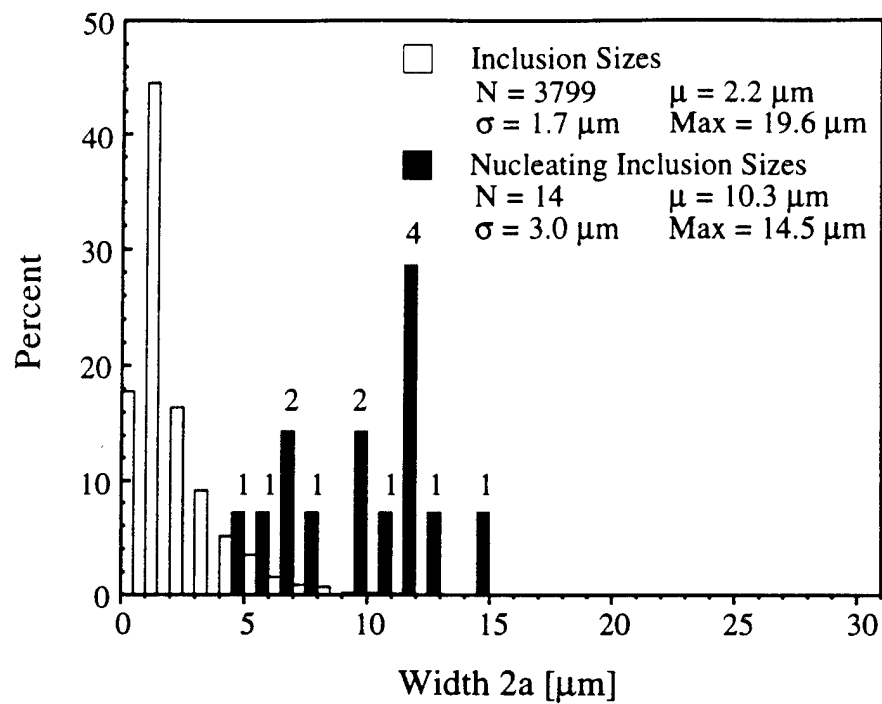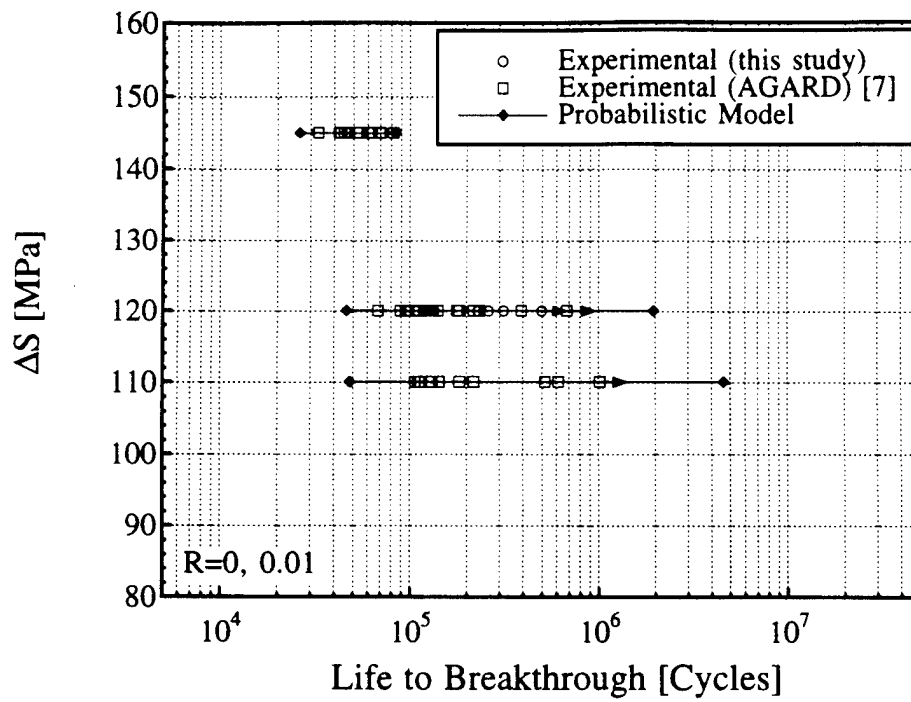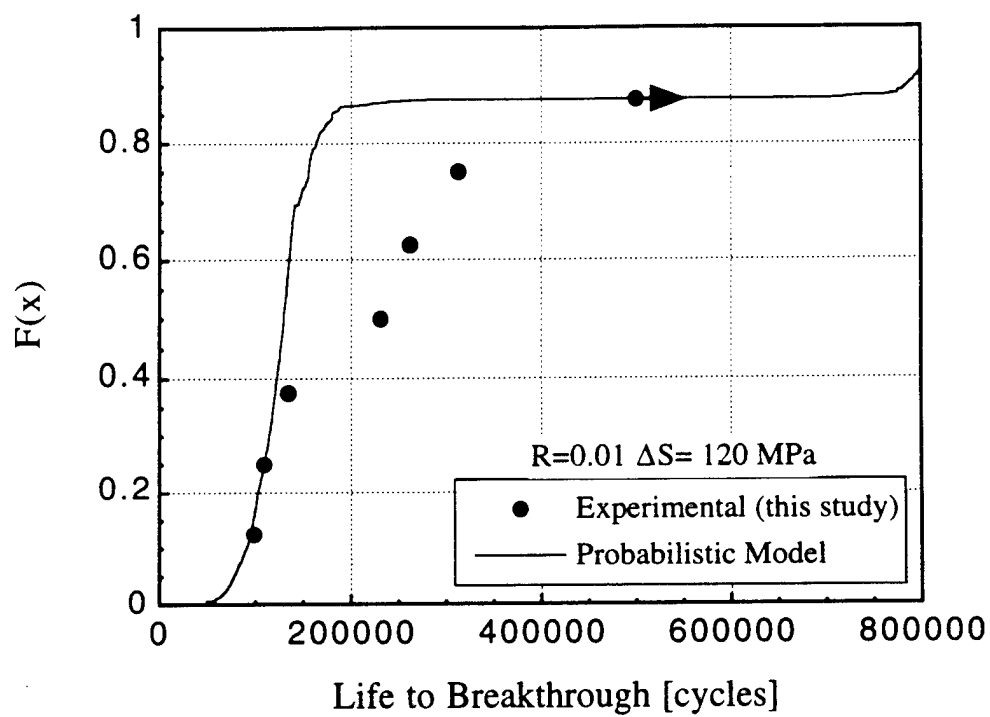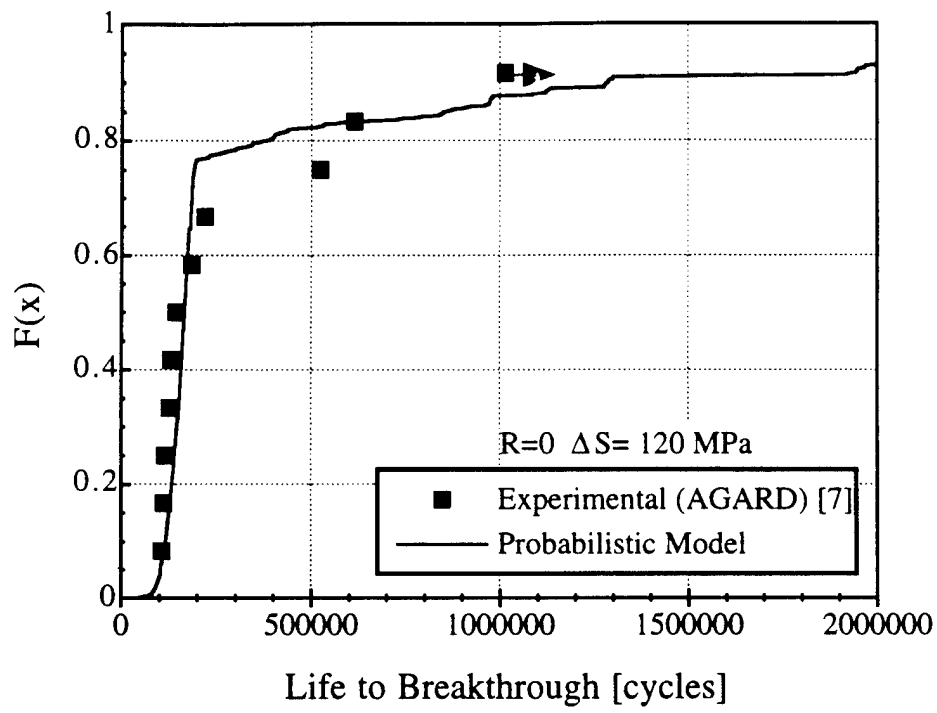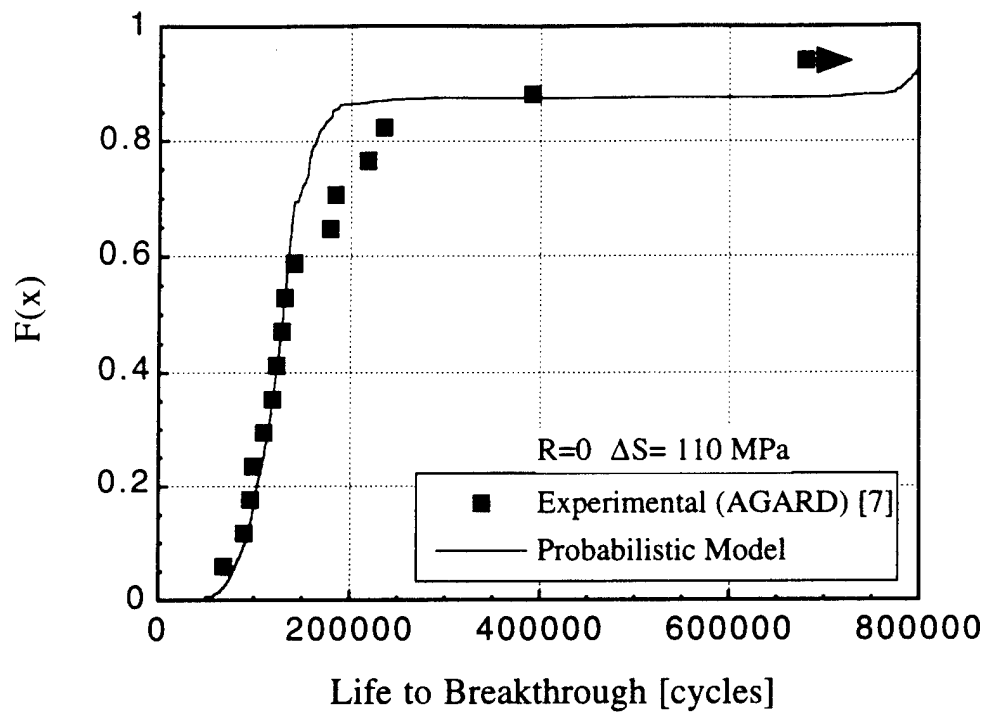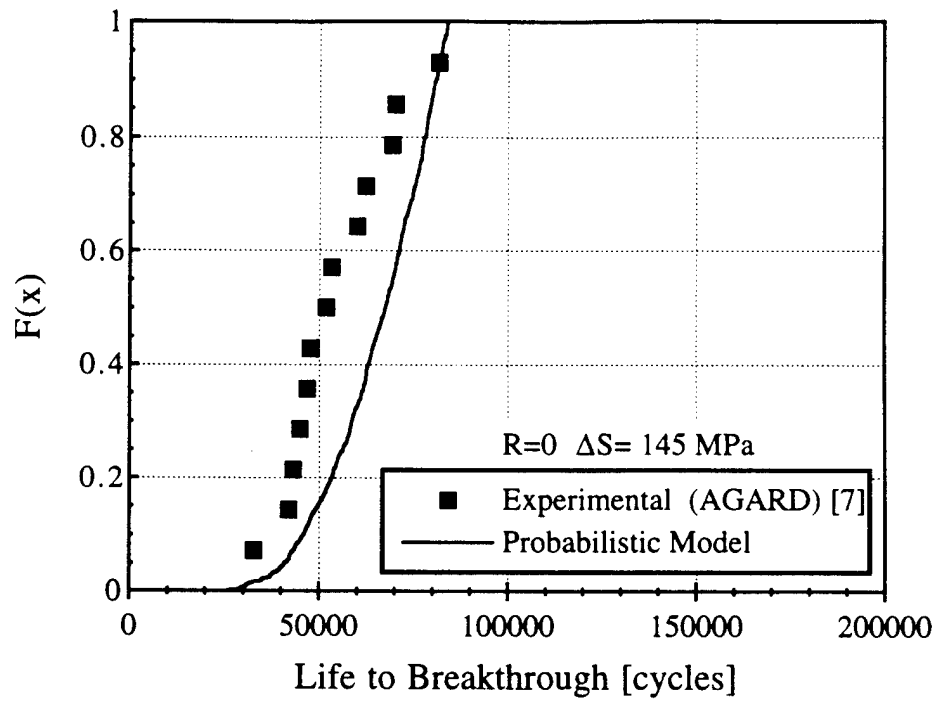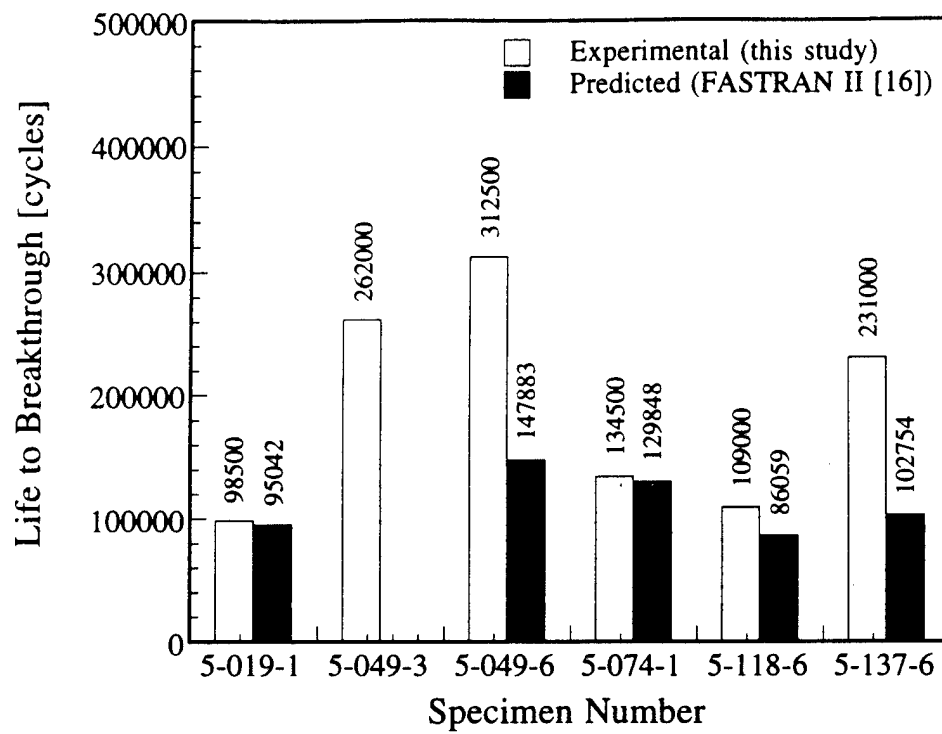
Loading Direction
Rolling Direction

ST plane

LT plane

LS plane

a   c

c

a

Top View

N = 3799
μ = 5.4 μm²
σ = 9.2 μm²
Max = 134.6 μm²
Threshold = 0.448 μm²
Scale = 0.364
Shape = 1.73

☐ Measured
— Log normal fit

R=0, 0.01 ΔS= 120 MPa

● Experimental (this study)
■ Experimental (AGARD) [7]

Life to Breakthrough [cycles]

25 μm

R=0.01 ΔS= 120 MPa
● Experimental (this study)
— Probabilistic Model

Life to Breakthrough [cycles]

R=0 ΔS= 120 MPa

■ Experimental (AGARD) [7]
—— Probabilistic Model

Life to Breakthrough [cycles]

R=0 ΔS= 110 MPa

- ■ Experimental (AGARD) [7]
- —— Probabilistic Model

Life to Breakthrough [cycles]

R=0 ΔS= 145 MPa

■ Experimental (AGARD) [7]
—— Probabilistic Model

Characterization of Fracture and Fatigue Behavior of Bonded Composite Repairs

Mr. John Klug
Mr. Scott Maley
Dr. C. T. Sun
School of Aeronautics and Astronautics. Purdue University
West Lafayette. Indiana 47907

ABSTRACT

Composite patches are bonded to a cracked metallic surface either symmetrically (double-sided) or unsymmetrically (single-sided). The stresses in the metallic panel are greatly affected by the repair symmetry. Unsymmetric repairs present the greatest challenge due to the presence of out-of-plane bending. Thermal residual stresses are present due to the thermal coefficient mismatch of the patch and aluminum plate. Debonding along an adhesive-adherend interface can reduce the patch effectiveness. A simple analysis using Mindlin plate theory is investigated to model the host and repair plate. The two plates are connected by an adhesive layer modeled by effective springs. Large deflection theory is used in the case of unsymmetric repairs. The springs are ineffective in the debond zone and are removed. Both the aluminum and debond cracks are characterized by fracture mechanics using the stress intensity factor and strain energy release rate, respectively. Experiments on aluminum 2024-T3 plate, AS4/3501-6 carbon/epoxy composite patch, and FM73 adhesive include determining the thermal residual stresses in the aluminum plate and debonding observations using an ultrasonic C-scan. Tests are conducted to examine the metallic and debond crack growth interaction on unsymmetric repairs.

INTRODUCTION

In order to extend the service life of an aging aircraft, the cracked components must be replaced or repaired. If the number of cracks is small and the crack size is small relative to the size of the component, it is often most economical to employ crack arrestment methods to regain the load carrying capacity of the component. A repair method using composite patches to reinforce the cracked structure has been shown to be very promising owing to the light weight, high stiffness and strength of the composite [1].

One of the most challenging aspects of bonded repair technology is stress analysis of the repaired structure. The difficulty arises from the fact that a plane stress metallic panel under in-

plane loading would develop highly complicated 3-D stresses if composite patches are bonded to its surfaces either symmetrically (double-sided) or unsymmetrically (single-sided). Unsymmetric repairs present the greatest challenge in modeling due to the presence of out-of-plane bending. The two side views show the bending induced from thermal residual stresses due to the thermal mismatch and from the off axis loading. Although it has been shown that double-sided repairs exhibit the most effective reinforcement, single-sided repairs provide a clear advantage when it is difficult or not possible to access both sides of a structure.

Many analysis techniques have been proposed [1]-[4]. However, not much combined analytic and experimental verification has been done at the present time. Perhaps the most extensive work has been done by Baker [5] for double sided repairs. Predictions of fatigue life are made including debond effects for many loading conditions. Debond size is destructively examined by removing the repair at high temperature and examining the oxidized aluminum surface from the debond zone.

Bending can cause a large variation of the stress intensity factor through the plate thickness. This can lead to curvature of the crack front in thick aluminum plates and makes prediction of the crack growth difficult. Large deflection is expected to play a role in the behavior of the plate when the mechanical loading is applied causing the bending shown in Figure 1b. The most interesting case is when the mechanical loading is applied after the effects of the thermal residual stresses have been taken into account.

The use of a full 3-D finite element model to perform stress analysis is computationally costly and can even cause ill conditioning when high aspect ratio elements are used for the thin patch and adhesive. In this paper, a simple analysis using Mindlin plate theory is investigated to model the host and repair plate and spring elements model the connecting adhesive layer. The aluminum crack is characterized by fracture mechanics using the stress intensity factor. The distribution of the strain energy release rate for a debond is calculated. A comparison and contrast between a double and single sided repairs with both thick and thin patches is achieved both numerically and experimentally. Fatigue crack growth data is taken using an ultrasonic C-scan to observe the debond crack. An optical microscope is used for the single sided repair aluminum crack growth. Quantitative comparisons between analysis and experiments are made.

MODEL AND ANALYSIS DESCRIPTION

Figure 2 shows a typical single-sided patch configuration. A complete derivation of the finite element model is given in Reference [3]. The plate nodes are located on the mid-planes of the aluminum plate and patch. The adhesive nodes lie along the patch-adhesive and adhesive-aluminum plate interfaces. Constraint equations are imposed on the patch-adhesive and adhesive-aluminum interfaces in order to enforce compatibility. The adhesive layer is modeled by three springs for the transverse shear stiffness in the xz and yz-planes and the axial stiffness in the z-direction.

The modified crack closure technique [7] is used to calculate the strain energy release rate. It is assumed that the strain energy released during crack extension is equal to the work needed to

close the opened crack surfaces. It is also assumed that the adhesive cracks along the aluminum crack region. Generally, the nodal forces and relative displacements from the geometric nonlinearity are nonlinear, and the energy required to close the crack front is the summation of the work done for each increment. However, it has been found that the relation between the nodal forces and relative displacements are linear at the crack tip. Thus, the work done for each increment is linear and a single step closure approach can be taken.

The strain energy release rate is computed for Mode I fracture loading. The same procedure can be used for mixed mode loading. A 4-noded Mindlin plate element (S4R) is used to model the aluminum plate. Figure 3 shows a 2-D finite element model for the aluminum plate near the crack tip at point b. Assume the crack front extends from b to c. Since the extension, Δa, is very small, the crack opening displacements at b are taken to be the same as those at a. Thus, the strain energy release rate can be calculated as the work done by the nodal force (moment), F_y^b (M_x^b), in closing the crack opening displacement (rotation), u_y^a (ψ_y^a). The total strain energy release rate is obtained as

$$\overline{G}_{total} = \overline{G}_u + \overline{G}_\psi = \frac{1}{2\Delta a}\left\{F^b\left(u_y^a - u_y^{a'}\right)\right\} + \frac{1}{2\Delta a}\left\{M^b\left(\psi_y^a - \psi_y^{a'}\right)\right\} \tag{1}$$

where $\overline{G}_u$, $\overline{G}_\psi$ and $\overline{G}_{total}$ are the transitional, rotational, and total strain energy release rates, respectively. Note that these strain energy release rates are the respective energies released (over the total plate thickness) per crack tip.

The fracture parameter for the aluminum crack is often given in terms of the stress intensity factor. The maximum stress intensity factor is located on the tension side of the plate and is composed of

$$K_I = K_u + K_\psi\left(\frac{2z}{t_s}\right) = \sqrt{\frac{\overline{G}_u E_s}{t_s}} + \sqrt{\frac{3\overline{G}_\psi E_s}{t_s}}\left(\frac{2z}{t_s}\right) \tag{2}$$

Cracking along the bond line is a key mode of failure in patch repair. This debond crack may propagate in the adhesive-aluminum or adhesive-patch interface. To predict debond crack growth behavior, the strain energy release rate along the crack front must be evaluated. The present double plate model can be employed to perform this task.

The debond crack always initiates from the location of the original crack in the aluminum plate. Based on some experimental results, we assume that the debond crack lies in the adhesive-repair plate interface. In fact, using the present plate model in conjunction with linear springs to represent the adhesive, the strain energy release rates for the two possible debond cracks turn out to be identical. The difference in fracture toughness of these two interfaces would determine the actual location of the debond crack.

To illustrate the procedure for calculating the strain energy release rate, we consider a small region in the neighborhood of the debond crack front. Figure 4 shows part of the finite

element model that includes four (4-noded) plate elements for the aluminum plate and 9 spring nodes (a_j^3, b_j^3 and c_j^3, j = 1, 2, 3). The debond crack front is at the line $b_1 b_2 b_3$. The top (lower adhesive) nodes b_j^3 and c_j^3 are tied to the corresponding bottom (aluminum plate) nodes b_j^4 and c_j^4, respectively, by the constraint conditions. The two sets of nodes a_j^3 and a_j^4 are not constrained because of the debond crack. The constraints result in reaction forces N_x, N_y, and N_z and moments M_x and M_y at these nodes. Note that the spring nodes have only reaction forces. The reaction forces and moments at a node are equal to the respective sums of the nodal forces and moments of all of the elements sharing this node.

The closure energy can be determined by assuming that the crack front extends from the current location b_j^3 - b_j^4 to c_j^3 - c_j^4. Since the extension Δa is very small, the crack opening displacements at b_j^3 - b_j^4 are taken to be the same as those at a_j^3 and a_j^4 before the assumed crack extension. Thus, the crack closure energy associated with a pair of nodes (say b_2^3 and b_2^4) can be expressed in the form

$$2U_{b_2} = N_x^3 \Delta u_x^3 + N_y^3 \Delta u_y^3 + N_x^3 \Delta u_x^3$$
$$+ N_x^4 \Delta u_x^4 + N_y^4 \Delta u_y^4 + N_z^4 \Delta u_z^4$$
$$+ M_x^4 \Delta \psi_x^4 + M_y^4 \Delta \psi_y^4$$

(3)

where N_i^3 and N_i^4 (M_i^4) are nodal constraining forces (moments) before crack extension at nodes b_2^3 and b_2^4, respectively, and u_i^3 and u_i^4 (ψ_i^4) are the nodal displacements (rotations) at nodes a_j^3 and a_j^4, respectively. Also, Δu_i^3 denotes the difference of the nodal displacements between nodes a_j^3 and b_j^3, and Δu_i^4 denotes the relative displacements between nodes a_j^4 and b_j^4.

The strain energy released over an area associated with the assumed crack extension can be calculated using eqn (3). The average strain energy release rate is obtained by dividing the total strain energy released by the local area. For example, the total strain energy release rate at b_2 is calculated as

$$G = \frac{U_{b_2}}{A}$$

(4)

where

$$A = \Delta a \times \frac{(l_1 + l_2)}{2}$$

The accuracy of such calculation depends on the finite element mesh, especially at the crack front.

The material properties for the graphite/epoxy repair (AS4/3501) are shown in Table 1. Two thickness of composite repair are chosen for comparison of both the single and double sided

repairs. Both 4 ply 0.508 mm and 8 ply 1.016 mm thick repairs are used. The aluminum sheet thickness. t_s, and adhesive thicknesses are is 3.175 mm and 0.1016 mm. respectively.

The first step in analysis is to determine the effect of the thermal residual stresses. Conventionally, the value of the temperature drop. ΔT, is taken as the difference in the ambient room temperature of the component and the curing temperature. For a typical adhesive like FM 73, the curing ΔT temperature is 120 °C and ambient room temperature is 20 °C making a ΔT of -100 °C. However, the actual value of ΔT is not well defined due to such things as the adhesive not hardening at 120 °C. Because of this uncertainty, an effective temperature drop ΔT_{eff} is proposed and defined as the temperature drop which can be adopted in a model without using temperature dependent material properties.

Two methods of determining this effective temperature drop have been proposed. The first method consists of curing an uncracked panel of composite/adhesive/aluminum to create the thermal residual stress. A strain gages is placed at the center on the surface of the composite panel. Next, the aluminum is dissolved with caustic NaOH solution. After removal of the aluminum, a strain measurement is again taken. This strain is used to match the strain from a finite element model by varying ΔT. For the single sided repair curvature measurements are taken from a profilometer and matched with a finite element model. It is found that ΔT_{eff} for the double sided repair is about -40 °C, and the single sided repair is in the range of -60 °C to -80 °C. Presently, more accurate techniques are being examined to obtain the value for the single sided repair. For this analysis ΔT_{eff} is chosen to be -70 °C.

Table 1. Composite Material Properties

Property	Graphite/Epoxy
E_1 (GPa)	138
E_2 (GPa)	9.7
E_3 (GPa)	9.7
G_{12} (GPa)	6.9
G_{13} (GPa)	6.9
G_{23} (GPa)	3.2
ν_{12}	0.3
ν_{13}	0.3
ν_{23}	0.49
α_1 ($10^{-6}(°C)^{-1}$)	-0.7
α_2 ($10^{-6}(°C)^{-1}$)	27.0
α_3 ($10^{-6}(°C)^{-1}$)	27.0

Table 2. Aluminum and Adhesive Material Properties

Property	Aluminum 2024-T3	Adhesive FM 73
E (GPa)	72.0	2.15
v	0.3	0.4
$\alpha\ (10^{-6}(^{\circ}C)^{-1})$	23.0	---

Only one half of the single sided and one quarter of the double sided repairs need to be modeled due to symmetry. Initially, the boundary conditions for the repair and aluminum plates are free to model the thermal residual stresses due to cure. Next the boundary at $y = L_s$ (half the aluminum sheet length) is clamped to model the grip condition. Finally, the load is increased to the maximum stress, σ_{max}. The displacements at the grip are also constrained to be equal during the loading.

EXPERIMENTAL PREPARATION

Figure 5 shows the geometry of the reinforced edge-cracked specimen. The aluminum alloy and the composite repair are 2024-T3 and AS4/3501-6 graphite/epoxy, respectively. Prior to bonding, the edge crack was initiated with a jewelers saw (0.008 in blade). A fatigue crack was propagated to a total crack length of about 13 mm. Note that the edges of the repair are not stepped and will thus give high edge stresses. The specimen is next prepared for the high temperature bonding.

One of the most critical steps in the bonding procedure is the aluminum surface preparation. Reference [1] details the required steps of the aluminum preparation and are briefly summarized as follows:

1. Surface degreasing: the aluminum surface of the repair area is thoroughly cleaned with Methyl Ethyl Ketone (MEK).
2. Abrasion: the repair area is abraded with aluminum oxide abrasive paper to remove the oxide layer and expose a clean metal surface.
3. Primer: a 1% solution of silane primer (gamma-glycidoxypropyltrimethoxy silane) is brushed onto the repair area for 10 minutes. The specimen is then air dried. The surface of the composite patch is only degreased and abraded.

Curing of the adhesive is done immediately following the aluminum surface treatment. FM73 (American Cyanamid) adhesive film is cured at 120° C for one hour. Note the composite is cured prior to the adhesive bonding cycle.

RESULTS AND DISCUSSION

The results include numerical results from finite element analysis and fatigue tests of both single and double sided repairs. Ultrasonic C-scans are taken of the repair area to show debonding. A through transmission technique with an immersion tank is used to detect

debonding. Two 10 MHz transducers with a 38.1 in focal length are used. Fatigue tests are performed on a 250 KN MTS and crack length for single sided repairs is measured using an optical microscope.

It is well understood that the single sided repair can affect the global geometry of a cracked structure due to thermal residual stresses arising from cure and to a mechanical in-plane load as shown in Figure 1. The effects of this geometrical change on the aluminum crack structure are not simple. In fact large deflection theory may be required to solve the problem [6]. Figure 6 shows the curvature of the midplane of the aluminum plate along the y-axis for the 8 ply repair for both linear and nonlinear or large deflection theory analyses with ΔT = -70 °C. Initially, the plate is curved due to the thermal residual stresses. As the in-plane mechanical load is increased, the plate flattens. Further increase of the load causes the plate to curve in the opposite direction. The plot shows that for this geometry there is little difference between the nonlinear and linear analysis.

Figure 7 shows the normalized stress intensity factor at both the aluminum plate midplane, Km and free edge, Kf versus the applied stress for both the nonlinear and linear solutions. The aluminum crack length is 12.7 mm. The stress intensity factor is normalized by the plane strain critical value, K_{Ic} for aluminum 2024-T3. The data is shown for ΔT = -70 °C. There is little difference between the linear and nonlinear solutions. Interestingly, the magnitude of the stress intensity factor is about the same for the 4 and 8 ply repairs. However, at high loads the stress intensity factor for the 4 ply is slightly higher than the 8 ply repair. At zero load, the 8 ply repair stress intensity factor is higher due to greater thermal residual stresses. Also note that the stress intensity factor at zero load is larger at the midplane. This is due to bending stresses in the aluminum plate arising from the thermal residual stresses. The maximum value of the stress intensity factor is at the aluminum-adhesive interface as opposed to the free edge. So imagine for a cyclic load from 0 MPa to a load greater than 10 MPa, the maximum value of the stress intensity factor will also shift from the inside interface to the free edge of the plate.

The double side repair results for both repair thicknesses are shown in Figure 8. The stress intensity factor is higher for the thicker repair at zero load when including thermal residual stresses. As the applied load is increased, the thicker repair becomes more effective than the thinner patch in reducing the stress intensity factor.

Strain energy release rate distributions for the single and double sided repairs are shown in Figures 9 and 10. The debond front and aluminum crack fronts are assumed to coincide. An ellipse with aspect ratio b*/a* = 0.2 is used to make comparisons of the repair geometry's. The strain energy release rate is plotted from the x-axis at the aluminum crack tip to the y-axis. Figure 9 shows that for two debond sizes, the distribution of the strain energy release rate is nearly equal for each of the thick and thin repairs. Also, the strain energy release rate increases near the free edge of the edge cracked specimen. Thus, one would expect the greatest debond growth near the free edge. Figure 10 shows that for double sided repair the magnitude of the strain energy release rate is higher for the thin patch. The strain energy release rate also increases near the free edge of the specimen as well. So the debonding characteristics for the single sided repair are similar for the thick and thin patches, but are different for the double sided repair.

Images of the ultrasonic C-scan are shown in Figures 11-14. The images are from fatigue loading taken at various cycles during the testing. The fatigue ranges for the single and double sided repairs are $\Delta\sigma$ = 68.95 MPa, R = 0 and $\Delta\sigma$ = 137.9 MPa, R = 0, respectively. Note no effort is made to avoid the transverse deflection change in the single sided repair mentioned by Belason [8] and shown in Figure 6 by increasing the minimum applied stress. The number of cycles in thousand (K) and crack position for the single sided repair, a_f, are indicated below the images. The aluminum crack for the single sided repair is tracked on the reverse side of the repair using an optical microscope. True aluminum crack positions for the double sided repairs are not indicated. It is felt that the aluminum fatigue crack is too fine to accurately measure the true crack tip position from the C-scan image.

The images in Figures 11 and 12 show that the debond and aluminum growth for the thin and thick repairs are similar. It seems that initially the debonding is very small as shown by the first image in each figure. Also, the debond does not seem to significantly cover the length of the aluminum crack. As the aluminum crack begins to penetrate the repair edge as shown in the next image, the debonding increases. However, there does not seem to be significant debonding. In fact, the debonding along the repair edge seems to be as much as along the aluminum crack. The final image shows the debonding after the aluminum crack has grown a little distance away from the repair edge.

The debonding for the thin and thick repairs shown in Figures 13 and 14 appears to be different. The thin repair seems to have more debonding along the aluminum crack over the entire fatigue life. Although the thick repair initially has more debonding. Also there is some debonding along the repair edge.

Predictions of the fatigue life are made by numerically integrating a Paris law.

$$N = \int_{a_i}^{a_f} \frac{da}{C(\Delta K)^m}$$

where a_f and a_i are the initial and final aluminum crack lengths, respectively. The material constants used for aluminum 2024-T3 are C = 4.086×10^{-10} and m = 2.318 [8]. Normally the materials constants are dependent on the R ratio, which is defined as the ratio of the minimum to maximum applied stresses.

Fatigue life data and predictions for the single sided repair are shown in Figure 15. The test data is labeled Test 1 and 2. Both repairs increase the fatigue life approximately 3.5 times the unrepaired specimen. It is immediately apparent that the thicker repair does not significantly improve the fatigue life. Kmax (the value of the stress intensity factor at peak applied load) is used instead of ΔK (Kmax - Kmin) for the predictions. Since there is a Kmin (the minimum value of the stress intensity factor) at zero load (for R = 0) due to the thermal residual stresses, this leads to an effective R ratio. Presently, R ratio dependent material constants C and m are not used for the analysis. The effect of debonding on the stress intensity factor is neglected because it was found that there was not a significant increase in stress intensity until the aluminum crack penetrates the repair. At this point significant debonding occurs as the repair performs like a lap

joint. Fatigue life cycle predictions using the stress intensity at the free edge, Nf, midplane, Nm and root mean square value, Nrms are indicated. Callinan et al. [9] showed the root mean square stress intensity factor as follows

$$K_{rms} = \sqrt{\frac{1}{t_s} \int_{-t_s/2}^{t_s/2} K^2(z) dz}$$

By substituting in eqn (2) into K(z) the following equation can be derived

$$K_{rms}^2 = K_m^2 + \frac{1}{3} K_f^2$$

The prediction using the free edge and midplane stress intensity factors span the test data. It seems using Krms to compute the fatigue life gives a very good conservative prediction for both the thick and thin repairs.

Figure 16 shows the fatigue life data for the double sided repairs. The test data is only shown at the point where the fatigue crack penetrates or travels completely through the repair. It is evident that the thicker patch leads to a greater fatigue life. Analysis is performed to predict the number of cycles for the fatigue crack to penetrate the repair. Analysis without debonding can predict the results for the thick, but not the thin repair. Since the thin patch has significantly more debond growth over the entire aluminum crack length, the effects of debonding on the stress intensity factor is added. The debonding effects were achieved by assuming an elliptic debond of approximately the same size as the actual debond from the C-scan image. This leads to conservative predictions of the fatigue life as shown in the figure.

CONCLUSIONS

In this study, the bonded composite single and double sided patches are investigated. Thermal residual stresses in the aluminum panel induced during bonding can significantly affect the effectiveness of patching and therefore must be accurately determined. Double sided repairs are much more effective at increasing fatigue life. Increasing the thickness of a low coefficient of thermal expansion composite like graphite/epoxy may not have a significant effect on fatigue crack growth for single sided repairs. It seems that Kmax can be effectively used to estimate the fatigue life. Debond growth must be taken into account in the stress intensity factor and subsequent fatigue life when there is significant debonding along the aluminum crack. Since the stress intensity factor varies through the thickness for single sided repairs, the fatigue life computed using Krms seems to accurately estimate the fatigue life.

## ACKNOWLEDGMENTS

REFERENCES

[1] Baker, A. A. and Jones, R., *Bonded Repair of Aircraft Structure*, Martinus Nijhoff Publishers, Dordrecht, The Netherlands, (1988).

[2] Chue, C., Chang, L., and Tsai, J., "Bonded Repair of a Plate With Inclined Central Crack Under Biaxial Loading," *Composite Structures* **28**, pp. 39-45, (1994).

[3] Sun, C., Klug, J., and Arendt, C., "Analysis of Cracked Aluminum Plates Repaired with Bonded Composite Patches," *AIAA Journal* **34**, pp. 369-374, (1995).

[4] Young, A., Rooke, D. P., and Cartwright, D. J., "Analysis of Patched and Stiffened Cracked Panels Using the Boundary Element Method," *International Journal of Solid Structures* **29**, pp. 2201-2216, 1992.

[5] Baker, A., "Growth Characterization of Fatigue Cracks Repaired with Adhesively Bonded/Epoxy Patches,"

[6] Klug, J. and Sun, C. T., "Large Deflection Effects of Cracked Aluminum Plates Repaired with Bonded Composite Patches," *Proceeding of the First International Conference on Composite Science and Technology*, Durban, South Africa, June 18-20, 1996.

[7] Rybicki, E. and Kanninen, M., "A Finite Element Calculation of Stress Intensity Factors by a Modified Crack Closure Integral," *Engineering Fracture Mechanics* **9**, pp. 931-938, (1977).

[8] Belason, E., "Fatigue and Static Ultimate Tests of Boron/Epoxy Doublers Bonded to 7075-6 Aluminum With a Simulated Crack," *18th Symposium of the International Conference on Aeronautical Fatigue*, Melbourne, Australia, May, 4, (1995).

[9] P. Phillips, "Long Crack Growth Rate Data - Constant Amplitude and FALSTAFF Loading", AGARD Report No. 732.

[10]Callinan, R. J., Rose, L. R. F., Wang, C. H., "Three Dimensional Stress Analysis of Crack Patching,"

Top View   side view   side view
                               (a)   (b)

Aluminum Plate

Repair Plate
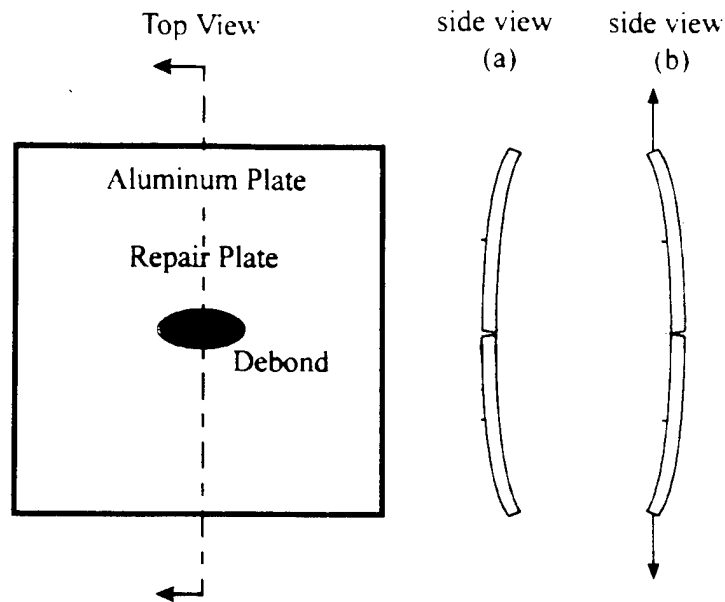
Debond

Figure 1 Curvature of single-sided repair due to a) thermal residual stresses and b) mechanical loading

$\blacktriangle y$

a
b   c $\blacktriangleright X$
a'

Δa Δa
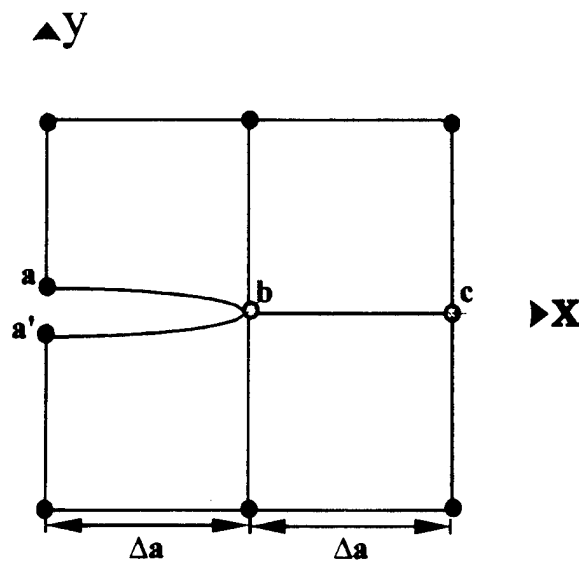
Figure 2 Aluminum plate crack tip elements (top view).
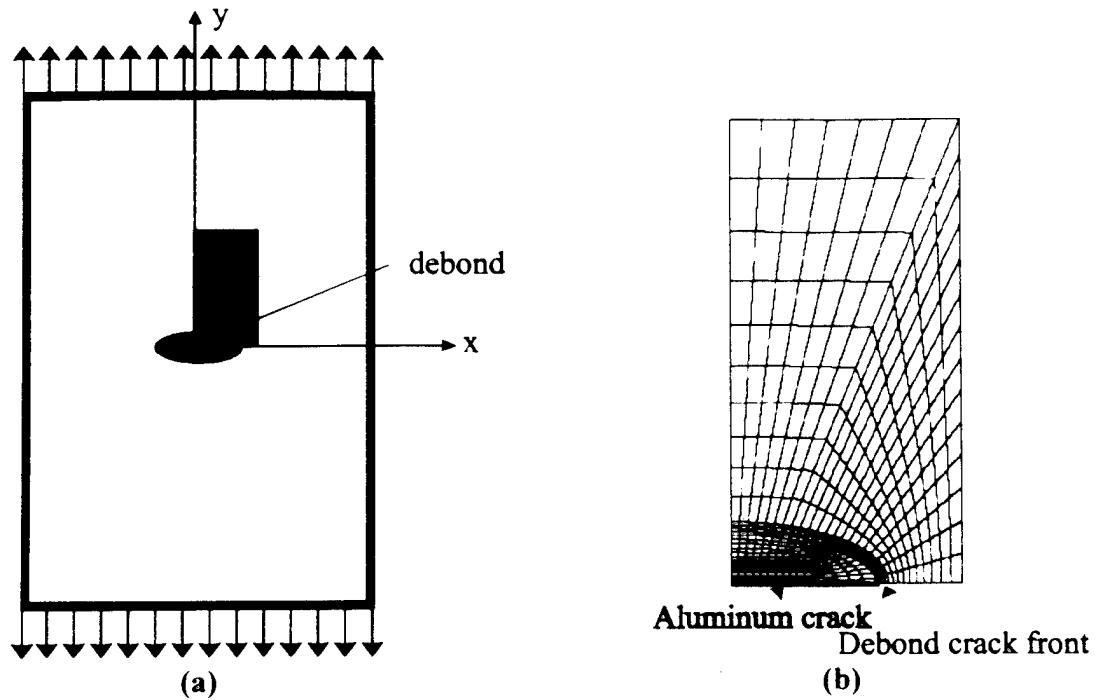
Figure 3 a) Configuration of a repaired center crack with debond and b) finite element mesh with debond (only quadrant of patch region shown).
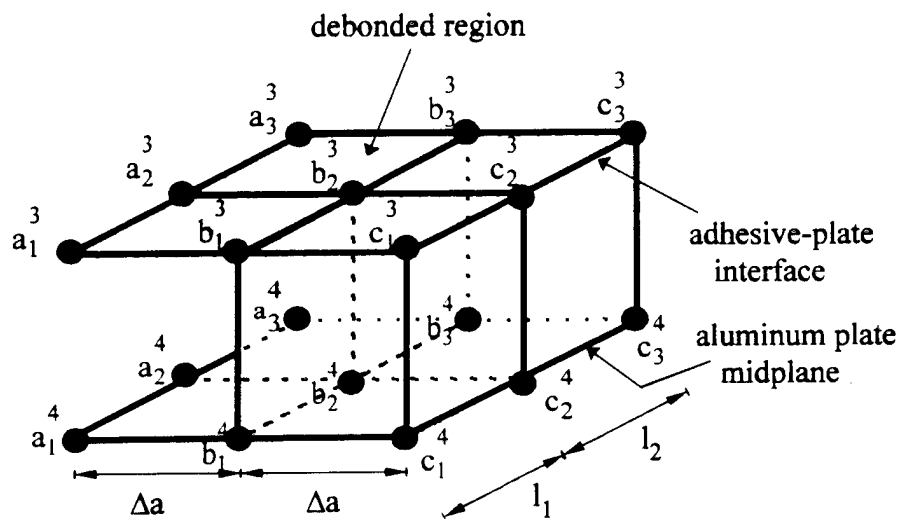
Figure 4 Schematic of debond crack front.
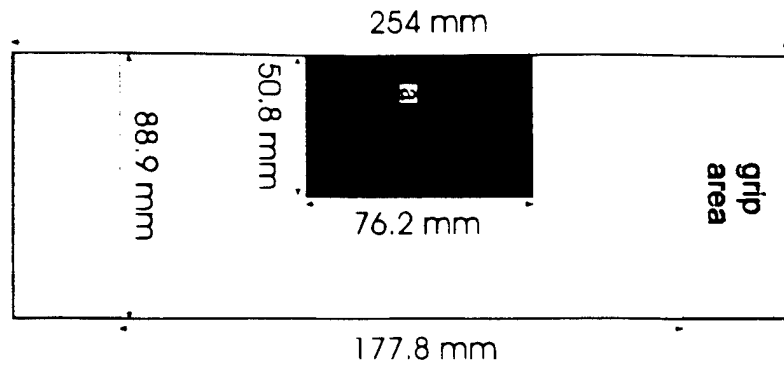
Figure 5 Geometry of composite repair.
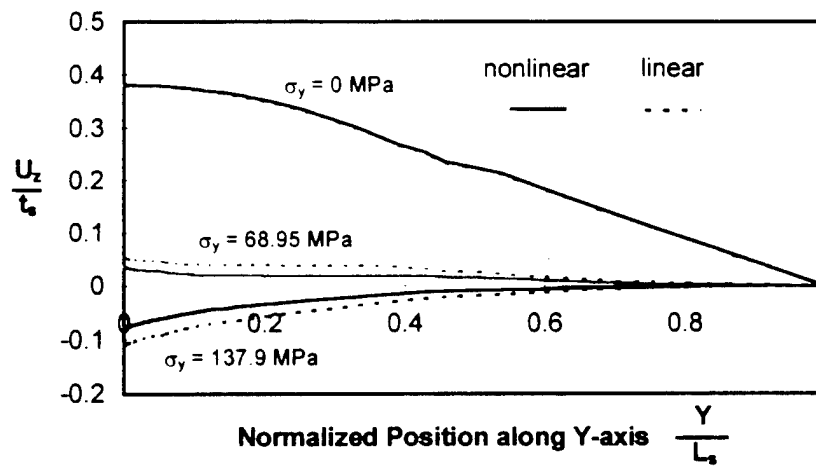
Figure 6 Curvature of aluminum plate midplane along y-axis for 8 ply composite repair.

(a)

(b)
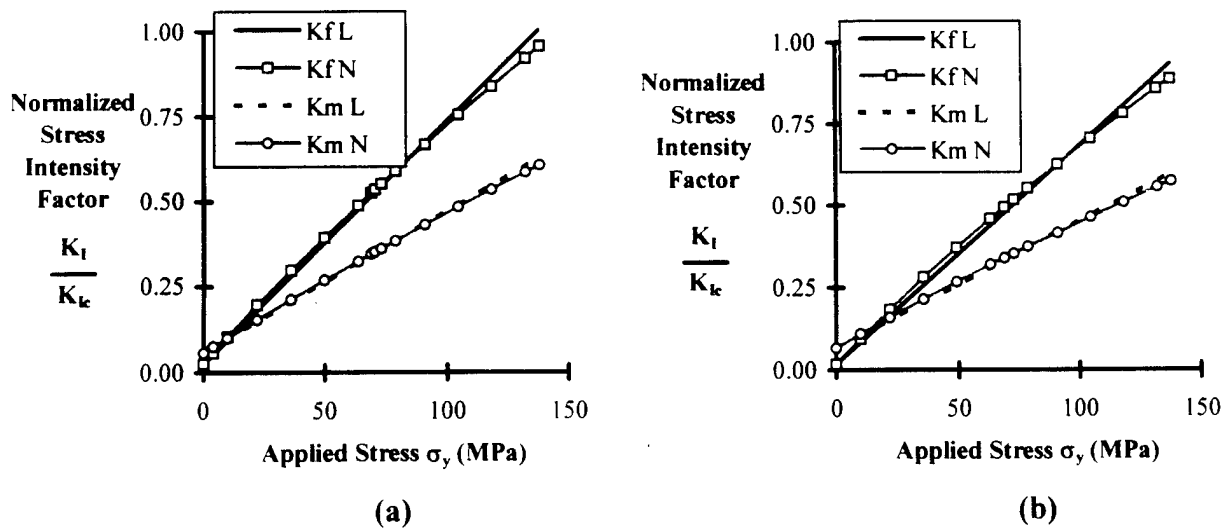
Figure 7 Normalized stress intensity factor with $\Delta T = -70\,^{\circ}C$ for the a) 4 ply and b) 8 ply repairs.
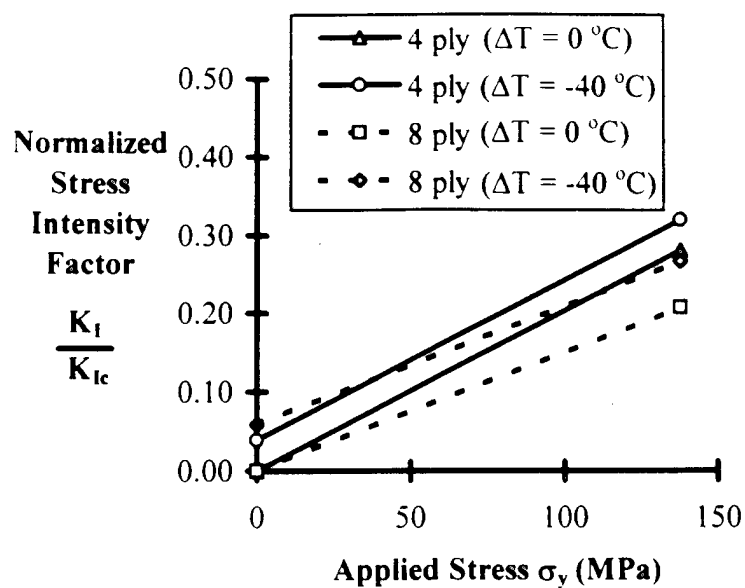
Figure 8 Normalized stress intensity factor for double sided repairs.
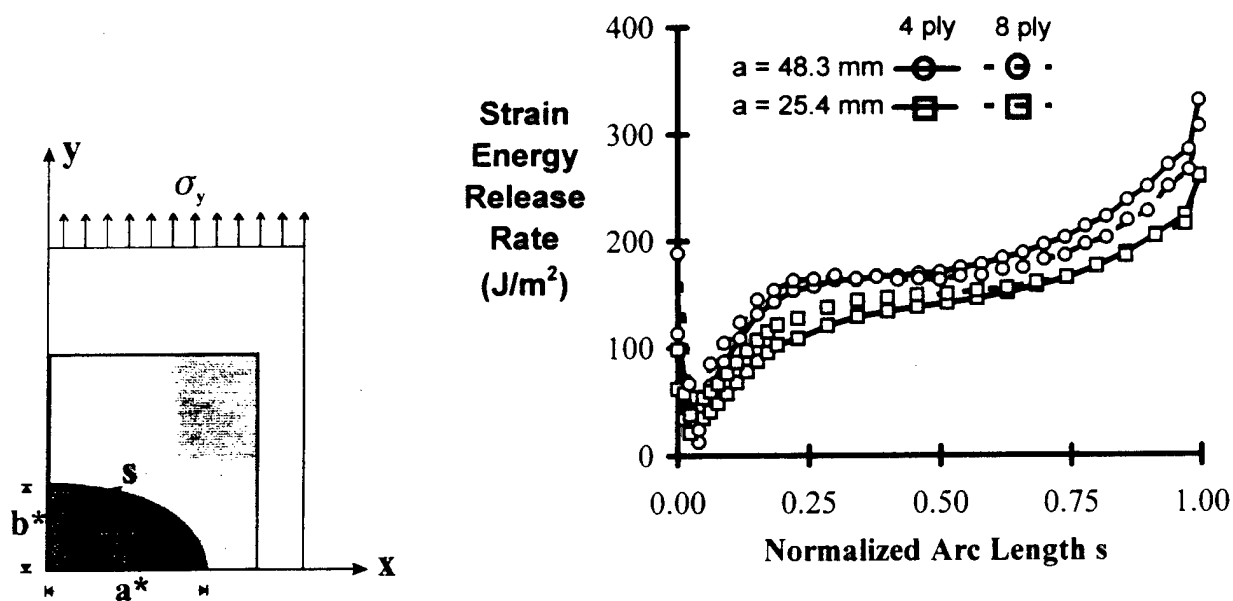
Figure 9 Debond crack strain energy release rate distributions for single sided repair.
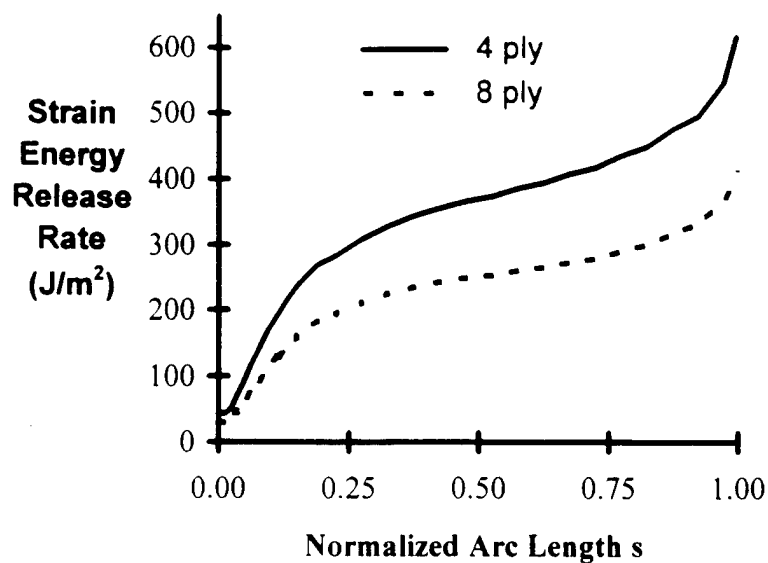
Figure 10 Debond crack strain energy release rate distributions for double sided repair.
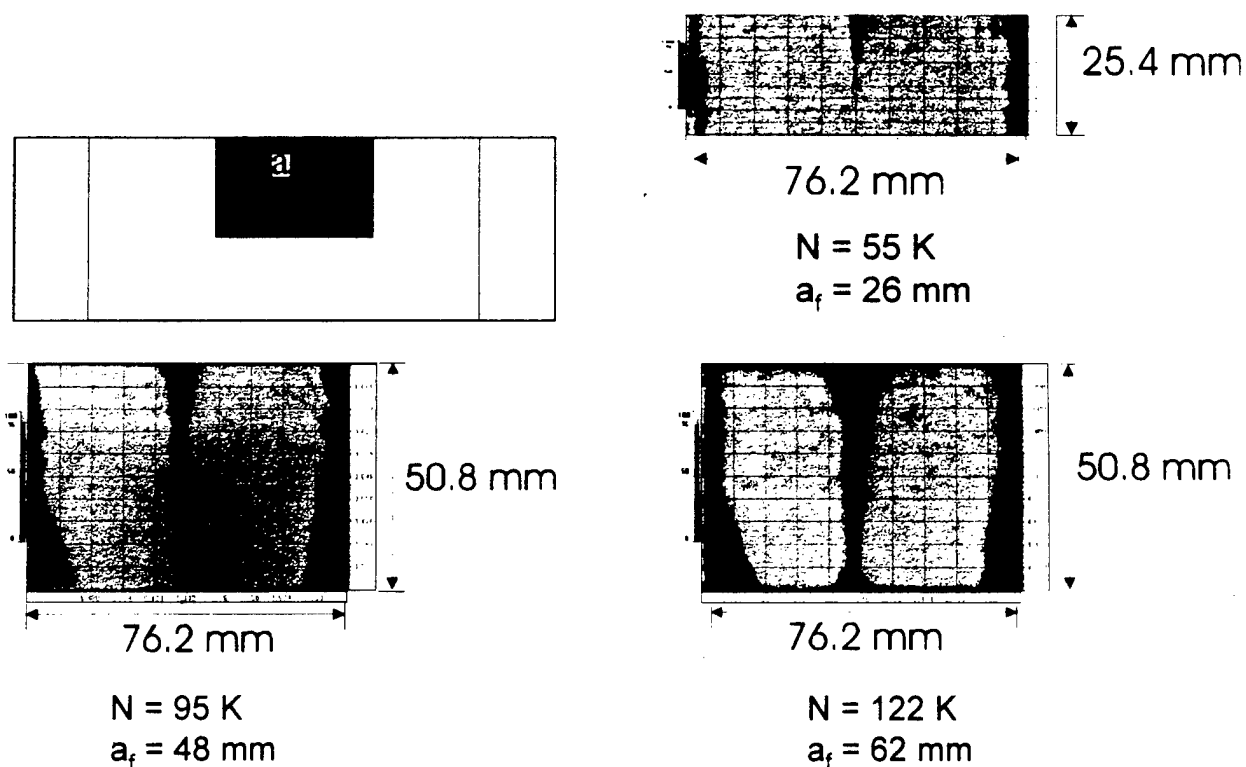
Figure 11 Ultrasonic C-scans of repair area 4 ply single sided repair with initial crack length 12 mm and σ = 68.95 MPa.
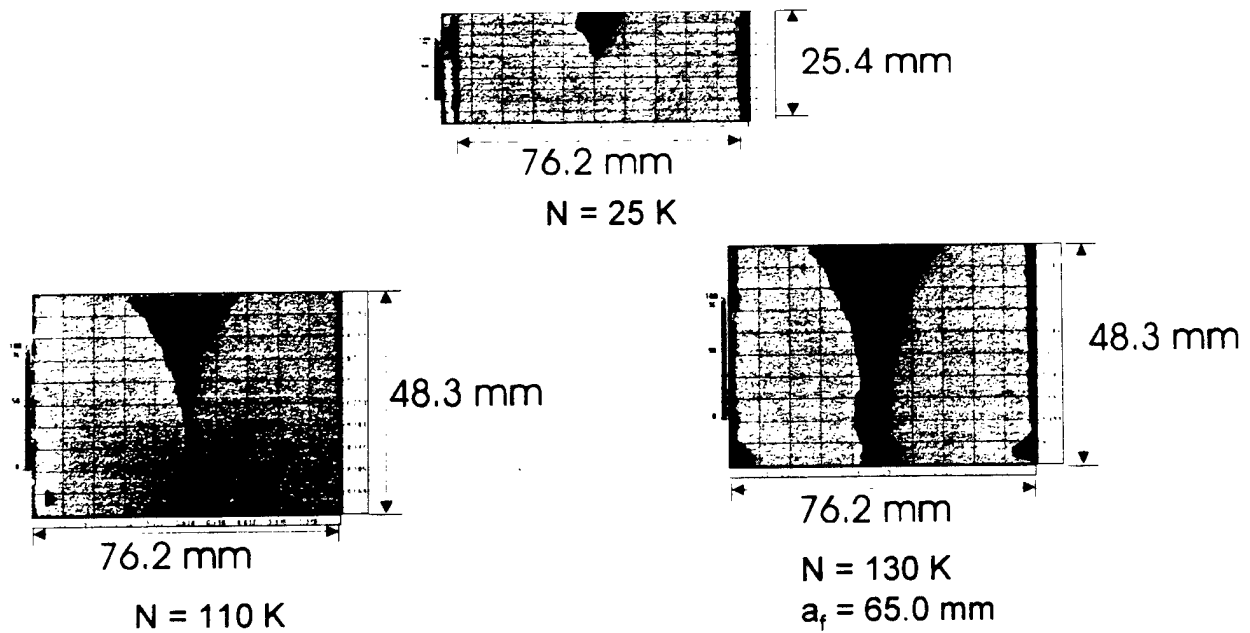
25.4 mm

76.2 mm

50.8 mm

76.2 mm
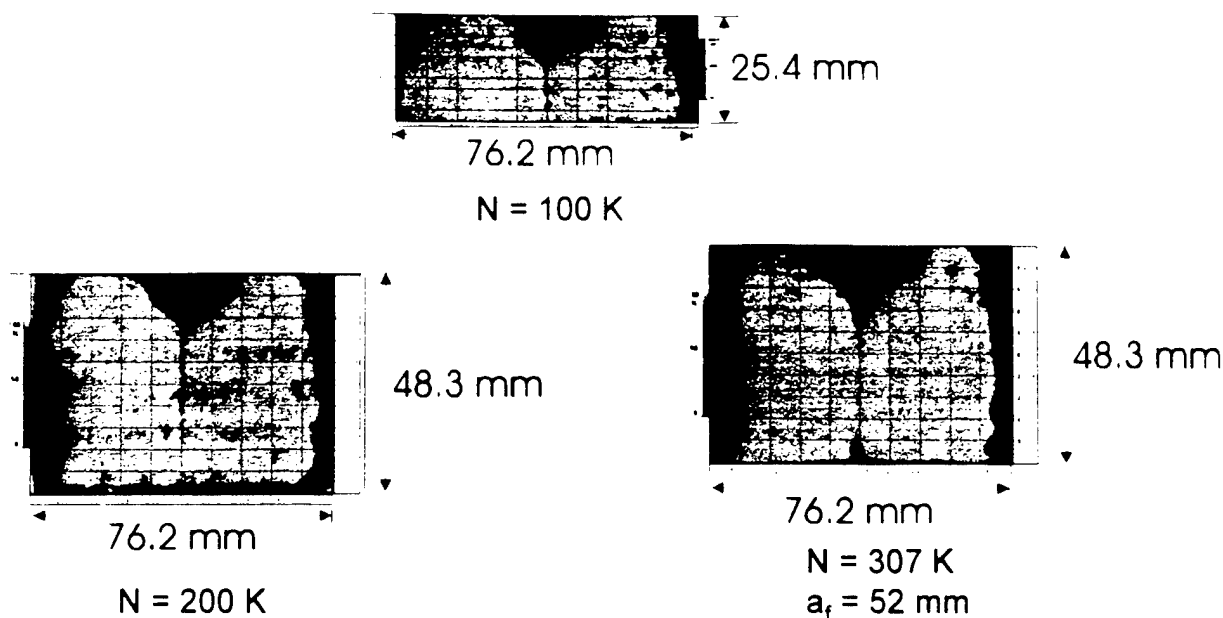N = 110 K
a_f = 51.6 mm

50.8 mm

76.2 mm
N = 132 K
a_f = 69.6 mm

Figure 12 Ultrasonic C-scans of repair area for 8 ply single sided repair with initial crack length 12 mm and $\Delta\sigma$ = 68.95 MPa.

25.4 mm

76.2 mm
N = 25 K

48.3 mm

76.2 mm
N = 110 K

48.3 mm

76.2 mm
N = 130 K
a_f = 65.0 mm

Figure 13 Ultrasonic C-scans of repair area for 4 ply double sided repair with initial crack length 13.5 mm and $\Delta\sigma$ = 137.9 MPa.

Figure 14 Ultrasonic C-scans of repair area for 8 ply double sided repair with initial crack length 13 mm and $\Delta\sigma$ = 137.9 MPa.
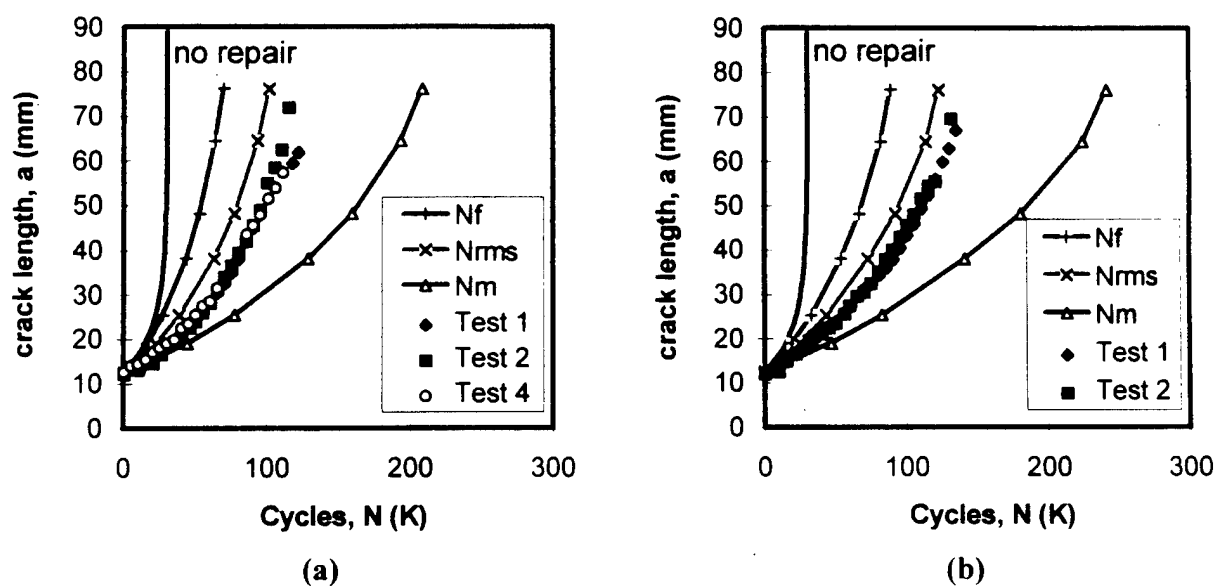

Figure 15 Crack length, a, versus cycles, N, for single sided repair with a) 4 plies of graphite epoxy and b) 8 plies of graphite epoxy composite.
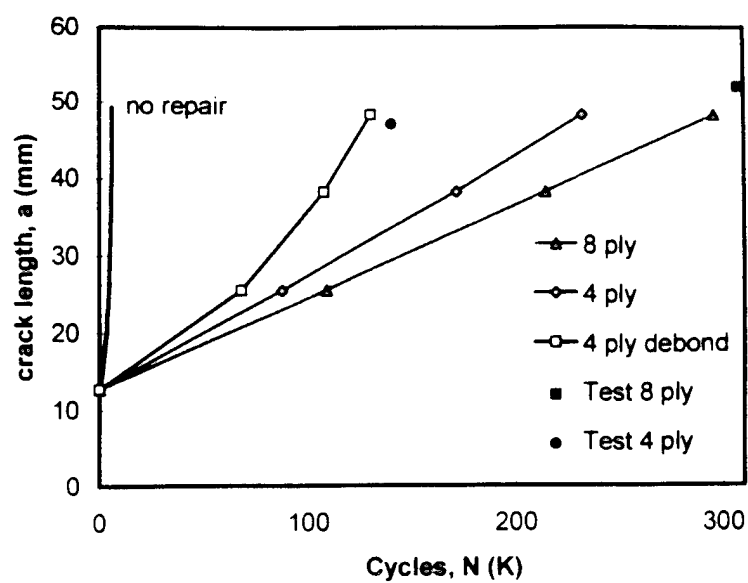
Figure 16 Crack length, a, versus cycles, N, for double sided repair.

Large Deflection Effects of Cracked Aluminum Plates Repaired with Bonded Composite Patches

J. C. Klug[*] and C. T. Sun[†]
School of Aeronautics and Astronautics, Purdue University
West Lafayette, Indiana 47907-1282

ABSTRACT

Highly complicated 3-D stresses in a metallic panel under in-plane loading are developed if composite patches are bonded to its surfaces either symmetrically (double-sided) or especially unsymmetrically (single-sided). Unsymmetric repairs present a great challenge in modeling due to the presence of out-of-plane bending. The problem is further complicated by thermal residual stresses arising from the thermal coefficient mismatch of the patch and aluminum plates. An efficient model using Mindlin plate theory and spring elements is used to model the both the host and repair plates and adhesive. Large deflection theory is used to study the effect of different variables including the thermal residual stresses and host and repair plate thicknesses.

1 INTRODUCTION

In order to extend the service life of an aging aircraft, the cracked components must be replaced or repaired. If the number of cracks is small and the crack size is small relative to the size of the component, it is often most economical to employ crack arrestment methods to regain the load carrying capacity of the component. A repair method using composite patches to reinforce the cracked structure has been shown to be

---

[*] Graduate Student, School of Aeronautics and Astronautics.
[†] Professor, School of Aeronautics and Astronautics

very promising owing to the light weight, high stiffness and strength of the composite.

Although it has been shown that a symmetric repair is the most effective reinforcement, unsymmetric repairs provide a clear advantage when it is difficult or not possible to access both sides of a structure. Unsymmetric repairs present a great challenge in modeling due to the presence of out-of-plane bending as shown in Figure 1. The two side views show the bending induced from thermal residual stresses due to the thermal coefficient mismatch and from the off axis mechanical loading.

Numerous models have been developed for the analysis of symmetric repairs using a wide variety of calculation techniques including the collocation method[2], boundary element method[3], finite element method[1,4,5], finite element alternating method[6], and approximate analytical solutions.[1] The unsymmetric repair has been approached approximately by correcting the plane stress finite element analysis with a global bending moment found by the difference in the loads of the patch and aluminum plate. Also, a full 3D finite element analysis[5] and the present plate-spring model[7] have been used. However, the effect of large deflection has not been addressed.

Large deflection theory has been used in the study of asymmetric laminates to accurately determine the plate deflection.[8] In linear laminated plate theory, asymmetric laminates will exhibit out-of-plane displacement from an in-plane load because the in-plane stress is coupled with the out-of-plane strain through the bending-extensional coupling. It was found that linear laminated plate theory overestimated the plate deflection because the strong bending-extensional coupling leads to a "large deflection"

effect at small loads. The large deflection effect increases for increasing bending-extensional coupling and decreasing extensional and bending stiffnesses. A single-sided repair can be considered as an unsymmetric laminate. The unsymmetry is caused by the offset in the neutral axis of the aluminum plate and the unbalanced lay-up of the composite aluminum plate structure.

The use of a full 3-D finite element model to perform stress analysis is computationally costly and can even cause ill conditioning when high aspect ratio elements are used for the thin patch and adhesive. In this paper, a simple analysis using Mindlin plate theory is investigated to model the host and repair plates with spring elements modeling the connecting adhesive layer. The crack ing the aluminum is characterized by fracture mechanics using the stress intensity factor. Many different variables affecting the large deflection solution are investigated including the effects of host and repair plate thicknesses and thermal residual stresses.

2 MODEL DESCRIPTION

Figure 2 shows a typical single-sided patch configuration. A complete derivation of the finite element model is given in Reference (7). The plate nodes are located on the mid-planes of the aluminum plate and patch. The adhesive nodes lie along the patch-adhesive and adhesive-aluminum plate interfaces. Constraint equations are imposed on the patch-adhesive and adhesive-aluminum interfaces in order to enforce the displacement compatibility. The adhesive layer is modeled by three springs for the transverse shear stiffnesses in the xz and yz-planes and the axial stiffness in the z-

direction, respectively. The model has been implemented into ABAQUS.

The modified crack closure technique[9] is used to calculate the strain energy release rate. It is assumed that the strain energy released during crack extension is equal to the work required to close the opened crack surfaces. It is also assumed that the adhesive cracks at the same place as the aluminum crack. Generally, the nodal forces and relative displacements due to the geometric nonlinearity are nonlinear, and the energy required to close the crack front is the summation of the work done for each increment. However, it will be demonstrated that the relation between the nodal forces and the cooresponding relative displacements are linear at the crack tip. Thus, the work done is linear and a single step closure approach can be implemented.

The strain energy release rate is computed for Mode I fracture loading. The same procedure can be used for mixed mode loading. A 4-noded Mindlin plate element is used to model the aluminum plate. Figure 3 shows a 2D finite element model for the aluminum plate near the crack tip at point b. Assume the crack front extends from b to c. Since the extension, Δa, is very small, the crack opening displacements at b are taken to be the same as those at a. Thus, the strain energy release rate can be calculated as the work done by the nodal force (moment), F_y^b (M_x^b), in closing the crack opening displacement (rotation), u_y^a (ψ_y^a). The total strain energy release rate is obtained as

$$\overline{G}_{total} = \overline{G}_u + \overline{G}_\psi = \frac{1}{2\Delta a}\left\{F_y^b\left(u_y^a - u_y^{a'}\right)\right\} + \frac{1}{2\Delta a}\left\{M_x^b\left(\psi_y^a - \psi_y^{a'}\right)\right\} \tag{1}$$

where $\overline{G}_u$, $\overline{G}_\psi$ and $\overline{G}_{total}$ are the translational, rotational, and total strain energy release

rates, respectively. Note that these strain energy release rates are the respective energies released (over the total plate thickness) per crack tip.

The fracture parameter for the aluminum crack is often given in terms of the stress intensity factor. The maximum stress intensity factor is located on the tension side of the plate and is composed of

$$K_I = K_u + K_\psi \left(\frac{2z}{t_s} \right) = \sqrt{\frac{\overline{G}_u E_s}{t_s}} + \sqrt{\frac{3\overline{G}_\psi E_s}{t_s}} \left(\frac{2z}{t_s} \right) \tag{2}$$

where the subscript s denotes parameters associated with the aluminum plate. K_u is the stress intensity factor due to the membrane action and is the value of K_I at the plate midplane. K_ψ is the stress intensity factor due to pure bending.

4 RESULTS AND DISCUSSION

The material properties and plate dimensions are listed in Table 1. The thickness of the aluminum and repair are listed for three configurations in Table 2. The aluminum crack length, 2a, is 50 mm. The boron/epoxy $0°$ fiber is in the y-direction, perpendicular to the aluminum crack. The first example is for a mechanical loading. The aluminum plate is subjected to an in-plane, uniform loading up to 150 MPa. Quarter model symmetry is used for the plate.

Table 1 Material Properties and Dimensions

Material	Material Properties	Dimensions (mm)	Thermal Expansion Coefficient
Aluminum	$E_s = 71.02$ GPa $v_s = 0.32$	$L_s = 180$ $W_s = 120$	$\alpha_s = 23.0 \times 10^{-6}/^\circ C$
Boron/Epoxy	$E_1 = 208$ GPa $E_2 = E_3 = 25.44$ GPa $G_{12} = G_{13} = 7.24$ GPa $G_{23} = 4.94$ GPa $v_{12} = v_{13} = 0.1677$ $v_{23} = 0.0350$	$L_r = 76$ $W_r = 38$ ply thickness = 0.127	$\alpha_1 = 4.5 \times 10^{-6}/^\circ C$ (fiber direction) $\alpha_2 = 23.0 \times 10^{-6}/^\circ C$ (transverse direction)
Adhesive	$G_a = 0.965$ GPa $v_a = 0.32$	$t_a = 0.1016$	

Table 2 Aluminum and Repair Plate Thicknesses

Case Number	Aluminum Plate Thickness, t_s (mm)	Repair Plate Thickness, t_r (mm)	$\dfrac{t_r}{t_s}$
1	2.29	0.762	3.0
2	2.29	0.127	18.0
3	22.90	7.620	3.0

The crack tip forces (moments) and displacements (rotations) using large deflection analysis are shown in Figure 4. These are the terms used for computing the strain energy release rate in equation (1). The values are normalized by the respective maximum and are compared to the straight line plotted from 0 to 1. As can be easily seen, the computed work done by crack closure is linear. Thus, the linear technique of crack closure is valid. Note that the applied load versus the maximum deflection is nonlinear.

Since the spring model contains simplifying assumptions, comparisons are made to a 20-noded 3D reduced integration element for the adhesive. The stress intensity factors of the 3D adhesive to the spring adhesive are shown in Figure 5 for Case 1 in Table 2. The stress intensity factor is normalized by the plane strain critical stress intensity factor, $K_{Ic} = 34$ MPa$\sqrt{m}$, for aluminum 2024-T3 and is plotted at two locations through the plate thickness, Kf at the free edge and Km at the midplane. The linear solution, labeled L, is constant over the applied stress. The 3D and spring adhesive solutions using large deflection theory are labeled N 3D and N Spring for nonlinear 3D and spring adhesives, respectively. It can be easily seen that the spring and 3-D adhesive models compare well. The plot shows that the stress intensity factor is largest at the free edge and can be over predicted by linear analysis.

For Case 1, the aluminum plate maximum deflection over plate thickness at a load of 5 MPa is 0.125 for the linear analysis while the nonlinear is 87% lower. Thus, the "nonlinear effect" is significant even for deflections that are usually considered small.

The stress intensity factor shown in Figure 5 is for the linear analysis is only 14% higher than the nonlinear. At a load of 150 MPa, the linear maximum deflection over thickness is 3.76 while the nonlinear is 680% lower. The linear analysis stress intensity factor is 76% higher than the nonlinear.

Figures 6 and 7 show the results for Cases 2 and 3. Figure 6 shows that as the ratio of the repair-to-aluminum thickness is decreased, the nonlinear effect on the stress intensity factor also decreases. Case 3 has a thicker aluminum sheet with the same repair-to-aluminum thickness ratio as Case 1. Figure 7 indicates that the linear and nonlinear solutions are nearly identical. The large deflection effect is quite complicated. Increasing the thickness of the aluminum while holding the repair-to-aluminum thickness changes all the terms in the stiffness matrix. The effect is small for Case 3 because the increase in bending rigidity is cubic with respect to the plate thickness while the increase in bending-extension stiffness is quadratic. This increased bending rigidity offsets the bending extensional coupling.

In second example, the effect of the thermal residual stresses due to the thermal coefficient mismatch of the aluminum and repair is demonstrated. Conventionally, the value of the temperature drop, ΔT, is taken as the difference in ambient room temperature of the component and the curing temperature. For a typical adhesive like FM 73, the curing ΔT temperature is 120 °C and ambient room temperature is 20 °C making a ΔT of -100°C. However, the actual value of ΔT is not well defined. Because of this uncertainty, a range of this effective temperature drop is examined.

The normalized stress intensity factor over a range of ΔT is shown for Cases 1 and 2 in Figure 8. The low coefficient of thermal expansion in the composite fiber direction results in thermal residual stresses causing the repair to be in residual compression and tension in the aluminum plate. The maximum value of the stress intensity factor is shifted to the aluminum-adhesive interface and is labeled Ki. The crack tip opening is larger at the adhesive-aluminum interface than at the free edge due to the curvature caused by the residual stresses. Also, the residual tension in the aluminum does not allow overlapping of the crack faces as the case of a cracked plate under pure bending.[8] As ΔT increases, the linear solution slightly under predicts the stress intensity factor. The difference in the peak out-of-plane deflection between the solutions is not significant.

In the final example uses the geometries of Cases 1 and 2 are used to examine the effect of the initial thermal residual stresses followed by a mechanical loading on the stress intensity factor. Figure 9 shows the normalized stress intensity factor at the free edge. Note that for lower applied stress levels, the maximum stress intensity factor will occur at the adhesive-aluminum interface. The two linear curves refer to the linear analysis with thermal residual stress of 0°C and -100°C, respectively. The difference between the solution with and without considering thermal residual stresses is very small. The plot shows that there is a large difference between the linear and nonlinear solutions. As the effective temperature drop increases, Kf significantly increases for the nonlinear solution. Figure 10 shows that as the thickness of the repair is reduced, there is a smaller large deflection effect.

Figure 11 shows the normalized curvature of the aluminum midplane along the y-axis from the center of the crack to the outer edge of the plate. The shaded area shows region of the aluminum which is covered by the repair. Two values of ΔT, -50°C and -100°C, are shown by the dashed and solid lines, respectively. The plot shows that the plate is initially curved due to the thermal residual stresses. As a mechanical load is applied, the plate straightens and eventually the curvature reverses by a very small amount. This change in curvature from the thermal residual stresses followed by the mechanical loading has been experimentally noted by Belason[10].

A comparison of the linear and nonlinear maximum deflections at the aluminum plate midplane for Case 1 is shown in Figure 12 at a ΔT of -50 °C. Initially, the deflections induced by thermal residual stresses obtained from the linear and nonlinear solutions, respectively are about equal. As the load is applied, the plot shows that the linear solution overpredicts the deflection as the plate changes curvature. Also, the nonlinear solution predicts that the plate straightens at a lower applied load.

A plot of the normalized stress intensity factor vesus crack length for Case 1 is shown in Figure 13. The stress intensity factor increases monotonically as the crack approaches the patch boundary. While the nonlinear solution is below the linear at both the free edge and midplane, the stress intensity factor increases with crack size as well. For comparison, the stress intensity factor for the double sided repair with the same effective patch thickness is shown. The solution is below the single sided repair for all crack sizes and approaches a limiting value as the crack size increases.

5 CONCLUSIONS

For one-sided repairs, the stress intensity factor in the cracked aluminum plate varies through the plate thickness. When the effect of thermal residual stresses is taken into account, the maximum value of the stress intensity factor in the aluminum plate is at the adhesive-aluminum interface. As a mechanical load is applied, the maximum stress intensity factor switches to the free edge of the aluminum plate. The effect of large deflection theory is pronounced for thin aluminum plates. The large deflection effect is important for the mechanical loading, but may not be significant for that due to initial thermal residual stresses. When thermal residual stresses are taken into account before the mechanical load is applied, the change in geometry due to residual stresses can have a substantial effect on the resulting stress intensity factor. In this case, the linear solution at first under predicts and later over predicts the stress intensity factor as the applied load increases.

6 ACKNOWLEDGMENT

7 REFERENCES

1. Baker, A. A. and Jones, R., *Bonded Repair of Aircraft Structure*, Martinus Nijhoff Publishers, Dordrecht, The Netherlands, 1988.

2. Dowrick, G., Cartwright, D. J., and Rooke, D. P., "The Effects of Repair Patches on the Stress Distribution in a Cracked Sheet," *Proceedings of the 2nd International*

Conference on Numerical Methods in Fracture Mechanics, (D. R. J. Owen and A. R. Luxmore, Editors) Swansea, U. K., 1980, pp. 763-775.

3. Young, A., Rooke, D. P., and Cartwright, D. J., "Analysis of Patched and Stiffened Cracked Panels Using the Boundary Element Method," *International Journal of Solid Structures* **29**, 1992, pp. 2201-2216.

4. Ratwani, M. M., "Charaterization of Fatigue Crack Growth in Bonded Structures," Air Force Flight Dynamics Lab, AFFDL-TR-77-31, Vols. 1 and 2, Wright-Patterson AFB, OH, June 1977.

5. Chue, C., Chang, L., and Tsai, J., "Bonded Repair of a Plate With Inclined Central Crack Under Biaxial Loading," *Composite Structures* **28**, 1994, pp. 39-45.

6. Park, J. H., Ogiso, T. And Atluri, S. N., "Analysis of Cracks in Aging Aircraft Structures, With and Without Composite-Patch Repairs," *Computational Mechanics*, Vol. 10, 1992, pp. 169-201.

7. Sun, C., Klug, J., and Arendt, C., "Analysis of Cracked Aluminum Plates Repaired with Bonded Composite Patches," *AIAA Journal* **34**, 1995, pp. 369-374.

8. Sun, C. T. and Chin, H., "Analysis of Asymmetric Composite Laminates", *AIAA Journal* **26**, 1988, pp. 714-718.

9. Rybicki, E. and Kanninen, M., "A Finite Element Calculation of Stress Intensity Factors by a Modified Crack Closure Integral," *Engineering Fracture Mechanics* **9**, 1977, pp. 931-938.

10. Belason, E., "Fatigue and Static Ultimate Tests of Boron/Epoxy Doublers Bonded to 7075-6 Aluminum With a Simulated Crack," *18th Symposium of the International Conference on Aeronautical Fatigue*, Melbourne, Australia, May, 4, 1995.
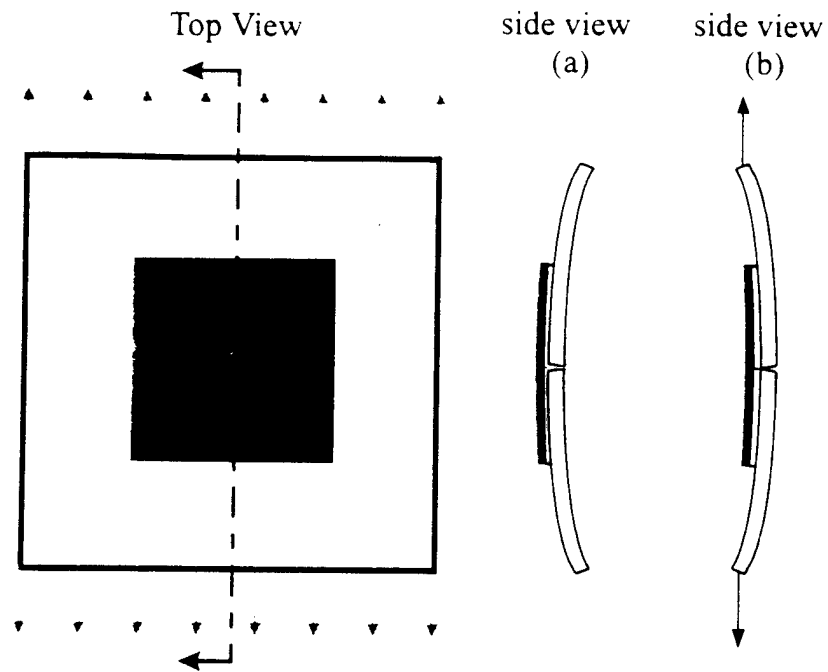
Figure 1 Curvature due to a) thermal residual stresses and b) mechanical load
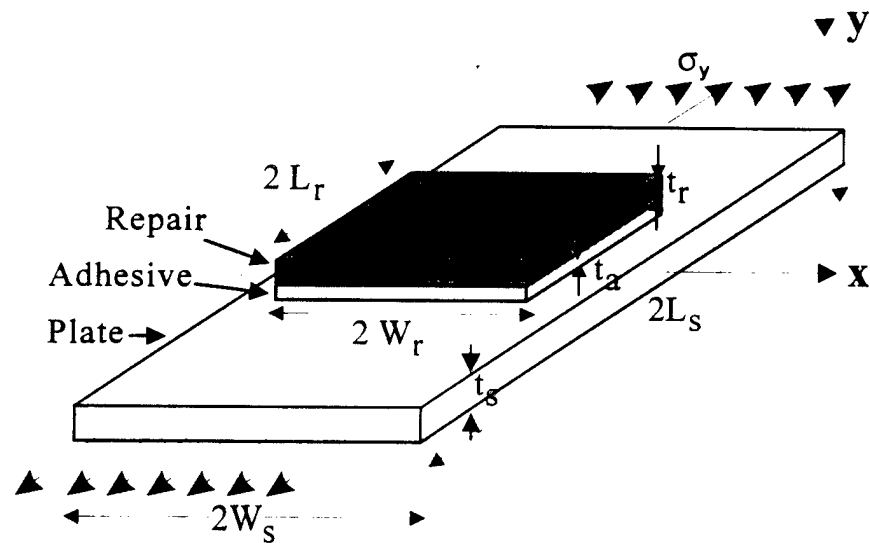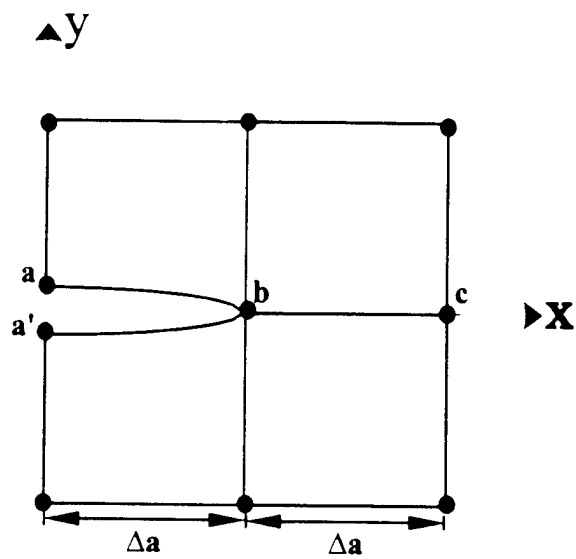

Figure 2 Sample bonded repair

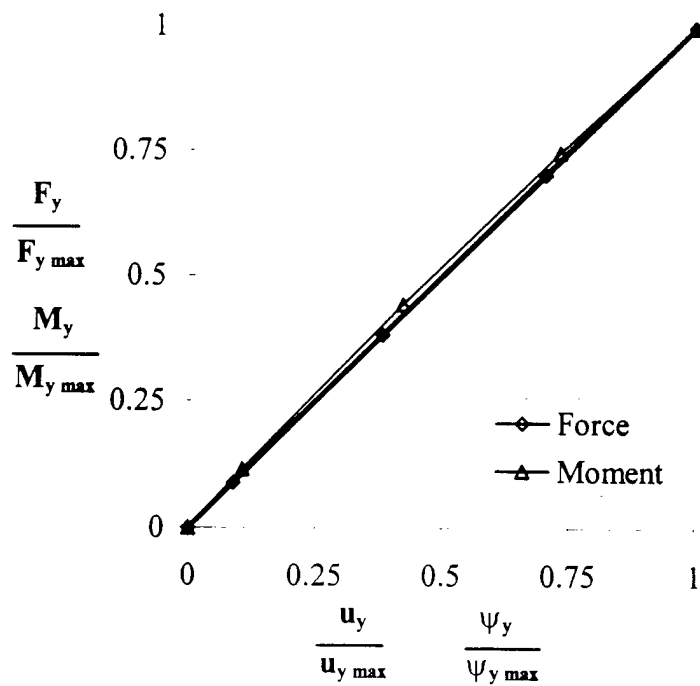**Figure 3 Aluminum plate crack tip elements (top view)**

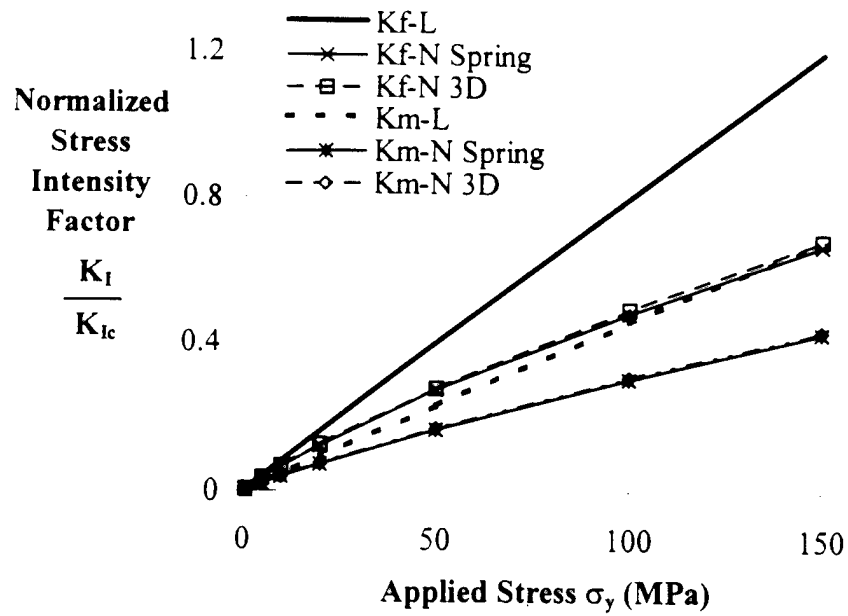**Figure 4 Crack closure force (moment) and displacement (rotation)**

Figure 5 Normalized stress intensity factor for Case 1
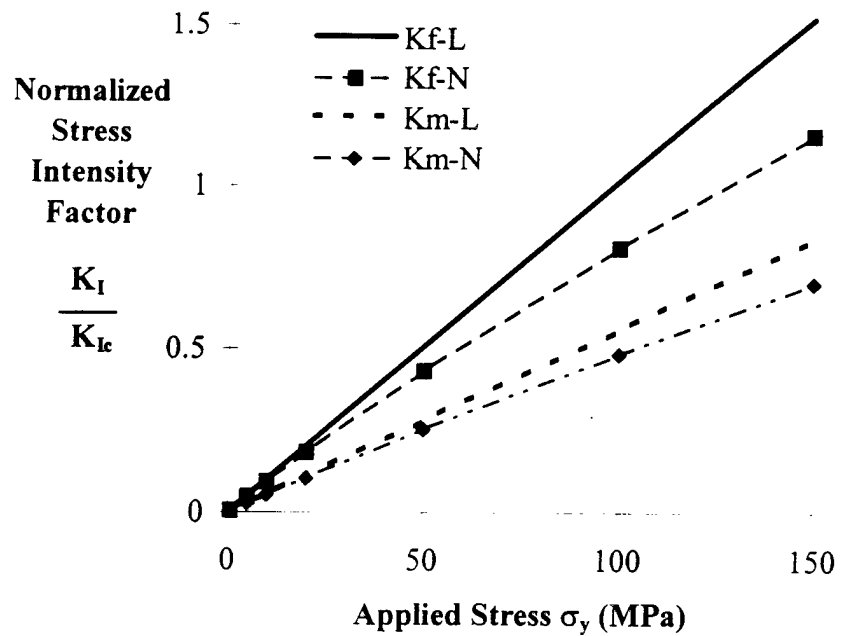

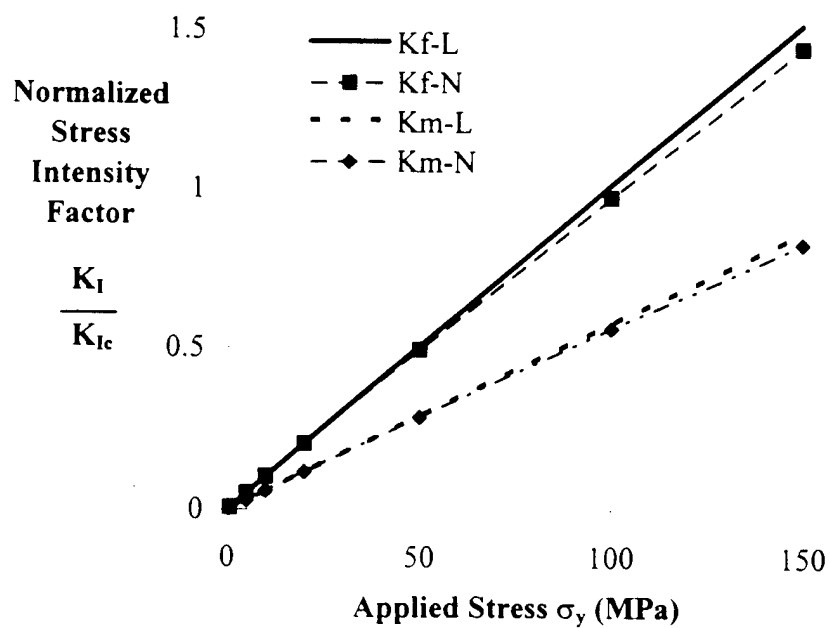**Figure 6 Normalized stress intensity factor Case 2**

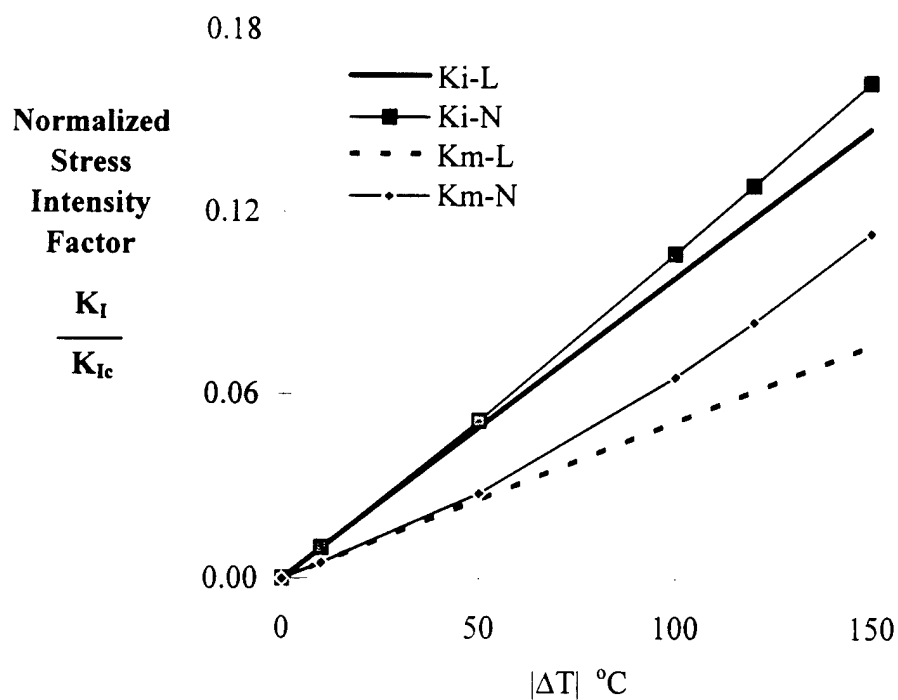**Figure 7 Normalized stress intensity factor Case 3**

Figure 8 Normalized stress intensity factor from thermal residual stresses for Case 1
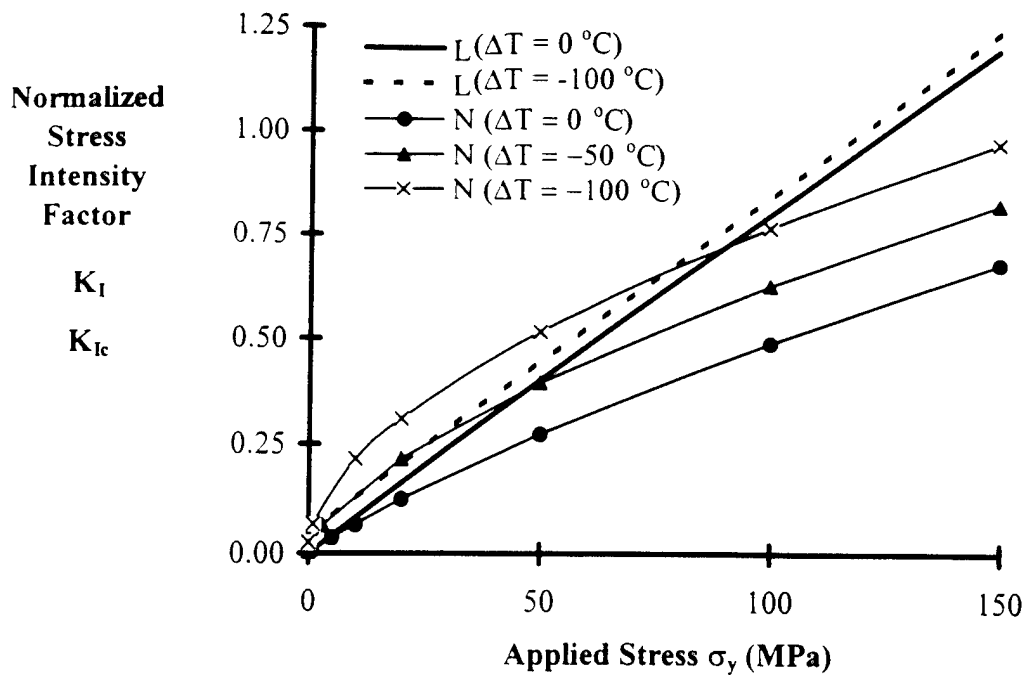
Figure 9 Normalized stress intensity factor with thermal residual stresses and mechanical load for Case 1
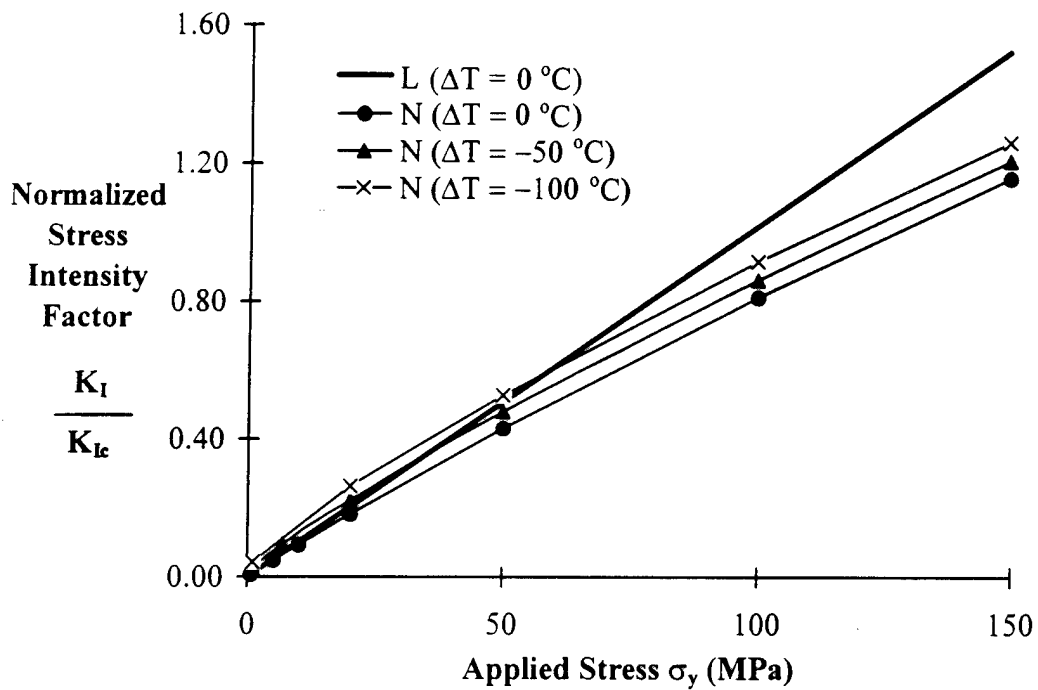

Figure 10 Normalized stress intensity factor with thermal residual stresses and mechanical load for Case 2
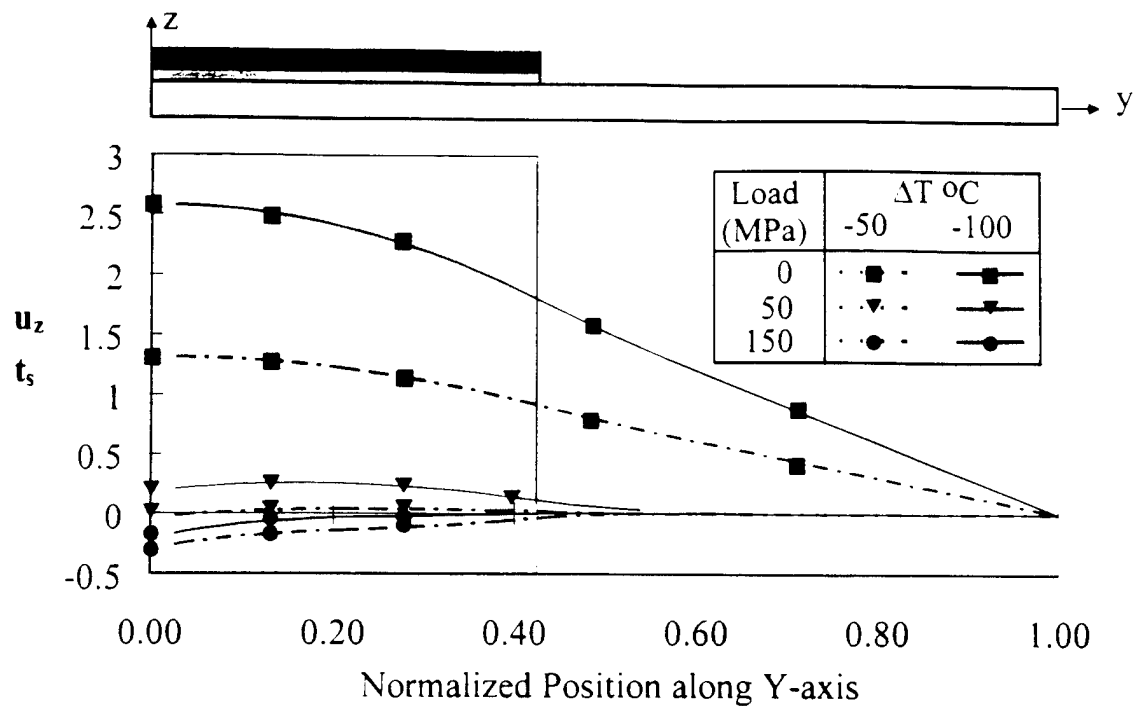
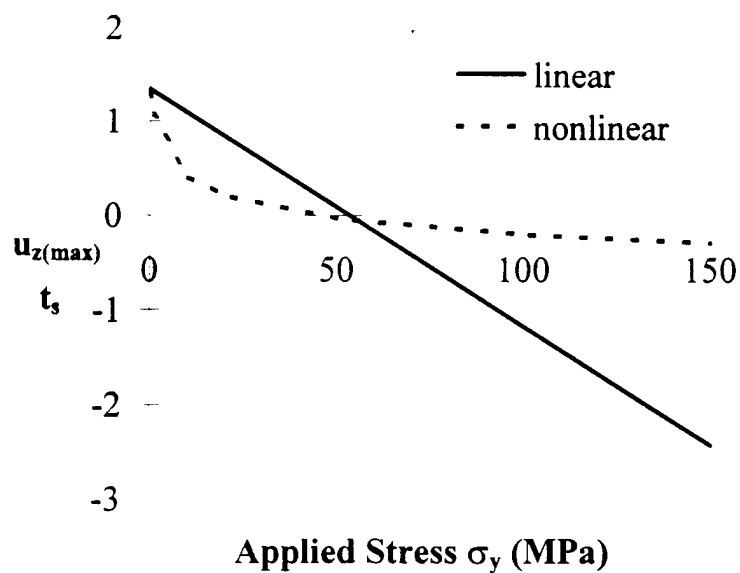**Figure 11 Curvature of aluminum plate midplane along y-axis for Case 1**

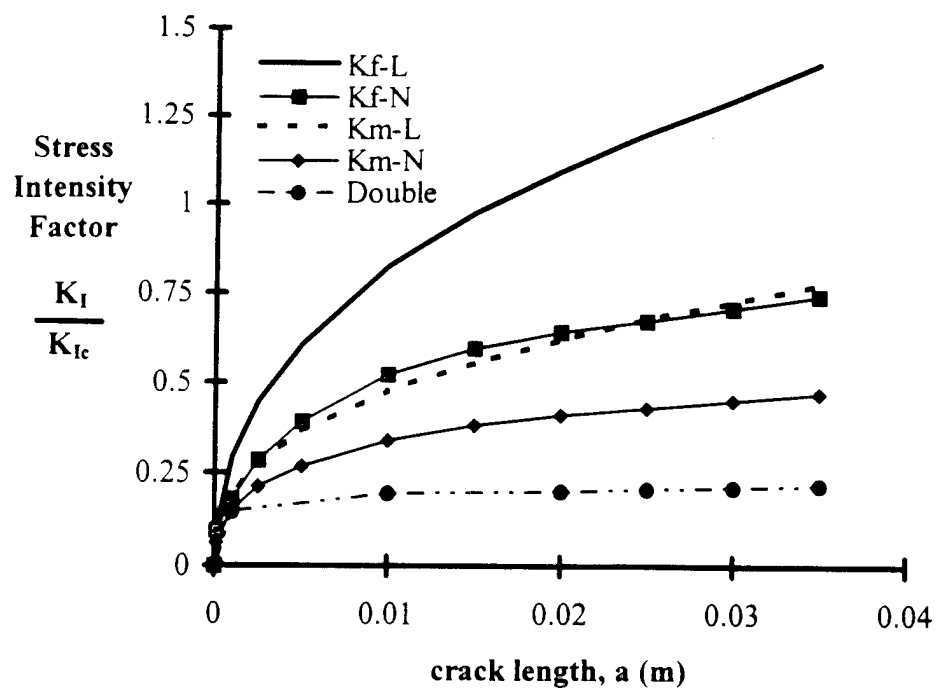**Figure 12 Maximum deflection of aluminum plate midplane at ΔT - 50°C for Case 1**

Figure 13 Stress Intensity Factor versus crack length for Case 1

Proc. FAA - NASA Symp. on Continued Airworthiness
of Aircraft Structures, Atlanta, August 1996

A16-1

EFFECT OF CRACK INTERACTION ON DUCTILE FRACTURE

C. T. Sun and X. M. Su
School of Aeronautics and Astronautics
Purdue University
West Lafayette, IN 47907-1282

SUMMARY

The interaction of a major crack and a small crack is analyzed by using a simple ductile fracture criterion based on critical equivalent stresses at the crack tip. To account for the three dimensional effect at the crack tip of cracked plates, a plane strain strip is used. With commercial finite element code ABAQUS, the crack interactions are analyzed for two materials with different hardening and yielding behaviors. The numerical results indicate that when the plastic zone of the major crack and that of the small crack coalesce, the small crack would extend rapidly toward the major crack, producing a drop in applied load.

INTRODUCTION

Interaction between a major crack and small cracks is of great concern in aircraft safety [1]. A large number of aging airplanes are in service beyond the lifetime they were designed for. Multiple site damages (MSD) in the aging aircraft, involving a large number of small fatigue cracks, may reduce the the residual strength of the aircraft in the presence of a major crack.

In a series of papers, Swift [1-3] approached the problem of the interaction of a major crack and small cracks by postulating that the major crack and a small crack would coalesce once the yield zones of the major crack and the small crack overlap. Swift based his analysis on elastic fracture mechanics and a crude estimation of the plastic zone. Its validity remains to be verified especially for ductile materials such as aluminum alloys used in aircraft structures.

Specimens under static monotonic loading and fractured with large scale yielding are noted to go through the stage of initial crack growth and the stage of steady state crack growth. Many parameters have been suggested to characterize the two stages. The J integral [4] and J-R curve were very popular in earlier studies. It was later found, however, that J integral and J-R curve are specimen size dependent [5]. Other parameters, such as plastic dissipation energy at the crack tip [6], CTOA [7], etc., have also been suggested.

1

By simulating more than 15 ductile fracture tests on grooved specimens performed by three different group of researchers, Su and Sun [8] have recently found that stresses, especially equivalent stresses, at a point within a critical distance from the crack tip remain constant during crack growth and are specimen size independent for fractures under plane strain deformation. Stresses, especially equivalent stresses, can be used as the parameter to characterize ductile fracture.

For ductile fracture of flat plates without side grooves, three dimensional effects at the crack tip must be considered. Recent analytical solution of three dimensional stresses at the crack tip for a cracked plate showed that singular stresses at the crack tip are plane strain throughout the plate thickness for elastic materials [9]. In other words, a plane strain core region exists around the crack tip where singular stresses dominate. Away from the crack tip, a state of plane stress prevails. The plane strain condition in ductile fracture has been investigated by Newman, et al [10], Narasimhan and Rosakis [11] and Nakamura and Park [12], among others. A moving plane strain core model, which accounts for plane strain deformation at the crack tip and plane stress deformation away from the crack tip has been developed successfully [13]. By using the moving plane strain core model, stresses, especially equivalent stresses at the crack tip, remain constant during steady static crack growth [13]. Stresses at the crack tip can be used together with the moving plane strain core model to characterize ductile fracture of flat plates.

In the present paper, the above mentioned ductile fracture criterion is used together with a simple version of the plane strain core model to study crack interactions in cracked plates under in-plane loading.

THE DUCTILE FRACTURE CRITERION

Recently, Su and Sun [8] simulated fifteen ductile fracture tests performed by three different research groups on grooved specimens to study local parameters during plane strain ductile fracture. The tests, reported by Hiser and Terrel [14], Joyce, Hackett and Roe [15] and Joyce and Link [16], used three different materials, i.e., A302B, HY100 and A533B, respectively. The specimens for A302B are standard compact tension specimens, with sizes ranging from 1/2T to 6T. The specimens for HY100 and A533B include single edge notched bending, single edge notched tension and double edge notched tension specimens.

Figure 1 gives the stresses at the first Gaussian point of the first element ahead of the current crack tip (referred to as G1-F1 later) for A302B. In the simulation, the same element size is used along the entire line of crack growth for every specimen. The stresses of G1-F1 are thus the stresses of a point with fixed position relative to the current crack tip. Figure 1 shows that stresses, especially equivalent stresses, are independent of specimen size and thus, can be used to characterize ductile fracture. This is also true for HY100 and A533B.

Stresses at a critical distance from the crack tip remain constant during steady static crack growth. A transition region exists before crack growth reaches the steady state. However, the transition is very short if equivalent stress is used to characterize ductile fracture. Here, a simple ductile fracture criterion is adopted which states that when the equivalent stress at a critical distance from the current

crack tip (say, G1-F1 for a specific mesh) reaches a critical value, the crack would grow. In using this criterion in cracked flat plates, the plane strain nature of the near tip stresses must be accounted for. This is accomplished by using a plane strain core that encompasses and moves with the crack tip. Beyond the plane strain core region, a state of plane stress is assumed.

To realize the moving plane strain core model using the commercial finite element code ABAQUS, user material subroutines must be used. Unfortunately, ABAQUS cannot be used to plot contours of plastic deformation when user material subroutines are used. Instead, a simplified version of the plane strain core model, i.e., plane strain strip model which was first suggested by Dawicke et al [17] is used in this study. For the plane strain strip model, a strip which spans the crack line is assumed to be in plane strain and the rest of the plate in plane stress. Although not precise, the plane strain strip model captures the plane strain characteristics of singular stresses at the crack tip.

THE NUMERICAL MODEL

The problem considered in this study is a flat plate under remote uniform tensile displacement. The two sides of the panel are traction free. A major crack of initial length 20 cm is at the center of the plate. Two smaller cracks, each of length 1.5 cm, are symmetrically located 5 cm away from the major crack on the crack line, as shown in Figure 2. Only a quarter of the plate needs to be analyzed. The finite element mesh used is shown in Figure 3. The thickness of the structure is assumed to be 2 cm and the width of the plane strain strip used is 0.6 cm. The element size is 1 mm along the crack line.

The commercial finite element code ABAQUS (1994) is used in the study with four nodal plane strain element CPE4 in the plane strain strip and four nodal plane stress element CPS4 for the rest of the plate. J_2 flow theory is the constitutive model. Crack growth is modeled by nodal release. Using the ductile fracture criterion to predict crack growth is an interactive process that requires consecutive redefining boundary conditions in accordance with the current crack length, which itself is being determined by the the results from current calculations. This interactive calculation is realized by using user subroutines "uel" and "uvarm". The user subroutine "uvarm" is used to read the equivalent stress at the first Gaussian point of the first element ahead of current crack tip. The user subroutine "uel" is the subroutine to define the user element. It is used here to define two nodal spring elements which lie below the line of crack growth. A shadow node is defined with the same coordinates but with a different nodal number for each of the nodes along the line of crack growth. Each of the spring elements connects a node along the crack growth line to its shadow which is rigidly supported. The spring element possesses an almost infinite stiffness before breaking; it breaks only when it is at the current crack tip and the equivalent stress at the first Gaussian point of the first element ahead of it reaches critical value.

In the ABAQUS execution, the equivalent stress at the first Gaussian point of the first element ahead of current crack tip is read by "uvarm" for each increment of loading and is compared with the given critical stress for crack growth. If the equivalent stress is equal to or larger than the critical

stress, a signal is sent to the subroutine "uel" so that the spring element below the current crack tip will break in the following calculations.

RESULTS OF CRACK INTERACTION

Two different materials are studied, i.e., A302 steel and 2024-T3 aluminum alloy. The stress and strain relations for the two materials are shown in Fig. 4. The aluminum alloy has a lower yield stress and does not harden as much as A302. The critical equivalent stresses for fracture at G1-F1 for crack growth with the element size of 1 mm are 390 MPa and 455 MPa for 2024-T3 and A302, respectively. The critical equivalent stresses are obtained from numerical simulations.

Figure 5(a) gives the load and displacement relations for A302. Initially, only the major crack grows, and the yielding zone of the major crack extends quickly, as shown in Figure 5(b). At the load level indicated by a circle in Fig. 5(a), the yielding zone of the major crack begins to join with that of the left crack tip of the small crack, as shown in Fig 5(c). As soon as the two yield zones overlap, the small crack grows towards the major crack. The speed of the growth of the small crack picks up quickly, and would surpass that of the major crack. The combined yield zone of the major crack and left tip of the small crack extends with loading and finally joins the yielding zone of the right tip of the small crack, as shown in Fig. 5(d). The load at which the two yield zones coalesce is depicted by a star in Fig. 5(a). After the yielding zone of the right tip of the small crack coalesces the combined yielding zone of the major crack and left tip of the small crack, the right tip of the small crack begins to grow to the right. The coalescence of the major crack and small crack is accelerated with further loading, and load and displacement curve has a jump when the major crack and small crack meet.

Obviously, for material A302, overlap of the yielding zone of the major crack and that of the small crack does not mean the two cracks will coalesce. Load can still increase after the overlapping.

Before turning to the results of 2024-T3, we need to elaborate the definition of crack length. For fracture tests carried out on 2024-T3, very severe tunneling effects are found, as shown in Fig. 6 for an 1T one inch thick specimen. When tunnelings are there, crack length measured on specimen surface or inferred by compliance calculation leads to overestimation of the load capacity of a structure [18]. An equivalent crack length, the average of crack length through the plate thickness has to be used in such cases. As shown in Figure 7, by using the equivalent crack length and plane strain core, fracture tests on 2024-T3 can be accurately simulated. In the following discussion, the crack length for 2024-T3 refers to the equivalent crack length.

Figure 8(a) presents the load and displacement relation for the material 2024-T3. The initial load-displacement relation is basically linear, where only the major crack grows stably. When the load reaches the value denoted in Fig. 8(a) by a circle, the yielding zones of the major crack and small crack overlap, as shown in Fig. 8(c). By then the major crack has already extended for 1.0 cm. The small crack begins to grow towards the major crack as the the yielding zones overlap. The small crack grows slowly initially, but picks up the pace very quickly. The right tip of the small crack starts growing as shown in Fig. 8(d) when its yielding zone merges with the combined yielding zone of the

major crack and the left tip of the small crack. The coalescence of the major crack and the small crack appears unstable as it is accompanied by an abrupt drop in loading. It is also noted that for 2024-T3, the coalescence of these cracks occurs almost immediately after the yielding zones overlap.

CONCLUSION

By comparing results for the two materials reported in the above sections, we conclude that plastic properties of materials, such as yielding and hardening, play an important role in the crack interactions in ductile materials. For 2024-T3 which exhibits little hardening, the merging of the crack tip plastic zone of the major crack and the small crack leads to almost immediate coalescence of the cracks and, correspondingly, a sharp drop in the applied load. The present numerical results appear to support Swift's postulation at least for aluminum alloys. Of course, to obtain accurate predictions using Swift's postulation, an accurate estimate of the crack tip plastic zone size should be used instead of the Irwin's model suggested by Swift.

Acknowledgment

REFERENCE

1. Swift, T.: Widespread Fatigue Damage Monitoring Issues And Concerns, in *Proc. Int. Conf. on Structural Airworthiness of New and Aging Aircraft*, Hamburg, 1993, pp. 113-150.

2. Swift, T.: Damage Tolerance in Pressurized Fuselages, *14th International Committee on Aeronautical Fatigue*, 1987. pp. 351-387.

3. Swift, T.: Damage Tolerance Capability, In: *Fatigue of Aircraft Materials, Proc. Specialists Cof.*, Delft, Oct., 1992, pp. 351-387.

4. Rice, J. R.: Mathematical analysis in th e mechanics of fracture, in *Fracture 2* (Edited by H. Liebowitz). Academic Press, New York, 1968.

5. Landes, J. D.: Extrapolation of the J-R Curve for Predicting Reactor Vessel Integrity, *NUREG/CR-5652*, US Nuclear Regulatory Commission, Washington D.C., 1992.

6. Saka. M. ; Shoji. T.; Takcheshi. H.; and Abe. H.: A Criterion Based on Crack Tip Energy Dissipation in Plane Strain Crack Growth under Large Scale Yielding. in: *Elastic-Plastic Fracture: second symposium. V.1-Inelastic Analysis. ASTM STP 803*. pp. I-130 - I-158.

7. Newman Jr.. J. C.: Booth. B. C.: and Shivakumar. K. N.: An Elastic Plastic Finite Element Analysis of the J Resistance Curve Using a CTOA Criterion, *Fracture Mechanics: eighteenth symposium. ASTM STP 945*. 1988. pp. 665-685.

8. Su. X. M.; and Sun. C. T.: A Ductile Fracture Criterion Derived from Numerical Simulations. in: *Proceedings of the 24th Midwest Applied Mechanics Conference*, Iowa State University. 1996, pp. 317-319.

9. Su. X. M.: and Sun. C. T.: On Singular Stress at the Crack Tip of a Thick Plate under In-plane Loading. *International Journal of Fracture*. to appear.

10. Newman Jr.. J. C.; Bigelow, C. A.; and Shivakumar. K. N.: Three Dimensional Elastic Plastic Finite Element Analysis of Constraint Variations in Cracked Bodies, *NASA TM-107704*. National Aeronautics and Space Administration, Washington , DC.,1992.

11. Narasimhan R.; and Rosakis, A. J.: Three-Dimensional Effects near a Crack Tip in a Ductile Three-Point Bend Specimen: Part I-a Numerical Investigation, *Journal of Applied Mechanics*. vol. 57, 1990, pp. 607-617.

12. Nakamura, T.; and Park, D. M.: Three-dimensional Crack Front Fields in a Thick Ductile Plate, *Journal of Mechanics Physics and Solids*, vol. 38, 1990, pp. 787-812.

13. Su, X. M.; and Sun, C. T: A Plane Strain Core Model for Crack Growth in Ductile materials. presented at the *Symposium on Fracture Mechanics for Ductile Materials, ASME WAM*, Atlanta, 1996.

14. Hiser, L. A.; and Terrel, J. B.: Size Effects on J-R Curves for A302-B Plate, *NUREG/CR-5265*. US Nuclear Regulatory Commission, Washington DC, 1989.

15. Joyce, J. A.; Hackett, E. M.; and Roe, C.: Comparison of J_{1c} and J-R Curves for Short Cracked Tensilely Loaded Specimen Geometries of High Strength Structural Steel, *NUREG/CR-5879*, US Nuclear Regulatory Commission, Washington DC., 1992.

16. Joyce, J. A.; and Link, R. E.: Effects of Tensile Loading on Upper Shelf Fracture Toughness, *NUREG/CR-6051*, US Nuclear Regulatory Commission, Washington DC., 1994.

17. Dawicke, D. S.; Sutton. M. A.; Newman, Jr.. J. C; and Bigelow, C. A.: Measurement and Analysis of Critical CTOA for an Aluminum Alloy Sheet, in *Fracture Mechanics: 25th Volume, ASTM STP 1220*, F. Erdogan, Ed., American Society for Testing and Materials, Philadelphia, 1995.

18. Su. X. M.: Three Dimensional Effects in Ductile Fracture, Ph.D thesis, School of Aeronautics and Astronautics, Purdue University, Dec., 1996.
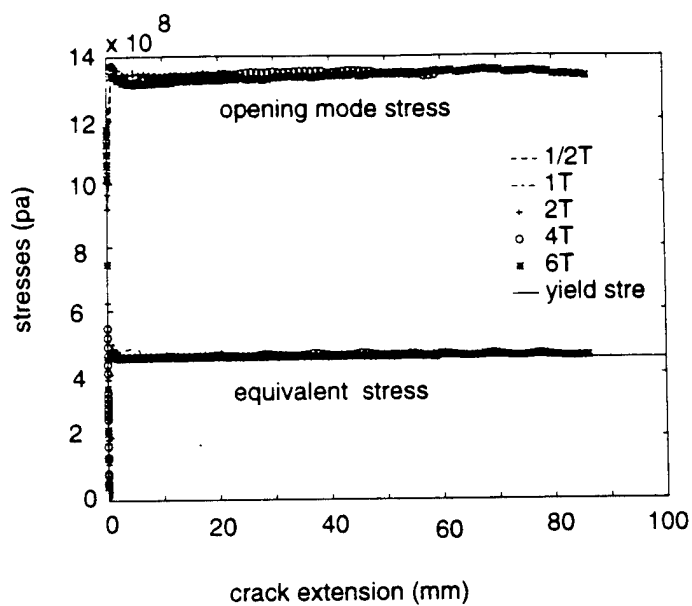
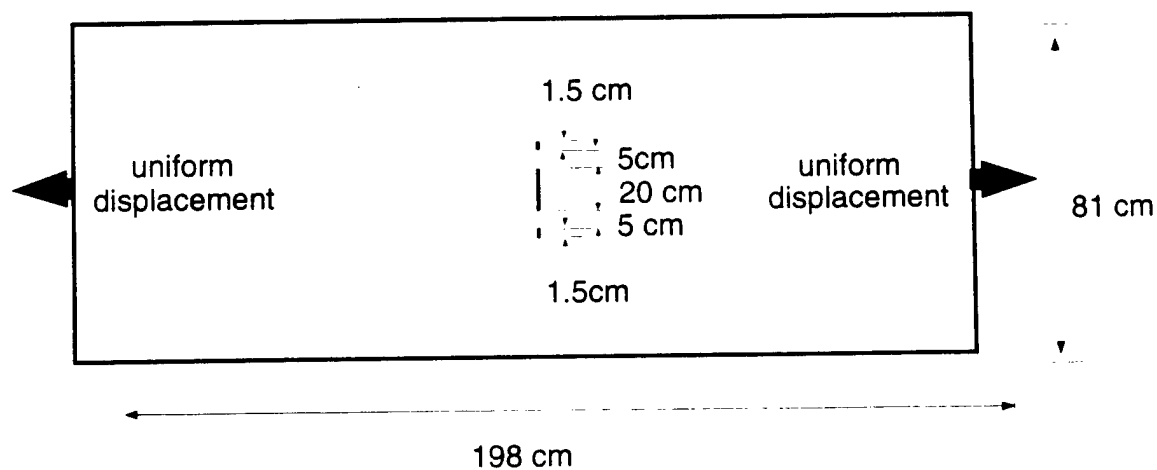Figure 1: Stresses at G1-F1 from numerical simulations

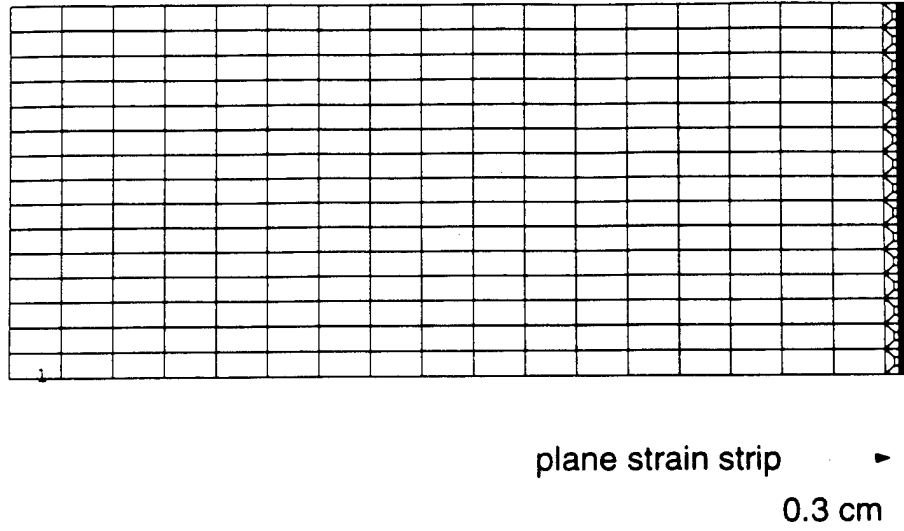Figure 2: A panel with a mjor crack and two small cracks
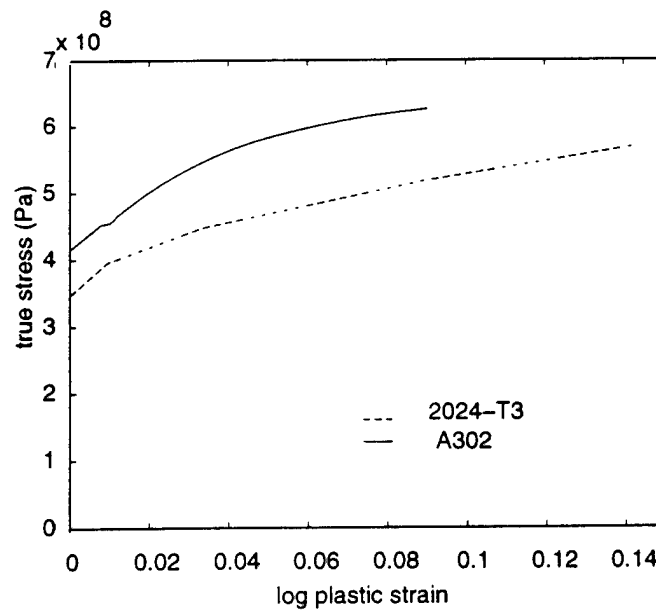
plane strain strip ► ◄

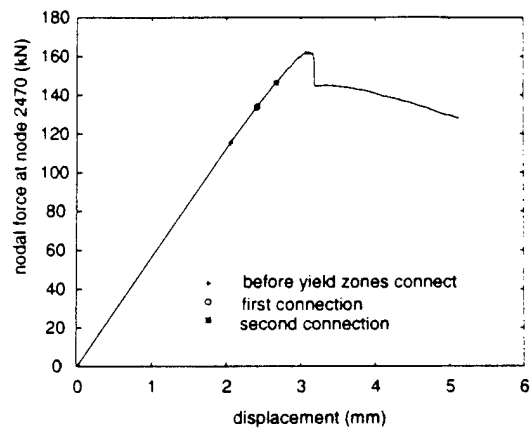0.3 cm

Figure 3: The mesh used in the analysis

Figure 4: Stress and strain curves for A302 and 2024-T3

(a) Load and displacement
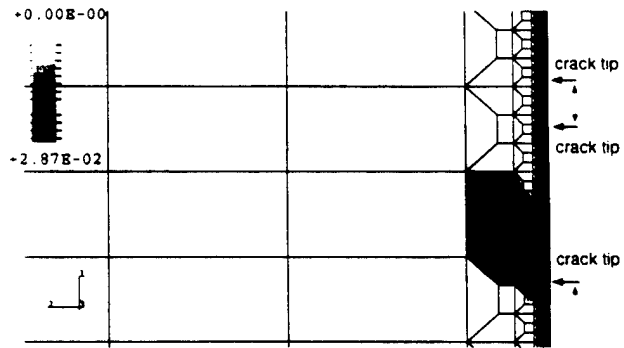
(b) yield zone for load at 'x'
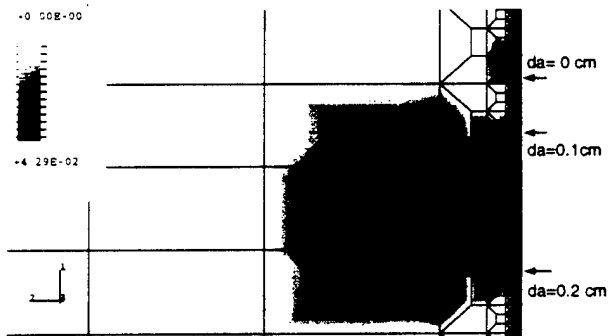
(c) Yield zone for load at 'o' in (a)

(d) Yield zone for load at '*' in (a)

Figure 5: Yield development during crack interaction for A302

crack front before
static loading

a_v

a_e

crack front after
2 mm surface crack growth

a_v : Visual crack length

a_e : Equivalent crack length

Figure 6: Fracture tests showing tunneling

Loadline disp. vs load (1/4" thick, core=1/2 thickness)

o   measured data
—   moving core simulation

load (kN)

loadline displacement (mm)

Figure 7: Load and loadline relation by using equivalent crack length
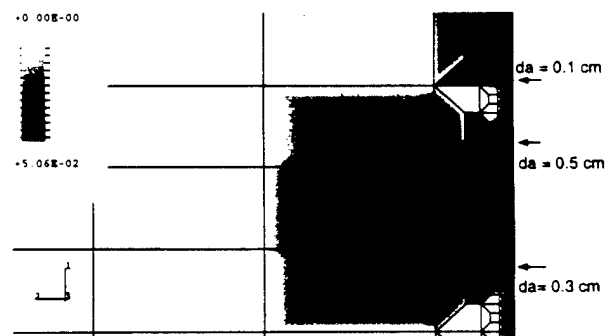
10

(a) Load and displacement curve

(b) yield zone for load at 'x'

(c) Yield zone for load at 'o' in (a)

(d) Yield zone for load at '*' in (a)

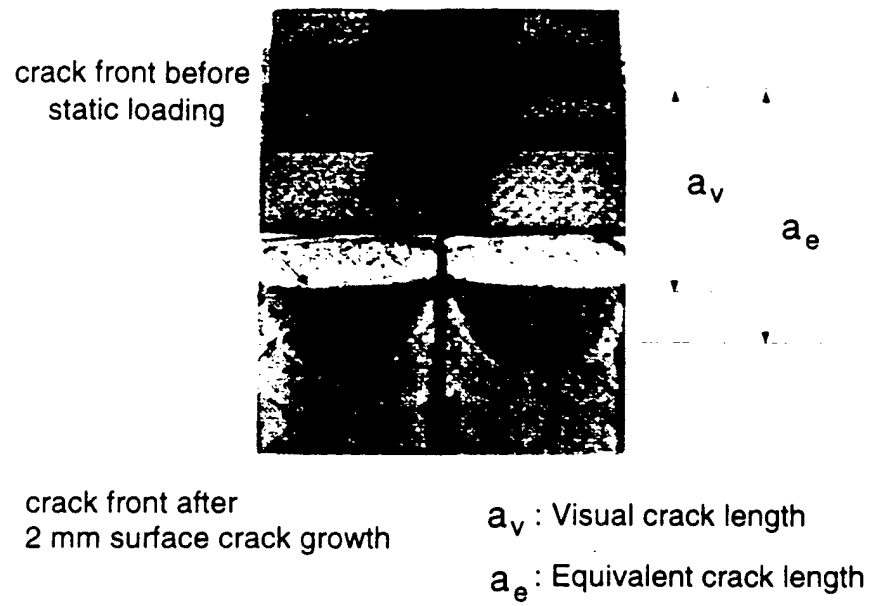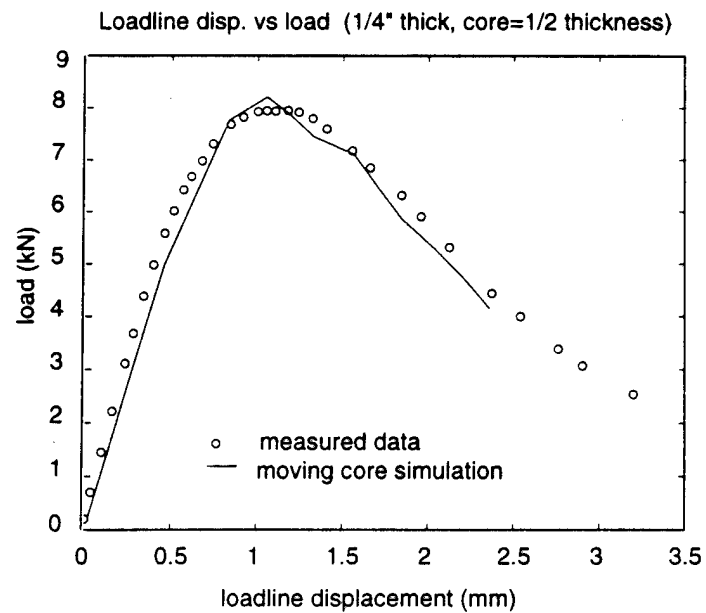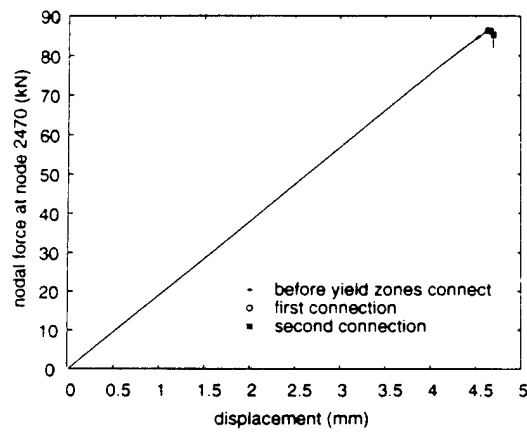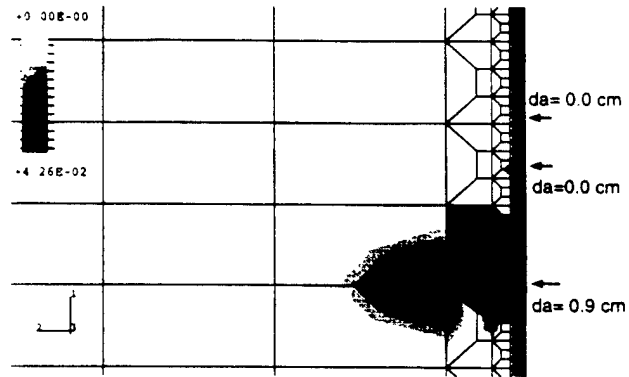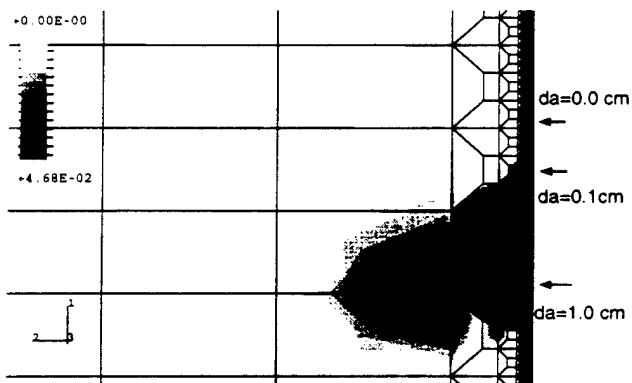Figure 8: Yield development during crack interaction for 2024-T3

11

4t7-1

On singular stress at the crack tip of a thick plate under in-plane loading

X.M. SU and C.T. SUN

School of Aeronautics and Astronautics, Purdue University, West Lafayette, Indiana 47907, USA

Abstract. By superposition of three asymptotic solutions, which collectively satisfy all the equilibrium and compatibility equations as well as boundary conditions, the three-dimensional crack tip stresses of a thick plate with a through-the-thickness cut are shown to be of square root singularity throughout the thickness. The near tip deformation is shown to be plane strain with stress intensity factor changing in the thickness direction. All components of the singular stresses vanish on plate surfaces. The profile of the stress intensity factor in the thickness direction cannot be determined by the asymptotic analysis alone.

1. Introduction

Crack-tip singularity and the profile of stress intensity in the thickness direction of a plate with a through-thickness cut are still open problems [1]. Earlier publications can be found in the review paper by Sih [2]. Several results are of interest, especially, those of Benthem [3], Kawai, Fujitani and Kumagai [4] and Sinclair [5]. Although most of the previous attempts followed to some degree Williams' separable eigenvalue approach [6], different coordinate systems and different approximations were used. Benthem [3] used spherical coordinates and concentrated his attention on the corner point (the intersection of the crack front and the plate surface). While boundary conditions at crack surface were satisfied exactly, the boundary conditions of the plate surfaces were only satisfied approximately. The results obtained by Benthem were characterized by a stress singularity less than square root at the corner point. This was true even if the crack tip was approached in a plane that is parallel to the free plate surface. Kawai et al. [4] also used spherical coordinates, but the boundary conditions on crack surfaces were satisfied approximately and those on plate surfaces exactly. The corresponding singularity was higher than square root. Sinclair [5] used cylindrical coordinates which were more or less similar to Sih's classical work [2]. The singularity in Sinclair's study was square root. However, the traction free boundary conditions of the plate surfaces were not satisfied completely by his solution, even though Sinclair was interested in stresses close to the plate surfaces.

In the present paper, the above crack problem is treated using a new approach. Recent developments in thick plate theory are exploited to obtain an asymptotic expansion of singular stresses at the crack tip that satisfy not only equilibrium and compatibility equations but also all boundary conditions exactly.

2. Basic equations

Consider a plate with a through-the-thickness cut. The plate is $2h$ thickness, and both upper and lower-plate surfaces and the crack surfaces are traction free. Loading is applied on the
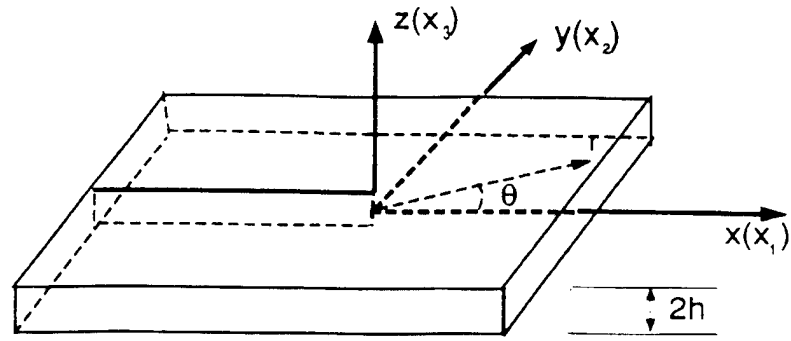
Figure 1. A thick plate with a through-the-thickness cut.

edges and is symmetric about the middle plane of the plate. A cylindrical coordinate system is established with the (r, θ) plane in the middle plane of the plate. The origin of the coordinate system is at the crack tip with the plane $\theta = 0$ parallel to the crack surface as shown in Figure 1.

The problem described above is among the thick plate problems which have been studied by Gregory [7]. Gregory has rigorously proved that the most general state of stress $\sigma_{ij}(i, j = 1, 2, 3)$ for the thick plate problem can be uniquely decomposed into three parts

$$\sigma_{ij} = \sigma_{ij}^{PS} + \sigma_{ij}^{S} + \sigma_{ij}^{PF}, \quad (i, j = 1, 2, 3),$$
(1)

where σ_{ij}^{PS} is the (exact) plane stress state; σ_{ij}^{S} the shear state stress; and σ_{ij}^{PF}, the so called Papkovich–Fadle state stress. The three stress fields are generated by three different stress functions. Following [7] the three stress states are described below.

Plane stress state

This is the well known (exact) plane stress [8]. The solution of the (exact) plane stress is a modification of the solution of plane stress in the conventional sense such that all the equilibrium and compatibility equations are satisfied. The stresses are obtained from stress function ψ as

$$\sigma_{11}^{PS} = \psi_{,22} + \frac{\nu(1 - 3(\frac{x_3}{h})^2)h^2}{6(1 + \nu)} \overline{\nabla}^2 \psi_{,22},$$
(2)

$$\sigma_{22}^{PS} = \psi_{,11} + \frac{\nu(1 - 3(\frac{x_3}{h})^2)h^2}{6(1 + \nu)} \overline{\nabla}^2 \psi_{,11},$$
(3)

$$\sigma_{12}^{PS} = -\psi_{,12} - \frac{\nu(1 - 3(\frac{x_3}{h})^2)h^2}{6(1 + \nu)} \overline{\nabla}^2 \psi_{,12},$$
(4)

$$\sigma_{13}^{PS} = \sigma_{23}^{PS} = \sigma_{33}^{PS} = 0,$$
(5)

where a comma indicates partial differentiation, ν is Poisson's ratio, and ψ is a two-dimensional function satisfying the biharmonic equation

$$\overline{\nabla}^2 \overline{\nabla}^2 \psi = \left(\frac{\partial^2}{\partial x_1^2} + \frac{\partial^2}{\partial x_2^2} \right) \left(\frac{\partial^2}{\partial x_1^2} + \frac{\partial^2}{\partial x_2^2} \right) \psi = 0.$$
(6)

Shear stress state

Shear stress state is derived from a three-dimensional potential function ϕ as

$$\sigma_{11}^S = 2\phi_{,12}, \tag{7}$$

$$\sigma_{22}^S = -2\phi_{,12}, \tag{8}$$

$$\sigma_{12}^S = \phi_{,22} - \phi_{,11}, \tag{9}$$

$$\sigma_{13}^S = \phi_{,23}, \tag{10}$$

$$\sigma_{23}^S = -\phi_{,13}, \tag{11}$$

$$\sigma_{33}^S = 0, \tag{12}$$

where

$$\nabla^2\phi = \frac{\partial^2\phi}{\partial x_1^2} + \frac{\partial^2\phi}{\partial x_2^2} + \frac{\partial^2\phi}{\partial x_3^2} = 0 \tag{13}$$

and

$$\phi_{,3}\,|_{x_3=\pm h} = 0, \tag{14}$$

$$\int_{-h}^{h} \phi\,\mathrm{d}x_3 = 0. \tag{15}$$

Papkovich–Fadle state

Papkovich–Fadle state stress is generated by a three-dimensional bi-harmonic function φ as

$$\sigma_{11}^{PF} = \varphi_{,1133} + \nu\nabla^2\varphi_{,22}, \tag{16}$$

$$\sigma_{22}^{PF} = \varphi_{,2233} + \nu\nabla^2\varphi_{,11}, \tag{17}$$

$$\sigma_{12}^{PF} = \varphi_{,1233} - \nu\nabla^2\varphi_{,12}, \tag{18}$$

$$\sigma_{13}^{PF} = -\overline{\nabla}^2\varphi_{,13}, \tag{19}$$

$$\sigma_{23}^{PF} = -\overline{\nabla}^2\varphi_{,23}, \tag{20}$$

$$\sigma_{33}^{PF} = \overline{\nabla}^2\overline{\nabla}^2\varphi, \tag{21}$$

where

$$\nabla^2\nabla^2\varphi = 0 \tag{22}$$

and

$$\varphi|_{x_3=\pm h} = \varphi_{,3}\,|_{x_3=\pm h}. \tag{23}$$

It can easily be confirmed that any combinations of the above three types of stresses satisfy not only the equilibrium equations and compatibility equations but also the boundary conditions on free plate surfaces.

It was shown by Gregory [7] that the decomposition of the three-dimensional stress field in a thick plate into PS, S and PF stresses is unique. On the other hand, one recalls that the conventional plane stress solution is unique once boundary conditions of the two-dimensional problem are prescribed. The PS state of stress, or the (exact) plane stress, shares the same stress function as the conventional plane stress problem if the stress function is determined with the boundary conditions obtained from averaging traction on the edges through-the-thickness. In the next section, the asymptotic PS state stress will be given first. The PS state stress obtained includes terms whose singularities are of higher order than that of inverse square root. These higher order singularity terms violate boundary conditions on crack surfaces. The S and PF state stresses are given subsequently. The three stresses are then combined to create the asymptotic solution that satisfies all the boundary conditions. All formulations in the paper are for mode I loading. The results for mode II are listed in Appendix II.

3. Asymptotic solution for mode I loading

3.1. EXPANSION OF PS, S AND PF STATE STRESS

PS state stress

PS state stress consists of two parts: conventional plane stress and the modification which is added to satisfy compatibility equations of elasticity. As noted in Section 2, the stress function of PS state stress is determined by solving a conventional plane stress problem with the boundary conditions obtained from averaging traction on the edges through-the-thickness. Boundary conditions for the stress function of the PS state are therefore

$$\frac{1}{h} \int_{-h}^{h} \sigma_{22} \mid_{\theta=\pm\pi} \, \mathrm{d}x_3 = \frac{1}{h} \int_{-h}^{h} \sigma_{\theta} \mid_{\theta=\pm\pi} \, \mathrm{d}z = 0, \tag{24}$$

$$\frac{1}{h} \int_{-h}^{h} \sigma_{12} \mid_{\theta=\pm\pi} \, \mathrm{d}x_3 = \frac{1}{h} \int_{-h}^{h} \sigma_{r\theta} \mid_{\theta=\pm\pi} \, \mathrm{d}z = 0. \tag{25}$$

Following Williams [6], the stress function in (6) is expanded in terms of r as

$$\psi(r,\theta) = r^{1+\lambda}\tilde{\psi}(\theta), \tag{26}$$

where λ is an arbitrary positive number. $\tilde{\psi}(\theta)$ is determined by

$$(1+\lambda)^2(\lambda-1)^2\tilde{\psi} + [(\lambda-1)^2 + (1+\lambda)^2]\tilde{\psi}'' + \tilde{\psi}'''' = 0. \tag{27}$$

The above differential equation is the result of substituting (26) into (6). The general solutions are

$$\tilde{\psi} = A \sin(\lambda-1)\theta + B \cos(\lambda-1)\theta + C \sin(1+\lambda)\theta + D\cos(1+\lambda)\theta. \tag{28}$$

The stress components are obtained by substituting (26) in (2–5). These stresses will satisfy boundary conditions in (24) and (25) only when

$$\sin 2\lambda\pi = 0, \tag{29}$$

which leads to eigenvalues

$$\lambda = \tfrac{1}{2}m, \quad m = 1, 2, 3, \ldots \tag{30}$$

The above eigenvalues are identical to the two-dimensional results obtained by Williams [6]. The negative integers are not included to avoid singular displacements. The even integers are associated with regular stresses. Thus, only the odd integers are associated with singular stresses and are taken for the asymptotic solutions.

For mode I (symmetric mode), we have

$$w = \left[B_1 \cos \tfrac{1}{2}\theta + D_1 \cos \tfrac{1}{2}3\theta \right] r^{3/2} + \left[B_2 \cos \tfrac{1}{2}\theta + D_2 \cos \tfrac{1}{2}5\theta \right] r^{5/2} + \cdots$$

$$+ [B_n \cos(n - \tfrac{3}{2})\theta + D_n \cos(n + \tfrac{1}{2})\theta] r^{n+1/2} + \cdots, \tag{31}$$

where B_n and D_n are constants. The corresponding stress components are

$$\sigma_{rr}^{PS} = -\tfrac{3}{2} B_1 k(z) \cos(\tfrac{1}{2}\theta) r^{-(5/2)} + \tfrac{3}{2} B_2 k(z) \cos(\tfrac{1}{2}\theta) r^{-(3/2)}$$

$$+ [\tfrac{5}{4} B_1 \cos \tfrac{1}{2}\theta - \tfrac{3}{4} D_1 \cos \tfrac{3}{2}\theta - \tfrac{15}{2} B_3 k(z) \cos \tfrac{3}{2}\theta] r^{-(1/2)} + \cdots, \tag{32}$$

$$\sigma_{\theta\theta}^{PS} = \tfrac{3}{2} B_1 k(z) \cos(\tfrac{1}{2}\theta) r^{-(5/2)} - \tfrac{3}{2} B_2 k(z) \cos(\tfrac{1}{2}\theta) r^{-(3/2)}$$

$$+ [\tfrac{3}{4} B_1 \cos \tfrac{1}{2}\theta + \tfrac{3}{4} D_1 \cos \tfrac{3}{2}\theta + \tfrac{15}{2} B_3 k(z) \cos \tfrac{3}{2}\theta] r^{-(1/2)} + \cdots, \tag{33}$$

$$\sigma_{r\theta}^{PS} = -\tfrac{3}{2} B_1 k(z) \sin(\tfrac{1}{2}\theta) r^{-(5/2)} - \tfrac{3}{2} B_2 k(z) \sin(\tfrac{1}{2}\theta) r^{-(3/2)}$$

$$+ [\tfrac{1}{4} B_1 \sin \tfrac{1}{2}\theta + \tfrac{3}{4} D_1 \sin \tfrac{3}{2}\theta + \tfrac{15}{2} B_3 k(z) \sin \tfrac{3}{2}\theta] r^{-(1/2)} + \cdots, \tag{34}$$

$$\sigma_{zz}^{PS} = \sigma_{rz}^{PS} = \sigma_{\theta z}^{PS} = 0. \tag{35}$$

In the above equations

$$k(z) = \frac{\nu(1 - 3(\tfrac{z}{h})^2)h^2}{6(1 + \nu)}. \tag{36}$$

It is noted that terms of singularity $r^{-(5/2)}$ and $r^{-(3/2)}$ appear in (32–34). These terms satisfy the two-dimensional conditions in (24–25) but violate exact three-dimensional boundary conditions on crack surfaces as $\sigma_{r\theta}^{PS}$ is not zero when $\theta = \pm\pi$. Thus, the S and PS state stresses are needed to make the crack surfaces traction free.

S state stress

Stress function ϕ is expanded as

$$\phi(r, \theta, z) = \sum_{n=1}^{\infty} \phi_n(r, \theta) \cos\left(\frac{n\pi z}{h}\right), \tag{37}$$

where ϕ_n is determined by

$$\overline{\nabla}^2 \phi_n - \left(\frac{n^2 \pi^2}{h^2}\right) \phi_n = 0, \tag{38}$$

which is obtained by substituting (35) into (13).

Each ϕ_n is again expanded as

$$\phi_n(r.\theta) = \sum_{k=1}^{\infty} \phi_{nk}(\theta) r^{k-(3/2)}. \tag{39}$$

After solving ϕ_{nk} by using asymptotic equations obtained by substituting (39) into (38), the above expansion can be arranged into

$$\phi_n(r.\theta) = (a_{n1} \sin \tfrac{1}{2}\theta) r^{-(1/2)} + (a_{n2} \sin \tfrac{1}{2}\theta) r^{1/2}$$
$$+ \left[a_{n3} \sin \frac{3\theta}{2} + \frac{1}{2} \left(\frac{n\pi}{h} \right)^2 (a_{n1} \sin \tfrac{1}{2}\theta) \right] r^{3/2} + \cdots, \tag{40}$$

where $a_{ni}(i = 1, \ldots,)$ are constants. The corresponding stress components are obtained after applying (37) and (40) in respective expressions in (7–12). We obtain

$$\sigma_{rr}^S = -\tfrac{3}{2} \cos \tfrac{1}{2}\theta \left(\sum a_{n1} \cos \frac{n\pi}{h}z \right) r^{-(5/2)} - \tfrac{1}{2} \cos \tfrac{1}{2}\theta \left(\sum a_{n2} \cos \frac{n\pi}{h}z \right) r^{-(3/2)}$$
$$+ \left[\tfrac{3}{2} \cos \tfrac{1}{2}3\theta \left(\sum a_{n3} \cos \frac{n\pi}{h}z \right) \right.$$
$$\left. + \tfrac{1}{4} \cos \tfrac{1}{2}\theta \left(\sum \left(\frac{n\pi}{h} \right)^2 a_{n1} \cos \frac{n\pi}{h}z \right) \right] r^{-(1/2)} + \cdots, \tag{41}$$

$$\sigma_{\theta\theta}^S = -\sigma_r^S, \tag{42}$$

$$\sigma_{r\theta}^S = -\tfrac{3}{2} \sin \tfrac{1}{2}\theta \left(\sum a_{n1} \cos \frac{n\pi}{h}z \right) r^{-(5/2)} + \tfrac{1}{2} \sin \tfrac{1}{2}\theta \left(\sum a_{n2} \cos \frac{n\pi}{h}z \right) r^{-(3/2)}$$
$$+ \left[-\tfrac{3}{2} \sin \tfrac{1}{2}3\theta \left(\sum a_{n3} \cos \frac{n\pi}{h}z \right) \right.$$
$$\left. + \tfrac{1}{4} \sin \tfrac{1}{2}\theta \left(\sum \left(\frac{n\pi}{h} \right)^2 a_{n1} \cos \frac{n\pi}{h}z \right) \right] r^{-(1/2)} + \cdots, \tag{43}$$

$$\sigma_{rz}^S = -\tfrac{1}{2} \cos \tfrac{1}{2}\theta \left(\sum a_{n1} \left(\frac{n\pi}{h} \right) \sin \frac{n\pi}{h}z \right) r^{-(3/2)}$$
$$- \tfrac{1}{2} \cos \tfrac{1}{2}\theta \left(\sum a_{n2} \left(\frac{n\pi}{h} \right) \sin \frac{n\pi}{h}z \right) r^{-(1/2)} + \cdots, \tag{44}$$

$$\sigma_{\theta z}^S = -\tfrac{1}{2} \sin \tfrac{1}{2}\theta \left(\sum a_{n1} \left(\frac{n\pi}{h} \right) \sin \frac{n\pi}{h}z \right) r^{-(3/2)}$$
$$+ \tfrac{1}{2} \sin \tfrac{1}{2}\theta \left(\sum a_{n2} \left(\frac{n\pi}{h} \right) \sin \frac{n\pi}{h}z \right) r^{-(1/2)} + \cdots, \tag{45}$$

$$\sigma_{zz}^S = 0. \tag{46}$$

PF stress state

The stress function is assumed to be (see [7])

$$\varphi(r, \theta, z) = \sum_\lambda \varphi_\lambda(r, \theta) E_\lambda(z). \tag{47}$$

where $E_\lambda(z)$ is defined by

$$E_\lambda(z) = \left(\frac{z}{h} - 1\right) \sin\left[\lambda\left(\frac{z}{h} + 1\right)\right] + \left(\frac{z}{h} + 1\right) \sin\left[\lambda\left(\frac{z}{h} - 1\right)\right] \tag{48}$$

and λ is the root of the equation

$$\sin 2\lambda + 2\lambda = 0. \tag{49}$$

Without losing generality, the summation in (47) will run only through roots whose real parts are positive (see [7]). The roots are thus in conjugate pairs.

Substituting (47) into (22) leads to

$$\overline{\nabla}^2 \varphi_\lambda - \left(\frac{\lambda}{h}\right)^2 \varphi_\lambda = 0. \tag{50}$$

Consistent with the expansions of PS stress, φ_λ is assumed to be

$$\varphi_\lambda = \sum_{k=1}^\infty \varphi_{\lambda k}(\theta) r^{k-(3/2)}. \tag{51}$$

With solutions of the asymptotic equations obtained by applying (51) in (50), (47) is expressed as

$$\varphi = \left[\cos\tfrac{1}{2}\theta \left(\sum d_{\lambda 1} E_\lambda(z)\right)\right] r^{-(1/2)} + \left[\cos\tfrac{1}{2}\theta \left(\sum d_{\lambda 2} E_\lambda(z)\right)\right] r^{1/2}$$
$$+ \left[\cos\tfrac{1}{2}3\theta \left(\sum d_{\lambda 3} E_\lambda(z)\right) + \tfrac{1}{2}\cos\tfrac{1}{2}\theta \left(\sum \left(\frac{\lambda}{h}\right)^2 d_{\lambda 1} E_\lambda(z)\right)\right] r^{3/2} + \cdots, \tag{52}$$

where $d_{\lambda i}$ are constants. The corresponding stress components are

$$\sigma_{rr}^{PF} = \left[\frac{3}{4}\left(\sum d_{\lambda 1} E_\lambda(z)''\right) - \tfrac{1}{4}3\nu \sum d_{\lambda 1}\left(\frac{\lambda^2}{h^2}E_\lambda(z) + E_\lambda(z)''\right)\right] \cos(\tfrac{1}{2}\theta) r^{-(5/2)}$$
$$+ \left[-\frac{1}{4}\left(\sum d_{\lambda 2} E_\lambda(z)''\right) + \tfrac{1}{4}\nu \sum d_{\lambda 2}\left(\frac{\lambda^2}{h^2}E_\lambda(z) + E_\lambda(z)''\right)\right] \cos(\tfrac{1}{2}\theta) r^{-(3/2)}$$
$$+ \left\{\left[\frac{3}{4}\left(\sum d_{\lambda 3} E_\lambda(z)''\right) - \tfrac{1}{4}3\nu \sum d_{\lambda 3}\left(\frac{\lambda^2}{h^2}E_\lambda(z) + E_\lambda(z)''\right)\right] \cos\tfrac{1}{2}3\theta\right.$$

$$-\left[\frac{3}{8}\left(\sum d_{\lambda 1}\frac{\lambda^2}{h^2}E_\lambda(z)''\right)\right.$$

$$\left.+\frac{1}{8}5\nu\sum d_{\lambda 1}\frac{\lambda^2}{h^2}\left(\frac{\lambda^2}{h^2}E_\lambda(z)+E_\lambda(z)''\right)\right]\cos\tfrac{1}{2}\theta\Bigg\}r^{-(1/2)}+\cdots \tag{53}$$

$$\sigma_{\theta\theta}^{PF}=\left[-\frac{3}{4}\left(\sum d_{\lambda 1}E_\lambda(z)''\right)+\frac{1}{4}3\nu\sum d_{\lambda 1}\left(\frac{\lambda^2}{h^2}E_\lambda(z)+E_\lambda(z)''\right)\right]\cos(\tfrac{1}{2}\theta)r^{-(5/2)}$$

$$+\left[\frac{1}{4}\left(\sum d_{\lambda 2}E_\lambda(z)''\right)-\frac{1}{4}\nu\sum d_{\lambda 2}\left(\frac{\lambda^2}{h^2}E_\lambda(z)+E_\lambda(z)''\right)\right]\cos(\tfrac{1}{2}\theta)r^{-(3/2)}$$

$$+\left\{\left[-\frac{3}{4}\left(\sum d_{\lambda 3}E_\lambda(z)''\right)+\frac{1}{4}3\nu\sum d_{\lambda 3}\left(\frac{\lambda^2}{h^2}E_\lambda(z)+E_\lambda(z)''\right)\right]\cos\tfrac{1}{2}3\theta\right.$$

$$+\left[\frac{5}{8}\left(\sum d_{\lambda 1}\frac{\lambda^2}{h^2}E_\lambda(z)''\right)\right.$$

$$\left.\left.+\frac{1}{8}3\nu\sum d_{\lambda 1}\frac{\lambda^2}{h^2}\left(\frac{\lambda^2}{h^2}E_\lambda(z)+E_\lambda(z)''\right)\right]\cos\tfrac{1}{2}\theta\right\}r^{-(1/2)}+\cdots, \tag{54}$$

$$\sigma_{r\theta}^{PF}=\left[\frac{3}{4}\left(\sum d_{\lambda 1}E_\lambda(z)''\right)-\frac{1}{4}3\nu\sum d_{\lambda 1}\left(\frac{\lambda^2}{h^2}E_\lambda(z)+E_\lambda(z)''\right)\right]\sin(\tfrac{1}{2}\theta)r^{-(5/2)}$$

$$+\left[\frac{1}{4}\left(\sum d_{\lambda 2}E_\lambda(z)''\right)-\frac{1}{4}\nu\sum d_{\lambda 2}\left(\frac{\lambda^2}{h^2}E_\lambda(z)+E_\lambda(z)''\right)\right]\sin(\tfrac{1}{2}\theta)r^{-(3/2)}$$

$$+\left\{\left[-\frac{3}{4}\left(\sum d_{\lambda 3}E_\lambda(z)''\right)+\frac{1}{4}3\nu\sum d_{\lambda 3}\left(\frac{\lambda^2}{h^2}E_\lambda(z)+E_\lambda(z)''\right)\right]\sin\tfrac{1}{2}3\theta\right.$$

$$-\left[\frac{1}{8}\left(\sum d_{\lambda 1}\frac{\lambda^2}{h^2}E_\lambda(z)''\right)\right.$$

$$\left.\left.-\frac{1}{8}\nu\sum d_{\lambda 1}\frac{\lambda^2}{h^2}\left(\frac{\lambda^2}{h^2}E_\lambda(z)+E_\lambda(z)''\right)\right]\sin\tfrac{1}{2}\theta\right\}r^{-(1/2)}+\cdots, \tag{55}$$

$$\sigma_{rz}^{PF}=\frac{1}{2}\left(\sum d_{\lambda 1}\frac{\lambda^2}{h^2}E_\lambda(z)'\right)\cos(\tfrac{1}{2}\theta)r^{-(3/2)}$$

$$-\frac{1}{2}\left(\sum d_{\lambda 2}\frac{\lambda^2}{h^2}E_\lambda(z)'\right)\cos(\tfrac{1}{2}\theta)r^{-(1/2)}+\cdots, \tag{56}$$

$$\sigma_{\theta z}^{PF}=\frac{1}{2}\left(\sum d_{\lambda 1}\frac{\lambda^2}{h^2}E_\lambda(z)'\right)\sin(\tfrac{1}{2}\theta)r^{-(3/2)}$$

$$+ \frac{1}{2} \left(\sum d_{\lambda 2} \frac{\lambda^2}{h^2} E_\lambda(z)' \right) \sin(\tfrac{1}{2}\theta) r^{-(1.2)} + \cdots. \tag{57}$$

$$\sigma_{zz}^{PF} = \sum d_{\lambda 1} \left(\frac{\lambda^4}{h^4} E_\lambda(z) \right) \cos(\tfrac{1}{2}\theta) r^{-\frac{1}{2}} + \cdots. \tag{58}$$

3.2. ASYMPTOTIC SOLUTION OF THE SINGULAR STRESS FIELD

In the above, PS, S and PF stresses are expanded asymptotically around the crack tip. Now the three stresses are combined so that an asymptotic solution to the three-dimensional crack problem can be obtained. The three stresses individually satisfy not only all equilibrium equations and compatibility equations but also the boundary conditions at the two plate surfaces. However, the boundary conditions at the crack surfaces are satisfied only when the three stresses are combined. These crack surface boundary conditions are

$$\sigma_\theta|_{\theta=\pm\pi} = 0, \tag{59}$$

$$\sigma_{r\theta}|_{\theta=\pm\pi} = 0, \tag{60}$$

$$\sigma_{z\theta}|_{\theta=\pm\pi} = 0. \tag{61}$$

Asymptotic analysis of order $r^{-(5/2)}$

Adding the three stresses obtained in Section 3.1, the amplitudes of stresses of order $r^{-(5/2)}$ are

$$\sigma_{rr}^{(-(5/2))} = -\tfrac{3}{2} B_1 k(z) \cos \tfrac{1}{2}\theta - \tfrac{3}{2} \cos \tfrac{1}{2}\theta \left(\sum a_{n1} \cos \frac{n\pi}{h} z \right)$$
$$+ \left[\frac{3}{4} \left(\sum d_{\lambda 1} E_\lambda(z)'' \right) - \tfrac{1}{4} 3\nu \sum d_{\lambda 1} \left(\tfrac{\lambda^2}{h^2} E_\lambda(z) + E_\lambda(z)'' \right) \right] \cos(\tfrac{1}{2}\theta), \tag{62}$$

$$\sigma_{\theta\theta}^{(-(5/2))} = \tfrac{3}{2} B_1 k(z) \cos \tfrac{1}{2}\theta + \tfrac{3}{2} \cos \tfrac{1}{2}\theta \left(\sum a_{n1} \cos \frac{n\pi}{h} z \right)$$
$$+ \left[-\frac{3}{4} \left(\sum d_{\lambda 1} E_\lambda(z)'' \right) + \tfrac{1}{4} 3\nu \sum d_{\lambda 1} \right.$$
$$\left. \times \left(\frac{\lambda^2}{h^2} E_\lambda(z) + E_\lambda(z)'' \right) \right] \cos(\tfrac{1}{2}\theta), \tag{63}$$

$$\sigma_{r\theta}^{(-(5/2))} = -\tfrac{3}{2} B_1 k(z) \sin \tfrac{1}{2}\theta - \tfrac{3}{2} \sin \tfrac{1}{2}\theta \left(\sum a_{n1} \cos \frac{n\pi}{h} z \right)$$
$$+ \left[\frac{3}{4} \left(\sum d_{\lambda 1} E_\lambda(z)'' \right) - \frac{3\nu}{4} \sum d_{\lambda 1} \left(\frac{\lambda^2}{h^2} E_\lambda(z) + E_\lambda(z)'' \right) \right] \sin(\tfrac{1}{2}\theta), \tag{64}$$

$$\sigma_{rz}^{(-(5/2))} = \sigma_{\theta z}^{(-(5/2))} = \sigma_{zz}^{(-(5/2))} = 0, \tag{65}$$

where the superscript $(-(5/2))$ denotes the stress amplitude associated with the singular term $r^{-(5/2)}$. The boundary conditions in (59–61) lead to

$$-\tfrac{3}{2}B_1k(z) - \frac{3}{2}\sum a_{n1}\cos\frac{n\pi}{h}z + \frac{3}{4}\sum\left[(1-\nu)E_\lambda(z)'' - \nu\frac{\lambda^2}{h^2}E_\lambda(z)\right]d_{\lambda1} = 0. \quad (66)$$

It is easy to see that the above equation leads to the conclusion

$$\sigma_{rr}^{(-(5/2))} = \sigma_{\theta\theta}^{(-(5/2))} = \sigma_{r\theta}^{(-(5/2))} = \sigma_{rz}^{(-(5/2))} = \sigma_{\theta z}^{(-(5/2))} = \sigma_{zz}^{(-(5/2))} = 0. \quad (67)$$

Asymptotic analysis of order $r^{-(3/2)}$

Similar to the analysis of order $r^{-(5/2)}$, the boundary conditions in (59)–(61) yield

$$-\tfrac{3}{2}B_2k(z) + \frac{1}{2}\sum a_{n2}\cos\frac{n\pi}{h}z + \frac{1}{4}\sum\left[(1-\nu)E_\lambda(z)'' - \nu\frac{\lambda^2}{h^2}E_\lambda(z)\right]d_{\lambda2} = 0 \quad (68)$$

and

$$\sum_{n=1}^{\infty}\frac{n\pi}{h}a_{n1}\sin\frac{n\pi}{h}z = \sum\frac{\lambda^2}{h^2}d_{\lambda1}E_\lambda(z)'. \quad (69)$$

Using the above relations, all stresses of this order can be shown to vanish identically.

Asymptotic solution of order $r^{-(1/2)}$

Boundary conditions in (59–61) require

$$-\left\{\frac{15}{2}B_3k(z) - \frac{3}{2}\sum a_{n3}\cos\frac{n\pi}{h}z - \frac{3}{4}\sum\left[(1-\nu)E_\lambda(z)'' - \nu\frac{\lambda^2}{h^2}E_\lambda(z)\right]d_{\lambda3}\right\}$$

$$= -\left\{\frac{1}{4}\sum\frac{n^2\pi^2}{h^2}a_{n1}\cos\frac{n\pi}{h}z - \frac{1}{8}\sum\frac{\lambda^2}{h^2}\left[(1-\nu)E_\lambda(z)'' - \nu\frac{\lambda^2}{h^2}E_\lambda(z)\right]d_{\lambda1}\right\}, \quad (70)$$

$$\sum_{n=1}^{\infty}a_{n2}\frac{n\pi}{h}\sin\frac{n\pi}{h}z + \sum\frac{\lambda^2}{h^2}d_{\lambda2}E_\lambda(z)' = 0. \quad (71)$$

The amplitudes of stresses of order $r^{-(1/2)}$ are, after applying (70) and (71) in conjunction with (69)

$$\sigma_{rr}^{(-(1/2))} = \frac{1}{4}\left\{B_1 + \frac{1}{2}\sum_\lambda\frac{\lambda^2}{h^2}\left[\nu\frac{\lambda^2}{h^2}E_\lambda(z) + (1+\nu)E_\lambda(z)''\right]d_{\lambda1}\right\}$$

$$\left(5\cos\tfrac{1}{2}\theta - \cos\tfrac{1}{2}3\theta\right), \quad (72)$$

$$\sigma_{\theta\theta}^{(-(1/2))} = \frac{1}{4}\left\{B_1 + \frac{1}{2}\sum_\lambda\frac{\lambda^2}{h^2}\left[\nu\frac{\lambda^2}{h^2}E_\lambda(z) + (1+\nu)E_\lambda(z)''\right]d_{\lambda1}\right\}$$

$$\left(3\cos\tfrac{1}{2}\theta + \cos\tfrac{1}{2}3\theta\right), \quad (73)$$

$$\sigma_{r\theta}^{(-(1/2))} = \frac{1}{4}\left\{B_1 + \frac{1}{2}\sum_\lambda \frac{\lambda^2}{h^2}\left[\nu\frac{\lambda^2}{h^2}E_\lambda(z) + (1+\nu)E_\lambda(z)''\right]d_{\lambda 1}\right\}$$

$$\left(\sin\tfrac{1}{2}\theta + \sin\tfrac{1}{2}3\theta\right). \tag{74}$$

$$\sigma_{rz}^{(-(1/2))} = 0. \tag{75}$$

$$\sigma_{\theta z}^{(-(1/2))} = 0. \tag{76}$$

$$\sigma_{zz}^{(-(1/2))} = \left(\sum_\lambda \frac{\lambda^4}{h^4}E_\lambda(z)d_{\lambda 1}\right)\cos\tfrac{1}{2}\theta. \tag{77}$$

In the above formulas, $d_{\lambda 1}$ are restricted by (66) and (69). Integration of (69) gives

$$\sum_{n=1}^\infty a_{n1}\cos\frac{n\pi}{h}z = -\sum\frac{\lambda^2}{h^2}d_{\lambda 1}E_\lambda(z) - \sum\frac{4\lambda}{h^2}d_{\lambda 1}. \tag{78}$$

The last term in the equation above comes from the integration constant which is determined by using (15). Substituting (78) into (66) gives the sole condition for $d_{\lambda 1}$ as

$$2B_1k(z) = \sum_\lambda\left[(2-\nu)\frac{\lambda^2}{h^2}E_\lambda(z) + (1-\nu)E_\lambda(z)'' + \frac{8\lambda}{h^2}\right]d_{\lambda 1}. \tag{79}$$

The lowest order nonzero displacements that correspond to the $r^{-(1/2)}$ singular stresses given by (72)–(77) are listed in Appendix I.

4. Discussion of the singular stress field.

From the asymptotic analysis in the section above, it appears that the lowest order nonzero three-dimensional crack tip stresses of a plate are of inverse square root singularity with the amplitudes given by (72–77).

Denote

$$K(z) = \left\{1 + \frac{1}{2B_1}\sum_\lambda\frac{\lambda^2}{h^2}\left[\nu\frac{\lambda^2}{h^2}E_\lambda(z) + (1+\nu)E_\lambda(z)''\right]d_{\lambda 1}\right\}B_1 \tag{80}$$

as the stress intensity factor. The singular stresses in (72–77) can then be expressed as

$$\sigma_{\alpha\beta} = K(z)\tilde{\sigma}_{\alpha\beta}r^{-(1/2)},$$

$$\sigma_{z\alpha} = 0 \qquad (\alpha,\beta = r,\theta), \tag{81}$$

$$\sigma_{zz} = \left(\sum_\lambda\frac{\lambda^4}{h^4}E_\lambda(z)d_{\lambda 1}\right)\cos\left(\tfrac{1}{2}\theta\right)r^{-(1/2)},$$

where $\tilde{\sigma}_{\alpha J}$ are the amplitudes of the classical plane strain singular stresses.

$$\tilde{\sigma}_{rr} = \tfrac{1}{4}(5 \cos \tfrac{1}{2}\theta - \cos \tfrac{1}{2}3\theta).$$

$$\tilde{\sigma}_{\theta\theta} = \tfrac{1}{4}(3 \cos \tfrac{1}{2}\theta + \cos \tfrac{1}{2}3\theta). \tag{82}$$

$$\tilde{\sigma}_{r\theta} = \tfrac{1}{4}(\sin \tfrac{1}{2}\theta + \sin \tfrac{1}{2}3\theta).$$

The in-plane components of the three-dimensional near tip singular stress field are thus expressed as singular plane strain stresses with the intensity factor $K(z)$ varying in the thickness direction. The natural question is whether the near tip deformation is a state of plane strain, i.e., $\varepsilon_{zz} = 0$.

As stated in Section 3, the constants $d_{\lambda 1}$ in (80) are restricted only by (79). Differentiating the two sides of (79) twice with respect to z gives

$$-\frac{2\nu}{1+\nu}B_1 = \sum_\lambda \left[(2-\nu)\frac{\lambda^2}{h^2}E_\lambda'' + (1-\nu)E_\lambda'''' \right] d_{\lambda 1}. \tag{83}$$

However, it is easily established by the definition of E_λ in (48) that

$$E_\lambda'''' = -\frac{2\lambda^2}{h^2}E_\lambda'' - \frac{\lambda^4}{h^4}E_\lambda. \tag{84}$$

Substituting (84) into (83) gives another form of (79), i.e.

$$2\nu B_1 = (1-\nu^2)\sum_\lambda \frac{\lambda^4}{h^4}E_\lambda d_{\lambda 1} - \nu(1+\nu)\sum_\lambda \frac{\lambda^2}{h^2}E_\lambda'' d_{\lambda 1}. \tag{85}$$

With (85), it is now possible to show that the singular stresses in (72–77) represent the plane strain deformation. Substitution of results from (72–77) into the following expression

$$\varepsilon_{zz} = \frac{1+\nu}{E}\sigma_{zz} - \frac{\nu}{E}(\sigma_{rr} + \sigma_{\theta\theta} + \sigma_{zz}) \tag{86}$$

leads to

$$\varepsilon_{zz} = \frac{1}{E}\left[-2\nu B_1 + (1-\nu^2)\sum_\lambda \frac{\lambda^4}{h^4}E_\lambda d_{\lambda 1} - \nu(1+\nu)\sum_\lambda \frac{\lambda^2}{h^2}E_\lambda'' d_{\lambda 1} \right] \cos \tfrac{1}{2}\theta = 0, \tag{87}$$

as terms in the bracket are terms in (85).

The result that plane strain deformation prevails over the entire thickness of the plate near the crack tip is somewhat unexpected. One would anticipate a plane stress state close to the traction free plate surfaces, where $\sigma_{zz} = 0$ but not necessarily $\varepsilon_{zz} = 0$. To further investigate this paradox, we note that (85) reduces to

$$2B_1 = -(1+\nu)\sum_\lambda \frac{\lambda^2}{h^2}E_\lambda(\pm h)'' d_{\lambda 1}, \tag{88}$$

at $z = \pm h$ since $E_\lambda(\pm h) = 0$ by definition. It is easy to see from (80) that

$$K(\pm h) = 0. \tag{89}$$

Consequently, all the components of the singular stress field vanish identically on the free plate surfaces. Thus, on plate surfaces, the distinction between the plane stress and plane strain states vanishes.

The implication of the above finding is that the stress intensity factor $K(z)$ vanishes on the plate surfaces. In fact, the displacements (see Appendix I) associated with the singular stresses also vanish on the plate surfaces. These results are consistent with the finite element results obtained by Shivakumar and Raju [9] which indicate that the strain energy release rate seems to drop to zero when approaching the plate surfaces.

At this point, one may surmise whether there is a unique functional form for $K(z)$. Since $K(z)$ depends on $d_{\lambda 1}$ (see (80)), to answer the above question, we must find out whether the coefficients $d_{\lambda 1}$ can be determined unambiguously. Unfortunately, except for the trivial case when $\nu = 0$, $d_{\lambda 1}$ cannot be determined uniquely by the crack tip asymptotic analysis alone.

For the case $\nu = 0$, we have $k(z) = 0$ by (36), and (79) reduces to

$$\sum_\lambda \left[2\frac{\lambda^2}{h^2} E_\lambda(z) + E_\lambda(z)'' + \frac{8\lambda}{h^2} \right] d_{\lambda 1} = 0 \Rightarrow d_{\lambda 1} = 0, \tag{90}$$

which leads to $K(z) = B_1$ and $\sigma_{zz} = 0$ in (80) and (81). The solution given by (81) for $\nu = 0$ is thus the conventional two-dimensional solution. This is the natural outcome since the in-plane deformation of the plate will no longer cause deformation in the z-direction for $\nu = 0$.

To prove the non-uniqueness of $d_{\lambda 1}$ for an arbitrary ν, we introduce the function

$$\overline{\varphi}(x, z) = \sum d_{\lambda 1} E_\lambda(z)\, e^{-(\lambda x/h)} \Rightarrow \overline{\varphi}|_{x=0} = \sum d_{\lambda 1} E_\lambda(z), \tag{91}$$

in which $\overline{\varphi}$ can be identified as the symmetric part of the so called Papkovich–Fadle expansion which has been well studied by Smith [10] and Gregory [11–12]. Gregory [12] proved that $\overline{\varphi}$ as defined by (91) is the general form of the solution of the biharmonic equation

$$\left(\frac{\partial^2}{\partial x^2} + \frac{\partial^2}{\partial z^2} \right) \left(\frac{\partial^2}{\partial x^2} + \frac{\partial^2}{\partial z^2} \right) \overline{\varphi} = 0 \tag{92}$$

with boundary conditions

$$\overline{\varphi}(x, \pm h) = \frac{\partial \overline{\varphi}}{\partial z}\bigg|_{z \pm h} = 0 \tag{93}$$

and

$$\frac{\partial^2 \overline{\varphi}}{\partial x^2}\bigg|_{x=0} = f(z), \quad z \in (-h, h), \tag{94}$$

$$\frac{\partial^2 \overline{\varphi}}{\partial z^2}\bigg|_{x=0} = g(z), \quad z \in (-h, h), \tag{95}$$

where f and g are symmetric functions of z and satisfy the so-called 'consistent condition', i.e.

$$f(\pm h) = \left.\frac{\partial^2 \overline{\varphi}}{\partial x^2}\right|_{x=0 \& z=\pm h} = 0, \tag{96}$$

$$f'(\pm h) = \left.\frac{\partial^3 \overline{\varphi}}{\partial x^2 \partial z}\right|_{x=0 \& z=\pm h} = 0, \tag{97}$$

$$\int_{-h}^{h} g\,dz = 0, \qquad \int_{-h}^{h} zg\,dz = 0. \tag{98}$$

With the above delineation, $d_{\lambda 1}$ in (79) is uniquely given by

$$d_{\lambda 1} = \frac{h^4 \tan^2 \lambda}{16\lambda^4} \int_{-h}^{h} \left[(f+g)E_\lambda(z)'' - f\frac{4\lambda}{h^2}\cos\lambda\cos\lambda z\right] dz. \tag{99}$$

Note that $d_{\lambda 1}$ is dependent on both f and g which are two arbitrary functions as long as they satisfy the 'consistent condition'. From (91), (94) and (95), it is seen that f and g are related to $d_{\lambda 1}$ by

$$f(z) = \sum \frac{\lambda^2}{h^2} E_\lambda(z) d_{\lambda 1}, \tag{100}$$

$$g(z) = \sum E_\lambda(z)'' d_{\lambda 1}. \tag{101}$$

By using relations in (100) and (101), (79) becomes

$$2B_1 k(z) = (2-\nu)f + (1-\nu)g - \int_{-h}^{h} f\,dz. \tag{102}$$

Since two arbitrary functions f and g appear in (102) and f and g are both needed in determining $d_{\lambda 1}, d_{\lambda 1}$ is non-unique. Thus, the z-profile of the stress intensity factor cannot be uniquely defined based on the asymptotic solution alone. The three-dimensional solution satisfying complete boundary conditions (including remote boundary conditions) may be needed to determine the distribution of the stress intensity factor over the plate thickness for each individually posed problem.

5. Conclusions

A three-dimensional asymptotic analysis has been carried out for singular crack tip stresses of a plate with a through-the-thickness cut. For both mode I and mode II loading, stress singularity at the crack tip is of the $r^{-(1/2)}$ type, while the stress intensity factor is a function of the thickness-wise coordinate. On the plate surfaces, all singular stress and strain components vanish, thus satisfying both plane stress and plane strain conditions. The deformation associated with the singular stress field is plane strain. The profile of the stress intensity factor as a function of the thickness-wise coordinate cannot be determined by the asymptotic analysis alone.

Appendix I: Lowest order nonzero displacements for mode I

Corresponding to the stresses in (72–77), the displacements of mode I deformation are

$$
u_r = \frac{1+\nu}{2E} \left\{ B_1 + \frac{1}{2} \sum \frac{\lambda^2}{h^2} \left[\nu \frac{\lambda^2}{h^2} E_\lambda(z) + (1+\nu) E_\lambda(z)'' \right] d_{\lambda 1} \right\}
$$
$$
\times [(5 - 8\nu) \cos \tfrac{1}{2}\theta - \cos \tfrac{1}{2}3\theta] r^{1/2}
\tag{103}
$$

$$
u_\theta = \frac{1+\nu}{2E} \left\{ B_1 + \frac{1}{2} \sum \frac{\lambda^2}{h^2} \left[\nu \frac{\lambda^2}{h^2} E_\lambda(z) + (1+\nu) E_\lambda(z)'' \right] d_{\lambda 1} \right\}
$$
$$
\times [-(7 - 8\nu) \sin \tfrac{1}{2}\theta + \sin \tfrac{1}{2}3\theta] r^{1/2}.
\tag{104}
$$

$$
u_z = \frac{1+\nu}{E} \left\{ \sum \frac{\lambda^2}{h^2} \left[\frac{7+\nu}{6} E_\lambda(z)''' - \tfrac{1}{6}(2-\nu) \frac{\lambda^2}{h^2} E_\lambda(z)' \right] d_{\lambda 1} \cos \tfrac{1}{2}3\theta \right.
$$
$$
\left. - \frac{1}{2} \sum \frac{\lambda^2}{h^2} \left[(1-\nu) E_\lambda(z)''' + (2-\nu) \frac{\lambda^2}{h^2} E_\lambda(z)' \right] d_{\lambda 1} \cos \tfrac{1}{2} \right\} r^{3/2}.
\tag{105}
$$

Appendix II: Mode II singular stresses

Mode II loading can be analyzed with the same procedure as for mode I loading. The lowest nonzero singular stresses are

$$
\sigma_r = \frac{1}{4} \left\{ A_1 + \frac{1}{2} \sum \frac{\lambda^2}{h^2} \left[\nu \frac{\lambda^2}{h^2} E_\lambda(z) + (1+\nu) E_\lambda(z)'' \right] c_\lambda^1 \right\}
$$
$$
\times (5 \sin \tfrac{1}{2}\theta - 3 \sin \tfrac{1}{2}3\theta) r^{-(1/2)},
\tag{106}
$$

$$
\sigma_\theta = \frac{1}{4} \left\{ A_1 + \frac{1}{2} \sum \frac{\lambda^2}{h^2} \left[\nu \frac{\lambda^2}{h^2} E_\lambda(z) + (1+\nu) E_\lambda(z)'' \right] c_\lambda^1 \right\}
$$
$$
\times (3 \sin \tfrac{1}{2}\theta + 3 \sin \tfrac{1}{2}3\theta) r^{-(1/2)},
\tag{107}
$$

$$
\sigma_{r\theta} = -\frac{1}{4} \left\{ A_1 + \frac{1}{2} \sum \frac{\lambda^2}{h^2} \left[\nu \frac{\lambda^2}{h^2} E_\lambda(z) + (1+\nu) E_\lambda(z)'' \right] c_\lambda^1 \right\}
$$
$$
\times (\cos \tfrac{1}{2}\theta + 3 \cos \tfrac{1}{2}3\theta) r^{-(1/2)},
\tag{108}
$$

$$
\sigma_{rz} = 0,
\tag{109}
$$

$$
\sigma_{\theta z} = 0,
\tag{110}
$$

$$\sigma_z = \left(\sum \frac{\lambda^4}{h^4} E_\lambda c_\lambda^1 \right) \sin \tfrac{1}{2}\theta r^{-(1/2)}. \tag{111}$$

where c_λ^1 satisfies the condition

$$2A_1 k(z) = \sum \left[(2-\nu)\frac{\lambda^2}{h^2} E_\lambda(z) + (1-\nu)E_\lambda(z)'' + \frac{8\lambda}{h^2} \right] c_\lambda^1. \tag{112}$$

Acknowledgment

References

1. M.L. Williams. *Fracture Mechanics: 22nd Symposium, ASTM STP 1131*, H.A. Ernst et al. (eds.), Philadelphia (1992) 5–33.
2. G.C. Sih. *International Journal of Fracture Mechanics* 7 (1971) 39–61.
3. J.P. Benthem. *International Journal of Solids and Structures* 13 (1977) 479–492.
4. T. Kawai, Y. Fujitani and K. Kumagai. *Proceedings of the International Conference on Fracture Mechanics and Technology*, Hong Kong (1977) 1157–1163.
5. G.B. Sinclair. *Proceedings of the 7th Canadian Congress of Applied Mechanics* 43 (1976) 479–481.
6. M.L. Williams. *Transactions of ASME, Journal of Applied Mechanics* 19 (1952) 526–528.
7. R.D. Gregory. *Journal of Elasticity* 28 (1992) 1–28.
8. S. Timoshenko and J.N. Goodier. *Theory of Elasticity*, McGraw-Hill, New York (1970).
9. K. N. Shivakumar and I.S. Raju. *Fracture Mechanics: 21st Symposium, ASTM STP 1074*, J.P. Gudas et al. (eds.), Philadelphia (1990) 470–489.
10. R.C.T. Smith. *Australian Journal of Scientific Research* A5(1952) 227–237.
11. R.D. Gregory. *Journal of Elasticity* 9 (1979) 283–309.
12. Ibid. 14 (1984) 27–64.

On singular stress at the crack tip of a thick plate under in-plane loading

X.M. SU and C.T. SUN
School of Aeronautics and Astronautics, Purdue University, West Lafayette, Indiana 47907, USA

Abstract. By superposition of three asymptotic solutions, which collectively satisfy all the equilibrium and compatibility equations as well as boundary conditions, the three-dimensional crack tip stresses of a thick plate with a through-the-thickness cut are shown to be of square root singularity throughout the thickness. The near tip deformation is shown to be plane strain with stress intensity factor changing in the thickness direction. All components of the singular stresses vanish on plate surfaces. The profile of the stress intensity factor in the thickness direction cannot be determined by the asymptotic analysis alone.

1. Introduction

Crack-tip singularity and the profile of stress intensity in the thickness direction of a plate with a through-thickness cut are still open problems [1]. Earlier publications can be found in the review paper by Sih [2]. Several results are of interest, especially, those of Benthem [3], Kawai, Fujitani and Kumagai [4] and Sinclair [5]. Although most of the previous attempts followed to some degree Williams' separable eigenvalue approach [6], different coordinate systems and different approximations were used. Benthem [3] used spherical coordinates and concentrated his attention on the corner point (the intersection of the crack front and the plate surface). While boundary conditions at crack surface were satisfied exactly, the boundary conditions of the plate surfaces were only satisfied approximately. The results obtained by Benthem were characterized by a stress singularity less than square root at the corner point. This was true even if the crack tip was approached in a plane that is parallel to the free plate surface. Kawai et al. [4] also used spherical coordinates, but the boundary conditions on crack surfaces were satisfied approximately and those on plate surfaces exactly. The corresponding singularity was higher than square root. Sinclair [5] used cylindrical coordinates which were more or less similar to Sih's classical work [2]. The singularity in Sinclair's study was square root. However, the traction free boundary conditions of the plate surfaces were not satisfied completely by his solution, even though Sinclair was interested in stresses close to the plate surfaces.

In the present paper, the above crack problem is treated using a new approach. Recent developments in thick plate theory are exploited to obtain an asymptotic expansion of singular stresses at the crack tip that satisfy not only equilibrium and compatibility equations but also all boundary conditions exactly.

2. Basic equations

Consider a plate with a through-the-thickness cut. The plate is $2h$ thickness, and both upper and lower-plate surfaces and the crack surfaces are traction free. Loading is applied on the
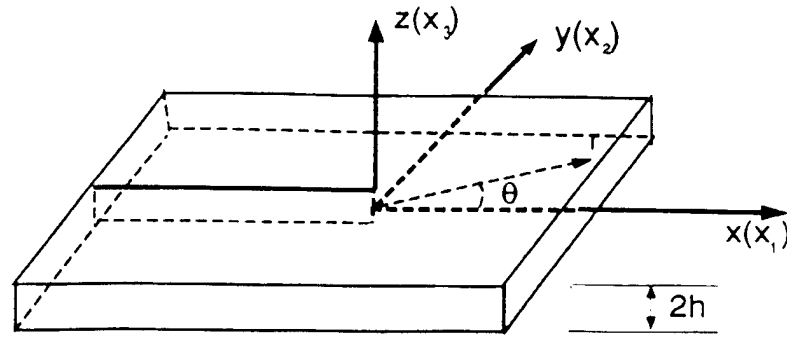
Figure 1. A thick plate with a through-the-thickness cut.

edges and is symmetric about the middle plane of the plate. A cylindrical coordinate system is established with the (r, θ) plane in the middle plane of the plate. The origin of the coordinate system is at the crack tip with the plane $\theta = 0$ parallel to the crack surface as shown in Figure 1.

The problem described above is among the thick plate problems which have been studied by Gregory [7]. Gregory has rigorously proved that the most general state of stress $\sigma_{ij}(i, j = 1, 2, 3)$ for the thick plate problem can be uniquely decomposed into three parts

$$\sigma_{ij} = \sigma_{ij}^{PS} + \sigma_{ij}^{S} + \sigma_{ij}^{PF}, \quad (i, j = 1, 2, 3), \tag{1}$$

where σ_{ij}^{PS} is the (exact) plane stress state; σ_{ij}^{S} the shear state stress; and σ_{ij}^{PF}, the so called Papkovich–Fadle state stress. The three stress fields are generated by three different stress functions. Following [7] the three stress states are described below.

Plane stress state

This is the well known (exact) plane stress [8]. The solution of the (exact) plane stress is a modification of the solution of plane stress in the conventional sense such that all the equilibrium and compatibility equations are satisfied. The stresses are obtained from stress function ψ as

$$\sigma_{11}^{PS} = \psi_{,22} + \frac{\nu(1 - 3(\frac{x_3}{h})^2)h^2}{6(1 + \nu)} \overline{\nabla}^2 \psi_{,22}, \tag{2}$$

$$\sigma_{22}^{PS} = \psi_{,11} + \frac{\nu(1 - 3(\frac{x_3}{h})^2)h^2}{6(1 + \nu)} \overline{\nabla}^2 \psi_{,11}, \tag{3}$$

$$\sigma_{12}^{PS} = -\psi_{,12} - \frac{\nu(1 - 3(\frac{x_3}{h})^2)h^2}{6(1 + \nu)} \overline{\nabla}^2 \psi_{,12}, \tag{4}$$

$$\sigma_{13}^{PS} = \sigma_{23}^{PS} = \sigma_{33}^{PS} = 0, \tag{5}$$

where a comma indicates partial differentiation, ν is Poisson's ratio, and ψ is a two-dimensional function satisfying the biharmonic equation

$$\overline{\nabla}^2 \overline{\nabla}^2 \psi = \left(\frac{\partial^2}{\partial x_1^2} + \frac{\partial^2}{\partial x_2^2} \right) \left(\frac{\partial^2}{\partial x_1^2} + \frac{\partial^2}{\partial x_2^2} \right) \psi = 0. \tag{6}$$

Shear stress state

Shear stress state is derived from a three-dimensional potential function ϕ as

$$\sigma_{11}^S = 2\phi_{,12}, \tag{7}$$

$$\sigma_{22}^S = -2\phi_{,12}, \tag{8}$$

$$\sigma_{12}^S = \phi_{,22} - \phi_{,11}, \tag{9}$$

$$\sigma_{13}^S = \phi_{,23}, \tag{10}$$

$$\sigma_{23}^S = -\phi_{,13}, \tag{11}$$

$$\sigma_{33}^S = 0, \tag{12}$$

where

$$\nabla^2 \phi = \frac{\partial^2 \phi}{\partial x_1^2} + \frac{\partial^2 \phi}{\partial x_2^2} + \frac{\partial^2 \phi}{\partial x_3^2} = 0 \tag{13}$$

and

$$\phi_{,3} \, |_{x_3 = \pm h} = 0, \tag{14}$$

$$\int_{-h}^{h} \phi \, \mathrm{d}x_3 = 0. \tag{15}$$

Papkovich–Fadle state

Papkovich–Fadle state stress is generated by a three-dimensional bi-harmonic function φ as

$$\sigma_{11}^{PF} = \varphi_{,1133} + \nu \nabla^2 \varphi_{,22}, \tag{16}$$

$$\sigma_{22}^{PF} = \varphi_{,2233} + \nu \nabla^2 \varphi_{,11}, \tag{17}$$

$$\sigma_{12}^{PF} = \varphi_{,1233} - \nu \nabla^2 \varphi_{,12}, \tag{18}$$

$$\sigma_{13}^{PF} = -\overline{\nabla}^2 \varphi_{,13}, \tag{19}$$

$$\sigma_{23}^{PF} = -\overline{\nabla}^2 \varphi_{,23}, \tag{20}$$

$$\sigma_{33}^{PF} = \overline{\nabla}^2 \overline{\nabla}^2 \varphi, \tag{21}$$

where

$$\nabla^2 \nabla^2 \varphi = 0 \tag{22}$$

and

$$\varphi|_{x_3 = \pm h} = \varphi_{,3} \, |_{x_3 = \pm h}. \tag{23}$$

It can easily be confirmed that any combinations of the above three types of stresses satisfy not only the equilibrium equations and compatibility equations but also the boundary conditions on free plate surfaces.

It was shown by Gregory [7] that the decomposition of the three-dimensional stress field in a thick plate into PS, S and PF stresses is unique. On the other hand, one recalls that the conventional plane stress solution is unique once boundary conditions of the two-dimensional problem are prescribed. The PS state of stress, or the (exact) plane stress, shares the same stress function as the conventional plane stress problem if the stress function is determined with the boundary conditions obtained from averaging traction on the edges through-the-thickness. In the next section, the asymptotic PS state stress will be given first. The PS state stress obtained includes terms whose singularities are of higher order than that of inverse square root. These higher order singularity terms violate boundary conditions on crack surfaces. The S and PF state stresses are given subsequently. The three stresses are then combined to create the asymptotic solution that satisfies all the boundary conditions. All formulations in the paper are for mode I loading. The results for mode II are listed in Appendix II.

3. Asymptotic solution for mode I loading

3.1. EXPANSION OF PS, S AND PF STATE STRESS

PS state stress

PS state stress consists of two parts: conventional plane stress and the modification which is added to satisfy compatibility equations of elasticity. As noted in Section 2, the stress function of PS state stress is determined by solving a conventional plane stress problem with the boundary conditions obtained from averaging traction on the edges through-the-thickness. Boundary conditions for the stress function of the PS state are therefore

$$\frac{1}{h} \int_{-h}^{h} \sigma_{22} \mid_{\theta=\pm\pi} \, \mathrm{d}x_3 = \frac{1}{h} \int_{-h}^{h} \sigma_\theta \mid_{\theta=\pm\pi} \, \mathrm{d}z = 0, \tag{24}$$

$$\frac{1}{h} \int_{-h}^{h} \sigma_{12} \mid_{\theta=\pm\pi} \, \mathrm{d}x_3 = \frac{1}{h} \int_{-h}^{h} \sigma_{r\theta} \mid_{\theta=\pm\pi} \, \mathrm{d}z = 0. \tag{25}$$

Following Williams [6], the stress function in (6) is expanded in terms of r as

$$\psi(r, \theta) = r^{1+\lambda} \tilde{\psi}(\theta), \tag{26}$$

where λ is an arbitrary positive number. $\tilde{\psi}(\theta)$ is determined by

$$(1 + \lambda)^2 (\lambda - 1)^2 \tilde{\psi} + [(\lambda - 1)^2 + (1 + \lambda)^2] \tilde{\psi}'' + \tilde{\psi}'''' = 0. \tag{27}$$

The above differential equation is the result of substituting (26) into (6). The general solutions are

$$\tilde{\psi} = A \sin(\lambda - 1)\theta + B \cos(\lambda - 1)\theta + C \sin(1 + \lambda)\theta + D \cos(1 + \lambda)\theta. \tag{28}$$

The stress components are obtained by substituting (26) in (2–5). These stresses will satisfy boundary conditions in (24) and (25) only when

$$\sin 2\lambda\pi = 0, \tag{29}$$

which leads to eigenvalues

$$\lambda = \tfrac{1}{2}m, \quad m = 1, 2, 3, \ldots \tag{30}$$

The above eigenvalues are identical to the two-dimensional results obtained by Williams [6]. The negative integers are not included to avoid singular displacements. The even integers are associated with regular stresses. Thus, only the odd integers are associated with singular stresses and are taken for the asymptotic solutions.

For mode I (symmetric mode), we have

$$\psi = \left[B_1 \cos \tfrac{1}{2}\theta + D_1 \cos \tfrac{1}{2}3\theta \right] r^{3/2} + \left[B_2 \cos \tfrac{1}{2}\theta + D_2 \cos \tfrac{1}{2}5\theta \right] r^{5/2} + \cdots$$

$$+[B_n \cos(n - \tfrac{3}{2})\theta + D_n \cos(n + \tfrac{1}{2})\theta]r^{n+1/2} + \cdots, \tag{31}$$

where B_n and D_n are constants. The corresponding stress components are

$$\sigma_{rr}^{PS} = -\tfrac{3}{2}B_1 k(z) \cos(\tfrac{1}{2}\theta)r^{-(5/2)} + \tfrac{3}{2}B_2 k(z) \cos(\tfrac{1}{2}\theta)r^{-(3/2)}$$

$$+[\tfrac{5}{4}B_1 \cos \tfrac{1}{2}\theta - \tfrac{3}{4}D_1 \cos \tfrac{3}{2}\theta - \tfrac{15}{2}B_3 k(z) \cos \tfrac{3}{2}\theta]r^{-(1/2)} + \cdots, \tag{32}$$

$$\sigma_{\theta\theta}^{PS} = \tfrac{3}{2}B_1 k(z) \cos(\tfrac{1}{2}\theta)r^{-(5/2)} - \tfrac{3}{2}B_2 k(z) \cos(\tfrac{1}{2}\theta)r^{-(3/2)}$$

$$+[\tfrac{3}{4}B_1 \cos \tfrac{1}{2}\theta + \tfrac{3}{4}D_1 \cos \tfrac{3}{2}\theta + \tfrac{15}{2}B_3 k(z) \cos \tfrac{3}{2}\theta]r^{-(1/2)} + \cdots, \tag{33}$$

$$\sigma_{r\theta}^{PS} = -\tfrac{3}{2}B_1 k(z) \sin(\tfrac{1}{2}\theta)r^{-(5/2)} - \tfrac{3}{2}B_2 k(z) \sin(\tfrac{1}{2}\theta)r^{-(3/2)}$$

$$+[\tfrac{1}{4}B_1 \sin \tfrac{1}{2}\theta + \tfrac{3}{4}D_1 \sin \tfrac{3}{2}\theta + \tfrac{15}{2}B_3 k(z) \sin \tfrac{3}{2}\theta]r^{-(1/2)} + \cdots, \tag{34}$$

$$\sigma_{zz}^{PS} = \sigma_{rz}^{PS} = \sigma_{\theta z}^{PS} = 0. \tag{35}$$

In the above equations

$$k(z) = \frac{\nu(1 - 3(\tfrac{z}{h})^2)h^2}{6(1 + \nu)}. \tag{36}$$

It is noted that terms of singularity $r^{-(5/2)}$ and $r^{-(3/2)}$ appear in (32–34). These terms satisfy the two-dimensional conditions in (24–25) but violate exact three-dimensional boundary conditions on crack surfaces as $\sigma_{r\theta}^{PS}$ is not zero when $\theta = \pm\pi$. Thus, the S and PS state stresses are needed to make the crack surfaces traction free.

S state stress

Stress function ϕ is expanded as

$$\phi(r, \theta, z) = \sum_{n=1}^{\infty} \phi_n(r, \theta) \cos\left(\frac{n\pi z}{h}\right), \tag{37}$$

where ϕ_n is determined by

$$\overline{\nabla}^2 \phi_n - \left(\frac{n^2\pi^2}{h^2}\right) \phi_n = 0, \tag{38}$$

which is obtained by substituting (35) into (13).

Each ϕ_n is again expanded as

$$\phi_n(r.\theta) = \sum_{k=1}^{\infty} \phi_{nk}(\theta) r^{k-(3/2)}. \tag{39}$$

After solving ϕ_{nk} by using asymptotic equations obtained by substituting (39) into (38), the above expansion can be arranged into

$$\phi_n(r.\theta) = (a_{n1} \sin \tfrac{1}{2}\theta) r^{-(1/2)} + (a_{n2} \sin \tfrac{1}{2}\theta) r^{1/2}$$
$$+ \left[a_{n3} \sin \frac{3\theta}{2} + \frac{1}{2} \left(\frac{n\pi}{h} \right)^2 (a_{n1} \sin \tfrac{1}{2}\theta) \right] r^{3/2} + \cdots. \tag{40}$$

where $a_{ni}(i = 1, \ldots,)$ are constants. The corresponding stress components are obtained after applying (37) and (40) in respective expressions in (7–12). We obtain

$$\sigma_{rr}^S = -\tfrac{3}{2} \cos \tfrac{1}{2}\theta \left(\sum a_{n1} \cos \frac{n\pi}{h} z \right) r^{-(5/2)} - \tfrac{1}{2} \cos \tfrac{1}{2}\theta \left(\sum a_{n2} \cos \frac{n\pi}{h} z \right) r^{-(3/2)}$$
$$+ \left[\tfrac{3}{2} \cos \tfrac{1}{2}3\theta \left(\sum a_{n3} \cos \frac{n\pi}{h} z \right) \right.$$
$$\left. + \tfrac{1}{4} \cos \tfrac{1}{2}\theta \left(\sum \left(\frac{n\pi}{h} \right)^2 a_{n1} \cos \frac{n\pi}{h} z \right) \right] r^{-(1/2)} + \cdots, \tag{41}$$

$$\sigma_{\theta\theta}^S = -\sigma_r^S, \tag{42}$$

$$\sigma_{r\theta}^S = -\tfrac{3}{2} \sin \tfrac{1}{2}\theta \left(\sum a_{n1} \cos \frac{n\pi}{h} z \right) r^{-(5/2)} + \tfrac{1}{2} \sin \tfrac{1}{2}\theta \left(\sum a_{n2} \cos \frac{n\pi}{h} z \right) r^{-(3/2)}$$
$$+ \left[-\tfrac{3}{2} \sin \tfrac{1}{2}3\theta \left(\sum a_{n3} \cos \frac{n\pi}{h} z \right) \right.$$
$$\left. + \tfrac{1}{4} \sin \tfrac{1}{2}\theta \left(\sum \left(\frac{n\pi}{h} \right)^2 a_{n1} \cos \frac{n\pi}{h} z \right) \right] r^{-(1/2)} + \cdots, \tag{43}$$

$$\sigma_{rz}^S = -\tfrac{1}{2} \cos \tfrac{1}{2}\theta \left(\sum a_{n1} \left(\frac{n\pi}{h} \right) \sin \frac{n\pi}{h} z \right) r^{-(3/2)}$$
$$- \tfrac{1}{2} \cos \tfrac{1}{2}\theta \left(\sum a_{n2} \left(\frac{n\pi}{h} \right) \sin \frac{n\pi}{h} z \right) r^{-(1/2)} + \cdots, \tag{44}$$

$$\sigma_{\theta z}^S = -\tfrac{1}{2} \sin \tfrac{1}{2}\theta \left(\sum a_{n1} \left(\frac{n\pi}{h} \right) \sin \frac{n\pi}{h} z \right) r^{-(3/2)}$$
$$+ \tfrac{1}{2} \sin \tfrac{1}{2}\theta \left(\sum a_{n2} \left(\frac{n\pi}{h} \right) \sin \frac{n\pi}{h} z \right) r^{-(1/2)} + \cdots, \tag{45}$$

$$\sigma_{zz}^{S} = 0. \tag{46}$$

PF stress state

The stress function is assumed to be (see [7])

$$\varphi(r, \theta, z) = \sum_{\lambda} \varphi_{\lambda}(r, \theta) E_{\lambda}(z). \tag{47}$$

where $E_{\lambda}(z)$ is defined by

$$E_{\lambda}(z) = \left(\frac{z}{h} - 1 \right) \sin \left[\lambda \left(\frac{z}{h} + 1 \right) \right] + \left(\frac{z}{h} + 1 \right) \sin \left[\lambda \left(\frac{z}{h} - 1 \right) \right] \tag{48}$$

and λ is the root of the equation

$$\sin 2\lambda + 2\lambda = 0. \tag{49}$$

Without losing generality, the summation in (47) will run only through roots whose real parts are positive (see [7]). The roots are thus in conjugate pairs.

Substituting (47) into (22) leads to

$$\overline{\nabla}^{2} \varphi_{\lambda} - \left(\frac{\lambda}{h} \right)^{2} \varphi_{\lambda} = 0. \tag{50}$$

Consistent with the expansions of PS stress, φ_{λ} is assumed to be

$$\varphi_{\lambda} = \sum_{k=1}^{\infty} \varphi_{\lambda k}(\theta) r^{k-(3/2)}. \tag{51}$$

With solutions of the asymptotic equations obtained by applying (51) in (50), (47) is expressed as

$$\varphi = \left[\cos \tfrac{1}{2}\theta \left(\sum d_{\lambda 1} E_{\lambda}(z) \right) \right] r^{-(1/2)} + \left[\cos \tfrac{1}{2}\theta \left(\sum d_{\lambda 2} E_{\lambda}(z) \right) \right] r^{1/2}$$

$$+ \left[\cos \tfrac{1}{2} 3\theta \left(\sum d_{\lambda 3} E_{\lambda}(z) \right) + \tfrac{1}{2} \cos \tfrac{1}{2}\theta \left(\sum \left(\frac{\lambda}{h} \right)^{2} d_{\lambda 1} E_{\lambda}(z) \right) \right] r^{3/2} + \cdots, \tag{52}$$

where $d_{\lambda i}$ are constants. The corresponding stress components are

$$\sigma_{rr}^{PF} = \left[\frac{3}{4} \left(\sum d_{\lambda 1} E_{\lambda}(z)'' \right) - \tfrac{1}{4} 3\nu \sum d_{\lambda 1} \left(\frac{\lambda^{2}}{h^{2}} E_{\lambda}(z) + E_{\lambda}(z)'' \right) \right] \cos(\tfrac{1}{2}\theta) r^{-(5/2)}$$

$$+ \left[-\frac{1}{4} \left(\sum d_{\lambda 2} E_{\lambda}(z)'' \right) + \tfrac{1}{4}\nu \sum d_{\lambda 2} \left(\frac{\lambda^{2}}{h^{2}} E_{\lambda}(z) + E_{\lambda}(z)'' \right) \right] \cos(\tfrac{1}{2}\theta) r^{-(3/2)}$$

$$+ \left\{ \left[\frac{3}{4} \left(\sum d_{\lambda 3} E_{\lambda}(z)'' \right) - \tfrac{1}{4} 3\nu \sum d_{\lambda 3} \left(\frac{\lambda^{2}}{h^{2}} E_{\lambda}(z) + E_{\lambda}(z)'' \right) \right] \cos \tfrac{1}{2} 3\theta \right.$$

$$+ \left[\frac{3}{8} \left(\sum d_{\lambda 1} \frac{\lambda^2}{h^2} E_\lambda(z)'' \right) \right.$$

$$\left. + \frac{1}{8} 5\nu \sum d_{\lambda 1} \frac{\lambda^2}{h^2} \left(\frac{\lambda^2}{h^2} E_\lambda(z) + E_\lambda(z)'' \right) \right] \cos \frac{1}{2}\theta \Big\} r^{-(1/2)} + \cdots \qquad (53)$$

$$\sigma_{nn}^{PF} = \left[-\frac{3}{4} \left(\sum d_{\lambda 1} E_\lambda(z)'' \right) + \frac{1}{4} 3\nu \sum d_{\lambda 1} \left(\frac{\lambda^2}{h^2} E_\lambda(z) + E_\lambda(z)'' \right) \right] \cos(\tfrac{1}{2}\theta) r^{-(5/2)}$$

$$+ \left[\frac{1}{4} \left(\sum d_{\lambda 2} E_\lambda(z)'' \right) - \frac{1}{4}\nu \sum d_{\lambda 2} \left(\frac{\lambda^2}{h^2} E_\lambda(z) + E_\lambda(z)'' \right) \right] \cos(\tfrac{1}{2}\theta) r^{-(3/2)}$$

$$+ \left\{ \left[-\frac{3}{4} \left(\sum d_{\lambda 3} E_\lambda(z)'' \right) + \frac{1}{4} 3\nu \sum d_{\lambda 3} \left(\frac{\lambda^2}{h^2} E_\lambda(z) + E_\lambda(z)'' \right) \right] \cos \tfrac{1}{2} 3\theta \right.$$

$$+ \left[\frac{5}{8} \left(\sum d_{\lambda 1} \frac{\lambda^2}{h^2} E_\lambda(z)'' \right) \right.$$

$$\left. \left. + \frac{1}{8} 3\nu \sum d_{\lambda 1} \frac{\lambda^2}{h^2} \left(\frac{\lambda^2}{h^2} E_\lambda(z) + E_\lambda(z)'' \right) \right] \cos \tfrac{1}{2}\theta \right\} r^{-(1/2)} + \cdots, \qquad (54)$$

$$\sigma_{r\theta}^{PF} = \left[\frac{3}{4} \left(\sum d_{\lambda 1} E_\lambda(z)'' \right) - \frac{1}{4} 3\nu \sum d_{\lambda 1} \left(\frac{\lambda^2}{h^2} E_\lambda(z) + E_\lambda(z)'' \right) \right] \sin(\tfrac{1}{2}\theta) r^{-(5/2)}$$

$$+ \left[\frac{1}{4} \left(\sum d_{\lambda 2} E_\lambda(z)'' \right) - \frac{1}{4}\nu \sum d_{\lambda 2} \left(\frac{\lambda^2}{h^2} E_\lambda(z) + E_\lambda(z)'' \right) \right] \sin(\tfrac{1}{2}\theta) r^{-(3/2)}$$

$$+ \left\{ \left[-\frac{3}{4} \left(\sum d_{\lambda 3} E_\lambda(z)'' \right) + \frac{1}{4} 3\nu \sum d_{\lambda 3} \left(\frac{\lambda^2}{h^2} E_\lambda(z) + E_\lambda(z)'' \right) \right] \sin \tfrac{1}{2} 3\theta \right.$$

$$- \left[\frac{1}{8} \left(\sum d_{\lambda 1} \frac{\lambda^2}{h^2} E_\lambda(z)'' \right) \right.$$

$$\left. \left. - \frac{1}{8}\nu \sum d_{\lambda 1} \frac{\lambda^2}{h^2} \left(\frac{\lambda^2}{h^2} E_\lambda(z) + E_\lambda(z)'' \right) \right] \sin \tfrac{1}{2}\theta \right\} r^{-(1/2)} + \cdots, \qquad (55)$$

$$\sigma_{rz}^{PF} = \frac{1}{2} \left(\sum d_{\lambda 1} \frac{\lambda^2}{h^2} E_\lambda(z)' \right) \cos(\tfrac{1}{2}\theta) r^{-(3/2)}$$

$$- \frac{1}{2} \left(\sum d_{\lambda 2} \frac{\lambda^2}{h^2} E_\lambda(z)' \right) \cos(\tfrac{1}{2}\theta) r^{-(1/2)} + \cdots, \qquad (56)$$

$$\sigma_{\theta z}^{PF} = \frac{1}{2} \left(\sum d_{\lambda 1} \frac{\lambda^2}{h^2} E_\lambda(z)' \right) \sin(\tfrac{1}{2}\theta) r^{-(3/2)}$$

$$+ \frac{1}{2} \left(\sum d_{\lambda 2} \frac{\lambda^2}{h^2} E_\lambda(z)' \right) \sin(\tfrac{1}{2}\theta) r^{-(1/2)} + \cdots. \tag{57}$$

$$\sigma_{zz}^{PF} = \sum d_{\lambda 1} \left(\frac{\lambda^4}{h^4} E_\lambda(z) \right) \cos(\tfrac{1}{2}\theta) r^{-\frac{1}{2}} + \cdots. \tag{58}$$

3.2. ASYMPTOTIC SOLUTION OF THE SINGULAR STRESS FIELD

In the above, PS, S and PF stresses are expanded asymptotically around the crack tip. Now the three stresses are combined so that an asymptotic solution to the three-dimensional crack problem can be obtained. The three stresses individually satisfy not only all equilibrium equations and compatibility equations but also the boundary conditions at the two plate surfaces. However, the boundary conditions at the crack surfaces are satisfied only when the three stresses are combined. These crack surface boundary conditions are

$$\sigma_\theta|_{\theta=\pm\pi} = 0, \tag{59}$$

$$\sigma_{r\theta}|_{\theta=\pm\pi} = 0, \tag{60}$$

$$\sigma_{z\theta}|_{\theta=\pm\pi} = 0. \tag{61}$$

Asymptotic analysis of order $r^{-(5/2)}$

Adding the three stresses obtained in Section 3.1, the amplitudes of stresses of order $r^{-(5/2)}$ are

$$\sigma_{rr}^{(-(5/2))} = -\tfrac{3}{2} B_1 k(z) \cos \tfrac{1}{2}\theta - \tfrac{3}{2} \cos \tfrac{1}{2}\theta \left(\sum a_{n1} \cos \frac{n\pi}{h} z \right)$$
$$+ \left[\frac{3}{4} \left(\sum d_{\lambda 1} E_\lambda(z)'' \right) - \tfrac{1}{4} 3\nu \sum d_{\lambda 1} \left(\tfrac{\lambda^2}{h^2} E_\lambda(z) + E_\lambda(z)'' \right) \right] \cos(\tfrac{1}{2}\theta), \quad (62)$$

$$\sigma_{\theta\theta}^{(-(5/2))} = \tfrac{3}{2} B_1 k(z) \cos \tfrac{1}{2}\theta + \tfrac{3}{2} \cos \tfrac{1}{2}\theta \left(\sum a_{n1} \cos \frac{n\pi}{h} z \right)$$
$$+ \left[-\frac{3}{4} \left(\sum d_{\lambda 1} E_\lambda(z)'' \right) + \tfrac{1}{4} 3\nu \sum d_{\lambda 1} \right.$$
$$\left. \times \left(\frac{\lambda^2}{h^2} E_\lambda(z) + E_\lambda(z)'' \right) \right] \cos(\tfrac{1}{2}\theta), \tag{63}$$

$$\sigma_{r\theta}^{(-(5/2))} = -\tfrac{3}{2} B_1 k(z) \sin \tfrac{1}{2}\theta - \tfrac{3}{2} \sin \tfrac{1}{2}\theta \left(\sum a_{n1} \cos \frac{n\pi}{h} z \right)$$
$$+ \left[\frac{3}{4} \left(\sum d_{\lambda 1} E_\lambda(z)'' \right) - \frac{3\nu}{4} \sum d_{\lambda 1} \left(\frac{\lambda^2}{h^2} E_\lambda(z) + E_\lambda(z)'' \right) \right] \sin(\tfrac{1}{2}\theta), \quad (64)$$

$$\sigma_{rz}^{(-(5/2))} = \sigma_{\theta z}^{(-(5/2))} = \sigma_{zz}^{(-(5/2))} = 0, \tag{65}$$

where the superscript $(-(5/2))$ denotes the stress amplitude associated with the singular term $r^{-(5/2)}$. The boundary conditions in (59–61) lead to

$$-\tfrac{3}{2}B_1 k(z) - \frac{3}{2}\sum a_{n1} \cos\frac{n\pi}{h}z + \frac{3}{4}\sum \left[(1-\nu)E_\lambda(z)'' - \nu\frac{\lambda^2}{h^2}E_\lambda(z)\right]d_{\lambda1} = 0. \quad (66)$$

It is easy to see that the above equation leads to the conclusion

$$\sigma_{rr}^{(-(5/2))} = \sigma_{\theta\theta}^{(-(5/2))} = \sigma_{r\theta}^{(-(5/2))} = \sigma_{rz}^{(-(5/2))} = \sigma_{\theta z}^{(-(5/2))} = \sigma_{zz}^{(-(5/2))} = 0. \quad (67)$$

Asymptotic analysis of order $r^{-(3/2)}$

Similar to the analysis of order $r^{-(5/2)}$, the boundary conditions in (59)–(61) yield

$$-\tfrac{3}{2}B_2 k(z) + \frac{1}{2}\sum a_{n2} \cos\frac{n\pi}{h}z + \frac{1}{4}\sum \left[(1-\nu)E_\lambda(z)'' - \nu\frac{\lambda^2}{h^2}E_\lambda(z)\right]d_{\lambda2} = 0 \quad (68)$$

and

$$\sum_{n=1}^{\infty} \frac{n\pi}{h}a_{n1} \sin\frac{n\pi}{h}z = \sum \frac{\lambda^2}{h^2}d_{\lambda1}E_\lambda(z)'. \quad (69)$$

Using the above relations, all stresses of this order can be shown to vanish identically.

Asymptotic solution of order $r^{-(1/2)}$

Boundary conditions in (59–61) require

$$-\left\{\tfrac{15}{2}B_3 k(z) - \frac{3}{2}\sum a_{n3} \cos\frac{n\pi}{h}z - \frac{3}{4}\sum \left[(1-\nu)E_\lambda(z)'' - \nu\frac{\lambda^2}{h^2}E_\lambda(z)\right]d_{\lambda3}\right\}$$

$$= -\left\{\frac{1}{4}\sum \frac{n^2\pi^2}{h^2}a_{n1} \cos\frac{n\pi}{h}z - \frac{1}{8}\sum \frac{\lambda^2}{h^2}\left[(1-\nu)E_\lambda(z)'' - \nu\frac{\lambda^2}{h^2}E_\lambda(z)\right]d_{\lambda1}\right\}, \quad (70)$$

$$\sum_{n=1}^{\infty} a_{n2}\frac{n\pi}{h} \sin\frac{n\pi}{h}z + \sum \frac{\lambda^2}{h^2}d_{\lambda2}E_\lambda(z)' = 0. \quad (71)$$

The amplitudes of stresses of order $r^{-(1/2)}$ are, after applying (70) and (71) in conjunction with (69)

$$\sigma_{rr}^{(-(1/2))} = \frac{1}{4}\left\{B_1 + \frac{1}{2}\sum_\lambda \frac{\lambda^2}{h^2}\left[\nu\frac{\lambda^2}{h^2}E_\lambda(z) + (1+\nu)E_\lambda(z)''\right]d_{\lambda1}\right\}$$

$$\left(5\cos\tfrac{1}{2}\theta - \cos\tfrac{1}{2}3\theta\right), \quad (72)$$

$$\sigma_{\theta\theta}^{(-(1/2))} = \frac{1}{4}\left\{B_1 + \frac{1}{2}\sum_\lambda \frac{\lambda^2}{h^2}\left[\nu\frac{\lambda^2}{h^2}E_\lambda(z) + (1+\nu)E_\lambda(z)''\right]d_{\lambda1}\right\}$$

$$\left(3\cos\tfrac{1}{2}\theta + \cos\tfrac{1}{2}3\theta\right), \quad (73)$$

$$\sigma_{r\theta}^{(-(1/2))} = \frac{1}{4} \left\{ B_1 + \frac{1}{2} \sum_{\lambda} \frac{\lambda^2}{h^2} \left[\nu \frac{\lambda^2}{h^2} E_\lambda(z) + (1+\nu) E_\lambda(z)'' \right] d_{\lambda 1} \right\}$$

$$\left(\sin \frac{1}{2}\theta + \sin \frac{1}{2}3\theta \right),$$
(74)

$$\sigma_{rz}^{-(1/2)} = 0,$$
(75)

$$\sigma_{\theta z}^{(-(1/2))} = 0,$$
(76)

$$\sigma_{zz}^{(-(1/2))} = \left(\sum_{\lambda} \frac{\lambda^4}{h^4} E_\lambda(z) d_{\lambda 1} \right) \cos \frac{1}{2}\theta.$$
(77)

In the above formulas, $d_{\lambda 1}$ are restricted by (66) and (69). Integration of (69) gives

$$\sum_{n=1}^{\infty} a_{n1} \cos \frac{n\pi}{h} z = -\sum \frac{\lambda^2}{h^2} d_{\lambda 1} E_\lambda(z) - \sum \frac{4\lambda}{h^2} d_{\lambda 1}.$$
(78)

The last term in the equation above comes from the integration constant which is determined by using (15). Substituting (78) into (66) gives the sole condition for $d_{\lambda 1}$ as

$$2B_1 k(z) = \sum_{\lambda} \left[(2-\nu) \frac{\lambda^2}{h^2} E_\lambda(z) + (1-\nu) E_\lambda(z)'' + \frac{8\lambda}{h^2} \right] d_{\lambda 1}.$$
(79)

The lowest order nonzero displacements that correspond to the $r^{-(1/2)}$ singular stresses given by (72)–(77) are listed in Appendix I.

4. Discussion of the singular stress field.

From the asymptotic analysis in the section above, it appears that the lowest order nonzero three-dimensional crack tip stresses of a plate are of inverse square root singularity with the amplitudes given by (72–77).
Denote

$$K(z) = \left\{ 1 + \frac{1}{2B_1} \sum_{\lambda} \frac{\lambda^2}{h^2} \left[\nu \frac{\lambda^2}{h^2} E_\lambda(z) + (1+\nu) E_\lambda(z)'' \right] d_{\lambda 1} \right\} B_1$$
(80)

as the stress intensity factor. The singular stresses in (72–77) can then be expressed as

$$\sigma_{\alpha\beta} = K(z) \tilde{\sigma}_{\alpha\beta} r^{-(1/2)},$$

$$\sigma_{z\alpha} = 0 \qquad (\alpha, \beta = r, \theta),$$
(81)

$$\sigma_{zz} = \left(\sum_{\lambda} \frac{\lambda^4}{h^4} E_\lambda(z) d_{\lambda 1} \right) \cos \left(\frac{1}{2}\theta \right) r^{-(1/2)},$$

where $\tilde{\sigma}_{\alpha\beta}$ are the amplitudes of the classical plane strain singular stresses.

$$\tilde{\sigma}_{rr} = \tfrac{1}{4}(5 \cos \tfrac{1}{2}\theta - \cos \tfrac{1}{2}3\theta),$$

$$\tilde{\sigma}_{\theta\theta} = \tfrac{1}{4}(3 \cos \tfrac{1}{2}\theta + \cos \tfrac{1}{2}3\theta), \tag{82}$$

$$\tilde{\sigma}_{r\theta} = \tfrac{1}{4}(\sin \tfrac{1}{2}\theta + \sin \tfrac{1}{2}3\theta).$$

The in-plane components of the three-dimensional near tip singular stress field are thus expressed as singular plane strain stresses with the intensity factor $K(z)$ varying in the thickness direction. The natural question is whether the near tip deformation is a state of plane strain, i.e., $\varepsilon_{zz} = 0$.

As stated in Section 3, the constants $d_{\lambda 1}$ in (80) are restricted only by (79). Differentiating the two sides of (79) twice with respect to z gives

$$-\frac{2\nu}{1+\nu}B_1 = \sum_\lambda \left[(2-\nu)\frac{\lambda^2}{h^2}E_\lambda'' + (1-\nu)E_\lambda''''\right]d_{\lambda 1}. \tag{83}$$

However, it is easily established by the definition of E_λ in (48) that

$$E_\lambda'''' = -\frac{2\lambda^2}{h^2}E_\lambda'' - \frac{\lambda^4}{h^4}E_\lambda. \tag{84}$$

Substituting (84) into (83) gives another form of (79), i.e.

$$2\nu B_1 = (1-\nu^2)\sum_\lambda \frac{\lambda^4}{h^4}E_\lambda d_{\lambda 1} - \nu(1+\nu)\sum_\lambda \frac{\lambda^2}{h^2}E_\lambda'' d_{\lambda 1}. \tag{85}$$

With (85), it is now possible to show that the singular stresses in (72–77) represent the plane strain deformation. Substitution of results from (72–77) into the following expression

$$\varepsilon_{zz} = \frac{1+\nu}{E}\sigma_{zz} - \frac{\nu}{E}(\sigma_{rr} + \sigma_{\theta\theta} + \sigma_{zz}) \tag{86}$$

leads to

$$\varepsilon_{zz} = \frac{1}{E}\left[-2\nu B_1 + (1-\nu^2)\sum_\lambda \frac{\lambda^4}{h^4}E_\lambda d_{\lambda 1} - \nu(1+\nu)\sum_\lambda \frac{\lambda^2}{h^2}E_\lambda'' d_{\lambda 1}\right]\cos\tfrac{1}{2}\theta = 0, \tag{87}$$

as terms in the bracket are terms in (85).

The result that plane strain deformation prevails over the entire thickness of the plate near the crack tip is somewhat unexpected. One would anticipate a plane stress state close to the traction free plate surfaces, where $\sigma_{zz} = 0$ but not necessarily $\varepsilon_{zz} = 0$. To further investigate this paradox, we note that (85) reduces to

$$2B_1 = -(1+\nu)\sum_\lambda \frac{\lambda^2}{h^2}E_\lambda(\pm h)'' d_{\lambda 1}, \tag{88}$$

at $z = \pm h$ since $E_\lambda(\pm h) = 0$ by definition. It is easy to see from (80) that

$$K(\pm h) = 0. \tag{89}$$

Consequently, all the components of the singular stress field vanish identically on the free plate surfaces. Thus, on plate surfaces, the distinction between the plane stress and plane strain states vanishes.

The implication of the above finding is that the stress intensity factor $K(z)$ vanishes on the plate surfaces. In fact, the displacements (see Appendix I) associated with the singular stresses also vanish on the plate surfaces. These results are consistent with the finite element results obtained by Shivakumar and Raju [9] which indicate that the strain energy release rate seems to drop to zero when approaching the plate surfaces.

At this point, one may surmise whether there is a unique functional form for $K(z)$. Since $K(z)$ depends on $d_{\lambda 1}$ (see (80)), to answer the above question, we must find out whether the coefficients $d_{\lambda 1}$ can be determined unambiguously. Unfortunately, except for the trivial case when $\nu = 0$, $d_{\lambda 1}$ cannot be determined uniquely by the crack tip asymptotic analysis alone.

For the case $\nu = 0$, we have $k(z) = 0$ by (36), and (79) reduces to

$$\sum_\lambda \left[2 \frac{\lambda^2}{h^2} E_\lambda(z) + E_\lambda(z)'' + \frac{8\lambda}{h^2} \right] d_{\lambda 1} = 0 \Rightarrow d_{\lambda 1} = 0, \tag{90}$$

which leads to $K(z) = B_1$ and $\sigma_{zz} = 0$ in (80) and (81). The solution given by (81) for $\nu = 0$ is thus the conventional two-dimensional solution. This is the natural outcome since the in-plane deformation of the plate will no longer cause deformation in the z-direction for $\nu = 0$.

To prove the non-uniqueness of $d_{\lambda 1}$ for an arbitrary ν, we introduce the function

$$\overline{\varphi}(x, z) = \sum d_{\lambda 1} E_\lambda(z) e^{-(\lambda x/h)} \Rightarrow \overline{\varphi}|_{x=0} = \sum d_{\lambda 1} E_\lambda(z), \tag{91}$$

in which $\overline{\varphi}$ can be identified as the symmetric part of the so called Papkovich–Fadle expansion which has been well studied by Smith [10] and Gregory [11–12]. Gregory [12] proved that $\overline{\varphi}$ as defined by (91) is the general form of the solution of the biharmonic equation

$$\left(\frac{\partial^2}{\partial x^2} + \frac{\partial^2}{\partial z^2} \right) \left(\frac{\partial^2}{\partial x^2} + \frac{\partial^2}{\partial z^2} \right) \overline{\varphi} = 0 \tag{92}$$

with boundary conditions

$$\overline{\varphi}(x, \pm h) = \frac{\partial \overline{\varphi}}{\partial z} \bigg|_{z \pm h} = 0 \tag{93}$$

and

$$\frac{\partial^2 \overline{\varphi}}{\partial x^2} \bigg|_{x=0} = f(z), \quad z \in (-h, h), \tag{94}$$

$$\frac{\partial^2 \overline{\varphi}}{\partial z^2} \bigg|_{x=0} = g(z), \quad z \in (-h, h), \tag{95}$$

where f and g are symmetric functions of z and satisfy the so-called 'consistent condition', i.e.

$$f(\pm h) = \left.\frac{\partial^2 \overline{\varphi}}{\partial x^2}\right|_{x=0\,\&\,z=\pm h} = 0. \tag{96}$$

$$f'(\pm h) = \left.\frac{\partial^3 \overline{\varphi}}{\partial x^2 \partial z}\right|_{x=0\,\&\,z=\pm h} = 0. \tag{97}$$

$$\int_{-h}^{h} g\,dz = 0, \qquad \int_{-h}^{h} zg\,dz = 0. \tag{98}$$

With the above delineation, $d_{\lambda 1}$ in (79) is uniquely given by

$$d_{\lambda 1} = \frac{h^4 \tan^2 \lambda}{16\lambda^4} \int_{-h}^{h} \left[(f+g)E_\lambda(z)'' - f\frac{4\lambda}{h^2}\cos\lambda\cos\lambda z \right] dz. \tag{99}$$

Note that $d_{\lambda 1}$ is dependent on both f and g which are two arbitrary functions as long as they satis. the 'consistent condition'. From (91), (94) and (95), it is seen that f and g are related to $d_{\lambda 1}$ by

$$f(z) = \sum \frac{\lambda^2}{h^2} E_\lambda(z) d_{\lambda 1}, \tag{100}$$

$$g(z) = \sum E_\lambda(z)'' d_{\lambda 1}. \tag{101}$$

By using relations in (100) and (101), (79) becomes

$$2B_1 k(z) = (2-\nu)f + (1-\nu)g - \int_{-h}^{h} f\,dz. \tag{102}$$

Since two arbitrary functions f and g appear in (102) and f and g are both needed in determining $d_{\lambda 1}, d_{\lambda 1}$ is non-unique. Thus, the z-profile of the stress intensity factor cannot be uniquely defined based on the asymptotic solution alone. The three-dimensional solution satisfying complete boundary conditions (including remote boundary conditions) may be needed to determine the distribution of the stress intensity factor over the plate thickness for each individually posed problem.

5. Conclusions

A three-dimensional asymptotic analysis has been carried out for singular crack tip stresses of a plate with a through-the-thickness cut. For both mode I and mode II loading, stress singularity at the crack tip is of the $r^{-(1/2)}$ type, while the stress intensity factor is a function of the thickness-wise coordinate. On the plate surfaces, all singular stress and strain components vanish, thus satisfying both plane stress and plane strain conditions. The deformation associated with the singular stress field is plane strain. The profile of the stress intensity factor as a function of the thickness-wise coordinate cannot be determined by the asymptotic analysis alone.

Appendix I: Lowest order nonzero displacements for mode I

Corresponding to the stresses in (72–77), the displacements of mode I deformation are

$$u_r = \frac{1+\nu}{2E} \left\{ B_1 + \frac{1}{2} \sum \frac{\lambda^2}{h^2} \left[\nu \frac{\lambda^2}{h^2} E_\lambda(z) + (1+\nu) E_\lambda(z)'' \right] d_{\lambda 1} \right\}$$
$$\times [(5 - 8\nu) \cos \tfrac{1}{2}\theta - \cos \tfrac{1}{2}3\theta] r^{1/2} \tag{103}$$

$$u_\theta = \frac{1+\nu}{2E} \left\{ B_1 + \frac{1}{2} \sum \frac{\lambda^2}{h^2} \left[\nu \frac{\lambda^2}{h^2} E_\lambda(z) + (1+\nu) E_\lambda(z)'' \right] d_{\lambda 1} \right\}$$
$$\times [-(7 - 8\nu) \sin \tfrac{1}{2}\theta + \sin \tfrac{1}{2}3\theta] r^{1/2}. \tag{104}$$

$$u_z = \frac{1+\nu}{E} \left\{ \sum \frac{\lambda^2}{h^2} \left[\frac{7+\nu}{6} E_\lambda(z)''' - \tfrac{1}{6}(2-\nu) \frac{\lambda^2}{h^2} E_\lambda(z)' \right] d_{\lambda 1} \cos \tfrac{1}{2}3\theta \right.$$
$$\left. - \frac{1}{2} \sum \frac{\lambda^2}{h^2} \left[(1-\nu) E_\lambda(z)''' + (2-\nu) \frac{\lambda^2}{h^2} E_\lambda(z)' \right] d_{\lambda 1} \cos \tfrac{1}{2} \right\} r^{3/2}. \tag{105}$$

Appendix II: Mode II singular stresses

Mode II loading can be analyzed with the same procedure as for mode I loading. The lowest nonzero singular stresses are

$$\sigma_r = \frac{1}{4} \left\{ A_1 + \frac{1}{2} \sum \frac{\lambda^2}{h^2} \left[\nu \frac{\lambda^2}{h^2} E_\lambda(z) + (1+\nu) E_\lambda(z)'' \right] c_\lambda^1 \right\}$$
$$\times (5 \sin \tfrac{1}{2}\theta - 3 \sin \tfrac{1}{2}3\theta) r^{-(1/2)}, \tag{106}$$

$$\sigma_\theta = \frac{1}{4} \left\{ A_1 + \frac{1}{2} \sum \frac{\lambda^2}{h^2} \left[\nu \frac{\lambda^2}{h^2} E_\lambda(z) + (1+\nu) E_\lambda(z)'' \right] c_\lambda^1 \right\}$$
$$\times (3 \sin \tfrac{1}{2}\theta + 3 \sin \tfrac{1}{2}3\theta) r^{-(1/2)}, \tag{107}$$

$$\sigma_{r\theta} = -\frac{1}{4} \left\{ A_1 + \frac{1}{2} \sum \frac{\lambda^2}{h^2} \left[\nu \frac{\lambda^2}{h^2} E_\lambda(z) + (1+\nu) E_\lambda(z)'' \right] c_\lambda^1 \right\}$$
$$\times (\cos \tfrac{1}{2}\theta + 3 \cos \tfrac{1}{2}3\theta) r^{-(1/2)}, \tag{108}$$

$$\sigma_{rz} = 0, \tag{109}$$

$$\sigma_{\theta z} = 0, \tag{110}$$

$$\sigma_z = \left(\sum \frac{\lambda^4}{h^4} E_\lambda c_\lambda^1 \right) \sin \tfrac{1}{2}\theta r^{-(1/2)}.$$

(111)

where c_λ^1 satisfies the condition

$$2A_1 k(z) = \sum \left[(2 - \nu)\frac{\lambda^2}{h^2} E_\lambda(z) + (1 - \nu) E_\lambda(z)'' + \frac{8\lambda}{h^2} \right] c_\lambda^1.$$

(112)

Acknowledgment

References

1. M.L. Williams. *Fracture Mechanics: 22nd Symposium, ASTM STP 1131*, H.A. Ernst et al. (eds.), Philadelphia (1992) 5–33.
2. G.C. Sih. *International Journal of Fracture Mechanics* 7 (1971) 39–61.
3. J.P. Benthem. *International Journal of Solids and Structures* 13 (1977) 479–492.
4. T. Kawai, Y. Fujitani and K. Kumagai. *Proceedings of the International Conference on Fracture Mechanics and Technology*, Hong Kong (1977) 1157–1163.
5. G.B. Sinclair. *Proceedings of the 7th Canadian Congress of Applied Mechanics* 43 (1976) 479–481.
6. M.L. Williams. *Transactions of ASME, Journal of Applied Mechanics* 19 (1952) 526–528.
7. R.D. Gregory. *Journal of Elasticity* 28 (1992) 1–28.
8. S. Timoshenko and J.N. Goodier. *Theory of Elasticity*. McGraw-Hill, New York (1970).
9. K. N. Shivakumar and I.S. Raju. *Fracture Mechanics: 21st Symposium, ASTM STP 1074*, J.P. Gudas et al. (eds.), Philadelphia (1990) 470–489.
10. R.C.T. Smith. *Australian Journal of Scientific Research* A5(1952) 227–237.
11. R.D. Gregory. *Journal of Elasticity* 9 (1979) 283–309.
12. Ibid. 14 (1984) 27–64.